Hybrid Photomechanical Analyses of Finite Isotropic and Orthotropic Composite Structures Containing Various Geometric Discontinuities

by

Narin Sara Fatima

A dissertation submitted in partial fulfillment of

the requirements for the degree of

Doctor of Philosophy

(Mechanical Engineering)

at the

University of Wisconsin – Madison

2019

Date of final oral examination: 01/18/2019

The dissertation is approved by the following members of the Final Oral Committee:

Robert Rowlands, Emeritus, Mechanical Engineering (Co-adviser)

Tim Osswald, Professor, Mechanical Engineering (Adviser)

Robert Witt, Associate Professor, Engineering Mechanics and Astronautics

Douglass Henderson, Professor, Engineering Mechanics and Astronautics

Lih-Sheng Turng, Professor, Mechanical Engineering

Hybrid Photomechanical Analyses of Finite Isotropic and Orthotropic Composite Structures Containing Various Geometric Discontinuities

Narin Sara Fatima

Under the Supervision of Professor Robert Rowlands and Professor Tim Osswald

At University of Wisconsin – Madison

Abstract

Perforated finite structures are prevalent in engineering and their mechanical integrity is often controlled by the stresses near geometric discontinuities. Theoretical stress analyses are virtually impossible and numerical analyses can be challenging for finite structures containing discontinuities. Theoretical and numerical analyses both necessitate knowing the loading, but such information is typically unavailable in practice. This thesis therefore presents an effective experimental-analytical-numerical hybrid-method to determine the stresses/strains/displacements reliably at and near geometric discontinuities in loaded, finite orthotropic or isotropic members. The technique processes measured information with a combination of Airy stress functions, conformal mapping, analytic continuation and least squares. Knowing the external loading is unnecessary. Since one often does not know a priori where the most serious stresses will occur in such structures, full-field analyses are required. Measured information at or near discontinuities is also typically unreliable. In addition to overcoming the latter difficulty, hybridizing experimentally measured data with the indicated analytical and numerical tools satisfies equilibrium, compatibility

and local traction-free boundary conditions. The approach is applied to round and elliptical holes and cracks in finite orthotropic composite plates as well as to perforated or notched isotropic members. In the latter cases, the structurally critical locations are far from any reliable measured input data.

The technique provides reliable stresses and/or displacements throughout the structure, including along the edge of geometric discontinuities, from only a single component of measured information. Measured thermal or displacement data are employed. Stress intensity factors are available by post-processing the hybrid-determined stresses or displacements with fracture mechanics concepts. An advantage of the displacement-based approach is that it does not involve physically differentiating the measured data to obtain strains/stresses. Rather the method is established on strong mechanics-based algorithms. Results by the hybrid-method are validated using FEA, force equilibrium, strain-gages and other published information.

The present hybrid-method can analyze extremely finite plates of any material properties containing virtually any types/sizes of holes or cracks. Ability to obtain reliable results at important locations but which are located very far from reliable measured input is a desirable feature of the current hybrid technique. The displacement-based approach is particularly well-suited to non-laboratory-type environments.

Acknowledgements

First and Foremost, all praise goes to The Almighty Allah.

The two most valuable persons that have been beside me throughout this journey is my husband Aminul Islam and my son Nadith Amin. This dissertation was only possible because of their patience, support and kindness. I would like to thank my son Nadith Amin and my daughter Navera Amin for being such wonderful children. Their level of patience at times were higher than mine. This dissertation is dedicated to my husband, my son and my daughter.

I am blessed to have the privilege to work under the guidance of Professor Robert E. Rowlands. His continuous support, technical and insightful guidance and immense engagement was a contributing factor in the successful completion of this thesis. I am ever grateful to him for his motivation, encouragement and his valuable time that he dedicated toward me.

I would like to thank my father Dr. Md. Jahirul Islam. Growing up as a child of a PhD graduate student and seeing my father work as a research scientist motivated me since childhood to pursue higher education. I would like to thank my mother Jesmin Islam and sister Sharin Sara Fatima for their continuous support and contribution. Last but not the least I would like to thank all my family members, friends, colleagues at UW and the Mechanical Engineering department. The journey would have not been the same without your presence and support.

Table of Contents

List of Figures

List of Tables

List of Symbols

a	Half central or full edge crack length; length of triangular/oval/square cutout side
a, b, a', b'	Ellipse major and minor radii
a/b	Elliptical hole opening ratio
a/W, $2a/W$, D/W	Plate finite-width ratio
a_{ij}, $a_{i'j'}$	Elastic compliances
a_j, b_j	Real Airy coefficients
A_j, B_j, C_j, D_j, E_j	Complex quantities
a_n, b_n, c_n, d_n, A_0, B_0, C_0, D_0, A_1, B_1, a'_n, b'_n, c'_n, d'_n, A'_1, B'_1	Airy stress real coefficients
$[A]$	Airy matrix
B, C	Complex material quantities
c	Correlation coefficient
C	Condition number
C_0, D_1, D_2	Constants related to rigid body motions

$\{c\}$	Vector of Airy coefficients
c_j	Complex Airy coefficients
$\bar{c}_j$	Complex conjugate of c_j
c_k^*	Mapping coefficients
c_p	Specific heat at constant pressure
d	Recorded displacements
d_{int}	Integration path dimension
ds	Arc length along integration path
d'	Reconstructed displacements
D, D_i, D_0	Hole diameter
D, D', D_1, D_2	Domains
D_c	Characteristic size of a structure with crack
D_j	Differential operator
E, E_{xx}, E_{yy}, E_{11}, E_{22}	Elastic moduli
E_{11}/E_{22}	Degree of material anisotropy
F, F_1, F_2	Airy stress functions

$f, f^{-1}, f(z), f_1(z), f_2(z)$	Analytic functions
F^*	Applied load
F_c^*	Computed load
$f(x)$, $g(y)$	Functions of rigid body motion
g_{0M}, g_{1M}, g_M, g_{0N}, g_{1N}, g_N	Terms of a finite series
G, G_{xy}	Shear moduli
G, G_{I}, G_{II}	Energy release rates
$H(a/W)$, $H(\alpha_c)$	Geometric correction factor
h, h_1, h_2, h_3	Number of imposed conditions
Im	Imaginary part
I_1, I_2	Pixel intensities
J	Integral
j, k, m, n	Integers
k	Number of Airy coefficients
K	TSA calibration coefficient
K_T	Stress concentration factor

K_T^{∞}	Stress concentration factor for infinite geometry
K_{I}, K_{II}	Stress intensity factors
L	Length
L_1, L_2, L_3, L_4	Complex material coefficients
M, N	Termination indices of summation series
m, n	Tangential direction-based terms
M_f	Magnification factor
M_j, N_j	Real stress coefficients
M_{1j}, M_{2j}	Complex material coefficients
n_{DIC}, n_{TSA}, n_{FEA}	Number of experimental/predicted input data values
n_s	Number of sides of polygon
n_t, n_{total}	Total number of input values
n_x, n_y	Normal direction components
p_j, q_j	Complex material quantities

q	Constant related to radius of curvature of parabolic notch
Q	Center of hole from nearest vertical outer edge
r, θ	Polar coordinates
R, R_i, R_0	Hole radii
R_c	Hole size coefficients
R_z, R'_z	Regions in the physical z-plane
R_ζ, R'_ζ	Regions in mapped ζ-plane
Re	Real part
S, S_{new}	Load-induced TSA isopachic stress data
S_{ij}	Elastic stiffness
S_1, S_2, R^*	Rigid body motions
S^*	Recorded load-induced thermal data
$S^{*'}$	Reconstructed load-induced thermal data
$\boldsymbol{T}$	Traction vector
t	Thickness

T_k	Coefficient related to number of sides of a polygon
$\boldsymbol{u}$	Displacement vector
u, v	Cartesian displacement components
U	Uncalibrated TSA signal
u_r, u_θ	Polar displacement components
u_0, v_0, w	Rigid body motion components
$u_{1'}$, $u_{2'}$	Local crack displacement components
W	Width
W_s	Strain energy density
x, y	Rectangular coordinates in physical plane or local crack coordinates
X, Y	Global rectangular coordinates in physical plane
x_c, y_c	Rectangular coordinates of discontinuity center
X_n, Y_n	External forces
$x_{1'}$, $x_{2'}$, x', y'	Crack/inclined cutout's local coordinate system

$Y(\rho)$	Material orthotropy correction factor
z_j, z_k	Complex variables
z_c	Location of center of cracks/holes
Z_k, Y_k	Complex functions
$\bar{Z}_k, \bar{Y}_k$	Complex functions from integrating Z_k, Y_k
z_0	Arbitrary point in the z-plane
α	Angle
α_c	Crack size to structure's characteristic size, D_c, ratio
α, α_j, γ	Distinct real part of complex material properties, μ_j
α_T, α_{T1}, α_{T2}	Coefficients of thermal expansion
α^*_1, β^*_1	Elastic material coefficients
β, β_j, δ	Distinct imaginary part of complex material properties, μ_j
γ_j	Stress coefficients
γ_{2N}	Number of stress coefficients

Γ	Contour of integration path
Γ_z, Γ'_z	Traction-free boundary in physical z-plane
Γ_ζ, Γ'_ζ	Traction-free boundary in mapped ζ-plane
ε	Strain
ε_{xx}, ε_{yy}, ε_{xy}, γ_{xy}	Cartesian strain components
$\varepsilon_{1'1'}$, $\varepsilon_{2'2'}$, $\gamma_{1'2'}$	Crack local strain components
ε'_{xx}, ε'_{yy}, γ'_{xy}	Lagrangian strain components
ζ	Complex plane
ζ_0	Arbitrary constant along the real axis in ζ-plane
ζ_j	Complex variables
κ	Location along plate's horizontal center-line with respect to major ellipse radius, a
λ, ρ	Dimensionless coefficients from elastic compliances
λ_T	Elliptical hole sharpness or rectangular hole side ratio
μ_j	Complex material properties

ν_{xy}, ν_{12}, ν_{21}	Poisson's ratio
ξ, η	Complex coordinates in mapped plane
π_1, π_2, π_3, π_4	Transformation coefficients
ρ_n	Radius of curvature of a parabolic notch
ρ_m	Mass density
σ_N	Nominal stress with respect to structural characteristic size
σ_{net}	Nominal stress with respect to net area
σ_{xx}, σ_{yy}, σ_{xy}	Cartesian stress components
σ_{rr}, $\sigma_{\theta\theta}$, $\sigma_{r\theta}$	Polar stress components
σ_0	Far-field stress
σ_{I}, σ_{II}, σ_{III}	Principal stresses
$\sigma_{1'1'}$, $\sigma_{2'2'}$, $\sigma_{1'2'}$, $\sigma_{2'1'}$	Local crack stress components
Φ, Ψ	Airy stress functions
Φ', Ψ'	Differentiation of Airy stress functions
ω_j	Mapping function

ω'_j	Differentiation of the Mapping function

Acronyms

AOI	Area of interest
BEM	Boundary element method
CASI	Computer aided speckle interferometry
CC	Central crack
CCD	Charge-coupled device
CNC	Computer numerical control
CTE	Crack-tip element
DEC	Double-edge cracks
DIC	Digital image correlation
DSCM	Digital speckle correlation method
DSPI	Digital speckle pattern interferometry
DT	Delta Therm
EDM	Electrical discharge machining

ESP	Electronic speckle photography
ESPI	Electronic speckle pattern interferometry
FD	Finite difference
FEA	Finite element analysis
FEM	Finite element method
FWCF	Finite width correction factor
LEFM	Linear elastic fracture mechanics
NFC	Natural fiber composite
PSA	Photoelastic stress analysis
QPE	Quarter-point element
RMS	Root mean square
SCF	Stress concentration factor
SIF	Stress intensity factor
SEC	Single-edge crack
SPATE	Stress pattern analysis by thermal emission
TSA	Thermoelastic stress analysis

XFEM	Extended finite element method
ZFEM	Complex-variable finite element method
2-/3D	Two or three dimensional, respectively

Chapter 1. Introduction

1.1. Background

The structural reliability of engineering members tends to be highly influenced by their stresses. This thesis emphasizes the ability to stress analyze components fabricated of isotropic homogeneous or orthotropic composite materials by hybridizing experimental, analytical and numerical tools.

Advanced composite structures are popular in a wide variety of engineering applications because of their high performance, low-weight, strength and designable properties. High strength-to-weight ratios of composites makes them an attractive choice in designing moving structures due to the high performance-to-energy requirements. Safety-critical structures such as aerospace, automotive or marine structures, windmill blades and highway-bridge retrofits require designs that assure structural integrity for twenty years or more. Composite materials can be suitable for such structures as it is possible to manufacture composites with the desired properties. Desired constitutive composite properties can be achieved by using different fiber-matrix combinations, changing the fiber-to-matrix proportions, lamina orientations and stacking sequence [1]. High stiffness/strength, low maintenance, low thermal conductivity and fire-resistance properties are additional advantages composites can offer over other conventional monolithic materials.

Real world structures and machine components frequently contain various cutouts due to their design requirements, access holes for assembling and/or feed-through cutouts for cables, wires and/or pipelines. Moreover, due to the manufacturing, handling and assembling processes, small cracks or voids can develop over time in a structure under normal operating conditions. The

presence of any discontinuities may significantly degrade structural strength and/or stiffness or give rise to locations of high stress concentration. Detailed knowledge on the behavior of loaded structures is necessary to ensure structural integrity. This requires stress analysis, especially near or at the edges of the discontinuities to guarantee safe operation. Of the common three ways of stress analyzing structures; theoretical, numerical and experimental methods only the latter is capable of doing so when the external loads are not known. This is typically the situation in practice. Stress/failure analysis in composites is much more complex than those in classical (isotropic, homogenous) materials.

Theoretical stress analyses are based on fundamental principles of equilibrium and compatibility. They require knowing accurately the loading and boundary conditions and tend to be restricted to simple infinite geometries with simple loading. Anisotropy complicates analytical approaches to composites. Finite composite structures with complicated loading and geometry makes theoretical stress analyses virtually impossible. A numerical technique such as finite element analysis (FEA) is an attractive way to analyze such complicated structures. FEA simulates a physical phenomenon of a known geometry under the given loading and boundary conditions. It is effective for stress analyzing structures, reduces the need for physical prototypes and experiments, and improves productivity by allowing product optimization in their design phase. However, like analytical analysis, FEA requires knowing the geometry, material properties and the applied loading. Difficulty in providing accurate boundary and loading conditions greatly compromises the accuracy of the FEA results. On the other hand, experimental techniques are capable of analyzing structures which cannot be analyzed analytically or numerically. However, purely experimental techniques tend to be incapable of providing accurate information near or along the edge of structural discontinuities. The edges of structural discontinuities typically contain

the most critical stresses. Fatigue analyses in composites are sometimes based on residual stresses which can necessitate experimental analyses [2]. The inability of purely experimental methods to capture the high stresses/strains near geometric discontinuities can therefore miss the most serious stresses and consequently over-estimate structural integrity.

The virtual inability to stress analyze finite structures theoretically or numerically when the applied loads are unknown motivates developing experimental-based approaches for such situations. The present research focuses on hybridizing experimental techniques with analytical and numerical tools to develop effective ways to full-field stress analyze perforated finite structures made of homogenous isotropic or composite materials. Because of their prevalence and structural consequences, cases involving cutouts are emphasized. Such hybrid techniques can overcome the difficulties associated with each of these techniques when used individually to analyze complicated situations.

1.2. Research Objective

A main objective of this study is to develop simple, non-destructive, non-contacting means of conducting full-field stress analyses of loaded, finite composite structures containing discontinuities based on mechanics-based principles. This is accomplished by employing only a single component of measured information and without requiring knowledge of the external loading. The general method is able to analyze structures having a variety of holes, notches or cracks and can be simplified to be applicable to isotropic materials.

1.3. Hybrid Stress Analysis Method

The word ***hybrid stress analysis*** is used in this research to define an approach combining experimental-analytical-numerical techniques to stress analyze loaded, finite, mostly orthotropic composite structures. Measured information is processed using an Airy stress function in conjunction with concepts such as conformal mapping, analytic continuation, least squares and power-series expansion. Equilibrium, compatibility and traction-free conditions are satisfied analytically. Advantages of the hybrid stress analysis approach include the following: (1) not requiring knowing the external boundary conditions or loading; (2) processing, filtering and extrapolating measured data using mechanics-based principles instead of using arbitrary techniques; (3) not depending on measured information close to the traction-free boundaries (where most purely experimental techniques are unreliable); (4) analytically incorporating essential features of a loaded structure such as compatibility, equilibrium and traction-free boundary conditions in the analysis; (5) simultaneous smoothing and inherent stress separation capabilities and (6) not requiring differentiation of measured quantities. When analyzing members made of isotropic materials, with thermoelastic data the hybrid stress analysis does not require knowing the structure's material properties. The developed technique enjoys the unique feature of being able to provide reliable full-field states of stress and displacement information of a loaded structure with paucity of or absent experimental input data at structurally important locations either due to the configuration of the structure or experimental factors. Most purely experimental techniques fail to reliably stress analyze structures under such situations. The hybrid-method uses a combination of complex variables Airy stress functions, conformal mapping, analytic continuation, power-series expansion and measured information, and without requiring knowledge of the external boundary or loading conditions, to evaluate full-field stresses of finite, orthotropic

members containing discontinuities. Quantitative experimental techniques such as digital image correlation (DIC) and thermoelastic stress analysis (TSA) are used to obtain the measured data. All mathematical calculations and plots are generated using commercial numerical software MATLAB. Results are validated using FEA (ANSYS APDL) and/or commercial strain-gages.

A big advantage of the hybrid-method is its ability to handle virtually any shaped finite structure whose external loading is unknown. This is unlike purely numerical or theoretical approaches. Example includes boundary collocation where accuracy heavily depends on knowing all the exact boundary conditions [3]. Using an appropriate mapping function, the presented method is able to stress analyze orthotropic/isotropic structures having virtually any type of discontinuities such as circular, elliptical, triangular, square, polygonal openings and cracks which are anywhere located at any orientation. An additional excellent feature of this method is to provide reliable results when a paucity of experimentally measured information prevails at locations critical to ensure the structural integrity.

1.4. Analytical Approach

1.4.1. Airy Stress Function [4]

For a two-dimensional member in the absence of body forces, the Airy stress function is a continuous function which satisfies equilibrium and compatibility. The Airy stress function was first proposed in 1862 by Royal George Biddel Airy at the Royal Society of London. He provided solutions to a 2D finite rectangular beam under flexure using his proposed theorem. Airy's proposed paper was reviewed by Clerk Maxwell. Maxwell noticed a few deficiencies in the proposed theory and provided a more general function that satisfy the structural equilibrium based

on the theory of elasticity. It was Maxwell who first satisfied the stress equilibrium in a 2D member by introducing a stress function. Maxwell proposed to name the method as 'Airy's Function of Stress'. The theorem is commonly known as the Airy stress function or the Maxwell's approach. Over time the theory has been accepted and its application extended by many researchers. The initial theory was extended to find the solution of Maxwell's bi-harmonic equations in polar and rectangular coordinates, to determine *u* and *v* displacements, to analyze structures with regular or arbitrary shaped cutouts and also extended to the theory of anisotropic elasticity. Some of the important contributions toward developing the concept of Airy stress function will be discussed. John H. Michell was the first to provide the solution of the bi-harmonic equation in the polar coordinates. Mikhail Filonenko-Borodich showed how selecting the coordinate origin at locations other than the center of a hole can lead to multi-valued stresses. Emile Leonard Mathieu was the first to provide full mathematical properties of the bi-harmonic equation. Edouard Goursat proposed an arbitrary bi-harmonic function represented by two analytic functions to apply the concept to anisotropic media. Nikoloz Muskhelishvili also provided a similar theory as that of Goursat. Gury Kolosov introduced the concept of complex variables Airy stress functions to 2D elastic problems. Later Muskhelishvili considerably extended the theory by introducing the concept of Cauchy-integral and conformal mapping [4]. Using a compliance-based formalism, the fundamental solutions of 2D anisotropic elastic bodies were first provided by Sergei Gheorgievich Lekhnitskii [5].

Detailed mathematical principles of the Airy stress function relevant to the presently proposed hybrid stress analysis technique are provided in Chapter 2.

1.4.2. Conformal Mapping

Conformal mapping employs a function that transforms a certain geometry from one coordinate system to different geometry in a different coordinate system while preserving angles of the object in between the two different coordinate systems. The word 'conformal' refers to 'same form' or 'shape'. In some cases, conformal mapping preserves both angles and geometric shape but not necessarily the size.

Around the 1500s conformal mapping was introduced in stereographic projection. Robust improvement and use of conformal mapping started during the nineteenth century by mathematicians like Carl Friedrich Gauss, Leonhard Euler and Bernhard Riemann. Conformal mapping was first introduced in the field of theory of elasticity by Kolosov and Muskhelishvili in the early 1900s. Since then conformal mapping has been successfully used in structural analyses involving holes of regular/arbitrary shapes and cracks. Its application has been extended to anisotropic materials [3,5–9].

Conformal mapping is employed in structural analysis, fluid flow, heat transfer (both steady and transient), vibrations, acoustics, buckling analyses, electromagnetics, computer graphics, computer aided designs and in medical fields [10].

If a geometry in the complex $z = x + iy$ plane is transformed to another complex plane $\zeta = \xi + i\eta$, then this transformation can be achieved using a complex mapping function of the complex variable $\omega = f(z)$. The latter is known as the conformal mapping function. The function 'ω' is analytic and during the mapping preserves magnitude and direction of angles between intersecting arcs. Laplace's equation ($\nabla^2 f = 0$) is satisfied in both the original and mapped coordinates. The solution governing Laplace's partial differential equation remains invariant if a complicated

geometry from the original plane is transformed to a simpler or more convenient geometry in a mapped plane. The transformation is one-to-one and reversible. The conformal mapping function $\omega = f(z)$ defines the forward transformation and $z = f^{-1}(\omega)$ the inverse [10].

For a function to be considered as conformal, some mathematical properties need to be fulfilled. The mapping function should be analytic, i.e., single-valued and differentiable in the defined domain. Angles should be preserved during the transformation. The singe-valued property ensures the one-to-one mapping and the differentiability over the entire region (holomorphic function) is required to preserve the angles during the transformation. A holomorphic function, f, that maps a domain D into a domain D' is called conformal if an inverse, f^{-1}, of the holomorphic function exists mapping back domain D' into domain D and its derivatives are non-zero everywhere on the domain. If the function is anti-holomorphic (conjugate to holomorphic function) it still preserves angles but reverses their orientation. In addition, the property of differentiability ensures continuity. An easy way to check the analyticity of a function is whether it is expandable by a finite series. If a function can be expanded by the Taylor or Laurent series then it satisfies analyticity [10,11].

The conformal mapping of any two simply-connected regions exists if the Riemann mapping theorem is satisfied. The derivative of $f(z)$ exists at point z if and only if the partial derivative of ξ and η exists and satisfies the following Cauchy-Riemann relationship [12]

$$\frac{\partial \xi}{\partial x} = \frac{\partial \eta}{\partial y} \quad \text{and} \quad \frac{\partial \xi}{\partial y} = -\frac{\partial \eta}{\partial x} \tag{1-1}$$

Mapping functions relevant to and used in the proposed hybrid stress analysis technique of this research are provided in Chapter 2.

1.4.3. Analytic Continuation

An important mathematical concept that is used in conjunction with conformal mapping is analytic continuation. If function $f_1(z)$ is defined in domain D_1 and $f_2(z)$ in domain D_2, and if D_1 and D_2 have a subregion for which $f_1(z) = f_2(z)$, then $f_2(z)$ is considered as the analytic continuation of $f_1(z)$. Analytic continuation is closely linked to Taylor and Laurent series and plays a role in Schwarz reflection principle [10]. Analytic continuation is employed advantageously in this thesis to satisfy traction-free boundary conditions.

1.5. Measured Information

Various forms of measured data can be processed by the hybrid-method to stress analyze a structure. Examples include displacements (from DIC, moiré, interferometry), stress (from TSA, PSA) and strain (from strain-gage, extensometer) data. However, in this research full-field experimental techniques of DIC and TSA were used due to their relative simplicity regarding experimental requirements. Point-wise techniques such as strain-gages and extensometers can lack the required spatial resolution to reliably capture the high-fidelity behavior of composites. The maximum strain can occur spatially at a length scale smaller than the size of the finite gages [13]. Moiré requires the application of rulings and traditionally necessitates the use of both in-plane displacement information to full-field stress analyze loaded components. Interferometric

techniques require special light sources and vibration isolation. Moreover, its results can be highly sensitive to environmental factors.

DIC is used in this study to obtain experimental data in the form of in-plane displacements. It is one of the simplest non-contact, full-field experimental techniques in terms of experimental set-up and preparation. Images of an undeformed and deformed structure are captured and stored by the DIC system in digital form. Image analysis is performed based on correlating each image of the deformed pattern to the state of the undeformed pattern [14]. TSA is another full-field stress analysis technique. It records the thermoelastic effect, i.e., load-induced temperature changes of a cyclically loaded structure. Between DIC and TSA, DIC is probably more preferable due to not requiring cyclic loading and the additional testing needed to evaluate the thermoelastic coefficient. Not requiring cyclic loading of the structure renders DIC applicable for practical applications beyond a laboratory environment. While utilizing DIC-recorded displacement data with the current hybrid-method to conduct full-field structural analysis, unlike other displacement-based methods, does not require physically differentiating the displacement data to obtain strains and stresses. But like most experimental techniques, DIC also has its own perils. DIC data can be noisy due to the correlation process. Procedures such as use of filters to reduce noise can mask high strain gradients prevailing near the edge of a discontinuity. Spatial resolution, i.e., number of pixels near the discontinuity and correlation variables such as subset size and step size can affect the quality of DIC-measured displacements [13]. Some of these challenges are overcome by the present hybrid-method as it does not rely on the correlation algorithm of commercial DIC software packages to calculate strains from recorded displacement data. By considering measured data away from edges, the present hybrid-method also enhances DIC results, particularly relative to evaluating stress

concentrations. Using DIC-measured information renders the present method a practical quantitative tool in stress analyzing structures in their actual operating environment.

1.6. Summary

The present hybrid stress analysis method is a very effective technique for assessing the structural integrity of engineering structures. It overcomes the challenges associated with purely theoretical, numerical or experimental means of stress analyses, especially for orthotropic materials. The present hybrid concept overcomes the limitations that most traditional displacement-based experimental techniques face while evaluating strain from measured displacement information, i.e., their inability to provide displacements/strains/stresses at the boundary of the structural discontinuities where the most critical stresses typically exist. The method does not require the (frequently unreliable) measured information close to the edge of a discontinuity. By employing measured quantities away from the location of interest, the method can effectively provide accurate information throughout a structure and at those locations where reliable experimental data are unavailable. It has the capability to work in presence of unreliable or missing data at structurally critical locations. The method can effectively analyze structures containing virtually any types of holes or cracks. Stress analysis is based on rigorous mechanics-based algorithm rather than arbitrary schemes. Equilibrium, compatibility and traction-free boundary conditions are satisfied. Processing measured information using concepts of stress functions, conformal mapping and analytic continuation enable one to stress analyze finite structures. The method does not require knowing the external loading or boundary conditions. It does not involve differentiation of the measured data. Moreover, all these are achieved by just

utilizing a single component of measured information, i.e., one measured displacement field or one recorded temperature. The method can reliably stress analyze a finite structure under situations where most other purely experimental techniques fail due to inadequate material or structural information or where theoretical/numerical analyses are impossible due to structural and loading complexities.

Chapter 2. Analytical Analysis of Isotropic and Anisotropic Materials

2.1. Hybrid Stress Analysis Method

The present method demonstrates the analytical ability to stress analyze loaded, finite, orthotropic elastic engineering members by processing measured information. The in-plane displacements and stresses are evaluated full-field, including at the edge of the geometric discontinuities. Complex variables Airy stress functions are used to analytically represent the loaded structure. The process of combining measured data with the analytical representation of the Airy stress functions is referred to here as the 'hybrid stress analysis method'. The method satisfies equilibrium, strain compatibility and traction-free boundary conditions. The technique is valid for plane-stress and plane-strain problems assuming no body forces are present. It is applicable to both isotropic and anisotropic materials. For isotropy the Airy stress function is the solution of a bi-harmonic equation in terms of real variables whereas orthotropy involves complex variables. Using a measured single component of in-plane displacement is emphasized.

2.2. Orthotropic Material

Orthotropic materials with at least two planes of material symmetry requires nine elastic compliances in their constitutive matrices of the generalized Hooke's law of equation (2-1).

$$\begin{Bmatrix} \varepsilon_{11} \\ \varepsilon_{22} \\ \varepsilon_{33} \\ \varepsilon_{23} \\ \varepsilon_{13} \\ \varepsilon_{12} \end{Bmatrix} = \begin{bmatrix} a_{11} & a_{12} & a_{13} & 0 & 0 & 0 \\ a_{12} & a_{22} & a_{23} & 0 & 0 & 0 \\ a_{13} & a_{23} & a_{33} & 0 & 0 & 0 \\ 0 & 0 & 0 & a_{44} & 0 & 0 \\ 0 & 0 & 0 & 0 & a_{55} & 0 \\ 0 & 0 & 0 & 0 & 0 & a_{66} \end{bmatrix} \begin{Bmatrix} \sigma_{11} \\ \sigma_{22} \\ \sigma_{33} \\ \sigma_{23} \\ \sigma_{13} \\ \sigma_{12} \end{Bmatrix} \tag{2-1}$$

where a_{ij} are the elastic compliances and can be expressed in terms of the elastic engineering properties as

$$a_{ij} = \begin{cases} \frac{1}{E_{ij}} \text{ for } i = j \\ -\frac{\nu_{ij}}{E_{ii}} \text{ for } i \neq j \end{cases} \text{ for } i, j = 1, 2, 3 \text{ and } a_{ij} = \frac{1}{G_{ij}} \text{ for } i = j = 4, 5, 6 \tag{2-2}$$

2.3. Plane-Stress Orthotropy

For an orthotropic two-dimensional loaded member under plane-stress ($\sigma_{zz} = \sigma_{yz} = \sigma_{zx} = 0$), the stress-strain relationship of equation (2-1) is simplified such that

$$\varepsilon_{xx} = a_{11}\sigma_{xx} + a_{12}\sigma_{yy} + a_{16}\sigma_{xy} \tag{2-3}$$

$$\varepsilon_{yy} = a_{21}\sigma_{xx} + a_{22}\sigma_{yy} + a_{26}\sigma_{xy} \tag{2-4}$$

$$\gamma_{xy} = a_{16}\sigma_{xx} + a_{26}\sigma_{yy} + a_{66}\sigma_{xy} \tag{2-5}$$

2.4. Equilibrium and Compatibility

The fundamental equations for loaded elastic bodies are equilibrium and compatibility. To stress analyze a loaded engineering member analytically, stress equilibrium and strain compatibility must be fulfilled throughout the structure under the given boundary conditions. In absence of body forces, stress components in a body (isotropic or anisotropic) must satisfy the following equilibrium equations [5]

$$\frac{\partial \sigma_{xx}}{\partial x} + \frac{\partial \sigma_{xy}}{\partial y} = 0, \quad \frac{\partial \sigma_{yy}}{\partial y} + \frac{\partial \sigma_{xy}}{\partial x} = 0 \tag{2-6}$$

The strain-displacement relationships, experiencing small deformation are

$$\varepsilon_{xx} = \frac{\partial u}{\partial x}, \quad \varepsilon_{yy} = \frac{\partial v}{\partial y}, \quad \gamma_{xy} = 2\varepsilon_{xy} = \left(\frac{\partial u}{\partial y} + \frac{\partial v}{\partial x}\right) \tag{2-7}$$

Combining derivatives of *u* and *v* of equation (2-7) provides the following compatibility equation

$$\frac{\partial^2 \varepsilon_{xx}}{\partial y^2} + \frac{\partial^2 \varepsilon_{yy}}{\partial x^2} = 2\frac{\partial^2 \varepsilon_{xy}}{\partial x \partial y} = \frac{\partial^2 \gamma_{xy}}{\partial x \partial y} \tag{2-8}$$

Under plane-elasticity in the absence of body forces, stresses in either isotropic or anisotropic members must satisfy the equilibrium condition of equations (2-6) and the strains must satisfy the compatibility relationship of equation (2-8) [5,15].

Moreover, the surface equilibrium condition in terms of the external forces X_n and Y_n in the x and y directions, respectively, with respect to a unit area and directions normal, n, to the component's surface is

$$\begin{bmatrix} \sigma_{xx} & \sigma_{xy} \\ \sigma_{xy} & \sigma_{yy} \end{bmatrix} \begin{Bmatrix} \cos(n,x) \\ \cos(n,y) \end{Bmatrix} = \begin{Bmatrix} X_n \\ Y_n \end{Bmatrix} \tag{2-9}$$

2.5. Airy Stress Functions in Complex Variables

The stress equilibriums of loaded structures are the same irrespective whether the material responses are isotropic or anisotropic. Stress equilibrium is not analytically affected by the material's anisotropic behavior. Moreover, one can assume an Airy stress function, $F(x, y)$, in the x-y rectangular Cartesian coordinates and satisfy the equilibrium by representing the stresses σ_{xx}, σ_{yy} and σ_{xy} of the equilibrium equations (2-6) in terms of the Airy stress function as

$$\sigma_{xx} = \frac{\partial^2 F}{\partial y^2}, \quad \sigma_{yy} = \frac{\partial^2 F}{\partial x^2}, \quad \sigma_{xy} = -\frac{\partial^2 F}{\partial y \partial x} \tag{2-10}$$

Introducing the expressions of in-plane strains from the Hooke's law of equations (2-3) through (2-5) into the compatibility equation (2-8), and then expressing the stress components in terms of the Airy stress function, $F(x, y)$, according to equation (2-10), for orthotropic components the following compatibility equation is obtained

$$\frac{\partial^4 F}{\partial x^4} - \frac{2a_{26}}{a_{22}} \frac{\partial^4 F}{\partial x^3 \partial y} + \frac{(2a_{12} + a_{66})}{a_{22}} \frac{\partial^4 F}{\partial x^2 \partial y^2} - \frac{2a_{16}}{a_{22}} \frac{\partial^4 F}{\partial x \partial y^3} + \frac{a_{11}}{a_{22}} \frac{\partial^4 F}{\partial y^4} = 0 \quad (2\text{-}11)$$

This homogenous, partial differential equation (2-11) with constant coefficients, a_{ij}, is the compatibility equation for orthotropic components and must be satisfied by the stress functions. For orthotropic members, the solution of any elastic problem would only require solving this compatibility equation (2-11) based on the appropriate boundary conditions of equation (2-9). Thus, under classical theory of plane-elasticity, any problem can be reduced to just finding a stress function, $F(x, y)$, such that it satisfies equation (2-11) under the subjected boundary conditions. Equation (2-11) can be written symbolically with linear differential operators in the following form

$$D_1 D_2 D_3 D_4 F = 0 \quad (2\text{-}12)$$

For an orthotropic material the operators D_j for $j = 1, 2, 3, 4$ of equation (2-12) are defined as

$$D_j = \frac{\partial}{\partial y} - \mu_j \frac{\partial}{\partial x}, \quad j = 1, 2, 3, 4 \quad (2\text{-}13)$$

where μ_j are the complex material properties. For an orthotropic member relative to the principal axes of orthotropy, μ_j are the roots of the following characteristic equation (2-14) associated with the compatibility equation (2-11).

$$a_{11}\mu^4 - 2a_{16}\mu^3 + (2a_{12} + a_{66})\mu^2 - 2a_{26}\mu + a_{22} = 0 \quad (2\text{-}14)$$

In general, the complex roots take the following form, $\mu_1 = \alpha + i\beta$, $\mu_2 = \gamma + i\delta$, $\mu_3 = \bar{\mu}_1 = \alpha - i\beta$ and $\mu_4 = \bar{\mu}_2 = \gamma - i\delta$. Quantities α, β, γ and δ represent real numbers and both β and δ are positive. The complex roots, μ_j, can be either complex or purely imaginary but cannot be real numbers. They can be of the following three types: i) the roots are purely imaginary and unequal, $\mu_1 = i\beta$ and $\mu_2 = i\delta$, ii) purely imaginary and equal $\mu_1 = \mu_2 = i\beta$, and iii) distinct and complex $\mu_1 = \alpha \pm i\beta$ and $\mu_2 = -\alpha \pm i\beta$ or $\mu_2 = \gamma \pm i\delta$. For orthotropic materials loaded along the axes of material symmetry, i.e., directions 1 or 2, the roots are completely imaginary, $\mu_1 = i\beta$, $\mu_2 = i\delta$ ($\alpha = \gamma = 0$, $\beta > 0$, $\delta > 0$, $a_{16} = a_{26} = 0$). For isotropic materials the roots are as $\mu_1 = \mu_2 = i$ ($\alpha = \gamma = 0$ and $\beta = \delta = 1$).

In the absence of body forces under plane-stressed condition, the Airy stress function for orthotropic materials are expressed as the summation of two arbitrary analytic functions of the complex variables z_j for $j = 1, 2$, [5] as such

$$F = 2Re[F_1(z_1) + F_2(z_2)] \tag{2-15}$$

where $F_1(z_1)$ and $F_2(z_2)$ are analytic functions of the complex variables z_1 and z_2, respectively, and '*Re*' represents the real part of the complex quantities. The complex variables, z_j, for an orthotropic material are

$$z_j = x + \mu_j y, \qquad j = 1, 2 \tag{2-16}$$

When the orthotropic member is physically loaded along a principal axis of orthotropy, i.e., along direction 1 (typically the strong/stiff fiber direction) or 2 (transverse to strong/stiff fiber direction) the orthotropic characteristic equation (2-14) reduces to

$$a_{11}\mu^4 + (2a_{12} + a_{66})\mu^2 + a_{22} = 0 \quad (2\text{-}17)$$

For such a loaded orthotropic structure, i.e., loaded along one of the axes of material symmetry, the elastic compliances of the generalized Hooke's law, a_{ij}, reduce to

$$a_{11} = \frac{1}{E_{11}}, a_{12} = \frac{-\nu_{21}}{E_{22}}, a_{21} = -\frac{\nu_{12}}{E_{11}}, a_{22} = \frac{1}{E_{22}}, a_{66} = \frac{1}{G_{12}}, a_{16} = a_{26} = 0 \quad (2\text{-}18)$$

and

$$\frac{\nu_{21}}{E_{22}} = \frac{\nu_{12}}{E_{11}} \text{ and } a_{12} = a_{21} \quad (2\text{-}19)$$

Subscripts 1 and 2 represent directions parallel and perpendicular to the strong/stiff fiber direction of the laminate, respectively. Using the expressions of the elastic compliances from equation (2-18) into equation (2-17) the orthotropic characteristic equation consequently takes the following form

$$\mu^4 + \left(\frac{E_{xx}}{G_{xy}} - 2\upsilon_{xy}\right)\mu^2 + \left(\frac{E_{xx}}{E_{yy}}\right) = 0 \quad (2\text{-}20)$$

In equations (2-18) and (2-20), the material's strong/stiff 1-direction is considered along the *x*-axis of the loaded member.

The complex material properties, μ_j for j = 1, 2, can also be determined directly from the following closed-form equations [16,17] such that

$$\beta^* = \pm\sqrt{\frac{1}{2}\left(\frac{a_{66}+2a_{12}}{2a_{11}} + \sqrt{\frac{a_{22}}{a_{11}}}\right)} \tag{2-21}$$

$$\alpha^* = \pm\sqrt{\frac{1}{2}\left(\frac{a_{66}+2a_{12}}{2a_{11}} - \sqrt{\frac{a_{22}}{a_{11}}}\right)} \tag{2-22}$$

and expressing the complex variables z_j for $j = 1, 2$, as

$$z_1 = x + i(\beta^* + \alpha^*)y \quad \text{and} \quad z_2 = x + i(\beta^* - \alpha^*)y \tag{2-23}$$

where

$$\mu_1 = i(\beta^* + \alpha^*) \quad \text{and} \quad \mu_2 = i(\beta^* - \alpha^*) \tag{2-24}$$

Knowing the orthotropic constitutive properties, the complex roots μ_1 and μ_2 are known either from the characteristic equation (2-17) or from equation (2-24) combined with equations (2-21) and (2-22). The in-plane stresses and displacements in the rectangular x-y coordinates of the physical plane, $z = x + \mu_j y$ for $j = 1, 2$, are then expressed in terms of the complex variables Airy stress functions as [5]

$$\sigma_{xx} = 2Re[\mu_1^2\Phi'(z_1) + \mu_2^2\Psi'(z_2)] \tag{2-25}$$

$$\sigma_{yy} = 2Re[\Phi'(z_1) + \Psi'(z_2)] \tag{2-26}$$

$$\sigma_{xy} = -2Re[\mu_1\Phi'(z_1) + \mu_2\Psi'(z_2)] \tag{2-27}$$

$$u = 2Re[p_1\Phi(z_1) + p_2\Psi(z_2)] - w_0 y + u_0 \tag{2-28}$$

$$v = 2Re[q_1\Phi(z_1) + q_2\Psi(z_2)] + w_0 x + v_0 \tag{2-29}$$

where the Airy stress functions, $\Phi(z_1) = \frac{dF_1(z_1)}{dz_1}$ and $\Psi(z_2) = \frac{dF_2(z_2)}{dz_2}$, and the primes of these functions represent differentiation with respect to the complex variables z_j for j = 1, 2. These functions are also analytic in the complex z_j plane. The stresses of equations (2-25) through (2-27) satisfy equilibrium and the associated strains satisfy compatibility. The displacement component u is in the x-direction and v is in the y-direction. The constants u_0, v_0 and w_0 in equations (2-28) and (2-29) are from integrating the in-plane strains of equations (2-7) to obtain the in-plane displacements u and v. The constants u_0 and v_0 represent rigid body translations and w_0 represents rigid body rotation. When testing a member physically and holding it securely between the grips, the contribution from rigid body motion can be ignored, i.e., $u_0 = v_0 = w_0 = 0$. Quantities p_1, p_2, q_1 and q_2 present in the expressions for the in-plane displacements of equations (2-28) and (2-29) depend only on the orthotropic elastic material properties and are defined as

$$p_1 = a_{11}\mu_1^2 + a_{12} - a_{16}\mu_1 \qquad p_2 = a_{11}\mu_2^2 + a_{12} - a_{16}\mu_2$$
$$q_1 = a_{12}\mu_1 + \frac{a_{22}}{\mu_1} - a_{26} \qquad q_2 = a_{12}\mu_2 + \frac{a_{22}}{\mu_2} - a_{26} \tag{2-30}$$

When a member is physically loaded ($u_0 = v_0 = w_0 = 0$) in a direction of material orthotropy ($a_{16} = a_{26} = 0$), the displacement components of equations (2-28) and (2-29) and the variables p_j and q_j (for $j = 1, 2$) of equation (2-30) reduce to

$$u = 2Re[p_1\Phi(z_1) + p_2\Psi(z_2)] \tag{2-31}$$

$$v = 2Re[q_1\Phi(z_1) + q_2\Psi(z_2)] \tag{2-32}$$

and

$$p_1 = a_{11}\mu_1^2 + a_{12} \qquad p_2 = a_{11}\mu_2^2 + a_{12}$$
$$q_1 = a_{12}\mu_1 + \frac{a_{22}}{\mu_1} \qquad q_2 = a_{12}\mu_2 + \frac{a_{22}}{\mu_2} \tag{2-33}$$

For plane-stress conditions, the stress-strain relationship in an orthotropic structure is expressed as equation (2-34). Therefore, from the evaluated in-plane stresses and measured orthotropic constitutive properties the in-plane strains can readily be derived, i.e.,

$$\begin{Bmatrix}\varepsilon_{11}\\ \varepsilon_{22}\\ \gamma_{12}\end{Bmatrix} = \begin{bmatrix}a_{11} & a_{12} & 0\\ a_{21} & a_{22} & 0\\ 0 & 0 & a_{66}\end{bmatrix}\begin{Bmatrix}\sigma_{11}\\ \sigma_{22}\\ \sigma_{12}\end{Bmatrix} \tag{2-34}$$

It should be noted that the $[0_{13}/90_5/0_{13}]$ graphite-epoxy laminate used in this research has a balanced, symmetric construction. In addition to the displacements and strains being uniform through the thickness, and while 26 plies have their fibers in the loading direction and five plies have their fibers transverse to the direction of loading, the elastic laminate properties are based on the average through-the-thickness stresses. The stresses of equations (2-25) through (2-27) similarly represents through-the-thicknesses average stresses. The actual stresses in the 90° layers are different from those in the 0° layers, and both may be different from the averaged stresses.

The concept of the complex variables Airy stress functions can be simplified to be applicable to isotropic materials. For an isotropic material with elastic modulus, E, Poisson's ratio, ν, and shear modulus, G, the elastic material properties are related as such, $E_{11} \approx E_{22} = E$, $\nu_{12} = \nu_{21} = \nu$ and $G = E/2(1 + \nu)$. Thus, for isotropy the elastic compliances of equation (2-18) take the following form

$$a_{11} = a_{22} = \frac{1}{E}, \qquad a_{12} = a_{21} = -\frac{\nu}{E}, \qquad a_{66} = \frac{1}{G} \text{ and } a_{16} = a_{26} = 0 \tag{2-35}$$

Equation (2-12) then simplifies to the following bi-harmonic expression

$$\nabla^4 F = \nabla^4 \Phi = 0 \tag{2-36}$$

where in the Cartesian x-y coordinates

$$\nabla^4 = \frac{\partial^4}{\partial x^4} + 2\frac{\partial^4}{\partial x^2 \partial y^2} + \frac{\partial^4}{\partial y^4} \tag{2-37}$$

Using the expressions of the isotropic elastic compliances from equation (2-35) into the characteristic equation (2-17), the complex material properties for isotropy become $\mu_1 = \mu_2 = i$ and the complex variable as $z = x + iy$.

2.6. Conformal Mapping

The concept of Airy stress functions can be used to solve two-dimensional problems analytically if under the subjected boundary conditions, the stress functions $\Phi(z_1)$ and $\Psi(z_2)$ are selected such that the stresses associated with these stress functions satisfy equilibrium, associated strains satisfy compatibility and the traction-free boundary condition are also analytically satisfied. The Airy stress functions satisfy equilibrium and compatibility. However, the stress functions can also be made to satisfy the traction-free boundary conditions along the edges of any present geometric discontinuities. This is accomplished by introducing the concept of conformal mapping. Analytical solutions of the Airy stress functions are mostly available for simple geometries. When stress analyzing engineering components with complicated geometries and loadings, conformal mapping can be an effective and useful tool to simplify the analytical procedure.

In general, a complex geometry in a certain coordinate system can be transformed to a different geometry in a different coordinate system by using an appropriate mapping function.

Angles are preserved during the mapping. Solutions from the new mapped region are mapped back to the original coordinate. Despite being solved in different coordinates, these solutions are still valid for the original coordinate system. In order to aid mathematical computations in this study, a complicated geometry from the physical *z*-plane is mapped to a comparatively simpler geometry in the imaginary ζ-plane, Figure 2-1 and Figure 2-2.

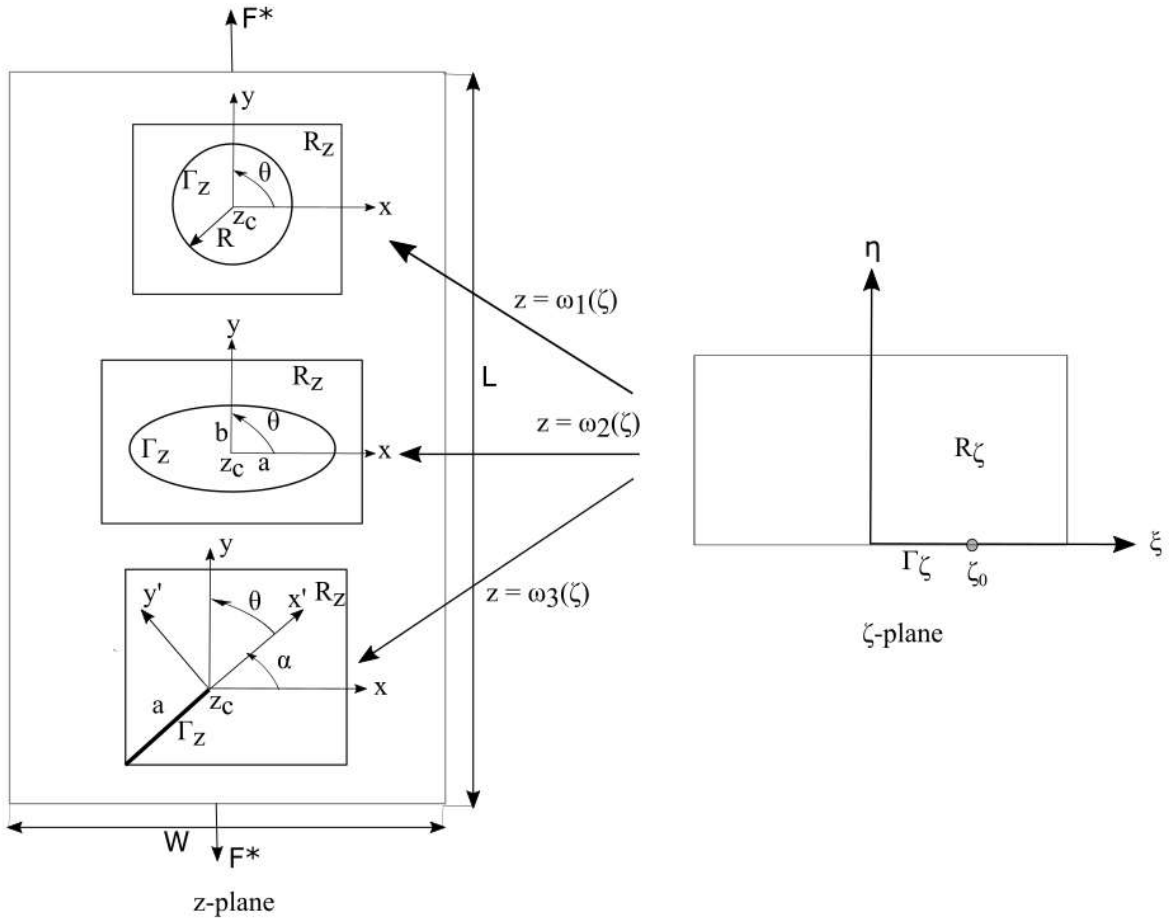

Figure 2-1: Conformal mapping of a half-plane from the ζ-plane into complicated geometries (such as a circular hole, elliptical hole or crack) in physical *z*-plane

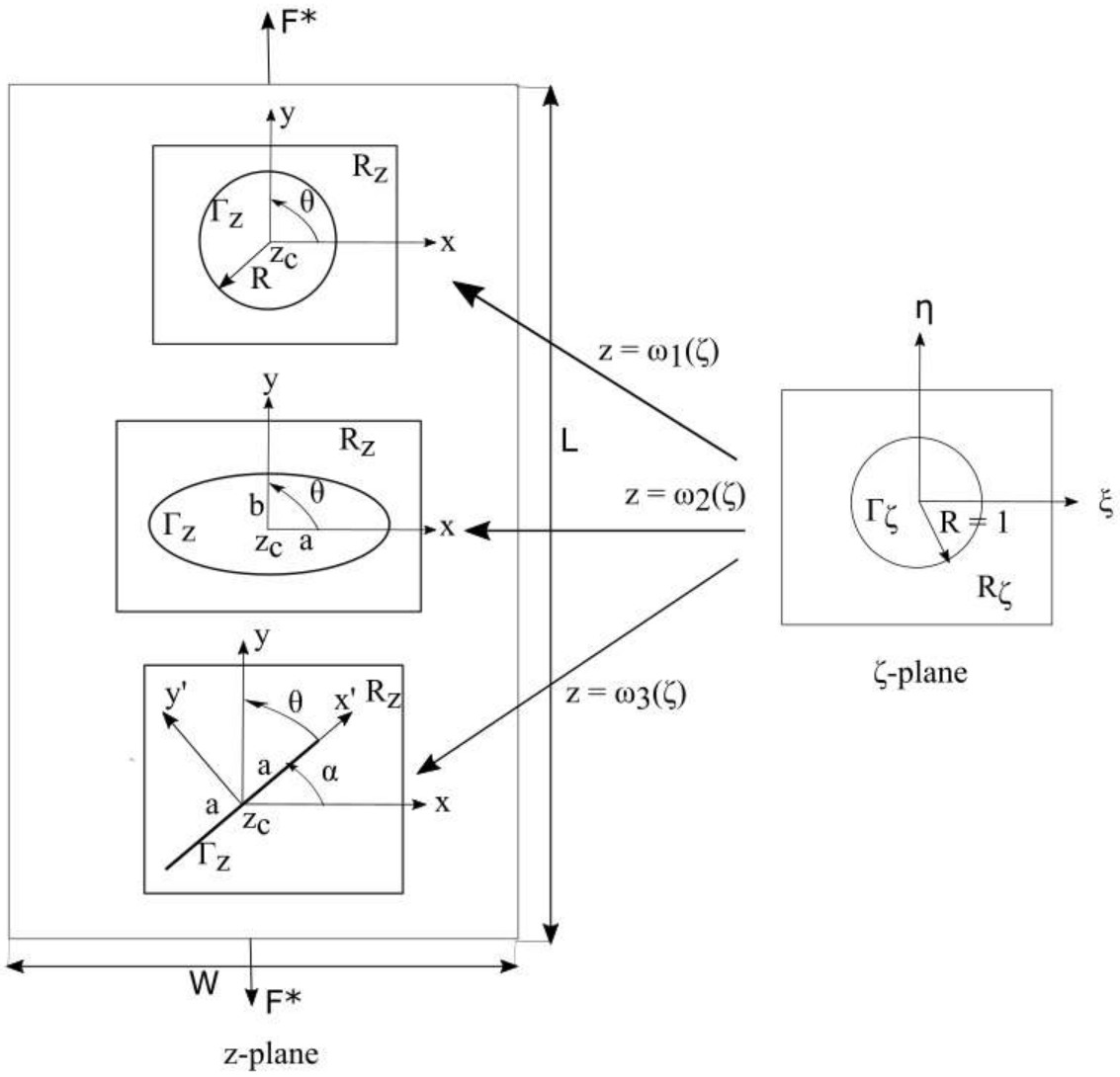

Figure 2-2: Conformal mapping of a unit circular hole from the ζ-plane into complicated geometries (such as a circular hole, elliptical hole or crack) in physical z-plane

The concept of conformal mapping is employed in the present hybrid stress analysis method to enable the complex variables Airy stress functions to analytically satisfy the traction-free boundary conditions and also to simplify the related analytical procedures. By expressing the Airy stress functions in the expressions of the in-plane stress, strain and displacement components (equations (2-25) through (2-29) and equation (2-34)) with respect to the complex variables ζ_j (for

$j = 1, 2$) of the mapped plane, the analytical procedure is simplified and the stresses/displacements analytically satisfy the traction-free boundary conditions.

In general, a function, $z = \omega(\zeta)$ maps a region R_ζ of a simple shape in the $\zeta = \xi + i\eta$ plane into probably a more complicated region R_z in the physical $z = x + iy$ plane of a loaded structure, Figure 2-1 or Figure 2-2. The comparatively simple shapes in the ζ-plane are usually in the form of a half-plane (Figure 2-1) or a unit circle (Figure 2-2). For orthotropic materials, the auxiliary planes are expressed as $z_j = x + \mu_j y$ and $\zeta_j = \xi + \mu_j \eta$ for $j = 1, 2$, and the associated mapping function according to equation (2-38). These induced mapping functions are invertible and perform one-to-one affine transformation.

$$z_j = x + \mu_j y = \omega_j(\zeta_j), \qquad j = 1, 2 \tag{2-38}$$

It is now possible to express the Airy stress functions, $\Phi(z_1)$ and $\Psi(z_2)$, as analytic functions of ζ_1 and ζ_2, respectively, as such

$$\Phi(z_1) = \Phi[\omega_1(\zeta_1)] \equiv \Phi(\zeta_1) \tag{2-39}$$

$$\Psi(z_2) = \Psi[\omega_2(\zeta_2)] \equiv \Psi(\zeta_2) \tag{2-40}$$

Similarly, the derivative of the stress functions of equations (2-39) and (2-40) with respect to z_j, can also be expressed as analytic functions of ζ_1 and ζ_2, respectively, i.e.,

$$\Phi'(z_1) = \Phi'(\zeta_1)\frac{d\zeta_1}{dz_1} = \frac{\Phi'(\zeta_1)}{\omega_1'(\zeta_1)} \tag{2-41}$$

$$\Psi'(z_2) = \Psi'(\zeta_2)\frac{d\zeta_2}{dz_2} = \frac{\Psi'(\zeta_2)}{\omega_2'(\zeta_2)} \tag{2-42}$$

where differentiation of the mapping function, ω_j, of equation (2-38) with respect to ζ_j (for j = 1, 2) results in the following

$$\frac{dz_j}{d\zeta_j} = \omega_j'(\zeta_j), \quad j = 1, 2 \tag{2-43}$$

Equation (2-43) is used in equations (2-41) and (2-42) to replace $\frac{d\zeta_j}{dz_j}$ by $\frac{1}{\omega_j'(\zeta_j)}$ for j = 1, 2. The new form of the stress functions obtained from combining equations (2-41) and (2-42) with equation (2-43) is now used in equations (2-25) through (2-27) and the obtained in-plane stresses are

$$\sigma_{xx} = 2Re\left[\mu_1^2\frac{\Phi'(\zeta_1)}{\omega_1'(\zeta_1)} + \mu_2^2\frac{\Psi'(\zeta_2)}{\omega_2'(\zeta_2)}\right] \tag{2-44}$$

$$\sigma_{yy} = 2Re\left[\frac{\Phi'(\zeta_1)}{\omega_1'(\zeta_1)} + \frac{\Psi'(\zeta_2)}{\omega_2'(\zeta_2)}\right] \tag{2-45}$$

$$\sigma_{xy} = -2Re\left[\mu_1\frac{\Phi'(\zeta_1)}{\omega_1'(\zeta_1)} + \mu_2\frac{\Psi'(\zeta_2)}{\omega_2'(\zeta_2)}\right] \tag{2-46}$$

As the mapping functions are also analytic functions of ζ_1 and ζ_2, equilibrium and compatibility are satisfied throughout the region R_z of the physical z-plane in the above expressions of the in-plane stresses of equations (2-44) through (2-46). Expressing the stress functions as analytic functions of ζ_j for $j = 1, 2$, according to equations (2-39) and (2-40) and substitution into equations (2-31) and (2-32) similarly provides the in-plane displacements as analytic functions of ζ_1 and ζ_2 as

$$u = 2Re[p_1\Phi(\zeta_1) + p_2\Psi(\zeta_2)] \tag{2-47}$$

$$v = 2Re[q_1\Phi(\zeta_1) + q_2\Psi(\zeta_2)] \tag{2-48}$$

2.7. Analytic Continuation

Analytic continuation is another useful tool to stress analyze orthotropic structures. At regions close to the traction-free edge of a cutout, analytic continuation allows the stress functions $\Phi(z_1)$ and $\Psi(z_2)$ to be related to each other. This simplifies the expressions for the in-plane stresses and displacements of equations (2-44) through (2-48) by employing only one stress function. Mathematical details of analytic continuation are now provided.

In regions close to a traction-free boundary, R_z, analytic continuation enables the two stress functions $\Phi(z_1)$ and $\Psi(z_2)$ to be expressed in terms of each other [8,9,18]. For a component of orthotropic material, if the traction-free boundary, Γ_z, and its exterior region, R_z, are mapped from the physical z-plane to a half-plane, R_ζ, in the mapped ζ-plane with the traction-free boundary, Γ_ζ,

along the real axis, ξ, analytical continuation relates the two stress functions throughout region, R_ζ, and along the traction-free boundary, Γ_ζ, i.e., [7–9,18]

$$\Psi(\zeta_2) = B\overline{\Phi(\bar{\zeta}_2)} + C\Phi(\zeta_2) \tag{2-49}$$

where B and C are complex material quantities and defined as

$$B = \frac{\bar{\mu}_2 - \bar{\mu}_1}{\mu_2 - \bar{\mu}_2} \tag{2-50}$$

$$C = \frac{\bar{\mu}_2 - \mu_1}{\mu_2 - \bar{\mu}_2} \tag{2-51}$$

Similarly, for orthotropy when the traction-free boundary, Γ_z, and its adjacent exterior region, R_z, from the physical z-plane are mapped along the traction-free boundary, Γ_ζ, of a unit circle and to its exterior region, R_ζ, then analytic continuation relates the two stress functions in region, R_ζ, close to the traction-free boundary, Γ_ζ, as following [8,19]

$$\Psi(\zeta_2) = B\overline{\Phi\left(\frac{1}{\bar{\zeta}_2}\right)} + C\Phi(\zeta_2) \tag{2-52}$$

Therefore, no matter how the mapping is conducted, analytic continuation allows both the stress functions, $\Phi(\zeta_1)$ and $\Psi(\zeta_2)$, to be expressed as a single stress function $\Phi(\zeta_j)$ for j = 1, 2.

2.8. Mapping Collocation

2.8.1. General Comments

The individual stresses and displacements (equations (2-44) through (2-48)) of a loaded orthotropic structure either using equation (2-49) or (2-52) can now be evaluated using a single stress function, $\Phi(\zeta_j)$ for $j = 1, 2$. This requires knowing the stress function $\Phi(\zeta_j)$ to stress analyze the structure. For this purpose, the concept of finite power-series expansion of a function is utilized in this thesis. The single stress function, $\Phi(\zeta_j)$, is expressed as a finite power-series expansion whose unknown complex coefficients are determined experimentally. Knowing the complex coefficients, the stress functions $\Phi(\zeta_1)$ and $\Psi(\zeta_2)$ are evaluated and hence the individual stresses and displacements are available throughout the structure from equations (2-44) through (2-48). Once stresses are known, using them along with the orthotropic constitutive properties in equations (2-3) through (2-5) or equation (2-34), the in-plane strains are determined.

Either a truncated Taylor series or a Laurent series is used to expand the stress functions. Gerhardt [8] provided information on when to use a Taylor series or when to use a Laurent series. For problems where the mapping is such that the boundary of a discontinuity is mapped from the physical z-plane to along the real axis of the ζ-plane, the Taylor series is used to express the stress function $\Phi(\zeta_j)$ (for $j = 1, 2$). If the mapping function maps the boundary of the traction-free cutout from the physical z-plane to a unit circle in the ζ-plane, the Laurent series is employed [8].

2.8.2. Taylor Series Expansion

A truncated Taylor series maps a portion of the real axis, Γ_ζ, of the imaginary ζ-plane and its adjacent region, R_ζ, onto the traction-free boundary of a cutout, Γ_z, and its exterior region, R_z, of the physical z-plane, Figure 2-1. For orthotropy the stress function $\Phi(\zeta_j)$ for j = 1, 2, in the ζ-plane using the Taylor series are expressed as [8]

$$\Phi(\zeta_1) = \sum_{j=0}^{N} \{c_j(\zeta_1 - \zeta_0)^j\} \tag{2-53}$$

Introducing equation (2-53) for ζ_2 into equation (2-49), the expression for $\Phi(\zeta_2)$ and hence for $\Psi(\zeta_2)$ is obtained as such [8,18]

$$\Psi(\zeta_2) = \sum_{j=0}^{N} \{(\bar{c}_j B + c_j C)(\zeta_2 - \zeta_0)^j\} \tag{2-54}$$

where c_j are the unknown complex Airy coefficients and $\bar{c}_j$ are the complex conjugate of c_j. The constant ζ_0 is an arbitrary point along the real ξ-axis (η = 0) of the ζ-plane. The unknown complex Airy coefficients, c_j, are complex numbers, i.e., $c_j = a_j + ib_j$, where a_j and b_j are real numbers and are evaluated in this research from measured information. It is typically not possible to stress analyze finite structures of orthotropic materials purely analytically. Measured quantities are thereby combined with analytical representations to solve for the system unknowns. This transforms the stress analysis procedure into an experimental-analytical method. This simplifies the system complexity. Since interest here is mainly in finite structures, the present concept of processing measured quantities often provides the additional advantage of automatically imposing

the structure's finiteness. The solutions of this hybrid-method thereby inherently account for the finite geometry of the structure. The finite boundary conditions can also be manually imposed.

The stresses of equations (2-44) through (2-46) consists of the derivatives of the stress functions, $\Phi'(\zeta_1)$ and $\Psi'(\zeta_2)$. When using Taylor series to express $\Phi(\zeta_1)$ and $\Psi(\zeta_2)$ as equations (2-53) and (2-54), derivatives of these two stress functions with respect to ζ_1 and ζ_2, respectively, are

$$\Phi'(\zeta_1) = \sum_{j=1}^{N} \{c_j j(\zeta_1 - \zeta_0)^{j-1}\} \tag{2-55}$$

and

$$\Psi'(\zeta_2) = \sum_{j=1}^{N} \{j(\bar{c}_j B + c_j C)(\zeta_2 - \zeta_0)^{j-1}\} \tag{2-56}$$

Thus, using the concept of analytic continuation of equation (2-49) to relate the stress functions of equations (2-44) through (2-46) as a single stress function, $\Phi(\zeta_j)$ for j = 1, 2, and expanding the latter using the Taylor series expansion, the in-plane stresses are obtained by combining equations (2-55) and (2-56) in equations (2-44) through (2-46), i.e.,

$$\sigma_{xx} = 2\sum_{j=1}^{N} Re\left\{\left[\frac{j\mu_1^2}{\omega_1'(\zeta_1)}(\zeta_1 - \zeta_0)^{j-1} + \frac{j\mu_2^2 C}{\omega_2'(\zeta_2)}(\zeta_2 - \zeta_0)^{j-1}\right]c_j + \left[\frac{j\mu_2^2 B}{\omega_2'(\zeta_2)}(\zeta_2 - \zeta_0)^{j-1}\right]\bar{c}_j\right\} \tag{2-57}$$

$$\sigma_{yy} = 2\sum_{j=1}^{N} Re\left\{\left[\frac{j}{\omega_1'(\zeta_1)}(\zeta_1 - \zeta_0)^{j-1} + \frac{jC}{\omega_2'(\zeta_2)}(\zeta_2 - \zeta_0)^{j-1}\right]c_j + \left[\frac{jB}{\omega_2'(\zeta_2)}(\zeta_2 - \zeta_0)^{j-1}\right]\bar{c}_j\right\} \tag{2-58}$$

$$\sigma_{xy} = -2\sum_{j=1}^{N} Re\left\{\left[\frac{j\mu_1}{\omega_1'(\zeta_1)}(\zeta_1 - \zeta_0)^{j-1} + \frac{j\mu_2\, C}{\omega_2'(\zeta_2)}(\zeta_2 - \zeta_0)^{j-1}\right]c_j + \left[\frac{j\mu_2 B}{\omega_2'(\zeta_2)}(\zeta_2 - \zeta_0)^{j-1}\right]\bar{c}_j\right\} \tag{2-59}$$

where B and C are complex quantities which depends on the material's elastic properties and are defined in equations (2-50) and (2-51) and $\omega'_j(\zeta_j)$ are the derivatives of the mapping functions of equation (2-38) with respect to the complex variables, ζ_j, for $j = 1, 2$. In the summation series, $j = 0$ represents a constant related to the rigid body motion and is omitted.

In a similar way, using equations (2-39), (2-40) and (2-49) with the expressions for the in-plane displacements of equations (2-31) and (2-32), and expressing the stress functions as a Taylor series expansion according to equations (2-53) and (2-54), expressions for the in-plane displacements are obtained as

$$u = 2\sum_{j=1}^{N} Re\{[p_1(\zeta_1 - \zeta_0)^j + p_2 C(\zeta_2 - \zeta_0)^j]c_j + [p_2 B(\zeta_2 - \zeta_0)^j]\bar{c}_j\} \tag{2-60}$$

$$v = 2\sum_{j=1}^{N} Re\{[q_1(\zeta_1 - \zeta_0)^j + q_2 C(\zeta_2 - \zeta_0)^j]c_j + [q_2 B(\zeta_2 - \zeta_0)^j]\bar{c}_j\} \tag{2-61}$$

Thus, to evaluate the in-plane stress and displacement components from equations (2-57) through (2-61), one only needs to find the unknown Airy coefficients, c_j.

2.8.3. Laurent Series Expansion

The Laurent series expansion is used when the boundary of the traction-free cutout is mapped from the physical z-plane to a unit circle in the complex ζ-plane. The Laurent series representation of the stress functions are

$$\Phi(\zeta_1) = \sum_{\substack{j=-m \\ j\neq 0}}^{j=m} c_j \zeta_1^j \tag{2-62}$$

$$\Psi(\zeta_2) = \sum_{\substack{j=-m \\ j\neq 0}}^{j=m} \left(\bar{c}_j B \zeta_2^{-j} + c_j C \zeta_2^j\right) \tag{2-63}$$

As mentioned previously, the Airy coefficients c_j are complex numbers, i.e., $c_j = a_j + ib_j$, where a_j and b_j are real numbers. B and C are complex material quantities which are obtained from equations

(2-50) and (2-51). The value of $j = 0$ in the summation series is related to the rigid body motion. As the plate is securely held between the grips when physically loaded, there is no contribution from the rigid body motions, $j \neq 0$. Moreover, if the situation is such that one has symmetry over the four quadrants, the value of j is not an even number, $m \neq 2n$ for $n = 1, 2, 3 \ldots \infty$. The series only sums the odd values of j, i.e., $m = 2n - 1$. For cases with geometric and loading symmetry about the x-y axes, analyzing just one quadrant is sufficient. Information in the other quadrants is known through symmetry.

Derivatives of the stress functions of equations (2-62) and (2-63) with respect to the complex variables ζ_j for $j = 1, 2$, are

$$\Phi'(\zeta_1) = \sum_{\substack{j=-m \\ j \neq 0}}^{j=m} j c_j \zeta_1^{j-1} \tag{2-64}$$

$$\Psi'(\zeta_2) = \sum_{\substack{j=-m \\ j \neq 0}}^{j=m} \left(-j\bar{c}_j B \zeta_2^{-j-1} + j c_j C \zeta_2^{j-1}\right) \tag{2-65}$$

Furthermore, substitution of equations (2-64) and (2-65) into equations (2-41) and (2-42), the derivatives of the stress functions with respect to the complex variables z_j for $j = 1, 2$, are obtained as

$$\Phi'(z_1) = \frac{\Phi'(\zeta_1)}{\omega_1'(\zeta_1)} = \sum_{\substack{j=-m \\ j\neq 0}}^{j=m} \frac{jc_j\zeta_1^{j-1}}{\omega_1'(\zeta_1)} \tag{2-66}$$

$$\Psi'(z_2) = \frac{\Psi'(\zeta_2)}{\omega_2'(\zeta_2)} = \sum_{\substack{j=-m \\ j\neq 0}}^{j=m} \frac{-j\bar{c}_j B\zeta_2^{-j-1} + jc_j C\zeta_2^{j-1}}{\omega_2'(\zeta_2)} \tag{2-67}$$

Combining equations (2-52), (2-62) and (2-63), with equations (2-47) and (2-48) provides the in-plane displacements in *x*- and *y*-directions as

$$u = 2\left(\sum_{\substack{j=-m \\ j\neq 0}}^{j=m} Re\left\{\left[p_1\zeta_1^j + p_2\left(C\zeta_2^j + B\zeta_2^{-j}\right)\right]a_j + i\left[p_1\zeta_1^j + p_2\left(C\zeta_2^j - B\zeta_2^{-j}\right)\right]b_j\right\}\right) \tag{2-68}$$

$$v = 2\left(\sum_{\substack{j=-m \\ j\neq 0}}^{j=m} Re\left\{\left[q_1\zeta_1^j + q_2\left(C\zeta_2^j + B\zeta_2^{-j}\right)\right]a_j + i\left[q_1\zeta_1^j + q_2\left(C\zeta_2^j - B\zeta_2^{-j}\right)\right]b_j\right\}\right) \tag{2-69}$$

Similarly, combining equations (2-66) and (2-67) with equations (2-44) through (2-46) gives the following expressions for the in-plane stresses

$$\sigma_{xx} = 2\left(\sum_{\substack{j=-m \\ j\neq 0}}^{j=m} Re\left[\mu_1^2 \frac{jc_j\zeta_1^{j-1}}{\omega_1'(\zeta_1)} + \mu_2^2 \frac{-j\bar{c}_j B\zeta_2^{-j-1} + jc_j C\zeta_2^{j-1}}{\omega_2'(\zeta_2)}\right]\right) \tag{2-70}$$

$$\sigma_{yy} = 2\left(\sum_{\substack{j=-m \\ j\neq 0}}^{j=m} Re\left[\frac{jc_j\zeta_1^{j-1}}{\omega_1'(\zeta_1)} + \frac{-j\bar{c}_j B\zeta_2^{-j-1} + jc_j C\zeta_2^{j-1}}{\omega_2'(\zeta_2)}\right]\right) \tag{2-71}$$

$$\sigma_{xy} = -2\left(\sum_{\substack{j=-m \\ j\neq 0}}^{j=m} Re\left[\mu_1 \frac{jc_j\zeta_1^{j-1}}{\omega_1'(\zeta_1)} + \mu_2 \frac{-j\bar{c}_j B\zeta_2^{-j-1} + jc_j C\zeta_2^{j-1}}{\omega_2'(\zeta_2)}\right]\right) \tag{2-72}$$

where ω'_j are the derivatives of the mapping functions ω_j for $j = 1, 2$, of equation (2-38). Once the stresses in the *x*-*y* rectangular Cartesian coordinates are determined from equations (2-70) through (2-72), using coordinate transformation matrix of equation (2-73) the stresses can be transformed from the Cartesian coordinates to the polar coordinates. The in-plane strains are available from a stress-strain relationship such as that of equation (2-34).

$$\begin{Bmatrix}\sigma_{rr}\\ \sigma_{\theta\theta}\\ \sigma_{r\theta}\end{Bmatrix} = \begin{bmatrix}\cos^2\theta & \sin^2\theta & 2\sin\theta\cos\theta\\ \sin^2\theta & \cos^2\theta & -2\sin\theta\cos\theta\\ -\sin\theta\cos\theta & \sin\theta\cos\theta & \cos^2\theta - \sin^2\theta\end{bmatrix}\begin{Bmatrix}\sigma_{xx}\\ \sigma_{yy}\\ \sigma_{xy}\end{Bmatrix} \tag{2-73}$$

By using conformal mapping and analytic continuation, the stresses of equations (2-57) through (2-59) or equations (2-70) through (2-72) can be made to satisfy local traction-free

boundary conditions and equilibrium throughout the entire structure. The associated strains satisfy compatibility.

The current approach can be extended to isotropic materials according to elastic modulus, $E_{11} = E_{22} = E$, Poisson's ratio, ν, and shear modulus, $G = E/2(1 + \nu)$. This method is capable of processing measured data in a variety of forms, i.e., the Airy stress coefficients can be determined from virtually any measured data. Examples include measured displacement u or v in equation (2-60) or (2-61) or in equation (2-68) or (2-69). Measured isopachic stresses can be used in a combination of equations (2-57) and (2-58) or of equations (2-70) and (2-71). Although applicable to a variety of experimental techniques, this research emphasizes stress analyzing loaded structures using a single displacement component measured by digital image correlation (DIC). With rapid advancements in image technologies and computer processing power, DIC is becoming a highly promising and convenient experimental tool for structural assessment.

To facilitate solving various real-world applications involving orthotropic structures with discontinuities, conformal mapping functions of several commonly found cutouts in mechanical structures or machine components are provided here.

2.9. Common Mapping Functions

2.9.1. Circular Cutouts, Notches and Fillets

2.9.1.1. Taylor Series

Consider an orthotropic component with a circular hole, notch or fillet of radius R and center located at z_c, Figure 2-1. To map a region, $R\zeta$, (half-plane) from the ζ-plane into a region,

R_z, adjacent to the circular opening of the physical z-plane, the following mapping function is used [9]

$$z_j = \omega_j(\zeta_j) = \frac{iR}{2}\left[(1 - i\mu_j)e^{-i\zeta_j} - (1 + i\mu_j)e^{i\zeta_j}\right] + z_c, \quad j = 1, 2 \tag{2-74}$$

The region along the real axis, $\Gamma_{\zeta,}$ in the ζ-plane is mapped onto the traction-free boundary, Γ_z, of the z-plane. Such mapping functions are employed when expressing the stress functions using the Taylor series expansion. The following inverse of the mapping function of equation (2-74) maps the circular hole of radius R and region, R_z, adjacent to it from the physical z-plane to a half-plane, R_ζ, along and above the real axis of the ζ-plane.

$$\zeta_j = \omega_j^{-1}(z_j) = i \ln\left[\frac{z_j - z_c \pm \sqrt{(z_j - z_c)^2 - R^2(1 + \mu_j^2)}}{i R(1 - i\mu_j)}\right], \quad j = 1, 2 \tag{2-75}$$

The branch of the square root of equation (2-75) is chosen so that $Im(\zeta_j) \geq 0$, i.e., $| e^{i\zeta_j} | \geq 1$ for $j = 1, 2$. The center of the cutout is at $z_c = x_c + \mu_j y_c$ for $j = 1, 2$. Keeping the origin of the coordinate system at the center of the circular hole eliminates z_c, i.e., $z_c = 0$ in equations (2-74) and (2-75).

2.9.1.2. Laurent Series

Consider an orthotropic component with a circular hole, notch or fillet of radius R and center located at z_c, Figure 2-2. According to the Laurent series expansion, to transform the unit

circle from the ζ-plane to a circular boundary of radius R in the z-plane, the mapping function of equation (2-76) is used to map the traction-free boundary, Γ_ζ, of the unit circle and its exterior adjacent region, R_ζ, from ζ-plane onto the traction-free edge, Γ_z, of the circular hole and its exterior region, R_z, in the z-plane, Figure 2-2, [8]. The inverse of this function maps the original circular cutout/fillet of radius R from the z-plane to the unit circle in the ζ-plane, equation (2-77).

$$z_j = \omega_j(\zeta_j) = \frac{R}{2}\left[(1 - i\mu_j)\zeta_j + \frac{1 + i\mu_j}{\zeta_j}\right] + z_c, \qquad j = 1, 2 \tag{2-76}$$

and

$$\omega^{-1}(z_j) = \zeta_j = \frac{z_j - z_c \pm \sqrt{(z_j - z_c)^2 - R^2(1 + \mu_j^2)}}{R(1 - i\mu_j)}, \qquad j = 1, 2 \tag{2-77}$$

The branch of the square root of the above equation (2-77) is chosen so that, $|\zeta_j| \geq 1$ for $j = 1, 2$.

2.9.2. Elliptical Cutouts or Notches

2.9.2.1. Taylor Series

For an orthotropic loaded structure with an elliptical cutout of major radius, a, and minor radius, b, and the ellipse center located at z_c, the mapping function to map the region R_ζ from the ζ-plane into the region R_z of the z-plane (Figure 2-1) is [8]

$$z_j = \omega_j(\zeta_j) = \frac{a - ib\mu_j}{2}\left(\frac{i - \zeta_j}{i + \zeta_j}\right) + \frac{a + ib\mu_j}{2}\left(\frac{i + \zeta_j}{i - \zeta_j}\right) + z_c, \quad j = 1, 2 \qquad (2\text{-}78)$$

The above mapping function considers the major radius of the ellipse, a, to be along the x-axis and minor radius, b, along the y-axis. Using the inverse of the mapping function of equation (2-78), the traction-free elliptical boundary, Γ_z, and its exterior adjacent region, R_z, from the physical z-plane is mapped into a half-plane of region, R_ζ, with the traction-free boundary mapped along a section of the real ξ-axis ($\eta = 0$) in the ζ-plane as

$$\zeta_j = \omega_j^{-1}(z_j) = i\frac{a - ib\mu_j - \left(z_j - z_c + \sqrt{(z_j - z_c)^2 - a^2 - b^2{\mu_j}^2}\right)}{a - ib\mu_j + \left(z_j - z_c + \sqrt{(z_j - z_c)^2 - a^2 - b^2{\mu_j}^2}\right)}, \qquad (2\text{-}79)$$

$$j = 1, 2$$

The branch of the square root of equation (2-79) is chosen so that $Im\zeta_j \leq 0$ for $j = 1, 2$. Selecting the coordinate origin at the center of the elliptical cutout will simplify the mapping function by eliminating z_c.

2.9.2.2. Laurent Series

To conformally map the same elliptical cutout just discussed from a unit circle the Laurent series expansion is used. To map the boundary of a unit circle and its exterior region from the ζ-plane into the exterior region of the elliptical hole in the z-plane, Figure 2-2, the mapping function

of equation (2-80) is used. This function maps the boundary of a unit circle, Γ_ζ, and region, R_ζ, adjacent to it from the ζ-plane to the traction-free boundary, Γ_z, along an elliptical hole of radii a and b, and region, R_z, exterior to it in the physical z-plane as [8]

$$z_j = \omega_j(\zeta_j) = \frac{a + ib\mu_j}{2}\frac{1}{\zeta_j} + \frac{a - ib\mu_j}{2}\zeta_j + z_c, \quad j = 1, 2 \tag{2-80}$$

The inverse of the mapping function of equation (2-80) maps the boundary of the elliptical hole, Γ_z, and region, R_z, close to it from the physical z-plane onto along the boundary, Γ_ζ, of a unit circle and region, R_ζ, exterior to it in the mapped ζ-plane.

$$\zeta_j = \omega_j^{-1}(z_j) = \frac{z_j - z_c \pm \sqrt{(z_j - z_c)^2 - a^2 - b^2\mu_j^2}}{a - ib\mu_j}, \quad j = 1, 2 \tag{2-81}$$

The branch of the square root of equation (2-81) is chosen in such a way that, $|\zeta_j| \geq 1$ for $j = 1, 2$.

While equations (2-80) and (2-81) theoretically assumes infinite geometry [5], Chapter 5 demonstrates these are applicable for highly finite members.

2.9.3. Inclined Elliptical Cutouts

2.9.3.1. Laurent Series

For an elliptical hole inclined at an angle α to the x-axis (x-axis aligned along strong/stiff material direction 1) and with the coordinate origin at the center of the hole ($z_c = 0$), Figure 2-3,

the mapping function to map the region, R_ζ, adjacent to a unit circle in the ζ-plane to an elliptical hole oriented at an angle α and its exterior region, R_z, in the physical z-plane, (similar to Figure 2-2) is [20]

$$z_j = \omega_j(\zeta_j) = \frac{a' - i\mu_j b'}{2}\zeta_j + \frac{\overline{a'} + i\mu_j \overline{b'}}{2}\zeta_j^{-1}, \qquad \text{for } j = 1, 2 \tag{2-82}$$

where

$$a' = a\cos\alpha + ib\sin\alpha \quad \text{and} \quad b' = b\cos\alpha + ia\sin\alpha \tag{2-83}$$

Quantities $\overline{a'}$ and $\overline{b'}$ are the complex conjugates of a' and b', respectively.

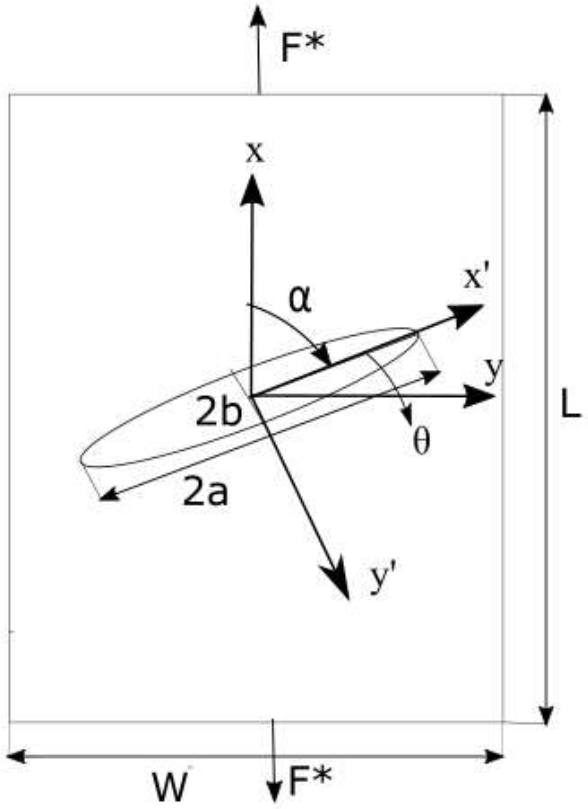

Figure 2-3: Orthotropic plate with inclined elliptical hole

After re-arranging, the inverse of the mapping function of equation (2-82) is [3]

$$\zeta_j = \frac{z_j + \sqrt{z_j^2 \ \pm (a^2\pi_1 + b^2\pi_2)}}{a\pi_3 \pm ib\pi_4}, \qquad j = 1, 2 \tag{2-84}$$

where

$$\pi_1 = \cos^2\alpha + \mu_j^2 \sin^2\alpha + \mu_j \sin 2\alpha \qquad \pi_3 = \cos\alpha + \mu_j \sin 2\alpha$$

$$\pi_2 = \sin^2\alpha + \mu_j^2 \cos^2\alpha \pm \mu_j \sin 2\alpha \qquad \pi_4 = \mu_j \cos\alpha \pm \sin\alpha \tag{2-85}$$

The branch of the square root of equation (2-84) is chosen so that $|\zeta_j| \geq 1$ for $j = 1, 2$. For the $z_j = x + \mu_j y$ plane, expressions for x and y are

$$x = a\cos\theta\cos\alpha \pm b\sin\theta\sin\alpha$$
$$y = a\sin\alpha\cos\theta + b\cos\alpha\sin\theta \tag{2-86}$$

2.9.4. Cracks

2.9.4.1. Taylor Series

For an orthotropic material with a crack located at $y' \rightarrow 0$ and $x' \leq 0$ and inclined at an angle α with the x-axis, the mapping function to map the region, R_ζ, (half-plane) from the ζ-plane to the region surrounding the crack, R_z, in the physical z-plane is [18,21]

$$z_j = \omega_j(\zeta_j) = -\zeta_j^2, \qquad j = 1, 2 \tag{2-87}$$

The local coordinate system x'-y' is aligned and normal to the crack and x-y are the plate's global Cartesian coordinates, Figure 2-1. The inverse of the mapping function of equation (2-87) and which maps the traction-free region of the crack from the z-plane onto a section of the real axis of the ζ-plane, is

$$\zeta_j = \omega_j^{-1}(z_j) = i\sqrt{z_j}, \qquad j = 1, 2 \tag{2-88}$$

The branch of the square root of equation (2-88) is chosen so that $Im(\zeta_j) \geq 0$ for $j = 1, 2$.

2.9.4.2. Laurent Series

Consider a crack of length $2a$ with center located at z_c and oriented at an angle α with respect to the plate's orthotropic material direction x, Figure 2-2. Equation (2-89) maps a region, R_ζ, surrounding a unit circle in the ζ-plane into a region, R_z, close to the traction-free boundary of the crack into the physical z-plane [22]

$$z_j = \omega_j(\zeta_j) = \frac{a}{2}\left(cos\alpha + u_j sin\alpha\right)\left(e^{-i\alpha}\zeta_j + e^{i\alpha}\zeta_j^{-1}\right) + z_c, \qquad j = 1, 2 \tag{2-89}$$

The inverse of the above mapping function of equation (2-89) is

$$\zeta_j = \frac{e^{i\alpha}\left[\left(z_j - z_c\right) \pm \sqrt{\left(z_j - z_c\right)^2 - a^2\left(cos\alpha + \mu_j sin\alpha\right)^2}\right]}{a(cos\alpha + \mu_j sin\alpha)}, \quad j = 1, 2 \tag{2-90}$$

For a crack aligned along the x-axis, i.e., $\alpha = 0$, equations (2-89) and (2-90) simplifies to

$$z_j = \omega_j(\zeta_j) = \frac{a}{2}\left(\zeta_j + \zeta_j^{-1}\right) + z_c, \qquad j = 1, 2 \tag{2-91}$$

and

$$\zeta_j = \frac{\left[(z_j - z_c) \pm \sqrt{(z_j - z_c)^2 - a^2}\right]}{a}, \quad j = 1, 2 \tag{2-92}$$

The branch of the square root of the above equations (2-90) and (2-92) are chosen so that, $|\zeta_j| \geq 1$ for $j = 1, 2$.

2.9.5. Straight lines

2.9.5.1. Taylor Series

Equation (2-93) maps a half-plane, R_ζ, from the ζ-plane into a region, R_z, adjacent to a straight line inclined at an angle α with the x-axis in the physical z-plane, Figure 2-4 [9]

$$z_j = \omega_j(\zeta_j) = (cos\alpha + \mu_j sin\alpha)\zeta_j + z_0, \quad j = 1, 2 \tag{2-93}$$

The inverse of the above mapping function is

$$\zeta_j = \omega_j^{-1}(z_j) = \frac{z_j - z_0}{cos\alpha + \mu_j sin\alpha}, \quad j = 1, 2 \tag{2-94}$$

where $z_0 = x_0 + \mu_j y_0$ is an arbitrary point in the physical z-plane.

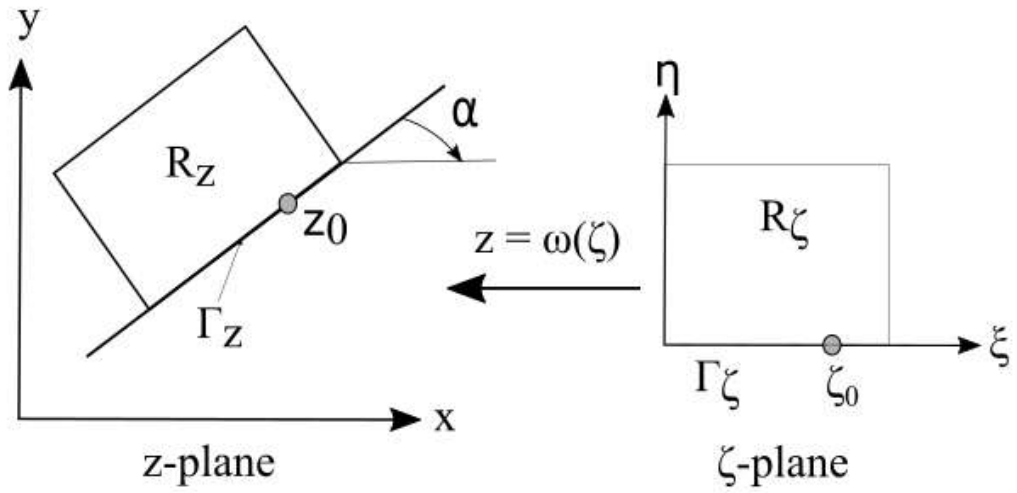

Figure 2-4: Mapping a half-plane from ζ-plane into a region close to a straight line in z-plane

2.9.6. Parabolic Notch

2.9.6.1. Taylor Series

For a parabolic notch with a radius of curvature ρ_n at its root (Figure 2-5) the following mapping function maps a half-plane, R_ζ, from the ζ-plane to the region adjacent to the parabolic notch, R_z, in the z-plane as such [9]

$$z_j = \omega_j(\zeta_j) = \mu_j\zeta_j^2 + 2q\zeta_j - \mu_j q^2, \quad j = 1, 2 \tag{2-95}$$

The inverse of the mapping function that maps the region R_z from the physical z-plane to R_ζ in the ζ-plane is

$$\zeta_j = \omega_j^{-1}(z_j) = -\frac{q}{\mu_j} + \sqrt{q^2\left(1 + \frac{1}{\mu_j^2}\right) + \frac{z_j}{\mu_j}}, \quad j = 1, 2 \tag{2-96}$$

The branch of the square root of equation (2-96) is chosen so that $Im(\zeta_j) \leq 0$ for $j = 1, 2$.

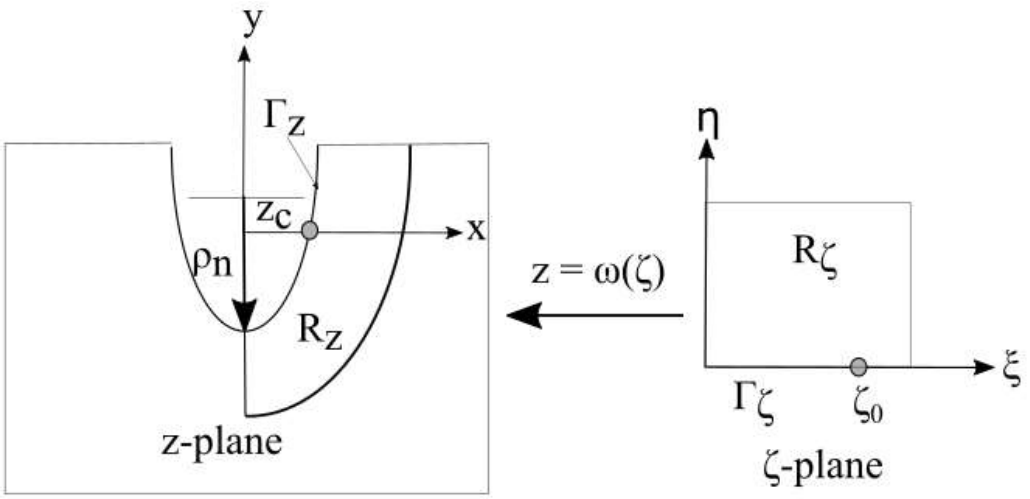

Figure 2-5: Mapping a half-plane from ζ-plane into a region close to a parabolic notch in z-plane

The parabolic notch of Figure 2-5 is represented as

$$y = \frac{x^2}{2\rho_n} - \frac{\rho_n}{2} \text{ and } q = \sqrt{\frac{\rho_n}{2}} \tag{2-97}$$

2.9.7. Rectangular Opening

2.9.7.1. Laurent Series

For a rectangular hole of major length $2a$ and minor length or width $2b$ and inclined at an angle α with the x-axis (Figure 2-6), the mapping function to map an region, R_ζ, exterior to a unit

circle in the ζ-plane into an area exteriorly adjacent to the rectangular boundary, R_z, in the z-plane is [6,23,24]

$$z = \omega(\zeta) = R_c \left(\zeta + \sum_{k=1}^{2n-1} \frac{c_k^*}{\zeta^k} \right) \tag{2-98}$$

where R_c is a hole size constant and c_k^* for $k = 2j - 1$ and $j = 1, 2, 3 \ldots n$, are the mapping function coefficients. The mapping coefficients, c_k^*, are defined as [24]

$$c_1^* = \frac{1}{2}\left(e^{2i(\lambda_T+\alpha)} + e^{-2i(\lambda_T-\alpha)}\right)$$

$$c_3^* = \frac{1}{24}\left(e^{2i(\lambda_T+\alpha)} - e^{-2i(\lambda_T-\alpha)}\right)^2 \tag{2-99}$$

$$c_5^* = \frac{1}{80}\left(e^{4i(\lambda_T+\alpha)} - e^{-4i(\lambda_T-\alpha)}\right)\left(e^{2i(\lambda_T+\alpha)} - e^{-2i(\lambda_T-\alpha)}\right)$$

where α is the inclination of the rectangular hole with the x-axis and λ_T is characterization side ratio of the rectangular hole, i.e., $\lambda_T = a/b$, Figure 2-6. Details regarding the mapping function can be found in Reference [24].

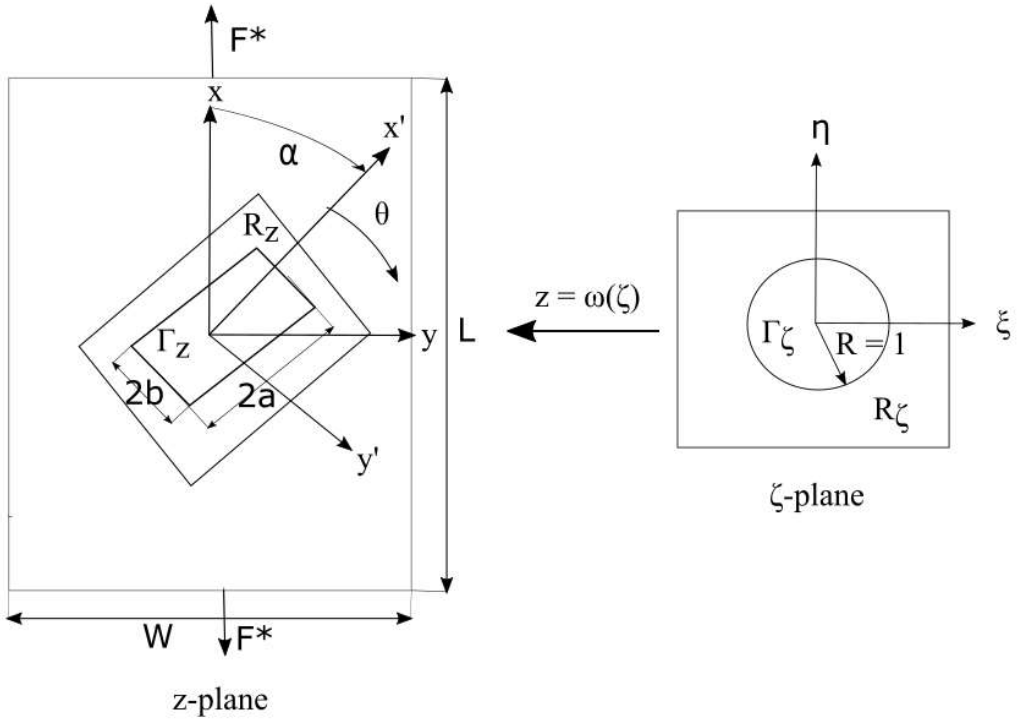

Figure 2-6: Mapping a unit circle from the ζ-plane into a region close to a rectangular boundary in the z-plane

For an orthotropic material, by substituting $z = x + iy$ as $z_j = x + \mu_j y$ for $j = 1, 2$, into the mapping function of equation (2-98), the mapping function subsequently takes the following form [24]

$$z_j = \omega_j(\zeta_j) = \frac{R_c}{2}\left[(1 + i\mu_j)\left(\frac{1}{\zeta_j} + \sum_{k=1}^{2n-1} c_k^* \zeta_j^k\right) + (1 - i\mu_j)\left(\zeta_j + \sum_{k=1}^{2n-1} \frac{c_k^*}{\zeta_j^k}\right)\right] \quad (2\text{-}100)$$

The summation series consider the odd values of k, i.e., $k = 2n - 1$ for $n = 1, 2, 3, \ldots$

2.9.8. Other Cutouts

The mapping functions for few other commonly-shaped cutouts are provided in this section. The functions of equations (2-101) through (2-103) map regions, R_ζ, above a half-plane in the ζ-plane into regions, R_z, adjacent to a square hole, triangular hole or oval hole, respectively, in the physical z-plane, Figure 2-7. Equation (2-101) is used to map a square hole with rounded corners and side length a from the ζ-plane into the physical z-plane [9]

$$z = \omega(\zeta) = R_c\left(\frac{1}{\zeta} - \frac{\zeta^3}{6} + \frac{1}{56}\zeta^7\right) + z_c \tag{2-101}$$

where R_c is a constant related to the scale and orientation of the square opening. Equation (2-102) is useful in mapping an equilateral triangular hole with side length a [25]

$$z = \omega(\zeta) = \frac{\sqrt{3a}}{4}\left(\zeta - \frac{1}{3}\zeta^{-2} + \frac{1}{45}\zeta^{-5}\right) + z_c \tag{2-102}$$

The following approximate mapping function can be employed for an oval opening with major and minor radii of a and $a/3$, respectively, [25]

$$z = \omega(\zeta) = \frac{17}{24}a\left(\zeta + \frac{8}{17}\zeta^{-1} - \frac{1}{17}\zeta^{-3}\right) + z_c \tag{2-103}$$

where z_c is the center of the cutouts.

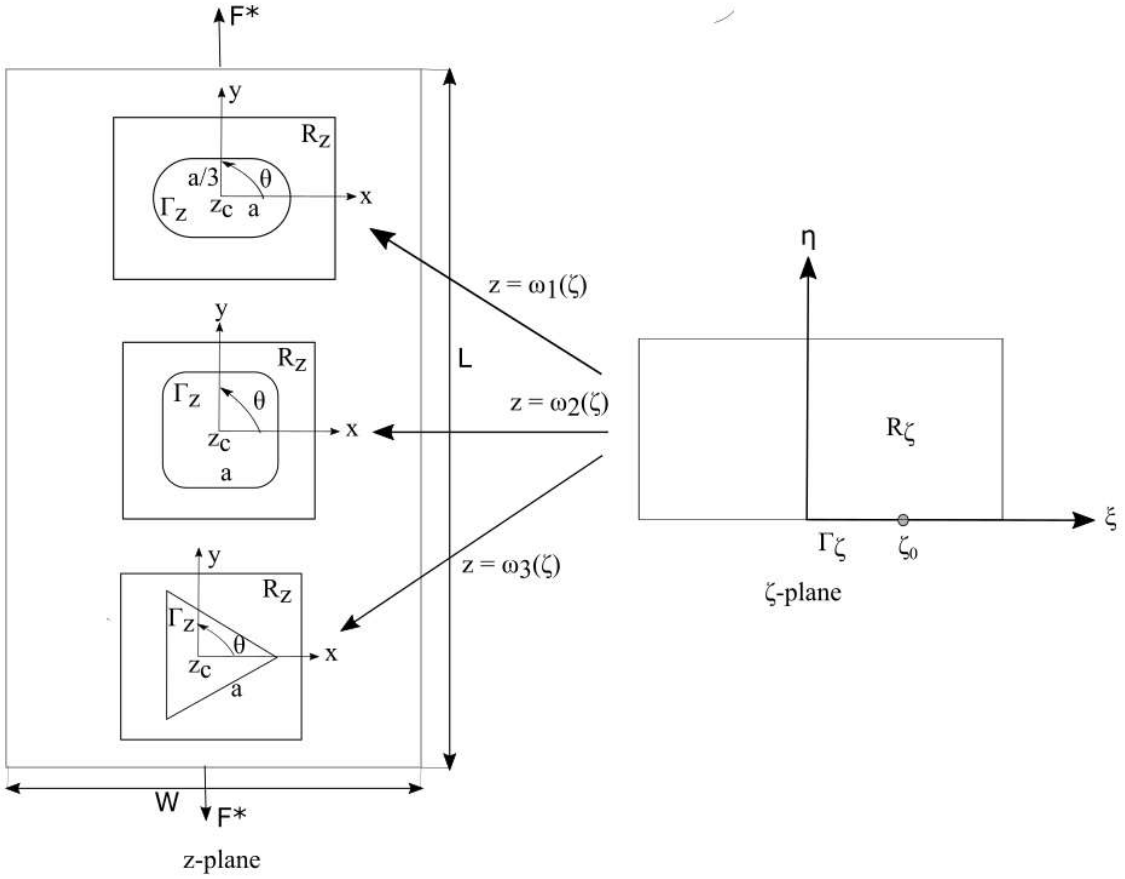

Figure 2-7: Mapping a half-plane from ζ-plane to various shaped cutouts (oval, square or triangle) in physical z-plane

Determining the inverse of the mapping functions of equations (2-101) through (2-103) requires the equations be arranged in the form of polynomial equations with the complex variable ζ as the roots. For example, equation (2-101) can be re-arranged as equation (2-104). The roots of the polynomial equation (2-104) contain the inverse of the mapping function and can be numerically obtained. The root that satisfies the condition $|\zeta| \leq 1$ is selected as the inverse of the mapping function [9].

$$3\zeta^8 - 28\zeta^4 - \frac{168z}{R}\zeta + 168 = 0 \tag{2-104}$$

The mapping function of equation (2-101) can be simplified by retaining only the first two terms as such [25]

$$z = \omega(\zeta) = R\left(\frac{1}{\zeta} - \frac{\zeta^3}{6}\right) \tag{2-105}$$

In this case the polynomial equation to solve for the inverse mapping function also simplify to

$$\zeta^4 + \frac{6z}{R}\zeta - 6 = 0 \tag{2-106}$$

To apply these mapping functions for orthotropic members, the complex variables $z_j = x + \mu_j y$ for $j = 1, 2$, needs to be combined individually with equations (2-101) through (2-103).

Equations (2-107) and (2-109) can be used to map a region, R_z, adjacent to a hole having n_s number of sides, i.e., a polygon into the physical z-plane, from an area, R_ζ, adjacent to a unit circle in the ζ-plane and vice-versa [26]

$$z = \omega(\zeta) = R_c\zeta + R_c\zeta^{(1-kn_s)}\sum_{k=1}^{N}\frac{\prod_{j=1}^{k}(j-1)n_s - 2}{n_s^k(1-n_s k)(k!)} \tag{2-107}$$

where n_s is the number of sides of the polygon, R_c is the hole size coefficient and Π represents the products of the terms in the series. R_c is obtained from the theory that the given polygon will be inscribed in a circle with a diameter equal to $2R_c(1 + T_k)$, where T_k is

$$T_k = \sum_{k=1}^{N} \frac{\prod_{j=1}^{k}(j-1)n_s - 2}{n_s^k(1 - n_s k)(k!)} \tag{2-108}$$

By introducing the complex parameters μ_j for j = 1, 2, the mapping function of equation (2-107) takes the following form for orthotropic members

$$z_j = \omega_j(\zeta_j) = \frac{R_c}{2}\left[\left(a_j\zeta_j^{-1} + b_j\zeta_j\right) + \left(a_j\zeta_j^{-(1-kn_s)} + b_j\zeta_j^{(1-kn_s)}\right)\sum_{k=1}^{N}\frac{\prod_{j=1}^{k}(j-1)n_s - 2}{n_s^k(1 - n_s k)(k!)}\right], \quad j = 1, 2 \tag{2-109}$$

where

$$a_j = 1 + i\mu_j \text{ and } b_j = 1 - i\mu_j, \quad j = 1, 2 \tag{2-110}$$

The technique of using conformal mapping in the hybrid stress analysis method becomes comparatively complicated when treating anisotropic structures with highly complicated-shaped cutouts. An alternative in these cases can be the Schwarz-Christoffel mapping. Another alternative can be approximate solutions based on a characterization parameter accounting for the deviation of a certain cutout from that of an elliptical or circular opening [27]. However, these techniques have their own limitations.

This thesis considered some of these mapping functions, i.e., analyzed finite orthotropic plates with a circular cutout, elliptical cutout or double-edge cracks experimentally and plates with central or single-edge crack or a circular annular plate numerically. Additional mathematical details for each of these cases are included in the respective chapters.

2.10. Airy Stress Function with Real Variables

For isotropic materials under plane-stress or plane-strain conditions in the absence of body forces, the Airy stress function is the solution of the following bi-harmonic equation that satisfy equilibrium and compatibility [28]

$$\nabla^4 \Phi = 0 \tag{2-111}$$

where ∇^2 is the Laplacian operator and in the polar coordinates is expressed as

$$\nabla^2 = \frac{\partial}{\partial r^2} + \frac{1}{r}\frac{\partial}{\partial r} + \frac{1}{r^2}\frac{\partial}{\partial \theta^2} \tag{2-112}$$

The general solution of the bi-harmonic equation (2-111) in the polar coordinates is

$$\Phi = a_0 + b_0 \ln r + c_0 r^2 + d_0 r^2 lnr + (A_0 + B_0 lnr + C_0 r^2 + D_0 r^2 lnr)\theta$$
$$+ \left(a_1 r + b_1 r lnr + \frac{c_1}{r} + d_1 r^3\right) sin(\theta)$$
$$+ \left(\acute{a_1} r + \acute{b_1} r lnr + \frac{\acute{c_1}}{r} + \acute{d_1} r^3\right) cos(\theta) + (A_1 r$$
$$+ B_1 r lnr)\theta sin(\theta) + \left(\acute{A_1} r + \acute{B_1} r lnr\right)\theta cos(\theta) \quad (2\text{-}113)$$
$$+ \sum_{n=2,3,4\ldots}^{\infty} \left(a_n r^n + b_n r^{n+2} + c_n r^{-n} + d_n r^{-(n-2)}\right) sin(n\theta)$$
$$+ \sum_{n=2,3,4\ldots}^{\infty} \left(\acute{a_n} r^n + \acute{b_n} r^{n+2} + \acute{c_n} r^{-n} + \acute{d_n} r^{-(n-2)}\right) cos(n\theta)$$

where r is the radial coordinate and θ is the angle measured counter-clockwise from the x-axis.

The individual components of stresses are expressed in terms of the Airy stress function, Φ, as (initially provided by Soutas-Little [28] but corrected according to Foust's thesis [29])

$$\sigma_{rr} = \frac{1}{r}\frac{\partial \Phi}{\partial r} + \frac{1}{r^2}\frac{\partial^2 \Phi}{\partial \theta^2} \quad (2\text{-}114)$$

$$\sigma_{\theta\theta} = \frac{\partial^2 \Phi}{\partial r^2} \quad (2\text{-}115)$$

$$\sigma_{r\theta} = -\frac{\partial}{\partial r}\left(\frac{1}{r}\frac{\partial \Phi}{\partial \theta}\right) \quad (2\text{-}116)$$

Using the expression of the Airy stress function, Φ, of equation (2-113) into equations (2-114) through (2-116), the individual stresses in the polar coordinate are expressed as

$$\sigma_{rr} = \frac{b_0}{r^2} + 2c_0 + d_0(2lnr + 1) + \frac{B_0\theta}{r^2} + 2C_0\theta + D_0(2lnr + 1)\theta$$
$$+ \left(\frac{b_1}{r} - \frac{2c_1}{r^3} + 2rd_1\right) sin(\theta) + \left(\frac{b_1'}{r} - \frac{2c_1'}{r^3} + 2rd_1'\right) cos(\theta)$$
$$+ \frac{2A_1}{r} cos(\theta) - \frac{2A_1'}{r} sin(\theta) + \frac{B_1}{r}\theta sin(\theta) + \frac{B_1'}{r}\theta cos(\theta)$$
$$+ \left(\frac{2B_1}{r} lnr\right) cos(\theta) - \left(\frac{2B_1'}{r} lnr\right) sin(\theta)$$
$$- \sum_{n=2,3,\ldots}^{N} \{a_n n(n-1)r^{n-2} + b_n(n+1)(n-2)r^n$$
$$+ c_n n(n+1)r^{-(n+2)} + d_n(n-1)(n+2)r^{-n}\} \sin(n\theta)$$
$$- \sum_{n=2,3,\ldots}^{N} \{a_n' n(n-1)r^{n-2} + b_n'(n+1)(n-2)r^n$$
$$+ c_n' n(n+1)r^{-(n+2)} + d_n'(n-1)(n+2)r^{-n}\} \cos(n\theta)$$

(2-117)

$$\sigma_{\theta\theta} = \frac{-b_0}{r^2} + 2c_0 + d_0(2lnr + 3) - \frac{B_0\theta}{r^2} + 2C_0\theta + D_0(2lnr + 3)\theta$$

$$+ \left(\frac{b_1}{r} + \frac{2c_1}{r^3} + 6rd_1\right) sin(\theta) + \left(\frac{b_1'}{r} + \frac{2c_1'}{r^3} + 6rd_1'\right) cos(\theta)$$

$$+ \frac{B_1}{r}\theta sin(\theta) + \frac{B_1'}{r}\theta cos(\theta)$$

$$+ \sum_{n=2,3,\ldots}^{N} \{a_n n(n-1)r^{n-2} + b_n(n+1)(n+2)r^n \qquad (2\text{-}118)$$

$$+ c_n n(n+1)r^{-(n+2)} + d_n(n-1)(n-2)r^{-n}\} sin(n\theta)$$

$$- \sum_{n=2,3,\ldots}^{N} \{a_n' n(n-1)r^{n-2} + b_n'(n+1)(n+2)r^n$$

$$+ c_n' n(n+1)r^{-(n+2)} + d_n'(n-1)(n-2)r^{-n}\} cos(n\theta)$$

$$\sigma_{r\theta} = \frac{A_0}{r^2} + B_0\frac{lnr-1}{r^2} - C_0 - D_0(lnr+1)\theta + \left(-\frac{b_1}{r} + \frac{2c_1}{r^3} - 2rd_1\right)cos(\theta)$$
$$-\left(-\frac{b_1'}{r} + \frac{2c_1'}{r^3} - 2rd_1'\right)sin(\theta) - \frac{B_1}{r}sin(\theta) - \frac{B_1'}{r}cos(\theta)$$
$$-\frac{B_1}{r}\theta cos(\theta) + \frac{B_1'}{r}\theta sin(\theta)$$
$$-\sum_{n=2,3,\ldots}^{N}\{a_n n(n-1)r^{n-2} + b_n n(n+1)r^n \qquad (2\text{-}119)$$
$$-c_n n(n+1)r^{-(n+2)} - d_n n(n-1)r^{-n}\}cos\,(n\theta)$$
$$+\sum_{n=2,3,\ldots}^{N}\{a_n' n(n-1)r^{n-2} + b_n' n(n+1)r^n$$
$$+c_n' n(n+1)r^{-(n+2)} + d_n' n(n-1)r^{-n}\}sin(n\theta)$$

where N is the terminating index of the finite summation series. The Airy coefficients for isotropy are real numbers. The coefficients a_0, a_1 and a_1' are absent in the above equations (2-117) through (2-119) due to differentiation of the Airy stress function of equation (2-113) according to equations (2-114) through (2-116). Based on the geometry and external loading, one can often omit many of the Airy coefficients. This simplifies the Airy stress function hence the associated stress, strain and displacement components. The number of Airy coefficients can often be further reduced depending on finite or infinite geometry, symmetry about specific axis/axes, location of the coordinate's origin, any self-equilibrated boundaries, and ensuring that the stresses/strains/displacements are single valued functions. One can sometimes advantageously impose known boundary conditions discretely or analytically.

Having determined the Airy coefficients, the individual in-plane stresses are evaluated from the equations (2-117) through (2-119). Knowing the stresses, equations (2-120) and (2-121) provide the individual in-plane strain components. The strain-displacement relationship (under small deformation) of these equations (2-120) and (2-121) can also be utilized to find the in-plane displacement components.

$$\varepsilon_{rr} = \frac{\partial u_r}{\partial r} = \frac{1}{E}(\sigma_{rr} - \nu\sigma_{\theta\theta}) \tag{2-120}$$

$$\varepsilon_{\theta\theta} = \frac{1}{r}\frac{\partial u_\theta}{\partial \theta} + \frac{u_r}{r} = \frac{1}{E}(\sigma_{\theta\theta} - \nu\sigma_{rr}) \tag{2-121}$$

2.11. Summary and Conclusions

The present experimental-analytical hybrid-method to stress analyze structures fabricated from isotropic or anisotropic materials only requires knowing the unknown Airy coefficients to stress analyze the structures. The unknown Airy coefficients can be determined using displacement components measured by DIC or isopachic stresses recorded by TSA. This hybrid-method fulfills equilibrium, satisfy strain compatibility and local traction-free boundary conditions.

Purely analytical solutions tend to be available for only simple, finite geometries subjected to simple loading. Real-world problem often involves complex, finite shapes and complicated boundary conditions. The present technique of processing measured data using stress functions enable one to obtain solutions to complicated, finite shapes subjected to complicated loading. However, one should be careful while analyzing certain cases using this technique. For example,

while results of Chapter 5 demonstrates reliable results for a finite elliptically-perforated component, the mapping function employed assumes infinite geometry.

Chapter 3. Experimental Techniques

3.1. General Comments

Increasing energy cost and a need for reduction in carbon emissions have necessitated the interest in designing safety-critical aerospace, naval and automotive structures using light-weight composite materials. Accurate assessment of structural integrity is critical for such structures. Analytical theories, finite element analyses and experimental techniques are common ways to evaluate structural integrity. However, when treating structures with complicated geometry and loading, all of the above-mentioned approaches face challenges and involve compromises in the final results. Material anisotropy can further complicate the situation.

Among the numerous available full-field experimental techniques to stress analyze composite materials non-destructively are photoelasticity (PSA), thermoelastic stress analysis (TSA) and optical forms such as interferometric or non-interferometric optical techniques. Common interferometric techniques are holography, moiré and speckle interferometry and non-interferometric techniques include grid methods and digital image correlation (DIC) [30].

Each of the above methods faces limitations regarding the type of applied load, any surface preparation or experimental requirements, plus what mechanical quantities or experimental data are extracted. Such examples are PSA requiring sensitive coating on opaque materials, TSA requires cyclic loading to ensure adiabatic condition and interferometric techniques have strict stability requirements [31]. Interferometric methods such as digital/electrical speckle pattern interferometry (DSPI) or laser shearography can be difficult to use outside the laboratory due to their high sensitivity to environmental conditions, rigid body motion, vibration and air-flow. Slight

interruption in any of these factors can affect the reliability of the displacement/strain measurements. Examples include where vibration isolation is needed [32]. However, DSPI possibly offers the highest sensitivity and accuracy for full-field displacement measurements of very small displacements.

Many challenges associated with several of the above-mentioned experimental techniques are overcome by DIC and TSA. DIC is becoming an extremely popular and robust experimental mechanics tool due to its minimal surface preparation requirements, ease of implementation, simple testing requirements and capability at various scales [33–35] and speed [36]. DIC-measurements tend to be less sensitive to rigid body motions than some other methods [32]. However, due to the speckle pattern requirements and its sensitivity to fluctuation in source light intensity, DIC can be challenging when working with very large deformations or under elevated temperature conditions. Reference [32] discusses aspects such as suitable DIC paints and illuminations to employ for very large deformation measurements. TSA is another contactless technique for full-field stress analysis of loaded members. TSA requires cyclically loading the structure, which might not always be practical. However, an advantage of TSA is not requiring differentiating the recorded data.

3.2. Digital Image Correlation (DIC)

3.2.1. General Overview

DIC is an effective optical tool for full-field deformation measurements [14]. It can provide important information regarding structural design, optimization, mechanical integrity, quality control and assurance. DIC is based on the principle of tracking common points on two or more

images. Advancement in computer processing power and imaging technologies are contributing factors in the rapid popularity and prevalence of DIC. It finds applications in experimental mechanics and optics for deformation, shape and motion measurements. DIC has been addressed in the literature by several different names, e.g., digital speckle correlation method (DSCM), texture correlation, electronic speckle photography (ESP) and computer-aided speckle interferometry (CASI) [30].

DIC offers large measurement ranges and is suitable for static and dynamic measurements. DIC surface deformation measurements range from macroscopic to microscopic to nanoscopic scale [32]. The methodology is based on processing grey-scale values of digital images representing the specimen surface before and after deformation. The associated data analysis software is based on well-established subset-based correlation algorithms. DIC has evolved into a very effective and popular experimental technique due to the simplicity it offers in full-field, non-contact displacement and hence strain measurements. DIC can be used to quantitatively determine the deformation fields for virtually any materials and loads. These includes metals, composites, woods, polymers and biological materials under mechanical, thermal or other forms of loading [30,32].

Measurement accuracy in DIC can be affected by several factors, e.g., sub-pixel optimization algorithm, subset shape function, subset size, sub-pixel intensity interpolation scheme, camera resolution, camera lens optical quality, lens distortion and image noise [30]. When using DIC to stress analyze composite materials, additional factors such as laminate ply orientation, anisotropic material properties, size of any discontinuities and filter size can affect accuracy [13]. DIC-measurements are also influenced by human handling factors [30].

3.2.2. Basic Working Principle of DIC

DIC is an optical method that utilizes techniques such as image tracking and registration to accurately measure two-dimensional or three-dimensional changes in digital images [14]. It compares the speckle patterns between any two deformation states of a loaded structure's surface. The applied speckle pattern imposes a certain grey-value distribution over the surface of interest and thus creates a virtual grid of subsets of a certain size and shape. A camera is used to record this pattern when the loaded structure undergoes deformation [14,37].

3.2.3. Advantages of DIC

Advantages of using DIC over other experimental techniques include the following: provides full-field displacement information, non-contacting, non-destructive and does not require cyclic loading. DIC is a relatively inexpensive, simple but accurate technique. It requires minimal surface preparation and is cost effective compared to other techniques such as speckle interferometry. The DIC experiments can easily be repeated and provide better result accuracy than manual measurements. Moreover, DIC is not limited to laboratory environment. The method essentially requires no special lighting and for self-textured materials does not even require any surface preparation.

3.2.4. Applications of DIC

DIC is applicable to a wide variety of engineering problems. Examples include [38] displacement/strain measurement in diverse range of materials, fracture studies to locate crack-tip

and monitor crack propagation, detecting damage development in anisotropic members, fatigue [39], structural deflection monitoring, high temperature strain mapping such as in laser welding [40,41], vibrational analysis, impact studies, infrastructure inspection and assessment and medical image tracking and scanning.

3.2.5. Historical Development of DIC

Though in the early 1950's Gilbert Hobrough first attempted a form of DIC, the ground-breaking developments of DIC started in the early 1980's. In 1982 Peters and Ranson [42] first proposed the use of DIC-like computer-based image acquisition and deformation measurements in material systems. With developed numerical algorithms and optically recorded images, Sutton and colleagues [14,43,44] significantly contributed in developing the original concept of DIC and made it practically suitable for variety of applications. Around 2005 DIC made rapid development in the field of experimental mechanics and optics [14,30]. The DIC correlation algorithm gradually developed and hence improved DIC accuracy and efficiency. The original DIC concept by Peters and Ranson [42] had one-pixel accuracy, while Sutton et al. [43], using a technique called coarse-fine method and bi-linear interpolation between the pixels, improved the accuracy. Bruck et al. [44] subsequently introduced the Newton-Rapson search method and bi-cubic pixel interpolation which improved the measurement accuracy and computational time by an order of a magnitude. Chen et al. [45] further improved the DIC accuracy by using spline interpolation. Methods such as the gradient method [46] and curve fitting method [47] are faster than the Newton-Rapson method but less accurate. Pan et al. [48–51] made significant contribution in decreasing the computational time of the Newton-Rapson based DIC algorithms.

3.2.6. Principle of Correlation Algorithm

DIC measures displacement by tracking grey-scale pattern in small neighborhoods (typically called subsets) of the unloaded and loaded structure during the deformation process. In general, the correlation algorithm used in DIC calculates a correlation coefficient, *c*, that represents the similarity between the grey-scale distribution of the subsets in different images of a structure. The correlation coefficient, *c*, is defined in equation (3-1) as [32]

$$c(\Delta x, \Delta y) = \frac{\sum_x \sum_y I_1(x,y) I_2(x+\Delta x, y+\Delta y)}{\sqrt{\sum_x \sum_y I_1^2(x,y) I_2^2(x+\Delta x, y+\Delta y)}} \tag{3-1}$$

where, subscripts 1 and 2 represent image 1 (typically, the undeformed situation) and image 2 (the deformed configuration), respectively. I_1 and I_2 are the pixel intensities at location (x, y) of image 1 and at location ($x + \Delta x$, $y + \Delta y$) of image 2, respectively. The maximum value of the correlation coefficient, *c*, is one. At $c = 1$ represents the grey-scale distribution of the two subsets being identical. Thus, the closer the value of *c* is to one, the more similar the two subsets are. This is the fundamental principle of the correlation techniques. DIC tracks a point by finding the maximum correlation coefficient, *c*, for all the subsets between the initial (undeformed) and subsequent (deformed) images to provide full-field displacement measurements of a loaded structure [32]. Once the displacements are measured by DIC, these displacement data are then numerically differentiated to obtain strains. Among other factors, accuracy of the DIC strains also depends on the type of equations used to evaluate strains from the measured displacements. The following Lagrangian strain model is well suited for determining strains in DIC [32]

$$\varepsilon'_{xx} = \frac{\partial u}{\partial x} + \frac{1}{2}\left[\left(\frac{\partial u}{\partial x}\right)^2 + \left(\frac{\partial v}{\partial x}\right)^2 + \left(\frac{\partial w}{\partial x}\right)^2\right] \tag{3-2}$$

$$\varepsilon'_{yy} = \frac{\partial v}{\partial y} + \frac{1}{2}\left[\left(\frac{\partial u}{\partial y}\right)^2 + \left(\frac{\partial v}{\partial y}\right)^2 + \left(\frac{\partial w}{\partial y}\right)^2\right] \tag{3-3}$$

$$\gamma'_{xy} = \frac{1}{2}\left[\frac{\partial u}{\partial y} + \frac{\partial v}{\partial x} + \frac{\partial u}{\partial x}\frac{\partial u}{\partial y} + \frac{\partial v}{\partial x}\frac{\partial v}{\partial y} + \frac{\partial w}{\partial x}\frac{\partial w}{\partial y}\right] \tag{3-4}$$

where ε'_{xx}, ε'_{yy} and γ'_{xy} are Lagrangian normal and shear strains in *x*-*y* coordinates, respectively. Equations (3-2) through (3-4) shows that for accurate DIC strain determination involving large deformations, a 3D-DIC is needed as it provides information regarding the out-of-plane motion, *w*. The Lagrangian strains can be transformed to engineering and true strains with the help of relevant transformation equations.

3.2.7. Experimental Details for DIC

Displacement measurement using DIC involves the use of high-performance digital cameras with CCD sensors and a high-quality optical lens, and high-capacity data acquisition and post-processing software. In addition to laboratory customized and designed DIC packages, there are several powerful commercially available DIC packages.

To perform a DIC test necessitates a random speckle pattern to be applied to the specimen surface. For 2D-DIC, the surface to be analyzed must be flat and parallel to the camera's CCD sensor. This is to ensure that the camera's optical axis is perpendicular to the test specimen's

surface. For 2D-DIC, the out-of-plane motion (acknowledging the Poisson's effect) of the loaded specimen should be small enough to be neglected. Image noise should be minimal. Digital images of the loaded structures are typically recorded at certain load intervals. A digital image of the unloaded structure is also taken to serve as a reference image for the correlation process. The DIC images are captured and post-processed by the correlation algorithm-based software.

3.2.8. Speckle Pattern

A random speckle pattern on the specimen surface is a pre-requisite for DIC. The random pattern works as unique markers to correlate displacement between the undeformed and deformed states of the loaded member. The random speckle pattern provides a random grey-intensity distribution over the DIC specimen. When the structure is loaded, the speckle pattern deforms along with the specimen and serves as a carrier for the deformation information [30]. Many techniques have been used to generate unique and reproducible speckle patterns. The natural textures of certain material surfaces can serve as the speckle pattern or the latter can be artificially applied by using paints (either by spraying/stamping or otherwise), hand drawing, chemical etching, computer generated images, atomization process, laser-beam and speckle-projections [52]. Errors in the DIC-measurements based on how the speckle patterns were applied have been analyzed. The naturally-textured surfaces provide the least unique pattern and can result in high measurement errors. The technique of manual drawing on the test object is time consuming and not practical for large scale or bulk quantity testing. Laser-beam and speckle-projection techniques face the challenge of adverse refection effects. Computer-generated images are popular due to their uniqueness, ease to generate, well-controlled deformation and reduced-noise characteristics.

However, the most popular way of generating speckle patterns for DIC-measurements is the paint-spraying technique. For specimens with paint sprayed speckle patterns, the DIC-measurements contained the least amount of error. However, manually applied speckle pattern quality can be highly dependent on personal features of the person applying the paint. Thus sprayed speckle patterns might not always provide the least amount of DIC-measurement errors [52–54].

DIC-measurement heavily depends on the quality of the applied speckle pattern. Speckle quality refers to the grey-scale distribution characteristics, speckle sizes, density and contrast between the applied dots and its background. Minimizing errors in DIC-measurements necessitates a systematic unique speckle pattern with repeatability [52]. Measurements have been taken to evaluate the quality of the speckle pattern using standard parameters such as image histogram, mean speckle size, mean subset grey-value fluctuation and sum of the squares of subset intensity gradients [52,54]. Optimal subset size typically varies from 2 to 5 speckles per pixel. High mean intensity gradient and subset fluctuation are desirable in the speckle pattern as they contribute to less error in the DIC-measurements [52].

3.2.9. Image Source

The correlation process of DIC is not restricted to certain kinds of optical images, thus allowing for a wide range of sources and flexibility for the DIC images. Surface roughness maps, conventional CCD or personal digital cameras, high speed videos, macroscopic or microscopic images can all be used as DIC images [38].

3.2.10. Illumination Source

Initially both the white-light speckle patterns (patterns with random grey-scale intensity) and laser-speckle patterns were used in DIC. However, laser-speckle patterns require a coherent light source such as a laser to illuminate the test objects surface. Highly unacceptable de-correlation effects were found when using laser-speckle pattern under some conditions. Thus, the white-light speckle pattern method has become the most popular form of DIC. White-light speckle pattern DIC employs white light, halogen light or natural light illumination [30].

3.2.11. Calibration

Calibration of the DIC system is performed before recording the speckle images. Calibration is done to obtain the DIC results in physical units rather than in pixels. The DIC calibration process creates a 3D-coordinate system on the specimen's surface and removes measurement bias. The process also calculates the camera's intrinsic and extrinsic parameters, triangulates the camera's position and removes lens distortions [55].

The DIC system calibration can be done in two different ways. For 2D-DIC utilizing one camera, simple and easy software-based calibration is done. The image contains a known distance on the specimen surface. Using the correlation software, a physical dimension is used manually to replace the pixels of the previously known distance. The second process is a nearly automatic calibration process which is used when conducting 3D-DIC using two cameras. The system calibration is achieved by moving, imaging and analyzing a rigid calibration target in front of the pair of stereo cameras. A rigid calibration target or grid is typically included with a commercial DIC package (Correlated Solution, Inc., for the current research). The grids come in various sizes.

A calibration grid of a size that is compatible with the size of the specimen's area of interest, is considered appropriate for the calibration process [55].

3.2.12. Subset Size

A subset size directly determines the unit area of the specimen surface being used to track the displacements between the reference and target images of the unloaded and loaded specimens, respectively. The subset size is user-defined and must be selected before conducting the image correlation procedure. The subset size can vary from several pixels to more than a hundred pixels depending on the speckle quality and the size of the specimen's area of interest [54]. Accuracy of the DIC-measured displacements may depend heavily on an appropriate selection of the subset size. The subset should be large enough to contain sufficient distinct intensity pattern to be distinguishable from other subsets. However, for a small subset the load-induced deformation can be readily and accurately approximated with a first or second-order subset shape function. Larger subset size usually gives rise to larger error while approximating the underlying deformations. Therefore to achieve reliable displacement measurements from DIC, a smaller subset size is desirable [54]. Smaller subsets also have a better capability in suppressing random noise [56]. Based on the practical engineering problem and the applied speckle density, an optimum choice for subset size is made from these two contradictory demands on the size of the subset.

In practical applications attributes due to personal handling makes the subset size selection more complicated. While using the paint spraying technique to apply the speckle pattern, if the speckle pattern is applied to identical specimens but by different people, then it is most likely that the DIC results of these identical specimens under the same load and test conditions will not be

the same. Due to personal features the speckle patterns will have slightly different image contrast and speckle sizes, thus slight differences in the grey-scale distribution and substantially small differences in the DIC-measurements [54]. Moreover, the reason behind the correlation process taking place over a square subset rather than on an individual pixel is that the square subset offers more uniqueness due to it having wider variation in the grey-levels [30].

.

3.2.13. Step Size

Step size defines the spacing of the points that are analyzed in DIC. A step size of one means that the correlation analysis will be performed at every pixel over the user-defined area of interest. DIC analysis time is inversely proportional to the square of the step size [55]. A small step size means more data for the analysis and thus will require longer correlation process time.

3.2.14. Experimental Aspects to Improve DIC-Measurement Accuracy

While working with DIC both experimental factors and correlation algorithm details have the potential to influence accuracy of the result. In most cases DIC users have very little control over the commercial correlation algorithm, other than selecting some correlation variables such as the image grid size, computation speed and the filter size. However, users have full control over the experimental set-ups and procedure. Making small changes in the DIC experimental details have the potential to significantly improve the accuracy. To ensure better accuracy while using DIC the following measures should be taken [30]:

- High contrast speckle pattern - obtained in this research by using a combination of black and white paints.
- Placement of camera lens absolutely parallel to the specimen surface.
- Use of telecentric lens or placing the DIC camera slightly away from the specimen surface.
- Use of high-quality, low noise stereo cameras.
- Keep the camera stable - a tripod was used presently for this purpose.
- Ensure even illumination during specimen loading.
- Take care in selecting subset, step and filter sizes.
- Not allowing anything bright or reflective to be placed behind the test specimen.

3.2.15. Limitations and Challenges of DIC

3.2.15.1. DIC-Measurement Accuracy

The correlation algorithm details can affect the accuracy of the DIC-measured displacements. The underlying algorithm details include sub-pixel registration algorithm, shape function and pixel interpolation scheme. Related studies have suggested using higher order interpolation schemes and second order shape functions in the correlation algorithm to reduce the systematic errors in the DIC computed displacements [30]. Moreover, noise in various forms is unavoidably present in the recorded digital images of the loaded structure. These noises are commonly in the form of shot noise (variation in the number of photons sensed by the image sensor at a given exposure level), thermal noise, and cut-off noise. Illumination light fluctuation during specimen loading often induces noise in the images. Measured displacement accuracy decreases proportionally with increase in noise variance [57]. Image noise can be alleviated by the use of

high-performance hardware, frame averaging during image acquisition and by the use of correct correlation criterion.

3.2.15.2. Strain Measurements from DIC

Strains involve displacement gradients and are obtained by numerical differentiation of the DIC displacements. For the displacement gradients, the initial pixel position is obtained from the reference image and final position from the deformed image. To numerically conduct the differentiation process of the DIC-measured displacements to obtain the displacement gradients or strains, algorithms such as Genetic, Newton-Raphson, and Lavenberg-Marquart are commonly used. Any error or noise associated with the measured displacements will be amplified by the numerical differentiation process [58]. Though the numerical differentiation of displacements to obtain strains is mathematically possible, in practice it can be an extremely unreliable and risky procedure. An example of how image noise or errors in the DIC-measured displacements affect the DIC strain accuracy is presented here from a review on DIC by Pan et al. [30]. For DIC-estimated displacements, if there is a ± 0.02 pixels error in the displacement estimation, and the grid step is 5 pixels, then the error in the computed strains by forward difference is $\Delta\varepsilon = (|\pm 0.02| + |\pm 0.02|)/5 = 8{,}000\ \mu\varepsilon$ and from central difference is $\Delta\varepsilon = (|\pm 0.02| + |\pm 0.02|)/10 = 4{,}000\ \mu\varepsilon$. Such errors will likely mask the underlying strain of the tested object. Thus to improve the accuracy of the estimated strains, smoothing of the DIC-measured displacement data are done before differentiating them [30].

Accuracy of the DIC-estimated strains highly depends on the accuracy of the DIC-measured displacements and on the local displacement filtering window size. To improve strain

accuracy, smoothing of the displacement data before the displacement-differentiation process is a standard procedure employed in commercial DIC software. Selecting the appropriate filtering window size for the smoothing process is extremely critical. A smaller window size might not properly filter out the noise in the DIC images, hence in the DIC-measured displacements. On the other hand, a larger window size has the possibility to corrupt the estimated strain data by masking out the high/critical strain values [13,30,58].

3.2.15.3. In-situ Application of DIC

When working with DIC outside of the laboratory environment, one might face additional difficulties associated with environmental effects, e.g., temperature/humidity/air-flow effects, changes in surface conditions due to weathering and/or oxidation, fluctuation in image illumination intensity, issues with specimen size and geometry and difficulty with accessing a good optical view of the specimen surface [38]. However, its less sensitive experimental requirements and not requiring cyclic loading or a coherent light source makes DIC a better choice for practical in-situ applications than most other experimental techniques.

3.3. Thermoelastic Stress Analysis (TSA) [59]

3.3.1. General Overview

Thermoelastic stress analysis (TSA) is an experimental technique for full-field, non-destructive stress assessment of structures under cyclic loading. TSA measures the small temperature changes associated with stress changes, i.e., the thermoelastic effect of a cyclically

loaded structure. The cyclic loading is applied at a frequency that provides adiabatic thermal condition in the test object. TSA is applicable virtually to any material and used in a variety of applications where stress or damage assessment is necessary. It has sensitivity similar to that of commercial strain-gages. Stress sensitivity depends on the material's thermoelastic coefficient, *K*.

3.3.2. Basic Working Principle of TSA

The thermoelastic behavior of a solid is somewhat similar to that of a gaseous substance subjected to variation in volume. When compressed, the temperature of gas increases and when expanded it decreases. A similar phenomenon occurs in solids. The temperature of a solid structure increases under compression and decreases under tension. However, such temperature variations in a loaded structure are quite insignificant and previously were hard to measure. With advanced infrared photon detectors and imaging technologies, it is now possible to effectively and accurately measure these small load-induced temperature variations. Staring array sensors have enabled instantaneous full-field data recording.

3.3.3. Advantages of TSA

TSA is a contactless, full-field experimental technique. TSA requires little to no surface preparation. Neither vibration isolation nor special external illumination are required. TSA does not involve differentiating the measured data. The latter is a computationally unreliable procedure.

3.3.4. Applications of TSA

Under sufficient cyclic loading TSA applies to almost all kind of materials, be they isotropic or orthotropic. TSA has been successfully performed on metals, metal-alloys, ceramics, composites, polymers, woods, bones, bricks and concretes. TSA has a variety of applications in structural integrity analysis, fracture mechanics, fatigue, residual stress analysis, vibrational analysis and in medical science.

3.3.5. Historical Development of TSA

In 1853 Lord Kelvin [60] was the first to theoretically describe the thermoelastic effect in solids. Compton and Webster [61] experimentally verified Kelvin's theory in 1915. In 1950 Biot [62] modified the basic theory to extend it to anisotropic materials. The first TSA-measurements were done by Belgen [63] in 1967. Mountain and Webber [64] were the first to develop a commercial TSA (SPATE) system. With developments in infrared cameras and computer processing power, TSA has become an effective experimental tool to assess structural integrity and is used in many studies.

3.3.6. Thermoelasticity Theory

For a cyclically loaded isotropic member under adiabatic and reversible conditions, the variations of in-phase temperatures are related to the changes in the first stress invariant or the sum of the principal stresses/strains. In 1953 the fundamental equation to describe the thermoelastic effect was introduced by Darken and Gurry [65] as

$$\frac{\delta T}{T} = -K.\delta\sigma \tag{3-5}$$

where T is the ambient temperature, $\sigma = \sigma_{\mathrm{I}} + \sigma_{\mathrm{II}} + \sigma_{\mathrm{III}}$ is the first stress invariant, and K is the thermoelastic coefficient. K is a function of the elastic material properties and defined as

$$K = \frac{\alpha_T}{\rho_m c_p} \tag{3-6}$$

where α_T is the coefficient of thermal expansion, ρ_m is the mass density and c_p is the specific heat at constant pressure. For an isotropic member, the thermoelastic effect of equation (3-5) is directly proportional to the first stress invariant, which is related to the variation of volume. The negative sign indicates that a positive $\delta\sigma$ corresponds to a negative variation in temperature and vice-versa. For an isotropic material under plane-stressed condition equation (3-5) can be written as [59]

$$S^* = K\Delta(\sigma_{\mathrm{I}} + \sigma_{\mathrm{II}}) = K\Delta S \tag{3-7}$$

where S^* is the measured thermal signal, σ_{I} and σ_{II} are the principal stresses and S is the isopachic stress. The basic principle of thermoelasticity (equations (3-5) and (3-7)) assumes that the material's elastic and thermal properties remains constant throughout the process.

Anisotropy complicates the material's thermoelastic response. For a cyclically loaded orthotropic member, the thermoelastic effect is expressed as [66]

$$\frac{\delta T}{T} = -\frac{1}{\rho_m c_p}\sum_{j=1}^{6} \alpha_{T_j}\,\delta\sigma_j \tag{3-8}$$

For plane-stress, equation (3-8) simplifies to

$$\frac{\delta T}{T} = -\frac{1}{\rho c_p}\left(\alpha_{T_1}\delta\sigma_{11} + \alpha_{T_2}\delta\sigma_{22}\right) = -(K_1\delta\sigma_{11} + K_2\delta\sigma_{22}) \tag{3-9}$$

where the subscripts 1 and 2 represent principal material directions.

3.3.7. TSA Experimental Procedure

The main component of the TSA system is a highly sensitive infrared camera capable of detecting small temperature changes in a cyclically loaded specimen. The infrared detector converts the incident radial energy from the loaded structure into electrical signals. Modern TSA cameras employ a sensitive focal-plane array sensor. These cameras require manual focusing.

The present TSA research uses a commercial Delta Therm system (by Stress Photonic, Inc., Madison, WI). The provided Delta Therm DT1410 camera consists of an indium antimonide (InSb) focal-plane array with a photon response wave bandwidth of 3-5 μm. The 256 × 230 or 256 × 256 arrays are commonly used, but infrared detectors with 1,024 × 1,024 array resolution are also available.

To improve the camera's infrared detectivity and reduce background radiation effects, one typically cools the camera detector to about 77 K when recording. For this the camera detector is

surrounded by a dewar filled with liquid nitrogen to keep it sufficiently cool. The detector cooling process takes about 20 minutes to an hour to achieve thermal stability.

To perform a thermoelastic test the specimen is cyclically loaded at a suitable frequency to achieve adiabaticity. The applied cyclic load is selected such that without damaging the specimen it ensures good TSA signals with low signal-to-noise ratio [66]. The load-induced temperature variations of the loaded specimen surface are recorded by the infrared camera. The system is equipped with an analog lock-in unit device. The lock-in unit serves as the system's signal processing unit. The applied load is indicated in the lock-in unit as the reference signal. The reference signal is usually generated by the loading-frame's function generator. The lock-in unit combines and filters the reference signal with the infrared detector's output signal from which it extracts the specimen's actual thermoelastic response. The present Stress Photonics infrared camera captures several images of the loaded specimen surface per unit time (1,000 frames per second) to compensate for signal noise. The TSA images are processed and correlated to the associated dynamic stresses by algorithms based on thermodynamics principles.

3.3.8. TSA Surface Preparation

TSA specimens require minimum surface preparation. To improve thermal emissivity and reduce reflection of incident radiations from the test object's surface, a thin black coating is typically applied on the test surface before performing TSA. Metals and materials with gloss-finish surfaces mostly requires the black coating. To avoid non-adiabatic effects and reduced thermoelastic response from the TSA specimen, the coating thickness should be within 20-30 μm

and the loading frequency between 5–200 Hz [59]. Commercial high-temperature flat black paints with emissivity greater than 0.9 are suitable for the TSA surface coating.

3.3.9. TSA Calibration

Performance and reliability of TSA depends on calibrating the temperature changes of the system signal, S^*, with the load-induced stress, S, in the structure. A common TSA calibration procedure is to experimentally evaluate the test material's thermoelastic coefficient, K. The calibration specimens generally employ a simple geometry and loading. Examples of common types of calibration specimens include uniaxial tensile coupons, beams subjected to four-point bending and diametrically loaded disks. The TSA calibration specimen and test structure must be of the same material and have the same surface coating. They should be tested on the same day using the same loading frequency and under the same environmental conditions. Orthotropic materials require testing two calibration coupons, one in each of the two in-plane principal material directions.

3.3.10. Adiabaticity and Phase Condition Monitoring

The fundamental concept of TSA assumes system adiabaticity and reversibility. Therefore, the selected load frequency should ensure adiabatic material response. A suitable frequency required to achieve (essentially) adiabaticity depends on the test material's thermal conductivity and stress gradients present in the loaded structure. The loading frequency is a function of the

material's thermal conductivity. For aluminum and graphite-epoxy composite the 20-25 Hz frequency range is typically suitable to ensure adiabatic response under cyclic loading.

The adiabatic condition of the loaded system is monitored by checking the phase-shift between the response and reference signals. Any heat transfer occurring within the test specimen or surface coating will be indicated by a shift between the two signals, i.e., a phase-shift will indicate non-adiabatic response. Adiabaticity can be a major concern in laminated composite structures as there is a possibility of heat transfer between the adjacent laminate plies as well as high stress gradients at the edge of cutouts. Heat transfer between a loaded component (of virtually any material) and its surrounding is assumed to be negligible.

3.3.11. Limitations and Challenges with TSA

3.3.11.1. Orthotropic Material Testing

Stress distribution in composite materials depends on its constitutive material properties, fiber orientation and laminate ply stacking sequence. This complicates TSA in composites. In laminated composites, internal heat transfer between adjacent plies might be significant. Thermoelastic response might therefore no longer only depend on the external surface-ply response.

3.3.11.2. Image Noise

TSA images typically contain some noise, especially near edges and therefore require noise filtration. For structures with cracks and notches that give rise to large spatial gradients or singularities when loaded, TSA signal filtering can mask the most critical stresses. This affects the measurement accuracy.

3.3.11.3. Unreliable Edge Data

Recorded TSA information at and near edges is typically unreliable. This is due to the detector having finite spatial resolution. The camera's infrared detector, when detecting a pixel along an edge, takes information partly from the loaded specimen and partly from the stress-free background. TSA information along an edge is hence unreliable. The quality of the TSA-measured edge information is further affected adversely by the applied cyclic loading. As a result of the cyclic loading, an individual point on the specimen surface will generate different radiation signals while occupying different spatial locations.

3.3.11.4. Adiabaticity Concerns

Inadequate loading frequencies, anisotropic material response and the surface coating can compromise the adiabatic response of a thermoelastic analysis. If working with TSA outside the laboratory environment, cyclically loading of the structure might not be possible. Also, under hostile environmental conditions (elevated temperature and high humidity) the surface coating might experience viscoelastic changes and contaminate the TSA results.

3.4. Discussion and Conclusions

TSA and DIC are versatile structural stress assessment techniques. Both methods are comparatively simple relative to experimental and specimen requirements. The availability of advanced software and hardware, signal and image processing technologies, and computers having high processing capability, enable new developments and applications of TSA and DIC. However, each of the method faces some challenges. The cyclic loading requirement of TSA is not always practical for real world and/or industrial applications. Differentiating DIC-measured displacement data to obtain strains is not a numerically reliable procedure. Regions close to or along the edges of structural discontinuities typically contain the most critical stresses. However, neither DIC nor TSA provides reliable information near the boundaries of a cutout. Fortunately, many of these challenges can be overcome by processing the recorded information (thermal or displacement) using stress functions as done in this thesis.

Chapter 4. Hybrid Photomechanical Stress Analysis of Finite Orthotropic Plate with Central Circular Hole using Single Measured Displacement Component

4.1. Introduction

Stresses, particularly those at geometric discontinuities, can influence structural integrity of engineering components. Motivated by the prevalence of cutouts in components, the objective of this study is to demonstrate ability to stress analyze finite, circularly-perforated, orthotropic composite plates whose external loading may be unknown. Recognizing difficulties in obtaining purely theoretical or numerical solutions, this study presents a hybrid means of stress analyzing such structures. Individual stresses, including on the edge of the hole, are obtained in a loaded, finite, graphite-epoxy $[0_{13}/90_5/0_{13}]$ laminated composite containing a round hole by processing measured values of a single displacement component with an Airy stress function in complex variables. Displacement information is obtained by digital image correlation (DIC). Traction-free conditions are satisfied analytically at the edge of the hole using conformal mapping and analytic continuation. Stresses satisfy equilibrium and strains satisfy compatibility. Significant features of the technique include its wide applicability, it smooths the measured information, does not require knowing the applied loading, and the rigorous mechanics foundation by which strains are determined from measured displacements. Results agree with those from FEM and force equilibrium.

4.2. General Overview

Composite structures with geometric discontinuities are widely used as load bearing components in various engineering applications. High strength- and stiffness-to-weight ratios often make composite materials popular over conventional isotropic, monolithic materials. Structural integrity is influenced by the stresses. While extensive stress information associated with holes or notches is available for isotropic materials, relatively little such data exists for orthotropic materials [67]. Stresses in composite structures depend on the material properties. Anisotropy often complicates the stress distributions near geometric discontinuities and their determination is important to prevent failure [68,69]. The orthotropic behavior can influence where along the boundary of a hole the most serious stresses occur [70]. Few theoretical analyses of finite orthotropic structures having cutouts are available. Like finite element analyses, they require knowing the boundary conditions. Such are often unknown in practice. Purely experimental techniques tend not to provide reliable data near the edge of a geometric discontinuity. Moreover, traditional displacement-based experimental methods of stress analysis have the additional challenge of having to differentiate the displacement data to obtain stresses. Differentiating measured data can be unreliable. Recognizing these difficulties, this study utilizes a hybrid complex variables method to perform full-field stress analysis of a loaded, finite, orthotropic plate containing a central circular hole from recorded single component of displacement. Needing only one displacement field is advantageous. For example, experimental techniques such as moiré, holography, grids or electronic speckle pattern interferometry (ESPI) necessitate additional rulings and/or optics to record two versus one in-plane component of displacement. Situations can also occur where there is a paucity or inferior quality of one or other of the in-plane displacements.

The present method of combining recorded displacement data with complex variables Airy stress functions, conformal mapping, analytic continuation and least squares is effective for full-field stress analyzing perforated, finite, orthotropic structures using only a single component of displacement without requiring knowledge of the external loading conditions. The digital image correlation (DIC)-measured displacement data in the loading direction starting slightly away from the cutout are processed with an Airy stress function which satisfies equilibrium. Using conformal mapping and analytic continuation techniques, traction-free conditions are satisfied along the boundary of the circular hole.

The present hybrid technique simultaneously smooths the measured displacement data, satisfies equilibrium and compatibility, and determines individual stresses full-field, including on the edge of the hole without requiring measured information near the cutouts or knowledge of the external loading. Fatigue analysis and strength criteria necessitate knowing the independent stresses. An additional strength of the present approach is the rigorous mechanics foundation by which strains are determined from measured displacement data. Experimental reliability is demonstrated by FEM and force equilibrium.

4.3. Literature Review

Lekhnitskii [5] and Savin [6] pioneered stress analyzing perforated infinite anisotropic plates using complex variables techniques. Analytical solutions were provided for such structures based on a complex variables method which was originally proposed by Muskhelishvili [15].

Recent researchers have advantageously utilized some of these concepts by processing measured data with Airy stress functions. Experimental techniques such as moiré, strain-gages, photoelasticity (PSA), thermoelasticity (TSA) and DIC have been employed for isotropic materials. Examples include those to cracks and holes. However, orthotropy complicates the situation by introducing two complex variable planes not coinciding with the physical plane.

Publications [18,19,22,71–74] utilized complex-variables Airy stress functions to experimentally stress analyze orthotropic plates containing geometric discontinuities. These studies used strain-gage, moiré or TSA-measured information or in some cases FEA-simulated data. Lin and Rowlands [18] employed TSA to stress analyze a loaded perforated composite plate, where Taylor series representation of the stress functions with relevant mapping functions were used. Their study contributed significantly to the development of the analytical background of the present hybrid stress analysis method. Baek and Rowlands employed a somewhat similar hybrid concept as here to stress analyze orthotropic materials based on moiré [72] and strain-gage data [71]. Using similar fundamental mathematical principles, Baek et al. [73] and Khaja [74] subsequently stress analyzed a perforated glass-epoxy orthotropic plate using FEM-simulated displacement data. The input information in these approaches were FEM-predicted displacement data instead of experimentally measured information. Rhee and Rowlands used conformal mapping and stress analyzed orthotropic plates using thermoelastic information [22] and hybrid-FEM [75]. Chen [76] used conformal mapping and complex Airy stress functions to stress analyze composites plates with elliptical cutout with his developed hybrid-FEM. Lin et al. [77] employed a somewhat similar mathematical approach and Taylor expansion to stress analyze loaded plates containing cracks. Emery and Dulieu-Barton [78] employed TSA calibrated strain data to analyze a glass reinforced polymer composite plate having a circular cutout.

Gerhardt [8] also used conformal mapping and gave information on when to use a Taylor series and when to use a Laurent series. Lagattu et al. [79] and Ashrafi and Tuttle [13] employed DIC-measured displacement information to stress analyze orthotropic composites containing round holes. These latter two stress analyses necessitated measured values of both in-plane displacement components and experienced difficulties in obtaining reliable stresses on the edge of the hole. Caminero et al. [80] used DIC-estimated strain data and X-ray radiography to analyze and monitor damage in a circularly-perforated composite plate. In their study DIC-provided strain values were compared with FEA-predictions. Laurin et al. [81] studied damage patterns in composite plates with multiple circular holes using DIC.

Influenced by Lekhnitskii [5] and Gerhardt [8], a Laurent series and complex variables Airy stress functions are utilized here to process a single component of DIC-recorded displacement data and thereby evaluate the Airy coefficients. Whereas the previous moiré analyses necessitated employing both measured u- and v-displacements, the present stress analysis employs only a single component of measured displacement and is capable of providing reliable results near and at the hole's boundary. Moreover, DIC is a more simple and practical experimental approach compared to TSA, PSA and moiré.

4.4. Relevant Equations

The analytical analysis was performed based on the mathematical concepts elaborated in Chapter 2. Stresses and in-plane displacements in rectangular coordinates (x, y) of the physical plane, $z_j = x + \mu_j y$ for $j = 1, 2$; of an orthotropic plate can be expressed as a combination of Airy stress functions, conformal mapping, analytic continuation and power-series expansion (from

equations (2-68) through (2-72)). Moreover, the in-plane displacements and stresses are found to be a function of the complex variables in the mapped plane ζ_j (j = 1, 2), orthotropic elastic properties and the Airy stress coefficients c_j as [8]

$$u = 2\left(\sum_{\substack{j=-m \\ j\neq 0}}^{j=m} Re\left\{\left[p_1\zeta_1^j + p_2\left(C\zeta_2^j + B\zeta_2^{-j}\right)\right]a_j + i\left[p_1\zeta_1^j + p_2\left(C\zeta_2^j - B\zeta_2^{-j}\right)\right]b_j\right\}\right) \tag{4-1}$$

$$v = 2\left(\sum_{\substack{j=-m \\ j\neq 0}}^{j=m} Re\left\{\left[q_1\zeta_1^j + q_2\left(C\zeta_2^j + B\zeta_2^{-j}\right)\right]a_j + i\left[q_1\zeta_1^j + q_2\left(C\zeta_2^j - B\zeta_2^{-j}\right)\right]b_j\right\}\right) \tag{4-2}$$

and

$$\sigma_{xx} = 2\left(\sum_{\substack{j=-m \\ j\neq 0}}^{j=m} Re\left[\mu_1^2\frac{jc_j\zeta_1^{j-1}}{\omega_1'(\zeta_1)} + \mu_2^2\frac{-j\bar{c}_jB\zeta_2^{-j-1} + jc_jC\zeta_2^{j-1}}{\omega_2'(\zeta_2)}\right]\right) \tag{4-3}$$

$$\sigma_{yy} = 2\left(\sum_{\substack{j=-m \\ j\neq 0}}^{j=m} Re\left[\frac{jc_j\zeta_1^{j-1}}{\omega_1'(\zeta_1)} + \frac{-j\bar{c}_jB\zeta_2^{-j-1} + jc_jC\zeta_2^{j-1}}{\omega_2'(\zeta_2)}\right]\right) \tag{4-4}$$

$$\sigma_{xy} = -2\left(\sum_{\substack{j=-m \\ j\neq 0}}^{j=m} Re\left[\mu_1 \frac{jc_j\zeta_1^{j-1}}{\omega_1'(\zeta_1)} + \mu_2 \frac{-j\bar{c}_j B\zeta_2^{-j-1} + jc_j C\zeta_2^{j-1}}{\omega_2'(\zeta_2)}\right]\right) \tag{4-5}$$

The complex material properties, μ_j (for $j = 1, 2$), are the roots of the characteristic equation (2-17). The complex quantities p_j, q_j (for $j = 1, 2$), B and C are defined in equations (2-33), (2-50) and (2-51), respectively, and depends only on the orthotropic constitutive material properties. In these expressions of in-plane displacements and stresses the traction-free boundary conditions are satisfied by conformal mapping and analytic continuation (according to equation (2-52)) in regions adjacent to the cutout. Laurent series was used to expand the complex stress functions as the circular hole from the physical z-plane is mapped to a unit circle in the ζ-plane, Figure 4-1. The variables ζ_j for $j = 1, 2$ are obtained from the inverse of the mapping function and are also a function of the plates x-y coordinate locations and elastic properties.

For orthotropic plates with circular cutouts, the following mapping function is used for the conformal transformation of a unit circle and its exterior region, R_ζ, in the ζ-plane to a circular hole of radius R and its exterior region, R_z, in the z-plane, Figure 4-1, [19,22,73,74]

$$z_j = \omega_j(\zeta_j) = \frac{R}{2}\left[(1 - i\mu_j)\zeta_j + \frac{1 + i\mu_j}{\zeta_j}\right], \quad j = 1, 2 \tag{4-6}$$

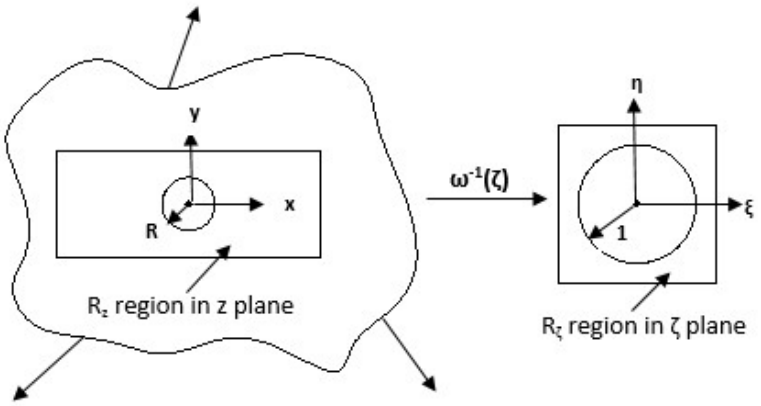

Figure 4-1: Mapping edge of circular hole from physical z-plane to unit circle in ζ-plane

The inverse of the mapping function in equation (4-7) maps the circular hole of radius R from the z-plane to a unit circle in the ζ-plane, Figure 4-1.

$$\omega_j^{-1}(z_j) = \zeta_j = \frac{z_j \pm \sqrt{z_j^2 - R^2(1 + \mu_j^2)}}{R(1 - i\mu_j)}, \qquad j = 1, 2 \tag{4-7}$$

The branch of the square root of the above equation (4-7) is chosen so that, $|\zeta_j| \geq 1$ for $j = 1, 2$. For convenience, the coordinate system is chosen so that, the coordinate origin is at the center of the plate's circular cutout. The variables $\omega'_j(\zeta_j)$ in the expression for the in-plane stresses of equations (4-3) through (4-5) are the derivatives of the mapping functions $\omega_j(\zeta_j)$ of equation (4-6) with respect to the complex variables ζ_j for $j = 1, 2$, as such

$$\omega_j'(\zeta_j) = \frac{R}{2}\left[(1 - i\mu_j) - \frac{1 + i\mu_j}{\zeta_j^2}\right], \qquad j = 1,2 \tag{4-8}$$

In the expressions for the in-plane displacements and stresses of equations (4-1) through (4-5) the only unknowns are the Airy coefficients c_j. The Airy coefficients c_j are complex numbers, i.e., $c_j = a_j + ib_j$, where a_j and b_j are real numbers. For the loaded plate with central hole, and due to the symmetry, the value of j never equals zero nor an even number. Moreover, as the plate is symmetric with respect to both the x- and y-axes, Figure 4-2, it is sufficient to analyze just one quadrant of the plate. Using DIC-measured displacement data in equation (4-1) or (4-2), combined with equation (4-7), the Airy coefficients c_j are evaluated. Knowing the Airy coefficients, the full-field stress analysis of the circularly-perforated orthotropic plate is possible from combining equations (4-1) through (4-5) with equations (4-7) and (4-8).

4.5. Material Properties

The orthotropic plate was made from a $[0_{13}/90_5/0_{13}]$ graphite-epoxy laminate. Material properties of the composite laminate were determined experimentally. Tension tests were conducted along each of the strong/stiff (highest fiber) direction, perpendicular to the strong/stiff direction and ± 45° to the strong/stiff direction to get E_{11}, E_{22}, ν_{12} and G_{12}, respectively, Table 4-1. Details on the tested material properties are attached in Appendix A.

Table 4-1: Material properties of the $[0_{13}/90_5/0_{13}]$ graphite-epoxy laminate according to the coordinates of Figure 4-2

Material Property	Symbol	Value	Units
Elastic modulus in strong/stiff direction	E_{11} or E_{xx}	104.1	GPa
Major Poisson's ratio	ν_{12} or ν_{xy}	0.155	Dimensionless
Elastic modulus perpendicular to strong/stiff direction	E_{22} or E_{yy}	28.1	GPa
Shear modulus	G_{12} or G_{xy}	3.0	GPa

4.6. Plate Preparation

4.6.1. Plate Geometry

A finite-width, orthotropic plate containing a central circular hole (Figure 4-2) was prepared and its displacement data were measured using DIC. The plate is L = 27.94 cm (11") long, W = 7.62 cm (3") wide and t = 5.28 mm (0.208") thick. The central circular hole has a diameter of D = 2.54 cm (1"), Figure 4-2 and Table 4-2. The plate is symmetric both about the horizontal and vertical axes.

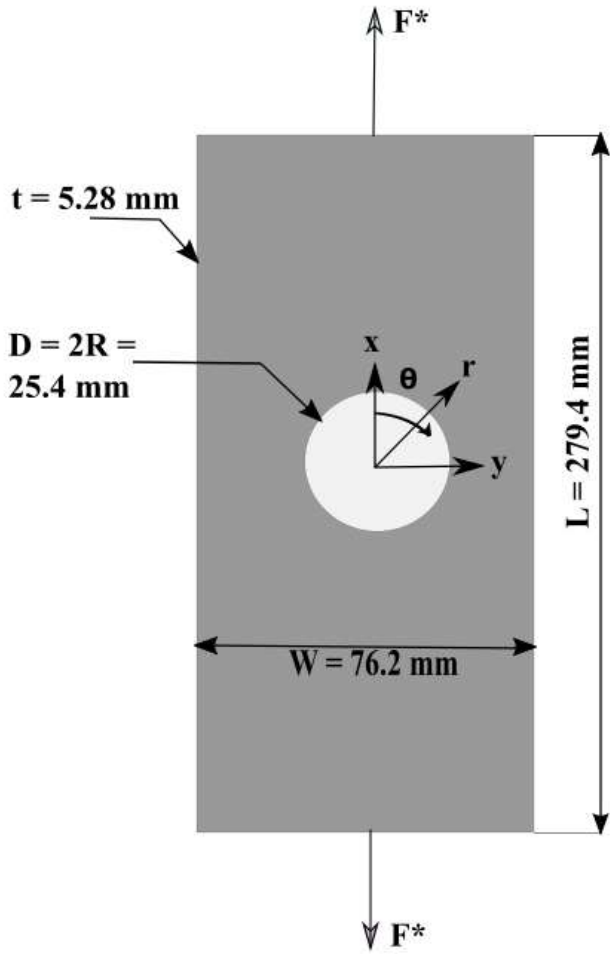

Figure 4-2: Circularly-perforated loaded [$0_{13}/90_5/0_{13}$] graphite-epoxy laminated plate

Table 4-2: Details of circularly-perforated orthotropic plate and loading

Material	$[0_{13}/90_5/0_{13}]$ graphite-epoxy orthotropic laminate
Supplier	Kinetic Composite, Inc., Oceanside, California
Thickness, t	5.28 mm (0.208")
Length, L	27.94 cm (11")
Width, W	7.62 cm (3")
Diameter, D	2.54 cm (1")
Plate finiteness, D/W	0.33
Symmetry	Both horizontally and vertically
Loading for DIC analysis	From 0 to 11.6 kN (2,600 lbs) in intervals of 889.6 N (200 lbs)
Load for DIC-hybrid stress analysis, F^*	4.5 kN (1,000 lbs)

4.6.2. Plate Fabrication

Water-jet cutting was used to prepare the composite plate with the central circular hole from a sheet of graphite-epoxy laminate. A water pressure of 413.69 MPa (60,000 psi) along with abrasive substances were used in this technique to generate the highly pressurized water-jet. Details on how to create finite orthotropic plates with cutouts using water-jet cutting and steps followed to avoid any fabrication induced defects in the plates are provided in Appendix B.

4.6.3. Application of Speckle Pattern

A speckle pattern needs to be applied on the plate's surface to conduct the DIC test. Using the pixel location of the speckle pattern on the unloaded plate, a correlation is made with the

patterns of the loaded plate. The speckle pattern must be random. White random dots on a black surface were used to create the speckle pattern, Figure 4-3. To avoid any reflection from the plate surface and to provide sharp contrast between the black background and white dots, the surface was first coated with a thin layer of black paint.

The machined plate surface was first lightly polished using 400-grit emery cloth and cleaned using a water-based mild cleaner (M-Prep Conditioner A followed by M-Prep Neutralizer 5A) from Vishay Precision Group - Micro-Measurements [82]. Special care was taken while polishing the plate, to avoid rounding off the hole boundary or changing the actual hole geometry. The cleaned surface was painted with Rust–Oleum Ultra Cover-Flat black paint and allowed to dry. Only a very thin layer of the black paint was applied so that it properly covers the entire surface area of the plate and does not change the shape of the surface or induce shearing effects due to coating thickness [83]. On top of the dried black paint, the white dots were created using Rust–Oleum Ultra Cover–Flat white paint. The dots were achieved by lightly applying pressure on the paint container trigger to get a discontinuous spray of paint. The paint container was held perpendicular at a distance from the plate's surface so that the paint drops randomly fall on the surface.

(a) (b)

Figure 4-3: (a) Plate covered with a thin layer of black paint and (b) Speckle pattern on the plate

4.7. Experimental Set-up and Details

4.7.1. Plate Loading

The 89 kN (20,000 lbs) capacity, open-loop, hydraulic-grip, MTS machine located at UW – Madison's Fatigue Lab was used to load the plate. The plate was carefully mounted between the hydraulic-grips to avoid any out-of-plane bending. To achieve symmetrical loading, care was taken to mount the plate symmetrically about the horizontal *y*-axis to ensure that the gripped areas on the top and bottom of the plate were exactly at the middle. A 3D-DIC test was conducted using two cameras. The 3D-DIC test includes information regarding the out-of-plane displacement, Figure C-1 of Appendix C. The plate was only subjected to uniaxial tensile load so there should

be no out-of-plane motion other than Poisson's effect. From the DIC-recorded data, the absence of the rigid out-of-plane motion while conducting the experiment was confirmed. Although both 2D- and 3D-DIC data were collected, the plane-stress analysis was conducted using the 2D-DIC information. The 3D-DIC testing was only conducted to ensure no out-of-plane motion occurred beyond the Poisson's effect.

Using the MTS loading machine, a vertical tensile static load varying from essentially zero to 11.6 kN (2,600 lbs) was applied in increments of 889.6 N (200 lbs) load in the strong/stiff direction of the plate (*x*-direction). National Instrument's universal analog input module was used to monitor the applied loads. For each load, a digital image of the plate's surface was taken using the Correlated Solution's data acquisition software Vic-Snap. Information from the 2D-DIC was utilized to conduct the stress analysis.

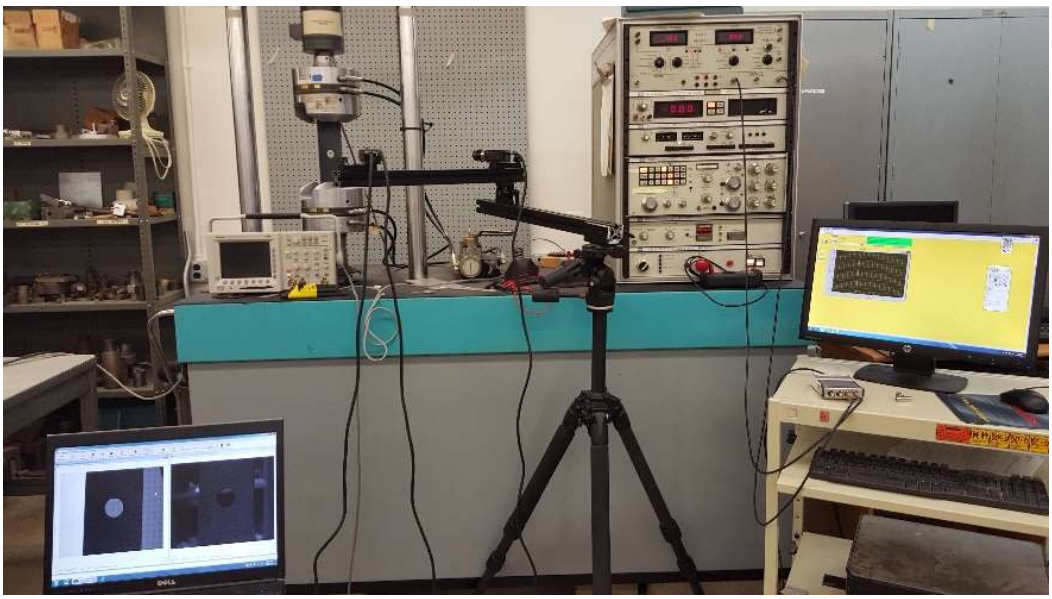

Figure 4-4: DIC experimental set-up

4.7.2. DIC Details [55]

Correlated Solution, Inc.'s (Columbia, SC 29063, USA) commercial DIC package equipped with high efficiency data acquisition and post-processing software was used in this research to measure the displacement information. The DIC package includes a pair of Point Gray digital cameras, several pairs of Schneider Xenoplan lenses with varying focal ratios and lengths, and Correlated Solution's Vic-Snap data acquisition and Vic-2D/3D post-processing software. The DIC package details are contained in the below Table 4-3.

.

Table 4-3: Correlated Solution, Inc.'s DIC details

Parameter	Equipment or Setting
Cameras	The Grasshopper (Point Grey Research), Model GRAS-50S5M-C
Imaging sensor	Sony ICX625 CCD, 2/3″ Sensor Format, 3.45 μm pixel size
Lens	CM120 BK 15 COMPACT-0901 (focal ratio: 1.9 and focal length: 35 mm)
Sensor/digitization	2,448 × 2,048 at 15 FPS (framing rate)
Pixel to inch conversion	1 pixel = 0.05 mm
Strain Resolution	50 $\mu\varepsilon$
Lighting	Ambient white light (for this research)

4.7.3. Calibration [55]

For calibrating the present DIC system using two cameras (3D-DIC), a calibration grid of the appropriate size was selected and placed over the area of interest. A calibration grid of the size

12 mm × 9 mm × 5 mm was used, Figure 4-5. Images of the calibration grid in different orientations and different angles were captured. These pictures were used subsequently to conduct the calibration analysis using the Correlation Solution's post-processing Vic-3D software. When using one camera (2D-DIC), the calibration was done by manually correlating pixel size for a known distance through Correlation Solution's Vic-2D software, i.e., marking a known distance and providing the length in terms of physical units.

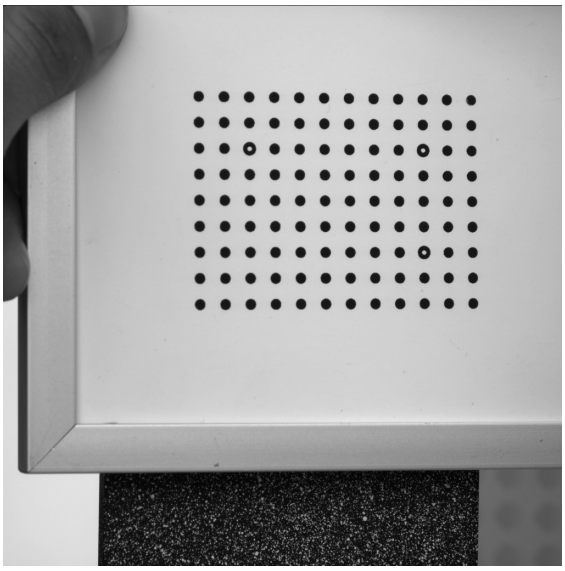

Figure 4-5: Orthotropic plate calibration with Correlated Solution, Inc.'s calibration grid

4.7.4. Subset and Step Size

DIC requires the use of a random and dense speckle pattern on the specimen that can provide unique markers to search for between the unloaded and loaded images. The DIC post-processing software assigns a predefined mesh of subsets or grids over the speckle image. From the random speckle pattern within each of these subsets, the correlation algorithm measures

displacements by matching the reference subsets in the undeformed image with the target subsets of the deformed images. The subset and step sizes are user defined. The accuracy of the measured displacement critically depends on the subset size and correlation speed on the step size. For this analysis, a subset size of 21 and a step size of 8 were used. Details on DIC systems working principles are provided in Chapter 3.

4.7.5. DIC Data Analysis

For the current analysis using Correlated Solution's Vic-2D software, the captured images were processed and correlated. In DIC, a set of images for the plate loaded at different loads need to be provided along with a reference image (digital image captured by the DIC system at zero load representing undeformed condition of the plate). The correlation algorithm tracks a group of pixels/subset and shifts the subset until the deformed image matches the reference image. Calibration scale is set using the Vic-2D/3D software so that the subset shifting can be expressed as physical units such as displacements. Once the reference image, area of interest (AOI) and calibration scale are set, the software can perform the analysis and find the speckle displacements.

User specifies the area of interest and subtracts any discontinuity from it, then using the selected subset size and step size the Vic-2D or Vic-3D software performs the analysis over the area of interest.

4.8. Finite Element Method

A motivation for developing the present technique is to enable stress analyzing orthotropic cases experimentally which cannot be analyzed numerically (e.g., inadequate knowledge of the external loads), yet FEM is used here. However, the present geometry and loading were selected so that one could obtain reliable FEM results with which to compare those from the present hybrid-method.

Having geometric and loading symmetry about both the *x*-*y* axes, only one quarter of the plate was modeled (Figure 4-6) numerically using commercial FEA tool ANSYS APDL. isoparametric elements, i.e., ANSYS element type Plane 182 with 4 nodes and 2 degrees of freedom per nodes were used to model the plate. The plate was modeled with the origin of the coordinate system located at the center of the hole. Symmetrical boundary conditions were manually imposed. High mesh density was utilized near the hole. A far-field stress of σ_0 = 11.05 MPa (1.6 ksi) was applied along the *x*-axis (strong/stiff direction) based on the applied load and the far-field cross-sectional area of the plate, using equation (4-9). The quarter-plate model consists of 26,000 elements and 26,371 nodes. The *x*-*y* coordinates of all the nodes, along with the displacement and stress components, were imported into MATLAB for post-processing and correlating the FEM-predictions with those from the DIC-hybrid analysis.

$$\sigma_0 = \frac{F^*}{Wt} = \frac{4{,}448.2}{76.2 \times 5.28}\left(\frac{\mathrm{N}}{\mathrm{mm}^2}\right) = 11.05\ \mathrm{MPa} \tag{4-9}$$

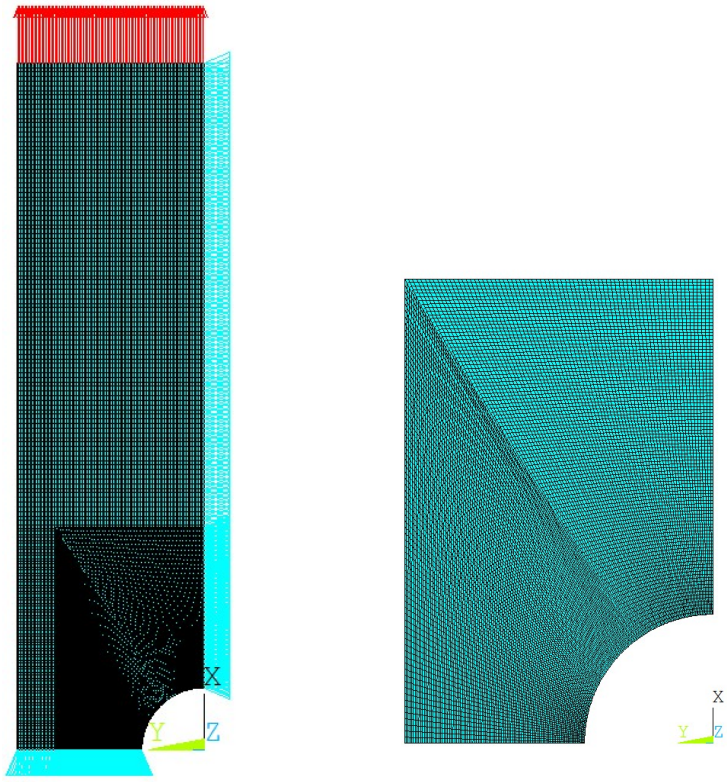

(a) (b)

Figure 4-6: FEM of the orthotropic plate with the central circular cutout

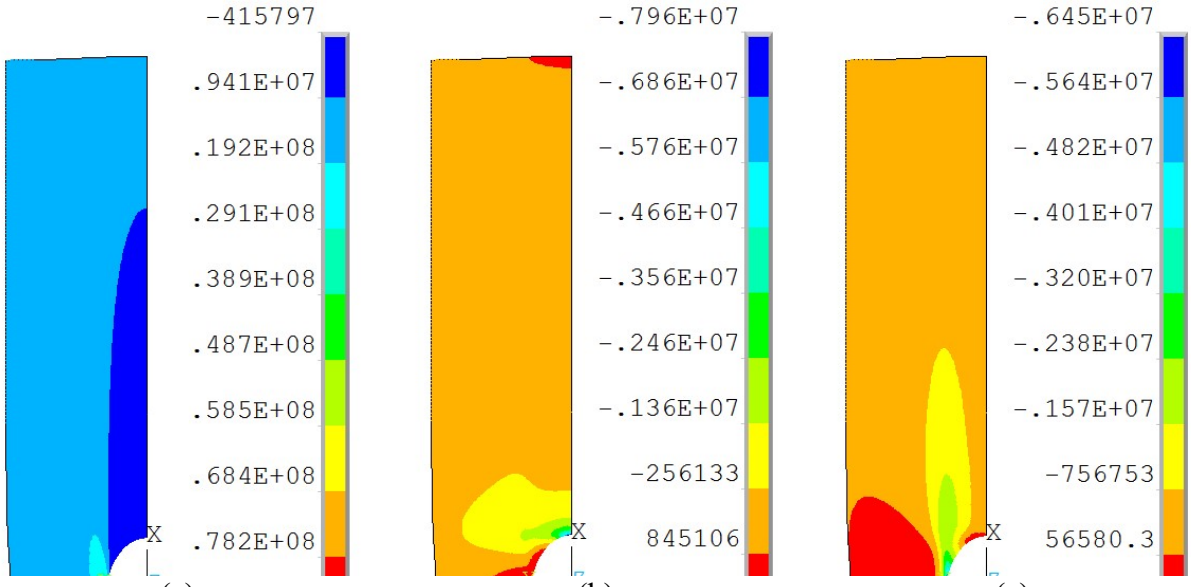

(a) (b) (c)

Figure 4-7: Contour plots for stresses (a) σ_{xx}, (b) σ_{yy} and (c) σ_{xy} from FEM (units in Pa)

4.9. Data Reduction and Analysis

The composite plate was physically loaded such that its top edge was stationary while the bottom edge moved vertically downward, Figure 4-8(a). To simulate the top and bottom ends of the laminate being extended equally, the DIC-recorded displacement data in the loading (strong/stiff direction, vertical x) direction of Figure 4-8(a) were post-processed to be zero along the horizontal ($x = 0$) axis. Acknowledging the then geometric and mechanical symmetry about the x- and y-axes, Figure 4-8(b) shows the resulting vertical displacements, u, throughout the first quadrant. Coordinate x is the loading direction. These measured u-displacements are processed as such because the analytical procedure considers the plate being extended equally from the plane passing through the coordinate origin located at the center of the hole/plate.

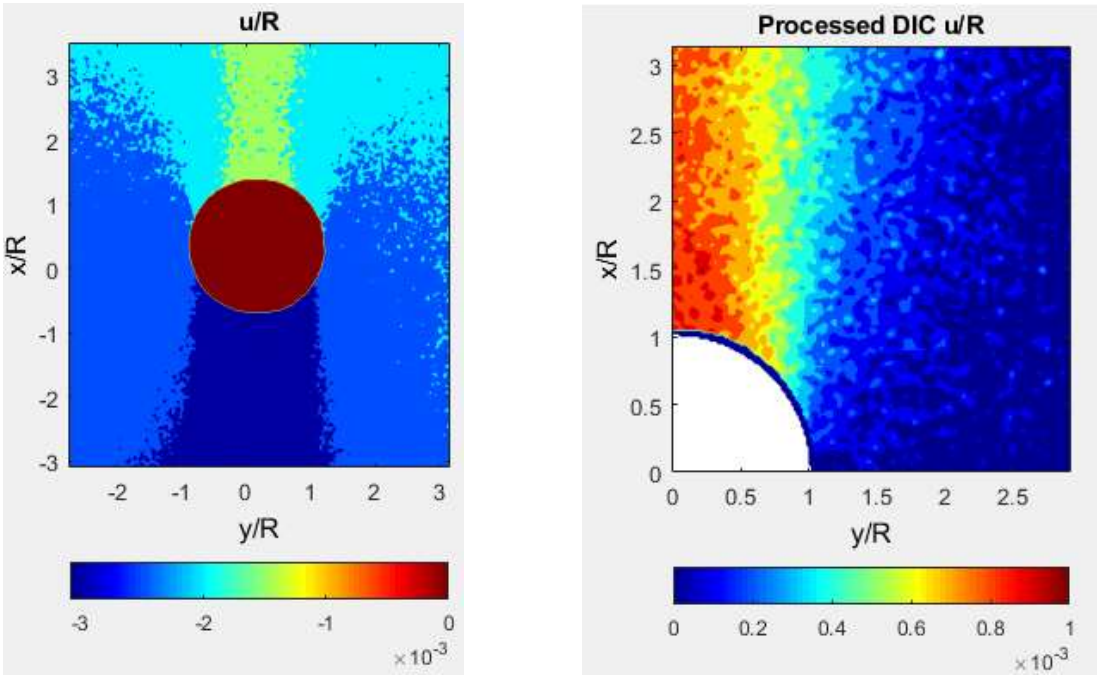

(a) (b)

Figure 4-8: DIC-measured vertical displacements u/R in vertical loading direction x, (a) DIC raw data and (b) Processed so $u = 0$ along y-axis at $x = 0$

From the u-displacement data of Figure 4-8(b), n_{DIC} = 6,448 essentially equally spaced DIC-recorded values of u were selected. Since DIC data at and near an edge are not reliable, no such displacement information was employed within a distance $0.1R$ (= 1.27 mm) from the edge of the hole (Figure 4-9). In addition to the n_{DIC} = 6,448 DIC-measured u-displacements, some symmetry and boundary conditions were employed. Stress $\sigma_{xy} = 0$ was imposed at h_1 = 3,601 equally spaced locations along $x = 0$, and $\sigma_{xy} = 0$ and $v = 0$ were similarly imposed at h_2 = 3,601 equally located points along $y = 0$. A total of $n_{total} = n_{DIC} + h_1 + 2 \times h_2 = 6{,}448 + 3{,}601 + 2 \times 3{,}601 = 17{,}251$ side conditions (pieces of information) were used to evaluate the Airy coefficients, where n_{DIC} = 6,448 are DIC-recorded u-displacement data and $h = h_1 + 2 \times h_2 = 10{,}803$ represents the applied conditions.

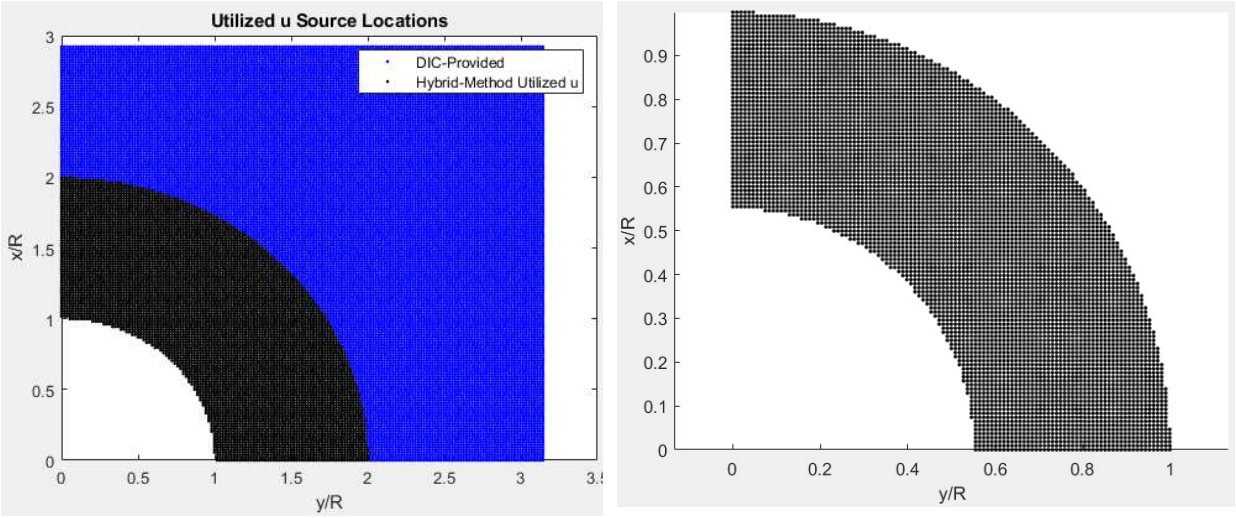

(a) (b)

Figure 4-9: Source locations of DIC evaluated u-displacements, (a) Available processed averaged over one quadrant of the plate and (b) n_{DIC} = 6,448 (black region in (a)) considered for the hybrid analysis

From equations (4-1), (4-2) and (4-5) one obtains,

$$\begin{Bmatrix} u \\ \sigma_{xy} = 0 \\ v = 0 \end{Bmatrix}$$

$$= 2Re\left(\begin{bmatrix} p_1\zeta_1^j + p_2\left(C\zeta_2^j + B\zeta_2^{-j}\right) & i\left[p_1\zeta_1^j + p_2\left(C\zeta_2^j - B\zeta_2^{-j}\right)\right] \\ -\mu_1\dfrac{j\zeta_1^{j-1}}{\omega_1'(\zeta_1)} + \mu_2\dfrac{jB\zeta_2^{-j-1} - jC\zeta_2^{j-1}}{\omega_2'(\zeta_2)} & i\left[-\mu_1\dfrac{j\zeta_1^{j-1}}{\omega_1'(\zeta_1)} + \mu_2\dfrac{-jB\zeta_2^{-j-1} - jC\zeta_2^{j-1}}{\omega_2'(\zeta_2)}\right] \\ q_1\zeta_1^j + q_2\left(C\zeta_2^j + B\zeta_2^{-j}\right) & i\left[q_1\zeta_1^j + q_2\left(C\zeta_2^j - B\zeta_2^{-j}\right)\right] \end{bmatrix}\begin{Bmatrix} a_j \\ b_j \end{Bmatrix}\right) \quad (4\text{-}10)$$

$$= 2Re\begin{Bmatrix} \text{Displacement data from DIC} \\ \text{Symmetry BC's(shear stresses)} \\ \text{BC's(transverse displacements)} \end{Bmatrix}$$

which can be written as

$$[A]_{n_{total}\times 2(m+1)}\{c\}_{2(m+1)\times 1} = \{d\}_{n_{total}\times 1} \quad (4\text{-}11)$$

where m = 1, 3…. and for $j = m$ there are 2(m+1) real Airy coefficients or k = (m + 1) complex Airy coefficients. In equation (4-11), matrix [A] depends on the plate's material properties and the x-y coordinate locations, vector $\{c\}$ consists of the Airy coefficients and $\{d\}$ includes the DIC-recorded displacement data along with the imposed symmetry and boundary conditions. The only unknowns in the above equation (4-11) are the Airy coefficients in vector $\{c\}$ which can be evaluated from equation (4-12) by least squares method. The backlash ('\') operator in MATLAB was used to evaluate the unknown complex Airy coefficients, c_j, according to equation (4-12).

$$\{c\} = [A]\backslash\{d\} \quad (4\text{-}12)$$

In the overdetermined system of linear equations (equation (4-11)), to account for experimental scatters in the measured quantities, the number of equations, n_{total}, is much greater than the number of evaluated real unknown coefficients, $2(m+1)$, i.e., $n_{total} >> 2(m+1)$.

4.9.1. Evaluating the Number of Airy Coefficients to Use

In this analysis for $n_{total} = 17{,}251$ data values, the complex coefficient $k = 2$ (motivated by Figure 4-10 through Figure 4-13) were found to be an appropriate number of complex Airy coefficients to use.

The number of Airy coefficients to use was initially determined by plotting the root mean squares (RMS) of the difference between the magnitudes of the $n_{DIC} = 6{,}448$ DIC-recorded u-displacements, $\{d\}$, with those $\{d'\}$ predicted by equation (4-1) and the $h = 10{,}803$ side conditions in equations (4-2) and (4-5), i.e., all measured information and side conditions in equation (4-10), Figure 4-10. The decision was narrowed down from the plots of condition numbers of Figure 4-11 and Figure 4-12. Although Figure 4-10 and Figure 4-12 suggests using $2 \leq k \leq 10$ and $k \leq 4$, respectively, would be reasonable, employing as few coefficients as acceptable minimizes the mathematical computation. Moreover, comparing the measured and the reconstructed displacements (from equation (4-1)) confirms the rational use of $k = 2$ complex coefficients, Figure 4-13(a). As the number of employed coefficients increases, the reproduced displacements of Figures 4-13(b) and (c) starts to deviate from the DIC-recorded data. Table 4-4 contains the values of the four real Airy coefficients.

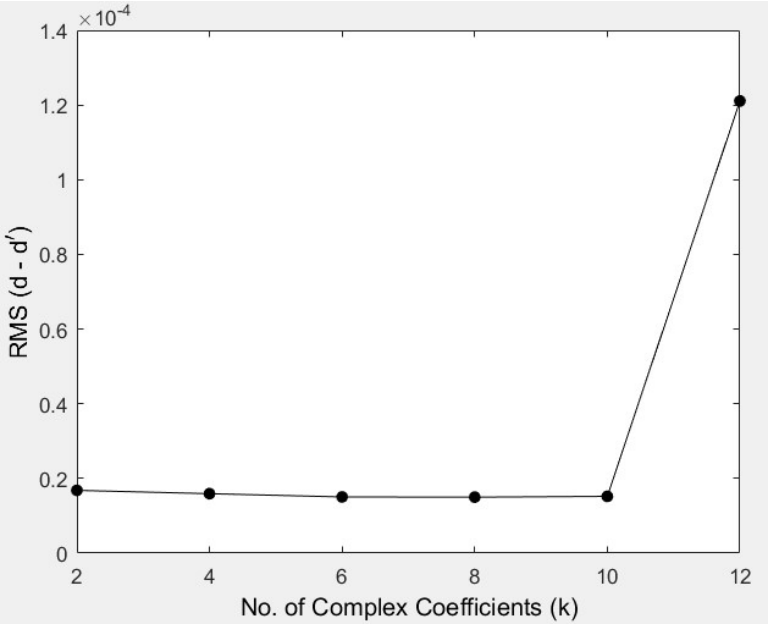

Figure 4-10: Plot of RMS versus number of complex coefficients, k, using n_{total} = 17,251 data values and Laurent series

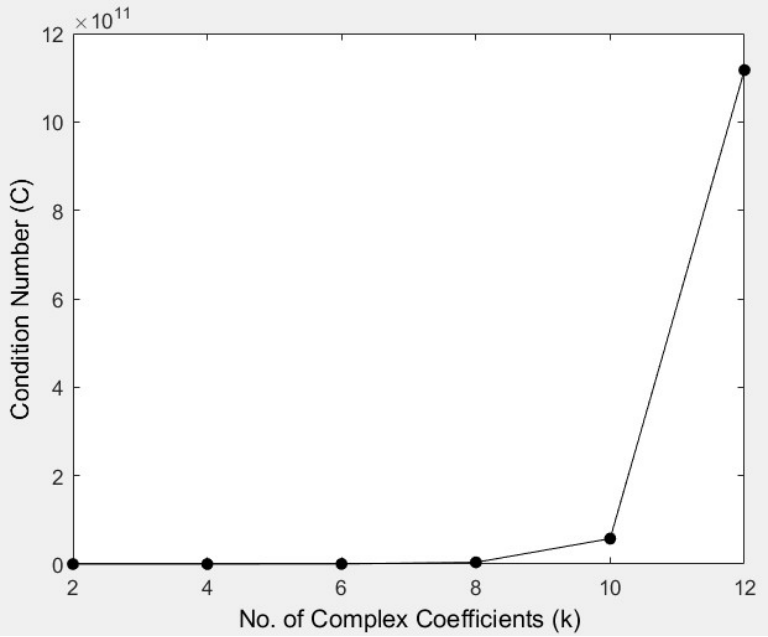

Figure 4-11: Plot of condition number, C, versus number of complex coefficients, k, using n_{total} = 17,251 data values and Laurent series

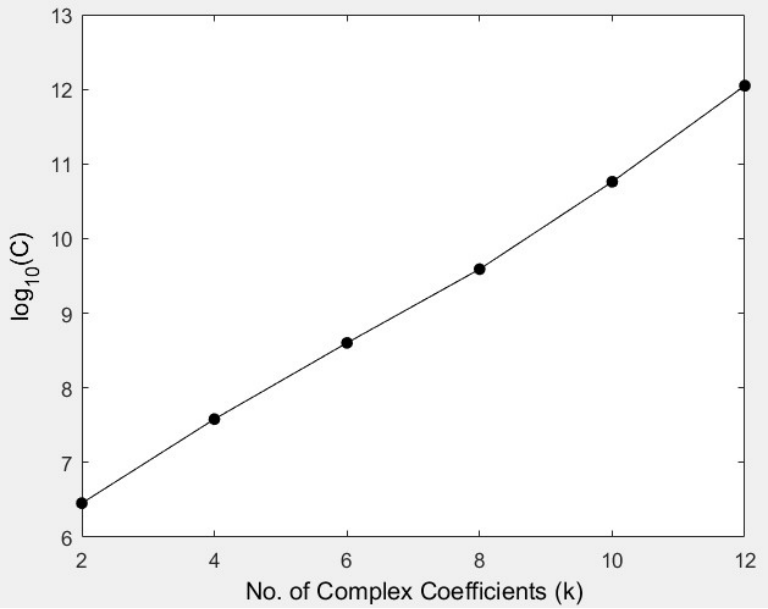

Figure 4-12: Plot of $\log_{10}(C)$ versus number of complex coefficients, k, using n_{total} = 17,251 data values and Laurent series

Table 4-4: Airy Coefficients, $c_j = a_j + ib_j$, from DIC-hybrid analysis involving a circularly-perforated, finite, graphite-epoxy plate

Airy Coefficients for m = 1 or k = 2	
a_{-1}	-49.32
b_{-1}	-0.28
a_1	-43.26
b_1	0.39

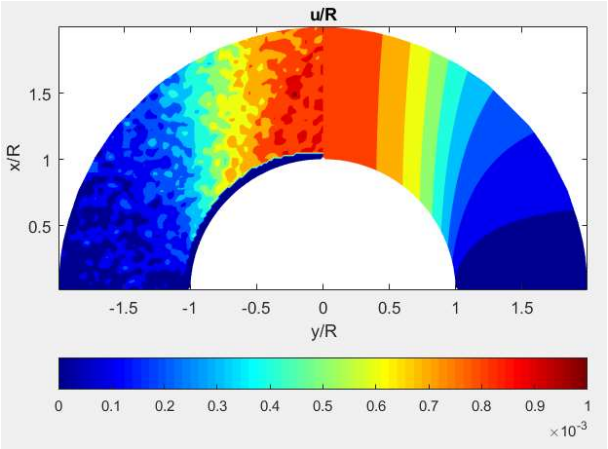

(a)

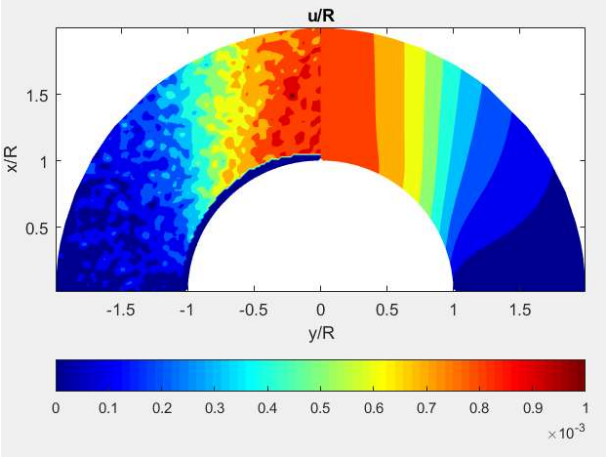

(b)

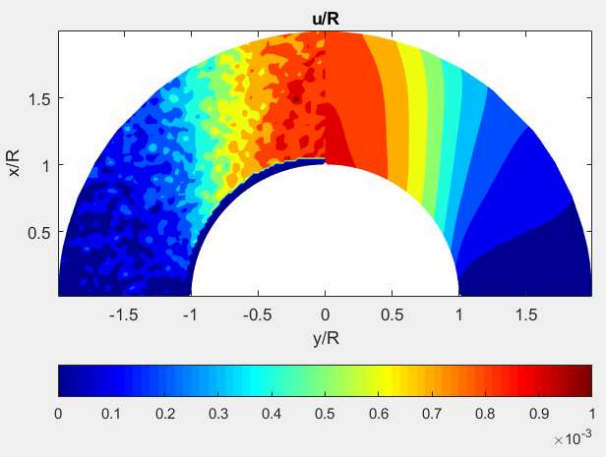

(c)

Figure 4-13: Comparing u/R-displacement contours obtained from DIC (left side) with reconstructed (right side) from the DIC-hybrid complex analysis for n_{total} = 17,251 and k =2, 4 and 10, respectively

4.10. Results

For the DIC-hybrid complex method, full-field stress analysis of the orthotropic plate was conducted employing the Laurent power series expansion, $n_{total} = n_{DIC} + h$ = 17,251 side conditions and k = 2 complex coefficients. From equation (4-10), the unknown Airy coefficients, c_j, were evaluated using displacements u at all the n_{DIC} = 6,448 locations selected in Figure 4-9(b) and the

h = 10,803 locations where symmetry and boundary conditions were imposed. Knowing the complex coefficients and their substitution into equations (4-1) through (4-5), the individual components of displacements and stresses are obtained. The results obtained from this method are compared with the FEM-predictions in Figure 4-14 through Figure 4-19. The v-displacement information of Figure 4-15 was obtained from equation (4-2) based on the DIC u-displacements determined Airy coefficients. All figures are generated using the commercial software MATLAB. Displacement components are normalized with respect to the radius, R, of the circular hole and the stress components are normalized with respect to the far-field applied stress, σ_0 = 11.05 MPa, according to equation (4-9).

All experimental results are based on the DIC-recorded u–displacement data. Good agreement prevails between the experimentally determined DIC-hybrid method results with the FEM-predictions. As expected, the DIC-hybrid analysis and FEM results for σ_{rr} and $\sigma_{r\theta}$ on the edge of the hole are extremely small, if not zero, Figure 4-19.

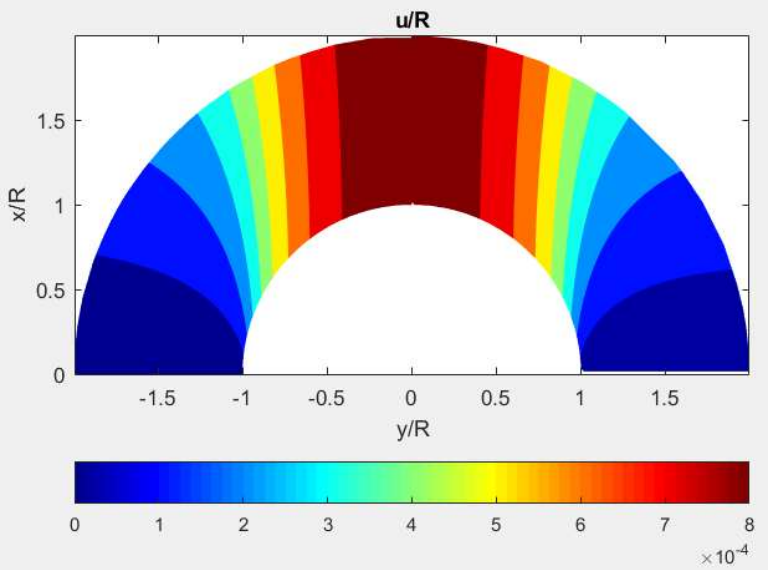

Figure 4-14: Contours of displacements u/R from FEA (left side) and DIC-hybrid method (right side) for $k = 2$ and $n_{total} = 17{,}251$ from measured u-displacements

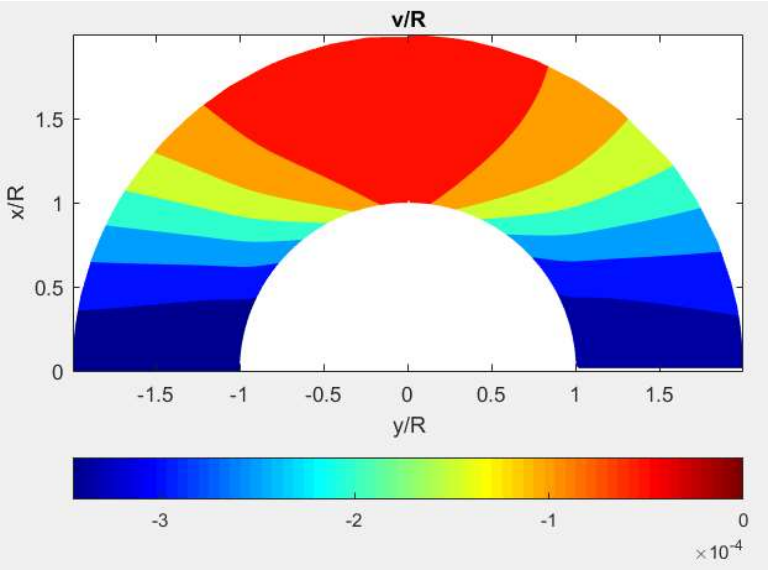

Figure 4-15: Contours of displacements v/R from FEA (left side) and DIC-hybrid method (right side) for $k = 2$ and $n_{total} = 17{,}251$ from measured u-displacements

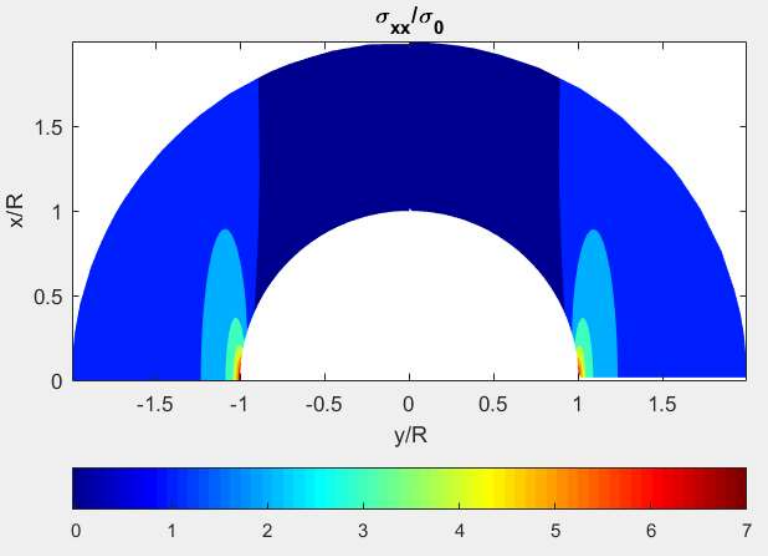

Figure 4-16: Contours of stresses σ_{xx}/σ_0 from FEA (left side) and DIC-hybrid method (right side) for $k = 2$ and $n_{total} = 17{,}251$ from measured u-displacements

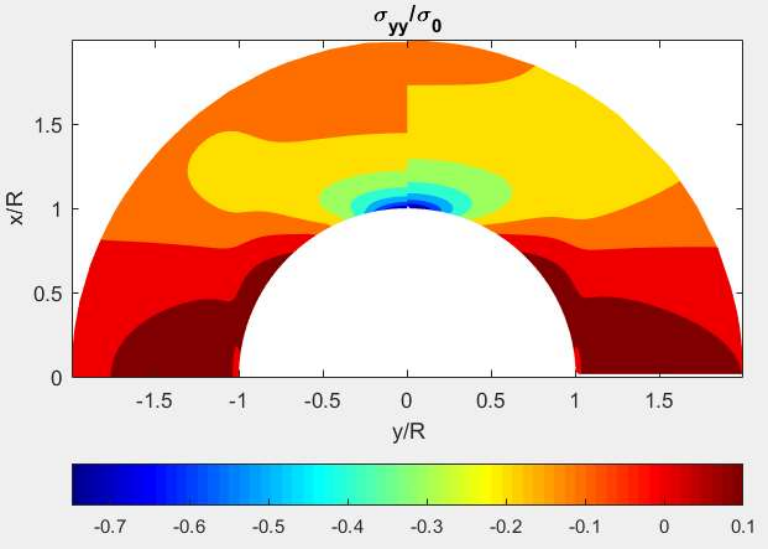

Figure 4-17: Contours of stresses σ_{yy}/σ_0 from FEA (left side) and DIC-hybrid method (right side) for $k = 2$ and $n_{total} = 17{,}251$ from measured u-displacements

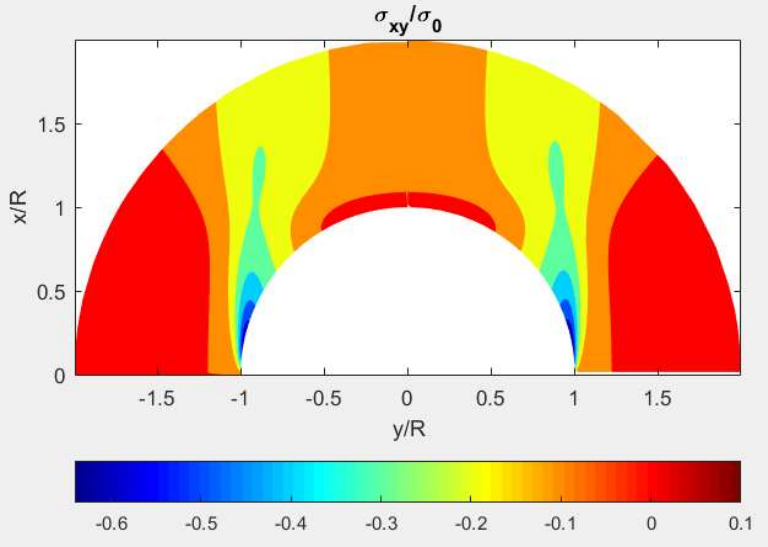

Figure 4-18: Contours of stresses σ_{xy}/σ_0 from FEA (left side) and DIC-hybrid method (right side) for $k = 2$ and $n_{total} = 17{,}251$ from measured u-displacements

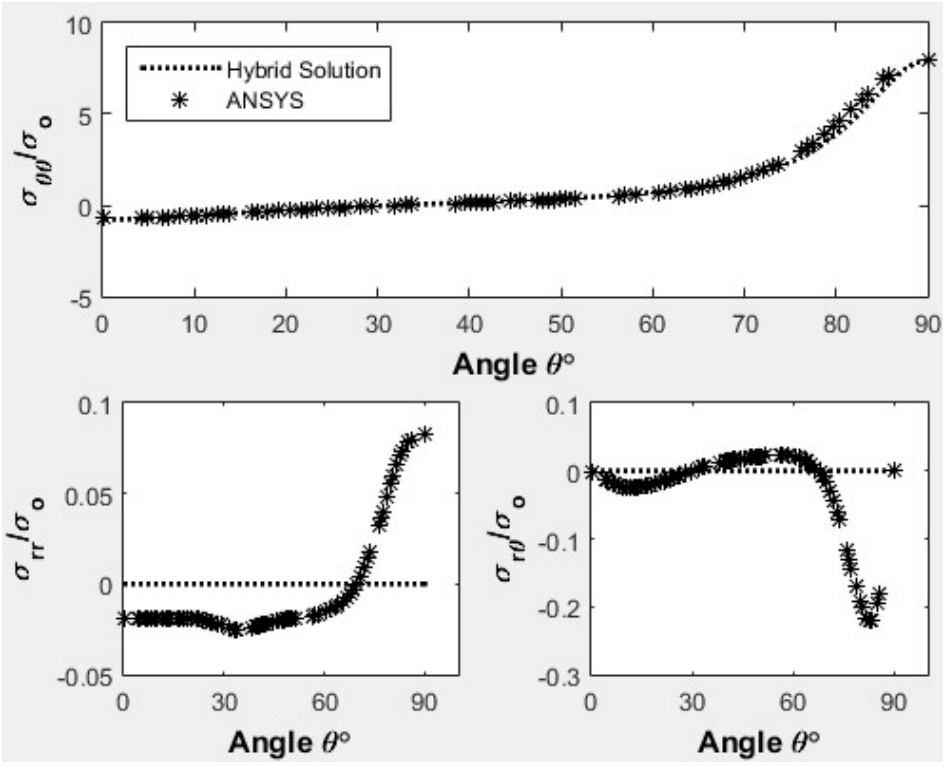

Figure 4-19: Plot of stresses $\sigma_{\theta\theta}/\sigma_0$, σ_{rr}/σ_0 and $\sigma_{r\theta}/\sigma_0$ along the boundary of the hole from ANSYS and DIC-hybrid analysis using $k = 2$ and $n_{total} = 17{,}251$ at $r = R$

The normalized tangential, radial and shear stress components along the boundary of the quarter of the round hole are plotted in Figure 4-19, from the DIC-hybrid complex analysis and are compared with the FEM-predictions. For the normalized tangential stresses, DIC-hybrid results agree well with those from FEM along the entire boundary of the cutout. These radial stress components are obtained from the rectangular components by stress transformation. For the normalized radial stresses and shear stresses along the traction-free region, the DIC-hybrid analysis gives zero stresses, which is expected theoretically. This is due to the fact that, theoretically along the traction-free region of a cutout $\sigma_{yy} = 0$ and $\sigma_{xy} = 0$. The FEM, due to complicated algorithms and processing, does not fully satisfy the traction-free conditions and is thus incapable of providing zero radial and shear stresses along the boundary of the cutout. However, these values are small.

4.11. Load Equilibrium

The reliability of the DIC-hybrid complex method was further evaluated by checking the load equilibrium from the stresses determined by this method in the loading direction. The load equilibrium is checked by integrating the DIC-based stresses σ_{xx} (based on DIC-recorded vertical displacement, u) over the width of the loaded plate using equation (4-13).

$$F_c^* = \int \sigma_{xx} dA = 2 \int_0^{\frac{W}{2}} \sigma_{xx} t dy \quad \text{at } x \geq R \tag{4-13}$$

where t is the thickness and W is the width of the plate. The trapezoidal rule of MATLAB was used to compute the integration. This was evaluated at various locations of x (= 0, R, 1.3R, 1.5R,

1.7*R*, 2*R*, *W*/2). The computed load was found to be within 2% of the physically applied 4.45 kN (1,000 lbs) load at each of these locations.

4.12. Summary, Discussion and Conclusions

The presented hybrid-DIC complex method is an effective tool to evaluate the stresses, including those on and near the edge of a discontinuity, in perforated, finite-width, tensile loaded orthotropic structures. The displacement data are synergized with a complex variables power series expansion of Airy stress functions, conformal mapping, analytic continuation and least squares. The technique was validated for a $[0_{13}/90_5/0_{13}]$ graphite-epoxy circularly-perforated, finite, orthotropic composite plate where the stresses are determined full-field from a single DIC-measured displacement field. Unlike finite element or theoretical/analytical analyses, the method does not require knowing far-field boundary conditions. This is important as external loads are often unknown in practice. Virtually all theoretically stressed orthotropic members are restricted to infinitely large geometry. Moreover, a difficulty with most purely experimental techniques is their inability to provide reliable information at and near the edge of cutouts [13,79]. The present DIC-hybrid analysis was done without experimental input data near the edge of the hole. Source data locations considered for the analysis were selected over a region away from the traction-free region; and for such cases the DIC-hybrid analysis gave results which are compatible with those from FEM and force equilibrium. Thus, this method overcomes the challenge that other methods face, i.e., which is not providing reliable data near the cutouts. Locations close to the cutout are the primary areas of interest as those locations typically contain the most serious stresses and displacements.

Many DIC approaches differentiate the displacements with schemes which lack a strong theoretical or analytical basis. Such processes can be highly sensitive to the quality and noise in the measured data and consequently give poor results [83]. This drawback is overcome in the present DIC-hybrid method where, to evaluate strains/stresses, the measured data are not differentiated using arbitrary methods. Instead the measured data are used in analytical formulations which are based on the Airy stress functions satisfying the equilibrium and compatibility. Moreover, conformal mapping and analytic continuation satisfy the traction-free boundary conditions.

One could measure the displacement data by other than DIC. However, the herein ability to need only one in-plane displacement field is significant. Recording both u and v by moiré, electronic speckle pattern interferometry (ESPI) or grids necessitates fairly complicated experimental set-ups. Irrespective of how the displacement data are recorded, it is not unusual to have locations where one of the u or v is of poor quality. The present need for only one of u or v is consequently advantageous.

In summary this hybrid-method is an effective and experimentally simple way to evaluate the full-field state of stress in finite composite members involving discontinuities in cases where the boundary conditions are unknown. Results of this chapter have been published [84].

Chapter 5. Hybrid Photomechanical Stress Analysis of Elliptically-Perforated Finite Orthotropic Plate using Single Measured Displacement Field

5.1. Introduction

An elliptically-perforated, finite, orthotropic laminate is stress analyzed by processing measured displacement data with a combination of Airy stress functions, conformal mapping, analytic continuation and least squares. Using only a single measured in-plane displacement field provides the complete displacements and stresses full-field, including at the edge of the hole. Compatible with real-world applications, this information is obtained without knowing either the external loading or measured values near the boundary of the cutout or having to differentiate the measured data. Unlike other techniques, virtually any shaped finite external boundary can be readily handled. Experimental results are supported by FEM and load equilibrium.

5.2. General Overview

The high stiffness- and strength-to-weight ratios of composite materials render them popular load bearing components for various applications. However, their orthotropy can greatly complicate their stress analyses, particularly with respect to holes and notches. One consequently does not enjoy the extensive stress concentration information with composites which is available for isotropic materials [67]. Stress analyzing finite-width orthotropic structures are challenging as theoretical analyses are mostly limited to infinite members with simple geometries. Moreover, like

with numerical analyses, their results are highly sensitive to the boundary conditions and loading. The latter are often unknown in practice. Purely experimental techniques often do not provide reliable data at the edges of geometric discontinuities. Traditional displacement-based experimental techniques are challenged by having to differentiate the measured information. Differentiating measured data is prone to errors. Engineering designs often involve cutouts, and the structural integrity must be ensured in the presence of such discontinuities. The use of elliptical openings in composite pressure vessels, aerospace and transportation members motivates having the ability to stress analyze finite, elliptically-perforated orthotropic structures from measured displacement data, Figure 5-1.

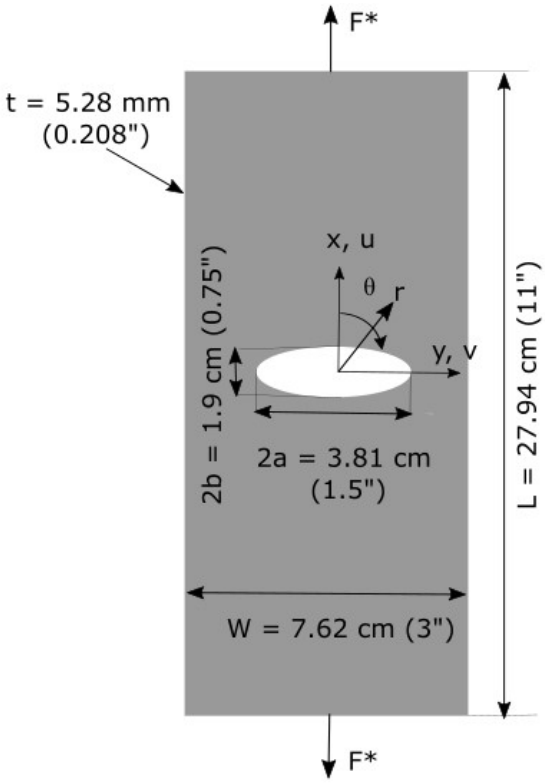

Figure 5-1: Schematic of finite composite plate with central-elliptical hole

The presented hybrid-method consists of complex variables Airy stress functions, least squares, conformal mapping, analytic continuation and power-series expansion of the stress functions and involves a digital image correlation (DIC) recorded single displacement field. The latter commence slightly away from the edge of the cutout. Traction-free conditions are satisfied along the boundary of the elliptical hole by conformal mapping and analytic continuation. Equilibrium and compatibility are satisfied by the Airy stress functions. Using either of the measured in-plane displacements provides the complete state of stress full-field. This method requires no knowledge of the external loading or measured data near the boundary of the cutout. Moreover, the measured displacement data are differentiated by employing a rigorous mechanics-based algorithm rather than using arbitrary polynomials. Although the basic equations theoretically assume infinite geometry, through extensive studies they are shown here to give reliable results for reasonably-finite structures.

5.3. Literature Review

The concept of complex variables technique developed by Lekhnitskii [5] and later modified by Savin [6] to stress analyze perforated infinite anisotropic plates is expanded here to stress analyze orthotropic plates of finite-width. Measured data are processed with Airy stress functions. In the previous Chapter 4 [84], an orthotropic plate with a circular cutout was stress analyzed with DIC-measured u-displacements. This study extends the previous work to investigate the hybrid-method's capability in handling cutout with aspect ratios other than $a/b = 1$ in orthotropic materials while utilizing DIC-measured displacement information. As the ellipse becomes narrower the stress concentration increases and can lead to more scatter in the

experimental behavior. This chapter also focuses on investigating how finite of a plate can be reliably analyzed by the current hybrid stress analysis approach. Moreover, the present analytical procedure is simplified to analyze isotropic plates.

Few studies involving perforated, finite, orthotropic members are found in literature. Samad and Rowlands [83,85] stress analyzed an elliptically-perforated symmetrical isotropic plate using DIC and with TSA for asymmetrical loading. Ambur and McGown [3] studied arbitrarily oriented, elliptically-notched composite plates using boundary collocation. They compared their numerical results with those from strain-gages. Lin and Ko [86] and Xu et al. [87] also employed boundary collocation to analyze elliptically-perforated composite plates. These studies by Ambur and McGowan [3], Lin and Ko [86] and Xu et al. [87] satisfied the boundary conditions at the hole by a mapping function and on the external edge by boundary collocation, and all three analyses involved rectangular external boundaries. Contrasted with using boundary collocation, the present ability to satisfy the internal boundary conditions analytically and external conditions experimentally is advantageous.

Alshaya et al. [88] stress analyzed an elliptically-perforated orthotropic plate from recorded thermal data. Lin and Rowlands [18], Lin [9] and Rhee and Rowlands [22] also stress analyzed orthotropic structures having cutouts using thermoelastic stress analysis (TSA) data, whereas Baek and Rowlands [71] employed strain-gage data. However, TSA requires cyclic loading which is often unrealistic for real-world applications. Baek and Rowlands [72] and Rhee et al. [70] stress analyzed orthotropic materials using moiré. Their methods necessitated using both measured u and v information. The present analysis employs only a single measured displacement component from DIC. Unlike with moiré or strain-gages, the latter is a non-contacting, full-field stress analysis technique. Unlike thermal elastic methods, DIC does not require cyclic loading. Since strain-gages

are finite in size and records only the local strains, it is difficult to evaluate the most serious stresses on the edge of a geometric discontinuity in an orthotropic composite using strain-gages unless one knows where it occurs a priori.

Gerhardt [8] utilized a hybrid-finite element to analyze perforated orthotropic plates. Using modified complex potentials, Zakharov and Becker [89] determined a theoretical solution for an elliptically-perforated orthotropic laminate having an elliptical external boundary and subjected to combined bending-extension. By applying variational concepts of equilibrium to the potential energy, Madenci et al. [90] obtained a system of equations containing unknown coefficients and whose solutions provide the stresses and displacements. The approach is applicable to external polygonal shapes and the boundary conditions at the cutout are satisfied using a mapping function. Tan [91] analytically related the ratio of stress concentration factors in finite and infinitely-wide perforated plates. His study [91] does not include any experimental finite width correction factor (FWCF) data for elliptically-perforated, finite, orthotropic composites.

Gerhardt [8], Ambur and McGowan [3], Chen [76], Lin and Ko [86] and Medanci et al. [90] also successfully used the mapping function used in this study to stress analyze elliptically-perforated, finite, orthotropic structures. Unlike References [3,86,87,89,90], the herein approach of combining DIC-measured information with analytical and numerical tools can readily handle virtually any externally-shaped boundary. Moreover, the current analysis includes rational means of assessing how many coefficients to retain in the series representation of the stress functions and whose magnitudes are obtained by least-squares. None of the cited relevant references seems to offer any such consideration. Experience indicates how many coefficients to retain is important.

Ashrafi and Tuttle [13] analyzed perforated composite plates from DIC-measured data and commercial DIC strain calculation algorithms. However, in addition to necessitating the use of both in-plane displacement components to obtain strains, results were unreliable at the edges of the holes.

5.4. Relevant Equations

For an orthotropic plate in absence of body forces and rigid body motion, using a combination of complex variables Airy stress functions, conformal mapping, analytic continuation and Laurent power-series expansion, the in-plane stress and displacement components in the rectangular coordinates (x, y) of the physical plane, $z_j = x + \mu_j y$ for $j = 1, 2$, are expressed as such [8,74]

$$\sigma_{xx} = 2\left(\sum_{\substack{j=-m \\ j\neq 0}}^{j=m} Re\left[\mu_1^2 \frac{jc_j\zeta_1^{j-1}}{\omega_1'(\zeta_1)} + \mu_2^2 \frac{-j\bar{c}_j B\zeta_2^{-j-1} + jc_j C\zeta_2^{j-1}}{\omega_2'(\zeta_2)}\right]\right) \tag{5-1}$$

$$\sigma_{yy} = 2\left(\sum_{\substack{j=-m \\ j\neq 0}}^{j=m} Re\left[\frac{jc_j\zeta_1^{j-1}}{\omega_1'(\zeta_1)} + \frac{-j\bar{c}_j B\zeta_2^{-j-1} + jc_j C\zeta_2^{j-1}}{\omega_2'(\zeta_2)}\right]\right) \tag{5-2}$$

$$\sigma_{xy} = -2\left(\sum_{\substack{j=-m \\ j\neq 0}}^{j=m} Re\left[\mu_1 \frac{jc_j\zeta_1^{j-1}}{\omega_1'(\zeta_1)} + \mu_2 \frac{-j\bar{c}_j B\zeta_2^{-j-1} + jc_j C\zeta_2^{j-1}}{\omega_2'(\zeta_2)}\right]\right) \tag{5-3}$$

$$u = 2\left(\sum_{\substack{j=-m \\ j\neq 0}}^{j=m} Re\left[\left(p_1\zeta_1^j + p_2 C\zeta_2^j\right)c_j + p_2 B\zeta_2^{-j}\bar{c}_j\right]\right) \tag{5-4}$$

$$v = 2\left(\sum_{\substack{j=-m \\ j\neq 0}}^{j=m} Re\left[\left(q_1\zeta_1^j + q_2 C\zeta_2^j\right)c_j + q_2 B\zeta_2^{-j}\bar{c}_j\right]\right) \tag{5-5}$$

where the complex material properties μ_j for $j = 1, 2$, are the roots of the characteristic expression of equation (2-20) (x-direction along the strong/stiff material direction 1) of Chapter 2 for a plane-stressed orthotropic material loaded along a principal axis of material orthotropy. Complex material quantities p_j and q_j for $j = 1, 2$, are defined in equations (2-33) and complex quantities B and C in equations (2-50) and (2-51), respectively. In equations (5-1) through (5-5), the Airy coefficients, c_j, are complex numbers, i.e., $c_j = a_j + ib_j$, where a_j and b_j are real numbers. Detailed derivations of these equations are provided in Chapter 2.

The DIC-hybrid method uses a conformal mapping in order to transform a complex geometry from the physical plane into a simpler geometry in the mapped plane while preserving angles during the mapping. As the stress functions are expressed here by the Laurent series, a mapping function that maps the elliptical hole between the original physical z-plane to the unit

circle in the mapped ζ-plane is required. The function $\omega_j(\zeta_j)$ of Figure 5-2, maps a region, R_ζ, adjacent to the unit circle in the $\zeta_j = \xi + \mu_j\eta$ plane into a region, R_z, exterior to an elliptical hole in the physical plane $z_j = x + \mu_j y$ for $j = 1, 2$; of the loaded structure, i.e., [5]

$$z_j = \omega_j(\zeta_j) = \frac{b + ia\mu_j}{2}\frac{1}{\zeta_j} + \frac{b - ia\mu_j}{2}\zeta_j, \quad j = 1, 2 \tag{5-6}$$

where a and b are the major and minor radii of the elliptical hole, respectively. The inverse of the mapping function is used to map the elliptical geometry from z-plane to the unit circle in the ζ-plane (Figure 5-2), i.e.,

$$\zeta_j = \omega_j^{-1}(z_j) = \frac{z_j \pm \sqrt{z_j^2 - b^2 - a^2\mu_j^2}}{b - ia\mu_j}, \quad j = 1, 2 \tag{5-7}$$

The branch of the square root of equation (5-7) is chosen so that, $|\zeta_j| \geq 1$ for $j = 1, 2$, and the system coordinate origin is at the center of the elliptical hole, $z_c = 0$. The quantity $\omega'_j(\zeta_j)$ in equations (5-1) through (5-3) represents differentiation of equation (5-6) with respect to the complex variables ζ_j for $j = 1, 2$, as equation (5-8). Details regarding the mapping function of equation (5-6) for the plate of Figure 5-1 are provided in Appendix D.

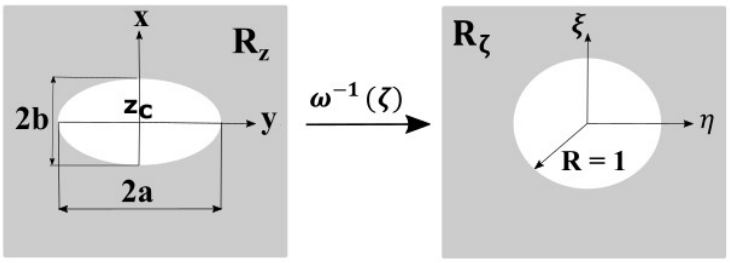

Figure 5-2: Mapping elliptical hole from physical z-plane to unit circle in ζ-plane and vice-versa

$$\omega_j'(\zeta_j) = \frac{b - ia\mu_j}{2} - \frac{b + ia\mu_j}{2}\frac{1}{\zeta_j^2}, \quad j = 1, 2 \tag{5-8}$$

The current orthotropic plate having $[0_{13}/90_5/0_{13}]$ graphite-epoxy lay-up is a balanced, symmetric laminate. Twenty-six plies have their fibers in the loading direction and five plies have their fibers transverse to the loading direction. The in-plane strains and displacements are uniform through the thickness. The elastic laminate properties and stresses of equations (5-1) through (5-3) are based on through-the-thickness average stresses.

The current analytical concept of complex variables Airy stress functions can be simplified to stress analyze isotropic members. For an isotropic material with elastic modulus, $E_{11} \approx E_{22} = E$, Poisson's ratio, $\nu_{12} = \nu_{21} = \nu$, and shear modulus, $G = E/2(1 + \nu)$, the elastic compliances are expressed according to equation (2-35). By substituting the expression of the isotropic elastic compliances from equation (2-35) into the characteristic equation (2-17), the complex material properties for isotopy are obtained as $\mu_1 = \mu_2 = i$.

5.5. Plate Preparation and Experimental Set-up

5.5.1. Plate Details

A finite-width, $[0_{13}/90_5/0_{13}]$ graphite-epoxy orthotropic plate containing a central elliptical cutout (Figure 5-1) was prepared and its displacement data were measured using DIC. The finite orthotropic laminate of length, L = 27.94 cm (11"), width, W = 7.62 cm (3") and thickness, t = 5.28 mm (0.208") contains a central elliptical cutout with a major radius a = 1.9 cm (0.75") and a minor radius b = 0.95 cm (0.375"), (Figure 5-1 and Table 5-1). The plate is symmetrical about both the horizontal and vertical axes.

Table 5-1: Elliptically-perforated orthotropic plate and loading details

Material	$[0_{13}/90_5/0_{13}]$ graphite-epoxy orthotropic laminate
Supplier	Kinetic Composite, Inc., Oceanside, California
Thickness, t	5.28 mm (0.208")
Length, L	27.94 cm (11")
Width, W	7.62 cm (3")
Ellipse major diameter, $2a$	3.81 cm (1.5")
Ellipse minor diameter, $2b$	1.9 cm (0.75")
Symmetry	Both horizontally and vertically
Loading for DIC analysis	From 0 to 11.6 kN (2,600 lbs) in intervals of 889.6 N (200 lbs)
Loading for DIC-hybrid stress analysis	4.5 kN (1,000 lbs)

5.5.2. Material Properties

From Table 4-1, the measured elastic properties of the orthotropic $[0_{13}/90_5/0_{13}]$ graphite-epoxy laminate are E_{11} = 104.1 GPa, E_{22} = 28.1 GPa, ν_{12} = 0.155 and G_{12} = 3.0 GPa, with the 1-direction being in the vertical x-orientation of Figure 5-1. Details regarding the composite laminate's material properties and their determination are provided in Appendix A.

5.5.3. Plate Fabrication

The elliptically-perforated plate of Figure 5-1 was machined from the $[0_{13}/90_5/0_{13}]$ graphite-epoxy orthotropic laminate provided by Kinetic Composite, Inc., Oceanside, CA. The 279.4 mm × 76.2 mm × 5.28 mm plate was fabricated from the composite laminate using an electric saw and the 38.1 mm × 19 mm elliptical hole was later introduced using a carbide end mill in a CNC milling machine.

5.5.4. Application of Speckle Pattern

The random speckle pattern required for DIC was applied on the elliptically-perforated, orthotropic plate following the standard guidelines for DIC speckle pattern application (details provided in Chapter 4, Section 4.6.3).

The dense, random speckle pattern of Figure 5-3 was applied to the surface of the plate for pixel correlation between the (essentially) unloaded and loaded conditions. Being careful not to round off the edges of the hole, the plate was lightly polished initially with 400-grit emery cloth

and cleaned with a water-based mild cleaner (Vishay Precision Group - Micro-Measurements M-Prep Conditioner A followed by M-Prep Neutralizer 5A) [82]. The cleaned plate was painted with a thin layer of black paint, after which a random pattern of white dots was applied. The random pattern was achieved by lightly applying pressure to the trigger of the white paint container while holding the container perpendicular to the surface of the plate to provide a discontinuous spray. Rust Oleum Ultra-Cover paints were used.

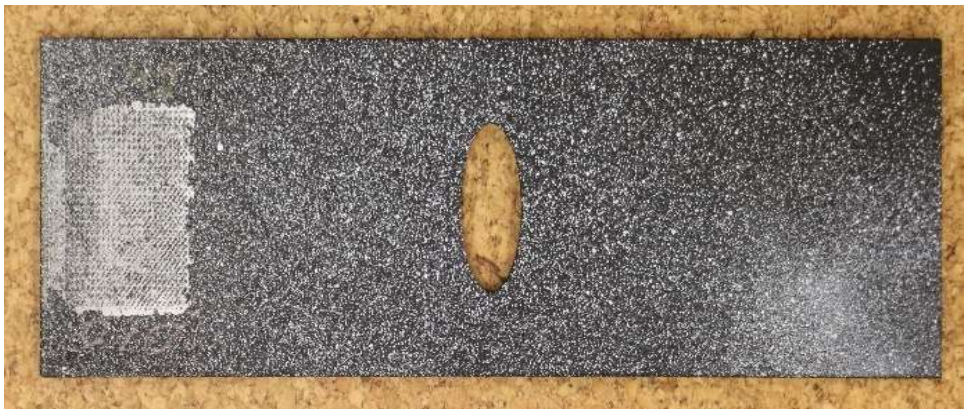

Figure 5-3: Elliptically-perforated plate with speckle pattern

5.5.5. Plate Loading

The plate was loaded in a 89 kN (20,000 lbs) capacity, closed-loop, hydraulic grip MTS machine taking care to ensure symmetrical loading and avoid any out-of-plane bending. To achieve symmetrical loading, special care was taken so that the plate was mounted symmetrically, Figure 5-4(a). The commercially available Correlated Solution, Inc.'s (Columbia, SC 29063, USA) DIC package was used to measure the displacements. The DIC package includes a pair of Point Gray digital cameras with 2,448 × 2,048-pixel resolution, three pairs of Schneider Xenoplan lenses

(lens pair with 1.9 focal ratio and 35 mm focal length were used), and Correlated Solutions' Vic-Snap data acquisition and Vic-2D/3D post-processing software (details in Table 4-3 of Chapter 4). A 3D-DIC test was conducted initially using two cameras to obtain the in- and out-of-plane displacement information and ensure there was no out-of-plane motion beyond the Poisson's effect. From the DIC-recorded data it can be seen that there was no out-of-plane motion while conducting the experiment, Figure E-1 of Appendix E. Being satisfied having no out-of-plane plate bending, a 2D-DIC test (Figure 5-4(b)) was done with the same loading set-up using one camera, the data from which were utilized for the stress analysis.

Vertical tensile static loading varying from essentially zero to 11.6 kN (2,600 lbs) was applied in the strong/stiff (*x*-) direction of the plate in 889.6 N (200 lbs) load increments. Reported results are those at 4.45 kN (1,000 lbs). An oscilloscope was used to monitor the applied loads. A digital image of the plate was taken using the Correlated Solution DIC camera coupled with Vic-Snap data acquisition software at each load increment using ambient lighting, Figure 5-4(b).

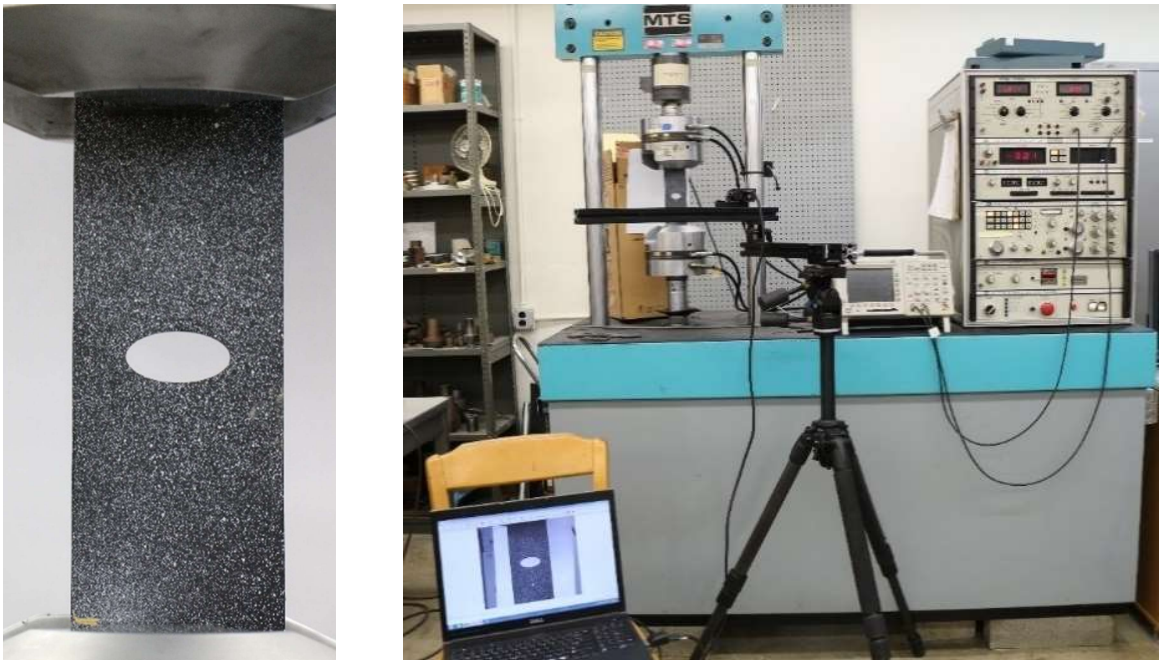

(a) (b)

Figure 5-4: (a) Loaded plate with speckle pattern and (b) Experimental set-up

5.5.6. Calibration

When using two cameras (3D-DIC), system calibration was achieved by moving, imaging and analyzing a rigid calibration grid (for the current study Correlated Solution Inc.'s 12 mm × 9 mm × 5 mm calibration grid was used) in front of the two cameras. When using one camera (2D-DIC), the calibration was done by manually correlating pixel size for a known distance through Vic-2D post-processing software, i.e., marking down a known distance and providing the length in terms of the physical units.

5.5.7. Subset and Step Size

A subset size of 21 and a step size of 5 were used.

5.5.8. DIC Data Analysis

The captured DIC images were processed and correlated using Correlated Solution Vic-2D correlation software to obtain the measured displacement information. A set of images at different loads were obtained along with a reference image at essentially zero load. Figure 5-5 shows how the analysis using the Vic-2D software is done. Figure 5-5(a) shows an image of the loaded plate captured by the DIC camera coupled with Vic-Snap software. The user specifies the area of interest, subtracts any discontinuity in the plate manually and specifies the subset and step size. In Figure 5-5(b) the shaded area is the area of interest (AOI) over which the analysis will take place. Figure 5-5(c) indicates the analysis completed by the Vic-2D software showing the displacement in the strong/stiff (vertical) x-direction.

Note that the Vic-Snap and Vic-2D software were only used to record the DIC images and extract the raw DIC displacement information by image correlation, respectively. Once this was obtained, the commercial software had no further use in this study. Rather, the DIC-recorded data were processed by the Airy stress functions.

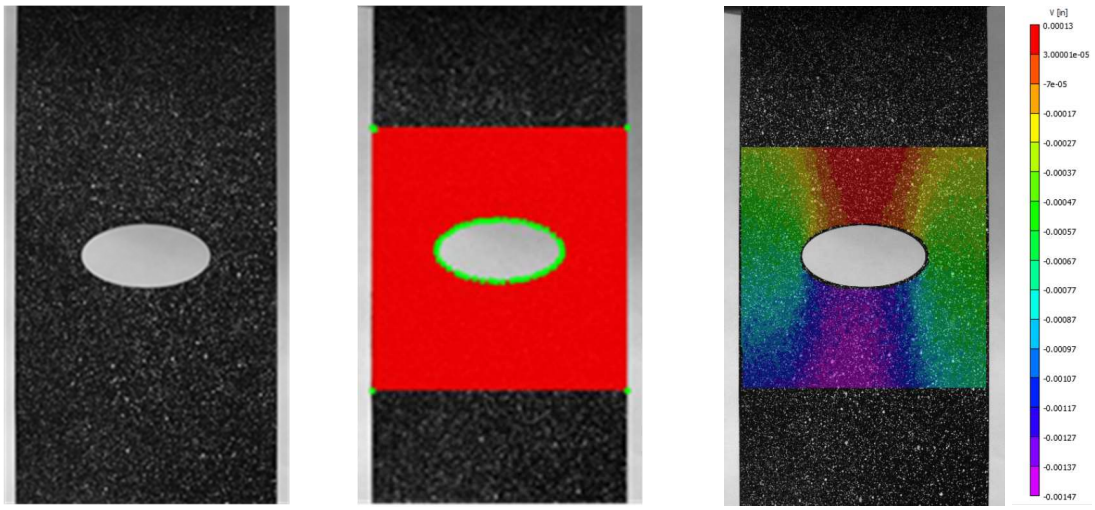

(a) (b) (c)

Figure 5-5: Processing of the digital images using Vic-2D post-processing software; (a) Initial captured DIC image, (b) Area of interest (AOI) selected using Vic-2D software and (c) Correlating the images conducting DIC analysis over the AOI (showing vertical displacement)

5.6. Finite Element Model

Having geometric and loading symmetry about both *x*-*y* axes, only one quarter of the plate was modeled in ANSYS APDL using isoparametric elements Plane 182 (4 nodes per element with translations *u* and *v* per node), Figure 5-6(a). The origin of the coordinate system is located at the center of the hole and symmetrical boundary conditions were numerically satisfied. Since the plate thickness is small compared to other dimensions, plane-stress with thickness option was used. The model had a very fine mesh at and near the edge of the hole. The mesh was refined until the maximum stress on the edge of the hole changed by less than 0.25% regardless of any further reduction in the element size. The final FEM quarter model involves 51,755 elements and 52,353 nodes. The plate experienced a far-field stress, σ_0 = 11.06 MPa (1.6 ksi), along *x*-axis based on the applied load and the far-field cross-sectional area of the plate according to equation (5-9). The coordinate values of all the nodes, along with the displacement and stress components of the FEM,

were imported into MATLAB for post-processing and correlating the data to those from the DIC-hybrid complex analysis.

$$\sigma_0 = \frac{F^*}{W \times t} = \frac{4{,}448.22 \text{ N}}{76.2 \text{ mm} \times 5.28 \text{ mm}} = 11.06 \text{ MPa } (1{,}604.12 \text{ psi}) \tag{5-9}$$

A stated motivation for developing the present technique is to enable stress analyze orthotropic cases experimentally which cannot be analyzed numerically due to the lack of knowledge on the actual loading and boundary conditions. However, FEM is used here. The geometry, loading and mesh quality of the plate (Figure 5-1) in this study were deliberately selected such that one could obtain reliable FEM results (Figure 5-7) with which to compare results of the present hybrid-method.

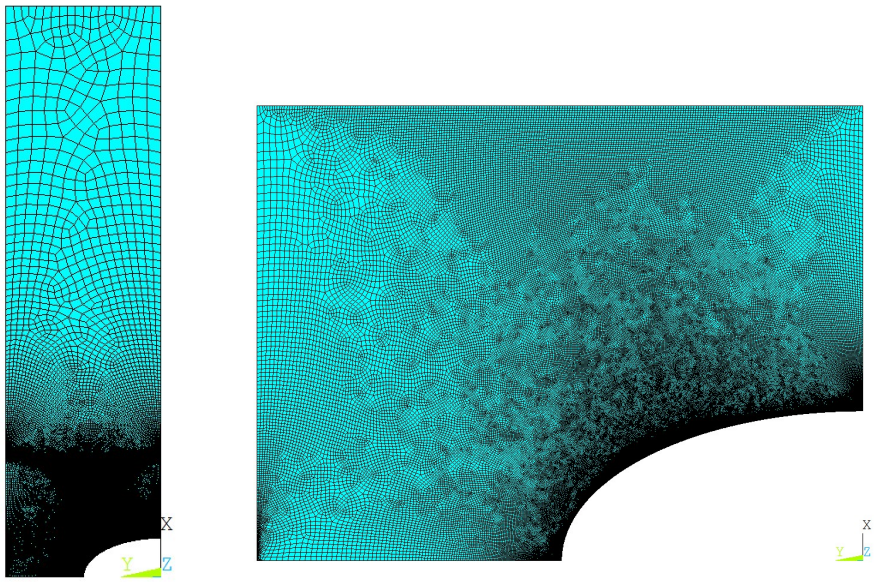

(a) (b)

Figure 5-6: (a) FEM of the elliptically-perforated quarter plate and (b) Area near the elliptical hole with dense element mesh

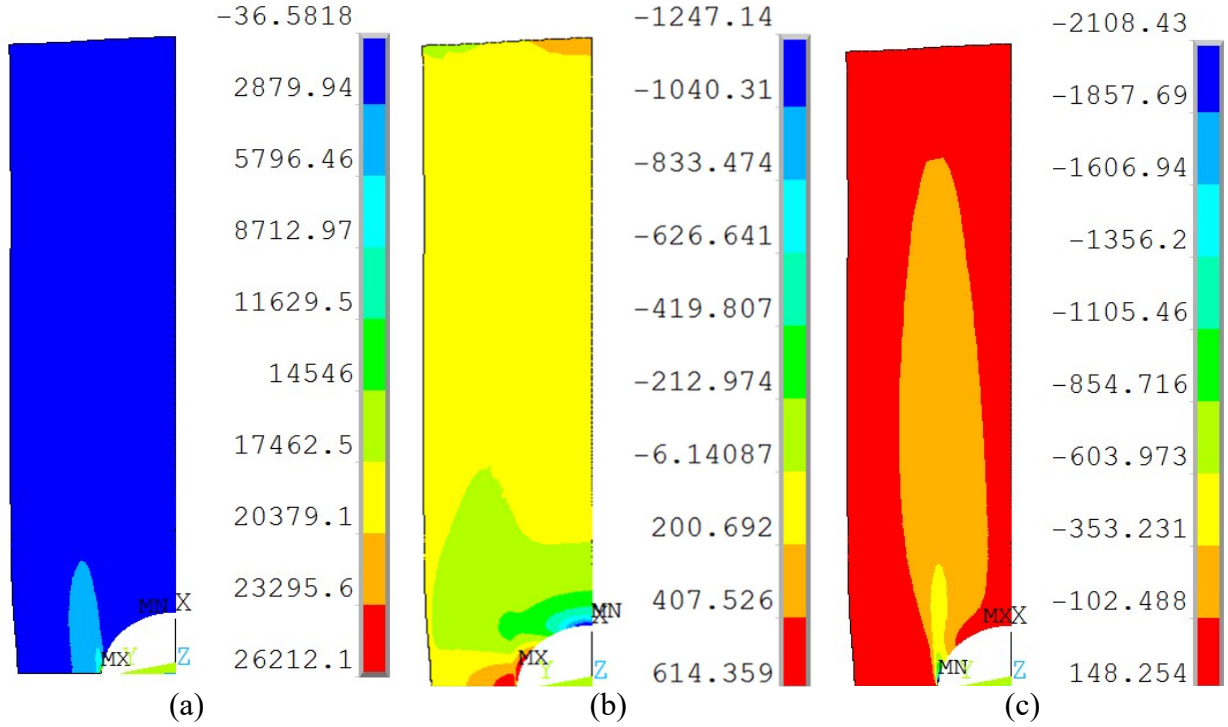

Figure 5-7: Contour plots, for stresses σ_{xx}, σ_{yy} and σ_{xy} from FEM (units in psi)

5.7. Data Reduction and Analysis

The plate is geometrically and mechanically symmetrical about both the *x*-*y* axes. The top grip of the MTS load frame (Figure 5-4(a)) is stationary and the bottom grip moves down to apply the tensile load. Figure 5-8(a) shows the associated non-symmetrical displacement pattern about the horizontal *y*-axis. These DIC-measured displacements in the loading direction (strong/stiff direction, *x*-direction) of Figure 5-8(a) were processed to shift the origin so it passes through the center of the hole and also to simulate both the top and bottom ends of the plate being equally extended vertically (Figure 5-8(b)), i.e., were post-processed considering the displacement in the loading direction should be zero along the horizontal center-line of the plate. These processed displacements were averaged over the four quadrants of the plate to cancel out any measurement

asymmetry and reduce scatters. The resulting averaged vertical displacements, u, are plotted throughout the top right quadrant of the plate in Figure 5-8(c).

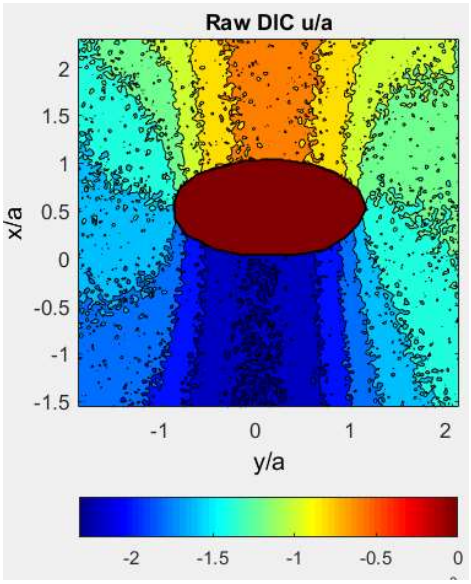

(a)

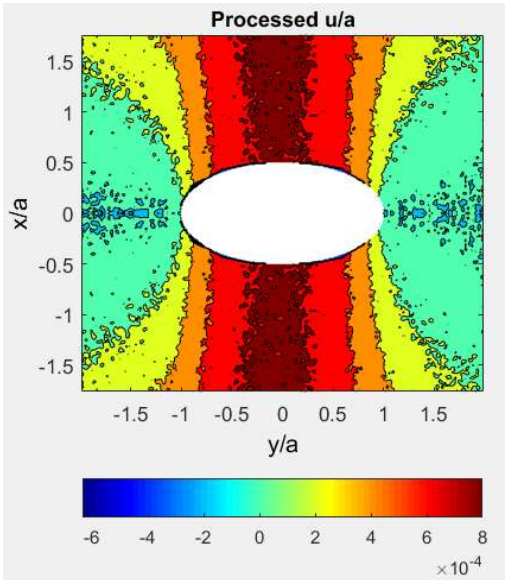

(b)

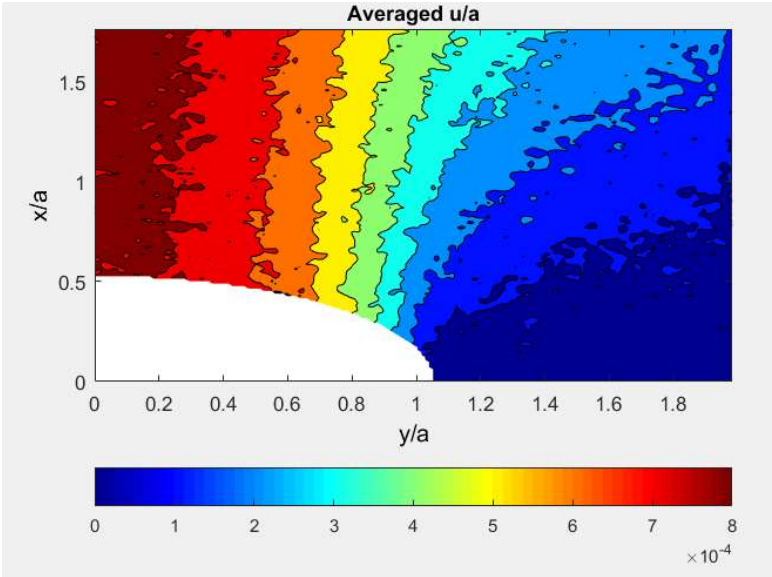

(c)

Figure 5-8: DIC-recorded displacement data, u/a, in vertical loading direction, x, : (a) DIC-recorded normalized u-data, (b) Processed so $u = 0$ at $x = 0$ (magnitude only) and (c) Averaged u-displacements over the four quadrants and discarding edge data

From the processed averaged vertical u-displacement data, n_{DIC} = 20,704 essentially equally spaced experimental values of u were selected, originating at a distance 0.05a (= 1 mm) away from the edge of the hole, Figure 5-8(c) and Figure 5-9. For these n_{DIC} = 20,704 source data values, the RMS plot of Figure 5-10 indicates employing $k \geq 4$ coefficients will yield less difference between the recorded, d, and reconstructed, d', displacement data. However, the plot of the condition number, C, and the natural logarithm of the condition number, $\log_{10}(C)$, of Figure 5-11 and Figure 5-12, respectively, suggests k = 2 to 8 would be an appropriate number of Airy coefficients to retain.

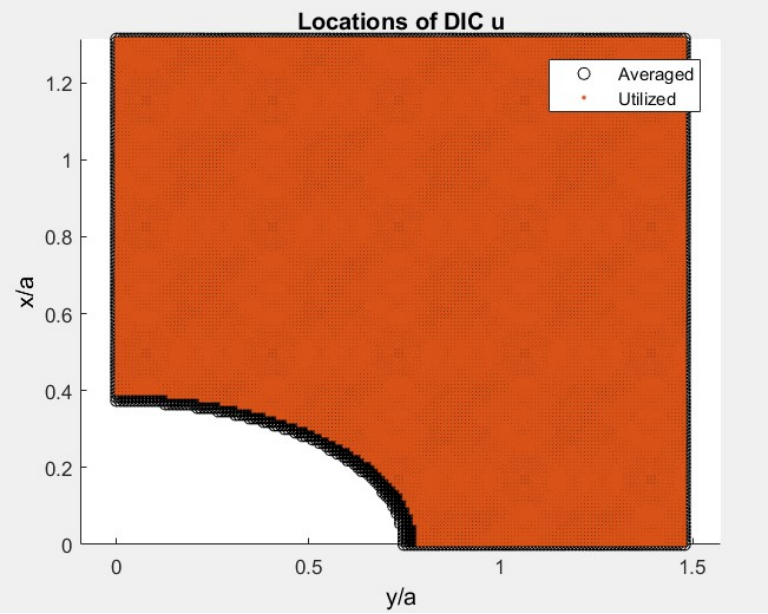

Figure 5-9: DIC data source locations, of n_{DIC} = 20,704 data points for the DIC-hybrid method

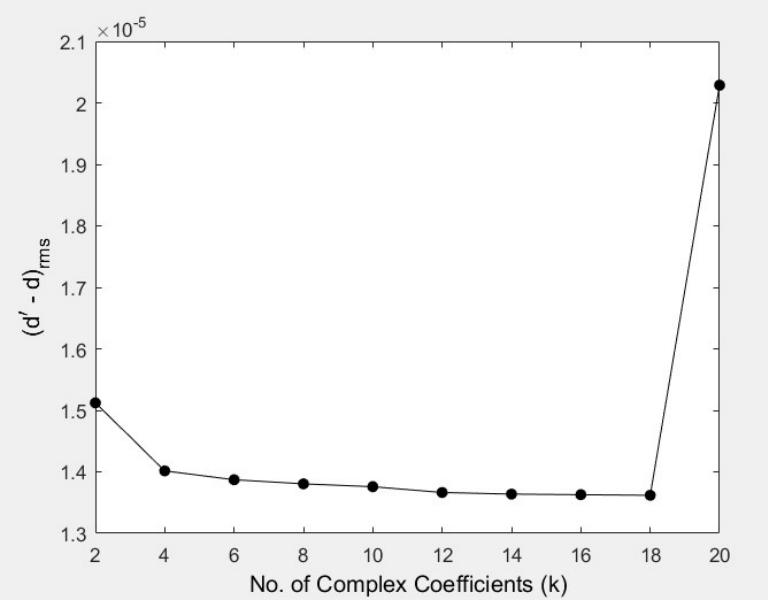

Figure 5-10: Plot of RMS versus number of complex coefficients, k, for n_{DIC} = 20,704 for vertical displacements, u

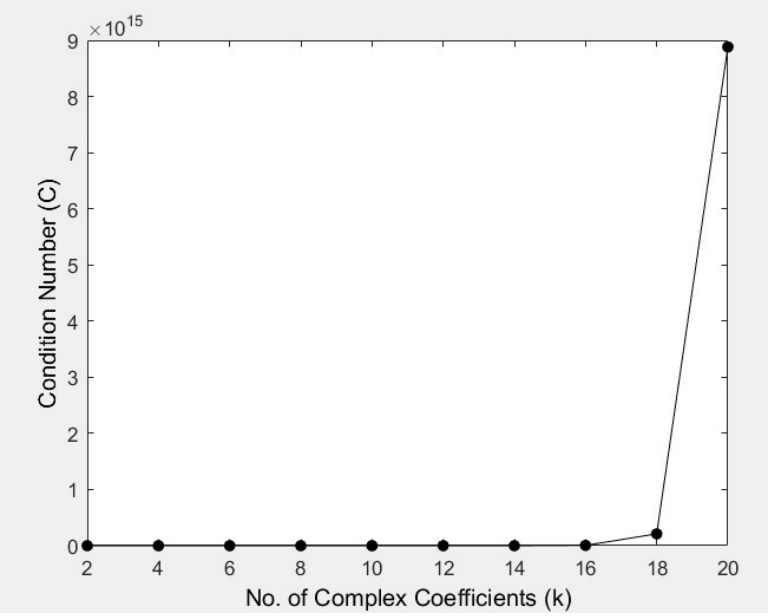

Figure 5-11: Plot of condition number, C, versus number of complex coefficients, k, for n_{DIC} = 20,704 for vertical displacements, u

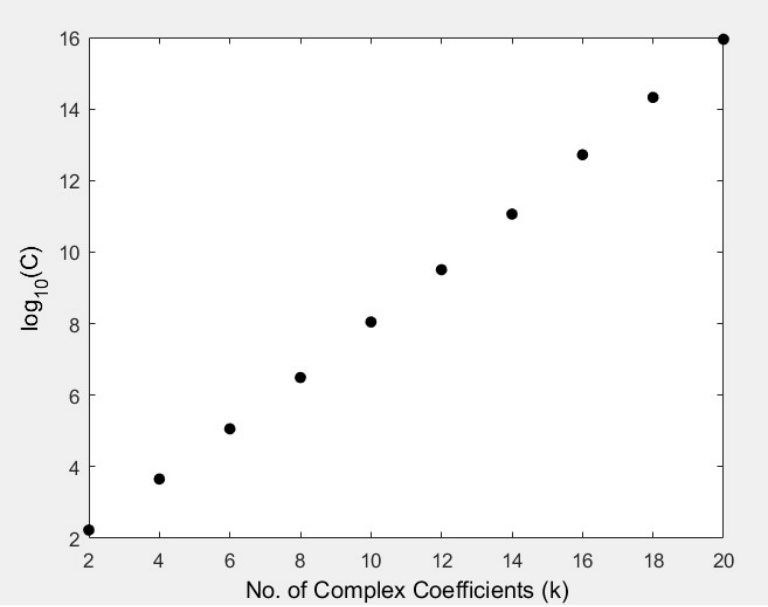

Figure 5-12: Plot of $\log_{10}(C)$ versus number of complex coefficients, k, for $n_{DIC} = 20{,}704$ for vertical displacements, u

To further aid in the selection of the number of coefficients to use in the summation series, the DIC-recorded u-displacement contours, d, were compared with the reconstructed u-displacement contours, d', from equation (5-4), for varying number of stress coefficients, k, in Figure 5-13. As the plate of Figure 5-1 has only a single central elliptical hole, there should not be any sudden deviation in the stress lines away from the boundary of the hole. Figure 5-13(b) shows that as the number of Airy coefficients is increased to $k = 4$ from $k = 2$ (Figure 5-13(a)), the stress lines at location 1 and 2 starts to show sudden slight deviations. This becomes more prominent in Figure 5-13(c) for $k = 6$. Moreover, unusual deviation in the stress lines at location 3 is observed in Figure 5-13(c). It should be kept in mind that traditional DIC methods are incapable of providing reliable results near or at the edges of a structure and this accounts for the large scatter in measured data near the right vertical edge of Figure 5-13(a).

Based on all the above-mentioned observations, for the n_{DIC} = 20,704 DIC-measured *u*-displacement information in the DIC-hybrid method to stress analyze the finite orthotropic plate of Figure 5-1, k = 2 is an optimum number of Airy coefficients to retain.

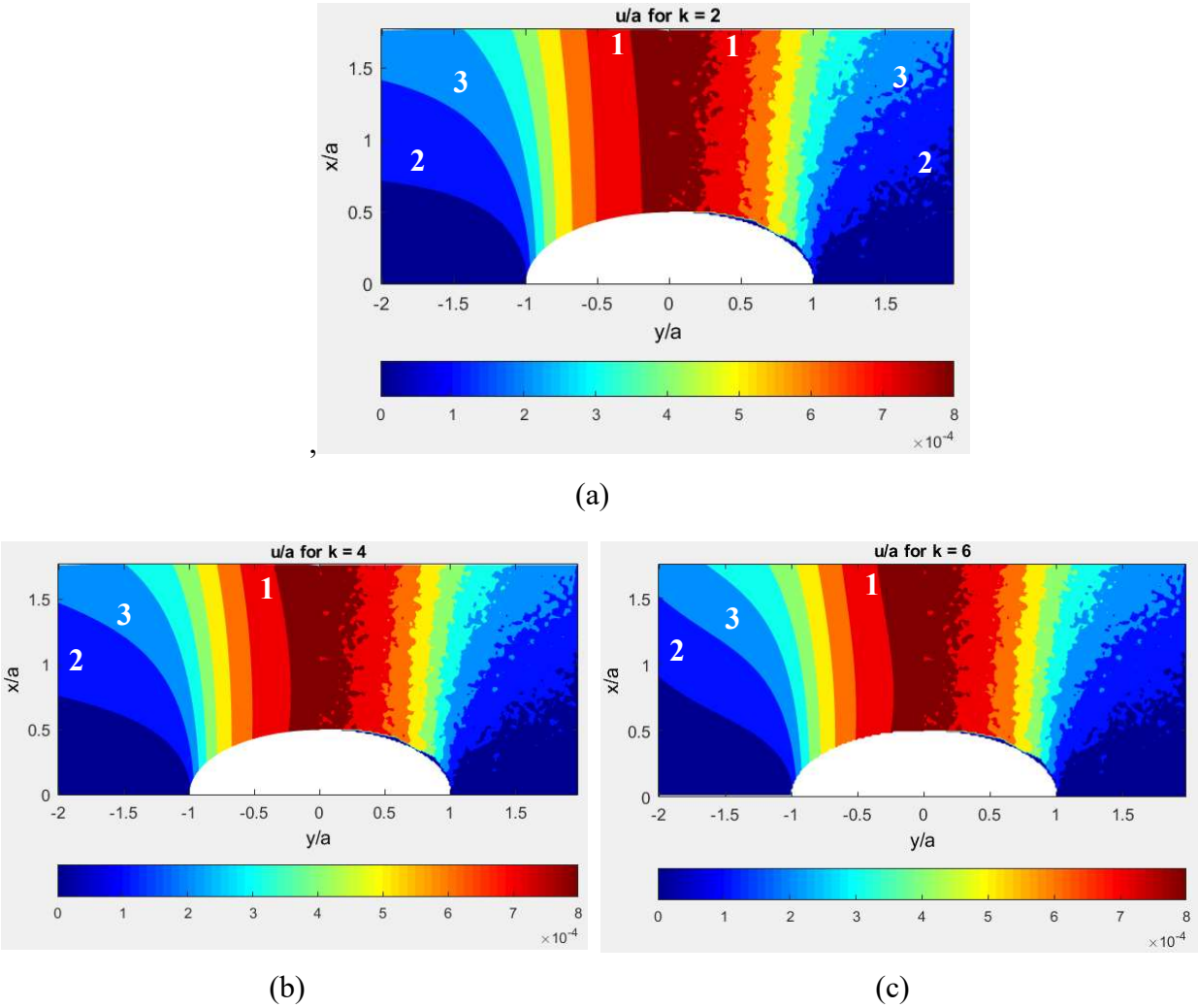

(a)

(b)

(c)

Figure 5-13: Comparing *u*/*a*-displacement contours obtained from DIC (right side) with reconstructed (left side) from the DIC-hybrid complex analysis for n_{DIC} = 20,704 *u*-displacements and k =2, 4 and 6, respectively

Note withstanding the above, it is worth observing that as the number of Airy coefficients was increased from $k = 2$ in equations (5-1) through (5-3), the stresses in the loading direction, σ_{xx}, showed slight change from the FEM-prediction, with a slight decrease in the maximum stress value from that of $k = 2$. However, the comparatively smaller stresses, i.e., the normal stresses in the direction transverse to the loading direction, σ_{yy}, and the shear stresses, σ_{xy}, showed significant deviation from the FEM-predictions for $k = 4$, Figure F-1 of Appendix F.

Acknowledging that the magnitudes of the displacements in the loading direction, u, are comparatively greater than those transverse to the loading direction, v, this DIC-based stress analysis emphasized using the former (higher magnitude) displacement data. However, to assess the reliability when employing the smaller displacement component, v, an additional DIC-hybrid stress analysis was conducted based on measured v-displacement data as input. Similar to the previous case, the DIC-recorded v-displacement data of Figure 5-14(a) were post-processed to be zero along vertical center-line $y = 0$. Due to appreciable scatter of the raw v-displacements about y-axis at $x = 0$, Figure 5-14(b), they were averaged over the four quadrants to minimize experimental scatter and asymmetry, Figure 5-14(c). From these processed and averaged experimental information, at a distance $0.05a \approx 1$ mm or greater from the boundary of the hole, $n_{DIC} = 20{,}704$ displacement v values were selected. This is the same number of measured v inputs as those of the u-displacements of Figure 5-9. When using DIC-recorded v-displacements, $k = 6$ was chosen based on RMS plot of Figure 5-15. This choice of $k = 6$ was also supported by the plots of the condition number of Figure 5-16 and Figure 5-17. Using either $k = 2$ or 8 in the summation series was found to have little effect on the DIC-hybrid computed in-plane stresses other than slight decrease in the maximum tangential stress along the boundary of the hole

compared to the FEM-prediction. This supports using $k = 6$ for the $n_{DIC} = 20{,}704$ horizontal v-displacement data to stress analyze the orthotropic plate.

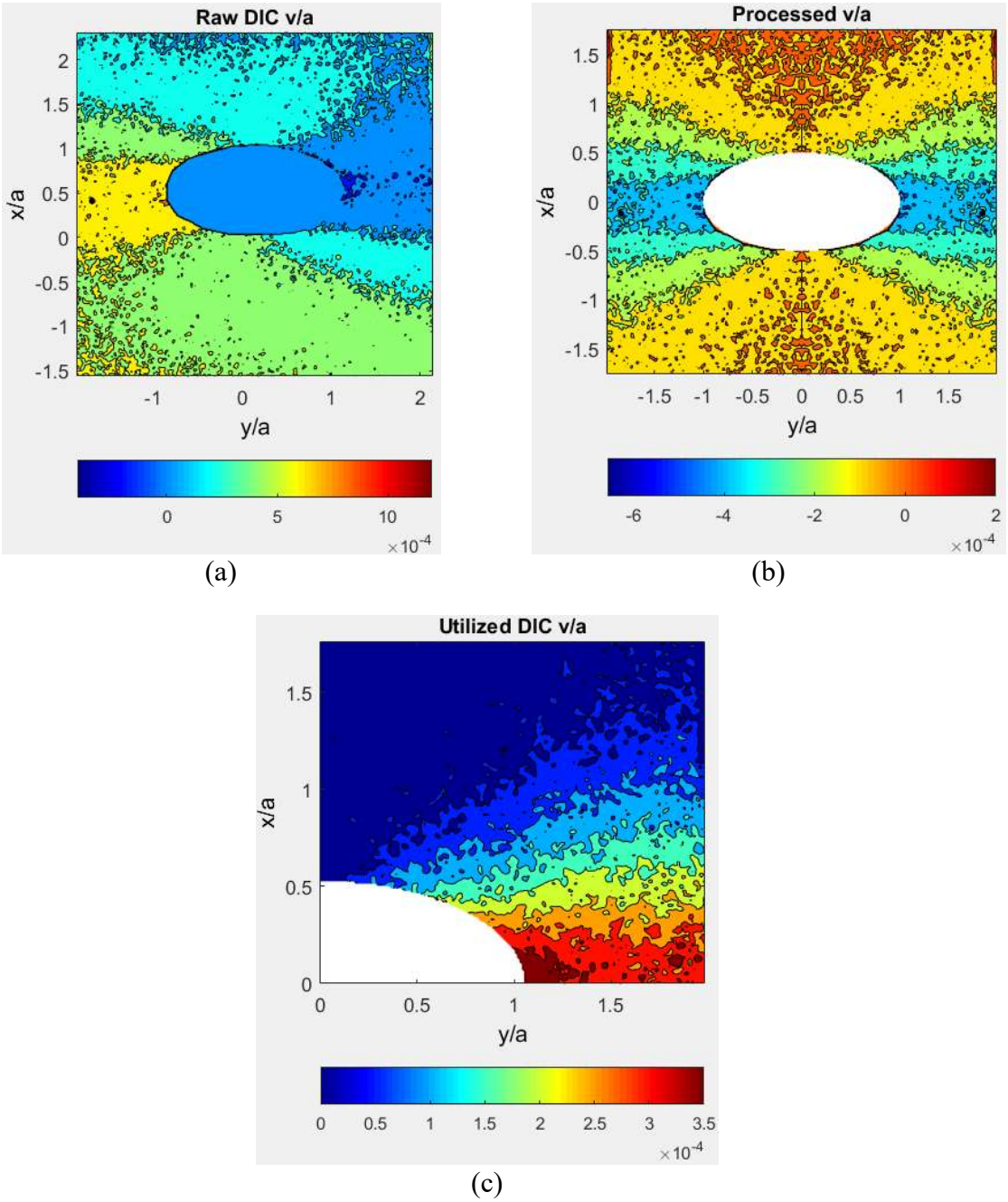

Figure 5-14: DIC-recorded v/a displacements transverse to loading direction x, (a) Raw DIC-recorded normalized v-data, (b) Processed so $v = 0$ at $y = 0$ (magnitude only) and (c) Averaged v-displacements over the four quadrants and discarding edge data

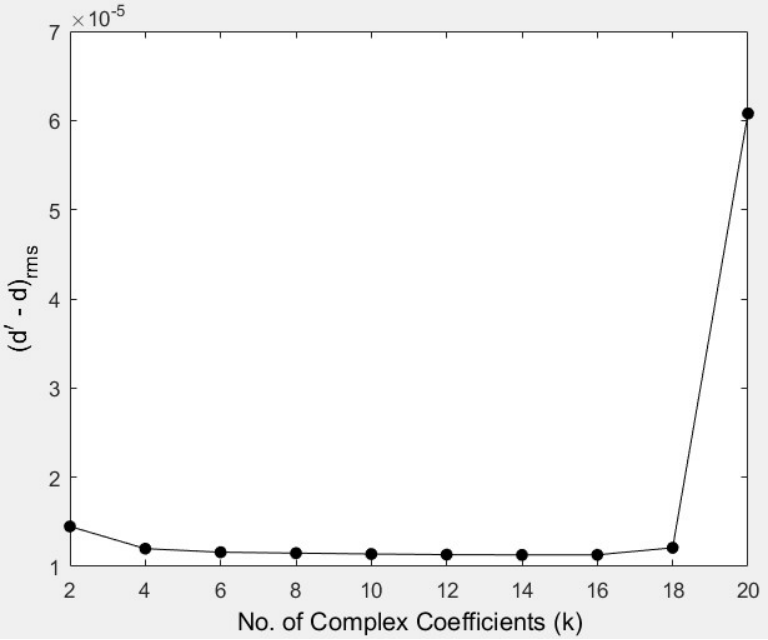

Figure 5-15: Plot of RMS versus number of complex coefficients, k, for n_{DIC} = 20,704 horizontal displacements, v

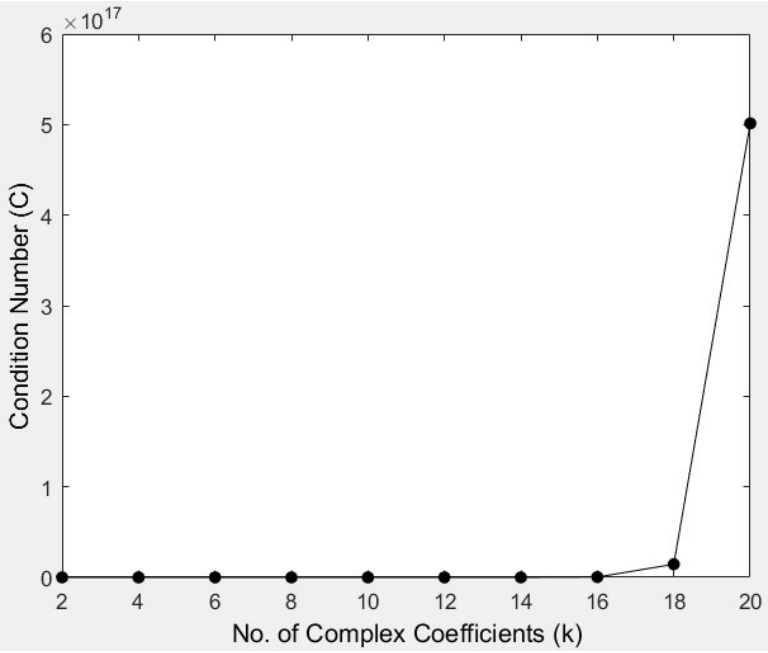

Figure 5-16: Plot of condition number, C, versus number of complex coefficients, k, for n_{DIC} = 20,704 horizontal displacements, v

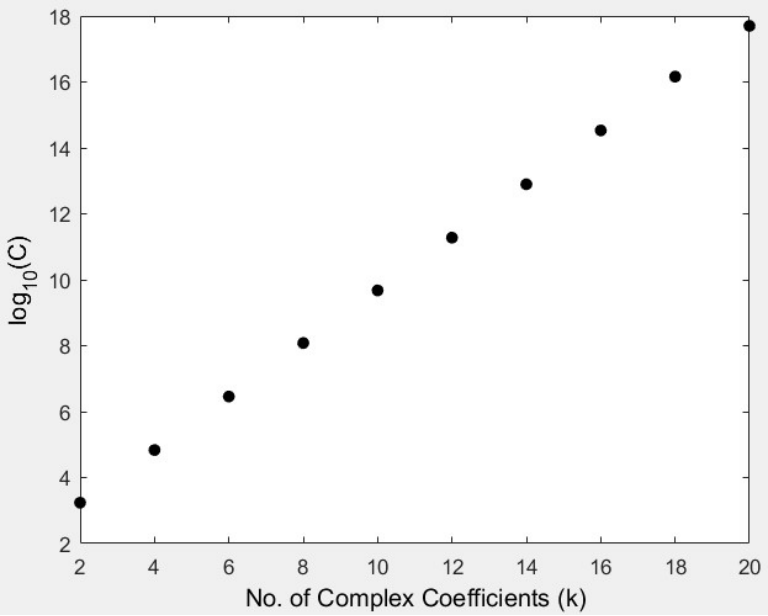

Figure 5-17: Plot of $\log_{10}(C)$ versus number of complex coefficients, k, for n_{DIC} = 20,704 horizontal displacements, v

Using the n_{DIC} = 20,704 DIC-measured u- or v-displacement data in either equation (5-4) or (5-5), the Airy coefficients can be evaluated, i.e.,

$$\{d\} = 2\sum_{\substack{j=-m \\ j\neq 0}}^{j=m} Re\left(\begin{bmatrix} s_1\zeta_1^j + s_2\left(C\zeta_2^j + B\zeta_2^{-j}\right) & i\left[s_1\zeta_1^j + s_2\left(C\zeta_2^j - B\zeta_2^{-j}\right)\right] \end{bmatrix}\begin{Bmatrix} a_j \\ b_j \end{Bmatrix}\right) = \{\text{DIC Displacement Data}\} \tag{5-10}$$

where $d = u$ or v and $s_j = p_j$ or q_j for u or v, respectively, and j = 1, 2. Equation (5-10) can be re-written as

$$[A]_{n_{DIC}\times 2(m+1)}\{c\}_{2(m+1)\times 1} = \{d\}_{n_{DIC}\times 1} \tag{5-11}$$

A simultaneous system of linear equations is formed according to equation (5-11) where the number of equations/input displacements, n_{DIC}, is much higher than the number of unknowns/real Airy coefficients, $2(m + 1)$, i.e., $n_{DIC} >> 2k = 2(m + 1)$. Matrix $[A]$ depends on the material properties, the mapping function and the source locations of the recorded input displacement values, vector $\{c\}$ involves the Airy coefficients and $\{d\}$ consists of the DIC-recorded displacement data. The only unknowns in the above equation (5-11) are the Airy coefficients in vector $\{c\}$. They are evaluated by the least-squares method. MATLAB's backlash operator of equation (5-12) is used for this purpose, i.e.,

$$\{c\} = [A]\backslash\{d\} \tag{5-12}$$

It should be noted that equation (5-11) solves for $2(m + 1)$ real coefficients (a_j and b_j) from which $k = (m + 1)$ complex coefficients, c_j, are obtained. Only the real part of the Airy coefficients, a_j, are utilized from equation (5-12) to evaluate the in-plane displacements and stresses from equations (5-1) through (5-5) combined with equations (5-7) and (5-8). For orthotropic materials with purely imaginary complex parameters ($\mu_1 = 5.87i$ and $\mu_2 = 0.34i$ for Figure 5-1 and Table 4-1) and direction of material symmetry parallel-perpendicular to the direction of applied loading, and with geometric-mechanical symmetry about the x- and y-axes requires retaining only the real and odd terms in the finite-series expansions of the stress functions, $\Phi(\zeta_1)$ and $\Psi(\zeta_2)$, of equations (2-62) and (2-63) [71]. The value $j = 0$ in equations (5-1) through (5-5), represents a rigid body constant which is omitted when the plate is loaded in a testing machine. Moreover, for the central elliptical hole, and due to the plate's symmetry about the x-y axes, the value of j never equals an even number. Thus, the value of j also never equals zero nor an even number. As the plate has

geometric and loading symmetry with respect to the *x*- and *y*-axes, Figure 5-1, just one quadrant of the plate was analyzed. Information in the other quadrants is obtained through symmetry.

This analysis is done without imposing any symmetry and/or near or far-field boundary conditions. A desirable feature of the present hybrid approach is that, it does not require knowing the external loading or boundary conditions. This is a big advantage over numerical techniques such as FEM, FD or boundary collocations where reliability depends heavily on the known external boundary conditions. This can be very useful in real-world applications involving complex geometry and/or loading as situations can occur where imposing boundary or symmetry conditions may not always be possible. Moreover, the actual external loading is often unknown in practice.

5.8. Results

Each of the DIC-measured *u* and *v* displacement components was used individually with the relevant equations (5-4) or (5-5) to evaluate the Airy coefficients. Knowing these coefficients, both in-plane displacements and the complete state of stress were available throughout the region engulfing the hole from equations (5-1) through (5-5). These results are compared in Figure 5-18 through Figure 5-23 with FEM-predictions. All figures were generated using MATLAB. Displacement components and distances are normalized with respect to the major elliptical hole radius, a = 1.9 cm, and the stresses are normalized with respect to the far-field applied stress, σ_0 = 11.06 MPa according to equation (5-9). Good agreement exists between the DIC-hybrid stress analyses and FEM-predictions. Discrepencies in Figure 5-19(b) and Figure 5-21(a) between the FEM-prediction and DIC-hybrid method are not significant. In the first case the σ_{yy} values are

smaller than σ_{xx}, the ones in the loading direction. The Figure 5-21(a) displacement in the loading direction, u, is computed from using the displacement transverse to loading direction, v, as input in the DIC-hybrid model.

Overall, good agreement prevails between the DIC-hybrid complex stress analyses and those obtained from the FEA, using Airy coefficients $k = 2$ for $n_{DIC} = 20{,}704$ values of vertical displacements, u, or $k = 6$ for $n_{DIC} = 20{,}704$ values of horizontal displacements, v, and using the Laurent series expansion to express the complex variables Airy stress functions. It must be noted that all of the DIC results are based on using either only the vertical, u, or horizontal, v, recorded displacement field as input data, not both together. This is unlike traditional displacement-based methods which require both u and v. Needing only one measured displacement field is advantageous since there can be situations where there is a paucity or poor quality of one or other of the recorded displacement fields.

The polar stress components of Figure 5-20 and Figure 5-23 were obtained by stress transformation from rectangular components of stress.

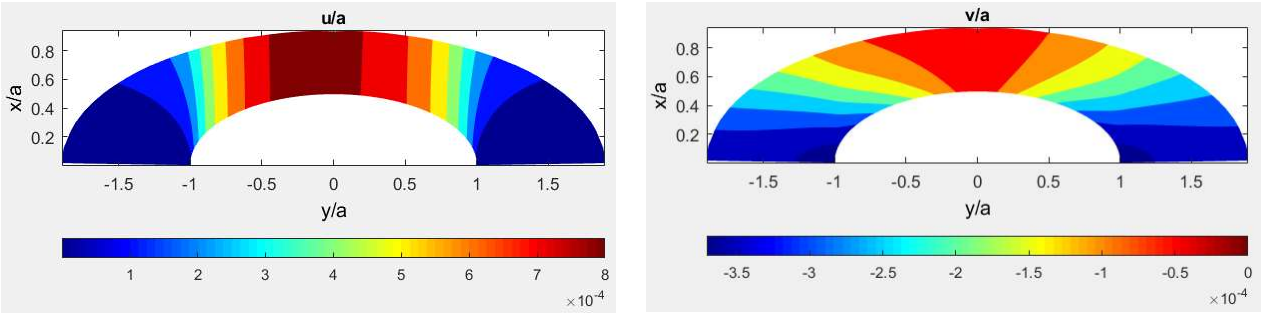

(a) (b)

Figure 5-18: Contours of (a) u/a and (b) v/a from FEM (left side) and hybrid-method based on DIC-measured displacement information, u, in the vertical loading direction (right side)

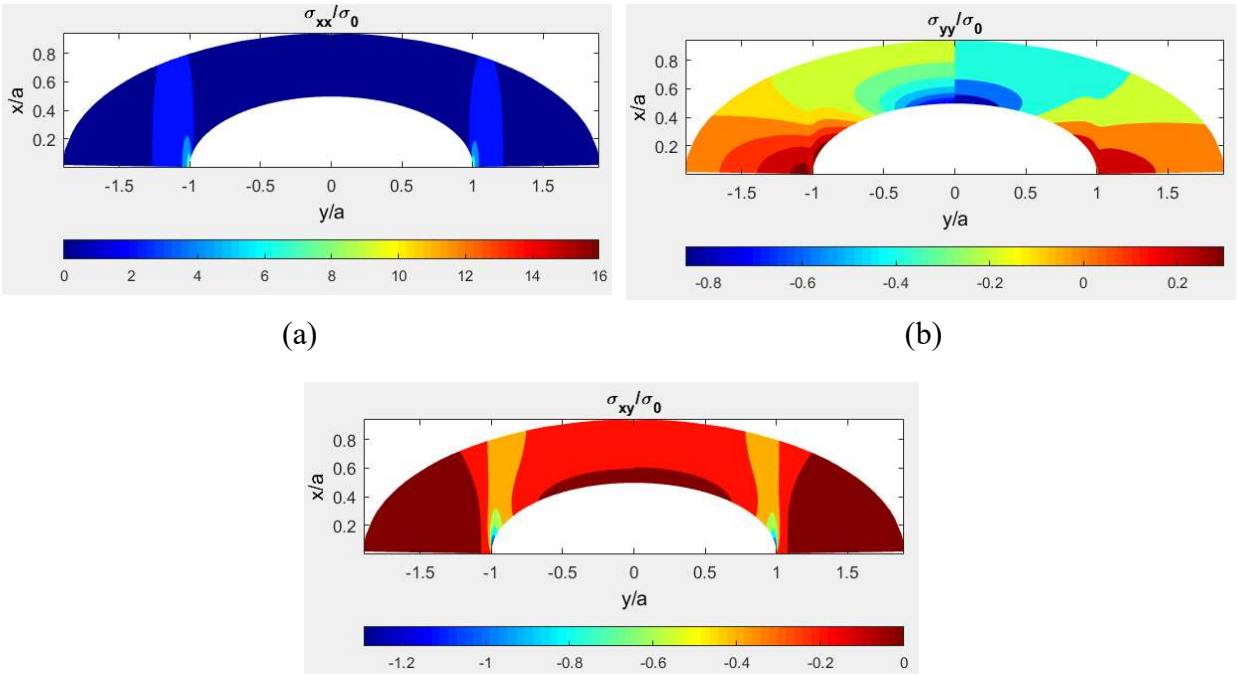

(a) (b)

(c)

Figure 5-19: Contours of (a) σ_{xx}/σ_0, (b) σ_{yy}/σ_0 and (c) σ_{xy}/σ_0 from FEM (left side) and hybrid-method based on DIC-measured displacement information, u, in vertical loading direction (right side)

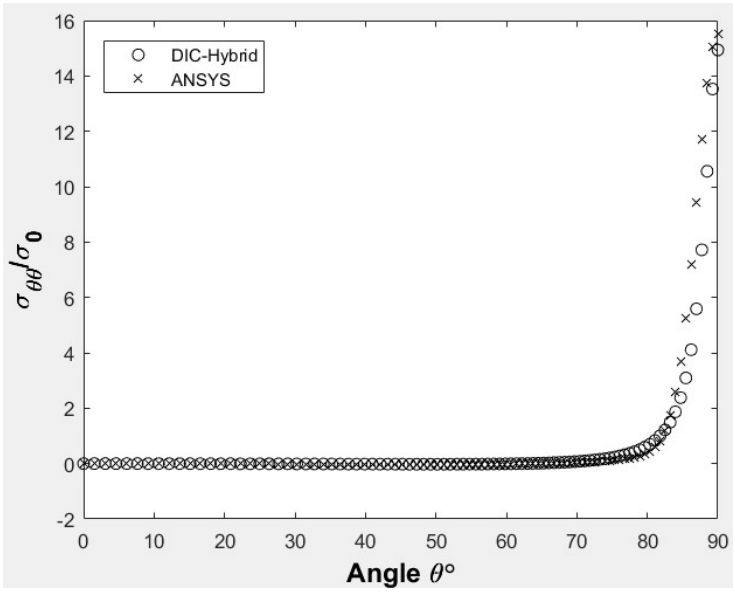

(a)

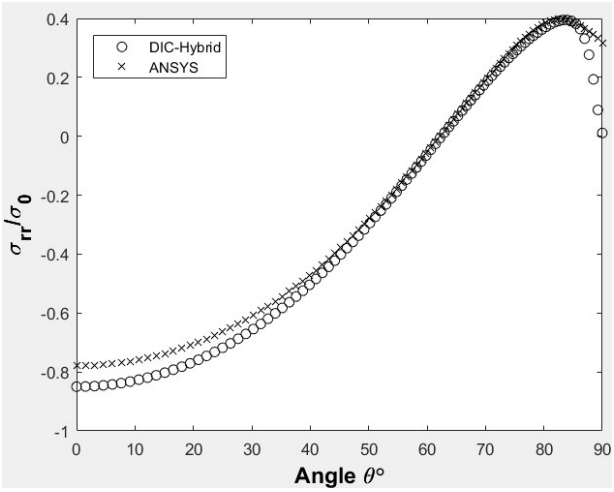

(b)

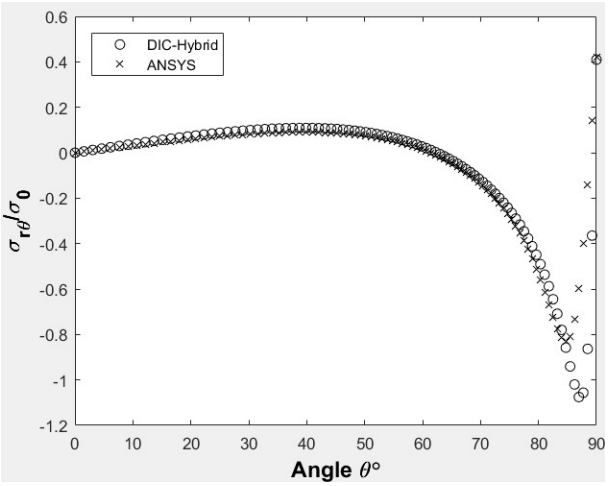

(c)

Figure 5-20: Plot of (a) $\sigma_{\theta\theta}/\sigma_0$, (b) σ_{rr}/σ_0 and (c) $\sigma_{r\theta}/\sigma_0$ along boundary of elliptical hole from hybrid-method based on DIC-measured displacement information, u, in vertical loading direction and FEM

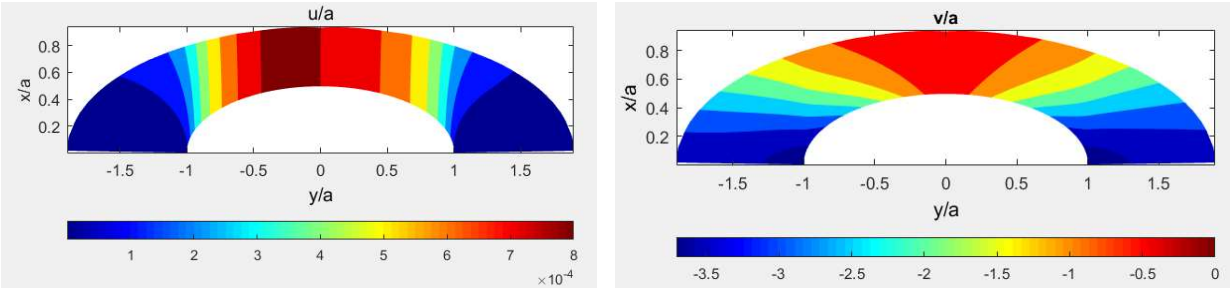

(a) (b)

Figure 5-21: Contours of (a) *u*/*a* and (b) *v*/*a* from FEM (left side) and hybrid-method based on DIC-measured displacement, *v*, in direction transverse to vertical loading direction (right side)

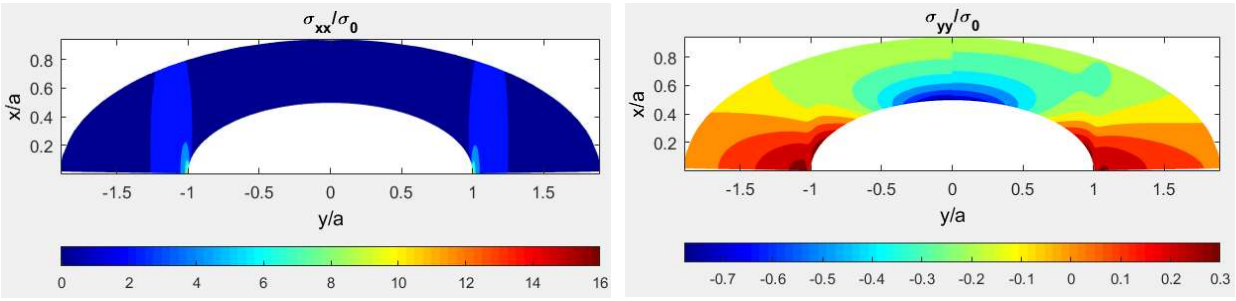

(a) (b)

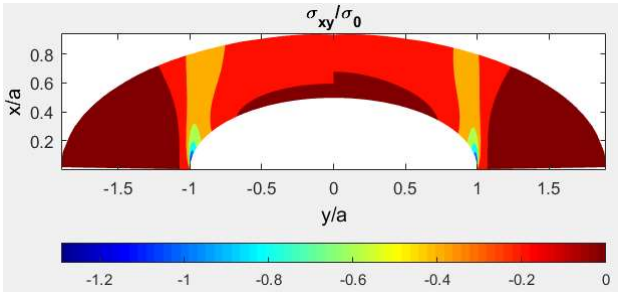

(c)

Figure 5-22: Contours of (a) σ_{xx}/σ_0, (b) σ_{yy}/σ_0 and (c) σ_{xy}/σ_0 from FEM (left side) and hybrid-method based on DIC-measured displacement information, *v*, in the direction transverse to vertical loading direction (right side)

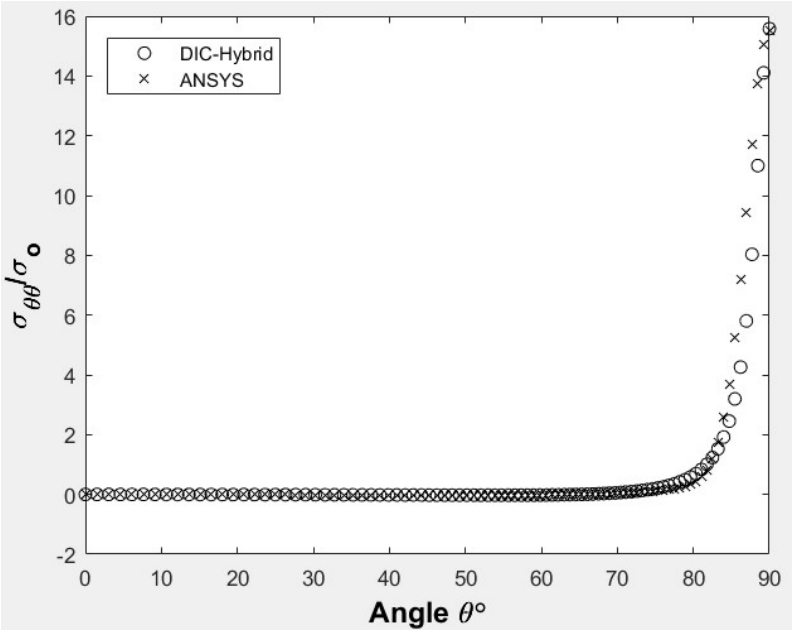

`(a)

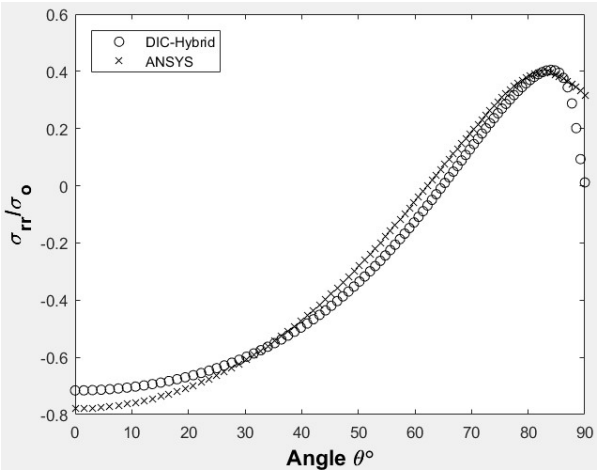

(b)

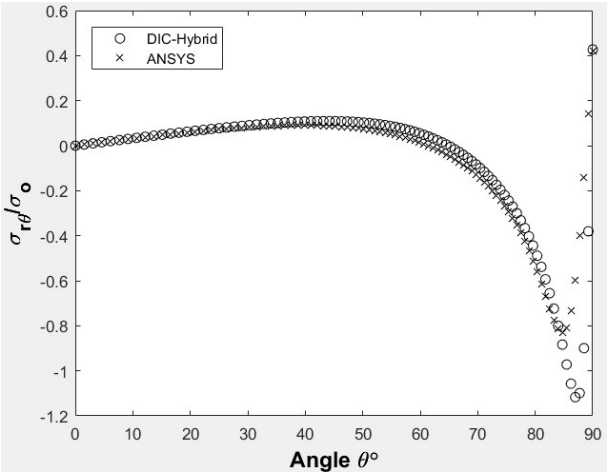

(c)

Figure 5-23: Plot of (a) $\sigma_{\theta\theta}/\sigma_0$, (b) σ_{rr}/σ_0 and (c) $\sigma_{r\theta}/\sigma_0$ along boundary of elliptical hole from hybrid-method based on DIC-measured displacement information, v, in the direction transverse to vertical loading direction and FEM

The normalized tangential stresses along the boundary of the elliptical hole (one quarter of the elliptical hole) is plotted in Figure 5-20 and Figure 5-23, based on the DIC-hybrid complex

analyses using the Laurent series expansion and is compared with the FEM-predictions. Hybrid results agree well with the FEM results of the tangential stresses along the entire edge of the hole.

5.8.1. Load Equilibrium

The load equilibrium was also checked to further assess the reliability of the DIC-hybrid method. By integrating the DIC-based computed stress component σ_{xx} along horizontal lines through the width of the loaded plate using equation (5-13), the computed load, F_c^*, from the DIC-hybrid analysis was determined, i.e.,

$$F_c^* = \int_{-\frac{W}{2}}^{\frac{W}{2}} \sigma_{xx} dA = 2 \int_{a}^{\frac{W}{2}} \sigma_{xx} t dy \quad \text{at } x = 0 \tag{5-13}$$

where t is the thickness and W is the width of the plate. Computing the integration using MATLAB's trapezoidal rule, the computed applied load at $x = 0$ is 4.63 kN (1,040 lbs) for the first case, where recorded u-displacements were used as input to compute σ_{xx}. For the second case, where σ_{xx} was calculated using recorded v-displacements as input, the computed load at $x = 0$ is 4.45 kN (1,001.6 lbs). These computed loads are within 4.06% and 0.16%, respectively, of the physically applied load. The DIC-hybrid method therefore satisfies the load equilibrium.

Figure 5-24 shows the effect of the number of Airy coefficients on the DIC-hybrid method computed load in the vertical x-direction at $x = 0$ from the load equilibrium of equation (5-13), when using u-displacements as input. The difference between the computed and physically applied loads increase as the number of Airy coefficients is increased to evaluate σ_{xx} from the DIC-hybrid

method. This further validates using $k = 2$ for $n_{DIC} = 20{,}704$ vertical displacements, u, as input in the DIC-hybrid method to stress analyze the finite orthotropic plate.

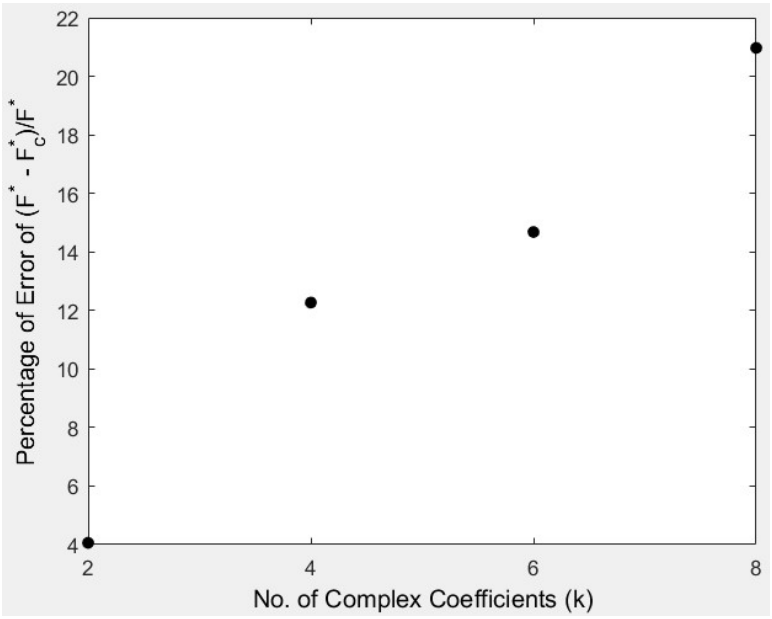

Figure 5-24: Plot of percentage of error between physically applied and DIC-hybrid method computed loads versus number of complex coefficients, k, for $n_{DIC} = 20{,}704$ vertical displacements, u, as input

Table 5-2 compares the real part, a_j, (imaginary part is zero) of the complex Airy coefficients from the DIC-hybrid analyses when separately using vertical u-displacements or horizontal v-displacements as input. It is observed that for both the cases the dominating Airy coefficients (a_{-1} and a_1 when using either u- or v-displacements as input) are quite similar to each other giving rise to similar results irrespective of using u or v-displacement data to stress analyze the plate.

Table 5-2: Comparing Airy coefficients from DIC-hybrid stress analysis involving an elliptically-perforated, finite, orthotropic plate from measured u- or v-displacement data

Airy coefficients a_j	From measured u and $k = 2$	From measured v and $k = 6$
a_{-1}	-69.47	-66.97
a_1	-59.59	-57.39
a_{-3}	-	2.28
a_3	-	1.89
a_{-5}	-	0.24
a_5	-	0.22

5.9. Validity of Presented Hybrid-Method for Finite-Width Plates

The reliability of the present experimental-analytical hybrid stress analysis method in treating a finite-width plate is demonstrated in this section. FEM analyses of the elliptically-perforated graphite-epoxy orthotropic plates were generated using ANSYS APDL for varying elliptical hole-opening, $2a$, to plate-width, W, ratios, i.e., for $0.2 \leq 2a/W \leq 0.9$. A plate with $2a/W$ close to 0.8 or above represents a very finite plate and those with $2a/W$ close to 0.2 represent a more infinitely-width plate.

FEM-simulated displacements, u, in the loading direction x, were used as input for the hybrid stress analysis method (in equation (5-4) to find c_j) and the plates were full-field stress analyzed (substituting c_j in equations (5-1) through (5-5)). The stress concentration factor (SCF), K_T, of a perforated plate is defined as the ratio of the maximum stress to nominal stress according to equation (5-14). For the elliptically-perforated graphite-epoxy plates similar to Figure 5-1 but with varying $2a/W$ ratios, when loaded along the strong/stiff fiber direction x, the maximum stress

occurs at the base of the elliptical hole, i.e., at $x = 0$, $y \rightarrow a$. This is observed from both FEM-predicted and DIC-hybrid (based on DIC-measured u or v input) computed σ_{xx} contours of Figure 5-19(a) and Figure 5-22(a), respectively. From the hybrid-method (using FEA-predicted u-displacements) computed in-plane stresses in the loading direction, σ_{xx}, the SCF, K_T, was evaluated using equation (5-14). These FEA-hybrid results are provided in Table 5-3. Similarly, the SCF, K_T, were determined directly by using the FEM-generated in-plane stresses in the loading direction, σ_{xx}, in equation (5-14), Table 5-3. Results of obtained K_T by FEA-hybrid method agree well with those derived from a direct FEA, Table 5-3 and Figure 5-25. The experimentally derived SCF from the DIC-hybrid method computed σ_{xx} using DIC-measured u-displacement data as input (for Figure 5-1) is overlaid with the FEA-hybrid and FEA, K_T in Figure 5-25. These experimental and FEA-based K_T results at $2a/W = 0.5$ agree well with each other. Note that all of the plates for these analyses (Table 5-3 and Figure 5-25) have an elliptical hole-opening ratio or sharpness of two, i.e., $a/b = 2$ and are of the same length, $L = 27.94$ cm (11"). All plates of Table 5-3 and Figure 5-25 have the same material properties, Table 4-1, and K_T were calculated using the gross cross-sectional area (equation (5-9)). Moreover, using FEA-predicted u-displacement data as input in the hybrid stress analysis method to stress analyze the plates is defined here as the FEA-hybrid method.

$$K_T = \frac{\sigma_{max}}{\sigma_0} = \frac{\sigma_{xx}(0, a)}{\sigma_0} \tag{5-14}$$

Tan [92] provided a closed-form equation to evaluate the SCF for an infinitely-wide orthotropic plate with an elliptical hole of major and minor radii a and b, respectively, as

$$K_T^{\infty} = 1 + \frac{a}{b}\sqrt{\frac{2}{S_{22}}\left(\sqrt{S_{11}S_{22}} - S_{12} + \frac{S_{11}S_{22} - S_{12}^2}{2S_{66}}\right)} \tag{5-15}$$

where S_{ij} are the in-plane stiffnesses of the laminate and subscripts 1- and 2- denote the directions parallel and transverse to the loading direction, respectively. For the current $[0_{13}/90_5/0_{13}]$ graphite-epoxy plate of Figure 5-1, the strong/stiff material direction 1 being parallel to the loading direction x, the above equation (5-15) can be re-written as

$$K_T^{\infty} = 1 + \frac{a}{b}\sqrt{2\left(\sqrt{\frac{E_{11}}{E_{22}}} - \nu_{12}\right) + \frac{E_{11}}{G_{12}}} \tag{5-16}$$

Tan also defined the ratio of the SCF, K_T, of a finite-width plate over the SCF for the same plate but of infinite-width with respect to the hole-opening $2a$, K_T^{∞}, as the finite width correction factor (FWCF) and this accounts for the effect of a plate's finite-width on its stress concentration [91], i.e.,

$$\text{FWCF} = \frac{K_T}{K_T^{\infty}} \tag{5-17}$$

For the present $[0_{13}/90_5/0_{13}]$ graphite-epoxy plate with $a/b = 2$ using the constitutive material properties of Table 4-1 and equation (5-16), K_T^{∞} is found to be 13.5. Using all this information in equation (5-17), i.e., the SCFs, K_T, evaluated for the graphite-epoxy plates with $a/b = 2$ and $0.2 \leq 2a/W \leq 0.9$ from FEA, FEA-hybrid and DIC-hybrid method and K_T^{∞} of 13.5, the

FWCF of the plates with varying $2a/W$ are determined, Table 5-3 and Figure 5-26. The obtained FWCF values by the three different methods, show good agreement.

Table 5-3: Comparison of SCF and FWCF for various ratios of $2a/W$ and $a/b = 2$

$2a/W$	K_T from FEM analysis directly	FWCF determined from FEM analysis directly	K_T based on FEM simulated displacement information in hybrid-method (FEA-hybrid)	FWCF based on FEM simulated displacement information in hybrid-method (FEA-hybrid)	K_T from DIC determined data for finite-width plate	FWCF based on DIC determined data for finite-width plate
0.2	15.32	1.14	15.5	1.16		
0.3	15.41	1.15	14.79	1.10		
0.35	15.52	1.16	14.86	1.11		
0.5	16.43	1.22	15.89	1.18	15	1.11
0.52	16.45	1.23	15.44	1.15		
0.54	16.75	1.25	15.65	1.17		
0.56	16.94	1.26	16.01	1.19		
0.58	17.32	1.29	16.22	1.21		
0.6	17.71	1.32	17.48	1.3		
0.62	18.08	1.35	17.94	1.34		
0.64	18.5	1.38	18.42	1.37		
0.75	22.66	1.69	21.31	1.59		
0.8	25.39	1.89	25.58	1.91		
0.85	31.12	2.32	29.89	2.23		
0.9	41.27	3.08	39.28	2.93		

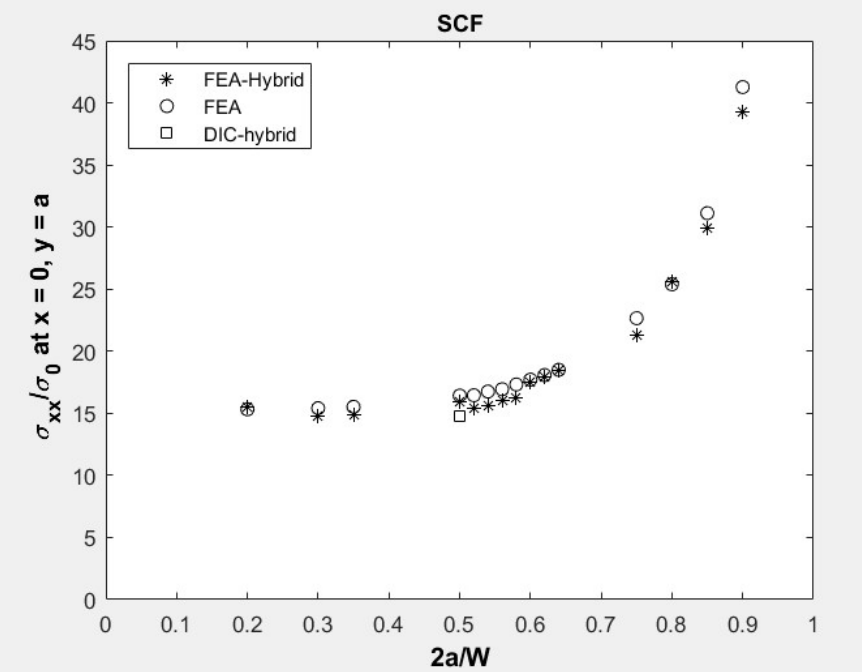

Figure 5-25: SCF, σ_{xx}/σ_0, of elliptically-perforated plates for various $2a/W$ ratios from FEA, FEA-hybrid and DIC-hybrid stress analyses

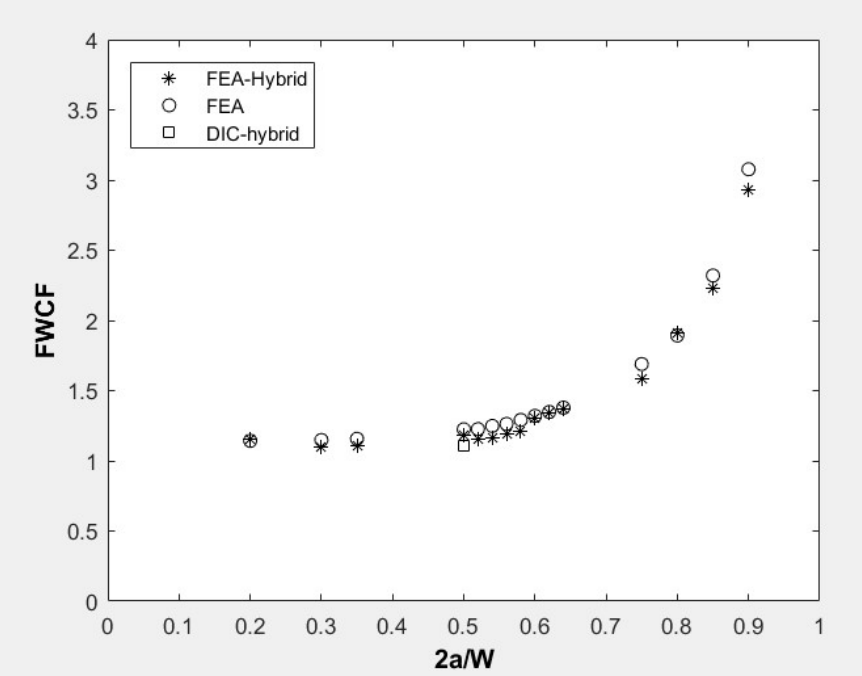

Figure 5-26: FWCF of elliptically-perforated plates for various $2a/W$ ratios from FEA, FEA-hybrid and DIC-hybrid stress analyses

Tan [91] developed closed-form solutions to estimate a plate's FWCF that account for the effect of the plate's finite-width on the SCF. For an orthotropic plate with an elliptical-opening the approximate FWCF is

$$\begin{aligned}\frac{K_T^{\infty}}{K_T} &= \frac{\lambda_T^2}{(1-\lambda_T)^2} + \frac{(1-2\lambda_T)}{(1-\lambda_T)^2}\sqrt{1+(\lambda_T^2-1)\left(\frac{2a}{W}\right)^2} \\ &- \frac{\lambda_T^2}{(1-\lambda_T)}\left(\frac{2a}{W}\right)^2\left[1+(\lambda_T^2-1)\left(\frac{2a}{W}\right)^2\right]^{-\frac{1}{2}} \\ &+ \frac{\lambda_T^7}{2}\left(\frac{2a}{W}\right)^6\left(K_T^{\infty}-1-\frac{2}{\lambda_T}\right)\left\{\left[1+(\lambda_T^2-1)\left(\frac{2a}{W}\right)^2\right]^{-\frac{5}{2}}\right. \\ &\left.-\left(\frac{2a}{W}\right)^2\left[1+(\lambda_T^2-1)\left(\frac{2a}{W}\right)^2\right]^{-\frac{7}{2}}\right\}\end{aligned} \tag{5-18}$$

Tan [91] later proposed the following modified version for the FWCF of the above equation (5-18)

$$\frac{K_T^{\infty}}{K_T} = \frac{\lambda_T^2}{(1-\lambda_T)^2} + \frac{(1-2\lambda_T)}{(1-\lambda_T)^2}\sqrt{1+(\lambda_T^2-1)\left(\frac{2a}{W}M_f\right)^2}$$
$$-\frac{\lambda_T^2}{(1-\lambda_T)}\left(\frac{2a}{W}M_f\right)^2\left[1+(\lambda_T^2-1)\left(\frac{2a}{W}M_f\right)^2\right]^{-\frac{1}{2}}$$
$$+\frac{\lambda_T^7}{2}\left(\frac{2a}{W}M_f\right)^6\left(K_T^{\infty}-1-\frac{2}{\lambda_T}\right)\left\{\left[1+(\lambda_T^2-1)\left(\frac{2a}{W}M_f\right)^2\right]^{-\frac{5}{2}}\right.$$
$$\left.-\left(\frac{2a}{W}M_f\right)^2\left[1+(\lambda_T^2-1)\left(\frac{2a}{W}M_f\right)^2\right]^{-\frac{7}{2}}\right\} \quad (5\text{-}19)$$

where $\lambda_T = b/a$, K_T^{∞} is a function of the plate's elastic material properties and the hole ratio a/b and is evaluated from equation (5-16). The quantity M_f is a magnification factor expressed in equation (5-20), and is only a function of the plate's $2a/W$ ratio.

$$M_f^2 = \frac{\sqrt{1-8\left[\frac{3\left(1-\frac{2a}{W}\right)}{2+\left(1-\frac{2a}{W}\right)^3}-1\right]}-1}{2\left(\frac{2a}{W}\right)^2} \quad (5\text{-}20)$$

For the current elliptically-perforated, finite orthotropic plate of Figure 5-1, in-plane stresses in the loading direction, x, along the horizontal center-line ($x = 0$) evaluated by the DIC-hybrid method were also checked against other approximate solutions available in the literature. For the plate coordinates of Figure 5-1, according to Tan's study [92], the normalized in-plane

stresses, σ_{xx}, in the loading direction x, along the plate's horizontal center-line at $x = 0$ from $y = a$ to $y = W/2$ can be represented as the following equation (5-21), where $\kappa = y/a$.

$$\frac{\sigma_{xx}(0,y)}{\sigma_0} = \frac{\lambda_T^2}{(1-\lambda_T)^2} + \frac{(1-2\lambda_T)\kappa}{(1-\lambda_T)^2\sqrt{\kappa^2-1+\lambda_T^2}} + \frac{\lambda_T^2\kappa}{(1-\lambda_T)(\kappa^2-1+\lambda_T^2)^{\frac{3}{2}}} - \frac{\lambda_T^7}{2}\left(K_T^\infty - 1 - \frac{2}{\lambda_T}\right)\left[\frac{5\kappa}{(\kappa^2-1+\lambda_T^2)^{\frac{7}{2}}} - \frac{7\lambda_T^2\kappa}{(\kappa^2-1+\lambda_T^2)^{\frac{9}{2}}}\right] \tag{5-21}$$

From a study by Bao et al. [93] for a tensile-loaded orthotropic plate of width W with an central notch of length $2a$, the SCF and the in-plane stresses in the loading direction (considered as x- here) along a horizontal center-line are expressed as

$$K_T = \sigma_0\sqrt{\pi a}Y(\rho)\left[1 - 0.025\left(\frac{2a}{W}\right)^2 + 0.06\left(\frac{2a}{W}\right)^4\right]\sqrt{\sec\frac{\pi a}{W}} \tag{5-22}$$

where for the plate of Figure 5-1,

$$\rho = \frac{(E_{11}E_{22})^{\frac{1}{2}}}{2G_{12}} - (\nu_{12}\nu_{21})^{\frac{1}{2}} \tag{5-23}$$

and

$$Y(\rho) = 1 + 0.1(\rho-1) - 0.016(\rho-1)^2 + 0.002(\rho-1)^3 \tag{5-24}$$

$$\frac{\sigma_{xx}(0,y)}{\sigma_0} = \frac{K_T}{\sigma_0\sqrt{2\pi r}} \tag{5-25}$$

where r is measured along the horizontal center-line ($x = 0$) of the plate of Figure 5-1 from $y \rightarrow a$ to $y = W/2$. As these equations were originally designed to treat orthotropic plates with cracks and consider the stress singularities near the crack-tip, the distance r is considered slightly away from the location $y = a$.

The in-plane stresses in the loading direction, σ_{xx}, computed from the DIC-hybrid stress analysis method (using u-displacements as input) is plotted in Figure 5-27, as are those evaluated from equation (5-21) and from combining equations (5-22) through (5-24) into equation (5-25), along the horizontal center-line passing through $y = a$ to $W/2$ at $x = 0$. The DIC-hybrid method computed stress distribution agrees with the approximate solutions provided by Tan [91] except at $x = 0$ for $y = a$ where the DIC-hybrid method provides higher maximum stress, Figure 5-27.

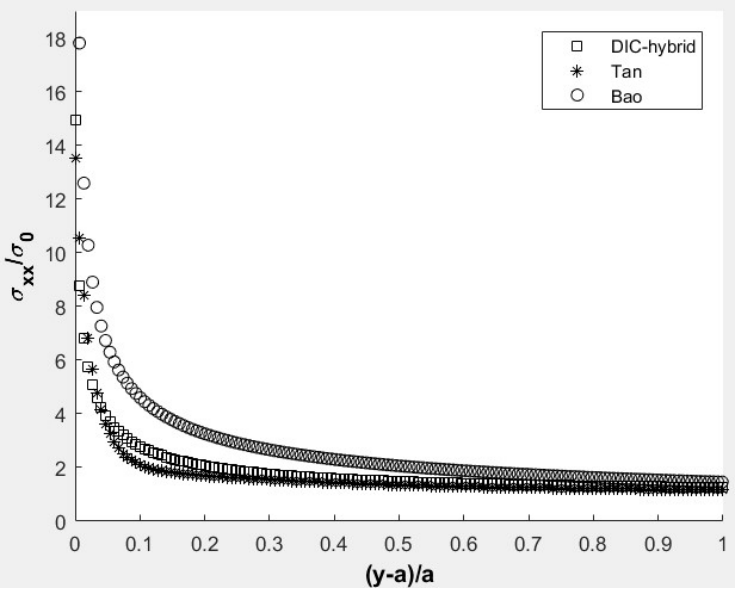

Figure 5-27: Normalized in-plane stresses in the loading direction, σ_{xx}/σ_0, from DIC-hybrid method, Tan's method [92] and Bao's method [93] of elliptically-perforated plate of Figure 5-1

For the current elliptically-perforated [$0_{13}/90_5/0_{13}$] graphite-epoxy plate of Figure 5-1, with $2a/W$ of 0.5, the SCF, K_T, was derived from all the above-mentioned approaches and compared with that experimentally obtained from the DIC-hybrid method computed stresses. All such results of K_T are summarized in Table 5-4. For the elastic properties of the plate (Table 4-1), the SCF for an infinitely-width plate, K_T^{∞}, is evaluated from equation (5-16). The K_T of the finite, elliptically-perforated plate is obtained from Tan's FWCF approach (equation (5-18)) and modified FWCF approach (equation (5-19)) and Bao's approach (equation (5-22)). In addition, K_T of the plate for $2a/W = 0.5$ from direct FEA-predictions and from using FEA predicted u-displacement data in the hybrid stress analysis method are obtained, i.e., FEA-hybrid method (from Table 5-3) and compared. The DIC-hybrid predicted K_T agrees well with those evaluated from these other approaches. This further validates the presented DIC-hybrid method's ability to reliably stress analyze finite-width plates.

Table 5-4: SCF and FWCF of the elliptically-perforated plate with $2a/W$ of 0.5

From	K_T	K_T^{∞}	K_T/ K_T^{∞}
Present DIC-Hybrid Stress Analysis	15	13.5 equation (5-16)	1.11
FEA-Hybrid Stress Analysis (input FEA simulated u)	15.89		1.18
FEA	16.43		1.22
Tan's FWCF ($a/b \leq 1$) (equation (5-18))	13.8		1.02
Tan's Modified FWCF ($a/b \leq 4$) (equation (5-19))	17.9		1.33
Bao's Method (essentially for plates with central cracks) (equation (5-22))	12.9		0.96

5.10. Hybrid-Method Validity for Various Hole-Opening Ratios (a/b)

In this section the effect of the plate's elliptical hole-opening sharpness, i.e., the ratio of the major to minor radii, a/b, on the SCF is studied. For the graphite-epoxy laminate of Table 4-1, FEAs were generated and analyzed in ANSYS for varying a/b and $2a/W$. The SCF of the different plates were determined directly from the FEA-predicted in-plane normal stresses in the loading direction and from those computed by the hybrid stress analysis by using FEA-predicted u-displacements as input, i.e., FEA-hybrid analysis. Results are presented in Table 5-5. All plates analyzed have the same length (L = 27.94 cm) and thickness (t = 5.28 mm). For the graphite-epoxy plates with varying a/b and $2a/W$, the K_T results obtained from FEA and FEA-hybrid method show good agreement.

Table 5-5: SCF of elliptically-perforated graphite-epoxy plates for material properties of Table 4-1 from FEA and FEA-hybrid

From	FEA	FEA-Hybrid	FEA	FEA-Hybrid	FEA	FEA-Hybrid
$2a/W$ \ a/b	1.5	1.5	2	2	2.5	2.5
0.4	11.65	11.69			20.16	19.36
0.5	12.42	12.32	16.43	15.89	20.59	19.62
0.6	13.77	13.62	17.71	17.48	21.81	20.40
0.7	16.19	15.91			24.85	22.18
0.8	20.87	20.63	25.39	25.58	30.89	27.42

5.11. Hybrid-Method Validity for Various Materials

The present DIC-hybrid stress analysis method is capable of analyzing both isotropic and orthotropic plates of essentially any elastic material properties. This is demonstrated here by analyzing plates with different material properties. The material properties of Table 5-6 were selected such that they represent an orthotropic member with very little anisotropy ($E_{11}/E_{22} = 1.03 \approx 1$), i.e., the loaded plate behavior is almost isotropic. FEAs of these new plates were generated for several hole-opening ratios (a/b) and hole-opening to plate-width ratios ($2a/W$). The SCF of these plates were evaluated directly from FEA and FEA-hybrid method, Table 5-7. As the orthotropic material properties of Table 5-6 are close to isotropy, the SCF of isotropic elliptically-perforated finite plates under axial loading from Isida [67] and Durelli et al. [94] (Appendix G) were obtained for several hole-opening to plate-width ratios, $2a/W$, for the hole-opening ratios, a/b of 2 and 4, Table 5-8. The obtained SCF for isotropic plates (Table 5-8) and slightly orthotropic plates of Table 5-6 (Table 5-7) are compared in Figure 5-28 for varying a/b and $2a/W$ ratios. Whereas the results of Table 5-8 are those determined by the respective authors, Figure 5-28 demonstrates good agreement between the K_T results obtained from the FEA-hybrid stress analysis method with those directly from FEA, Isida [67] and Durelli et al. [94].

Table 5-6: Slightly orthotropic elliptically-perforated plate's material properties

Properties	Symbol	Value	Units
Elastic modulus in strong/stiff direction	E_{11} or E_{xx}	210.29	GPa
Major Poisson's ratio	ν_{12} or ν_{xy}	0.25	Dimensionless
Elastic modulus perpendicular to direction -1	E_{22} or E_{yy}	203.39	GPa
Shear modulus	G_{12} or G_{xy}	82.74	GPa

Table 5-7: SCF for elliptically-perforated plate with material properties of Table 5-6

From	FEA	FEA-Hybrid	FEA	FEA-Hybrid	FEA	FEA-Hybrid
$2a/W$ \ a/b	2	2	3	3	4	4
0.4	5.88	5.78	8.08	8.09	10.51	10.38
0.5	6.53	6.51	8.86	8.85	11.22	11.13
0.6	7.58	7.55	10.06	10.07	12.59	12.51
0.7	9.39	9.15	12.11	12.08	14.95	14.89
0.8	13.04	12.42	16.17	15.66	19.57	19.26

Table 5-8: SCF for elliptically-perforated isotropic finite-width plates

From	Isida [67]		Durelli [94]	
$2a/W$ \ a/b	2	4	2	4
0.4	5.8	10.2	5.7	9.5
0.5	6.48	11.18	6.3	10.5
0.6	7.55	12.58	7.6	11.7
0.7	9.4	14.9	9.5	14.1
0.8	13	19.4	14.2	18.95

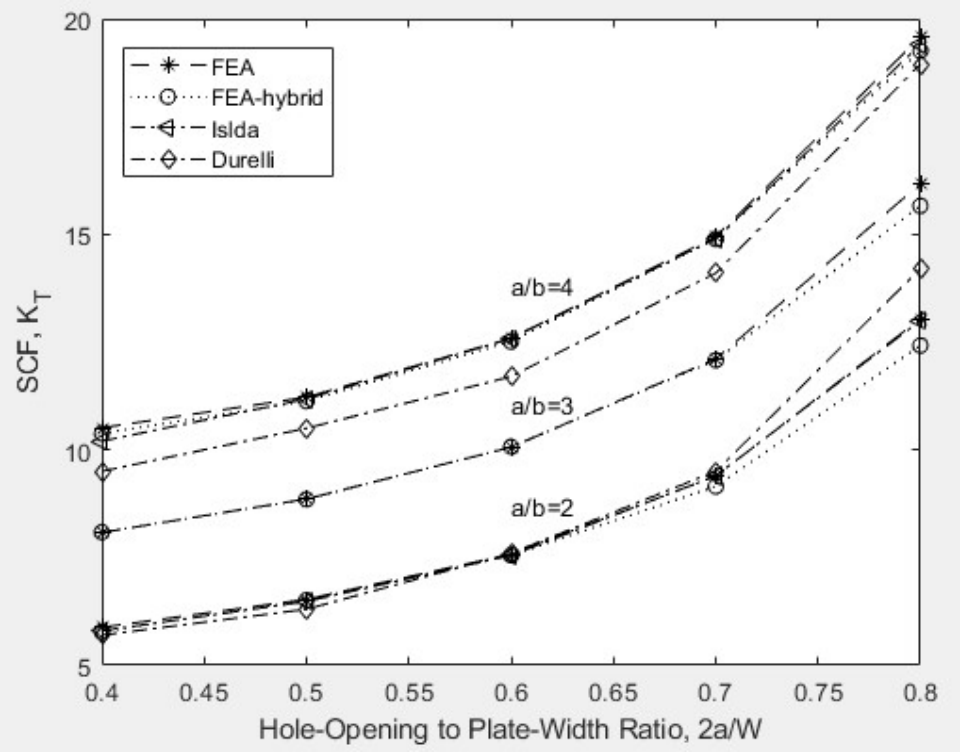

Figure 5-28: Comparison of SCF for slightly orthotropic elliptically-perforated plates (Table 5-6) from FEA, FEA-hybrid method and isotropic plates from Isida [67] and Durelli et al. [94]

The reliability of the hybrid stress analysis method in treating highly anisotropic plates was also demonstrated by analyzing such plates with material properties of Table 5-9 [95] for E_{11}/E_{22} = 19.19. FEAs of the plates were created in ANSYS APDL and K_T were evaluated directly from FEA-predictions and FEA-hybrid method using u-displacements as input, equation (5-14), Table 5-10. Good agreement exists between the FEA and FEA-hybrid method evaluated K_T values.

It can be concluded that the experimental-analytical hybrid means of stress analysis is capable of analyzing orthotropic finite-width plates of any degree of anisotropy, i.e., of virtually any elastic material properties.

Table 5-9: Material properties of highly anisotropic graphite-epoxy plate from Daniel and Ishai [95]

Parameters	Symbol	Value	Units
Elastic modulus in strong/stiff direction	E_{11} or E_{xx}	190	GPa
Major Poisson's ratio	ν_{12} or ν_{xy}	0.35	Dimensionless
Elastic modulus perpendicular to direction -1	E_{22} or E_{yy}	9.9	GPa
Shear modulus	G_{12} or G_{xy}	7.8	GPa

Table 5-10: SCF for highly anisotropic plates of Table 5-9

From	FEA	FEA-Hybrid	FEA	FEA-Hybrid
$2a/W$ \ a/b	2	2	4	4
0.4	14.68	14.73	35.42	35.49
0.5	15.18	15.16	36.26	35.89
0.6	16.56	16.15	36.88	36.34
0.7	19.33	19.19	38.28	38.48
0.8	24.65	24.36	45.67	45.21
0.9	39.24	39.63	66.36	66.96

A FEA of an isotropic plate with the same dimensions as those of the orthotropic graphite-epoxy plate of Figure 5-1, i.e., with $2a/W = 0.5$ and $a/b = 2$, was also analyzed. The SCF of the isotropic plate was evaluated individually from direct FEA and the FEA-hybrid method, Table 5-11. It is interesting to note that the present tensile SCF exceeds that for the equivalent isotropic case by approximately 132% ($K_{T\,|\,\text{Isotropic}} = 6.47$).

Table 5-11: SCF of an isotropic (aluminum) plate with $2a/W$ of 0.5

From	FEA	FEA-Hybrid	Isida	Durelli	Neuber
$2a/W$ \ a/b	2	2	2	2	2
0.5	6.49	6.47	6.5	6.3	7.2

In Figure 5-29 and Figure 5-30, the in-plane stress and displacement contours from FEA and FEA-hybrid analysis show excellent correlation. This further validates the hybrid stress analysis method's ability in providing reliable results for plates with virtually any type of material properties.

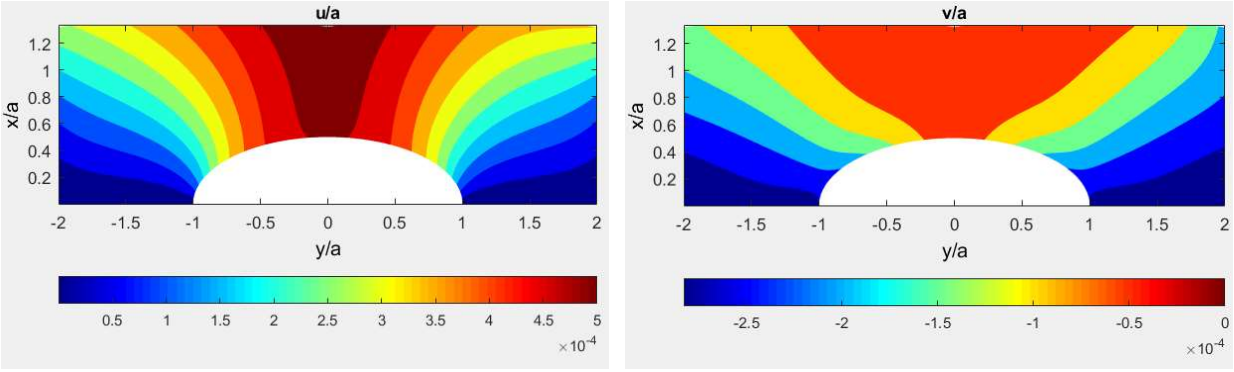

(a) (b)

Figure 5-29: Contours of (a) u/a and (b) v/a from FEA (left side) and FEA-hybrid method (right side) based on FEA-predicted displacement information, u, in loading direction for elliptically-perforated, $2a/W = 0.5$ and $a/b = 2$, isotropic plate (aluminum)

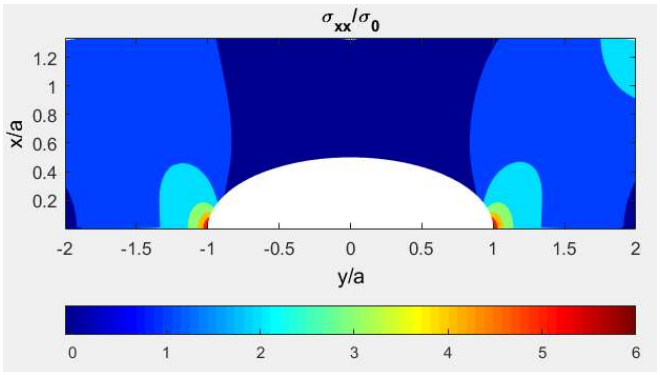

(a)

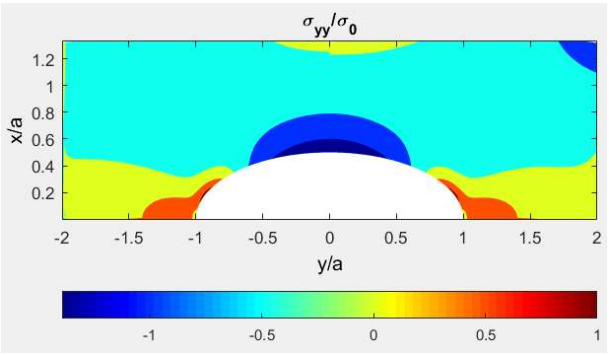

(b)

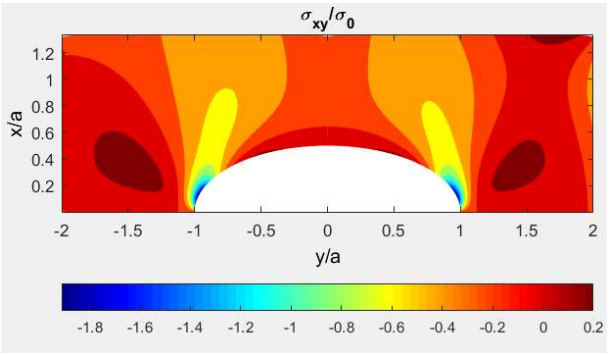

(c)

Figure 5-30: Contours of (a) σ_{xx}/σ_0, (b) σ_{yy}/σ_0 and (c) σ_{xy}/σ_0 from FEA (left side) and FEA-hybrid method (right side) based on FEA-predicted displacement information, u, in loading direction for elliptically-perforated, $2a/W = 0.5$ and $a/b = 2$, isotropic plate (aluminum)

These analyses demonstrate that, the hybrid stress analysis method can provide reliable results for virtually any type of plates, i.e., plates with any material properties (isotropic or orthotropic), any hole-opening sharpness, a/b, and of any plate width with respect to the hole size, $2a/W$. Although the herein-employed equations assume infinite geometry [5], the contents of Sections 5.9 through 5.11 illustrate that they can be used reliably for finite geometries (at least over wide ranges of $2a/W$, a/b and material properties), i.e., particularly for the present DIC-analyzed $[0_{13}/90_5/0_{13}]$ graphite-epoxy plate of Figure 5-1 with $2a/W = 0.5$. The method's ability to effectively analyze plates experiencing variety of loadings is also demonstrated in Appendix H.

5.12. Summary, Discussion and Conclusions

Hybridizing measured displacement data, i.e., processing them with a combination of complex variables Airy stress functions, conformal mapping, analytic continuation, least squares and power-series expansions provides an excellent method to evaluate the stresses, including those on and near the edge of a discontinuity, in loaded, perforated, finite-width orthotropic structures. This includes plates with elliptically-perforated holes. Advantages of this method over techniques such as numerical methods (finite elements, finite differences or boundary collocation), analytical models, purely experimental methods or commercial stress analysis packages include not requiring either of the following: (1) knowledge of the external loading or boundary conditions; (2) experimental data near the edge of any cutouts; (3) recorded information of both u and v displacements or (4) differentiating them using arbitrary methods. The simultaneous smoothing of the measured data and separation into the individual stress components are additional desirable features of the present approach. DIC avoids the contact requirements of strain-gage or moiré techniques, or the cyclic-loading needs of thermoelastic stress techniques.

The present study applies these hybrid concepts to determine the stresses and displacements in an elliptically-perforated $[0_{13}/90_5/0_{13}]$ graphite-epoxy orthotropic finite-width plate. The measured data were processed using strong mechanics-based analytical formulations of Airy stress functions satisfying equilibrium and compatibility, conformal mapping and analytic continuation satisfying traction-free boundary conditions. No additional symmetry or boundary conditions were imposed. DIC-hybrid results are supported by those from FEM, load equilibrium and other published information.

A previous study using DIC to stress analyze a perforated laminated plate reported difficulties in obtaining reliable results at the edge of the hole. Reference [13] used Correlated Solution, Inc.'s commercial correlation software to obtain the recorded displacement data and estimate strains. Their study failed to provide strain information near the edge of the hole. Displacements were calculated slightly away from the hole's edge resulting in no strain data along those areas. Strain distribution of laminated composites was also found to be highly depended on the spatial resolution, step, subset and filtering size when using commercial software to find strains from measured displacements. Use of higher filter sizes can lead to the possibility of masking the high strain gradients. Such challenges have no effect on the present technique. This is because the stress/strain components at and near the discontinuity are determined by excluding data near the cutout, i.e., maximum stress/strain gradients are evaluated from data away from the locations where the maximum values actually occur.

The DIC-hybrid technique is employed here to stress analyze an elliptically-perforated orthotropic plate. However, the general concepts are applicable to other composite problems, e.g., other shaped cutouts, other external geometries and/or more complicated loading and other forms of measured data. Although employing the recorded displacement data in the loading direction is emphasized here, the presently successful use of those in the transverse direction is illustrated. The author is unaware of any previous study whereby the displacement field transverse to the loading direction alone was used to stress analyze a perforated orthotropic structure. Unlike most of the herein cited analyses for finite composites, the presented technique can handle virtually any external geometry. The present ability to satisfy the internal boundary conditions analytically is also advantageous. The method is applicable for various types of loading, Appendix H.

Albeit the infinite-width assumption in the analytical expressions [5], the current DIC-hybrid method gives good results for finite laminate material up to at least $2a/W = 0.85$ to 0.9. This is well beyond the physically-tested case of $2a/W = 0.5$, Figure 5-1. Extensive studies conducted here demonstrates that the present equations are reliable for $2a/W$ up to at least 0.9 for a variety of orthotropic materials and for different elliptical-hole sharpness ratios, a/b. The technique can also reliably analyze isotropic members.

Chapter 6. Stress Analysis of Circularly-Perforated Tensile Plate with Absent Experimental Data Near the Edge of the Hole

6.1. Introduction

The present chapter experimentally assesses the structural integrity of a loaded, finite, asymmetrically-perforated plate with absent experimental input at critical locations near the cutout. Despite missing data at important locations, the technique of hybridizing measured quantities with analytical concepts and numerical tools is capable of providing reliable stress information at those important locations of missing data. This is accomplished by processing distant measured load-induced temperature information with an Airy stress function plus some applied boundary conditions. The approach involves neither knowing the plate's elastic properties or external loading condition, nor requires differentiating the measured data. Reliability is confirmed by force equilibrium and result from a strain-gage and FEM.

6.2. General Overview

Strength criteria, fatigue considerations or assessing the integrity of structural members necessitates knowing the stresses. However, stress analyses of asymmetrically-perforated loaded, finite plates are difficult by purely analytical or theoretical stress analysis methods. Such approaches tend to be limited to simple situations involving infinite geometries. Moreover, and like numerical approaches such as the finite element method (FEM), analytical/theoretical analyses

depend on reliable knowledge of the boundary conditions and external loading. The latter are commonly unknown in practice. Purely experimental techniques suffer from their inability to provide reliable information near the edge of the cutouts, these often being locations of greatest mechanical interest. Thermoelastic stress analysis (TSA) is a contemporary technique of determining stresses experimentally. Advantages of TSA include being applicable to both isotropic or orthotropic materials and virtually requires no surface preparation. In addition, TSA does not require knowing the constitutive material properties, nor is it necessary to differentiate the measured data. The relationship between the local temperature and state of stress in TSA presupposes an adiabatic response. This is usually addressed by cyclically loading the member of interest. However, depending on the loads needed, it can be problematic to cyclically load a member sufficiently rapidly to achieve adiabatic conditions in regions of high stress gradient, e.g., at fillets, where the most serious stress typically occurs. The prospects of not locally satisfying adiabaticity adequately, combined with the reality that recorded-TSA information is unreliable within several pixels of an edge, can render it challenging to obtain dependable important stresses in situations such as near-by multiple holes or notches, or at geometric discontinuities near member edges. While approaches have been proposed for correcting the local lack of adiabaticity, a method is provided here whereby reliable solutions are obtainable by just avoiding the use of unreliable experimental information. Therefore, the ability to reliably stress analyze, finite-width, perforated loaded members in the presence of unreliable/absent data can be important to ensure their structural integrity.

Recognizing the above, the present analysis demonstrates the ability to evaluate stresses experimentally at a structurally important location engulfed within a significantly large region throughout which there is no dependable input information. The particular case considered

involves a hole near an edge of the vertically loaded aluminum plate illustrated in Figure 6-1. The hole being located very close to the right vertical edge of the plate, no reliable experimental data are obtained at locations adjacent to the hole boundary close to the right edge of the plate. Under such condition, the quality of the stress at point A in Figure 6-1 is of major concern here.

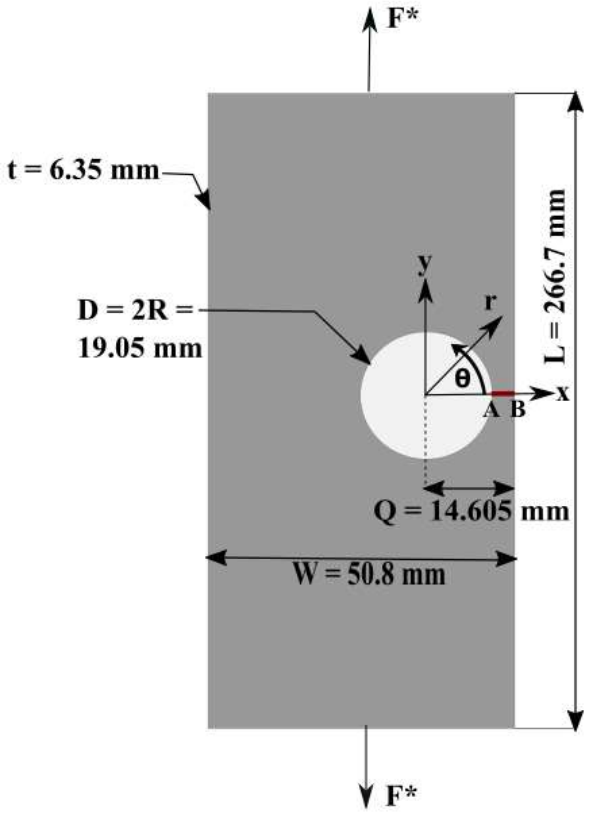

Figure 6-1: Schematic of off-axis perforated aluminum tensile plate

The present hybrid approach involves processing the measured thermal information with an Airy stress function. Notwithstanding the 'assumption' that there are no dependable measured input data within 19-pixels of location A, the TSA results agree with those from a strain-gage, FEM and force equilibrium. In practice, unreliable TSA information in a region surrounding point

A of Figure 6-1 could be due to effects such as inadequate adiabaticity and/or a deficient layer of black paint. Albeit, the cyclic loading effect could be more serious at the top and bottom of the hole than at location A in Figure 6-1. Issues associated with inadequate adiabatic response might be more serious in orthotropic composites because of their very high stress concentrations/gradients.

This study signifies the extent to which the hybrid stress analysis method (combining measured data with an Airy stress function) can be used to provide important reliable stress information in perforated-plates. Most other techniques would fail to do so due to the lack of measured information along the traction-free edges or at critical locations.

6.3. Literature Review

Lin et al. [96] used thermoelasticity with Airy stress function to stress analyze a finite plate with a near-edge circular hole under a concentrated load and Wang et al. [97] used photoelasticity (PSA) to study a similar situation involving a semi-finite plate using Hertz contact theory. One of the advantage of using TSA over PSA is that desired information is extracted from the TSA-measured isopachic stresses [96] using linear least squares whereas photoelastic isopachic stresses [97] requires non-linear least squares. Lin et al. [98] also used TSA-measured data and Airy stress function to stress analyze a loaded, finite, centrally-perforated rectangular plate, i.e., the cutout was located at the center of the plate instead near the edge of the plate and measured-information was available near the cutout. Ryall et al. [99] proposed a method that combines TSA, Airy stress function, non-linear least squares to evaluate both the first and second thermoelastic isopachic stresses to analyze perforated plates with cutouts.

Khaja [74], Lin et al. [100], Philip [101], Alshaya [19] and Paneerselvam et al. [102] all analyzed finite plates with near-edge cutouts under concentrated load using an Airy stress function and measured data. Apart from Philip [101], who analyzed a finite plate with an asymmetrical complex-shaped cutout, the other authors studied finite plates with circular cutouts. Paneerselvam et al. [102] worked with displacement data from DIC, whereas the other studies involved TSA data to stress analyze the finite plates. Though most of these studies employed a real variables Airy stress function, Alshaya [19] used complex variables Airy stress functions and conformal mapping for the stress analysis. Khaja [74] simplified the current Airy stress equations used in his study, which were previously used by Lin et al. [96,100]. All the above-mentioned studies involved a near edge cutout located under a concentrated compressive load in a finite plate and combined Airy stress function with measured data excluding data near the edges. All are capable of providing reliable information at and near the edge of the cutout.

Thermoelastically measured information can be highly sensitive to factors such as the paint-coating thickness, non-adiabaticity due to inadequate loading frequency or presence of any near-by edges. These can give rise to regions without any reliable TSA-measured data. McKelvie [103] and Mackenzie [104] have analyzed the thermoelastic consequences of factors such as variations in thickness of the paint coating, whereas Quinn and Dulieu-Barton [105] identified causes of non-adiabatic behavior. Joglekar [106] considered an aluminum tensile plate containing a hole near a vertical edge somewhat similar to the current situation. Unlike the present emphasis, his objective was to evaluate the influence of the amount and source locations of the recorded TSA information on the stresses. However, he encountered adiabatic concerns in that the initial testing system used was unable to cycle as rapidly as desired at the magnitude of the loads needed. He had to subsequently employ a different testing system in a different laboratory. References [107–

110] discuss non-adiabatic thermoelastic studies and in some cases provide means of correcting for the lack of adiabaticity.

The main highlight of this study is that the cutout being located extremely close to the plate's right vertical edge leads to a wide range of absent/unreliable measured data over a large region containing the most serious stresses. Despite having a significant amount of absent/unreliable data in regions close to the cutout, the present hybrid-method provides reliable stress information at and near the cutout by using a real-variables Airy stress function along with distant reliable TSA-recorded data. No knowledge of the external loading or the elastic material properties of the plate are required.

6.4. Relevant Equations

In absence of body forces and for plane-stressed problems involving isotropy, an Airy stress function is the solution of the bi-harmonic differential expression of equation (6-1) and which is the representation of equilibrium and compatibility [28].

$$\nabla^4 \Phi = 0 \tag{6-1}$$

$$\begin{aligned}\Phi = {} & a_0 + b_0 \ln r + c_0 r^2 + d_0 r^2 \ln r + (A_0 + B_0 \ln r + C_0 r^2 + D_0 r^2 \ln r)\theta \\ & + \left(a_1 r + b_1 r \ln r + \frac{c_1}{r} + d_1 r^3\right) \sin\theta \\ & + \left(\acute{a_1} r + \acute{b_1} r \ln r + \frac{\acute{c_1}}{r} + \acute{d_1} r^3\right) \cos\theta \\ & + (A_1 r + B_1 r \ln r)\theta \sin\theta + \left(\acute{A_1} r + \acute{B_1} r \ln r\right)\theta \cos\theta \\ & + \sum_{n=2,3,4\ldots}^{\infty} \left(a_n r^n + b_n r^{n+2} + c_n r^{-n} + d_n r^{-(n-2)}\right) \sin(n\theta) \\ & + \sum_{n=2,3,4\ldots}^{\infty} \left(\acute{a_n} r^n + \acute{b_n} r^{n+2} + \acute{c_n} r^{-n} + \acute{d_n} r^{-(n-2)}\right) \cos(n\theta)\end{aligned} \tag{6-2}$$

The expression for Φ consists of numerous terms, i.e., real Airy stress coefficients. Imposing certain information/conditions often enables one to simplify the expression for Φ by eliminating many of these coefficients. Such imposed conditions can be based on whether the structure of interest is finite or infinite, where the coordinate origin is located, whether the geometry is mechanically and/or geometrically symmetric about specific axis/axes, whether the relevant Airy stress function is an even or odd function and whether the desired engineering quantities are single-valued. For the finite plate of Figure (6-1), that things are symmetric about the horizontal *x*-axis, the coordinate origin is at the center of the circular hole and there is in no resultant force at the origin, simplifies the expression for Φ. That the displacements, strains or stresses are not multivalued functions of θ further simplifies the expression of the Airy stress function of equation (6-1). All these conditions of the present plate makes the following coefficients zero [96],

$$d_0 = B_0 = C_0 = D_0 = A_1 = \acute{A_1} = B_1 = \acute{B_1} = b_1 = \acute{b_1} = 0$$

Thus, for the finite plate of Figure 6-1, the Airy stress function of equation (6-2) reduces to (originally provided by Soutas-Little [28] but later corrected by Foust [29])

$$\begin{aligned}\Phi = a_0 + b_0 \ln r + c_0 r^2 + A_0\theta + \left(a_1 r + \frac{c_1}{r} + d_1 r^3\right)\sin\theta \\ + \left(a_1' r + \frac{c_1'}{r} + d_1' r^3\right)\cos\theta \\ + \sum_{n=2,3,4\ldots}^{N}\left(a_n r^n + b_n r^{n+2} + c_n r^{-n} + d_n r^{-(n-2)}\right)\sin(n\theta) \\ + \sum_{n=2,3,4\ldots}^{N}\left(a_n' r^n + b_n' r^{n+2} + c_n' r^{-n} + d_n' r^{-(n-2)}\right)\cos(n\theta)\end{aligned} \tag{6-3}$$

The plate being symmetric about the horizontal x-axis, the stresses at any angle, $\theta = +\beta$ are same as those at an angle $\theta = -\beta$. This suggests that the Airy stress function for the finite plate of Figure 6-1 is an even function, i.e., $\Phi(r, -\theta) = \Phi(r, \theta)$. This condition omits all the θ and sin θ terms from equation (6-3), i.e., A_0, a_1, c_1, d_1 and a_n, b_n, c_n, d_n (for $n \geq 2$) equates to zero. Therefore, the Airy stress function of equation (6-3) further reduces to

$$\begin{aligned}\Phi = a_0 + b_0 \ln r + c_0 r^2 + \left(a_1' r + \frac{c_1'}{r} + d_1' r^3\right)\cos\theta \\ + \sum_{n=2,3,4\ldots}^{N}\left(a_n' r^n + b_n' r^{n+2} + c_n' r^{-n} + d_n' r^{-(n-2)}\right)\cos(n\theta)\end{aligned} \tag{6-4}$$

where r is the radial coordinate measured from the center of the circular hole, θ is the angle measured counter-clockwise from the horizontal x-axis, Figure 6-1, and N is the terminating index of the finite summation series.

The individual components of the in-plane stresses are expressed in terms of the Airy stress function as [28]

$$\sigma_{rr} = \frac{1}{r}\frac{\partial \Phi}{\partial r} + \frac{1}{r^2}\frac{\partial^2 \Phi}{\partial \theta^2} \tag{6-5}$$

$$\sigma_{\theta\theta} = \frac{\partial^2 \Phi}{\partial r^2} \tag{6-6}$$

$$\sigma_{r\theta} = -\frac{\partial}{\partial r}\left(\frac{1}{r}\frac{\partial \Phi}{\partial \theta}\right) \tag{6-7}$$

Substituting equation (6-4) into equations (6-5) through (6-7), the final expressions for the in-plane stresses in the polar coordinates in terms of the Airy stress function, Φ, involving real coefficients become

$$\begin{aligned} \sigma_{rr} = {} & \frac{b_0}{r^2} + 2c_0 - \frac{2\acute{c}_1}{r^3}\cos\theta + 2r\acute{d}_1\cos\theta \\ & - \sum_{n=2,3\ldots}^{N} \left[\acute{a}_n n(n-1)r^{(n-2)} + \acute{b}_n(n-2)(n+1)r^n \right. \\ & \left. + \acute{c}_n n(n+1)r^{-(n+2)} + \acute{d}_n(n+2)(n-1)r^{-n}\right]\cos(n\theta) \end{aligned} \tag{6-8}$$

$$\sigma_{\theta\theta} = -\frac{b_0}{r^2} + 2c_0 + \frac{2\acute{c}_1}{r^3}\cos\theta + 6r\acute{d}_1\cos\theta$$
$$+ \sum_{n=2,3\ldots}^{N} \left[\acute{a}_n n(n-1)r^{(n-2)} + \acute{b}_n(n+2)(n+1)r^n \right. \tag{6-9}$$
$$\left. + \acute{c}_n n(n+1)r^{-(n+2)} + \acute{d}_n(n-2)(n-1)r^{-n}\right]\cos(n\theta)$$

$$\sigma_{r\theta} = -\frac{2\acute{c}_1}{r^3}\sin\theta + 2r\acute{d}_1\sin\theta$$
$$+ \sum_{n=2,3\ldots}^{N} \left[\acute{a}_n n(n-1)r^{(n-2)} + \acute{b}_n n(n+1)r^n \right. \tag{6-10}$$
$$\left. - \acute{c}_n n(n+1)r^{-(n+2)} - \acute{d}_n n(n-1)r^{-n}\right]\sin(n\theta)$$

Although for the present plate of Figure 6-1, in the reduced Airy stress function, Φ, of equation (6-4) the coefficients a_0 and a'_1 are present, they are absent in the expressions for the individual stress components of equations (6-8) through (6-10). This is due to the Airy stress function of equation (6-4) being differentiated according to equations (6-5) through (6-7), to obtain equations (6-8) through (6-10), respectively.

For isotropic materials under proportional loading, the TSA-recorded thermal information is linearly proportional to the change in the isopachic stress, S, which is the summation of the normal stresses, i.e.,

$$S^* = K\Delta S = K\{\Delta(\sigma_{rr} + \sigma_{\theta\theta} = \sigma_{xx} + \sigma_{yy})\} \tag{6-11}$$

where S^* is the system output signal associated with the local stress-induced temperature changes and K is the TSA calibration coefficient. Equation (6-11) assumes thermodynamic adiabaticity, which implies cyclically loading the structure. Combining equations (6-8) and (6-9), into equation (6-11), one obtains the following equation for the isopachic stress

$$S = \frac{S^*}{K} = 4c_0 + 8r\acute{d}_1 \cos\theta + \sum_{n=2,3\ldots}^{N} [b'_n 4(n+1)r^n - d'_n 4(n-1)r^{-n}]\cos(n\theta) \tag{6-12}$$

However, the individual stress components of equations (6-8) through (6-10), contains the Airy coefficients b_0, c'_1, a'_n, c'_n (for $n \geq 2$) which are absent in the expression for the isopachic stress of equation (6-12). Therefore, combining measured TSA data, S^*, with equation (6-12) is not sufficient to determine all the Airy stress coefficients. The present method is thus incapable of stress analyzing the current plate through the use of equations (6-8) through (6-10) while processing TSA-measured information in the isopachic stress, S, expression of equation (6-12). However, it is possible to overcome this situation by imposing the traction-free boundary conditions analytically along the boundary of the hole. Thus, by imposing the traction-free boundary conditions $\sigma_{r\theta} = \sigma_{rr} = 0$ at $r = R$ (= 9.53 mm or 0.375"), the in-plane stress components of equations (6-8) through (6-10) are re-written as [74]

$$\sigma_{rr} = \left(\frac{1}{r^2} - \frac{3r}{2R^3} + \frac{r^3}{2R^5}\right) b_0 + \left(2 - \frac{3r}{R} + \frac{r^3}{R^3}\right) c_0$$

$$+ \left(-\frac{2R^4}{r^3} + 2r\right) \acute{d}_1 \cos\theta + 3R^2 \left(1 - \frac{R^4}{r^4}\right) \acute{b}_2 \cos(2\theta)$$

$$+ \left(\frac{1}{R^2} + \frac{3R^2}{r^4} - \frac{4}{r^2}\right) \acute{d}_2 \cos(2\theta)$$

$$+ \left(\frac{24r}{R^6} - \frac{12r^3}{R^8} - \frac{12}{r^5}\right) \acute{c}_3 \cos(3\theta)$$

$$+ \left(\frac{18r}{R^4} - \frac{8r^3}{R^6} - \frac{10}{r^3}\right) \acute{d}_3 \cos(3\theta) \qquad (6\text{-}13)$$

$$+ \left\{ \sum_{n=4,5\ldots}^{N} [(n^2-1) r^{(n-2)} R^2 - (n+1)(n-2) r^n \right.$$

$$- (n+1) r^{-(n+2)} R^{(2n+2)}] \acute{b}_n \cos(n\theta)$$

$$+ \left[(n-1) r^{(n-2)} R^{-(2n-2)} - (1-n^2) r^{-(n+2)} R^2 \right.$$

$$\left. \left. - (n-1)(n+2) r^{-n}\right] \acute{d}_n \cos(n\theta) \right\}$$

$$\sigma_{\theta\theta} = \left(-\frac{1}{r^2} + \frac{3r}{2R^3} - \frac{5r^3}{2R^5}\right) b_0 + \left(2 + \frac{3r}{R} - \frac{5r^3}{R^3}\right) c_0$$

$$+ \left(\frac{2R^4}{r^3} + 6r\right) \acute{d}_1 \cos\theta + \left(-3R^2 + 12r^2 + \frac{3R^6}{r^4}\right) \acute{b}_2 \cos(2\theta)$$

$$- \left(\frac{1}{R^2} + \frac{3R^2}{r^4}\right) \acute{d}_2 \cos(2\theta)$$

$$+ \left(-\frac{24r}{R^6} + \frac{60r^3}{R^8} + \frac{12}{r^5}\right) \acute{c}_3 \cos(3\theta)$$

$$+ \left(-\frac{18r}{R^4} + \frac{40r^3}{R^6} + \frac{2}{r^3}\right) \acute{d}_3 \cos(3\theta) \qquad (6\text{-}14)$$

$$+ \left\{ \sum_{n=4,5\ldots}^{N} [-(n^2-1) r^{(n-2)} R^2 + (n+1)(n+2) r^n \right.$$

$$+ (n+1) r^{-(n+2)} R^{(2n+2)}] \acute{b}_n \cos(n\theta)$$

$$+ \left[-(n-1) r^{(n-2)} R^{-(2n-2)} + (1-n^2) r^{-(n+2)} R^2 \right.$$

$$\left. \left. + (n-1)(n-2) r^{-n}\right] \acute{d}_n \cos(n\theta) \right\}$$

$$\sigma_{r\theta} = \left[\frac{3r\tan(3\theta)}{2R^3} - \frac{3r^3\tan(3\theta)}{2R^5}\right] b_0 + \left[\frac{3r\tan(3\theta)}{R} - \frac{3r^3\tan(3\theta)}{R^3}\right] c_0$$
$$- \left(\frac{2R^4}{r^3} - 2r\right) \acute{d}_1 \sin\theta - \left(3R^2 - 6r^2 + \frac{3R^6}{r^4}\right) \acute{b}_2 \sin(2\theta)$$
$$- \left(\frac{1}{R^2} - \frac{3R^2}{r^4} + \frac{2}{r^2}\right) \acute{d}_2 \sin(2\theta)$$
$$- \left(\frac{24r}{R^6} - \frac{36r^3}{R^8} + \frac{12}{r^5}\right) \acute{c}_3 \sin(3\theta)$$
$$- \left(\frac{18r}{R^4} - \frac{24r^3}{R^6} + \frac{6}{r^3}\right) \acute{d}_3 \sin(3\theta) \qquad (6\text{-}15)$$
$$+ \left\{ \sum_{n=4,5\ldots}^{N} [-(n^2-1)r^{(n-2)}R^2 + n(n+1)r^n \right.$$
$$- (n+1)r^{-(n+2)}R^{(2n+2)}] \acute{b}_n \sin(n\theta)$$
$$+ \left[-(n-1)r^{(n-2)}R^{-(2n-2)} - (1-n^2)r^{-(n+2)}R^2 \right.$$
$$\left. \left. - n(n-1)r^{-n}\right] \acute{d}_n \sin(n\theta) \right\}$$

The new expression for the isopachic stress, S_{new}, based on equations (6-13) and (6-14) in equation (6-11) includes all the Airy stress coefficients present in the individual stress components of equations (6-13) through (6-15). It is therefore now possible to evaluate the three individual stress components from the TSA-measured S^* data.

$$
\begin{aligned}
S_{new} = & -\frac{2r^3}{R^5}b_0 + \left(4 - \frac{4r^3}{R^3}\right)c_0 + 8r\acute{d}_1\cos\theta + 12r^2\acute{b}_2\cos(2\theta) \\
& - \frac{4}{r^2}\acute{d}_2\cos(2\theta) + \frac{48r^3}{R^8}\acute{c}_3\cos(3\theta) \\
& + \left(\frac{32r^3}{R^6} - \frac{8}{r^3}\right)\acute{d}_3\cos(3\theta) \\
& + \sum_{n=4,5\ldots}^{N}\left[4(n+1)r^n\acute{b}_n\cos(n\theta) - 4(n-1)r^{-n}\acute{d}_n\cos(n\theta)\right]
\end{aligned}
\tag{6-16}
$$

Knowing the stresses in the polar coordinates, the stress transformation relationship of equation (6-17) is used to transfer the stresses from the polar coordinates into those in the Cartesian coordinates.

$$
\begin{Bmatrix}\sigma_{xx}\\ \sigma_{yy}\\ \sigma_{xy}\end{Bmatrix} = \begin{bmatrix}\cos^2\theta & \sin^2\theta & -2\sin\theta\cos\theta \\ \sin^2\theta & \cos^2\theta & 2\sin\theta\cos\theta \\ \sin\theta\cos\theta & -\sin\theta\cos\theta & \cos^2\theta - \sin^2\theta\end{bmatrix}\begin{Bmatrix}\sigma_{rr}\\ \sigma_{\theta\theta}\\ \sigma_{r\theta}\end{Bmatrix} \tag{6-17}
$$

6.5. Plate Preparation and Experimental Set-up

6.5.1. Plate Details

An aluminum (6061-T6) plate (Figure 6-1 and Table 6-1) of length, L = 26.67 cm (10.5"), width, W = 5.08 cm (2") and thickness, t = 6.35 mm (0.25") with an offset circular hole of radius R = 9.53 mm (0.375") was stress analyzed by processing the TSA-measured thermal data with an Airy stress function. The center of the hole is located at a distance 10.80 mm (0.425") from the

center of the plate. The plate was cyclically loaded at 1,334.47 N ± 889.64 N at 20 Hz frequency and had a TSA calibration coefficient, K, of 218.95 U/MPa.

Table 6-1: Details of perforated aluminum plate and TSA

Material	Aluminum 6061-T6
Thickness, t	6.35 mm (0.25")
Length, L	26.67 cm (10.5")
Width, W	5.08 cm (2")
Hole diameter, $D = 2R$	1.905 cm (0.75")
Symmetry	Horizontally
Elastic modulus, E	69 GPa (10×10^6 psi)
Poisson's ratio, v	0.33
Loading for TSA, F^*	1,334.47 N ± 889.64 N (300 lbs ± 200 lbs)
Loading frequency	20 Hz
Thermoelastic coefficient, K	218.95 U/MPa (1.51 U/psi)

6.5.2. Plate Surface Preparation

For TSA, minimum surface preparation is required compared to other full-field experimental techniques such as DIC. The aluminum plate was initially degreased (with CSM-2 by Vishay Precision Group) and polished with 400-grit emery cloth while taking extreme care not

to round off the edges of the hole. The polished plate was cleaned with a water-based mild cleaner (Vishay Precision Group - Micro-Measurements M-Prep Conditioner A followed by M-Prep Neutralizer 5A) and allowed to dry. Just prior to testing, the plate was sprayed with Krylon Ultra-Flat black paint and the paint allowed to dry for an hour. The plate was painted black to achieve uniform and enhanced thermal emissivity and also to avoid any reflection from the plate during testing; which might compromise the image quality.

6.5.3. TSA System

Using a commercially sensitive Delta Therm DT1410 infrared camera (by Stress Photonics, Inc., Madison, WI), the temperature information of the loaded plate was recorded, Figure 6-2. The Delta Therm camera employs an indium antimonide (InSb) focal-plane array sensor with 256 × 256 resolution. With the liquid nitrogen, the camera detectors are kept cooled to 77 K to improve the result accuracy. The camera responds in the 3–5 μm wavelength range with a peak response at 5.3 μm. It records at a speed of 1000 frames per second and the captured images have a temperature resolution of 0.001 °C. The system has a mechanical resolution compatible to that of commercial foil strain-gages.

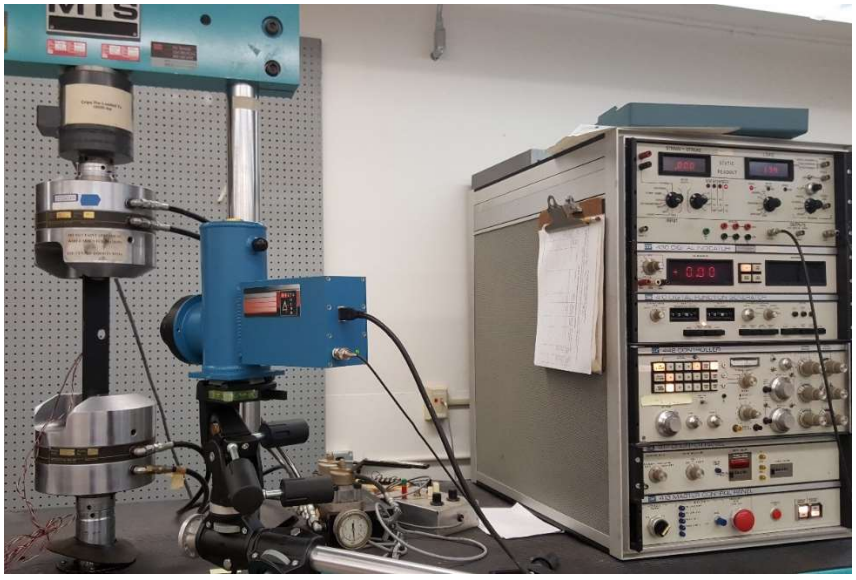

Figure 6-2: TSA experimental set-up

6.5.4. Loading and Data Acquisition

The plate was sinusoidally loaded at 1,334.47 N ± 889.64 N (300 lbs ± 200 lbs) at 20 Hz frequency using a 89 kN (20 kips) capacity, closed-loop, hydraulic-grip MTS machine, Figure 6-2. The mean load was 1,334.47 N (300 lbs) while the maximum and minimum loads were 2,224.11 N (500 lbs) and 444.83 N (100 lbs), respectively. An oscilloscope was used to monitor the frequency and applied load with precision. The 20 Hz cyclic frequency was selected based on prior experiences [59].

The load-induced TSA data, i.e., TSA images, were recorded using the TSA Delta Therm model DT1410 infrared camera and the phase condition and TSA images of the loaded plate were monitored using the TSA Stress Photonics Delta Vision data acquisition software. Phase condition monitoring is important to ensure that system adiabaticity is maintained at the selected cyclic loading frequency. The TSA Delta Therm model DT1410 infrared camera consists of a 256 × 256-

pixel sensor array and which is maintained at very low temperature to provide accurate load-induced temperature readings. Liquid nitrogen is used for this purpose. Care needs to be taken to mount the plate in the MTS grips to ensure symmetrical loading along the vertical *y*–axis and the camera needs to be mounted exactly perpendicularly to the plate's surface at a minimum distance of eight inch. The thermoelastic signals, S^*, were recorded and then processed by the TSA Delta Therm system. Using the Delta Therm DT1410 camera, a series of TSA images were captured over a time interval of two minutes and the data were stored and averaged over the time interval by the Delta Vision software. The TSA-recorded data were imported into Excel as a 256 × 256 matrix.

6.5.5. Maintaining Adiabatic Condition

High loading frequency of 20 Hz was selected as it was found to give good results in previous studies [59]. By keeping the loading frequency higher than the heat flow rate, it is possible to essentially avoid local heat transfer, i.e., ensure adiabaticity, Figure 6-3.

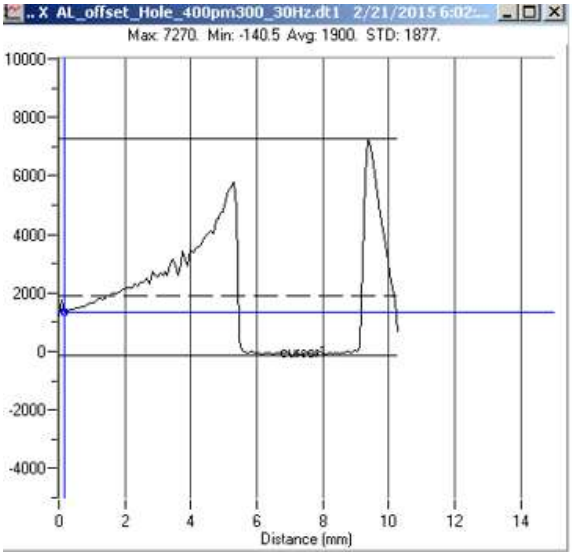

Figure 6-3: Checking TSA phase condition using Delta Vision software to ensure adiabaticity during the test, TSA load-induced temperature information, S^* (uncalibrated units U), plotted along y-axis

6.5.6. TSA Calibration

The thermoelastic coefficient, K, of equations (6-11) and (6-12) was determined from a separate 6061-T6 aluminum uniform L = 200.66 mm (7.9") long, W = 50.8 mm (2") wide and t = 6.35 mm (0.25") thick tensile coupon. The aluminum calibration coupon was painted and tested on the same day of painting and recording the TSA data of the perforated plate. Both the perforated plate and calibration coupon were loaded at the same frequency and under the same ambient condition. Reasons behind painting and testing the calibration and test coupons on the same day are provided in Appendix I. The calibration coupon was cyclically loaded at 8,446.08 N ± 6,227.51 N (1,900 lbs ± 1,400 lbs) at 20 Hz frequency and K was found to be 218.95 U/MPa (1.51 U/psi), where U denotes the uncalibrated TSA signal output, Figure 6-4.

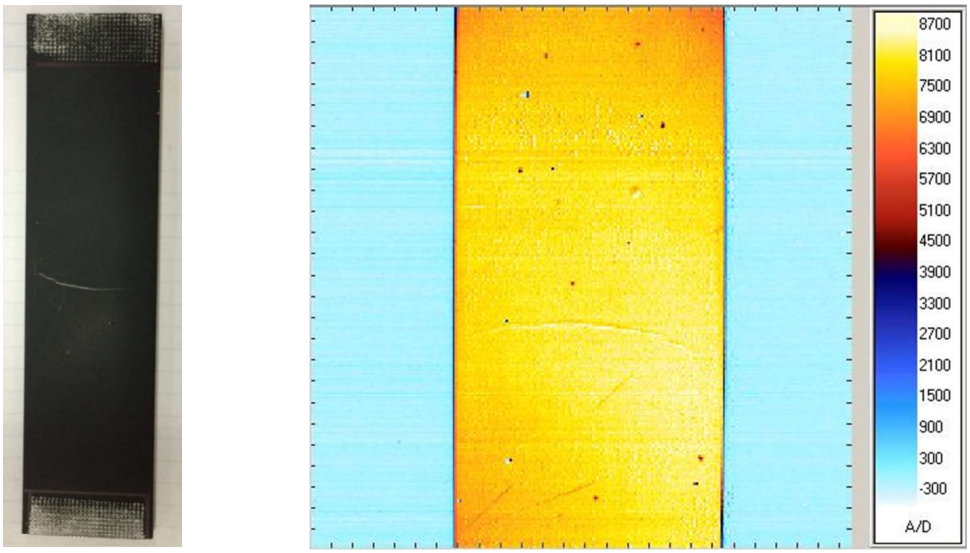

(a) (b)

Figure 6-4: TSA calibration tensile aluminum coupon (a) Surface prepared and (b) TSA load-induced temperature information, S^* (uncalibrated units U)

6.6. Experimental Data Analysis, Reduction and Selection

6.6.1. Data Processing

The raw thermoelastic data, which were recorded as a 256 × 256 matrix by the Delta Vision software, were subsequently converted to physical units knowing the dimensions of the plate and the thermoelastic coefficient, K. From the 65,563 pixels of the 256 × 256 matrix, a total of 29,304 pixels covered the loaded plate with a pixel spacing of 0.37 mm (0.0152"), Figure 6-5. The x-y coordinates were normalized by the hole radius, R, and the stress-induced thermoelastic data, S^*, by the far-field stress, $\sigma_0 = 5.52$ MPa according to equation (6-18), Figure 6-5 and Figure 6-6. The white space in Figure 6-5 represents no data while the colored contours represents the 29,304 pixels over the loaded plate.

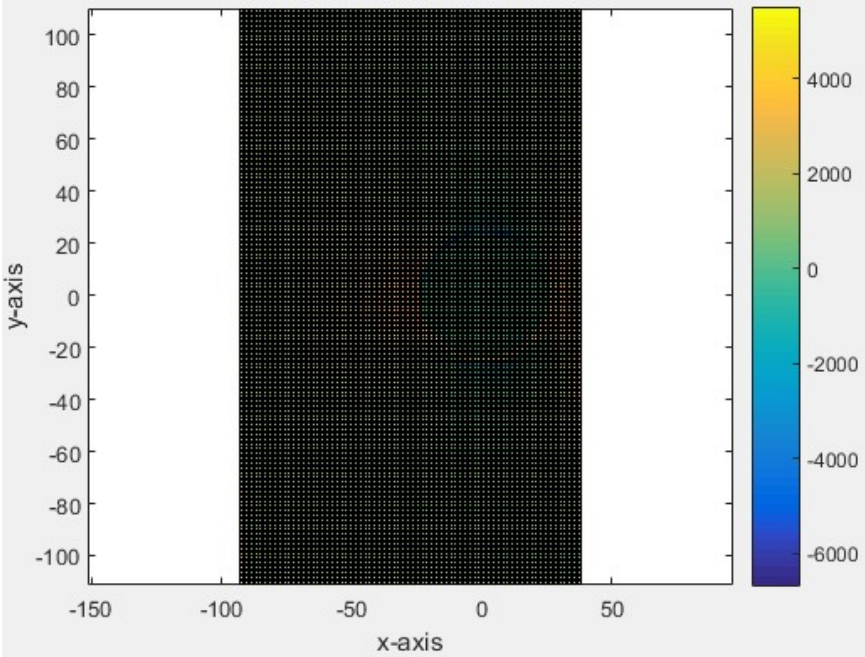

Figure 6-5: TSA-measured raw stress-induced thermal information provided in pixels

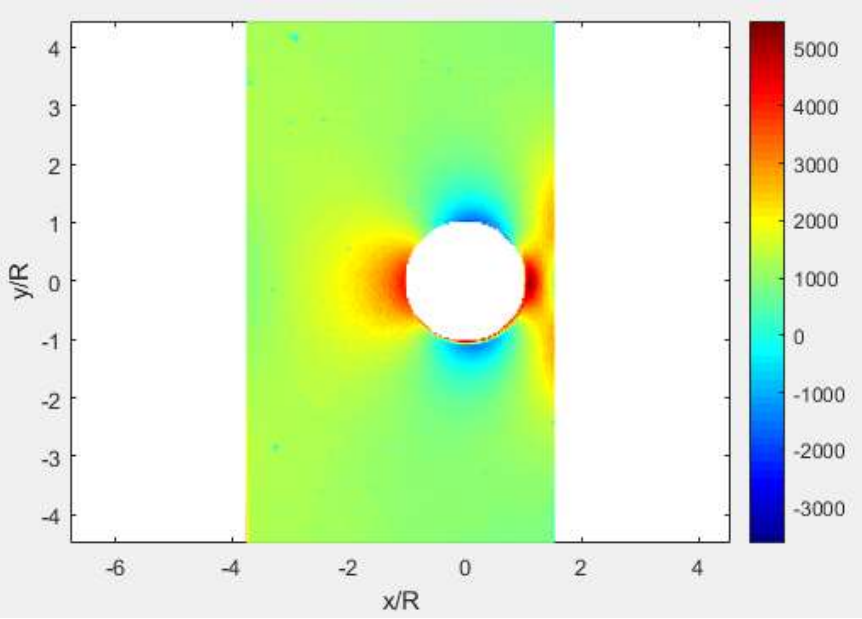

Figure 6-6: TSA-measured thermoelastic data, S^* (uncalibrated units U)

$$\sigma_0 = \frac{F^*}{W \times t} = \frac{1779.29\ \text{N}}{50.8\ \text{mm} \times 6.35\ \text{mm}} = 5.52\ \text{MPa (800 psi)} \tag{6-18}$$

Since the plate was geometrically and mechanically symmetrical about the *x*-axis, the TSA-recorded thermoelastic data, S^*, were averaged about the *x*-axis to cancel any possible scatter. The resulting averaged normalized S^* data are plotted throughout the top half of the plate in Figure 6-7.

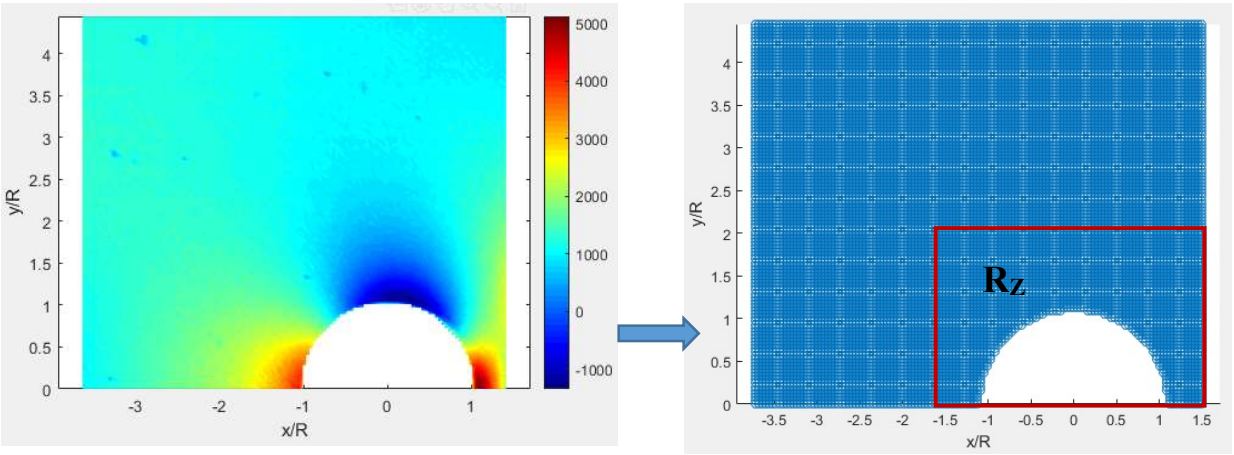

(a) (b)

Figure 6-7: (a) Averaged measured load-induced TSA data S^* (uncalibrated units *U*) and (b) Source locations of TSA averaged measured S^* and region R_z

Experimental techniques tend not to provide reliable data at or near edges. TSA can be particularly bad in this regard. In addition to the consequences of the cyclic motion, TSA-recorded values at and close to an edge are unreliable as pixels at an edge combines information partly from the stressed structure and partly from the stress-free background. No recorded thermal information was therefore used within 3 pixels from either of the sides (along the plates vertical edge) or around the edge of the plate's hole, i.e., within $0.1R$ ($\approx$ 1 mm) distance from the hole's boundary, Figure

6-8. The hole was located close to the right edge of the plate. Acknowledging that TSA information at and near edges is unreliable, there was, at best, then only a short region between the right edge of the hole and the neighboring edge of the plate within which reliable TSA data might prevail. In view of the above, and for the present purpose, it was assumed that no sufficiently reliable TSA data existed throughout the region to the right of the hole up as far as $y/R = 0.75$ in Figure 6-8. Such local data-deficient situations could occur due to a defective camera (damaged pixels), lack of thermal adiabaticity or an uneven layer of paint [103–106]. Excluding all the 'assumed' unreliable data, only a net number of $n_{TSA} = 12{,}592$ TSA-measured value of S^* were considered for the analysis, Figure 6-8. In addition to these n_{TSA} TSA-measured pieces of information, $\sigma_{xy} = \sigma_{xx} = 0$ were discretely imposed at $h = 122$ locations along the y-axis (61 locations on each vertical side) of the unloaded edges (at $x = Q$ and $x = -(W - Q)$), Figure 6-9.

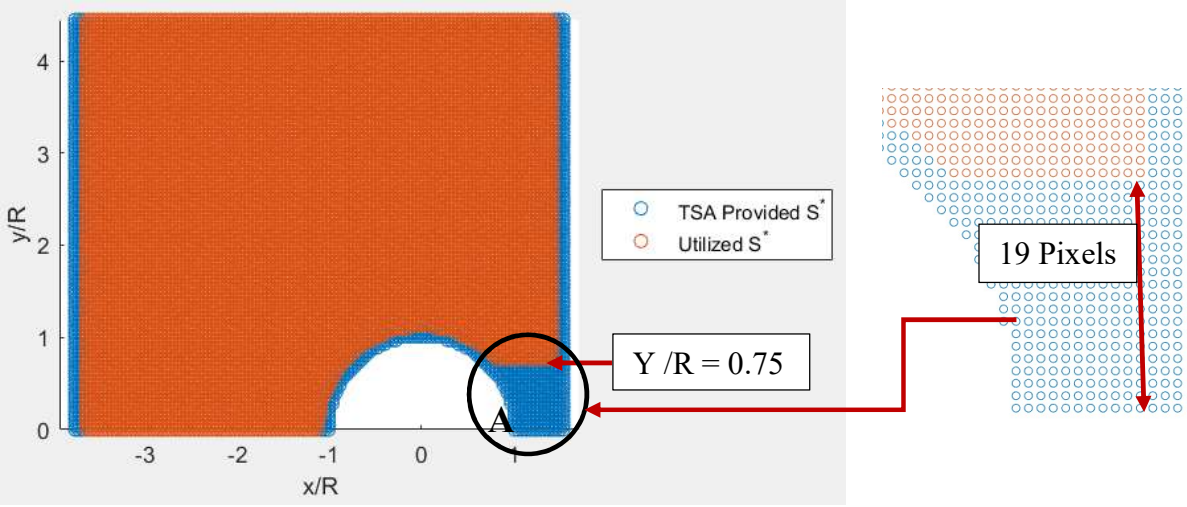

(a) (b)

Figure 6-8: (a) Source locations of recorded TSA data and (b) Nearest data considered from point 'A'

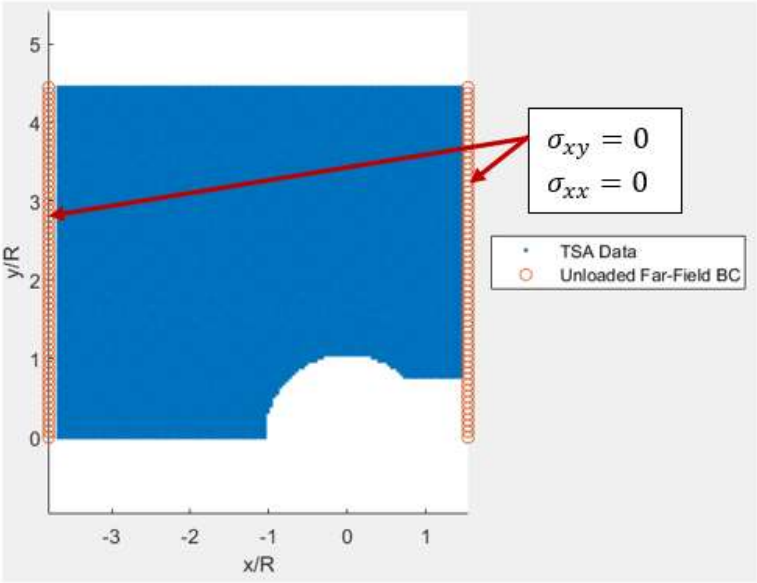

Figure 6-9: Source locations of utilized n_{TSA} = 12,592 TSA data and $2h$ = 244 boundary conditions

TSA-measured information can be noisy and involve some scatter. This is overcome by employing the number of side conditions, $n_t = n_{TSA} + 2h$, much higher than the number of the unknown Airy coefficients, k.

6.6.2. Computing the Unknown Airy Coefficients

The Airy coefficients of equations (6-13) through (6-15) are evaluated from the equally-spaced 12,592 TSA-measured values of S^* and the $2h$ = 244 imposed boundary conditions using equation (6-19). The latter, i.e., equation (6-19), employs S_{new} from equation (6-16) and σ_{xx} and σ_{xy} from equations (6-13) through (6-15) into polar to Cartesian stress transformation of equation (6-17). Equation (6-19) was solved employing the least squares method, where the number of

equations, n_t, substantially exceeds the number of unknown Airy coefficients, k, to compensate for the scatter in the measured TSA information.

$$\begin{bmatrix} S_{new}\,(b_0\ c_0\ \acute{d}_1\ \acute{b}_2\ \acute{d}_2\ \acute{c}_3\ \acute{d}_3\ \ldots.\ \acute{b}_n\ \acute{d}_n) \\ \sigma_{xy}(b_0\ c_0\ \acute{d}_1\ \acute{b}_2\ \acute{d}_2\ \acute{c}_3\ \acute{d}_3\ \ldots.\ \acute{b}_n\ \acute{d}_n) \\ \sigma_{xx}(b_0\ c_0\ \acute{d}_1\ \acute{b}_2\ \acute{d}_2\ \acute{c}_3\ \acute{d}_3\ \ldots.\ \acute{b}_n\ \acute{d}_n) \end{bmatrix} \begin{Bmatrix} b_0 \\ c_0 \\ \acute{d}_1 \\ \acute{b}_2 \\ \acute{d}_2 \\ \acute{c}_3 \\ \acute{d}_3 \\ \cdot \\ \vdots \\ \cdot \\ \acute{b}_n \\ \acute{d}_n \end{Bmatrix} = \begin{bmatrix} TSA\ (S^*/K) \\ BC's\ (\sigma_{xy} = 0) \\ BC's\ (\sigma_{xx} = 0) \end{bmatrix} \tag{6-19}$$

To apply the boundary conditions $\sigma_{xy} = 0$ and $\sigma_{xx} = 0$ in equation (6-19), the stresses in the polar coordinates were transformed to those in the Cartesian coordinates using the transformation relationship of equation (6-17). Equation (6-19) can be re-written as

$$[A]_{\{n_t \times k\}}\{c\}_{\{k \times 1\}} = \{s\}_{\{n_t \times 1\}} \tag{6-20}$$

where $k = 7 + 2(n - 3)$ for $n = 4, 5 \ldots N$. The matrix $[A]$ involves the locations (r and θ) of the n_{TSA} = 12,592 values of TSA-measured S^* data and the h = 122 locations (x, y) where boundary conditions $\sigma_{xy} = \sigma_{xx} = 0$ were imposed. Vector $\{c\}$ contains the unknown Airy coefficient's and vector $\{s\}$ consists of the TSA-measured S^* data and imposed boundary conditions. For the set of linear equations, the number of equations, n_t, is much higher than the number of unknown Airy coefficients, k, i.e., $n_t >> k$. Therefore, equation (6-20) becomes an overdetermined system of linear equations which can be numerically solved by least squares. This compensates for noise in the

measured data in the final results of the evaluated coefficients. Equation (6-20) was solved using the backslash operator ('\') in MATLAB, i.e., equation (6-21). The Airy coefficients were evaluated using n_{TSA} = 12,592 TSA-measured S^* in equation (6-16) and $2h$ = 244 imposed boundary conditions by combining equations (6-13) through (6-15) in equation (6-17), i.e., a total of $n_t = n_{TSA} + 2h$ = 12,836 input values. Knowing the values of the Airy coefficients, the individual stresses in the polar coordinates were evaluated using equations (6-13) through (6-15) throughout the region R_z of Figure 6-7(b), including along the edge of the cutout where the measured data were excluded and locations close to the plate's edge where measured data were missing.

$$\{c\} = [A]\backslash\{s\} \tag{6-21}$$

6.6.3. Evaluating Number of Coefficients to Employ

The Airy coefficients were evaluated using n_{TSA} = 12,592 TSA-measured S^* in equation (6-16) and $2h$ = 244 imposed boundary conditions, i.e., a total of $n_t = n_{TSA} + 2h$ = 12,836 input values. k = 21 real Airy stress coefficients were evaluated. Using these Airy coefficients in equations (6-13) through (6-15) provide the stresses throughout the plate of Figure 6-1. Therefore, one must assess a realistic number of Airy coefficients to employ. Too few Airy coefficients give poor results while too many coefficients can cause computational difficulties and/or the solution to blow up, i.e., become infinite.

The number of Airy coefficients to use was determined based on the plot of the root mean square (RMS) of equation (6-22) in Figure 6-10, the condition number of the matrix [A] (of equation (6-20)) in Figure 6-11 and by comparing contour plots of the experimentally recorded

TSA thermal data, S^*, and reconstructed, $S^{*\prime}$, (from equation (6-16) into equation (6-11)) in Figure 6-12 for different numbers of Airy coefficients, k.

The RMS of equation (6-22) is a measure of the difference between the experimentally derived TSA data $\{S^*\}$ and the reconstructed data $\{S^{*\prime}\}$ for varying k in equation (6-16) combined with equation (6-11), Figure 6-10. The RMS plot of Figure 6-10 suggests that using k = 9 to 23 real coefficients nearly has the same effect.

$$(S^{*\prime} - S)_{\mathrm{RMS}} = \sqrt{\sum_{j=1}^{12,836} \left(S_j^{*\prime} - S_j\right)^2 / 12,836} \tag{6-22}$$

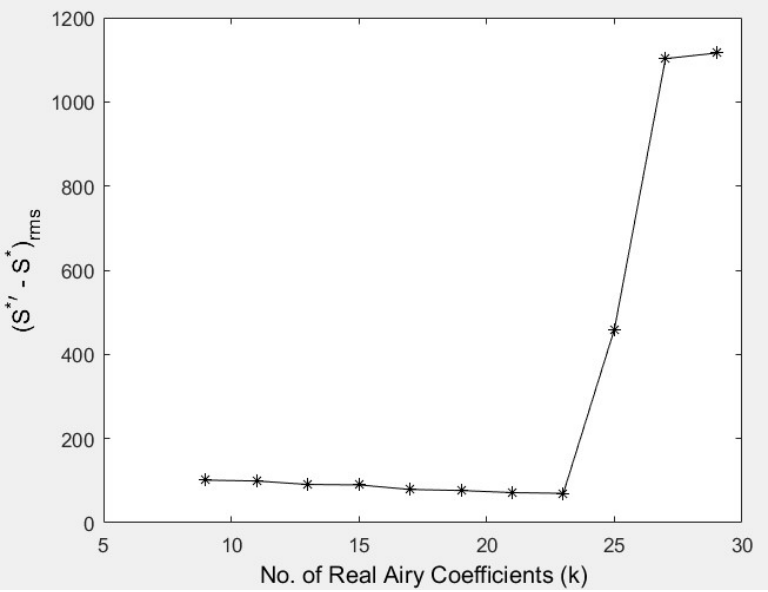

Figure 6-10: Root mean square of the measured and reconstructed TSA signal, ($S^{*\prime} - S^*$), versus the number of real Airy stress coefficients, k

The condition number of the matrix [A] of equation (6-20) was evaluated for different number of Airy coefficients. Figure 6-11 shows as the number of Airy coefficients, k, increases from 21 to 23, the condition number suddenly increases, affecting the accuracy of the result. Therefore, the number of Airy coefficients to use should be between k = 9 to 21.

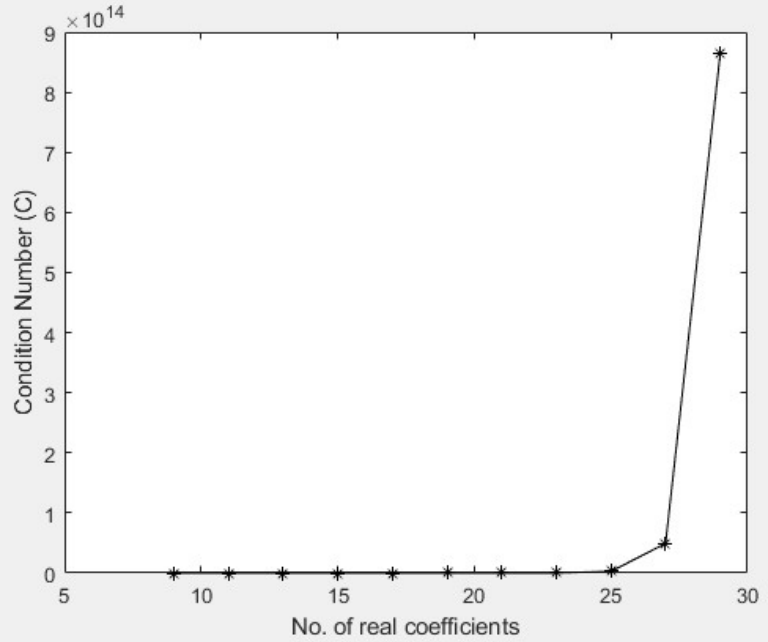

Figure 6-11: Plot of condition number, C, versus the number of real coefficients, k

The third method that was employed before finalizing the number of Airy coefficients to use was comparing the raw measured thermoelastic data S^* with those reconstructed by the TSA-hybrid method for varying number of Airy coefficients using equations (6-16) and (6-11) (Figure 6-12). The experimental data near the edge of the hole is unreliable or missing and S^* should be highest along the boundary of the hole. Figures 6-12(b) and (c) show that using either too few (k = 9) or too many (k = 25) Airy coefficients, the reconstructed thermoelastic values do not exceed

5125.2 U (uncalibrated units) which the original experimental TSA values gave, Figure 6-6. Reconstructed thermoelastic data of Figure 6-12 (b) do not represent the real stress distribution of the plate. For $\theta \rightarrow 0$, at a location $r = R$ the stress value should be higher than at any location of $r > R$. For too many Airy coefficients such as $k = 25$, the contour of the reconstructed thermoelastic data also starts to deviate from the ones originally obtained from TSA, (Figure 6-12 (c)). Using Airy coefficients k = 19 or 21 yields reconstructed thermoelastic data contours that match well with the ones obtained from TSA and give values higher than 5125.2 U at locations $r = R$ and $\theta \rightarrow 0$. However, between k = 19 and k = 21, Figure 6-10 shows k = 21 gives rise to slightly less difference between the measured and reconstructed TSA thermal information than using k = 19. Moreover, from the contour lines of Figure 6-13 it is seen that for k = 21 compared to k = 9 there is better match between the TSA-recorded and hybrid-method reconstructed stress induced thermal data distribution in regions between points 1 and 2 and along line number 3. Considering the results obtained from all these three different analyses suggests choosing k = 21 Airy coefficients. Table J-1 of Appendix J provides further support for selecting k = 21.

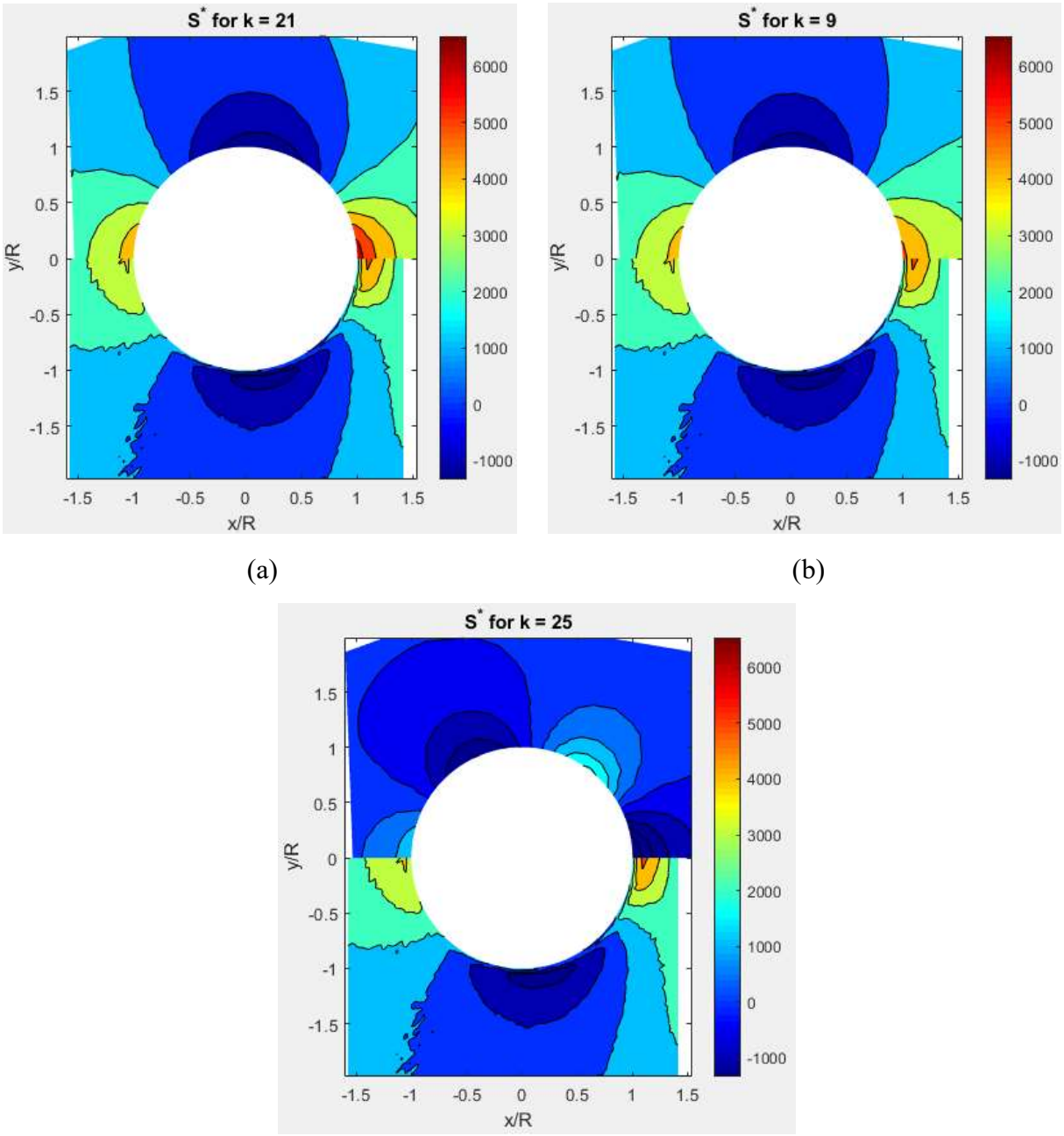

(a) (b)

(c)

Figure 6-12: (a) Experimental TSA S^* (bottom) and reconstructed $S^{*\prime}$ (top) contours for (a) $k = 21$ best match of contour lines, (b) $k = 9$ reconstructed thermoelastic data along the hole's right edge does not exceed the measured TSA thermal information slightly away from the right edge of the hole, and (d) $k = 25$ leads to computational errors

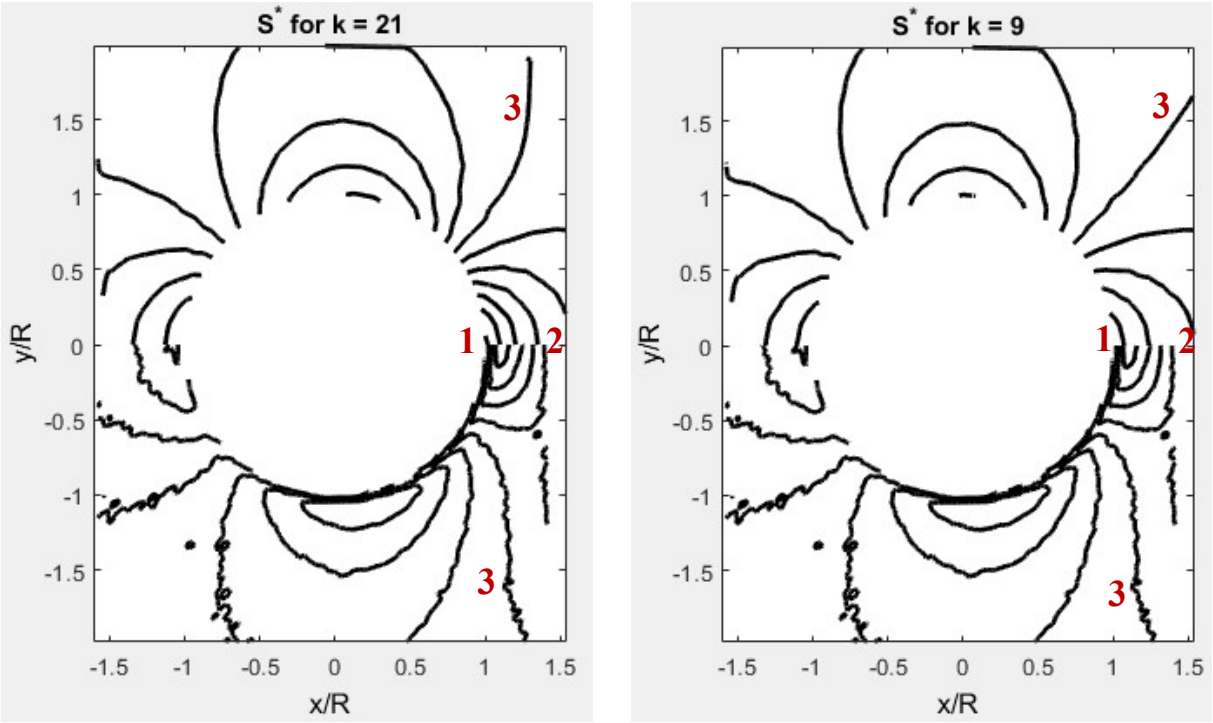

(a) (b)

Figure 6-13: Contour lines comparison between locations 1 to 2 and line 3 for experimental TSA, S^*, (bottom) and reconstructed, $S^{*\prime}$, (top) for (a) $k = 21$ and (b) $k = 9$

6.7. Finite Element Model

A motivation for formulating the ability to experimentally evaluate the stresses in loaded finite structures having a dearth of measured data acknowledges not having to know the external loading condition, something which FEA requires. However, the present situation was deliberately selected due to its known external boundary conditions and therefore able to obtain reliable FEA results with which to compare the TSA results.

The plate was modeled with commercial FEA tool, ANSYS APDL using isoparametric element Plane 182. These elements consist of four nodes with two degrees of freedom (translations

in nodal *x*-*y* directions) at each node. Plane-stress option was selected as the TSA analyzed plate is plane-stressed. Whereas the current analytical-experimental hybrid approach does not require knowing the material properties or external loading of the plate, the FEA requires knowing the material properties and external loading to provide accurate results with which to compare the TSA-based results. As the plate is symmetrical about the horizontal *x*-axis, only the top half of the plate was modeled, Figure 6-14. Appropriate symmetrical boundary conditions were imposed numerically. The origin of the coordinate system was located at the center of the off-set hole to make the FEA-simulated results compatible with the assumptions used to reduce the Airy stress function, Φ, according to equation (6-4). The plate dimensions, material properties and external loading for the FEM were those of Table 6-1. Knowing the plate dimensions and the effective load, $F^* = 1.8$ kN (400 lbs) on the plate during TSA testing, the FEM of the plate was subjected to a far-field uniform stress, σ_0, of 5.52 MPa (800 psi), using equation (6-18). The FEA model of one half of the physical plate consists of 4,365 elements and 4,515 nodes. ANSYS predicted nodal information such as in-plane displacements and stresses in polar coordinates (Figure 6-15) were exported to MATLAB to enable comparing the FEA results with those provided by the TSA-hybrid method.

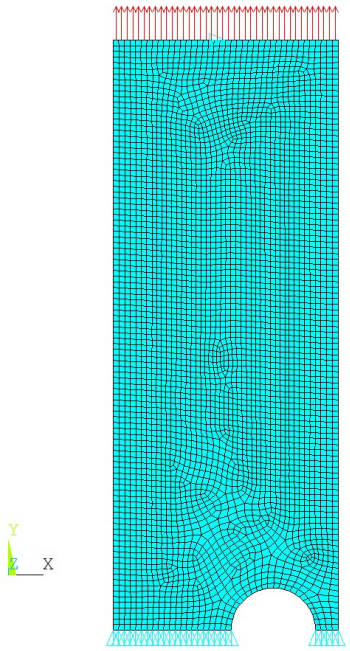

Figure 6-14: FEM of loaded off-axis perforated plate

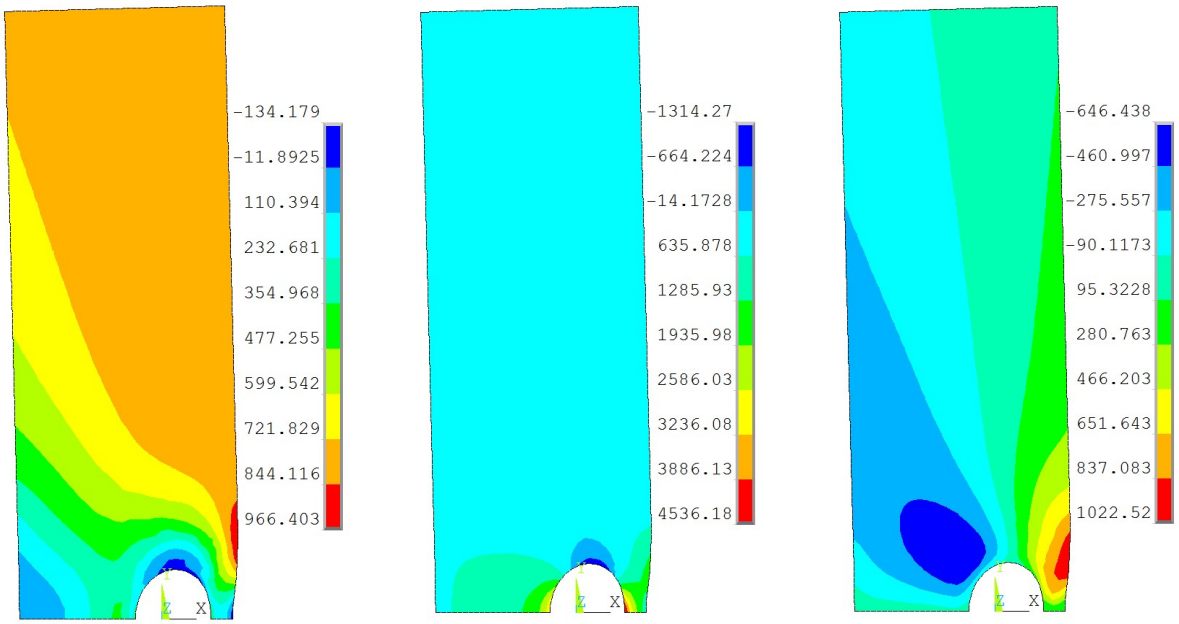

(a) (b) (c)

Figure 6-15: FEA-predicted in-plane stresses, (a) σ_{rr}, (b) $\sigma_{\theta\theta}$ and (c) $\sigma_{r\theta}$ of loaded off-axis perforated plate (units in psi)

6.8. Results

6.8.1. TSA Results

Results from the TSA-hybrid analysis were compared with those from FEA and good agreements were found. Figure 6-16 through Figure 6-18 compare the normalized stress contours for the individual polar component of stresses and Figure 6-19 compares the normalized stress contours of stresses in the loading y-direction in the Cartesian coordinates of the loaded plate from TSA-hybrid analysis and FEA. Figure 6-20 compares the TSA-hybrid method determined normalized tangential stresses along the boundary of the cutout with those predicted by the FEA, which again exhibits excellent agreement between the two methods. All coordinate values are normalized by the hole radius, R, and the stresses by the far-field uniform stress, σ_0 = 5.52 MPa (800 psi), according to equation (6-18).

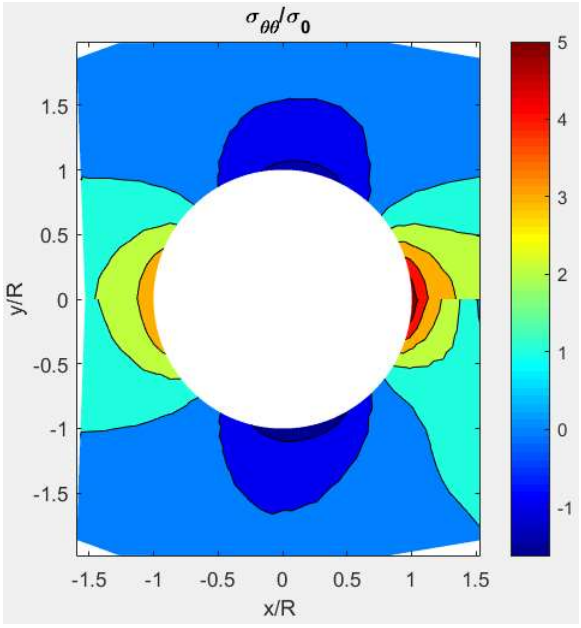

Figure 6-16: Stress contours of $\sigma_{\theta\theta}/\sigma_0$ from TSA-hybrid method (top) and FEM (bottom)

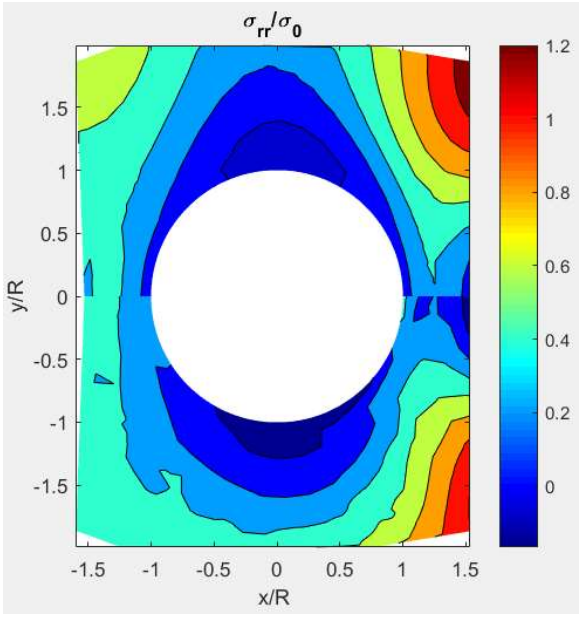

Figure 6-17: Stress contours of σ_{rr}/σ_0 from TSA-hybrid method (top) and FEM (bottom)

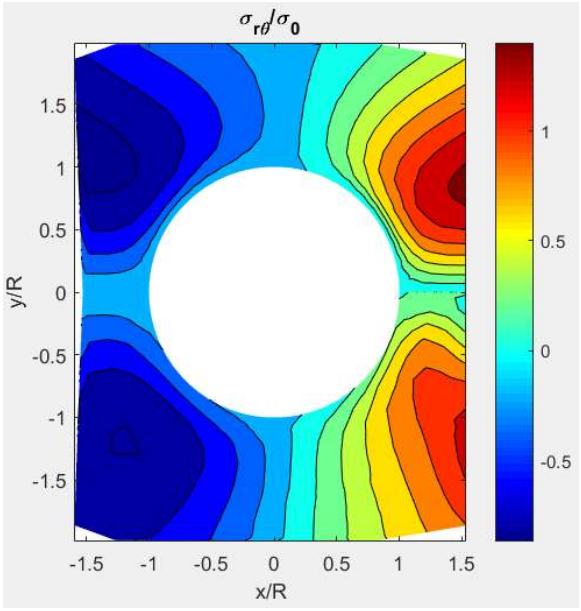

Figure 6-18: Stress contours of $\sigma_{r\theta}/\sigma_0$ from TSA-hybrid method (top) and FEM (bottom)

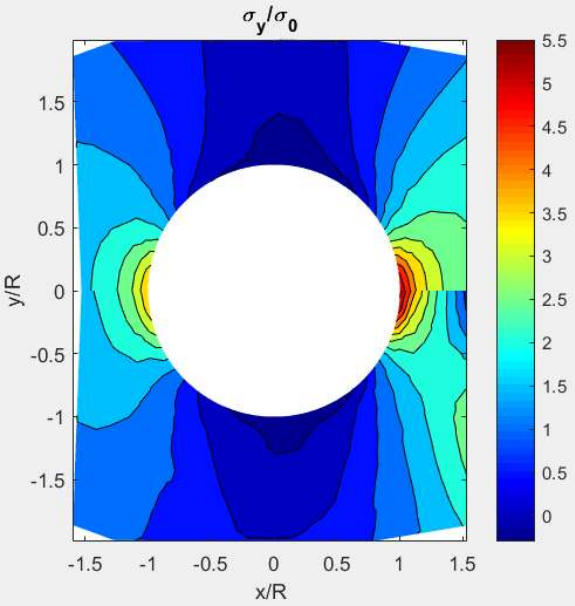

Figure 6-19: Stress contours of σ_{yy}/σ_0 from TSA-hybrid method (top) and FEM (bottom)

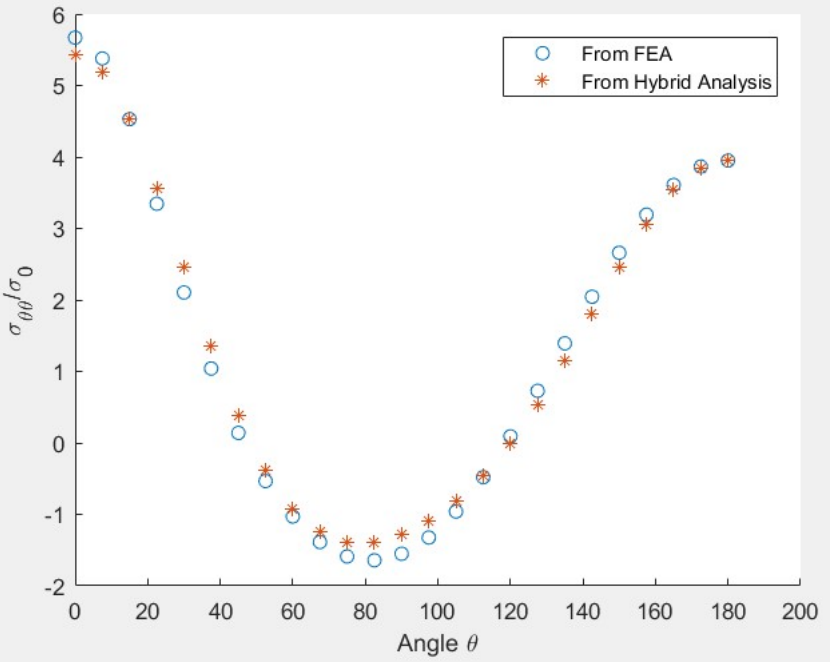

Figure 6-20: Plot of stresses $\sigma_{\theta\theta}/\sigma_0$ along edge of hole from FEM and TSA for n_t = 12,836 and k =21

6.8.2. Strain-Gage Analysis

Relative to the physical set-up of Figure 6-21, the reliability of the TSA method was further assessed by comparing the stresses at locations 'A' and 'B' (on the right boundary of the hole and right vertical edge of the plate; at $r = R$ or 9.5 mm and $r = Q$ or 14.6 mm, respectively, for $\theta = 0$ in Figure 6-1) evaluated by TSA-hybrid method and predicted by FEA with those obtained from strain-gages (Table 6-2 and Figure 6-22). The compared stresses are those in the Cartesian coordinate in the loading, y-direction. The lack of experimental information between the hole and right edge of the plate is manifested by poor TSA-based results at location B (outside edge of plate) in Figure 6-22. However, this is not highly significant structurally as the stress at point B is only 50% of that at location A. Figure 6-23 contains photographs of the strain-gaged plate. All gages employed were Micro-Measurement MM CEA-13-032UW-120 (gage factor: 2.13). Since the gages were self-compensated for aluminum, they were mounted and the plate tested at room temperature, no dummy gages were utilized.

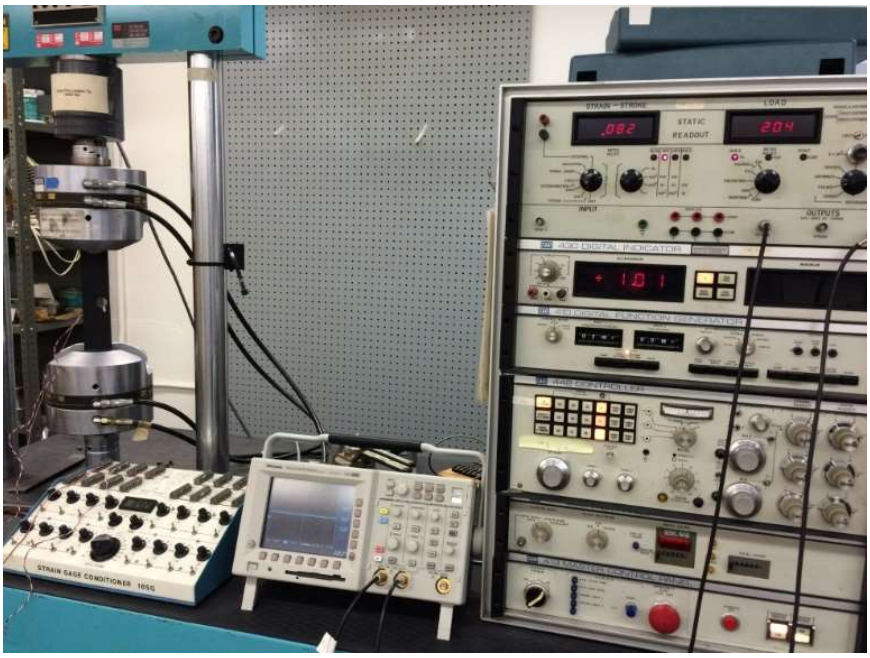

Figure 6-21: Strain-gage mounted loaded plate

Table 6-2: Comparison of stress at location ‘A’ from TSA, FEA and strain-gage for n_t = 12,836 and k =21

Normalized stress in loading direction, σ_{yy}/σ_0	TSA	FEA	Strain-Gage
At point ‘A’	5.43	5.67	5.34
Absolute % of error with TSA-hybrid method	-	4.51	1.49

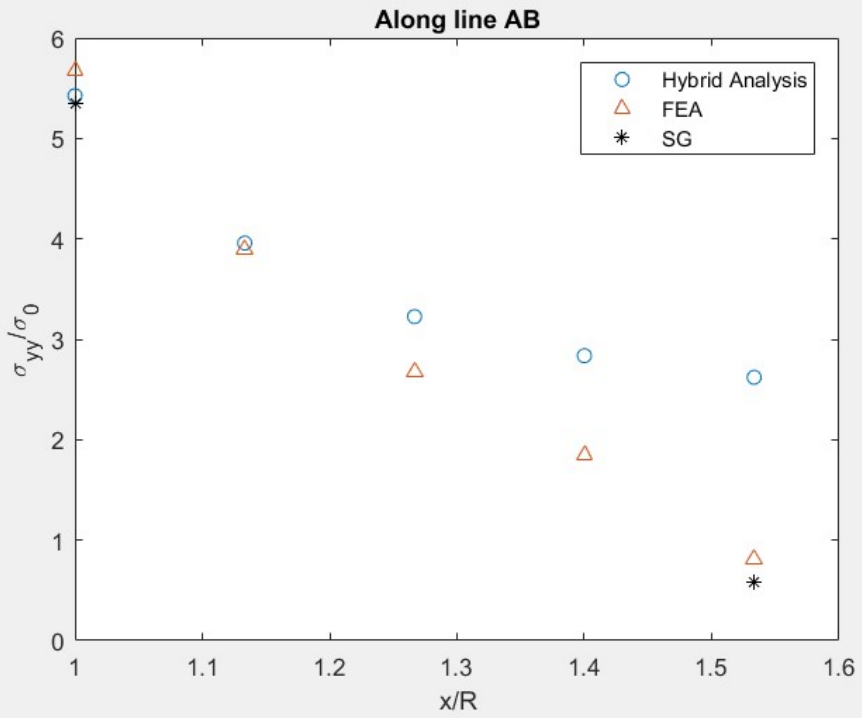

Figure 6-22: σ_{yy}/σ_0 from TSA, FEM and strain-gages at and between locations A and B

(a) (b)

Figure 6-23: Strain-gages mounted on (a) Inside edge of the hole at location 'A' and (b) On the right vertical boundary of the plate at location 'B'

6.8.3. Load Equilibrium

Load equilibrium is another effective mean of checking the reliability of the TSA-based hybrid stress analysis method. Load equilibrium was checked by numerically integrating the TSA-determined vertical stresses σ_{yy} along the x-axis at $y = R$ according to equation (6-23).

$$F_c^* = \int \sigma_{yy}\, dA = \int_{-(W-Q)}^{Q} \sigma_{yy} t dx\,, \quad \text{at} \quad y \geq R \tag{6-23}$$

where t, W, R and Q are the plate thickness, width, hole radius and distance of the hole center from nearest plate edge, respectively. The trapezoidal rule in MATLAB was used to compute the integration. The evaluated load was found to be 1,785.52 N (401.4 lbs) which is within 0.34% of the physically applied load of 1,779.3 N (400 lbs).

6.9. Summary, Discussion and Conclusions

When experimentally evaluating stresses in engineering members, it is not uncommon to encounter situations, or at least regions, of inferior or unreliable measured input information. Some factors contributing to unreliable TSA-recorded information are lack of local adiabaticity, uneven paint layer, light reflection from the tested specimen compromising the image quality, TSA camera sensor not properly cooled, improper evaluation of thermoelastic coefficient, K, or damaged specimen. In such cases an option might be to repeat the entire test procedure. However, that might not be possible to do so due to time or fiscal limitations. In some situations, an alternative might be to improve the initially measured unsatisfactory results through advance post-processing. For example, TSA methods have been proposed to handle non-adiabaticity [107–110]. Alternatively,

if a structurally important location is engulfed within a region of unreliable or inadequate experimental input information, but reliable measured information exits elsewhere at distant locations in the member, then combining analytical and numerical tools with the distant reliable experimental data might enable one to obtain accurate stresses at the location of interest. The strong mechanics-based concept processes the distant measured data with an Airy stress function. Available/suitable boundary conditions can also be utilized.

The present example demonstrates the ability to determine thermoelastically the stresses on the edge of an asymmetrically located hole in a finite tensile plate in the absence of local measured data by processing recorded distant load-induced temperature information with an Airy stress function. This is accomplished without knowing the constitutive material properties or the external loading. Moreover, this method does not require differentiating the measured data and the analysis can be done in isotropic materials with real variables. Reliability is supported by FEA, load equilibrium and strain-gage results. The ability to obtain reliable stresses along the boundary of the hole in the absence of local measured data is important. As mentioned earlier, one can encounter practical situations where there is a paucity of, or at least poor quality, measured information. Recognizing recorded TSA or DIC data are traditionally unreliable as one approaches an edge, such could occur whenever edges approach each other, such as happens in Figure 6-1.

Thermoelastic values are normally reliable only beyond approximately one millimeter (mm) inside an edge. When processing the measured information by a stress function, one therefore typically only uses recorded input data at least two or three pixels from and beyond an edge. In the present situation, the closest temperature information employed is 7.31 mm from the location of prime concern, i.e., point A in Figure 6-1.

The present approach is applicable to more complicated situations, different types/shapes of cutouts, to infinitely-width or finite-width plates with any shaped external boundaries. The concept is also extendable to stress analyze orthotropic composite materials by using complex variables. The present general concept could also be used with displacement-based techniques like moiré or DIC.

Appendix K considers results of variation of the present analysis. This study considers the consequence of omitting input data from one or two, rather than three pixels from along the vertical edges of the plate and enlarging the region between the hole and right plate edge where recorded TSA data are unreliable.

6.10. Acknowledgement

The TSA test data were collected by S. Gang.

Chapter 7. Stress Analysis of Diametrically-Loaded Isotropic Ring in Absence of Adequate Measured Displacement Information

7.1. Introduction

It is not uncommon in experimental mechanics to have regions with a paucity of, or poor quality, recorded data. The situation can be particularly serious if knowledge of the stresses in locations of inadequate experimental information is critical to the integrity of the machine or structural component. Motivated by this challenge, the objective of this study is to demonstrate the ability to evaluate stresses experimentally at a structurally important location engulfed within a significantly large region throughout which there is no dependable input information. An example is a diametrically-loaded ring and measured information of a single displacement component. Reliability is demonstrated by comparison with results from FEM and a strain-gage.

7.2. General Overview

The integrity of a machine or structural member can be highly influenced by its stresses. Purely analytical or theoretical stress analysis methods tend to be limited to situations involving simple infinite geometries, whereas most practical problems involve non-trivial, finite shapes. Moreover, like numerical approaches such as the finite element method (FEM), analytical/theoretical analyses depend on reliable knowledge of the external loading. The latter are commonly unknown in practice. Recognizing the above motivates the use of experimental methods

such as thermoelastic stress analysis (TSA) or digital image correlation (DIC). The capability of the hybrid experimental-analytical method to work with distant TSA information in the absence of adequate reliable measured information at structurally important locations was demonstrated in Chapter 6. The current study investigates the ability of the hybrid stress analysis method to effectively work with a limited amount of DIC data in similar situations, i.e., with missing measured information at critical locations of the loaded structure.

DIC is a popular and contemporary optical technique for recording displacements [14] and is applicable to both isotropic and orthotropic materials. It is more amendable than TSA to engineering applications beyond a laboratory environment. Although it enjoys the advantage of not requiring cyclic loading, DIC does necessitate the surface being interrogated to have a suitable random pattern. Moreover, the measured displacement data must be differentiated to obtain strains. Differentiating measured data can be unreliable. Stresses can be obtained from the strains if the constitutive material properties are known. DIC-determined information by traditional methods using commercial systems tends to be unavailable at and near geometric discontinuities due to an inability to track a group of pixels (subset) which lack neighboring pixels. Reference [83] illustrated the errors which can occur at the edge of a geometric discontinuity by traditional DIC. An inferior or damaged speckle pattern, poor user defined correlation variables such as unsuitable subset or step size, fluctuation in the image light and/or inappropriate filter size can produce unreliable displacements and inaccurately differentiated displacement data can result in erroneous strains. Therefore, both experimental factors and correlation variables, or either one of these, can contribute to unreliable DIC-measured information. An alternative can be re-doing the entire experiment which includes reapplying the speckle pattern, repeating the DIC test and redoing the post-processing. However, an alternative can be to work with the compromised measured

information, i.e., using distant reliable measured information to obtain reliable information at the critical locations containing inadequate/unreliable local measured information.

The present DIC-hybrid stress analysis technique involves processing a DIC-measured single displacement field by a strong mechanics-based algorithm based on a combination of Airy stress function, discretely imposed traction-free boundary conditions and numerical methods such as least squares to aid the mathematical computation.

The current study involves an annular aluminum plate with diametrically-loaded concentrated loads, Figure 7-1. Such plates are commonly used in load cells, rocket shells, gun barrels, high pressure piping and rock/concrete and earth excavation cutters [74]. The present full-field technique stress analyzes the isotropic ring, including along its traction-free boundaries, using a DIC-measured single displacement field away from the geometric discontinuities or edges. Major advantages of this method over other stress analyses techniques include the following: full-field, non-contacting stress analysis with simple and easy experimental requirements (unlike strain-gages), independent of external boundary conditions or loadings or unreliable edge data, does not require differentiating measured quantities using arbitrary methods, simultaneous smoothing and automatic stress separation of the experimental data, no cyclic loading or additional calibration coupon required like thermoelastic stress analysis and does not necessitate using both the in-plane displacement components (such as with moiré or electronic speckle).

The experimental data were not always deficient in some of the regions considered here to be so but are conjectured as such to demonstrate ability to obtain reliable results at important locations which are engulfed within a region whose experimental information is not dependable.

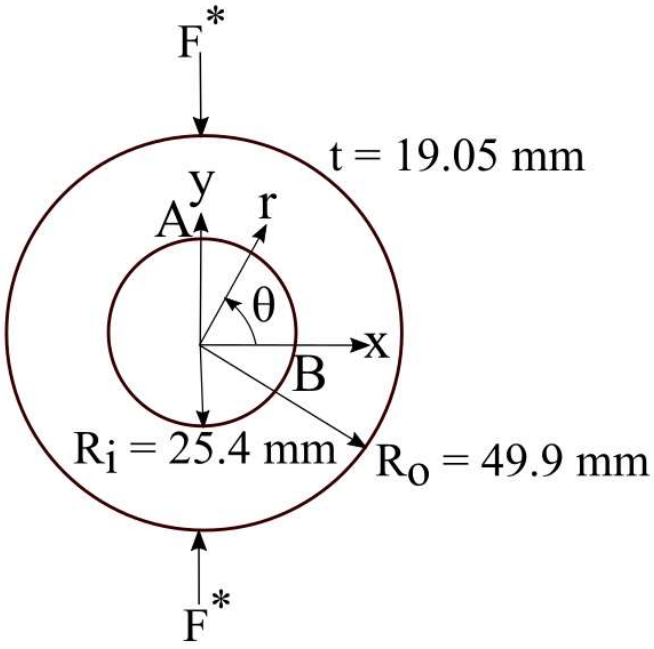

Figure 7-1: Diametrically-loaded aluminum ring

7.3. Literature Review

Theoretical analysis of annular plates are available but limited to only a fixed outer-to-inner diameter ratio of two [111]. Such structures with outer-to-inner diameter ratio other than two have been studied experimentally using techniques such as photoelasticity [67] and strain-gages [74]. A diametrically-loaded isotropic ring was studied by Khaja [74] using strain-gages. The ring, mounted with several strain-gages, necessitated multiply loadings in order to change the gage orientation with respect to the loading points. This was done to increase the number of data outputs from the limited number of mounted strain-gages and thereby to ensure sufficient input data for the stress analysis. The analytical expressions were based on Airy stress function with real variables. Serati et al. [112] investigated displacement and stress components of annular rings under different types of loading by employing the Michell's expansion in the polar coordinates and Fourier series representation of the boundary conditions. Stress concentration factors of

annular rings with various inner-to-outer diameter ratios have been reported in Reference [67] by using photoelasticity. The present study stress analyzes an annular ring using only a single DIC-measured displacement field and processing that information with Airy stress function and discretely imposing the boundary conditions. The present technique is applicable to a ring of any inner-to-outer diameter ratio using simple non-contacting full-field experimental set-ups and rigorous mechanics-based algorithms.

7.4. Relevant Equations

Acknowledging the ring's mechanical and geometric symmetry about the *x*- and *y*-axes, the inner and outer boundaries being self-equilibrated, the stresses, strains and displacements being single-valued functions of θ, under plane-stress and no body forces, equation (7-1) is a relevant Airy stress function, Φ, for the isotropic ring of Figure 7-1 [28,83].

$$\Phi = a_0 + b_0 \ln r + c_0 r^2 + \sum_{n\,=\,2,4\ldots}^{\infty} \left(a_n r^n + b_n r^{n+2} + c_n r^{-n} + d_n r^{-(n-2)}\right) \cos(n\theta) \tag{7-1}$$

Substituting the expression of the Airy stress function, Φ, from equation (7-1) into equations (6-5) through (6-7), the in-plane stresses in the polar coordinates are

$$\sigma_{rr} = \frac{b_0}{r^2} + 2c_0$$
$$- \sum_{n\,=\,2,4\ldots}^{N} \left[a_n n(n-1)r^{(n-2)} + b_n(n-2)(n+1)r^n \right. \tag{7-2}$$
$$\left. + c_n n(n+1)r^{-(n+2)} + d_n(n+2)(n-1)r^{-n}\right]\cos(n\theta)$$

$$\sigma_{\theta\theta} = -\frac{b_0}{r^2} + 2c_0$$
$$+ \sum_{n\,=\,2,4\ldots}^{N} \left[a_n n(n-1)r^{(n-2)} + b_n(n+2)(n+1)r^n \right. \tag{7-3}$$
$$\left. + c_n n(n+1)r^{-(n+2)} + d_n(n-2)(n-1)r^{-n}\right]\cos(n\theta)$$

$$\sigma_{r\theta} = \sum_{n\,=\,2,4\ldots}^{N} \left[a_n n(n-1)r^{(n-2)} + b_n n(n+1)r^n - c_n n(n+1)r^{-(n+2)} \right. \tag{7-4}$$
$$\left. - d_n n(n-1)r^{-n}\right]\sin(n\theta)$$

The polar radial coordinate, *r*, is measured from the center of the ring and angle θ is measured counter clock-wise from the horizontal *x*-axis. *N* is the terminating index of the summation series. Note that equation (7-1) does not account for the contacting top and bottom concentrated loads. In order to evaluate the Airy stress coefficients from the DIC-measured displacement data, expressions for the in-plane displacements for the current diametrically-loaded ring (Figure 7-1) need to be established. Utilizing Hooke's law and the stresses of equations (7-2)

and (7-3), expressions for the in-plane strains can be obtained, from which by integration the expressions of the in-plane displacements are established. Combining equations (7-2) and (7-3) with 2D-Hooke's law, the normal in-plane strain components in polar coordinates are

$$\frac{\partial u_r}{\partial r} = \varepsilon_{rr} = \frac{1}{E}(\sigma_{rr} - \nu\sigma_{\theta\theta}) \tag{7-5}$$

$$\frac{1}{r}\frac{\partial u_\theta}{\partial \theta} = \varepsilon_{\theta\theta} - \frac{u_r}{r} = \frac{1}{E}(\sigma_{\theta\theta} - \nu\sigma_{rr}) - \frac{u_r}{r} \tag{7-6}$$

The relationship between in-plane strains and displacements are utilized in equations (7-5) and (7-6). Rearranging equation (7-6) one obtains

$$\frac{\partial u_\theta}{\partial \theta} = \frac{r}{E}(\sigma_{\theta\theta} - \nu\sigma_{rr}) - u_r \tag{7-7}$$

Integrating equation (7-5) gives u_r, as equation (7-8). Substituting the expression of u_r from equation (7-8) into equation (7-7), and integrating, the in-plane displacement component in the polar coordinates u_θ is obtained, as equation (7-9).

$$u_r = \frac{1}{E}\Bigg[-\frac{b_0(1+\nu)}{r} + 2c_0(1-\nu)r - \sum_{n=2,4\ldots}^{N}\Big[a_n n(1+\nu)r^{n-1} + b_n[(n-2)+\nu(n+2)]r^{n+1} - c_n n(1+\nu)r^{-(n+1)} - d_n[(n+2)+\nu(n-2)]r^{-n+1}\Big]\cos(n\theta) + S_1 cos(\theta) - S_2\sin(\theta)\Bigg] \quad (7\text{-}8)$$

$$u_\theta = \frac{1}{E}\Bigg[\sum_{n=2,4\ldots}^{N}\Big[a_n n(1+\nu)r^{n-1} + b_n[n(1+\nu)+4]r^{n+1} + c_n n(1+\nu)r^{-(n+1)} + d_n[n(1+\nu)-4]r^{-n+1}\Big]\sin(n\theta) - S_1 cos(\theta) - S_2\sin(\theta) + R^* r\Bigg] \quad (7\text{-}9)$$

Quantities S_1, S_2 and R^* represent the rigid body motions and are present in these equations as a result of integrating strains to obtain displacements. When physically loading in a testing machine, S_1, S_2 and R^* are zero.

DIC provides displacements in the Cartesian *x*-*y* coordinates. Thus, to aid the mathematical procedure, the displacements in the polar coordinates, u_r and u_θ, (equations (7-8) and (7-9)) are transformed to those, *u* and *v*, in the *x*-*y* Cartesian coordinates according to Figure 7-2, i.e.,

$$u = u_r cos\theta - u_\theta sin\theta \tag{7-10}$$

$$v = u_r sin\theta + u_\theta cos\theta \tag{7-11}$$

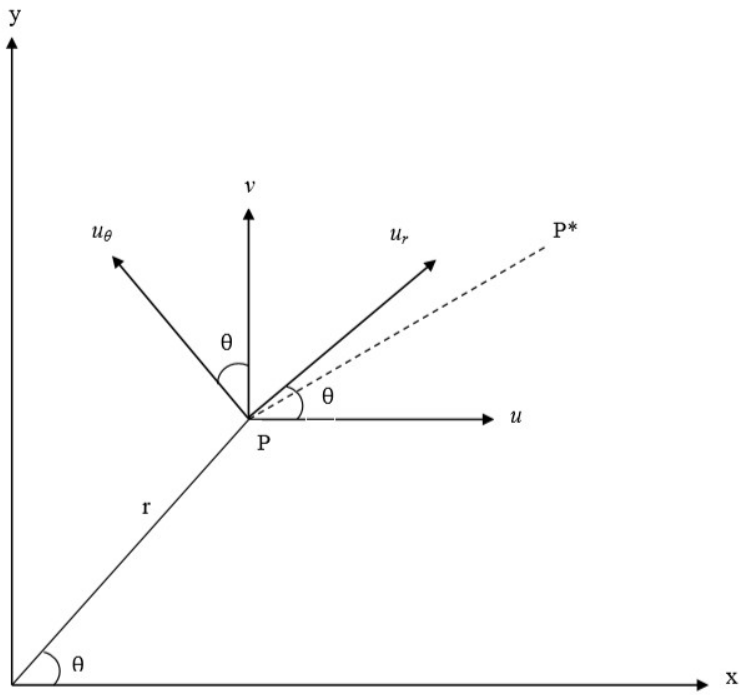

Figure 7-2: Relation between displacement components in polar and Cartesian coordinates

Using the expressions of u_r and u_θ from equations (7-8) and (7-9) in equation (7-11), the expression for the displacement component in the vertical loading direction-y in the Cartesian coordinate is as

$$
\begin{aligned}
v = \frac{1}{E}\Bigg[& -\frac{b_0(1+\nu)}{r} + 2c_0(1-\nu)r \\
& + \sum_{n=2,4\ldots}^{N} n[\sin(n\theta)\cos\theta - \cos(n\theta)\sin\theta](1+\nu)r^{n-1}a_n \\
& + ([(2-n)+\nu(n+2)]\cos(n\theta)\sin\theta \\
& + [n(1+\nu)+4]\sin(n\theta)\cos\theta)r^{n+1}b_n \\
& + n[\cos(n\theta)\sin\theta + \sin(n\theta)\cos\theta](1+\nu)r^{-(n+1)}c_n \\
& + ([(n+2)+\nu(n-2)]\cos(n\theta)\sin\theta \\
& + [n(1+\nu)-4]\sin(n\theta)\cos\theta)r^{-n+1}d_n\Bigg]
\end{aligned}
\tag{7-12}
$$

It should be noted that, when treating an isotropic perforated structure with an Airy stress function in real variables, the in-plane stresses of equations (7-2) through (7-4) are independent of the elastic material properties. However, the in-plane displacements of equations (7-8) through (7-12) are not, i.e., to evaluate the displacement components, or to use them to find the Airy coefficient, requires knowing the material properties *E* and *v*.

7.5. Ring Details

The aluminum 6061-T6 (from Weidenbeck, Inc., Madison, WI) ring had inner and outer radii of R_i = 25.4 mm (1.0") and R_0 = 49.9 mm (1.96"), respectively, and a thickness of *t* = 19.05 mm (0.75"), Table 7-1.

Table 7-1: Details of aluminum ring and loading

Material	Aluminum 6061-T6
Supplier	Weidenbeck, Inc., Madison, WI
Inner diameter, D_i	50.8 mm (2.00")
Outer diameter, D_0	99.8 mm (3.92")
Thickness, t	19.05 mm (0.75")
Elastic Modulus, E	69 GPa (10×10^6 psi)
Poisson's ratio, v	0.33
Symmetry	Both horizontally and vertically
Loading for DIC analysis	From 0 to 6.67 kN (1,500 lbs) in increments of 1.1 kN (250 lbs)
Loading for DIC-hybrid stress analysis	6.67 kN (1,500 lbs)

7.6. DIC Experimental Details

7.6.1. Ring Surface Preparation

Standard DIC surface preparation, i.e., speckle application protocol as mentioned in Chapter 4, was followed to apply the random speckle pattern on the ring. The plate was initially degreased using a solvent (CSM-2 by Vishay Precision Group), polished lightly with a fine (400-grit) emery cloth and cleaned with water-based mild cleaners. The cleaned surface was covered with a coat of white paint over which random black dots of paint were applied, Figure 7-3. Rust-

Oleum Ultra Cover paints were used. Details regarding application of speckle pattern are provided in Chapter 4, Section 4.6.3.

Figure 7-3: Aluminum ring with applied speckle pattern

7.6.2. Loading and Correlation Details

The prepared ring was loaded using a 4.45 kN (10,000 lbs) capacity, electro-mechanical, Sintech MTS machine from essentially 0 to 6.67 kN (1,500 lbs) in load increments of 1.1 kN (250 lbs), Figure 7-4. The reported results are for a load of 6.67 kN (1,500 lbs). The loading-frame is equipped with a computerized data acquisition and monitoring system through which the applied load on the ring was monitored. The DIC test was conducted using ambient lighting. While loading, the ring was placed on the compression fixture of the lower stationary crosshead and compressive load was applied through the compression fixture of the top crosshead. This simulated the ring being diametrically-compressed by concentrated loads from the two vertical ends.

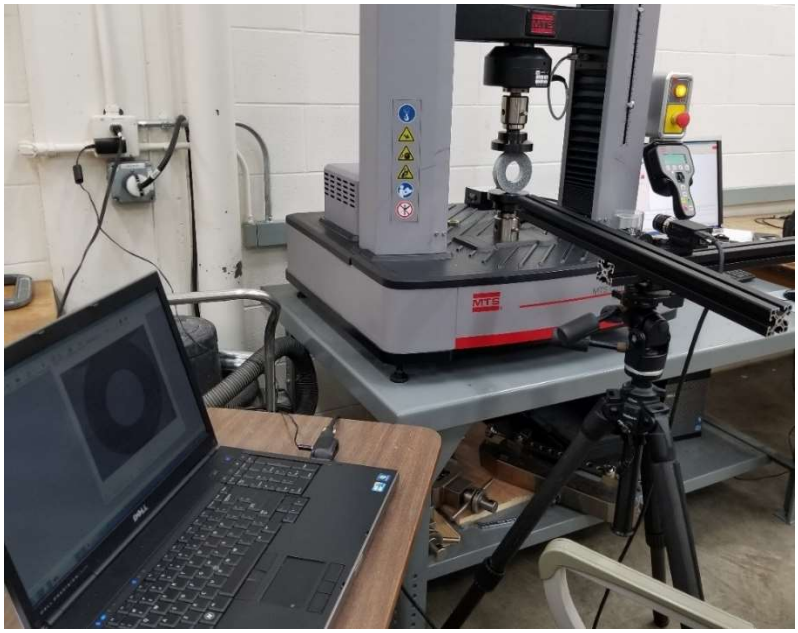

Figure 7-4: DIC experimental set-up for isotropic ring

For the DIC test of the ring, Correlated Solution, Inc.'s commercial DIC package was employed. Details regarding the DIC package are available in Chapter 4, Table 4-3. A single digital camera was used since the ring experiences no out-of-plane motion beyond the Poisson's effect (care was taken to ensure the camera is exactly perpendicular to the plate's surface). Digital images of the ring were taken with the digital camera controlled by Vic-Snap image acquisition software. The applied load on the ring was held constant while capturing the digital image for each load increment. The load for each DIC image was recorded manually. To calibrate the system, a picture of an appropriate calibration grid was taken by the DIC camera and Vic-Snap software. The supplier's calibration grid was placed on the load-frame's compression fixture at the exact same distance from the camera as was the aluminum ring. This was achieved by marking the location of the ring's front surface using a piece of tape, Figure 7-5, and later using the tape as a marker to place the calibration grid at the exact same location of the aluminum ring. Through this process

the same depth of field for the calibration image and the speckle images was achieved. The system was then calibrated using the thus obtained calibration image in Vic-2D correlation software's calibration scale option, i.e., previously known distance of the grid was marked and provided in physical units. A subset size of 26 and step size 5 were used. Vic-2D software was used to correlate the reference and deformed images and provide the DIC-measured displacements.

(a) (b)

Figure 7-5: Calibration of the DIC system, (a) Tape on compression fixture to indicate placement of the calibration grid and (b) DIC system capturing calibration image

7.7. Data Reduction and Analysis

When loaded physically, the bottom of the ring remained stationary while the top was vertically compressed. The recorded v-displacement data in the loading y-direction were consequently unsymmetrical about the horizontal x-axis, Figure 7-6(a). However, the ring is geometrically and mechanically symmetrical about the x-y axes. The recorded DIC vertical v-

displacement data were processed to shift the origin to the center of the ring and reorganized to simulate the plate being compressed vertically equally from its top and bottom, i.e., $v = 0$ along the horizontal center-line passing through $y = 0$ of Figure 7-1. The processed displacement data were then averaged over the four quadrants to remove any experimental scatter or any asymmetry. Figure 7-6(b) illustrates the averaged result in the first quadrant.

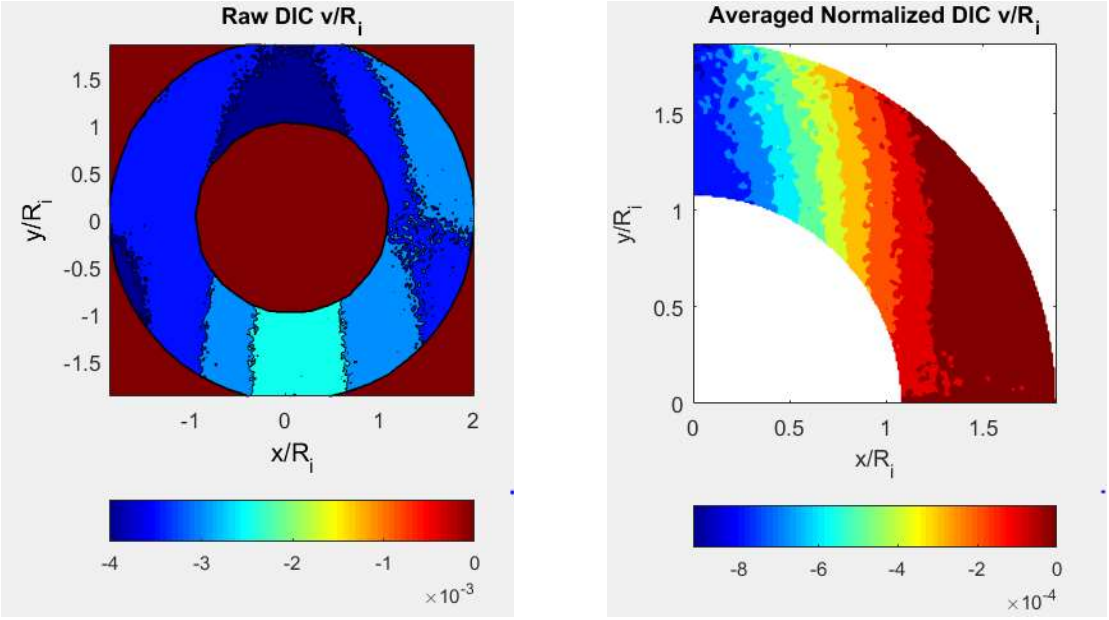

(a) (b)

Figure 7-6: DIC-measured v-displacements in loading direction y for the diametrically-loaded ring, (a) Recorded data after shifting the origin to the center of the ring and (b) Processed and averaged over the four quadrants, $v = 0$ at $y = 0$

The ability to determine reliably by DIC the tensile stress at point A on the inside of the diametrically-compressed ring of Figure 7-1 is now demonstrated. This is possible even though location A is contained within a large region throughout which there are no dependable measured displacement data. In reality, there was reasonable DIC information throughout the ring (except

near the edges). However, only that within the black region (n_{DIC} = 2,222) of Figure 7-7 is assumed here to be dependable. Moreover, only the vertical displacement information, v, is assumed to be available/reliable.

To observe the effect of the data selection range on the overall results of the DIC-hybrid stress analysis method, a second analysis was conducted with measured data over a slightly larger and distributed region (n_{DIC} = 3,326) of the ring as shown in Figure 7-8.

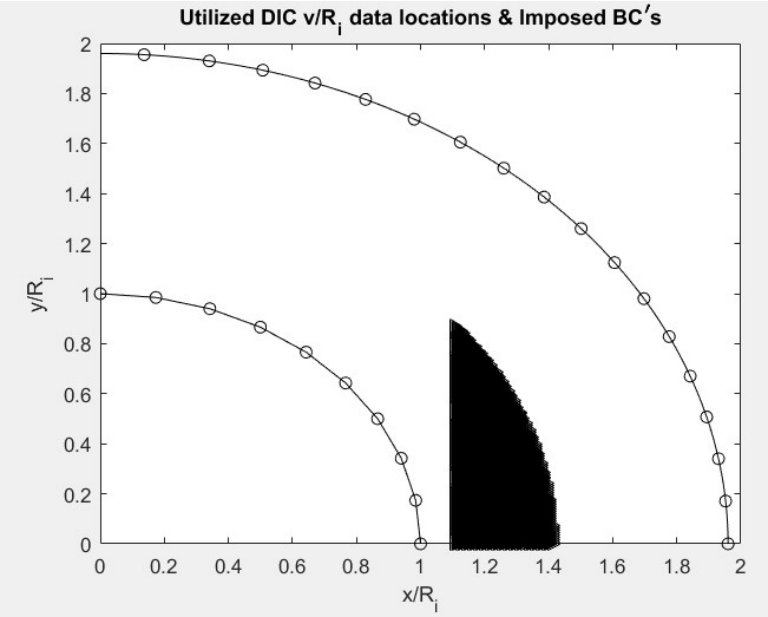

Figure 7-7: One quarter of the ring of Figure 7-1 showing region of reliable displacement data (black region) and locations of imposed boundary conditions (circular markers) for $n_{DIC} + h$ = 2,222 + 28

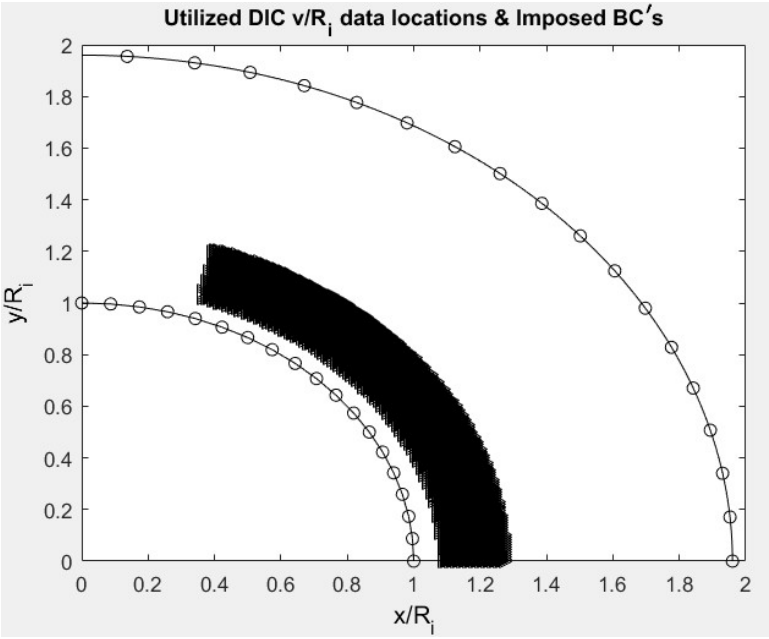

Figure 7-8: One quarter of the ring of Figure 7-1 showing region of reliable displacement data (black region) and locations of imposed boundary conditions (circular markers) for $n_{DIC} + h =$ 3,326 + 37

For both cases, in addition to processing the selected measured DIC v-displacement data with an Airy stress function, some boundary conditions were used to obtain the stresses at the location of interest, point A, Figure 7-1. The boundary condition $\sigma_{r\theta} = 0$ was applied discretely along R_i between $0 \leq \theta \leq 90°$ and along R_0 between $0 \leq \theta \leq 85°$. Although not done so, one could also impose $\sigma_{rr} = 0$ at discrete locations on the inner and outer radii of the ring. In addition, the averaged v-displacement data automatically satisfied the condition $v = 0$ at $y = 0$.

For the analysis of Figure 7-7, along with the $n_{DIC} = 2{,}222$ DIC-measured v-displacement information, the traction-free boundary condition $\sigma_{r\theta} = 0$ was imposed at $h_1 = 10$ equally spaced locations along $r = R_i$ and at $h_2 = 18$ equally spaced locations along $r = R_0$. Similarly, for the analysis of Figure 7-8 along with the $n_{DIC} = 3{,}326$ v-displacements, the number of imposed boundary conditions were $h_1 = 19$ and $h_2 = 18$ at $r = R_i$ and $r = R_0$, respectively.

These processed, averaged and selected DIC-measured displacement data in the loading direction, v, were used in equation (7-12) with the traction-free boundary condition $\sigma_{r\theta} = 0$ in equation (7-4) to evaluate the Airy coefficients. The response in the loaded ring can analytically be expressed as equation (7-13). This can further be expressed in terms of matrices of equation (7-14), where the matrix $[A]$ involves plate's material properties and the locations (r and θ) of the n_{DIC} locations of DIC-measured v-displacement data and the h ($= h_1 + h_2$) locations (r and θ) where boundary condition $\sigma_{r\theta} = 0$ was imposed. Vector $\{c\}$contains the unknown Airy coefficient's and vector $\{d\}$ includes the DIC-recorded displacement data and the imposed traction-free boundary conditions. In equation (7-14) the only unknowns are the Airy coefficients of vector $\{c\}$ and they were evaluated by least squares. For these studies the backslash operator '\' in MATLAB was used to compute the least square values of the Airy coefficients of vector $\{c\}$.

$$\begin{bmatrix} v\,(b_0\ c_0\ a_n\ b_n\ c_n\ d_n) \\ \sigma_{r\theta}(a_n\ b_n\ c_n\ d_n) \end{bmatrix} \begin{Bmatrix} b_0 \\ c_0 \\ a_n \\ b_n \\ c_n \\ d_n \end{Bmatrix} = \begin{bmatrix} \mathrm{DIC}(v) \\ \mathrm{BC's}\ (\sigma_{r\theta} = 0) \end{bmatrix} \tag{7-13}$$

$$[A]_{(n_{DIC}+h)\times k}\{c\}_{k\times 1} = \{d\}_{(n_{DIC}+h)\times 1} \tag{7-14}$$

Number $n = 2, 4, 6, \ldots N$ in the summation series of equations (7-4) and (7-12), and the number of Airy coefficients $k = (2n + 2)$ in equation (7-14). To account for experimental scatter in the DIC-recorded information, at $x \geq R$ the over-determined system of linear equations of equation (7-14) employs more side conditions, $n_{DIC} + h$, than the number of unknown Airy coefficients, k.

7.8. Finite Element Model

A finite element analysis of the aluminum ring was conducted against which to compare the results of the DIC-hybrid stress analysis method. As accuracy of the FEA results is highly dependent on the external loading and boundary conditions, the geometry, boundary conditions and loading of the present ring was deliberately selected to obtain accurate FEA results with which to compare the present DIC-hybrid results. The 2D-FEM with plane-stress condition was generated using commercial FEA tool ANSYS APDL. The plate having mechanical and geometrical symmetry about both the *x*-*y* axes, only one quarter of the plate was modeled with the coordinate origin located at the center of the ring. Appropriate symmetrical boundary conditions were numerically imposed. ANSYS isoparametric elements Plane 183 with eight nodes per element with translations *u* and *v* per node were used to model the ring, Figure 7-9. The annular ring was meshed throughout with quadrilateral elements and the mesh density was selected as such that increasingly denser meshes had no effect on the maximum stress concentration. A point load was applied at the top center of the ring to represent a concentrated load. As only a quarter of the ring was modeled, half of the physically applied 6.67 kN (1,500 lbs) load, i.e., 3.34 kN (750 lbs) load was applied. This results in an average/nominal stress of 7.18 MPa (= 1.04 ksi) according to equation (7-15). The final quarter-FEM ring had 2,911 nodes and 2,800 elements.

$$\sigma_{net} = \frac{F^*}{(D_0 - D_i) \times t} = \frac{6.67\ \text{kN}}{2\ \times\ (49.9\ -25.4)\ \text{mm}\ \times 19.05\ \text{mm}} = \ 7.18\ \text{MPa or}\ 1{,}041.67\ \text{psi} \tag{7-15}$$

Figure 7-10 and Figure 7-11 contains FEM results.

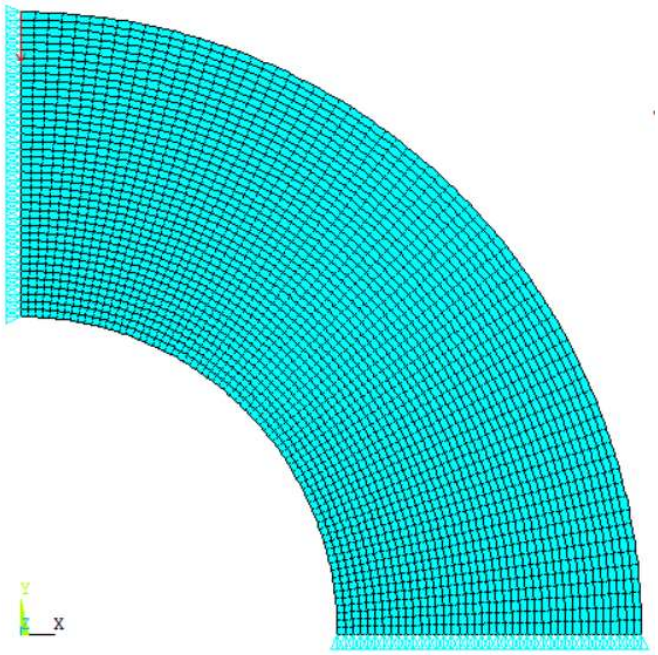

Figure 7-9: FEM of one quarter of the aluminum ring

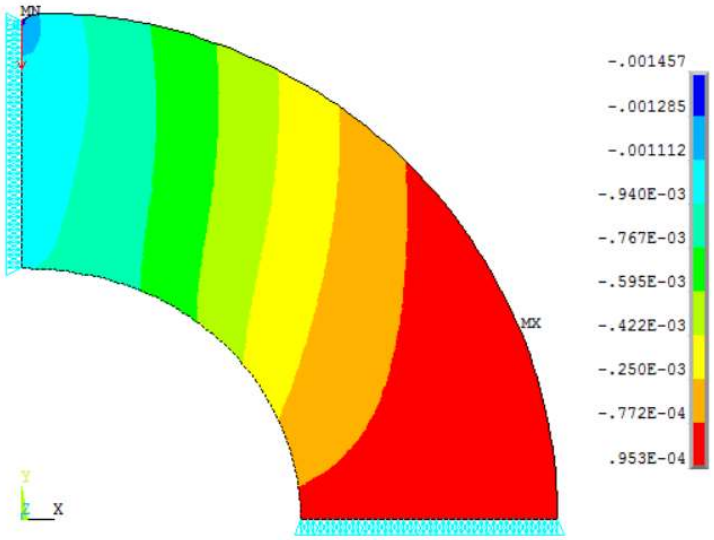

Figure 7-10: Contours of *v*-displacement from FEM (units in inches)

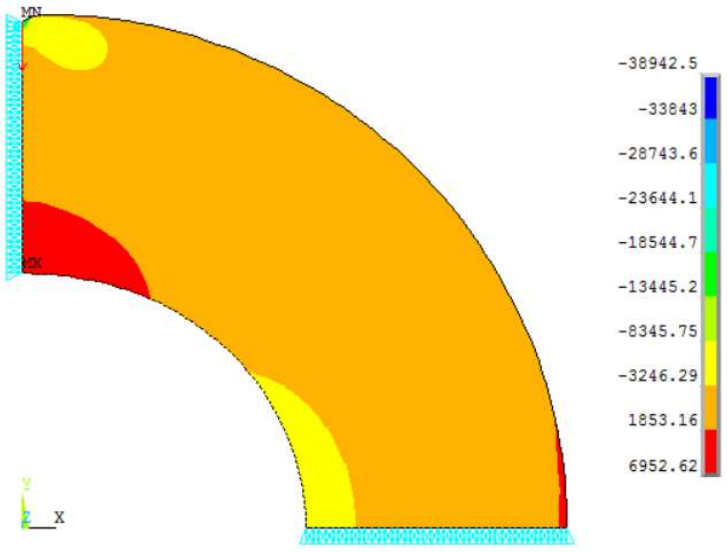

Figure 7-11: Contours of tangential stresses, $\sigma_{\theta\theta}$, from FEM (units in psi)

7.9. Strain-Gage Analysis

To further assess the reliability of the DIC-based stress analysis method, a strain-gage was mounted on the inner boundary of the ring (Figure 7-12) and loaded (Figure 7-13 and Figure 7-14), the results from which were compared with those from FEM and DIC. The Micro-Measurement's strain-gage was of type EA-06-015LA-120 with a gage factor of 2.01 and 1.2% transverse sensitivity. By rotating the ring with respect to the vertically applied loading, it was possible to record strains along the ring's inner circumference, $r = R_i$, from 0° to 90° at locations of 10° intervals (Figure 7-1), Figure 7-14. The gaged ring was loaded using the 4.45 kN (10,000 lbs), electro-mechanical, Sintech MTS loading-frame, coupled with National Instruments modular hardware and software for the strain measurements, Figure 7-13. The strain-gage being tuned for aluminum, it was mounted and the ring tested at room temperature without the use of any dummy gages. The elastic modulus, $E = 69$ GPa (10×10^6 psi) of the ring was used to convert the recorded strains to stresses.

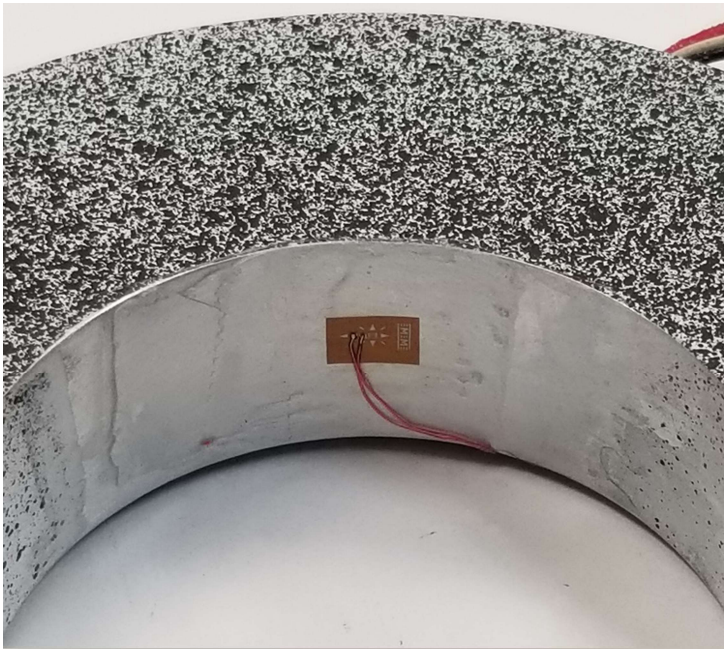

Figure 7-12: Mounted strain-gage on the inner surface of the aluminum ring

Figure 7-13: Loading and strain data acquisition of strain-gage mounted aluminum ring

(a) (b)

Figure 7-14: Ring loading with respect to strain-gage location to record (a) Tensile strain at location A and (b) Compressive strain at location B of Figure 7-1, respectively

7.10. Evaluating Number of Airy Coefficient to Employ

The present number of Airy coefficient to employ was chosen based on the root mean square (RMS) between the experimentally measured displacement data, d, and those reconstructed by the DIC-hybrid method, d', according to equation (7-13) (Figure 7-15 and Figure 7-16) and the condition number, C, of the matrix $[A]$ of equation (7-14) (Figure 7-17 and Figure 7-18). In addition, the contours of the tangential stress component of equation (7-3) for varying number of Airy stress coefficients, k, from the DIC-hybrid method are compared with those from FEM in Figure 7-19 and Figure 7-20. From the analyses, for $n_{DIC} = 3{,}326$ and $h = 37$ of Figure 7-8, $k = 10$ was found to be a reasonable choice. The RMS plot of Figure 7-15 suggest $k \geq 14$ but the condition number data of Figure 7-17(b) suggest $k \leq 10$ be retained in the summation series. The contour

plots of the tangential stresses from the DIC-hybrid method and FEM of Figure 7-19 show that for k = 6, the DIC-hybrid method over-estimates the maximum tangential stress and for k = 14 the stress contours start to deviate from the expected behavior. For the case of Figure 7-7, for n_{DIC} = 2,222 and h = 28, k = 6 was found to be a realistic choice for the DIC analysis of the compressed ring. The RMS plot of Figure 7-16 suggests use k = 10, 14 or 18 over k = 6, but the plot of the natural logarithm of the condition number, $\log_{10}(C)$, (Figure 7-18(b)) and the comparison of the tangential stress contours (Figure 7-20) highly recommend using k = 6. For values of k > 6, the system mathematically becomes ill-conditioned resulting in huge computational errors. As such k = 6 were selected for n_{DIC} = 2, 222 and h = 28, and k = 10 for n_{DIC} = 3,326 and h = 37.

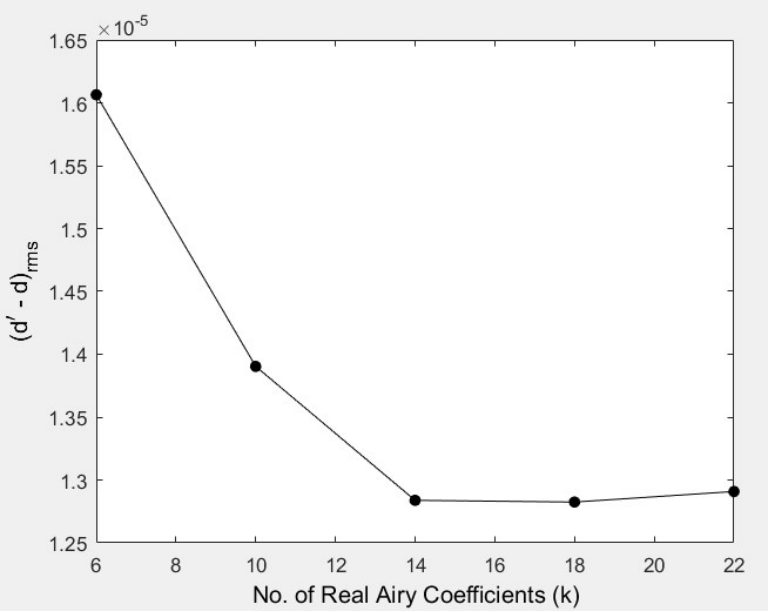

Figure 7-15: RMS of the measured and reconstructed displacement data versus the number of Airy stress coefficients, k, for n_{DIC} = 3,326 and h = 37 of Figure 7-8

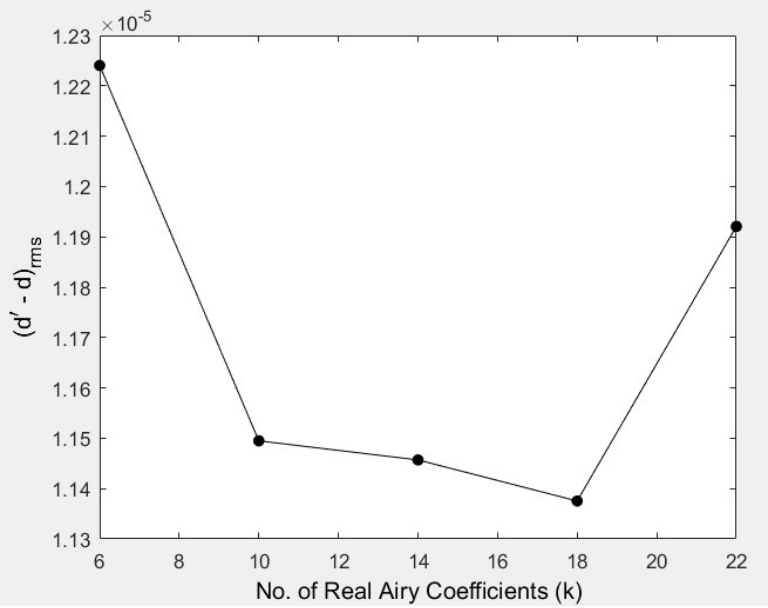

Figure 7-16: RMS of the measured and reconstructed displacement data versus the number of Airy stress coefficients, *k,* for n_{DIC} = 2,222 and h = 28 of Figure 7-7

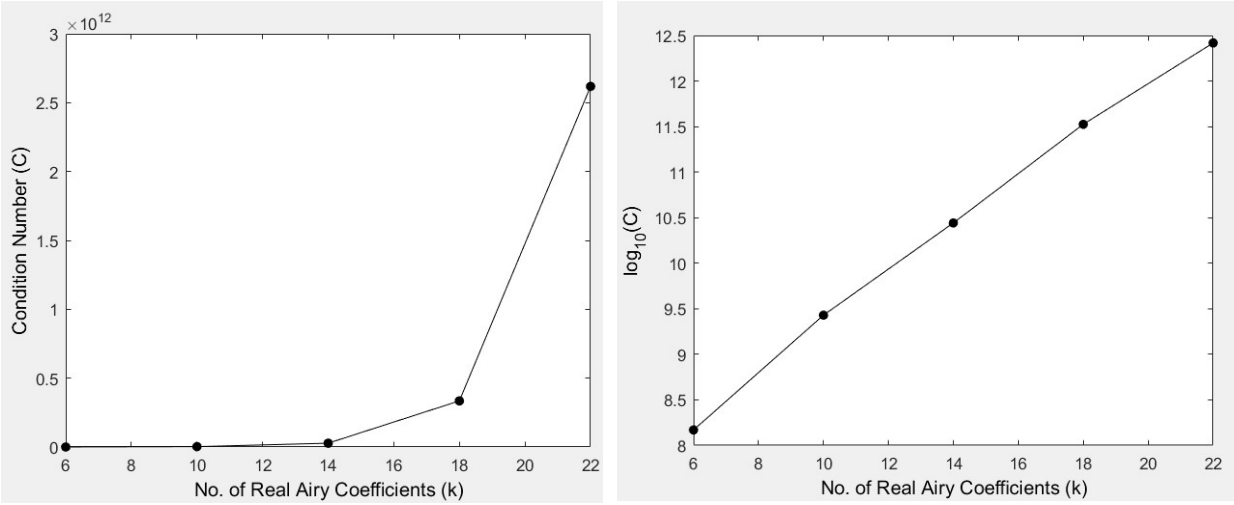

(a) (b)

Figure 7-17: (a) Condition number, C, and (b) $\log_{10}(C)$ for varying number of Airy stress coefficients, *k,* for n_{DIC} = 3,326 and h = 37 of Figure 7-8

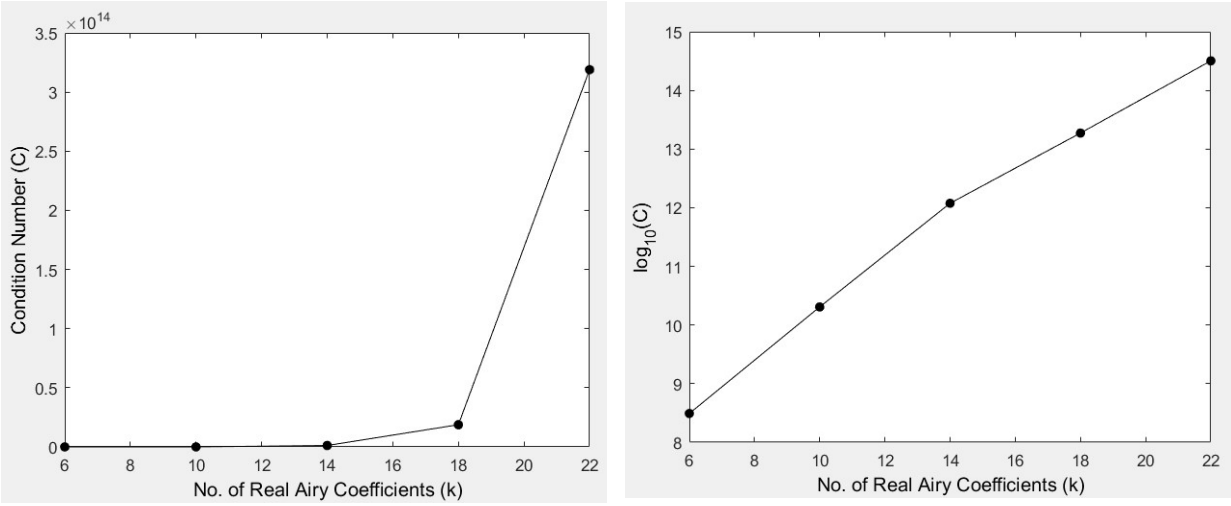

(a) (b)

Figure 7-18: (a) Condition number, C, and (b) $\log_{10}(C)$ for varying number of Airy stress coefficients, k, for n_{DIC} = 2,222 and h = 28 of Figure 7-7

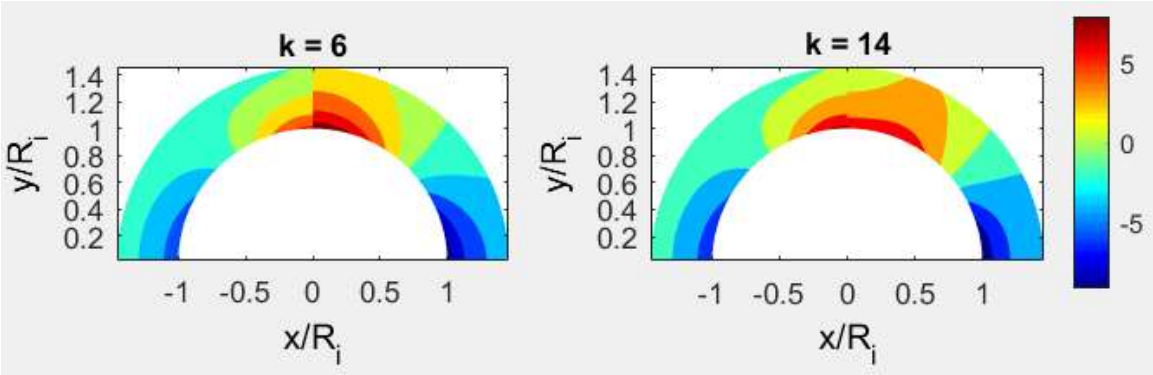

Figure 7-19: Contours of $\sigma_{\theta\theta}/\sigma_{net}$ from DIC-hybrid method (right) and FEM (left) for n_{DIC} = 3,326 and h = 37 of Figure 7-8 and Airy stress coefficients, k = 6 and k = 14, respectively

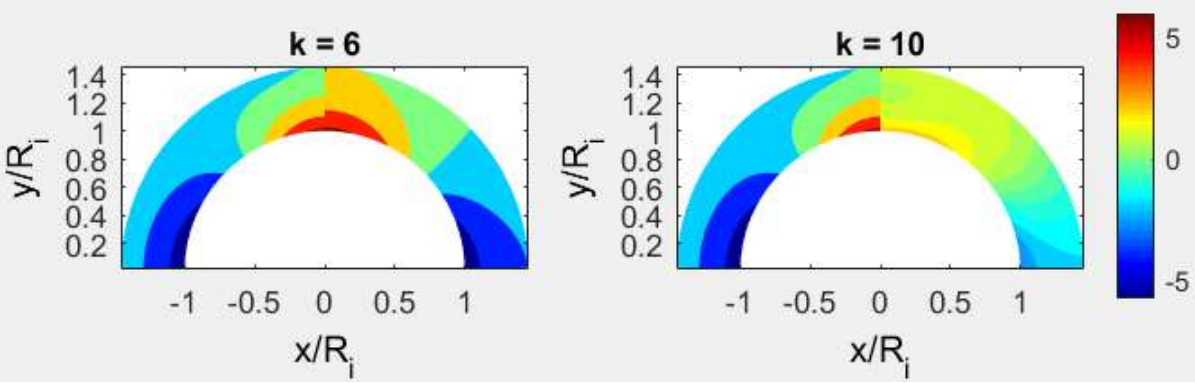

Figure 7-20: Contours of $\sigma_{\theta\theta}/\sigma_{net}$ from DIC-hybrid method (right) and FEM (left) for n_{DIC} = 2,222 and h = 28 of Figure 7-7 and Airy stress coefficients, k = 6 and k = 10, respectively

7.11. Results

The Airy coefficients are evaluated according to equation (7-13), from DIC-measured v-displacement field of equation (7-12) and imposed traction-free boundary condition of equation (7-4). Knowing the Airy coefficients, the in-plane stresses of the ring are determined from equations (7-2) through (7-4) and in-plane displacements in the polar coordinates from equations (7-8) and (7-9), whereas in Cartesian coordinates from equations (7-10) and (7-11).

Figure 7-21 through Figure 7-26 compare the results obtained from the DIC-measured displacement data with those predicted by FEM. All distances and displacements are normalized by the inner radius of the ring, R_i = 25.4 mm, and stresses with respect to the nominal stress, σ_{net} = 7.18 MPa of equation (7-15). The DIC-hybrid results are further supported by the strain-gage readings at locations of θ = 0° and 90° in Table 7-2, Figure 7-23 and Figure 7-26.

While using n_{DIC} = 2,222 of Figure 7-7 in this DIC-hybrid method, Figure 7-26 indicates appreciable discrepancies between DIC and FEM results away from θ = 0° or 90°. However, the

0° and 90° locations are structurally the most significant, and at those locations the agreement is excellent. Based on the results (Figure 7-21 through Figure 7-26 and Table 7-2), Figure 7-7 represents the worse of the two situations considered. The analysis of Figure 7-8, utilizes a larger number of DIC-measured v-displacement values and which are better distributed over the plate than that of Figure 7-7. The DIC-hybrid computed $\sigma_{\theta\theta}$ of Figure 7-8 in Figure 7-23 agrees somewhat better with the FEM-predictions and strain-gage results along the rings inner boundary from $\theta = 0°$ to 90° than just at locations $\theta = 0°$ and 90° as in Figure 7-26.

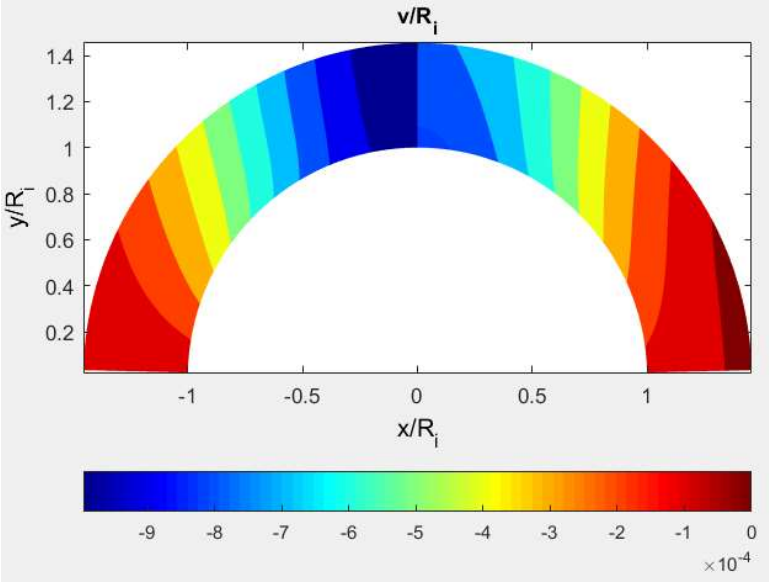

Figure 7-21: Contours of v/R_i displacements from DIC-hybrid method (right) and FEM (left) of the ring for n_{DIC} = 3,326 and h = 37 of Figure 7-8

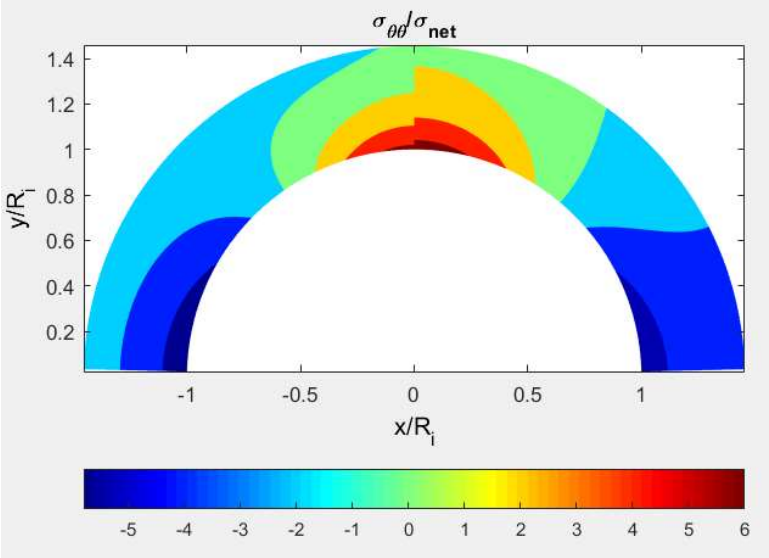

Figure 7-22: Contours of $\sigma_{\theta\theta}/\sigma_{net}$ tangential stresses from DIC-hybrid method (right) and FEM (left) of the ring for n_{DIC} = 3,326 and h = 37 of Figure 7-8

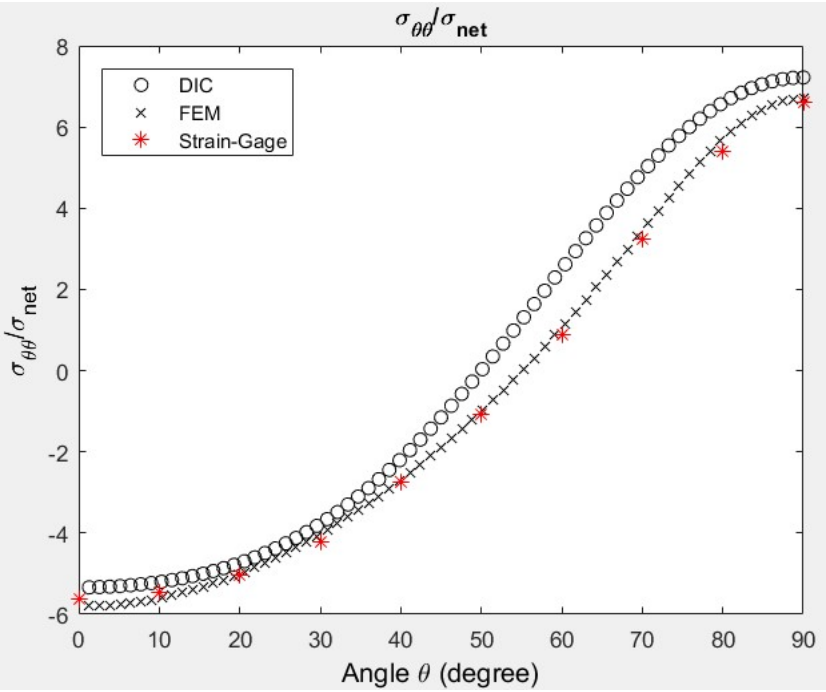

Figure 7-23: Plot of tangential stresses, $\sigma_{\theta\theta}/\sigma_{net}$, along edge of the inner radius of the ring from strain-gage, FEM and DIC-hybrid for n_{DIC} = 3,326 and h = 37 of Figure 7-8

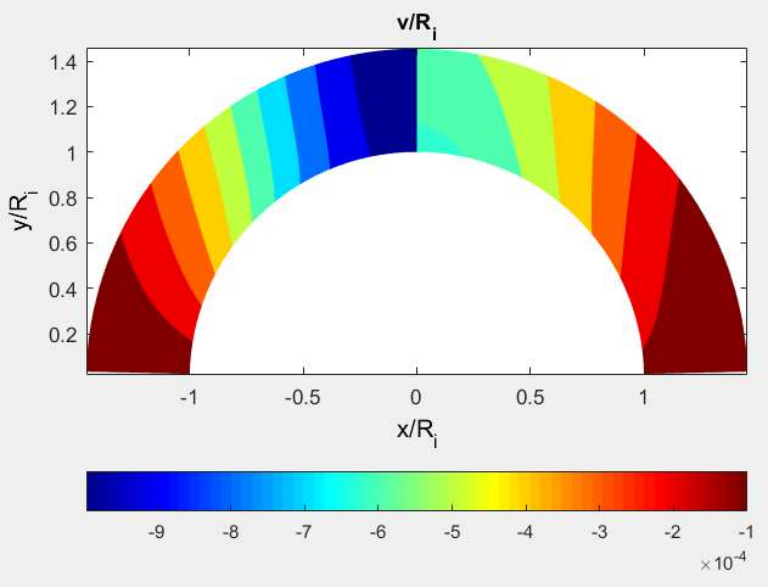

Figure 7-24: Contours of v/R_i displacements from DIC-hybrid method (right) and FEM (left) of the ring for n_{DIC} = 2,222 and h = 28 of Figure 7-7

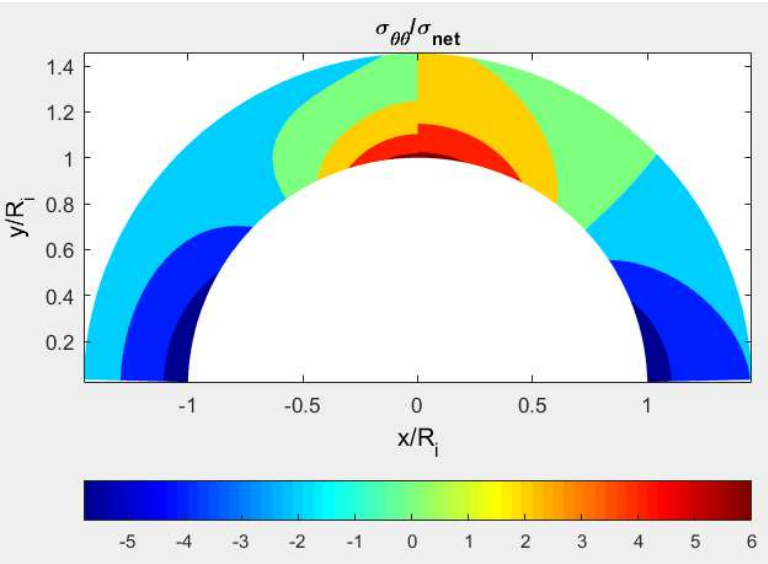

Figure 7-25: Contours of $\sigma_{\theta\theta}/\sigma_{net}$ stresses from DIC-hybrid method (right) and FEM (left) of the ring for n_{DIC} = 2,222 and h = 28 of Figure 7-7

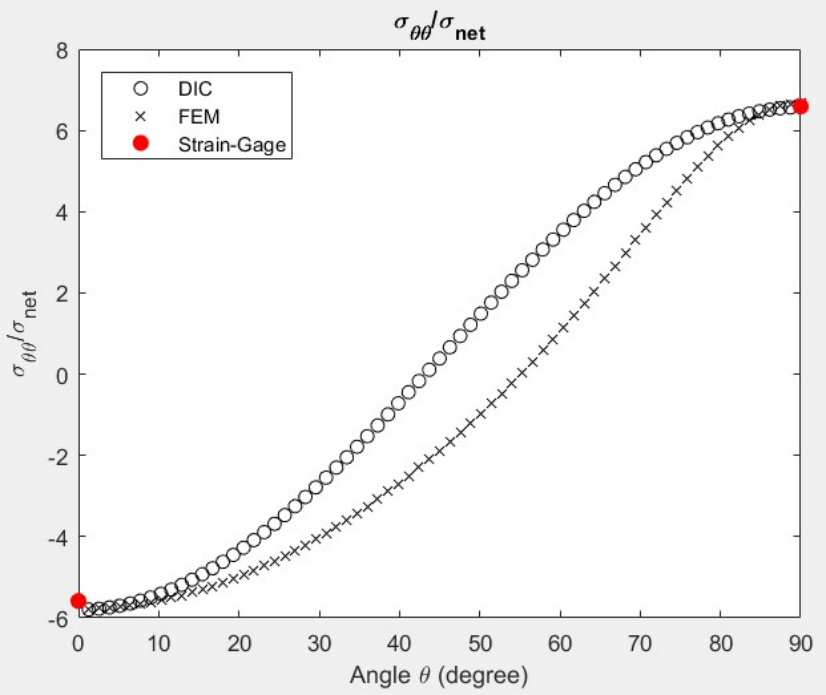

Figure 7-26: Plot of tangential stresses, $\sigma_{\theta\theta}/\sigma_{net}$, along edge of the inner radius of the ring from strain-gage, FEM and DIC-hybrid for n_{DIC} = 2,222 and h = 28 of Figure 7-7

Table 7-2: Comparison of stresses at location A and B (Figure 7-1) of the ring from DIC-hybrid, FEM and strain-gage

Angle θ	$\sigma_{\theta\theta}/\sigma_{net}$			
	DIC, n_{DIC} = 2,222 and h =28	DIC, n_{DIC} = 3,326 and h = 37	FEM	Strain-Gage
0°	-5.79	-5.34	-5.77	-5.58
90°	6.57	7.22	6.67	6.59

The DIC-recorded information of Figure 7-6 includes the effect of the top concentrated load. However, the stress function of equation (7-1), and hence the associated expressions for the

stresses and displacements, do not. This simplicity in the form of stress function contributes to the unreliable stress information in the upper region of the ring.

7.12. Summary, Discussion and Conclusions

DIC is a prevalent experimental method for evaluating stresses in engineering members. Like with any experimental technique, for a variety of reasons with DIC, one can encounter situations, or at least regions, of inferior or unreliable experimental information. An option might be to repeat the test, but that can face time and/or fiscal challenges. In some cases, initially unsatisfactory results can perhaps be improved post-experiment. For example, displacement smoothing in correlation algorithms. Alternatively, if the difficulty involves an important location within a region of unreliable or lacking experimental input information, but reliable measured data exists elsewhere in the member, it is demonstrated here that, at least in some cases, analytical and numerical tools can be combined with the distant reliable experimental data to obtain accurate stresses at the location of interest. The concept involves more than just extrapolation using a stress function. Available/suitable boundary conditions are also utilized. Importantly, the stress function possesses a strong mechanics basis. In the case of Figure 7-7, the closest reliable DIC input values are 30 mm, respectively, away from the locations of structural interest. As with the current ring, most practical serious concerns tend to involve a single stress component occurring at a traction-free re-entrant geometry (e.g., a hole or notch). An advantage of the current DIC-hybrid method is that it does not require knowing the external loading. This is a great advantage as most engineering problems have complicated geometry and loading, and the loading is unknown or poorly defined.

DIC typically records at least both in-plane displacements, but the present diametrically-compressed ring case assumes only some v information is available. This was motivated by the fact that, although moiré and electronic speckle are alternative means of recording displacement information, to measure more than one in-plane displacement by these latter techniques necessitates considerable effort beyond that when recording only a single in-plane displacement component.

Future prospects of developing superior and reliable techniques to obtain accurate stresses in situations involving poor or inadequate DIC-measured data exceeds the scope of this chapter. However, the present use of stress functions and boundary conditions are certainly applicable to orthotropic composite materials, and the concept of analytic continuation provides a powerful means of handling traction-free conditions when employing complex variables. The aluminum ring of Figure 7-1 was stress analyzed using the concepts of complex variables Airy stress functions, conformal mapping, analytic continuation and Laurent series, Appendix L and Appendix M. FEA-determined v-displacement data were processed with the complex variables technique in Appendix L, whereas the complex-hybrid analysis of Appendix M was done using DIC-measured v-displacement data.

Chapter 8. Review of Concepts to Determine Stress Intensity Factors for Orthotropic Plates

8.1. Introduction

This chapter considers a variety of techniques to analyze cracks in orthotropic materials and assesses their feasibility in providing important fracture information such as stress intensity factor (SIF) when combined with the herein proposed hybrid stress analysis method. By using an appropriate mapping function and displacement information, the hybrid-method is developed to obtain full-field state of stress in orthotropic structures with cracks. This includes regions close to the crack-tip with singular stress and displacement fields. The hybrid-method computed displacement and stress information is processed using fracture theories to obtain the SIF. The study numerically demonstrates/discusses the capability of this method to provide SIF from displacement information for virtually any cracked orthotropic plate, i.e., plate with any type of cracks, any crack-length to plate-width ratios and of any composite material properties. The reliability of the displacement-based hybrid-method is established in this chapter by comparing the obtained SIF results with those available in literature.

8.2. General Overview

Wide spread use of composite materials in structural designs have precipitated interest in studies of such configurations with holes, cracks or discontinuities of any other form. In linear elastic fracture mechanics (LEFM) for a member containing crack, the stress intensity factor (SIF)

characterizes the theoretical state of stress near the crack arising from the stress singularities present in that region. Accurate estimation of the SIF is important to reliably predict structural strength. Whether a crack will grow can be assessed by comparing the SIF of a loaded structure with its critical SIF. Anisotropy complicates fracture analysis of members made of orthotropic materials, relative to that of isotropic materials. Among other things, the magnitude of SIF now also depends on the orthotropic constitutive properties and the material directions [113]. SIF for a component with crack can be determined analytically, semi-analytically or using numerical techniques based on finite element method (FEM) or boundary element method (BEM).

For relatively simple infinite geometries and simple loading, it is possible to evaluate the SIF analytically or experimentally. Semi-analytical methods such as the weight function approach introduced by Bueckner [114] and generalized by Rice [115] is capable of solving a variety of fracture problems. The approach involves finding an arbitrary SIF from a reference solution for a certain mode of fracture, then uses a weight function to relate the arbitrary SIF to find the actual SIF for the same geometry but under different load. The method faces the challenge of finding a suitable reference solution for certain fracture problems [116].

For more complicated geometries and loadings, numerical techniques such as FEA and BEM can provide reasonable estimates of SIF. FEA-predicted results highly depend on the structure's exact loading and boundary conditions. In practice knowing the exact boundary condition and loading is not always possible. In most practical engineering situations, the loading is poorly defined or very complicated. Moreover, to accurately estimate the high stress gradients near a crack by FEA requires the use of special elements. BEM does not require discretization of the region close to the crack-tip like FEM does, but the theory related to BEM is more complicated than that of FEM.

Conventional FEA techniques are incapable of accurately representing the singular stress field adjacent to the crack-tip. This has led to the approach of including stress singularity over a finite region near the crack-tip in standard finite element analysis programs and superimposing the analytical and finite element solutions. This technique is commonly known as hybrid-FEA. Commercial FEA packages now include special crack-tip elements or process to skew the regular elements close to the crack-tip to accurately represent the crack nearby singular stress fields. However, numerical-analyses results face the challenge of heavily depending on accurate information of the loading and boundary conditions irrespective of what measures are taken to accurately represent the structure's behavior near the crack.

Experimental techniques of stress or SIF evaluation are another means of finding information of members containing cracks under complex situations. Such techniques include thermoelastic stress analysis (TSA), photoelastic stress analysis (PSA), digital image correlation (DIC), caustics and strain-gages. Besides not providing reliable edge data, traditional full-field experimental techniques have the drawback of not determining the individual stress components. TSA and PSA provide the sum and difference of the principal stresses, respectively, and DIC provides the displacements of the loaded structure. The first two techniques necessitate special experimental requirements (e.g., cyclic loading or special light source) and stress separation techniques. The latter typically requires differentiating the displacement data to obtain strains/stresses. Differentiating displacements to obtain strains is a numerically unreliable and risky procedure. The strain-gage determined SIF accuracy is affected by factors such as the crack's strain gradient effects on the finite gage size, exact orientation and location of the gage with respect to the crack and possible three-dimensional effects near the crack-tip [117].

All of the above challenges associated with theoretical, numerical and experimental stress analyses can be overcome by the present technique of stress analyzing loaded, finite, orthotropic components with cracks. The present study finds nearby crack-tip displacements/stresses and consequently SIF information based on DIC-recorded single displacement field at locations slightly away from the crack-tip. Stress separation and/or measured data differentiation are accomplished based on rigorous mechanics foundation by combining the measured data with a complex variables Airy stress function. The singularity does not need to be additionally imposed as it is inherently included in the measured quantities and included analytically by using an appropriate mapping function. The traction-free conditions of the crack-face is also imposed analytically by the mapping function and analytic continuation. This approach eliminates the need of using any FEA or hybrid-FEA programs with specially-formulated crack nearby elements. The method requires no information of the actual loading or boundary conditions. Once the stress fields in the plate are known including along the crack-face and adjacent to the crack-tip, the SIF can be determined subsequently by using concepts such as near crack stress/strain/displacement fields [16,17,22,118] or path independent integrals such as *J*-integral [77].

With developments in computers processing capability and major improvements in digital cameras, full-field structural information such as displacement measurement is now readily possible, such as with digital image correlation (DIC). Acknowledging the numerous advantages DIC offers over other available experimental techniques, the present study utilizes FEA-predicted displacement information to replicate the DIC-measured displacement information in the developed displacement-based complex hybrid-method to obtain nearby crack-tip states of stress and displacement. The herein displacement-based hybrid-methods which use FEM-predicted simulated measurement input data are analogous to the DIC-hybrid method.

8.3. Literature Review

8.3.1. FEA in Fracture Analysis

Finite element analysis (FEA) is a popular tool for fracture analysis. Field variables in traditional FEA are interpolated using polynomials and are incapable of accurately representing the crack-tip square root singular stress fields. Without employing any special elements or formulations for the near-crack elements, conventional FEA requires a very fine mesh near the crack-tip to provide reliable results in those locations. This leads to slow convergence and significantly increases the computation time. These difficulties motivated the development of special crack-tip elements (CTE) in FEA tools. CTE were introduced in FEA to analyze fracture problems in the 1970s. The special CTE's are formulated with shape functions that account for the crack-tip singular stress fields. This approach employs special element/elements in regions adjacent to the crack-tip and regular elements for rest of the structural domain and computes the crack analysis by matching the analytical solution of the region near the crack-tip with the finite element solution of its surrounding. This approach is commonly known as hybrid-finite element analysis. Though hybrid-FEA successfully fracture analyzes structures, the approach is mostly restricted to laboratory purposes. The major drawback that prevents hybrid-FEA to be used in commercial FEA programs is the shape function of the CTE not always being compatible with conventional FEM elements. Implementation of CTE in commercial FEA codes also causes algorithmic difficulties. However, these difficulties were overcome by the introduction of crack-tip quarter-point elements (QPE). Significant growth and development in fracture mechanics was made with the use of QPEs in commercial FEA tools. Barsoum [119] and Henshell and Shaw [120] individually first proposed the idea of QPEs. By placing the mid-side node near the crack-tip at a quarter-point position, an inverse square root singularity is generated in the element. This

singularity arises from the non-linear mapping between the original and shifted local coordinates in the element. Unlike CTE, the QPE allows the entire structure to be modeled using the same element. This automatically satisfies the compatibility of the shape functions between adjacent QPE and regular elements near the crack-tip. In this present research collapsed quarter-point eight-node quadrilateral elements are used by collapsing a side of an eight-node isoparametric quadrilateral element and moving the mid-side node of the crack-tip element to the quarter-point position [121]. Commercial FEA packages now include several in-built commands to calculate important fracture parameters such as SIF, *J*-integral, virtual crack extension and energy release rates. However, most of these commands are only applicable to homogenous isotropic materials. FEA packages ABAQUS and NASTRAN provides more flexibility in fracture analyzing cracked members. ABAQUS evaluates contour integrals for any linear fracture problem. However, quarter-points elements are automatically generated only in ANSYS and requires to be manually created in ABAQUS.

Recent developments such as extended finite element method (XFEM) and complex-variable finite element method (ZFEM) are enabling FEM to handle more complex, non-linear fracture problems. Commercial finite element software such as ALTAIR and ABAQUS have XFEM implemented in their algorithms.

8.3.2. Fracture Analysis of Composite Members

Composite materials with directional properties and high strength- and stiffness-to-weight ratios have gained much attention as mechanical structures for a variety of applications. This has led to increased research interest in the field of structural mechanics and similarly in fracture

mechanics for refining classical concepts to handle anisotropic elasticity and in finding analytical solutions/numerical techniques to fracture analyze anisotropic materials.

In solid mechanics Lekhnitskii [5] first provided analytical solutions for plane theory of rectilinear anisotropy using analytical functions of complex variables. Savin [6] refined some of these solutions and introduced several numerical solutions. In fracture mechanics, Sih, Paris and Irwin [122] were the pioneers to introduce rectilinear anisotropy.

Bowie et al. utilized variety of techniques to analyze fracture in elastic members [7,123–125]. Bowie and Neal [123] used complex variable techniques, i.e., a combination of a stress functions and conformal mapping with boundary collocation arguments in their modified boundary collocation method to analyze problems involving cracks. Stress functions were based on Muskhelishvili's [15] continuation arguments to satisfy the traction-free boundary conditions along the crack-face and collocation method was utilized for the remaining boundary conditions [123]. Bowie and Freese [7] used Airy stress functions, conformal mapping, Laurent power-series expansion, boundary collocation and least squares to find SIFs of orthotropic rectangular sheets with central cracks. Meyerson [126] and Li and Cheng [127] also used conformal mapping in fracture analyses.

Tong et al. [128] used the concept of complex variables technique with hybrid-FEA to successfully analyze cracks in homogenous materials. With the same efficiency and accuracy compared to isotropic materials, Tong [21] later extended this approach to rectilinear anisotropy. Joshi and Manepatil [129] employed boundary collocation to demonstrate the effects of variations in principal material directions and crack length on SIFs for inclined and/or eccentric cracks in finite orthotropic plates. Mandell et al. [130] obtained SIF for fractured anisotropic plates and

beams using hybrid stress model FEA which were supported by compliance tests. Saxce and Kang [131] used hybrid mongrel displacement FEA concept. Abdullah [132] compared the stress distributions in finite isotropic and orthotropic tensile plates containing a mode-I central crack. Arakere et al. [133] used FEA tool ANSYS along with FRANC3D fracture analysis software to determine mixed-mode SIF in an anisotropic foam material, results were supported experimentally.

Feng et al. [134,135] used moiré displacement data with a smoothing function to find SIF in orthotropic members. Rhee and Rowlands [22] used the concept of Airy stress functions, conformal mapping, Laurent power-series expansion and expressions for crack-tip nearby stress fields with TSA-measured thermal information to find SIFs in orthotropic cracked members. They obtained K_I for a central crack in a tensile glass-epoxy laminate by evaluating the associated stress functions from recorded thermoelastic data around the external boundary of a subregion containing the crack. Lin et al. [77] provided the concept of using TSA thermal data with Airy stress functions, conformal mapping, Taylor series expansion and *J*-integral to find SIF for orthotropic plates with cracks. Lin et al. analyzed an aluminum plate with centrally located crack from actual measured thermal data. Numerically-simulated input was employed for a central and single-edge crack orthotropic composite plates. He and Rowlands [136] again determined K_I for a central crack in a composite by evaluating the associated stress functions from recorded temperature information away from the crack. They employed decomposed stress functions. Khalil et al. [118] employing Airy stress functions and conformal mapping developed expressions for the crack-tip nearby stress fields in their developed hybrid-FEA. Ju and Rowlands determined SIF for orthotropic members by least squares with distant measured TSA data [137,138] or FEA-predicted displacement data [139] based on the analytical concept provided by Khalil et al. [118]. In reference [140] Ju and

Rowlands demonstrated a method to determine exact crack-tip coordinates from measured TSA data and least squares. Baek et al. [141] utilized simulated isochromatic data, Airy stress functions, conformal mapping, non-linear least squares to find SIF for mixed-mode problems. Farahani et al. [142] used a hybrid experimental-numerical method based on TSA thermal data and analytical expressions of crack-tip nearby stress fields from William's series to analyze mode-I fracture in an aluminum alloy.

Using the coherent gradient sensing method, Liu et al. [143] evaluated K_I for a crack extending vertically upward from the bottom edge of a composite beam subjected to four-point bending. Pariasamy and Tippur [144] also used coherent gradient sensing method to obtain crack-tip deformation and SIF in an acrylic plate with a single-edge crack. Dai et al. [145] studied the deformation and fracture behavior associated with an opening-mode single-edge crack in a tensile glass-reinforced composite by digital speckle correlation.

Shukla et al. [16] and Debaleena et al. [117] used strain-gages to find SIF in composite materials. Shukla et al. [16] determined K_I in a single-edge notched glass-epoxy composite from a strain-gage which was appropriately positioned and orientated relative to the crack.

Kim [146] numerically determined the SIFs in finite composites having single- and doubled-edge cracks using a path-independent *J*-integral which involves the tractions and displacements on a contour surrounding the crack. Perry and McKelvie [147] obtained the energy release rate in a cantilevered composite beam by evaluating the *J*-integral from recording both in-plane displacement components using interferometric moiré. Kawahara and Brandon [148] and Frediani [149] used strain-gages and *J*-integral as line integral to develop direct experimental technique of measuring *J*-integrals for isotropic rectangular plates with cracks. However, Rice

[150] was the first to introduce the concept of *J*-integral in fracture mechanics. He showed that in a two-dimensional strain field of an elastic or elastic-plastic material the contour path integral or *J*-integral is independent of the path around the tip of a crack. Vavrik and Jandejsek [151] used DIC-measured information to obtain various fracture information including *J*-integral and used X-ray radiography to observe the crack behavior in highly ductile aluminum alloys. Valaire et al. [152] used the concepts of *J*-integral to develop an approach to analyze fracture in composites and elastoplastic materials under mode-I and mixed-mode loading. Hein and Kuna [153] derived analytical expressions of *J*-integral to account for temperature dependent behavior of functionally graded materials, the approach was incorporated in FEM to analyze such material with a surface crack. Rabbolini et al. [154] processed DIC-measured information with least-squares regression algorithm to directly evaluate mode-I and mode-II stress intensity factor ranges for anisotropic single crystal materials. Dag et al. [155] developed a computational method established on *J*-integral concept to analyze functionally graded materials with mixed-mode fracture. The results of the computational method were compared with those obtained experimentally from DIC. Similar technique by Dag [156] based on equivalent domain integral provided mode-I SIF for functionally graded materials under thermal loading. Lee et al. [157] evaluated the mode-I and mixed-mode SIFs in a single-edge notched graphite-epoxy plate from DIC measurements combined with Sih et al. [122] provided fracture concepts for quasi-static loading and Stroh [158] formulation for impact loading. The following References involves the concept of *J*-integral in fracture analyzing anisotropic materials: Tracy et al. [159], Cahill et al. [160], Catalanotti et al. [161], Gonzáles et al. [162] and Hedan et al. [163].

DIC due to its simplicity and ease of implementation is widely used in fracture studies. Using equations from Reference [16] and DIC measured information, Mogadpalli and

Parameswaran [17] determined K_I for a single-edge crack aligned parallel to the fibers in a unidirectional laminate. Pataky et al. [164] measured stress intensity factors in anisotropic single-crystal stainless steel using DIC measurements. Samarasinghe and Kulasiri [165] used DIC data combined with fracture concepts from Sih et al. [122] to evaluate SIF of a wood block containing a single-edge crack under tangential-longitudinal opening-mode loading. Meite et al. [166] used DIC-measured displacements and FEM based on $M\theta$-integral to study mixed-mode fracture characteristics in wood. Nunes and Reis [167] studied fracture parameters in a glass-fiber reinforced polymer composite with a single-edge crack under three-point bending using DIC. Koohbor et al. [168] used DIC to analyze an orthogonally woven composite member containing single-edge crack. Mallon et al. [169] also analyzed orthogonally woven composites with cracks using 3D-DIC, where SIF was obtained by utilizing DIC-determined displacement and strain data with an over-deterministic approach. Han et al. [170] used DIC to find fracture information for CFRP composite with a single-edge crack under uniaxial tension and three-point bending. The study also involved investigating the effect of pre-stress on fracture components.

The analytical concepts behind the present hybrid experimental-analytical method are similar to the hybrid-FEA approach except this technique can conduct the crack analysis without requiring the need of any special element generation or its stiffness matrix formulation, nor requiring any FEA tools. The main advantages of this technique include not having to know the loading or boundary conditions like FEA or hybrid-FEA methods or not depending on experimental information near the crack-tip or edges which purely experimental techniques lack providing. It also offers inbuilt stress separation and simultaneous smoothing of the evaluated results and does not require differentiating measured displacement data.

The present approach utilizes a single displacement component to determine SIF for finite, tensile-loaded, orthotropic plates with fracture. The detail analytical approach of the fracture techniques to post-process the hybrid-method evaluated results are illustrated in this chapter. The method is validated using FEA-simulated data and the evaluated SIFs are compared with those found in the literature.

8.4. Analytical Fracture Analysis of Orthotropic Plates

8.4.1. General Comments

Relative to determine the SIF of an orthotropic plate with crack, this section initially develops a hybrid-model to evaluate the in-plane stress and displacement fields in a loaded, finite, orthotropic plate containing a crack. This is accomplished by processing numerically predicted information (mostly displacement information) with complex variables Airy stress functions, conformal mapping, analytic continuation, power-series expansion of the stress functions and least squares to evaluate the unknown Airy stress coefficients. Knowing the Airy stress coefficients, the in-plane stresses, strains and displacements at locations near the crack-tip are known from the hybrid-model. The second part of the analysis utilizes the hybrid-method computed in-plane stress, strain and displacement components to find the SIF. This can be done in several different ways. Here some established fracture analysis methods available in literature are discussed that can effectively evaluate the SIF by post-processing the hybrid-method evaluated states of stress and/or displacement.

Analytical procedures to evaluate SIF by these various methods are discussed in this section. However, details regarding the analytical background of the displacement-based hybrid-

method are discussed in Chapter 2. The relevant mapping functions used to develop the hybrid-method for stress analyzing orthotropic members with different crack configurations will be discussed subsequently.

8.4.2. Laurent Series and Mapping Functions

8.4.2.1. Central Crack

For a plate with a central crack of length $2a$ at an angle α with one of the orthotropic material directions and crack center at $z_c = x_c + \mu_j y_c$ for $j = 1, 2$, the general mapping function to map a unit circle, Γ_ζ, and its exterior from region, R_ζ, of the ζ-plane into a crack, Γ_z, and to its exterior region, R_z, in the physical z-plane is, Figure 8-1 [22,145]

$$z_j = \omega_j(\zeta_j) = \frac{a}{2}\left(cos\alpha + \mu_j sin\alpha\right)\left(e^{-i\alpha}\zeta_j + e^{i\alpha}\zeta_j^{-1}\right) + z_c, \quad j = 1, 2 \tag{8-1}$$

The following inverse of equation (8-1) maps the crack, Γ_z, and its exterior region, R_z, from the physical z-plane to a unit circle, Γ_ζ, and its exterior region, R_ζ, in the ζ-plane [22]

$$\zeta_j = \frac{e^{i\alpha}\left[\left(z_j - z_c\right) \pm \sqrt{\left(z_j - z_c\right)^2 - a^2\left(cos\alpha + \mu_j sin\alpha\right)^2}\right]}{a(cos\alpha + \mu_j sin\alpha)}, \quad j = 1, 2 \tag{8-2}$$

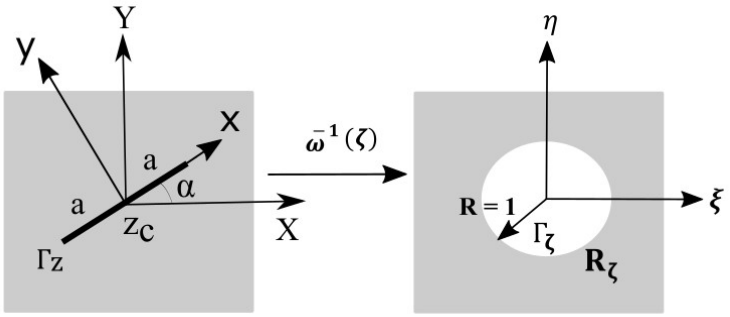

Figure 8-1: Conformal mapping of an inclined central crack from z-plane to unit circle in ζ-plane for a loaded orthotropic plate using equation (8-2)

For a crack aligned along the x-axis of the material orthotropy, i.e., for $\alpha = 0$, the expression for the mapping function of equation (8-1) and the inverse of the mapping function of equation (8-2) reduce to the following [7,22]

$$z_j = \omega_j(\zeta_j) = \frac{a}{2}\left[\zeta_j + \frac{1}{\zeta_j}\right] + z_c, \qquad j = 1, 2 \tag{8-3}$$

$$\omega_j^{-1}(z_j) = \zeta_j = \frac{(z_j - z_c) \pm \sqrt{(z_j - z_c)^2 - a^2}}{a}, \qquad j = 1, 2 \tag{8-4}$$

where a is the half crack length and $z_c = x_c + \mu_j y_c$ is the center of the crack. The branch of the square root of the above equation (8-4) is chosen so that, $|\zeta_j| \geq 1$ for $j = 1, 2$. The derivative of the mapping function, $\omega_j(\zeta_j)$, of equations (8-1) and (8-3) with respect to the complex variables ζ_j for $j = 1, 2$, are respectively,

$$\omega_j'(\zeta_j) = \frac{a}{2}(cos\alpha + u_j sin\alpha)\left[e^{-i\alpha} - \frac{e^{i\alpha}}{\zeta_j^2}\right], \qquad j = 1,2 \tag{8-5}$$

and

$$\omega_j'(\zeta_j) = \frac{a}{2}\left[1 - \frac{1}{\zeta_j^2}\right], \qquad j = 1,2 \tag{8-6}$$

8.4.2.2. Edge Crack

Consider a plate with an edge crack of length a within region R_z, and R'_z as the region containing the reflection of the edge crack, Figure 8-2. Equation (8-7) maps a unit circle, $\Gamma_\zeta + \Gamma'_\zeta$, and its exterior region, $R_\zeta + R'_\zeta$, of the ζ-plane to the edge crack and its reflection, $\Gamma_z + \Gamma'_z$, and its exterior region, $R_z + R'_z$, into the physical z-plane, Figure 8-2. The crack is perpendicular to the loading direction [171,172]. Details on the mapping function of equation (8-7) are provided in Appendix N.

$$\omega_j(\zeta_j) = z_j = \frac{ia\mu_j}{2}\left(\zeta_j^{-1} - \zeta_j\right) + z_c, \;\; j = 1, 2 \tag{8-7}$$

The inverse of the mapping function of equation (8-7) is

$$\zeta_j = \frac{-(z_j - z_c) \pm \sqrt{(z_j - z_c)^2 - a^2\mu_j^2}}{ia\mu_j}, \quad j = 1, 2 \tag{8-8}$$

where a is the edge crack length and z_c is the location of the edge of the crack. The branch of the square root of the above equation (8-8) is chosen so that, $|\zeta_j| \geq 1$ for $j = 1, 2$.

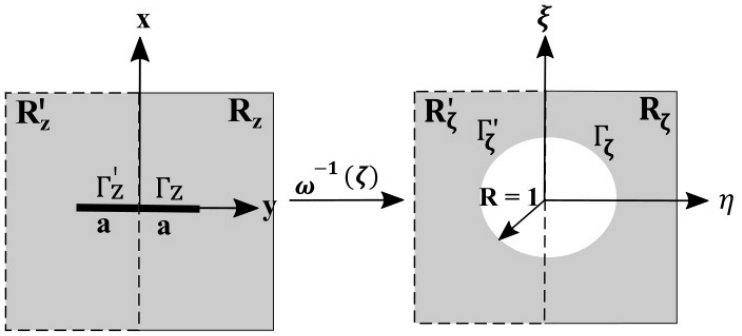

Figure 8-2: Conformal mapping of an edge crack from z-plane to unit circle in ζ-plane for a vertically loaded orthotropic plate according to the inverse mapping function of equation (8-8)

Differentiation of the mapping function of equation (8-7) with respect to the complex variables ζ_j for $j = 1, 2$, is

$$\omega_j'(\zeta_j) = -\frac{ia\mu_j}{2}\left(1 + \frac{1}{\zeta_j^2}\right), \quad j = 1, 2 \tag{8-9}$$

8.4.3. Stresses, Strains and Displacements

Combining the concepts of complex variables Airy stress functions, analytic continuation and Laurent power series expansion, the complete states of stress and displacement in a plane-stressed orthotropic member can be expressed as equations (2-70) through (2-72), and equations (2-68) and (2-69), respectively. Depending on the crack type and its orientation with respect to material direction x, the mapping function in equations (2-68) through (2-72) changes. For a centrally inclined crack one uses equations (8-2) and (8-5), for a central crack along material symmetry x-axis one employs equations (8-4) and (8-6), and for an edge crack one uses equations (8-8) and (8-9) as ζ_j and $\omega'_j(\zeta_j)$ for j = 1, 2, respectively, in equations (2-68) through (2-72). Once the expressions for the in-plane displacements and stresses are developed for a certain crack type, the DIC-recorded u- or v-displacement data (in this case FEA-predicted displacement information) selected at locations away from the crack-tip are incorporated into either equation (2-68) or equation (2-69), from which the unknown complex variables Airy stress coefficients, c_j, are derived. Knowing the Airy coefficients and using them in equations (2-68) and (2-69), the in-plane displacements and in equations (2-70) through (2-72), the in-plane stresses are obtained throughout the plate. This includes at locations close to the crack-tip. Substituting the known in-plane stresses of equations (2-70) through (2-72) into equation (2-34) gives the in-plane strains.

8.4.4. Taylor Series and Mapping Function

Although the use of the Laurent series to express the stress functions is emphasized here, the same could have been done using a Taylor series. A detailed example of this will be demonstrated in the following Chapter 9. When using the Taylor series, a mapping function that

maps a half-plane from the ζ-plane to a crack in the physical z-plane is selected, equation (8-10). The crack is considered to be located along the negative x-axis with the crack-tip at the coordinate origin, i.e., at $z = 0$ [21,77].

$$z_j = \omega_j(\zeta_j) = -\zeta_j^2, \qquad j = 1, 2 \tag{8-10}$$

The inverse of the mapping function of equation (8-10) is

$$\zeta_j = \omega_j^{-1}(z_j) = i\sqrt{z_j}\,, \qquad j = 1, 2 \tag{8-11}$$

The branch of the square root of the above equation is chosen so that $Im\zeta_j \geq 0$ for $j = 1, 2$. When using the Taylor series to expand the stress functions, in-plane stresses and displacements are evaluated from equations (2-57) through (2-61).

8.4.5. Evaluating the SIF

8.4.5.1. Method-1 (Khalil/Ju's Concept)

The technique was originally proposed by Khalil et al. [118] and later used by Ju and Rowlands [137] and Ju [139] to study orthotropic plates with inclined cracks. Khalil et al. [118] developed a super element for their hybrid-finite element approach to find SIF in anisotropic materials. To formulate the stiffness matrix of the super elements they used the mathematical concept of complex variables Airy stress functions for anisotropic members provided by Lekhnitskii [5] along with conformal mapping. The individual stress functions were expressed as

simple polynomials of the complex variables in the mapped plane and related to each other by the surface tractions on the boundaries. The crack-tip singularity of the stress field was included through the use of conformal mapping of equation (8-12). The coordinate system was taken such that the sharp crack lay along the negative portion of the z-plane with the crack-tip at $z = 0$ and $z_j = x + \mu_j y$ for $j = 1, 2$ [118].

$$z_j = \omega_j(\zeta_j) = \zeta_j^2, \qquad j = 1, 2 \tag{8-12}$$

The complex material properties, $\mu_j = \alpha_j \pm i\beta_j$, used in the expression of the complex variables, $z_j = x + \mu_j y$ for $j = 1, 2$, are obtained from the roots of the complex variables Airy stress functions characteristic equation (2-14).

The SIF of the plane anisotropic member near the crack-tip were evaluated based on the following expressions provided by Sih, Paris and Irwin [122]

$$\begin{aligned} K_{\mathrm{I}} + \frac{K_{\mathrm{II}}}{\mu_2} &= -\sqrt{2}\left(\frac{\mu_1}{\mu_2} - 1\right) \lim_{\zeta_1 \to 0} \Phi_1'(\zeta_1) \\ K_{\mathrm{I}} + \frac{K_{\mathrm{II}}}{\mu_1} &= \sqrt{2}\left(1 - \frac{\mu_2}{\mu_1}\right) \lim_{\zeta_2 \to 0} \Psi_2'(\zeta_2) \end{aligned} \tag{8-13}$$

Khalil expressed the near crack-tip displacement fields in an anisotropic material as [118,139]

$$u = \sum_{j=1}^{2N} D_j(z_1, z_2)\gamma_j \tag{8-14}$$

$$v = \sum_{j=1}^{2N} E_j(z_1, z_2)\gamma_j \tag{8-15}$$

The γ_j are stress coefficients and N is the number of displacement terms retained, where for $N = 1$, $j = 2N = 2$, i.e., for one displacement term there are two stress coefficients, γ_j and γ_{j+N}. The terms D_j and E_j are functions of the orthotropic material properties and coordinate locations as following

$$D_j = 2Re\left(p_1 z_1^{\frac{j}{2}} + p_2 M_{1j} z_2^{\frac{j}{2}}\right) \tag{8-16}$$

$$D_{j+N} = 2Re\left(ip_1 z_1^{\frac{j}{2}} + p_2 M_{2j} z_2^{\frac{j}{2}}\right) \tag{8-17}$$

$$E_j = 2Re\left(q_1 z_1^{\frac{j}{2}} + q_2 M_{1j} z_2^{\frac{j}{2}}\right) \tag{8-18}$$

$$E_{j+N} = 2Re\left(iq_1 z_1^{\frac{j}{2}} + q_2 M_{2j} z_2^{\frac{j}{2}}\right) \tag{8-19}$$

where p_j and q_j for $j = 1, 2$, are complex material properties and are defined in equations (2-30).

Also [118,139]

$$M_{1j} = -\frac{\beta_1}{\beta_2} \text{ and } M_{2j} = \frac{\alpha_2 - \alpha_1}{\beta_2} - i \quad \text{for odd values of } j \tag{8-20}$$

$$M_{1j} = -1 + i\frac{\alpha_1 - \alpha_2}{\beta_2} \text{ and } M_{2j} = -i\frac{-\beta_1}{\beta_2} \quad \text{for even values of } j \tag{8-21}$$

According to Khalil's concept the singular stress fields near the crack-tips are expressed as [118,137]

$$\sigma_{xx} = \sum_{j=1}^{2N} A_j(z_1, z_2)\gamma_j \tag{8-22}$$

$$\sigma_{yy} = \sum_{j=1}^{2N} B_j(z_1, z_2)\gamma_j \tag{8-23}$$

$$\sigma_{xy} = \sum_{j=1}^{2N} C_j(z_1, z_2)\gamma_j \tag{8-24}$$

where A_j, B_j and C_j are also functions of the orthotropic material properties and coordinate locations of the area being analyzed. These are expressed as [118,137]

$$A_j = jRe\left(\mu_1^2 z_1^{\frac{j-2}{2}} + \mu_2^2 M_{1j} z_2^{\frac{j-2}{2}}\right) \tag{8-25}$$

$$A_{j+N} = jRe\left(i\mu_1^2 z_1^{\frac{j-2}{2}} + \mu_2^2 M_{2j} z_2^{\frac{j-2}{2}}\right) \tag{8-26}$$

$$B_j = jRe\left(z_1^{\frac{j-2}{2}} + M_{1j}z_2^{\frac{j-2}{2}}\right) \tag{8-27}$$

$$B_{j+N} = jRe\left(iz_1^{\frac{j-2}{2}} + M_{2j}z_2^{\frac{j-2}{2}}\right) \tag{8-28}$$

$$C_j = -jRe\left(\mu_1 z_1^{\frac{j-2}{2}} + \mu_2 M_{1j}z_2^{\frac{j-2}{2}}\right) \tag{8-29}$$

$$C_{j+N} = -jRe\left(i\mu_1 z_1^{\frac{j-2}{2}} + \mu_2 M_{2j}z_2^{\frac{j-2}{2}}\right) \tag{8-30}$$

Khalil et al. showed that at locations very close to the crack-tip, the stresses are dominated by the two stress coefficients γ_1 and γ_{1+N}, which again can be expressed in terms of SIF, K_{I} and K_{II}, respectively, as [118,137,139]

$$K_{\mathrm{I}} = \sqrt{2\pi}\left[\left(1 - \frac{\beta_1}{\beta_2}\right)\gamma_1 + \left(\frac{\alpha_2 - \alpha_1}{\beta_2}\right)\gamma_{1+N}\right] \tag{8-31}$$

$$K_{\mathrm{II}} = -\sqrt{2\pi}\left[\left(\alpha_1 - \alpha_2\frac{\beta_1}{\beta_2}\right)\gamma_1 + \left(\beta_2 - \beta_1 + \alpha_2\frac{\alpha_2 - \alpha_1}{\beta_2}\right)\gamma_{1+N}\right] \tag{8-32}$$

Therefore, to evaluate the complete states of stress and displacement of an orthotropic member from equations (8-22) through (8-24) and equations (8-14) and (8-15), respectively, one needs to know the stress coefficients γ_j. This can be achieved by processing measured (FEM-predicted in this case) information with any one or a combination of these equations and using least squares. A

simultaneous system of linear equations is formed by utilizing measured information with individual/combined analytical expressions of the in-plane displacements and/or stresses. The number of utilized measured quantities are kept higher than the number of unknowns. Such examples include utilizing measured displacement data in the loading direction, *v*, in equation (8-15) to obtain equation (8-33), where E_j just depends on equations (8-18) through (8-21). If both the in-plane displacements, *u* and *v*, are utilized then by using equations (8-14) through (8-21) the expression of equation (8-34) is obtained. If the orthotropic plate's complete states of stress and displacement are used to find the stress coefficients, such can occur while using FEA-predicted information, then combining equations (8-14) through (8-30) gives equation (8-35).

$$\{v\} = [E_1 \quad E_2 \quad \dots \quad E_j \quad E_{j+1} \quad \dots \quad E_{2j-1} \quad E_{2j}] \begin{Bmatrix} \gamma_1 \\ \gamma_2 \\ \vdots \\ \gamma_j \\ \gamma_{j+1} \\ \vdots \\ \gamma_{2j-1} \\ \gamma_{2j} \end{Bmatrix} \tag{8-33}$$

or,

$$\begin{Bmatrix} u \\ v \end{Bmatrix} = \begin{bmatrix} D_1 & D_2 & \dots & D_j & D_{j+1} & \dots & D_{2j-1} & D_{2j} \\ E_1 & E_2 & \dots & E_j & E_{j+1} & \dots & E_{2j-1} & E_{2j} \end{bmatrix} \begin{Bmatrix} \gamma_1 \\ \gamma_2 \\ \vdots \\ \gamma_j \\ \gamma_{j+1} \\ \vdots \\ \gamma_{2j-1} \\ \gamma_{2j} \end{Bmatrix} \tag{8-34}$$

or,

$$\begin{Bmatrix} u \\ v \\ \sigma_{xx} \\ \sigma_{yy} \\ \sigma_{xy} \end{Bmatrix} = \begin{bmatrix} D_1 & D_2 & \dots & D_j & D_{j+1} & \dots & D_{2j-1} & D_{2j} \\ E_1 & E_2 & \dots & E_j & E_{j+1} & \dots & E_{2j-1} & E_{2j} \\ A_1 & A_2 & \dots & A_j & A_{j+1} & \dots & A_{2j-1} & A_{2j} \\ B_1 & B_2 & \dots & B_j & B_{j+1} & \dots & B_{2j-1} & B_{2j} \\ C_1 & C_2 & \dots & C_j & C_{j+1} & \dots & C_{2j-1} & C_{2j} \end{bmatrix} \begin{Bmatrix} \gamma_1 \\ \gamma_2 \\ \vdots \\ \gamma_j \\ \gamma_{j+1} \\ \vdots \\ \gamma_{2j-1} \\ \gamma_{2j} \end{Bmatrix} \tag{8-35}$$

Equations (8-33) through (8-35) can be re-written as equation (8-36) which can be solved for the stress coefficients, γ_j, using least squares.

$$\{\text{Input Values}\} = [\text{Constants}]\{\text{Stress Coefficients}(\gamma_j)\} \tag{8-36}$$

The number of terms to retain in the summation series can be determined based on any of the following techniques: (1) by checking the root mean square; (2) by comparing the contours between the input and reconstructed quantities or (3) by checking the condition number of the matrix [Constants] in equation (8-36) and all (1) - (3) techniques for varying number of stress coefficients. Knowing the stress coefficients, the respective SIFs can then be obtained from equations (8-31) and/or (8-32).

8.4.5.2. Method-2 (*J*-Integral Concept)

For 2-D problems the contour integral *J* is defined as [148–150]

$$J = \oint_{\Gamma} \left(W_s dx_{2'} - \boldsymbol{T}.\frac{d\boldsymbol{u}}{dx_{1'}} ds \right) \tag{8-37}$$

where Γ is a contour surrounding the crack, $W_s = \int_0^{\varepsilon} \sigma_{ij}\, d\varepsilon_{ij}$ is the strain energy density at points on Γ, $\boldsymbol{T}$ is the traction vector along Γ, $\boldsymbol{u}$ is the displacement vector for points on Γ, ds is a selected arc length on Γ and $x_{1'}$ and $x_{2'}$ are directions along and perpendicular to the crack-face, respectively, (Figure 8-3). If deformation-induced geometric changes are negligible in a material, then some properties of the *J*-integral are [148,150]

- The value of J is path-independent. The *J*-integral can be evaluated knowing the stresses/strains and displacement gradients either close or far from the crack-tip.
- The value of J is a measure of crack-tip stress-strain intensity field.
- With respect to the crack length, J equals the variation rate of the total potential energy.

According to the directions of the coordinate system and path Γ shown in Figure 8-3, the *J*-integral for a plane-stressed elastically deformed material can be written as [149]

$$J = \int_{\Gamma} \left[\frac{1}{2} (\sigma_{1'1'}\varepsilon_{1'1'} + \sigma_{2'2'}\varepsilon_{2'2'} + 2\sigma_{1'2'}\varepsilon_{1'2'}) dx_{2'} - \left(\sum\nolimits_{ij} \sigma_{ij} n_j \frac{\partial u_i}{\partial x_{1'}} \right) ds \right] \tag{8-38}$$

or,

$$J = \int_{\Gamma} \left[\frac{1}{2} (\sigma_{1'1'}\varepsilon_{1'1'} + \sigma_{2'2'}\varepsilon_{2'2'} + 2\sigma_{1'2'}\varepsilon_{1'2'}) dx_{2'} - (\sigma_{1'1'} n_{1'} \frac{\partial u_{1'}}{\partial x_{1'}} + \sigma_{1'2'} n_{2'} \frac{\partial u_{1'}}{\partial x_{1'}} + \sigma_{2'1'} n_{1'} \frac{\partial u_{2'}}{\partial x_{1'}} + \sigma_{2'2'} n_{2'} \frac{\partial u_{2'}}{\partial x_{1'}}) ds \right] \quad (8\text{-}39)$$

where direction 1' is along the crack length and direction 2' is perpendicular to the crack. The path Γ starts from the lower flank of the crack and proceed to the upper flank in a counter-clockwise direction. Typically, measurement of J along any path Γ is relatively difficult. However, this can be simplified by selecting suitable integration paths.

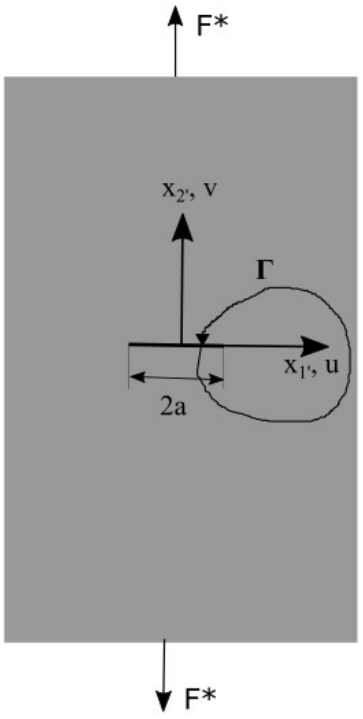

Figure 8-3: Coordinate system for *J*-integral

The in-plane stresses and strains required to evaluate the *J*-integral according to equation (8-39) are known from the hybrid stress analysis method. However, the displacement gradients need to be evaluated. This can be done by the same analytical concept used to find the in-plane stresses and displacements from the hybrid stress analysis approach. As the stress functions $\Phi(z_1)$ and $\Psi(z_2)$ are analytic functions, the Cauchy-Reimann condition for an analytic function $F(z)$ of equation (8-40) is applicable when differentiating the displacements u and v of equations (2-68) and (2-69), respectively, with any coordinate axis. For a crack along the negative x-axis, differentiating the displacement components of equations (2-47) and (2-48) with respect to x one can obtain the normal strain ε_{xx} and rotation component $\frac{\partial v}{\partial x}$ as equations (8-41) and (8-42), respectively.

$$\frac{\partial ReF(z)}{\partial x} = \frac{\partial ImF(z)}{\partial y} = Re\frac{dF(z)}{dz} \text{ and } \frac{\partial ImF(z)}{\partial x} = -\frac{\partial ReF(z)}{\partial y} = Im\frac{dF(z)}{dz} \quad (8\text{-}40)$$

and

$$\varepsilon_{xx} = \frac{\partial u}{\partial x} = 2Re\{p_1\Phi'(z_1) + p_2\Psi'(z_2)\} \quad (8\text{-}41)$$

$$\frac{\partial v}{\partial x} = 2Re\{q_1\Phi'(z_1) + q_2\Psi'(z_2)\} \quad (8\text{-}42)$$

Using the expressions of $\Phi'(z_1)$ and $\Psi'(z_2)$ from equations (2-66) and (2-67), respectively, in equations (8-41) and (8-42) the following new expressions for normal strain ε_{xx} and rotation component $\frac{\partial v}{\partial x}$ of equations (8-43) and (8-44), respectively, are obtained (when using a Laurent

series for the stress functions). Similarly, when using a Taylor series, the expressions of $\Phi'(z_1)$ and $\Psi'(z_2)$ from equations (2-55) and (2-56), respectively, into equations (8-41) and (8-42) give ε_{xx} and $\frac{\partial v}{\partial x}$ as equations (8-45) and (8-46), respectively.

$$\frac{\partial u}{\partial x} = \varepsilon_{xx} = 2\left(\sum_{\substack{j=-m \\ j\neq 0}}^{j=m} Re\left[p_1 \frac{jc_j\zeta_1^{j-1}}{\omega_1'(\zeta_1)} + p_2 \frac{-j\bar{c}_j B\zeta_2^{-j-1} + jc_j C\zeta_2^{j-1}}{\omega_2'(\zeta_2)} \right] \right) \tag{8-43}$$

and

$$\frac{\partial v}{\partial x} = 2\left(\sum_{\substack{j=-m \\ j\neq 0}}^{j=m} Re\left[q_1 \frac{jc_j\zeta_1^{j-1}}{\omega_1'(\zeta_1)} + q_2 \frac{-j\bar{c}_j B\zeta_2^{-j-1} + jc_j C\zeta_2^{j-1}}{\omega_2'(\zeta_2)} \right] \right) \tag{8-44}$$

or,

$$\frac{\partial u}{\partial x} = \varepsilon_{xx} = \sum_{j=1}^{N} Re\left\{ i\left(jp_1\zeta_1^{j-2} + jp_2 C\zeta_2^{j-2} \right)c_j - i\left(jp_2 B\zeta_2^{j-2} \right)\bar{c}_j \right\} \tag{8-45}$$

and

$$\frac{\partial v}{\partial x} = \sum_{j=1}^{N} Re\left\{ i\left(jq_1\zeta_1^{j-2} + jq_2 C\zeta_2^{j-2} \right)c_j - i\left(jq_2 B\zeta_2^{j-2} \right)\bar{c}_j \right\} \tag{8-46}$$

where the expressions for p_j, q_j (for $j = 1, 2$), B and C are provided in equations (2-30), (2-50) and (2-51), respectively.

To simplify the analytical procedures involved in computing the J-integration, the J-integral is evaluated along a square path ABCDEFG at a distance, d_{int}, from the crack-tip, $z = x + \mu_j y = 0$, Figure 8-4. For each line segment of the integration path the contribution to J-integral is derived separately and then added to find the total J-integral. For a crack aligned along x-axis, the contribution of the J-integral from the individual line segments according to Figure 8-4 are

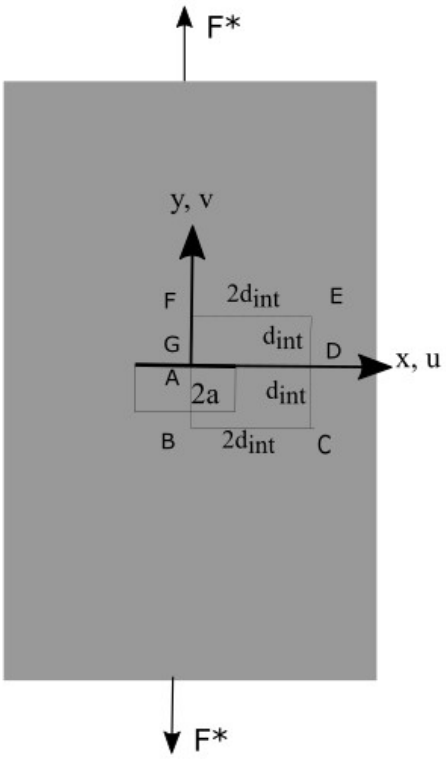

Figure 8-4: J-integral square path Γ

For line AB: $n_x = -1$, $n_y = 0$ and $\int_A^B ds = -\int_A^B dy$, equation (8-39) simplifies to

$$J_{AB} = \int_A^B \left[\frac{1}{2}\left(\sigma_{xx}\varepsilon_{xx} + \sigma_{yy}\varepsilon_{yy} + \sigma_{xy}\gamma_{xy}\right)dy - \left(\sigma_{xx}\frac{du}{dx} + \sigma_{xy}\frac{dv}{dx}\right)dy\right] \quad (8\text{-}47)$$

For line BC: $n_x = 0$, $n_y = -1$, $dy = 0$ and $\int_B^C ds = \int_B^C dx$, equation (8-39) simplifies to

$$J_{BC} = \int_B^C \left[\left(\sigma_{xy}\frac{du}{dx} + \sigma_{yy}\frac{dv}{dx}\right)dx\right] \quad (8\text{-}48)$$

For line CDE: $n_x = 1$, $n_y = 0$, $dx = 0$ and $\int_C^E ds = \int_C^E dy$, equation (8-39) simplifies to

$$J_{CE} = \int_C^E \left[\frac{1}{2}\left(\sigma_{xx}\varepsilon_{xx} + \sigma_{yy}\varepsilon_{yy} + \sigma_{xy}\gamma_{xy}\right)dy - \left(\sigma_{xx}\frac{du}{dx} + \sigma_{xy}\frac{dv}{dx}\right)dy\right] \quad (8\text{-}49)$$

For line EF: $n_x = 0$, $n_y = 1$, $dy = 0$ and $\int_E^F ds = -\int_E^F dx$, equation (8-39) simplifies to

$$J_{EF} = \int_E^F \left[\left(\sigma_{xy}\frac{du}{dx} + \sigma_{yy}\frac{dv}{dx}\right)dx\right] \quad (8\text{-}50)$$

For line FG: $n_x = -1$, $n_y = 0$ and $\int_F^G ds = -\int_F^G dy$, equation (8-39) simplifies to

$$J_{FG} = \int_F^G \left[\frac{1}{2}\left(\sigma_{xx}\varepsilon_{xx} + \sigma_{yy}\varepsilon_{yy} + \sigma_{xy}\gamma_{xy}\right)dy - \left(\sigma_{xx}\frac{du}{dx} + \sigma_{xy}\frac{dv}{dx}\right)dy\right] \quad (8\text{-}51)$$

As the integrands of *J* are comparatively complex, a numerical integration based on the Gaussian Quadrature rule and employing higher number of Gaussian points is used to compute the *J*-integral.

The integrations are conducted along the preselected path Γ, i.e., the square AB-BC-CD-DE-EF-FG of Figure 8-4. It is not necessary that the integration path and the region over which measured data are utilized to determine the Airy coefficients coincide. Knowing the Airy coefficients, in-plane stresses, strains and displacement slopes throughout the plate, including on the traction-free region and along the integration path, are evaluated from which the *J*-integral thus the SIF is determined.

J-integral is related to the SIF, *K*, and the Griffith's strain energy release rate function, *G*. For a plane-stressed, orthotropic, tensile-loaded plate with a crack along the negative *x*-axis and the strong/stiff material direction 1 aligned along the crack-face, i.e., along *x*-axis, Griffith's strain energy release rate function, *G*, and SIF, *K*, for opening-mode (mode-I, G_{I}, K_{I}) and shear-mode (mode-II, G_{II}, K_{II}) can be related as follows [77,173,174]

$$G_{\mathrm{I}} = \frac{K_{\mathrm{I}}^2}{\sqrt{(2E_{11}E_{22})}}\left[\left(\frac{E_{11}}{E_{22}}\right)^{\frac{1}{2}} + \frac{E_{11}}{2G_{12}} - \nu_{12}\right]^{\frac{1}{2}} \tag{8-52}$$

$$G_{\mathrm{II}} = \frac{K_{\mathrm{II}}^2}{E_{11}\sqrt{2}}\left[\left(\frac{E_{11}}{E_{22}}\right)^{\frac{1}{2}} + \frac{E_{11}}{2G_{12}} - \nu_{12}\right]^{\frac{1}{2}} \tag{8-53}$$

A more general expression to relate K_{I} and G_{I} in terms of orthotropic material's elastic compliances is [130]

$$G_{\mathrm{I}} = K_{\mathrm{I}}^2 \left\{ \left(\frac{a_{1'1'} a_{2'2'}}{2} \right)^{\frac{1}{2}} \left[\left(\frac{a_{2'2'}}{a_{1'1'}} \right)^{\frac{1}{2}} + \left(\frac{2a_{1'2'} + a_{6'6'}}{2a_{1'1'}} \right) \right]^{\frac{1}{2}} \right\} \tag{8-54}$$

where $a_{i'j'}$ are the elastic compliance from the generalized Hooke's law with direction $1'$ being parallel to the crack and direction $2'$ perpendicular to the crack. For linear elasticity, J is expressed in terms of both G_{I} and G_{II} as [150]

$$J = G_{\mathrm{I}} + G_{\mathrm{II}} \tag{8-55}$$

For mode-I crack, $K_{\mathrm{II}} = G_{\mathrm{II}} = 0$ and thus $G_{\mathrm{I}} = J$. Substituting this into equation (8-52) and re-arranging, the SIF can be expressed in terms of J-integral and orthotropic plate's material properties as

$$K_{\mathrm{I}}^2 = \frac{J\sqrt{E_{11}E_{22}}}{\sqrt{(\alpha_1^* + \beta_1^*)/2}} \tag{8-56}$$

where $\alpha_1^* = \sqrt{E_{11}/E_{22}}$ and $\beta_1^* = (E_{11}/2G_{12} - \nu_{12})$ and strong/stiff material direction 1 is parallel to the crack-face along x-direction. However, from equation (8-54), for a plate with a crack along the x-axis and the strong/stiff material direction 1 perpendicular to the crack, one can obtain the following relation between K_{I} and J

$$K_{\mathrm{I}}^2 = \frac{J\sqrt{E_{11}E_{22}}}{\sqrt{(\alpha_1^* + \beta_1^*)/2}} \tag{8-57}$$

where $\alpha_1^* = \sqrt{E_{22}/E_{11}}$ and $\beta_1^* = (E_{22}/2G_{12} - \nu_{12}E_{22}/E_{11})$ and strong/stiff material direction 1 is perpendicular to the crack which is located along the *x*-direction.

8.4.5.3. Method-3 (Mogadpalli and Parameswaran's Concept)

For an orthotropic member containing an edge crack, Shukla et al. [16] developed expressions for the crack-tip strain fields which Mogadpalli and Parameswaran [17] later expanded to crack-tip displacement fields. Shukla et al. [16] used the semi-inverse method suggested by Westergaard [175] and later modified by Sanford [176] to solve the biharmonic characteristic equation of the Airy stress function for mode-I crack, with the crack located at $y = 0$. For a crack in an orthotropic plate aligned along one of the principal material axes under opening-mode loading, the near crack-tip strain fields are expressed as [16]

$$\begin{aligned}\varepsilon_{xx} = {} & \frac{\alpha-\beta}{2\alpha}\{a_{12} - a_{11}(\alpha+\beta)^2\}ReZ_1 + \frac{\alpha+\beta}{2\alpha}\{a_{12} - a_{11}(\beta-\alpha)^2\}ReZ_2 \\ & + \frac{\beta}{2\alpha}\{a_{11}(\alpha+\beta)^2 - a_{12}\}ReY_1 + \frac{\beta}{2\alpha}\{a_{12} - a_{11}(\beta-\alpha)^2\}ReY_2\end{aligned} \tag{8-58}$$

$$\varepsilon_{yy} = \frac{\alpha-\beta}{2\alpha}\{a_{22} - a_{12}(\alpha+\beta)^2\}ReZ_1 + \frac{\alpha+\beta}{2\alpha}\{a_{22} - a_{12}(\beta-\alpha)^2\}ReZ_2 + \frac{\beta}{2\alpha}\{a_{12}(\alpha+\beta)^2 - a_{22}\}ReY_1 + \frac{\beta}{2\alpha}\{a_{22} - a_{12}(\beta-\alpha)^2\}ReY_2 \tag{8-59}$$

$$\gamma_{xy} = \frac{a_{66}}{2\alpha}(\alpha^2-\beta^2)\{ImZ_1 - ImZ_2\} - \frac{a_{66}\beta}{2\alpha}\{(\beta+\alpha)ImY_1 - (\beta-\alpha)ImY_2\} \tag{8-60}$$

where Z_k and Y_k for $k = 1, 2$ are complex functions and for a finite plate are

$$Z_k(z_k) = \sum_{j=0}^{M} M_j z_k^{j-\frac{1}{2}}, \quad k = 1, 2 \tag{8-61}$$

$$Y_k(z_k) = \sum_{j=0}^{N} N_j z_k^{j}, \quad k = 1, 2 \tag{8-62}$$

and

$$z_1 = x + i(\beta+\alpha)y, \quad z_2 = x + i(\beta-\alpha)y \quad \text{and} \quad i = \sqrt{-1} \tag{8-63}$$

$$2\beta^2 = \frac{a_{66}+2a_{12}}{2a_{11}} + \sqrt{\frac{a_{22}}{a_{11}}}, \quad 2\alpha^2 = \frac{a_{66}+2a_{12}}{2a_{11}} - \sqrt{\frac{a_{22}}{a_{11}}} \tag{8-64}$$

According to the strain-displacement relations of equation (2-7), integrating equation (8-58) with respect to *x* and equation (8-59) with respect to *y*, the *u* and *v* displacement components in the *x*-*y* plane are obtained as [17]

$$u = \frac{\alpha-\beta}{2\alpha}\{a_{12} - a_{11}(\alpha+\beta)^2\}Re\bar{Z}_1 + \frac{\alpha+\beta}{2\alpha}\{a_{12} - a_{11}(\beta-\alpha)^2\}Re\bar{Z}_2 + \frac{\beta}{2\alpha}\{a_{11}(\alpha+\beta)^2 - a_{12}\}Re\bar{Y}_1 + \frac{\beta}{2\alpha}\{a_{12} - a_{11}(\beta-\alpha)^2\}Re\bar{Y}_2 + g(y) \quad (8\text{-}65)$$

$$v = \frac{\alpha-\beta}{2\alpha}\{a_{22} - a_{12}(\alpha+\beta)^2\}\frac{Im\bar{Z}_1}{(\beta+\alpha)} + \frac{(\alpha+\beta)}{2\alpha}\{a_{22} - a_{12}(\beta-\alpha)^2\}\frac{Im\bar{Z}_2}{(\beta-\alpha)} + \frac{\beta}{2\alpha}\{a_{12}(\alpha+\beta)^2 - a_{22}\}\frac{Im\bar{Y}_1}{(\beta+\alpha)} + \frac{\beta}{2\alpha}\{a_{22} - a_{12}(\beta-\alpha)^2\}\frac{Im\bar{Y}_2}{(\beta-\alpha)} + f(x) \quad (8\text{-}66)$$

where

$$\bar{Z}_k(z_k) = \sum_{j=0}^{M} \frac{2}{2j+1} M_j z_k^{j+\frac{1}{2}}, \quad k = 1, 2 \quad (8\text{-}67)$$

$$\bar{Y}_k(z_k) = \sum_{j=0}^{N} \frac{1}{j+1} N_j z_k^{j+1}, \quad k = 1, 2 \quad (8\text{-}68)$$

The above-mentioned equations are derived by taking the origin of the coordinate at the crack-tip and crack aligned along *x*-axis at *y* = 0. Here a_{ij} are the elastic compliances of the orthotropic material. *M* and *N* in equations (8-61) through (8-62) and equations (8-67) and (8-68) are the number of terms required for accurate representation of the strain and displacement fields, respectively. The coefficients M_j and N_j are real and are chosen in such a way that the boundary conditions are satisfied. The terms *f*(*x*) and *g*(*y*) in the displacement expressions of equations (8-65)

and (8-66) are unknown functions of integration and expressed as equations (8-69) and (8-70), where C_0, D_1 and D_2 are constants from the structure's rigid body motion.

$$f(x) = C_0 x + D_1 \tag{8-69}$$

$$g(y) = -C_0 y + D_2 \tag{8-70}$$

Shukla et al. [16] showed that the coefficient M_0 is directly related to the opening-mode SIF, K_I, as

$$K_I = M_0\sqrt{2\pi} \tag{8-71}$$

To evaluate K_I from equation (8-71) one needs to know the coefficient M_0, which can be obtained by processing measured displacement data with equations (8-65) and/or (8-66). The process of using measured displacement data in the loading direction, v, to evaluate K_I will be demonstrated. To aid the analysis process, equation (8-66) is simplified and re-written as

$$v = L_1 Im\bar{Z}_1 + L_2 Im\bar{Z}_2 + L_3 Im\bar{Y}_1 + L_4 Im\bar{Y}_2 \tag{8-72}$$

where

$$L_1 = \frac{\alpha - \beta}{2\alpha(\alpha + \beta)}\{a_{22} - a_{12}(\alpha + \beta)^2\}, L_2 = \frac{\alpha + \beta}{2\alpha(\beta - \alpha)}\{a_{22} - a_{12}(\beta - \alpha)^2\},$$

$$L_3 = \frac{\beta}{2\alpha(\alpha + \beta)}\{a_{12}(\alpha + \beta)^2 - a_{22}\}, \tag{8-73}$$

$$L_4 = \frac{\beta}{2\alpha(\beta - \alpha)}\{a_{22} - a_{12}(\beta - \alpha)^2\}$$

For the physically loaded plate, the contribution from the rigid body motion, i.e., $f(x)$ can be neglected. Combining equations (8-67) and (8-68) into equation (8-72) (where L_j for j = 1 to 4 are provided in equation (8-73)) and re-writing in matrix form gives equation (8-74). The only unknowns in equation (8-74) are the coefficients M_j and N_j. All other values are either known measured values (v) or quantities that depend on the plate's material properties and x-y coordinate locations (equation (8-75)). Equation (8-74) can be written as (8-76) and solved for coefficients M_j and N_j using least squares.

$$\{v\} = Im[g_{0M} \quad g_{1M} \quad \cdots \quad g_M \quad g_{0N} \quad g_{1N} \quad \cdots \quad g_N] \begin{Bmatrix} M_0 \\ M_1 \\ \vdots \\ M_j \\ N_0 \\ N_1 \\ \vdots \\ N_j \end{Bmatrix} \tag{8-74}$$

where

$$g_{0M} = 2\left(L_1 z_1^{\frac{1}{2}} + L_2 z_2^{\frac{1}{2}}\right), g_{1M} = \frac{2}{3}\left(L_1 z_1^{\frac{3}{2}} + L_2 z_2^{\frac{3}{2}}\right),$$

$$g_M = \frac{2}{2j+1}\left(L_1 z_1^{j+\frac{1}{2}} + L_2 z_2^{j+\frac{1}{2}}\right), g_{0N} = L_3 z_1 + L_4 z_2, \tag{8-75}$$

$$g_{1N} = \frac{1}{2}(L_3 z_1^2 + L_4 z_2^2), g_N = \frac{1}{j+1}\left(L_3 z_1^{j+1} + L_4 z_2^2\right)$$

$$\{\text{Input Values}\} = [\text{Constants}]\{\text{Coefficients } (M_j + N_j)\} \tag{8-76}$$

Mogadpalli and Parameswaran suggested [17] using at least $M + N \geq 12$ terms in the series expansion of the displacements to obtain an accurate SIF.

8.4.5.4. Method-4 (Sih, Paris and Irwin's Concept)

Sih, Paris and Irwin's near crack-tip approximation for orthotropic materials in terms of the three modes of loading is utilized here. For an opening-mode or mode-I crack, the stresses and displacements in the vicinity of the crack-tip can be expressed as [22,122]

$$\sigma_{xx} = \frac{K_{\mathrm{I}}}{(2\pi r)^{\frac{1}{2}}} Re\left(\frac{\mu_1\mu_2}{\mu_1 - \mu_2}\left[\frac{\mu_2}{(\cos\theta + \mu_2 \sin\theta)^{1/2}} - \frac{\mu_1}{(\cos\theta + \mu_1 \sin\theta)^{1/2}}\right]\right) \tag{8-77}$$

$$\sigma_{yy} = \frac{K_{\mathrm{I}}}{(2\pi r)^{\frac{1}{2}}} Re\left(\frac{1}{\mu_1 - \mu_2}\left[\frac{\mu_1}{(\cos\theta + \mu_2 \sin\theta)^{1/2}} - \frac{\mu_2}{(\cos\theta + \mu_1 \sin\theta)^{1/2}}\right]\right) \tag{8-78}$$

$$\sigma_{xy} = \frac{K_{\mathrm{I}}}{(2\pi r)^{\frac{1}{2}}} Re\left(\frac{\mu_1\mu_2}{\mu_1 - \mu_2}\left[\frac{1}{(\cos\theta + \mu_1 \sin\theta)^{1/2}} - \frac{1}{(\cos\theta + \mu_2 \sin\theta)^{1/2}}\right]\right) \quad (8\text{-}79)$$

$$u = K_{\mathrm{I}}\sqrt{2\pi r} Re\left(\frac{1}{\mu_1 - \mu_2}\left[\mu_1 p_2\sqrt{\cos\theta + \mu_2 \sin\theta} - \mu_2 p_1\sqrt{\cos\theta + \mu_1 \sin\theta}\right]\right) \quad (8\text{-}80)$$

$$v = K_{\mathrm{I}}\sqrt{2\pi r} Re\left(\frac{1}{\mu_1 - \mu_2}\left[\mu_1 q_2\sqrt{\cos\theta + \mu_2 \sin\theta} - \mu_2 q_1\sqrt{\cos\theta + \mu_1 \sin\theta}\right]\right) \quad (8\text{-}81)$$

For mode-II loading the stresses and displacements in the vicinity of the crack-tip are as [22,122]

$$\sigma_{xx} = \frac{K_{\mathrm{II}}}{(2\pi r)^{\frac{1}{2}}} Re\left(\frac{1}{\mu_1 - \mu_2}\left[\frac{\mu_2^2}{(\cos\theta + \mu_2 \sin\theta)^{1/2}} - \frac{\mu_1^2}{(\cos\theta + \mu_1 \sin\theta)^{1/2}}\right]\right) \quad (8\text{-}82)$$

$$\sigma_{yy} = \frac{K_{\mathrm{II}}}{(2\pi r)^{\frac{1}{2}}} Re\left(\frac{1}{\mu_1 - \mu_2}\left[\frac{1}{(\cos\theta + \mu_2 \sin\theta)^{1/2}} - \frac{1}{(\cos\theta + \mu_1 \sin\theta)^{1/2}}\right]\right) \quad (8\text{-}83)$$

$$\sigma_{xy} = \frac{K_{\mathrm{II}}}{(2\pi r)^{\frac{1}{2}}} Re\left(\frac{1}{\mu_1 - \mu_2}\left[\frac{\mu_1}{(\cos\theta + \mu_1 \sin\theta)^{1/2}} - \frac{\mu_2}{(\cos\theta + \mu_2 \sin\theta)^{1/2}}\right]\right) \quad (8\text{-}84)$$

$$u = K_{\mathrm{II}}\sqrt{2\pi r} Re\left(\frac{1}{\mu_1 - \mu_2}\left[p_2\sqrt{\cos\theta + \mu_2 \sin\theta} - p_1\sqrt{\cos\theta + \mu_1 \sin\theta}\right]\right) \quad (8\text{-}85)$$

$$v = K_{\mathrm{II}}\sqrt{2\pi r} Re\left(\frac{1}{\mu_1 - \mu_2}\left[q_2\sqrt{\cos\theta + \mu_2 \sin\theta} - q_1\sqrt{\cos\theta + \mu_1 \sin\theta}\right]\right) \quad (8\text{-}86)$$

Coordinates r and θ are measured from the crack-tip. For a crack along the X-axis of material orthotropy, i.e., $\alpha = 0$, Figure 8-1, equations (8-78) and (8-84) give the SIF for mode-I and mode-II cracks at $\theta = 0$, $r << a$, respectively [22]

$$K_{\mathrm{I}} = \sigma_{yy}\sqrt{2\pi r} \tag{8-87}$$

$$K_{\mathrm{II}} = \sigma_{xy}\sqrt{2\pi r} \tag{8-88}$$

where σ_{yy} and σ_{xy} of equations (8-87) and (8-88) are obtained from the hybrid stress analysis method. For a plate with an inclined crack, i.e., $\alpha \neq 0$, a stress transformation between the plate's global and crack's local coordinates need to be established.

8.4.5.5. Method-5 (Bao's Concept)

According to Bao et al. [93], for a plane-stressed finite orthotropic member with a crack along principal directions of material symmetry and taking into account the rescaling from the plate's dimensionality, linearity and orthotropy, the SIF for an orthotropic material under opening-mode loading can be expressed as

$$K_{\mathrm{I}} = \sigma_0\sqrt{\pi a}Y(\rho)H\left(\frac{a}{W}\right) \tag{8-89}$$

where $Y(\rho)$ is the correction factor due to material orthotropy and $H(a/W)$ is the correction factor for geometry dependence (accounts for the plate's finite/infinite width with respect to the crack

length). For $\lambda^{1/4}(L/W) \geq 2.0$ the effect of plate's length over its width can be neglected. Here λ and ρ are dimensionless parameters expressed in terms of the composite's elastic compliances and were first proposed and defined by Suo [177] as

$$\lambda = \frac{a_{11}}{a_{22}}, \quad \rho = \frac{1}{2}(2a_{12} + a_{66})(a_{11}a_{22})^{-1/2} \tag{8-90}$$

where directions 1 and 2 represent the plate's orthotropic material directions and for Suo's analyses the material direction 1 was taken along the crack-face in the x-direction. Thus direction 1 is along the crack-face. Bao et al. [93] provided an single expression for the function $Y(\rho)$ which they claim is 95% - 98% accurate for a central, single-edge or double-edge notched plate. Bao's expression for $Y(\rho)$ is

$$Y(\rho) = 1 + 0.1(\rho - 1) - 0.016(\rho - 1)^2 + 0.002(\rho - 1)^3 \tag{8-91}$$

Bao et al. [93] showed that the rescaling factor $H(a/W)$ for geometry dependence of an orthotropic plate is the same function as that for isotropic materials provided by Tada et al. [178]. The expression of $H(a/W)$ for plates with three different types of cracks under opening-mode loading are [93]

$$H\left(\frac{a}{W}\right)=\begin{cases}\left[1+0.122\cos^4\frac{\pi a}{W}\right]\sqrt{\frac{W}{\pi a}\tan\frac{\pi a}{W}} & \text{DEC}\\ \sqrt{\frac{2W}{\pi a}\tan\frac{\pi a}{2W}}\,\frac{0.752+2.02\left(\frac{a}{W}\right)+0.37\left(1-\sin\frac{\pi a}{2W}\right)^3}{\cos\frac{\pi a}{2W}} & \text{SEC}\\ \left[1-0.025\left(\frac{2a}{W}\right)^2+0.06\left(\frac{2a}{W}\right)^4\right]\sqrt{\sec\frac{\pi a}{W}} & \text{CC}\end{cases} \tag{8-92}$$

where a is the half crack length for a central crack and length of each of the edge cracks for a single- or double-edge crack, W is the plate's width. Bao's expressions for SIF are typically valid for materials with $0 \le \rho \le 4$ and $0.05 \le \lambda \le 20$.

8.4.5.6. Shukla's Analytical Method for SIF in Single-Edge Crack Plate

Shukla et al. [16] provided a closed-form solution to find the SIF of orthotropic plates with a single-edge crack based on equations (8-93) and (8-94).

$$K_{\mathrm{I}} = H(a/W)\sigma_0\sqrt{a} \tag{8-93}$$

where $H(a/W)$ is a calibration factor of a SEC-plate and is defined in terms of the crack-length, a, to plate-width, W, ratio, a/W, as

$$H(\frac{a}{W}) = 1.99 - 0.41\left(\frac{a}{W}\right) + 18.7\left(\frac{a}{W}\right)^2 - 38.48\left(\frac{a}{W}\right)^3 + 53.85\left(\frac{a}{W}\right)^4 \tag{8-94}$$

8.5. Numerical Analyses

Four different plates were considered to demonstrate the displacement-based hybrid-method's ability to stress analyze fracture in orthotropic plates. The plates had different dimensions, crack types, material properties, fiber orientations and crack-opening to plate-width ratios. The plates were selected intentionally to observe the effect of these various factors (plate type/crack type/material type) on the DIC-hybrid (here based on using FEA-predicted displacement data) evaluated displacements and stresses.

8.5.1. Plate Details

The first orthotropic plate analyzed (plate-1) contains a centrally-located crack of $2a/W = 0.2$, Figure 8-5(a). The second orthotropic plate (plate-2) has a single-edge crack of $a/W = 0.3$, Figure 8-5(b). Plate details are provided in Table 8-1 (dimensions and loading) and in Table 8-2 (material properties). The two plates were analyzed by Lin et al. [77]. Plate-1 (plate with central crack) was also analyzed by Bowie and Freese [7] and by Saxce and Kang [131]. Plate-2 (plate with the single-edge crack) was originally analyzed by Mandell et al. [130] and then by Saxce and Kang [131]. Plate-1 has the principal material direction 1 along the crack surface in the x-direction. For plate-2 the principal material direction 1 is perpendicular to the crack-face and in the loading direction.

The second set of plates analyzed are orthotropic plates with a single-edge crack of $a/W = 0.37$ (plate-3), Figure 8-5(c), and double-edge cracks of $2a/W = 0.75$ (plate-4), Figure 8-5(d). Both of these plates have the strong/stiff material direction 1 along the crack-face in x-direction. Dimensions and loading details of the plates and their material properties are provided in Table

8-3 and Table 8-4, respectively. Plate-3 was originally analyzed by Mogadpalli and Parameswaran [17]. Plate-4 is the same as that of plate-3 except it has double-edge cracks instead of a single-edge crack. Plate-4 has $2a/W = 0.75$ whereas $a/W = 0.37$ for plate-3.

From the externally applied load, F^*, and the far-field dimensions of the plates, the far-field applied stress, σ_0, on the plates were calculated according to equation (8-95), Table 8-1 and Table 8-3.

$$\sigma_0 = F^*/Wt \tag{8-95}$$

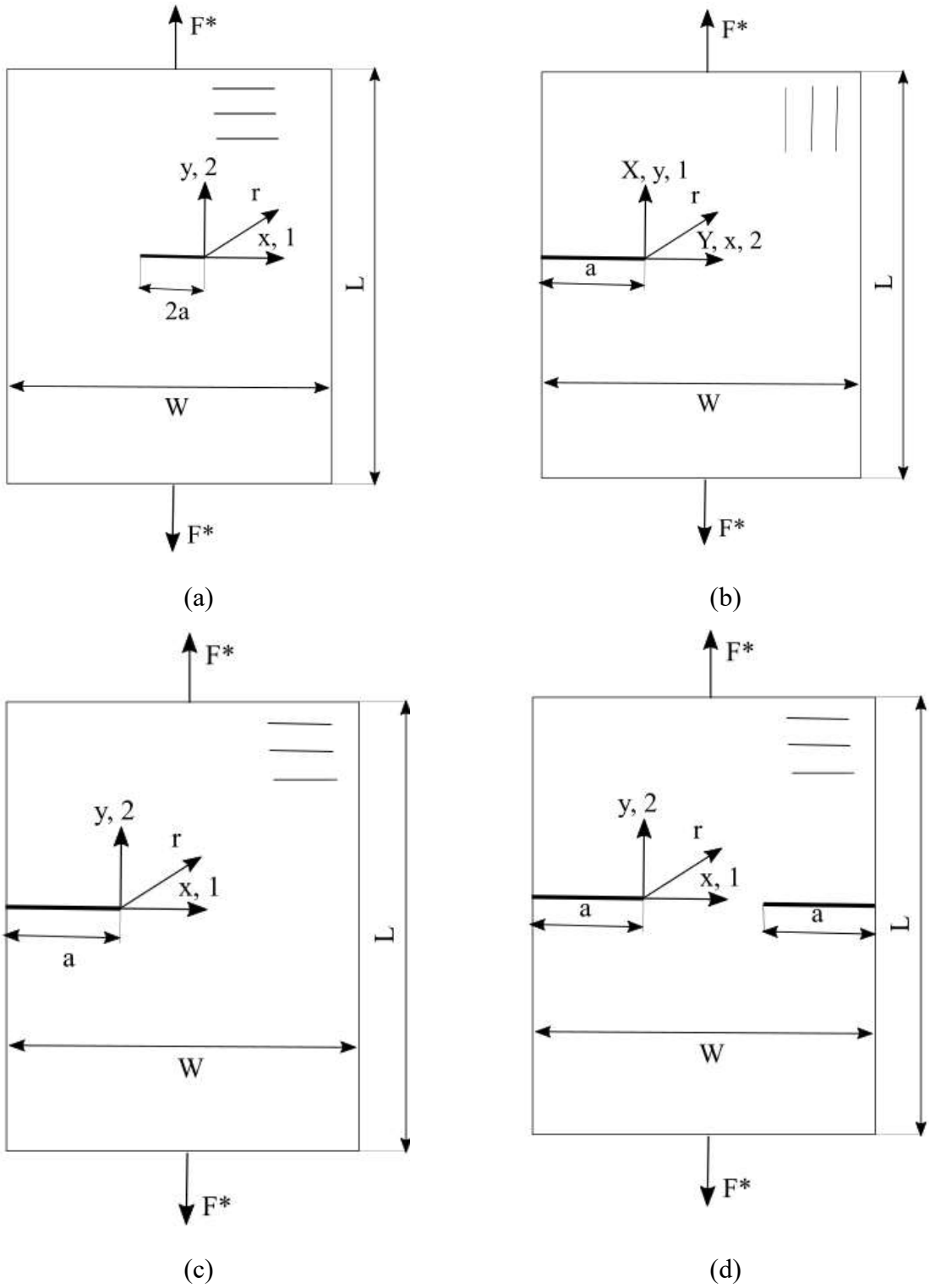

Figure 8-5: Nomenclatures for plate with (a) Central crack (Plate-1), (b) Single-edge crack (Plate-2), (c) Single-edge crack (Plate-3) and (d) Double-edge cracks (Plate-4). The coordinate directions are selected based on the respective mapping functions used to stress analyze the plates

Table 8-1: Details [77] for plate-1 with central crack from Bowie and Freese [7] and plate-2 with single-edge crack from Mandell et al. [130]

Plate Parameters	Central Crack (Plate-1)	Single-Edge Crack (Plate-2)
Crack length, a	12.7 mm (half of total crack length $2a$)	38.1 mm
Crack-opening to plate-width ratio	$2a/W = 0.2$	$a/W = 0.3$
Width, W	127 mm	127 mm
Length, L	127 mm	762 mm
Thickness, t	5.28 mm	5.28 mm
Applied load, F^*	4.45 kN (1,000 lbs)	4.45 kN (1,000 lbs)
Far-field stress, σ_0	6.64 MPa	6.64 MPa

Table 8-2: Material properties for plate-1 with central crack from Bowie and Freese [7] and plate-2 with single-edge crack from Mandell et al. [130]

Plate's Elastic Properties	Central Crack (Plate-1)	Single-Edge Crack (Plate-2)
Elastic modulus in strong/stiff direction, E_{11}	206.85 GPa (30×10^6 psi)	144.8 GPa (18.3×10^6 psi)
Elastic modulus in transverse direction, E_{22}	82.74 GPa (12×10^6 psi)	11.7 GPa (1.7×10^6 psi)
Major Poisson's ratio, ν_{12}	0.3	0.27
Shear modulus, G_{12}	50.47 GPa (7.32×10^6 psi)	8.3 GPa (1.2×10^6 psi)

Table 8-3: Details for plate-3 with single-edge crack from Mogadpalli and Parameswaran [17] and similar plate-4 with double-edge cracks

Plate Parameters	Single-Edge Crack (Plate-3)	Double-Edge Cracks (Plate-4)
Crack length, a	11.2 mm	11.2 mm
Crack-opening to plate-width ratio	$a/W = 0.37$	$2a/W = 0.75$
Width, W	30 mm	30 mm
Length, L	130 mm	130 mm
Thickness, t	3.6 mm	3.6 mm
Applied load, F^*	300 N (67.4 lbs)	300 N (67.4 lbs)
Far-field stress, σ_0	2.78 MPa	2.78 MPa

Table 8-4: Material properties for plate-3 with single-edge crack from Mogadpalli and Parameswaran [17] and similar plate-4 with double-edge cracks

Plate's Elastic Properties	SEC (Plate-3) and DEC (Plate-4)
Elastic modulus in strong/stiff direction, E_{11}	39.8 GPa (30×10^6 psi)
Elastic modulus in transverse direction, E_{22}	17.7 GPa (12×10^6 psi)
Major Poisson's ratio, ν_{12}	0.29
Shear modulus, G_{12}	5 GPa (7.32×10^6 psi)

8.5.2. Finite Element Model

FEA tool ANSYS APDL was used to generate FEAs of the four plates according to the dimensions and loading conditions provided in Table 8-1 and Table 8-3. All plates were modeled

using isoparametric element Plane 183 with eight-nodes per element. Plate-1 and plate-4 have geometric and loading symmetry about both the x- and y-axes so only one quarter of those plates were modeled. Plate-2 and plate-3, being symmetrical about the horizontal center-line, only half of these plates were modeled. Appropriate symmetrical boundary conditions were imposed and for all four plates the origin of the coordinate system was at the crack-tip. Assigned material properties are those of Table 8-2 and Table 8-4 for the respective plates. 'KSCON' command was used to generate focused mesh at the crack-tip and 'skewed element' option was used to make the crack-tip elements singular, Figure 8-6. The final quarter plate FEM model for plate-1 with central crack had 2,166 eight-node quadratic isoparametric elements (which includes 6 quarter-point elements at the crack-tip) and a total of 6,599 nodes, Figure 8-7(a). The half model of Plate-2, with the single-edge crack, had 6,135 quadratic isoparametric elements (including 6 quarter-point elements) and 18,676 nodes, Figure 8-7(b). The half FEM model of Plate-3 with the single-edge crack had a total of 3,391 elements (including the quarter-point elements) and 10,316 nodes, Figure 8-8(a). The quarter FEM model of Plate-4 (double-edge cracks) had 2,100 elements (including the quarter-point elements) and 6,443 nodes, Figure 8-8(b). Both plate-3 and -4 had 16 quarter-point elements at the crack-tips. Due to the far-field applied external load, F^*, and plate dimensions, all plates experienced a far-field stress of σ_0 according to equation (8-95).

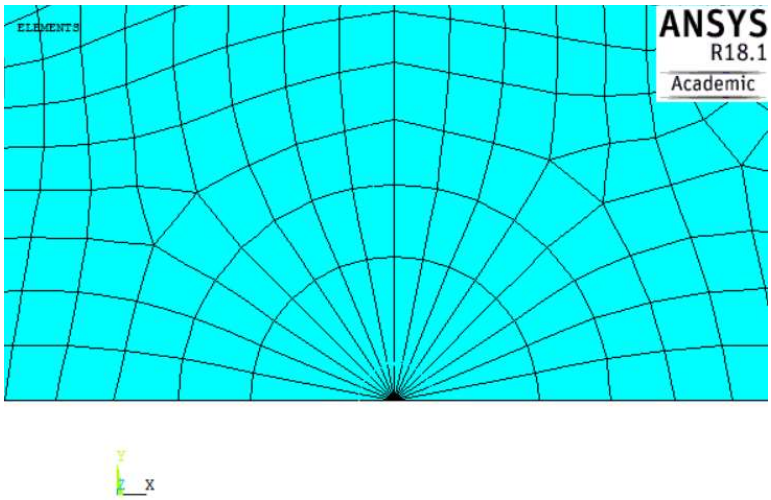

Figure 8-6: ANSYS quarter-point elements near crack-tip

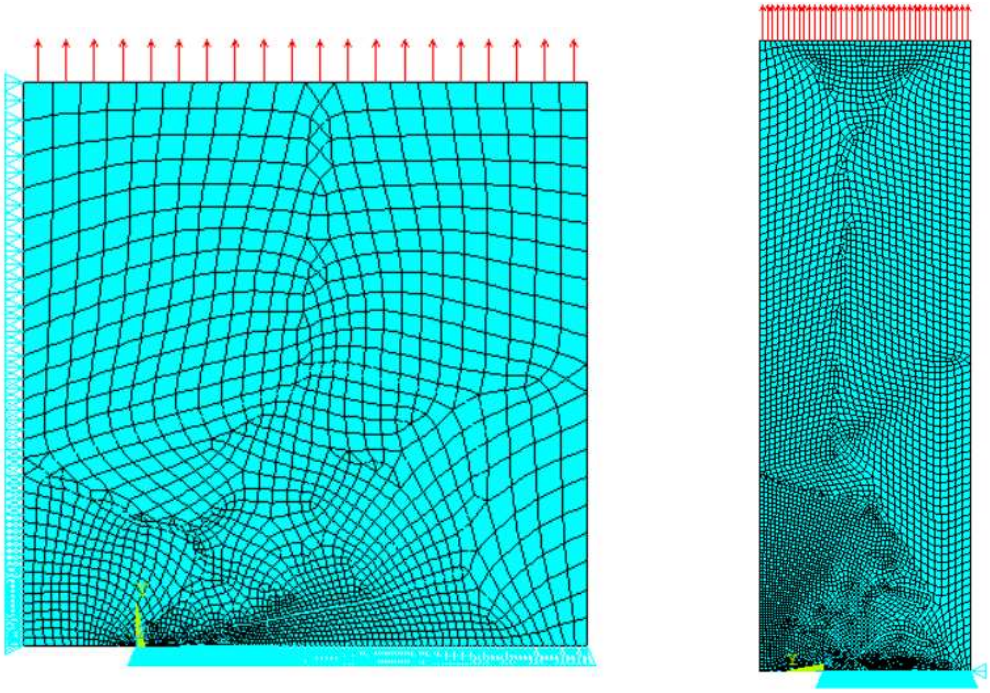

(a) (b)

Figure 8-7: FEMs of orthotropic plate with (a) Central crack (quarter model of plate-1) and (b) Single-edge crack (half model of plate-2)

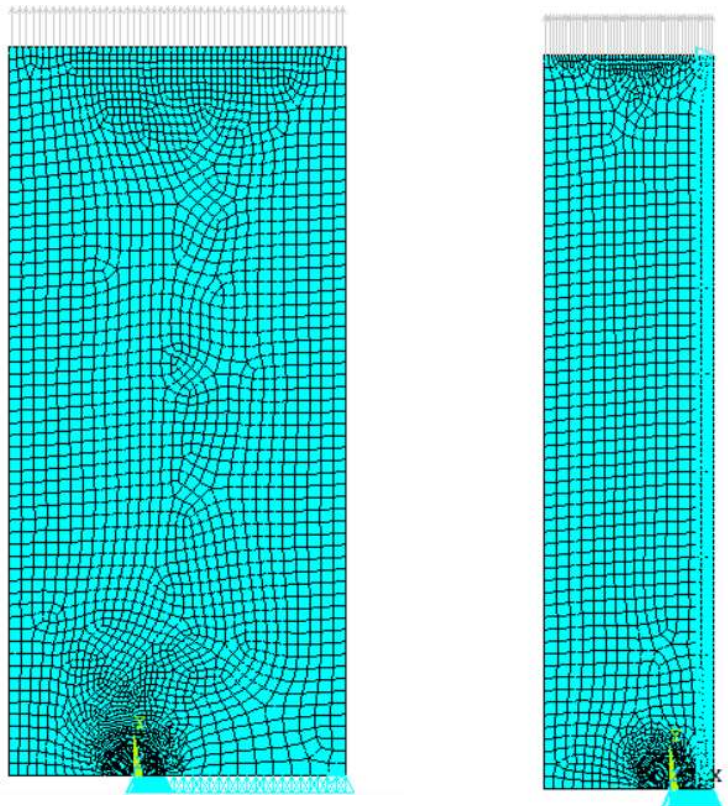

(a) (b)

Figure 8-8: FEMs of orthotropic plate with (a) Single-edge crack (half model of plate-3) and (b) Double-edge cracks (quarter model of plate-4)

8.6. Displacement-Based Hybrid Stress Analysis

8.6.1. Data Selection and Stress and Displacement Evaluation

All of the nodal information, i.e., node coordinates, stress and displacement information from ANSYS APDL computed FEA results were exported into Excel and post-processed using MATLAB to stress analyze the respective plates.

Using the mapping function of equation (8-3) for plate-1, a Laurent series expansion for the Airy stress functions of equations (2-68) through (2-72) enables one to full-field stress analyze the plate. By combining equation (8-4) with either equation (2-68) or (2-69) and using $n_{FEA} = 2{,}076$

FEA-predicted u- or v-displacements, respectively, it is possible to solve the developed system of linear equations for the unknown Airy coefficients, $c_j = a_j + ib_j$, by least squares. Employing the evaluated Airy coefficients, c_j, in equations (2-68) and (2-69) plus equation (8-4) provides the in-plane displacement components. By similarly combining equations (8-4) and (8-6) with equations (2-70) through (2-72) gives the in-plane stresses. The number of coefficients to use in equations (2-68) through (2-72) was selected based on the RMS plot of Figure 8-9 and by comparing the FEA-predicted and hybrid-method reconstructed input displacement contours. By these $k = 8$ was selected.

The same procedure as those for plate-1 were followed to full-field stress analyze plate-2 from FEA-predicted displacement data. The only difference is that the inverse mapping function of equation (8-8) was used to map the edge crack of plate-2 from the $Z = X + \mu_j Y$-plane to a unit circle in ζ-plane. This analysis was done using both the in-plane displacements u and v as input and applying the symmetry boundary condition $\sigma_{XY} = 0$ at $h = 81$ equally spaced locations beyond the crack, i.e., along $Y = 0$ to $(W - a)$ at $X = 0$. The plate was loaded in the X-direction as the mapping function considers the crack being transverse to the loading direction [171]. To evaluate the unknown coefficients $n_{FEA} = 2 \times 3{,}835$ FEA-predicted u- and v-displacements (in equations (2-68) and (2-69)) and $h = 81$ imposed symmetry conditions (in equation (2-72)) were utilized. The number of Airy coefficients to retain in the summation series was chosen based on the RMS plot of Figure 8-10 which suggests using $k = 8$.

Plate-3 and -4 were analyzed using the mapping function of equation (8-10) and the Taylor series expansion of the Airy stress functions. The inverse of the mapping function of equation (8-11) was used in equation (2-61) to obtain the expression for the in-plane v-displacement field. Using n_{FEA} (Table 8-5) FEA-predicted v-displacement values in this newly obtained expression of

v, the unknown Airy coefficients, c_j, were obtained by least squares. Substitution of the evaluated c_j in equations (2-57) through (2-61) enabled full-field stress/displacement analyses of the plates. Again, the number of Airy coefficients to full-field stress analyze the plates were chosen based on the RMS plot of Figure 8-11 and Figure 8-12. The RMS suggestions for k were re-checked by comparing the FEA-predicted and hybrid-method reconstructed input displacement contours for varying k. For plate-3 and -4, $k = 5$ and $k = 10$ were selected, respectively. For both plates $k \geq 5$ had no significant effect on the evaluated results.

Details on the hybrid-methods are provided in Table 8-5. It must be noted that the stress analyses for the plates were essentially done by just using either only v or u displacement data and without imposing any symmetry or finite boundary conditions, except for plate-2. This was done intentionally to investigate whether the accuracy of the hybrid-method depends on knowing the finite boundary conditions or not.

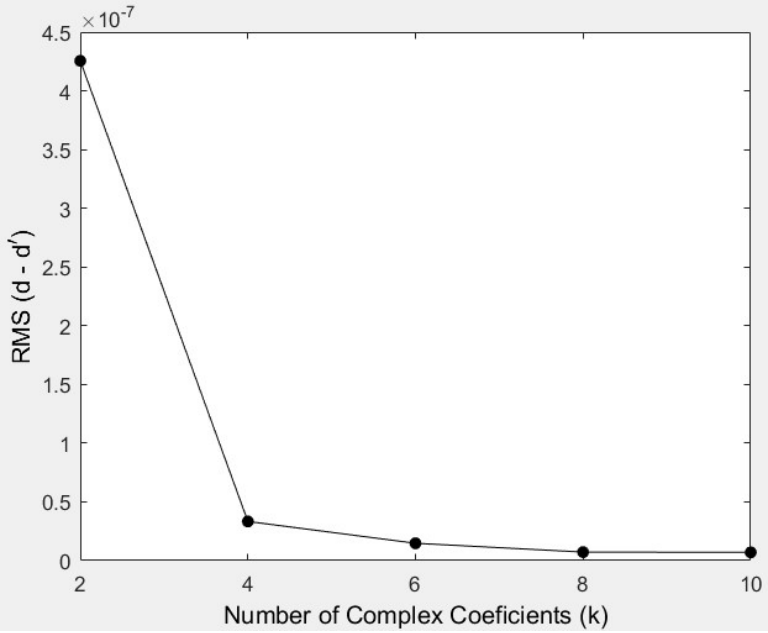

Figure 8-9: RMS of the FEA-predicted and reconstructed displacement data versus the number of Airy stress coefficients, *k,* for n_{FEA} = 2,076 *u*- or *v*-displacements of plate-1 and Laurent series

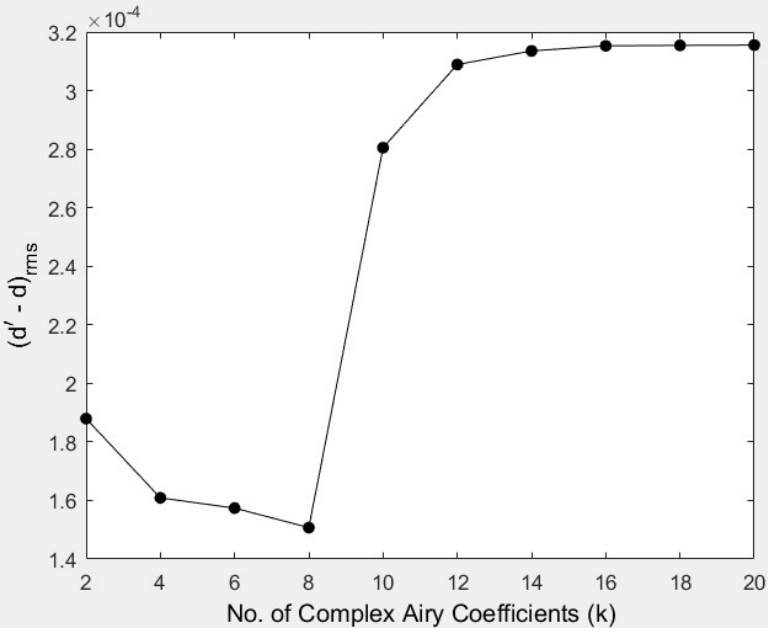

Figure 8-10: RMS of the FEA-predicted and reconstructed displacement data versus the number of Airy stress coefficients, *k,* for n_{FEA} = 2 × 3,835 *u*- and *v*- displacements plus *h* = 81 of plate-2 and Laurent series

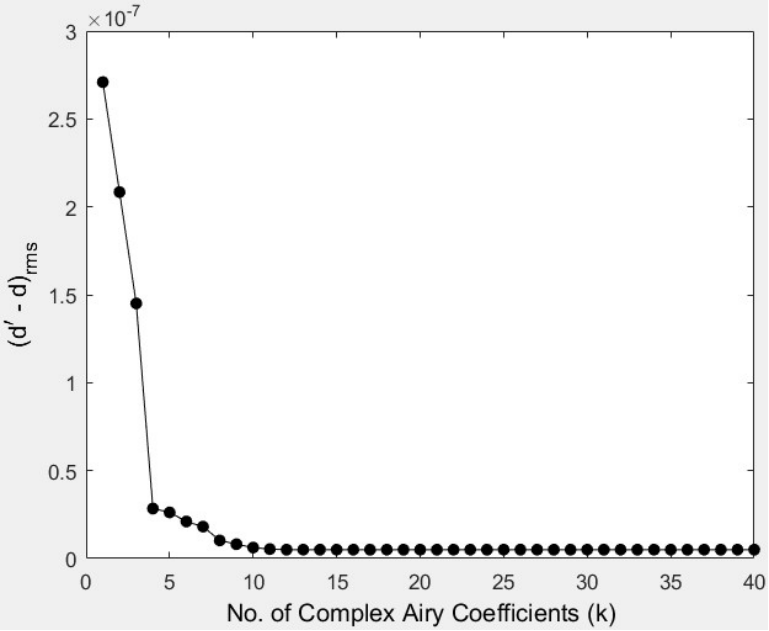

Figure 8-11: RMS of the FEA-predicted and reconstructed displacement data versus the number of Airy stress coefficients, *k,* for n_{FEA} = 3,499 *v*-displacements of plate-3 and Taylor series

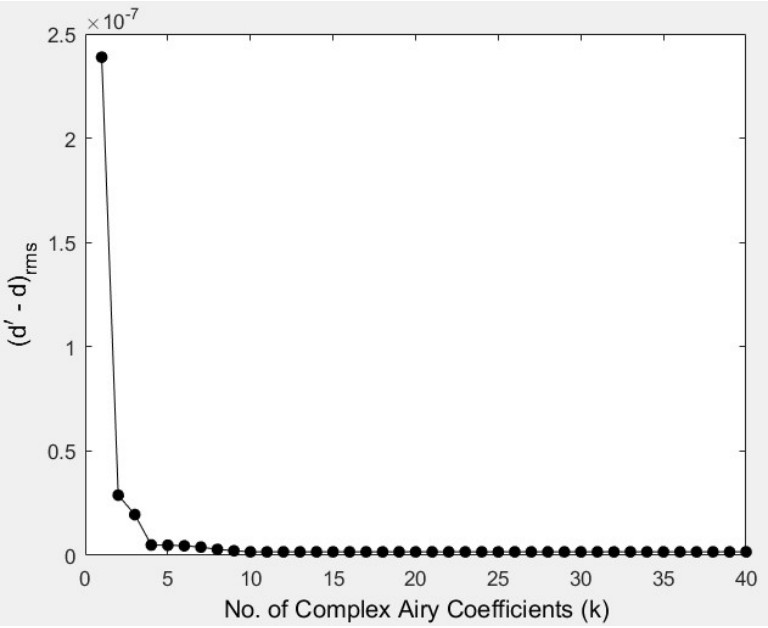

Figure 8-12: RMS of the FEA-predicted and reconstructed displacement data versus the number of Airy stress coefficients, *k,* for n_{FEA} = 2,277 *v*-displacements of plate-4 and Taylor series

Table 8-5: Hybrid analyses details for plate-1 through -4

Plate No.	Complex material properties	Hybrid-method's input quantity	Employed FEA-predicted displacements	Imposed boundary condition	No. of complex Airy coefficients employed
1	$\mu_1 = 1.58i$ $\mu_2 = i$	u or v	$n_{FEA} = 2{,}076$	$h = 0$	$k = 8$ (Laurent)
2	$\mu_1 = 3.73i$ $\mu_2 = 0.88i$	u, v and symmetrical BC	$n_{FEA} = 2\times3{,}835$	$h = 81$	$k = 8$ (Laurent)
3	$\mu_1 = 2.66i$ $\mu_2 = 0.56i$	v	$n_{FEA} = 3{,}499$	$h = 0$	$k = 5$ (Taylor)
4	$\mu_1 = 2.66i$ $\mu_2 = 0.56i$	v	$n_{FEA} = 2{,}277$	$h = 0$	$k = 10$ (Taylor)

8.6.2. Determination of SIF

Once the complete states of displacement and stress are known in an orthotropic, finite-width, member involving crack from the hybrid stress analysis method, the stress and/or displacement information can be used in any of the established crack analysis approaches to determine the SIF. Determination of SIF or other crack related parameters is thus just an additional post-processing of the hybrid-method provided information on the structure's state of stress. Accuracy of the obtained SIF strongly depends on the accuracy of results from the hybrid-method. Any reliable fracture technique can be coupled with the hybrid-method to evaluate the SIF. From the numerous fracture analysis techniques available in literature, five methods are mainly discussed here. The SIF results obtained from these methods based on the hybrid-method computed (based on FEM input data) or direct FEM-provided stress or displacement information

are compared with values reported in the literature. In some cases, SIF results from a closed form solution are also provided for comparison.

For plate-1 and -2 according to method-4 (Sih, Paris and Irwin's concept), the hybrid-method computed in-plane stresses in the loading direction are used in equation (8-87), respectively. From this the mode-I SIF, K_I, is evaluated. Results will be reported in Table 8-6 for plate-1 and Table 8-7 and Table 8-8 for plate-2. SIF determination is a post-processing of the hybrid-method evaluated results. For plate-2 the state of stress is obtained from the hybrid-method relative to the *X*-*Y* global coordinates and the SIF is obtained from the Sih, Paris and Irwin's method relative to the *x*-*y* crack local coordinates, Figure 8-5(b).

The concept of *J*-integral was also used to evaluate the SIF for plate-1. The hybrid-method provided complete states of displacement and stress near a crack were obtained from equation (2-68) through (2-72). Using the stresses of equations (2-70) through (2-72) and the elastic compliances of equation (2-18) in equations (2-3) through (2-5), the in-plane strains were obtained. Thus, the in-plane stresses and strains in the expression for *J*-integral of equation (8-39) are known. The expressions for the displacement gradients $\partial u/\partial x$ and $\partial v/\partial x$ used in equation (8-39) are obtained from equations (8-43) and (8-44). The *J*-integral is evaluated along a square path enclosing the crack in a counter clock-wise direction from the crack's lower flank to the upper flank according to Figure 8-4. The expression for the *J*-integral of equation (8-39) is simplified according to equations (8-47) through (8-51) for each of the path segments. The integration is computed using numerical integration based on the Gaussian Quadrature rule. The contributions of *J* from the various line segments are added to evaluate the total *J* value. SIF for mode-I loading, K_I, is obtained using the evaluated *J* in equation (8-56).

For plate-3 and -4, K_I are also evaluated using the concept of J-integral. The same procedure as that outlined for plate-1 is followed to evaluate K_I for plate-3 and -4 using J-integral. However, for these analyses the Airy stress functions were expanded by the Taylor series. The in-plane displacements and stresses were computed from equations (2-57) through (2-61) using the mapping function of equation (8-10). The displacement gradients $\partial u/\partial x$ and $\partial v/\partial x$ were evaluated from equations (8-45) and (8-46). K_I were also evaluated for plate-3 and -4 from Bao's [93] closed form solutions of equations (8-89) through (8-92).

8.7. Khalil's Concept

The states of stress/displacement and SIFs of plate-1 and -2 were also evaluated using the analytical procedure provided by Khalil et al. [118] and later utilized by Ju and Rowlands [137,139]. For both plates v-displacements were processed according to equation (8-15) combined with equations (8-18) through (8-21). The system can thus be expressed as equation (8-33). The unknown stress coefficients of equation (8-33) are evaluated by least squares according to equation (8-36). Knowing the stress coefficients, the displacement components u and v are evaluated using equations (8-14) through (8-21). Similarly, the in-plane stresses are obtained from equations (8-20) through (8-30). The SIF under mode-I loading is then obtained from equation (8-31). The data selection ranges of utilized v did not have significant effect on the evaluated results. These two analyses were done only using v-displacements $n_{FEA} = 2{,}031$ for plate-1 and $n_{FEA} = 2{,}858$ for plate-2. The selected FEA-predicted v-displacement data originated at a radial distance $r = 0.1a$ away from the crack-tip.

An additional analysis was done using both the in-plane displacements and all three of the in-plane stresses as input in this method to obtain better correlation for plate-1 between the FEA-predicted *v*-displacements and reconstructed *v*-displacements (from Khalil's method). This was achieved using the expression of u and v from equations (8-14) and (8-15) combined with equations (8-16) through (8-21) plus using the expressions of σ_{xx}, σ_{yy} and σ_{xy} from equations (8-22) through (8-30) along with equations (8-20) and (8-21). This provided a system of linear expressions of equations (8-35) and which was solved according to equation (8-36) using least squares.

The number of terms to retain in the summation series was selected based on the RMS plot of the FEA-predicted and Khalil's method reconstructed input quantity/quantities. While utilizing only *v*-displacement data to stress analyze the plates according to Figure 8-13 for plate-1, $\gamma_{2N} = 16$ and for plate-2 according to Figure 8-14, $\gamma_{2N} = 36$ was utilized. For the second analysis of plate-1 utilizing all in-plane displacements and stresses as input, Figure 8-15 suggests $\gamma_{2N} = 8$.

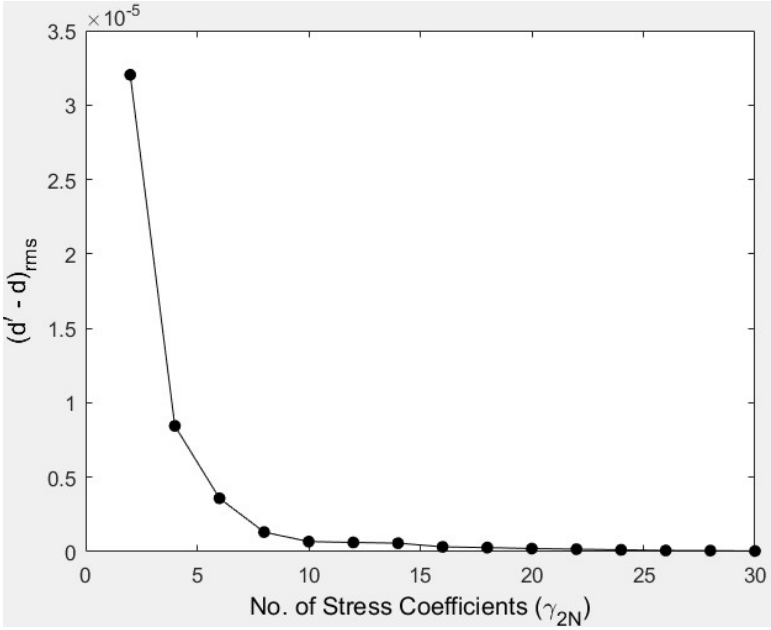

Figure 8-13 RMS versus number of stress coefficients, γ_{2N}, for plate-1 from Khalil's method using FEM-predicted *v*-displacements as input

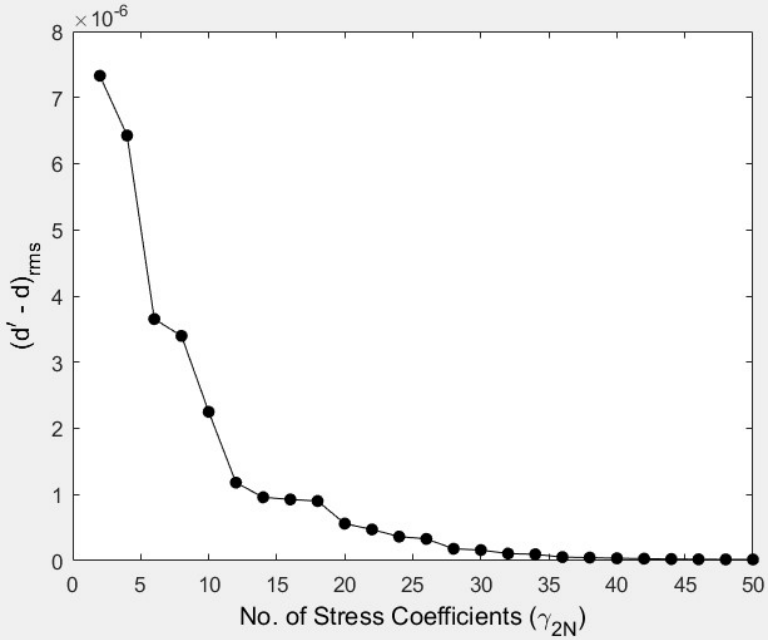

Figure 8-14: RMS versus number of stress coefficients, γ_{2N}, for plate-2 from Khalil's method using FEM-predicted *v*-displacements as input

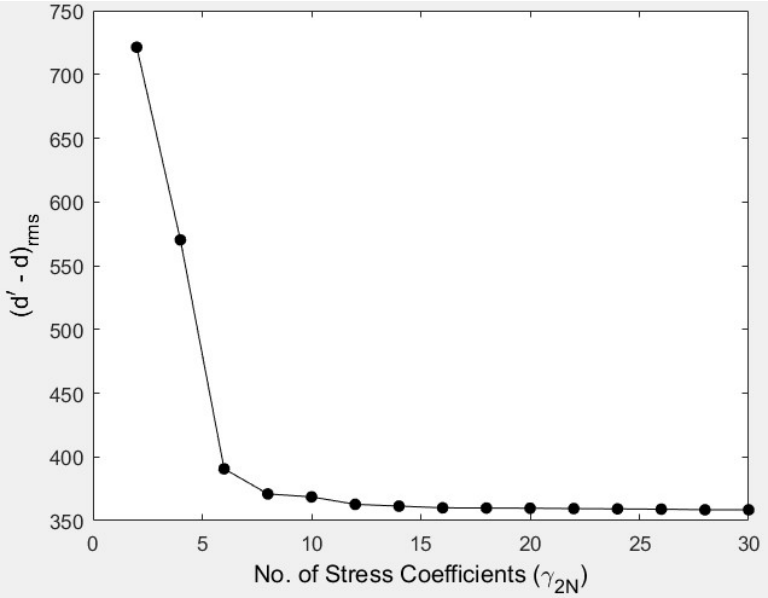

Figure 8-15: RMS versus number of stress coefficients, γ_{2N}, for plate-1 from Khalil's method using FEM-predicted u, v, σ_{xx}, σ_{yy} and σ_{xy} as input

8.8. Results

8.8.1. Hybrid Stress Analysis Results

Using only the FEA-predicted u- or v–displacement data in the hybrid stress analysis method for plate-1, -3 and -4, the in-plane displacements and stresses in the cracked plates were determined and compared with the direct FEA predictions. For plate-2, both u- and v-displacements were used along with imposed symmetrical boundary conditions. For each of the plates good agreement prevails between the reconstructed displacements and stresses from the hybrid complex stress analysis with those initially predicted by FEA. All location and displacement data are normalized by the crack length, a; for a central crack 'a' is half of the total crack length and for edge cracks 'a' is the length of an individual crack. The stresses are normalized by the far-field stress, σ_0, according to equation (8-95). Figure 8-16 through Figure 8-20 compare the hybrid-method computed in-plane displacements and stresses with the input

FEA-predictions for the four different plates. The good agreement between the hybrid (based on FEM simulated input) and direct/conventional FEM results indicates the high reliability of the hybrid-method. Accurate evaluation of SIFs by utilizing these hybrid-based results are therefore substantiated.

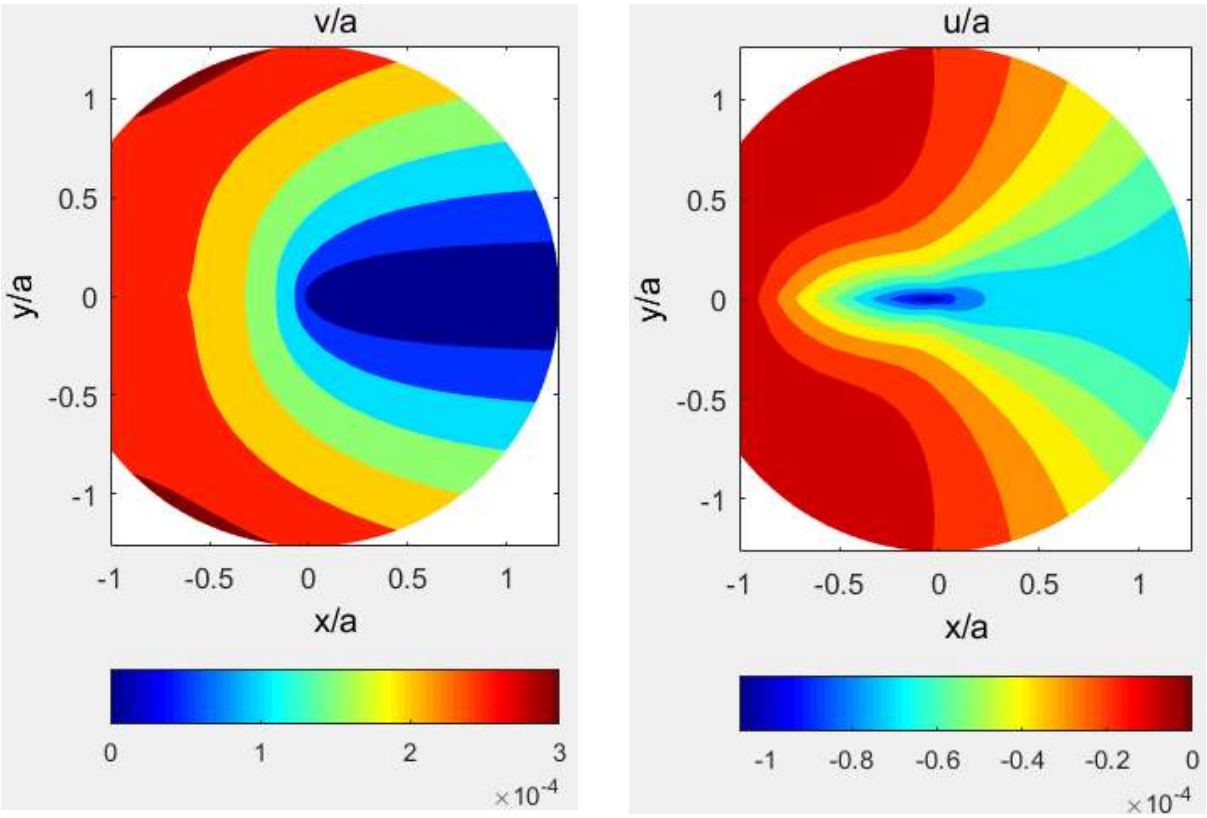

(a) (b)

Figure 8-16: Contours of (a) v/a and (b) u/a for plate-1 from hybrid-method (top half) using n_{FEA} = 2,076 FEM-predicted u-displacements, Laurent series expansion and k = 8 and from FEA (bottom half)

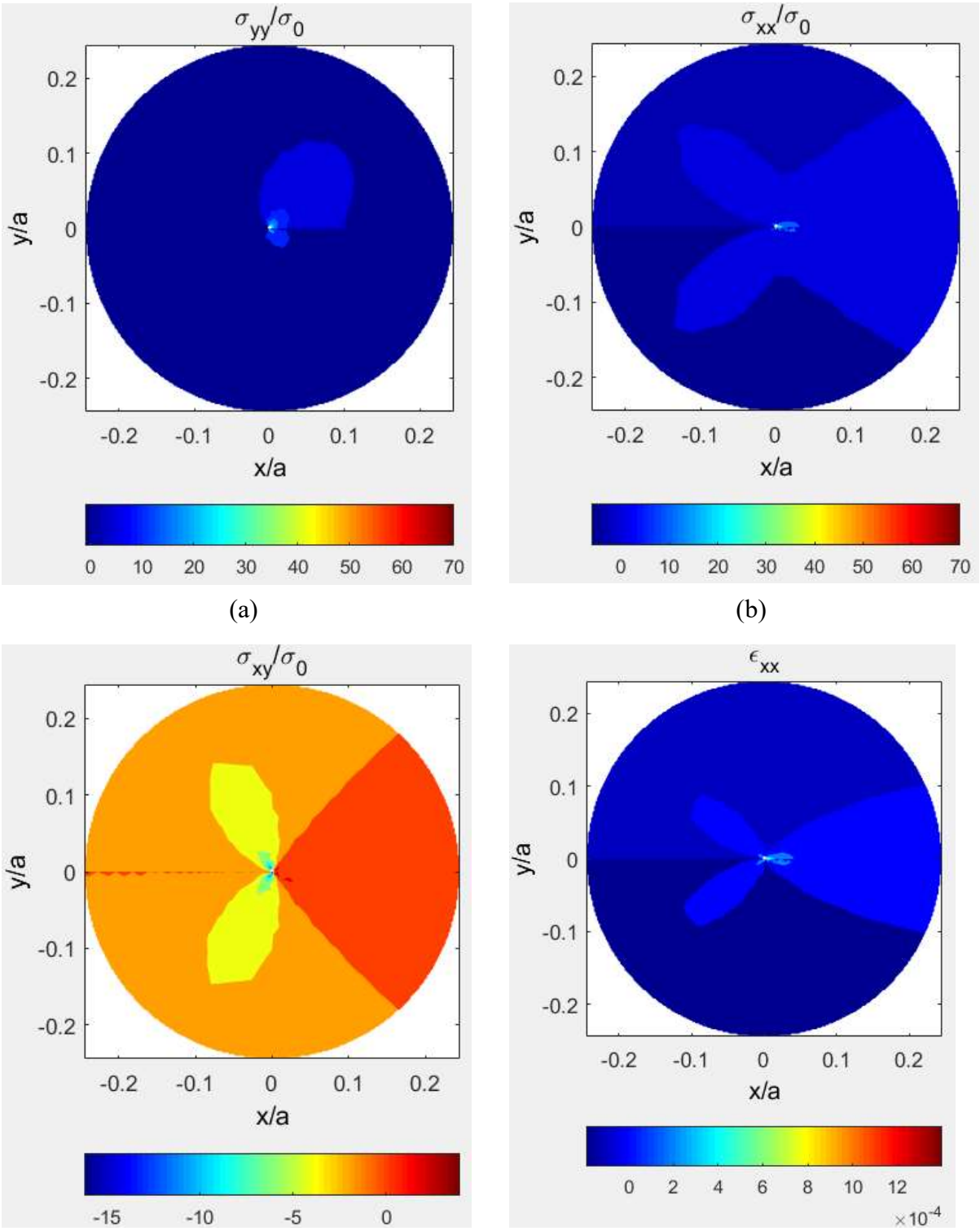

Figure 8-17: Contours of (a) σ_{yy}/σ_0, (b) σ_{xx}/σ_0, (c) σ_{xy}/σ_0 and (d) ε_{xx} for centrally-cracked plate-1 from hybrid-method (top half) using n_{FEA} = 2,076 FEM-predicted u-displacements, Laurent series and k = 8 and from FEA (bottom half)

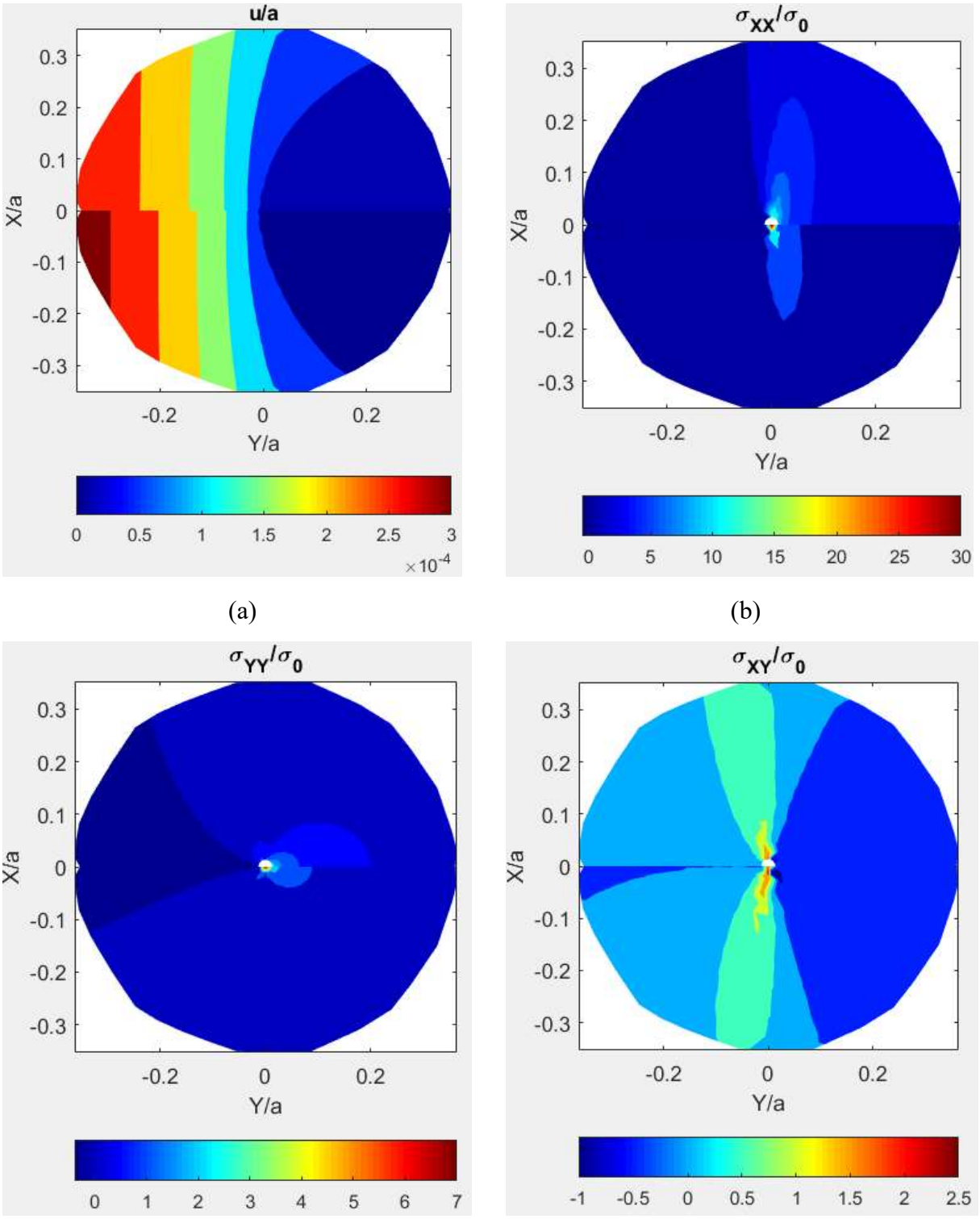

Figure 8-18: Contours of (a) u/a, (b) σ_{XX}/σ_0, (c) σ_{YY}/σ_0 and (d) σ_{XY}/σ_0 for SEC plate-2 from hybrid-method (top half) using n_{FEA}= 2 × 3,835 FEM-predicted u- and v-displacements, Laurent series and k = 8 and from FEA (bottom half)

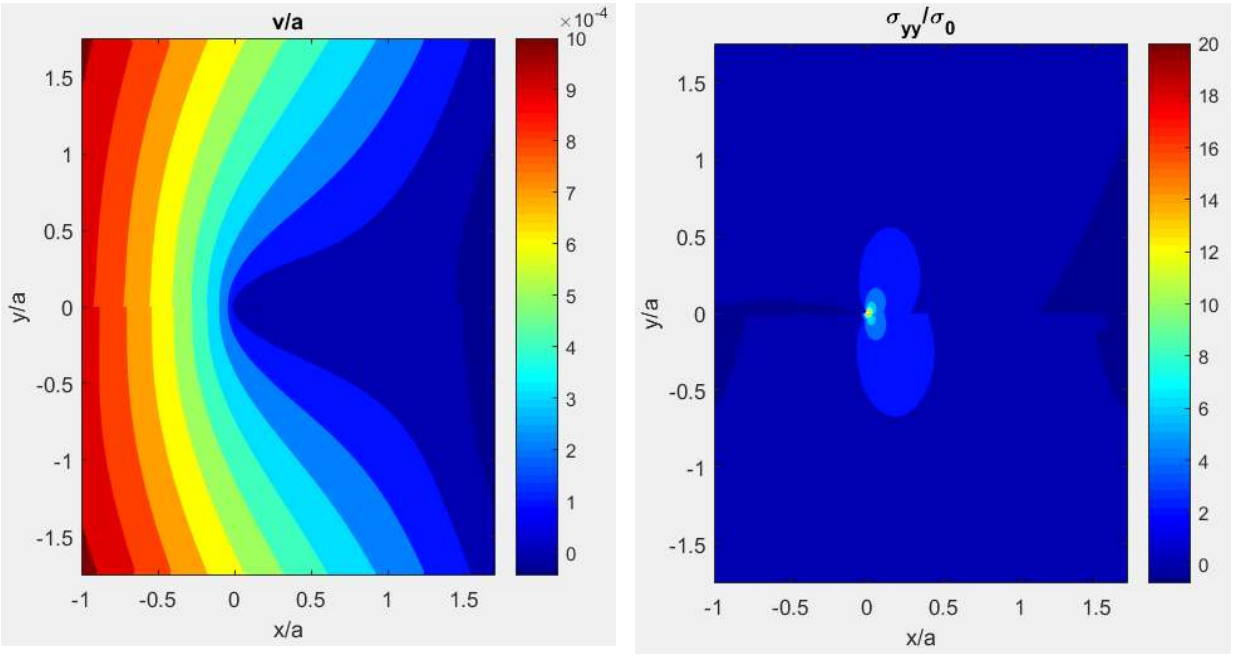

(a) (b)

Figure 8-19: Contours of (a) v/a and (b) σ_{yy}/σ_0 from hybrid-method (top half) for SEC plate-3 based on n_{FEA} = 3,499 FEM-predicted v-displacements, Taylor series and k = 5 and FEA (bottom half)

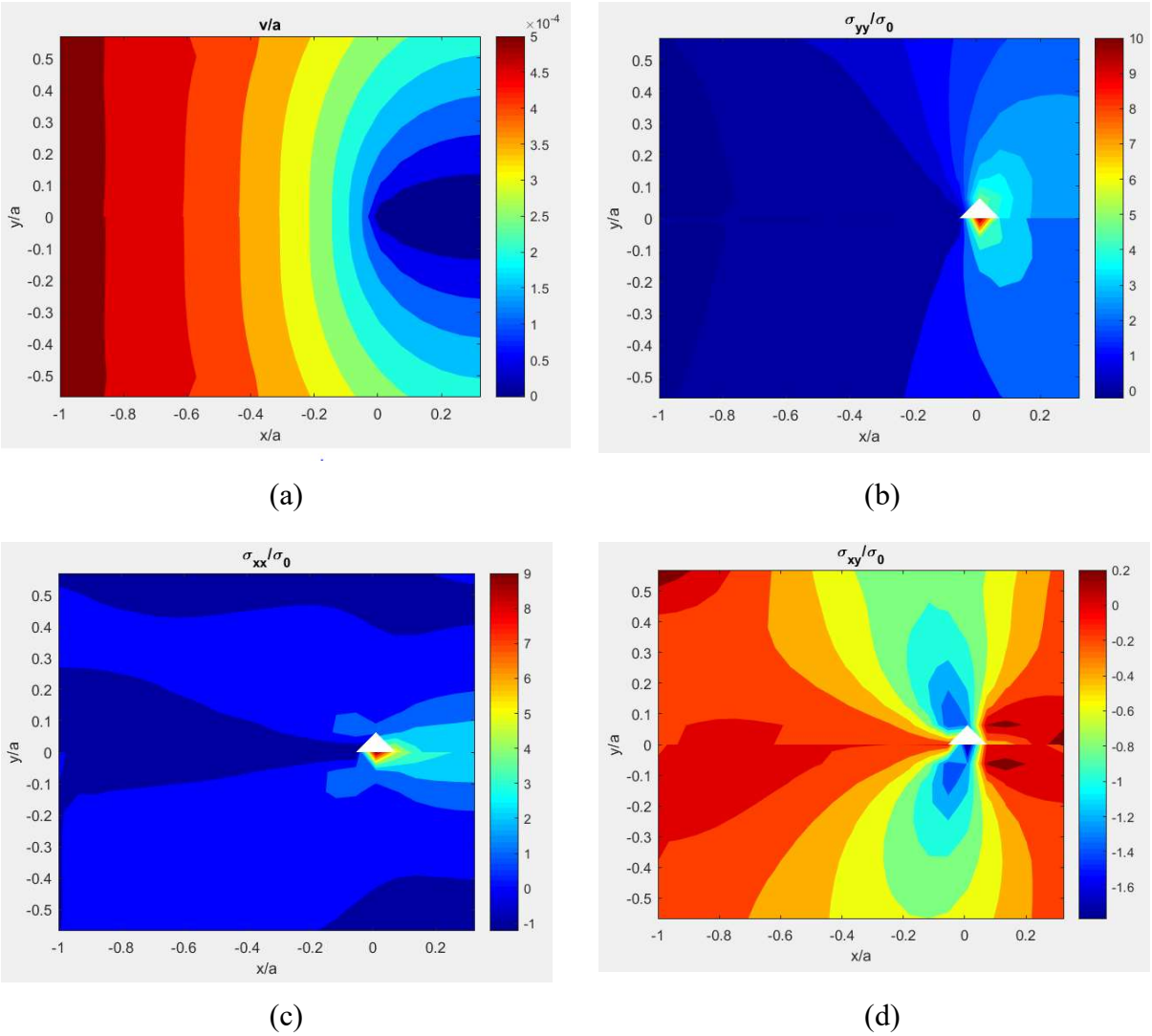

Figure 8-20: Contours of (a) v/a, (b) σ_{yy}/σ_0, (c) σ_{xx}/σ_0 and (d) σ_{xy}/σ_0 for DEC plate-4 from hybrid-method (top half) based on n_{FEA} = 2,277 FEM-predicted v-displacements, Taylor series and k = 10 and FEA (bottom half)

8.8.2. SIF Results

The SIFs for the four orthotropic plates are evaluated by processing the hybrid-method evaluated in-plane displacements and stresses with fracture analysis techniques available in the literature. For plate-1 the SIF is evaluated individually using the concept of *J*-integral (method-2) and Sih, Paris and Irwin concept (method-4), Table 8-6. The original results by Bowie and Freese [7] plus those by Saxce and Kang [131] and Lin et al. [77] are also provided in Table 8-6. The SIF evaluated by hybrid-method combined with the *J*-integral method or Sih, Paris and Irwin's concept exactly agree with those provided by Bowie and Freese [7], Saxce and Kang [131] and Lin et al. [77]. This validates the hybrid-method's ability to accurately evaluate the state of stress of a centrally-cracked orthotropic plate-1. That the hybrid result is independent of the *J*-integral path, d_{int}, or the distance from the crack-tip, r, for $r \ll a$ are also noticeable and significant.

Table 8-6: SIF results for plate-1 from hybrid-method and the literature

Distance from crack-tip, r or d_{int} =	Normalized SIF, $\frac{K_I}{\sigma_0\sqrt{\pi a}}$				
	Hybrid + *J*-integral with FEM v	Hybrid + Sih, Paris & Irwin's Method with FEM v	Bowie and Freese [7]	Saxce and Kang [131]	Lin et al. [77]
$0.1a$	1.0366	-			
$0.2a$	1.0367	1.040			
$0.3a$	1.0367	1.043	1.04	1.048	1.036
$0.5a$	1.0367	1.052			
$0.7a$	1.0368	1.067			

For plate-2 the SIF are obtained employing the Sih, Paris and Irwin's concept for varying distance, r, from the crack-tip using either a single displacement component or both the displacement components, Table 8-7 and Table 8-8, respectively. SIF results for plate-2 of Table 8-8 agree well with those originally provided by Mandell et al. [130] (hybrid-FEA supported by compliance tests) and later by Saxce and Kang [131] (hybrid-FEA). These results again demonstrate the reliability of the hybrid stress analysis method.

Table 8-7: SIF for plate-2 from hybrid-method (using only FEM-predicted u as input) and the literature

Distance from crack-tip, r =	Normalized SIF, $\frac{K_I}{\sigma_0\sqrt{\pi a}}$		
	Hybrid + Sih, Paris & Irwin's method and FEM v	Mandell at al. [130]	Saxce and Kang [131]
0.1a	1.751		
0.2a	1.645	1.768	1.758
0.3a	1.603		

Table 8-8: SIF for plate-2 from hybrid-method (using FEM-predicted both u and v as input) and the literature

Distance from crack-tip, r =	Normalized SIF, $\frac{K_I}{\sigma_0\sqrt{\pi a}}$		
	Hybrid + Sih, Paris & Irwin's method and FEM v and u	Mandell et al. [130]	Saxce and Kang [131]
$0.1a$	1.848	1.768	1.758
$0.2a$	1.842		
$0.3a$	1.838		
$0.5a$	1.838		
$0.7a$	1.866		

For plate-3 and -4 the SIFs are evaluated using the J-integral method, and the closed-form solutions provided by Bao et al. [93], Table 8-9. For plate-3 the obtained SIF results from the hybrid-method (with FEA predicted input) combined with the J-integral approach and directly from Bao's closed-form solutions are compared with that originally evaluated by Mogadpalli and Parameswaran [17]. The SIF results show good agreement, especially between those from the hybrid-method and Mogadpalli and Parameswaran. K_I for plate-3 was also obtained using the closed-form solution provided by Shukla et al., i.e., using equations (8-93) and (8-94), Table 8-9. For the similar DEC plate-4 the SIF obtained from hybrid-method results processed by J-integral agree well with that estimated by Bao's method.

Table 8-9: SIF results for SEC plate-3 and similar DEC plate-4

Plate type	$K_I/\sigma_0\sqrt{a}$ from			
	Hybrid and *J*-integral using FEM-predicted *v*-displacements	Bao et al. [93]	Directly from Mogadpalli and Parameswaran [17]	Shukla et al. [16]
SEC (Plate-3)	3.77	3.99 (K_I = 1.2 MPa.√m)	3.65 (K_I = 1.1 MPa.√m)	3.46
DEC (Plate-4)	2.90	2.75 (K_I = 0.82 MPa.√m)	-	-

8.8.3. Khalil's Fracture Analysis Method

Plate-1 was analyzed according to Khalil's method [118] by using FEA-predicted *v*-displacement (Figure 8-21) or all the in-plane displacements and stresses (Figure 8-22). Plate-2 was analyzed according to this method using only FEA-predicted *v*-displacement, Figure 8-23. The somewhat poor match (plate-1) between the FEA-provided and Khalil's method reconstructed displacement *v* of Figure 8-21(a), is what motivated further analyzing the plate utilizing FEA predicted all displacement and stress information, Figure 8-22.

The RMS plots of Figure 8-13 and Figure 8-15 for plate-1 suggested using $\gamma_{2N} \geq 16$ and $\gamma_{2N} \geq 8$, respectively, in the summation series for the respective analyses. The plots of the normalized SIF of Figure 8-24 and Figure 8-25 of plate-1 show that after $\gamma_{2N} = 10$ (Figure 8-24) and $\gamma_{2N} = 8$ (Figure 8-25) the evaluated K_I are reasonably constant. For second analysis of plate-1 the evaluated SIFs after $\gamma_{2N} = 8$ up to $\gamma_{2N} = 30$, changes within 1.22 % - 4.34 %, Figure 8-25 and Table 8-10. For

the first analysis of plate-1, $\gamma_{2N} = 16$ (Figure 8-21) and for the second analysis $\gamma_{2N} = 8$ (Figure 8-22) were used.

For plate-2 the RMS plot (Figure 8-14) suggests using $\gamma_{2N} \geq 36$ whereas the plot of normalized K_I for varying γ_{2N} in Figure 8-26 and Table 8-11 shows little difference between the evaluated SIF for $\gamma_{2N} = 28$ to 50. The stress analysis (Figure 8-23) was conducted for $\gamma_{2N} = 36$.

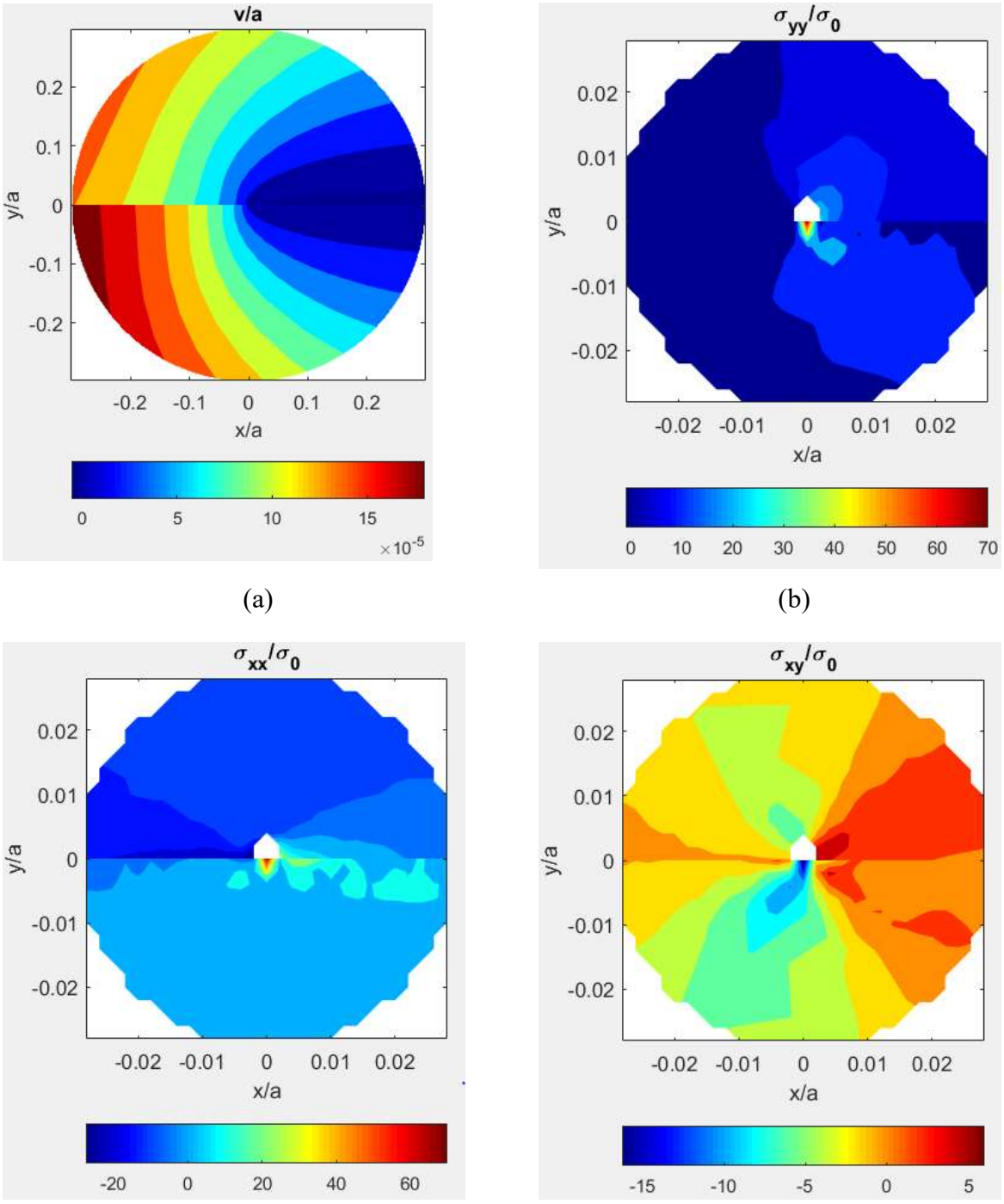

Figure 8-21: Contours of (a) v/a, (b) σ_{yy}/σ_0, (c) σ_{xx}/σ_0 and (d) σ_{xy}/σ_0 for plate-1 from Khalil's concept (top half) using n_{FEA} = 2,031 FEM-predicted v-displacements and γ_{2N} = 16 and from FEA (bottom half)

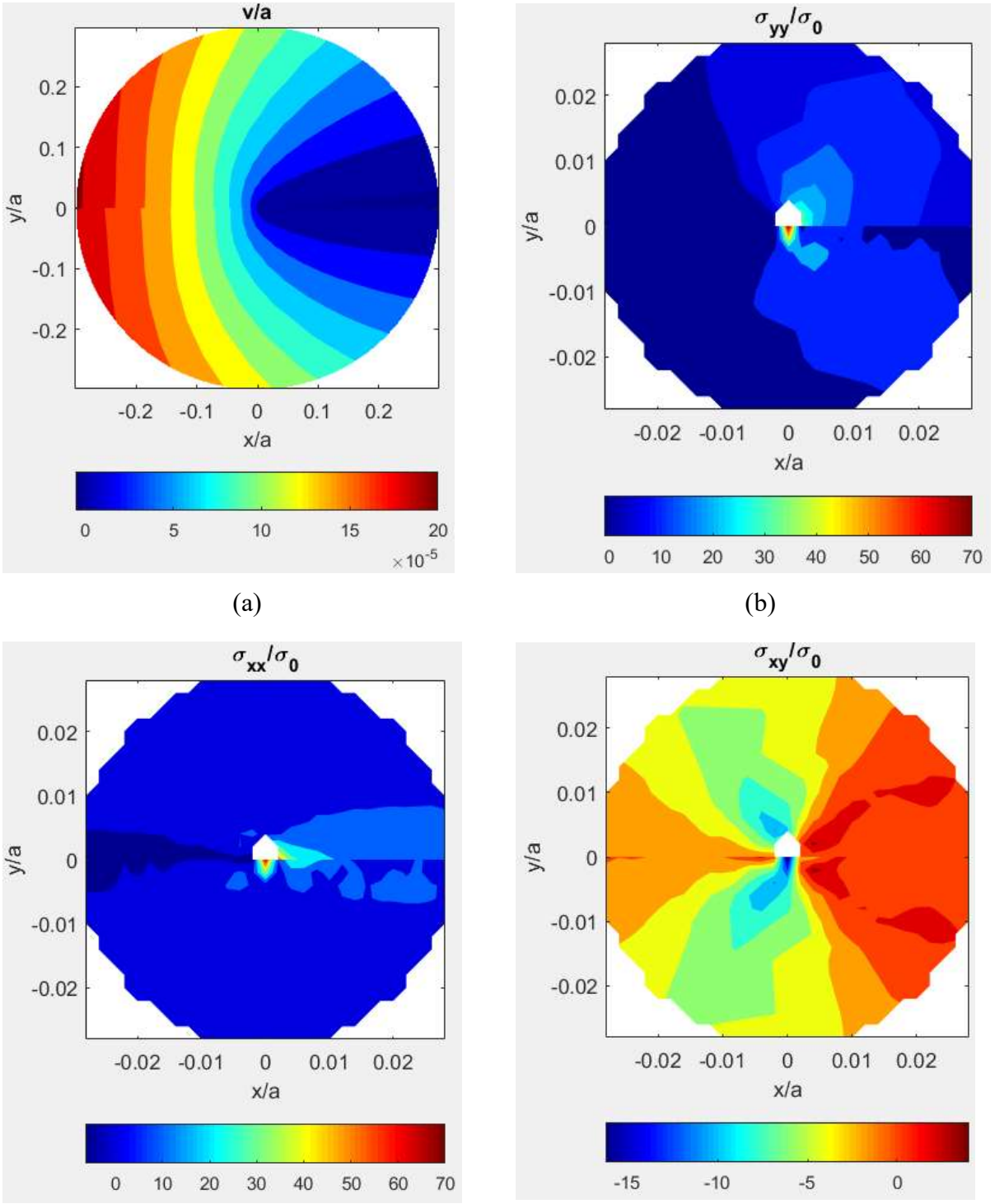

Figure 8-22: Contours of (a) v/a, (b) σ_{yy}/σ_0, (c) σ_{xx}/σ_0 and (d) σ_{xy}/σ_0 for plate-1 from Khalil's concept (top half) using $n_{FEA} = 5 \times 2{,}031$ u, v, σ_{xx}, σ_{yy} and σ_{xy} FEM-predicted displacements and stresses and $\gamma_{2N} = 8$ and from direct FEA (bottom half)

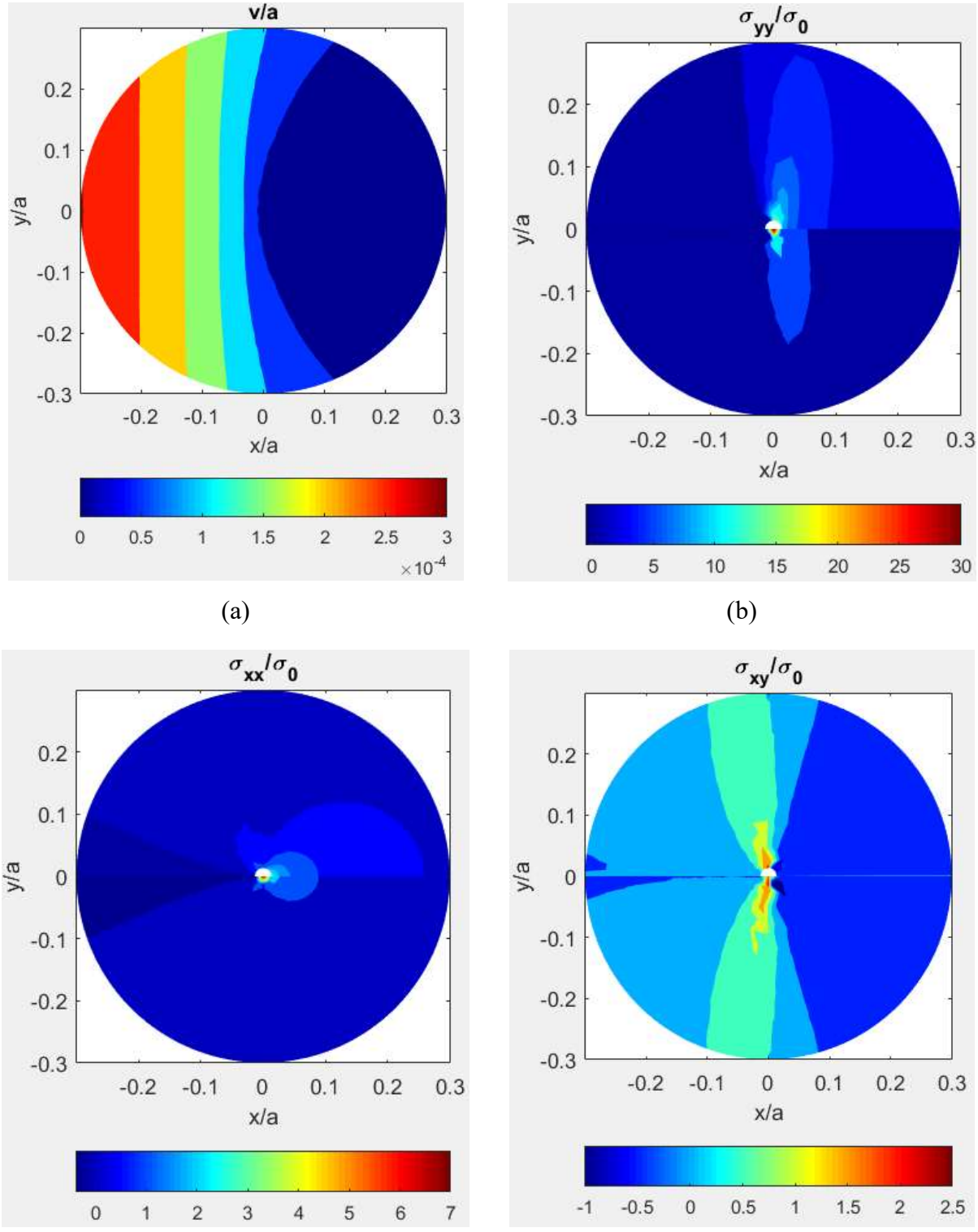

Figure 8-23: Contours of (a) v/a, (b) σ_{yy}/σ_0, (c) σ_{xx}/σ_0 and (d) σ_{xy}/σ_0 for plate-2 from Khalil's concept (top half) using n_{FEA} = 2,858 FEM-predicted v-displacements and γ_{2N} = 36 and from direct FEA (bottom half)

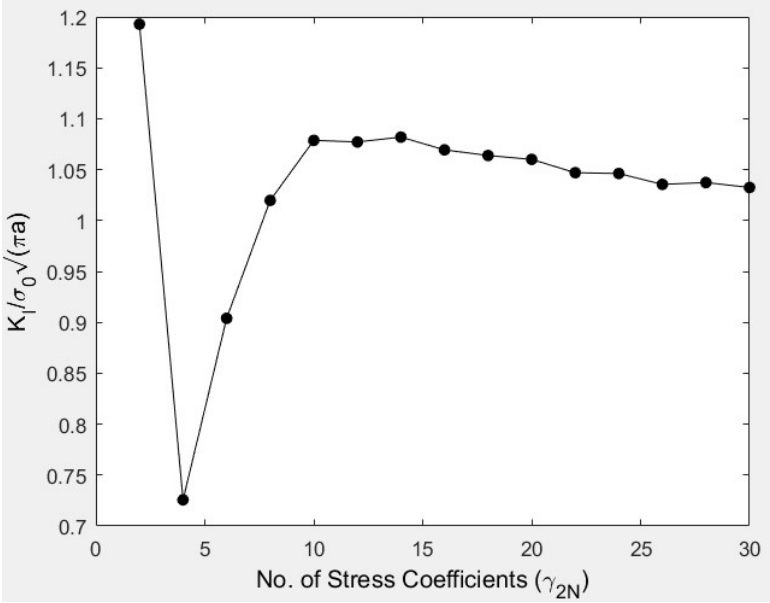

Figure 8-24: Effect of number of stress coefficients, γ_{2N}, utilized on the evaluated SIF for plate-1 from Khalil's concept using FEM-predicted *v*-displacements as input

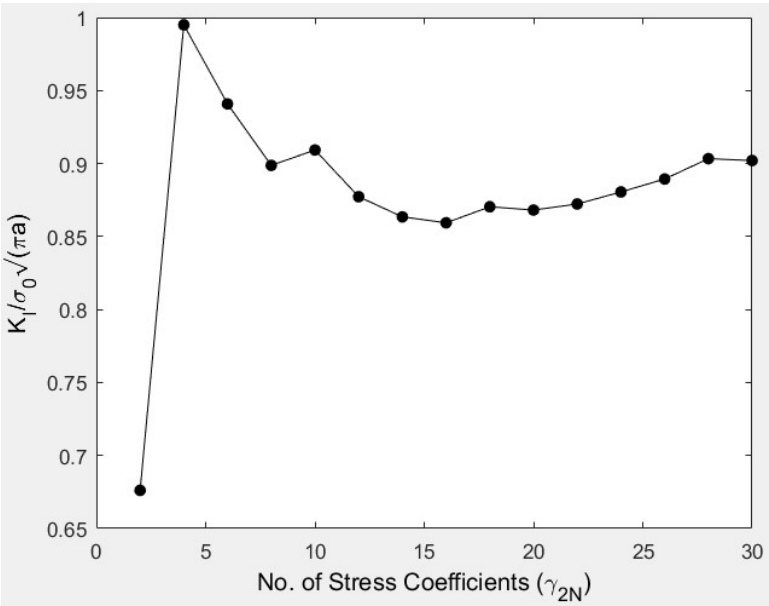

Figure 8-25: Effect of number of stress coefficients, γ_{2N}, utilized on the evaluated SIF for plate-1 from Khalil's concept using FEM-predicted displacements and stresses *u*, *v*, σ_{xx}, σ_{yy} and σ_{xy} as input

Table 8-10: Effect of number of employed stress coefficients on the evaluated SIF for plate-1 from Khalil's method using FEM-predicted v or u, v, σ_{xx}, σ_{yy} and σ_{xy} as input

No. of stress coefficients, γ_{2N}	Normalized SIF, $\frac{K_I}{\sigma_0\sqrt{\pi a}}$ for input of	
	FEM v	FEM u, v, σ_{xx}, σ_{yy} and σ_{xy}
8	1.02	0.899
10	1.08	0.91
16	1.07	0.86
20	1.06	0.87
30	1.03	0.90

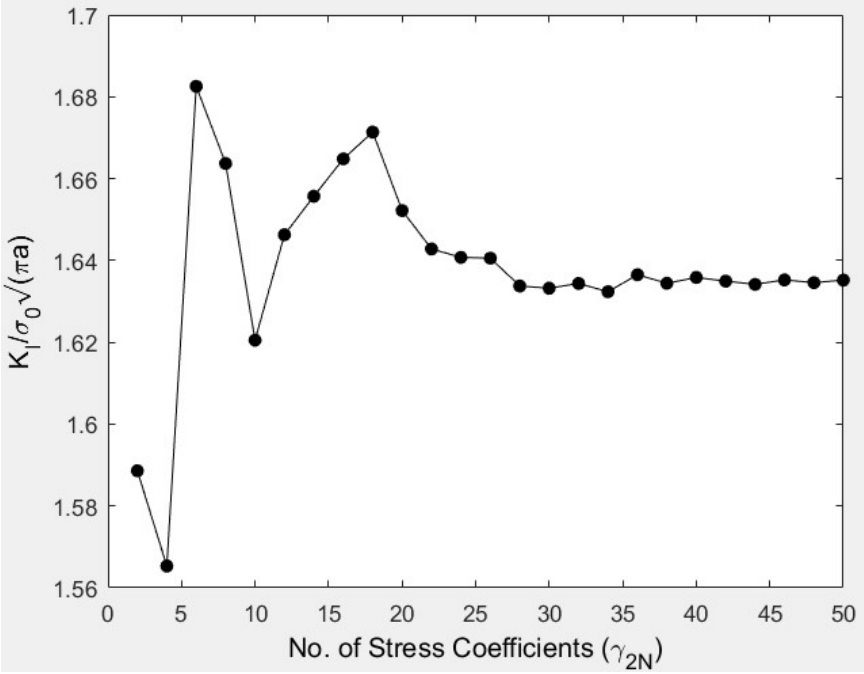

Figure 8-26: Effect of number of stress coefficients, γ_{2N}, utilized on the evaluated SIF for plate-2 from Khalil's concept using n_{FEA} = 2,858 FEM-predicted v-displacements

Table 8-11: Effect of number of employed stress coefficients on the evaluated SIF for plate-2 from Khalil's method using FEM-predicted *v*-displacements as input

No. of stress coefficients, γ_{2N}	Normalized SIF, $\frac{K_I}{\sigma_0\sqrt{\pi a}}$
28	1.6338
32	1.6344
36	1.6365
40	1.6358
44	1.6342
48	1.6346
50	1.6352

Results demonstrate that when working with the Khalil's method to stress analyze a plate, it is typically insufficient to employ only a single component of measured displacement as input, Figure 8-21. More input information is required to better predict the overall behavior of the loaded plate, Figure 8-22. A higher number of stress coefficients is also required when using only a single component of measured information, i.e., $\gamma_{2N} = 16$ (Figure 8-13) in Khalil's method compared to $k = 8$ (Figure 8-10) in hybrid-method for plate-1 when employing a single component of measured displacement to stress analyze the plate. The present hybrid-method (i.e., combining measured information with analytical expression) does not experience these limitations and can very easily predict the behavior of an orthotropic cracked plate using only a single component of measured displacement and by utilizing only a few Airy stress coefficients.

8.8.4. Results for Single-Edge Crack Orthotropic Plate

Table 8-12 compares the SIF obtained for plate-2 using results from various crack analysis studies with the plate available in literature, directly from Khalil's method [118] and from the hybrid-method coupled with Sih, Paris and Irwin's [122] fracture analysis method using FEA v- or both v- and u-displacement data. Also the SIF of the plate is obtained from the closed-form solutions provided by Bao et al. [93] and Shukla et al. [16] to find K_I in single-edge cracked orthotropic plate, i.e., using equations (8-89) through (8-92) and equations (8-93) and (8-94), respectively, Table 8-12.

All of these analyses are for the same orthotropic plate (Plate-2 details provided in Table 8-1 and Table 8-2) with a single-edge crack either from the various cited papers or which are evaluated by the author using FEM data for the various crack analyses techniques mentioned in this chapter.

Table 8-12: Comparison of SIF for plate-2 from various present methods and the literature

Methods used to evaluate SIF	$\frac{K_{\mathrm{I}}}{\sigma_0\sqrt{\pi a}}$
Hybrid-method (with FEM-predicted displacements in the loading direction as input and Laurent series expansion) plus Sih, Paris and Irwin's concept	1.67 (from analysis using FEM single displacement component in hybrid-method coupled with Sih, Paris and Irwin's approach)
Hybrid-method (with FEM-predicted both displacement components as input and Laurent series expansion) plus Sih, Paris and Irwin's concept	1.74 (from analysis using FEM both displacement components in hybrid-method coupled with Sih, Paris and Irwin's approach)
Khalil's method (with FEM-predicted displacements in loading direction as input)	1.63 (from analysis using FEM single displacement component in Khalil's method)
Mandell et al. [130]	1.79 (done by Mandell et al.)
Saxe and Kang [131]	1.78 (done by Saxce and Kang)
Lin et al. [77] (FEA-simulated isopachic stresses as input and Taylor series expansion)	1.70 (done by Lin et al. using S^* in hybrid-method and *J*-integral)
Bao et al. [93]	1.49 (using Bao's equations)
Shukla et al. [16]	1.66 (using Shukla's closed form equations)

8.9. Complex Variables Hybrid-Method and Concept of *J*-Integral in Isotropic Fracture Analysis

The ability of the displacement-based complex variables hybrid-method combined with the concepts of *J*-integral to fracture analyze isotropic plates containing cracks were investigated, Appendix O. FEA-determined displacements in the loading direction, *v*, were employed for an orthotropic plate with a very low degree of anisotropy (plate's material properties were close to isotropy) and a steel plate. Both plates had double-edge cracks. *J*-integral values obtained by post-processing the hybrid-method evaluated results were compared with those obtained from ANSYS APDL built-in command 'CINT' to calculate *J*-integral from linear fracture analysis of members made of isotropic materials, Appendix O. The study demonstrates the hybrid-method's ability to reliably fracture analyze isotropic plates containing cracks. The effect of the hybrid-method selected input data source locations on the evaluated hybrid results were also studied, Appendix P.

8.10. Summary, Discussion and Conclusions

This chapter demonstrates that processing a single component of displacement information with a combination of Airy stress functions, conformal mapping, analytic continuation, power-series expansion and least squares provides a hybrid means of stress/displacement analyzing of orthotropic members containing cracks. Subsequently processing the hybrid-method evaluated stress or displacement information in the neighborhood of the crack with fracture mechanics concepts provides an accurate value of the structure's SIF. Present results show the SIF can be accurately evaluated based on measured input data either at locations close to the crack-tip, i.e., *r*

or d_{int} = 0.1a; to at locations considerably away from the crack-tip, i.e., r or d_{int} = 0.7a. This demonstrates the method's independence on the near crack measured information and on the integration path. This has practical significance. Most of the provided SIFs are obtained utilizing only a single component of measured information. No symmetry or finite boundary conditions are required. Measured input information is not needed close to the crack-tip or crack surface. No knowledge of the external loading or boundary conditions is needed. The method can effectively analyze plates of any type (finite or infinite) with any type of cracks (SEC/CC/DEC) and of any material properties (isotropic or orthotropic with any degree of anisotropy).

The concept of the hybrid-method is established on strong mechanics-based algorithms. Along with the traction-free boundary conditions, the singular stress fields near the crack-tip are satisfied by the conformal mapping. The Airy stress functions satisfies equilibrium and compatibility. Displacement information is not differentiated by arbitrary numerical schemes which lack the required accuracy and reliability. Combining the hybrid concept with reliable fracture mechanics theory is an effective and reliable way to stress analyze cracked orthotropic structures. Reliability of the concept depends on the accuracy of the hybrid-method evaluated (stress, displacement) results. Once the states of stress and displacement are known, finding important fracture parameters such as the SIF involves only post-processing the evaluated hybrid-method results according to a fracture mechanics theory. Employing the Taylor series in the stress functions provides superior flexibility in analyzing any type of cracks located anywhere at any orientation utilizing a single mapping function. It is expected that employing mapping techniques such as the Schwarz-Christoffel mapping will enable the present technique to analyze more complicated crack shapes.

Chapter 9. Experimental Determination of Stress Intensity Factor of a Finite Orthotropic Plate with Double-Edge Cracks

9.1. Introduction

This method demonstrates the ability to find the stress intensity factor (SIF) in loaded, finite, orthotropic composite plate from a digital image correlation (DIC) provided single-displacement field. Combining experimental-analytical stress analysis with concepts such as reasonably-distant crack-tip stress/displacement fields or *J*-integral, the SIF of a double-edge cracked (DEC) loaded, finite-width, orthotropic plate is determined experimentally. Stress/strain/displacement information near the crack-tip are obtained by processing measured displacement data with complex variables Airy stress functions, conformal mapping, analytic continuation and numerical methods. Using the known stress and displacement fields in expressions for displacement/stress singular fields or closed form integrals such as the *J*-integrals, the SIF can be determined from a single measured information without knowing the external loading. Requiring neither knowledge of the external loading nor use of any hybrid-FEA tools nor depending on experimental information very near the crack-tip are some of the advantages of this technique over other crack analysis approaches available in literature.

9.2. General Overview

The experimental-analytical hybrid means of stress analysis, i.e., processing measured information with analytical expressions of Airy stress functions, conformal mapping, analytic continuation, power-series expansion and numerical methods such as least squares is expanded here to stress analyze, with distant measured data, orthotropic, finite-width, loaded, components involving cracks. The challenges in obtaining reliable experimental data near crack-tips motivated developing this method to stress analyze fracture problems in orthotropic members. Knowing the near-crack displacement/stress/strain fields from this hybrid stress analysis method, a variety of concepts can be used to evaluate stress intensity factors (SIFs). The method provides for any degree of anisotropy, any types of cracks (i.e., central, edge-, double-edge or inclined) or any plate-width to crack ratios. It is thus capable of analyzing a wide range of fracture-type problems in orthotropic plates under plane-stress condition. Not requiring knowing the external loading is an additional advantage of this method.

Digital image correlation (DIC) recorded single-displacement field was used to stress analyze a finite-width, graphite-epoxy orthotropic plate with double-edge cracks (DEC), Figure 9-1. As situations can occur where there is a paucity or poor quality, of either of the measured displacements, the present use of a single in-plane displacement field away from the crack-tip is advantageous. Recording reliable information reasonably near a crack-tip is a challenge for virtually any purely experimental technique.

Chapter 5 demonstrate this hybrid stress analysis method's capability in providing reliable results for elliptically-perforated finite-width plates with the ellipse size to plate-width ratio, $2a/W$, up to 0.85 ~ 0.9. For the current DEC-plate (Figure 9-1), the ratio of $2a/W$ is 0.6.

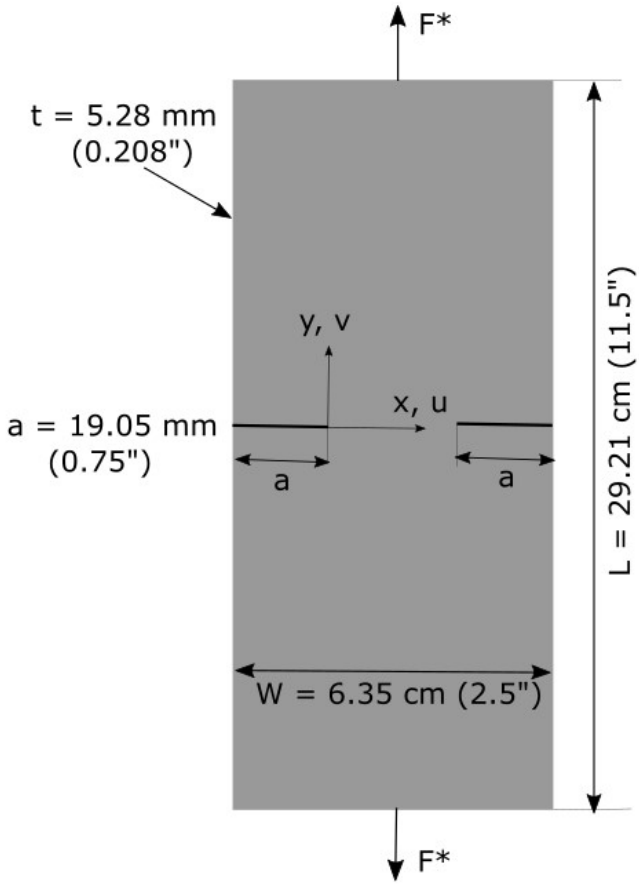

Figure 9-1: DEC finite-width, orthotropic plate

9.3. Literature Review

While the literature contains numerous experimental determinations of stress intensity factors in isotropic materials, there are comparatively few applications of experimental techniques to fracture in composites. Bowie and Freese [7] used conformal mapping along with modified boundary collocation method to evaluate the SIF in orthotropic, finite plates with central cracks. Tong et al. used conformal mapping in their developed super element for the hybrid-finite element analysis to determine SIF in isotropic materials having plane cracks [128]. Later Tong [21] expanded the concept to handle cracks in anisotropic materials. Khalil et al. [118] in their developed hybrid-finite element method, further modified Tong's [21] approach to incorporate

cracks inclined to the materials axes of symmetry. References [22,77,136–139] combined stress-induced temperature information with a variety of analytical/numerical tools to evaluate the SIFs associated with opening- or mixed-mode cracks in composite members. Lin et al. [77], without requiring the use of any super elements, directly determined the SIF in finite, orthotropic materials using FEA-simulated thermoelastic data in expressions of Airy stress functions and *J*-integrals. They analyzed a centrally-cracked aluminum plate from measured thermal data. Ju [139] and Ju and Rowlands [137] employed concepts from Khalil et al. [118] to thermoelastically determine K_I and K_{II} associated with inclined cracks in tensile composites. Rhee and Rowlands [22] obtained K_I for a central crack in a tensile glass-epoxy laminate by evaluating the associated stress functions from recorded thermoelastic data around the external boundary of a subregion containing the crack. He and Rowlands [136] again determined K_I for a central crack in a composite by evaluating the associated stress functions from recorded temperature information away from the crack. However, unlike Rhee's [22] subregion concept, they employed decomposed stress functions. Shukla et al. [16] determined K_I in a single-edge notched glass-epoxy composite from a strain-gage which was appropriately positioned and orientated relative to the crack. References [17] and [164] applied DIC to fracture-type problems involving orthotropic materials. Mogadpalli and Parameswaran [17] used DIC-measured displacement data in expressions for near crack-tip displacement fields to find the SIF of a single-edge cracked orthotropic plate. Pataky et al. [164] measured stress intensity factors in anisotropic single-crystal stainless steel. These methods faced some difficulties. The study done by Shukla et al. [16] required knowing a priori through complex algebraic calculations where to place the strain-gages. That by Mogadpalli and Parameswaran [17] suffered from difficulties associated with the correlation technique and analysis was sensitive to rigid body motion. Liu et al. [143] evaluated K_I for a crack extending vertically upward from the

bottom edge of a composite beam subjected to four-point bending. Dai et al. [145] studied the deformation and fracture behavior associated with an opening-mode single-edge crack in a tensile glass-reinforced composite by digital speckle correlation. By evaluating the *J*-integral from recording both in-plane displacement components using interferometric moiré, Perry and McKelvie [147] obtained the energy release rate in a cantilevered composite beam.

Although SIFs have been determined in several different finite composite structures from recorded thermoelastic information [22,77,136–138], that the technique necessitates cyclically loading the member renders the approach impractical for many engineering applications. Unlike the present approach, TSA is also not particularly suitable outside of a laboratory environment.

Huang and Kardomateas [179] analytically determined the SIFs for single- and double-edge cracks in infinite orthotropic plates, whereas Joshi and Manepatil [129] employed boundary collocation to demonstrate the effects of variations in principal material directions and crack length on SIFs for inclined and/or eccentric cracks in finite orthotropic plates. Employing FEA, References [130,131] analyzed centrally, single- and double-edge cracked finite orthotropic plates. Saxce and Kang [131] employed mongrel displacement FEA whereas numerically predicted SIF of Mandell et al. [130] was supported by compliance tests. Abdullah [132] compared the stress distributions in finite isotropic and orthotropic tensile plates containing a mode-I central crack. Kim [146] numerically determined the SIFs in single- and doubled-edged finite composites using a path-independent integral which involves the tractions and displacements on a contour surrounding the crack.

Bao et al. [93] provided closed-form solutions to find SIF in orthotropic materials by incorporating the material orthotropy with fracture equations for isotropic materials. The method

lacks guidance regarding the direction of material orthotropy with respect to the crack-face and has some limitations regarding its validity relative to certain orthotropic material properties. Bažant et al. [180] also conducted similar studies.

The author is unaware of any previous experimentally-determined SIF in a DEC, finite-width, orthotropic composite plate by utilizing only a single component of measured displacement.

9.4. Analytical Analyses

9.4.1. Stresses, Strains and Displacements

For an orthotropic plate under plane-stress containing a traction-free crack located at $y \rightarrow 0$ and $x \leq 0$, the following mapping function maps a section of the real axis of the ζ-plane, Γ_ζ, from the R_ζ region into the traction-free boundaries, Γ_z, of the region R_z surrounding the crack surface in the physical z-plane, Figure 9-2 [21,77]

$$z_j = \omega_j(\zeta_j) = -\zeta_j^2, \qquad j = 1, 2 \tag{9-1}$$

where

$$z_j = x + \mu_j y, \qquad -\pi < Arg(z_j) \leq \pi, \qquad \zeta_j = \xi + \mu_j \eta, \qquad j = 1, 2 \tag{9-2}$$

Knowing the orthotropic plate's constitutive elastic properties, the complex material properties, μ_j, are obtained from the roots of equation (2-17) (general expression) or (2-20) (especially for plate

of Figure 9-1). For the orthotropic plate under current consideration, the *y*-axis is perpendicular to the crack-face as shown in Figure 9-1.

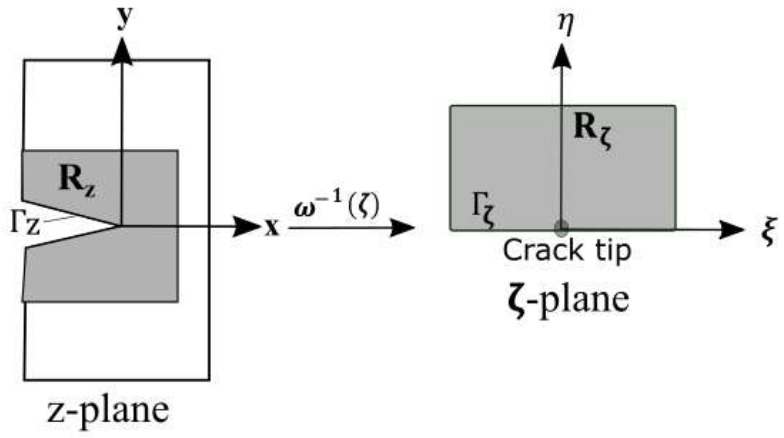

Figure 9-2: Conformal mapping of edge crack of a loaded orthotropic plate from *z*-plane to half-plane in ζ-plane

The inverse of the mapping function of equation (9-1) is

$$\zeta_j = \omega_j^{-1}(z_j) = i\sqrt{z_j}\,, \qquad j = 1, 2 \tag{9-3}$$

where $i = \sqrt{-1}$ and the branch of the square root of the above equation (9-3) is chosen so that $Im\zeta_j \geq 0$ for $j = 1, 2$.

For orthotropic members in absence of body forces and rigid body motions, and knowing the constitutive elastic properties, the in-plane components of stresses (of equations (2-25) through (2-27)) and displacements (of equations (2-31) and (2-32)) in the rectangular coordinates (x, y) of the physical plane, $z_j = x + \mu_j y$, for $j = 1, 2$, can be expressed using two complex Airy stress functions $\Phi(z_1)$ and $\Psi(z_2)$. Further, the concept of analytic continuation of equation (2-49) enables

these two complex Airy stress functions to be expressed in terms of each other while continuously satisfying the traction-free boundary conditions along the crack surface, Γ_z. The single stress function is further expressed using a truncated power-series expansion. For this analysis the stress functions are expressed using a finite Taylor series expansion as [21]

$$\Phi(\zeta_1) = -\sum_{j=1}^{N} ic_j\zeta_1^j \tag{9-4}$$

and

$$\Psi(\zeta_2) = -\sum_{j=1}^{N} i\left(-\bar{c}_jB + c_jC\right)\zeta_2^j \tag{9-5}$$

where the Airy coefficients, c_j, are complex numbers, i.e., $c_j = a_j + ib_j$, and a_j and b_j are real numbers. $\bar{c}_j$ are the complex conjugate of c_j. For the finite simply connected region R_ζ, the stress functions, $\Phi(\zeta_1)$ and $\Psi(\zeta_2)$, are single valued analytic functions. The complex quantities B and C are defined in equations (2-50) and (2-51).

The derivatives of the stress functions being analytic functions of ζ_1 and ζ_2, respectively, and re-writing equations (2-41) and (2-42), one obtains

$$\Phi'(z_1) = \frac{\Phi'(\zeta_1)}{\omega_1'(\zeta_1)} \quad \text{and} \quad \Psi'(z_2) = \frac{\Psi'(\zeta_2)}{\omega_2'(\zeta_2)} \tag{9-6}$$

The expression for the stress components of equations (2-25) through (2-27) requires the derivatives of the stress functions with respect to the complex variables z_j for $j = 1, 2$. Thus, according to equation (9-6), to express the stress components in terms of the complex stress functions requires the differentiation of both the mapping functions and the stress functions with respect to the complex variables ζ_j for $j = 1, 2$. Differentiating the mapping functions of equation (9-1) with respect to the complex variables ζ_j and differentiating equations (9-4) and (9-5) with respect to the complex variables ζ_j, the following equations (9-7) and (9-8) - (9-9) are obtained, respectively.

$$\omega_j'(\zeta_j) = -2\zeta_j, \qquad j = 1, 2 \tag{9-7}$$

and

$$\Phi'(\zeta_1) = -\sum_{j=1}^{N} ijc_j\zeta_1^{j-1} \tag{9-8}$$

$$\Psi'(\zeta_2) = -\sum_{j=1}^{N} ij\left(-\bar{c}_j B + c_j C\right)\zeta_2^{j-1} \tag{9-9}$$

Using the Taylor series to express the stress functions, the in-plane displacement and stress components are obtained by combining equations (9-4) and (9-5) with equations (2-31) and (2-32) or equations (2-47) and (2-48), and equations (9-7) through (9-9) with equations (2-44) through (2-46), respectively, as

$$u = 2\sum_{j=1}^{N} Re\{-i[p_1(\zeta_1)^j + p_2C(\zeta_2)^j]c_j + i[p_2B(\zeta_2)^j]\bar{c}_j\} \tag{9-10}$$

$$v = 2\sum_{j=1}^{N} Re\{-i[q_1(\zeta_1)^j + q_2C(\zeta_2)^j]c_j + i[q_2B(\zeta_2)^j]\bar{c}_j\} \tag{9-11}$$

$$\sigma_{xx} = \sum_{j=1}^{N} Re\{i(j\mu_1^2\zeta_1^{j-2} + j\mu_2^2C\zeta_2^{j-2})c_j - i(j\mu_2^2B\zeta_2^{j-2})\bar{c}_j\} \tag{9-12}$$

$$\sigma_{yy} = \sum_{j=1}^{N} Re\{i(j\zeta_1^{j-2} + jC\zeta_2^{j-2})c_j - i(jB\zeta_2^{j-2})\bar{c}_j\} \tag{9-13}$$

$$\sigma_{xy} = -\sum_{j=1}^{N} Re\{i(j\mu_1\zeta_1^{j-2} + j\mu_2C\zeta_2^{j-2})c_j - i(j\mu_2B\zeta_2^{j-2})\bar{c}_j\} \tag{9-14}$$

$$\begin{Bmatrix}\varepsilon_{xx}\\ \varepsilon_{yy}\\ \gamma_{xy}\end{Bmatrix} = \begin{bmatrix}a_{1'1'} & a_{1'2'} & 0\\ a_{2'1'} & a_{2'2'} & 0\\ 0 & 0 & a_{6'6'}\end{bmatrix}\begin{Bmatrix}\sigma_{xx}\\ \sigma_{yy}\\ \sigma_{xy}\end{Bmatrix} \tag{9-15}$$

where $a_{i'j'}$ are the elastic compliances and are defined below for the coordinate system shown in Figure 9-1

$$a_{1'1'} = \frac{1}{E_{22}}, a_{1'2'} = \frac{-\nu_{12}}{E_{11}} = \frac{-\nu_{21}}{E_{22}}, a_{2'2'} = \frac{1}{E_{11}} \text{ and } a_{6'6'} = \frac{1}{G_{12}} \tag{9-16}$$

Directions 1' and 2' are parallel and perpendicular to the crack-face and directions 1 and 2 are along and transverse to the strong/stiff orthotropic material directions, respectively. For the graphite-epoxy orthotropic plate of interest direction, y is along the strong/stiff orthotropic direction 1.

Once the in-plane stresses are known from equations (9-12) through (9-14), using those in equation (9-15), the stresses are transformed to strains. To find the complete state of stress of a member containing crack using the present analytical approach (finding in-plane displacements, stresses and strains from equations (9-10) through (9-15)), the only unknowns that needs to be found are the Airy stress coefficients, c_j. The presently defined DIC-hybrid method utilizes DIC-measured displacement data either in equation (9-10) or (9-11) and numerical techniques to evaluate the unknown Airy coefficients. Once the Airy coefficients are known, substituting those back into equations (9-10) through (9-15) enables one to evaluate the complete states of stress/strain and displacement of a loaded, finite-width, orthotropic plate containing a crack.

Therefore, knowing the complete state of stress of the orthotropic member having crack from the above-mentioned DIC-hybrid stress analysis method, this information can be combined with various well-established techniques to find the SIF. Four separate techniques are used in this study to individually evaluate the SIF of the DEC, finite-width, graphite-epoxy plate.

9.4.2. Determining SIF

9.4.2.1. Method-1 (Khalil's Concept)

The first technique used here was originally proposed analytically by Khalil et al. [118] and later exploited numerically by Ju [139] and experimentally by Ju and Rowlands [137] to study

fracture behavior of orthotropic plates with inclined cracks. Khalil et al. used Airy stress functions along with conformal mapping to formulate super elements in their hybrid-finite element approach to find SIFs in anisotropic materials. The traction-free condition of the crack-face was considered by the use of conformal mapping. For the coordinate system with the sharp crack along the negative portion of the z-plane and the crack-tip at $z = 0$, according to this method, displacement and stress fields near the crack-tip in an anisotropic material can be expressed as [118,137,139]

$$v = \sum_{j=1}^{2N} E_j(z_1, z_2)\gamma_j \tag{9-17}$$

$$\sigma_{yy} = \sum_{j=1}^{2N} B_j(z_1, z_2)\gamma_j \tag{9-18}$$

where $z_j = x + \mu_j y$, for $j = 1, 2$. The γ_j are the stress coefficients and N is the number of displacement terms retained, where for one displacement term, i.e., $N = 1$, there are two stress coefficients, γ_j and γ_{j+N}. The displacement component in the loading direction y, v, is utilized here to evaluate the SIF, K_I, for the present DEC graphite-epoxy plate. Expressions for the terms E_j of equation (9-17) are as below

$$E_j = 2Re\left(q_1 z_1^{\frac{j}{2}} + q_2 M_{1j} z_2^{\frac{j}{2}}\right) \tag{9-19}$$

$$E_{j+N} = 2Re\left(iq_1 z_1^{\frac{j}{2}} + q_2 M_{2j} z_2^{\frac{j}{2}}\right) \tag{9-20}$$

Also, expressions for B_j of equation (9-18) are

$$B_j = (-1)^p jRe\left(\mu_1^p z_1^{\frac{j-2}{2}} + \mu_2^p M_{1j} z_2^{\frac{j-2}{2}}\right) \tag{9-21}$$

$$B_{j+N} = (-1)^p jRe\left(i\mu_1^p z_1^{\frac{j-2}{2}} + \mu_2^p M_{2j} z_2^{\frac{j-2}{2}}\right) \tag{9-22}$$

here $(-1)^p = 1$ for $p = 0, 2$ and $(-1)^p = -1$ for $p = 1$.

And,

$$M_{1j} = -\frac{\beta_1}{\beta_2} \quad \text{and} \quad M_{2j} = \frac{\alpha_2 - \alpha_1}{\beta_2} - i \quad \text{for odd values of } j \tag{9-23}$$

$$M_{1j} = -1 + i\frac{\alpha_1 - \alpha_2}{\beta_2} \quad \text{and} \quad M_{2j} = -i\frac{-\beta_1}{\beta_2} \quad \text{for even values of } j \tag{9-24}$$

where $\mu_j = \alpha_j + i\beta_j$ for j =1, 2. For the coordinate system shown in Figure 9-1 and for in-plane stresses in the loading direction y, $p = 0$. To find in-plane displacement along the x-axis, q_j for j = 1, 2 in equations (9-19) and (9-20) only needs to be replaced by p_j. Similarly, to find in-plane normal stresses along the x-axis and in-plane shear stresses, the constant p in equations (9-21) and (9-22) is 2 and 1, respectively.

Khalil et al. and Ju et al. showed that, at locations very close to the crack-tip, stresses are dominated by the two stress coefficients γ_1 and γ_{1+N}, which again for mode-I loading can be expressed in terms of the SIF, K_I, as such [118,137,139]

$$K_{\mathrm{I}} = \sqrt{2\pi}\left[\left(1 - \frac{\beta_1}{\beta_2}\right)\gamma_1 + \left(\frac{\alpha_2 - \alpha_1}{\beta_2}\right)\gamma_{1+N}\right] \tag{9-25}$$

DIC-measured *v*-displacement data are used in equation (9-17) to evaluate the stress coefficients γ_j. Once the stress coefficients are known, their substitution into equation (9-25) provides K_{I}. Using DIC-measured data in Khalil/Ju's approach, one can use either of the in-plane displacements to evaluate the stress coefficients and thus the SIF. Note that one can also use the DIC-hybrid stress analysis method (rather than just DIC-measured displacement data) to determine all the in-plane displacements and stresses (i.e., equations (9-17) and/or (9-18)), providing flexibility in using any one of the in-plane displacement or stress expressions from Khalil/Ju's approach to find the SIF.

9.4.2.2. Method-2 (*J*-Integral Concept)

For an orthotropic plate with a crack lying along the negative *x*-axis and the *y*-axis being perpendicular to the crack's surface, the *J*-integral in Cartesian *x*-*y* coordinate can be written as [150]

$$J = \oint_{\Gamma}\left(W_s\, dy - \mathbf{T}.\frac{\partial \mathbf{u}}{\partial \mathrm{x}} ds\right) \tag{9-26}$$

where Γ is an arbitrarily preselected curve which surrounds the tip of the crack in Figure 9-3. $W_s = \int_0^{\varepsilon} \sigma_{ij}\, d\varepsilon_{ij}$ is the strain energy density, σ_{ij} and ε_{ij} are the stress and strain tensors, respectively, $\boldsymbol{T}$ is the traction vector defined according to the outward normal vector n along Γ, $T_i = \sigma_{ij} n_j$, $\boldsymbol{u}$ is the

displacement vector and *ds* is an element of arc length along Γ, Figure 9-3. The path Γ starts from the lower flank of the crack and proceeds to the upper flank in a counter-clockwise direction. For an elastically deformed material under plane-stress for a path Γ, the *J*-integral can be expressed as [77,149]

$$J = \int_{\Gamma} \left[\frac{1}{2} \left(\sigma_{xx}\varepsilon_{xx} + \sigma_{yy}\varepsilon_{yy} + \sigma_{xy}\gamma_{xy} \right) dy \right. \\ \left. - \left(\sigma_{xx} n_x \frac{\partial u}{\partial x} + \sigma_{xy} n_y \frac{\partial u}{\partial x} + \sigma_{yx} n_x \frac{\partial v}{\partial x} + \sigma_{yy} n_y \frac{\partial v}{\partial x} \right) ds \right] \tag{9-27}$$

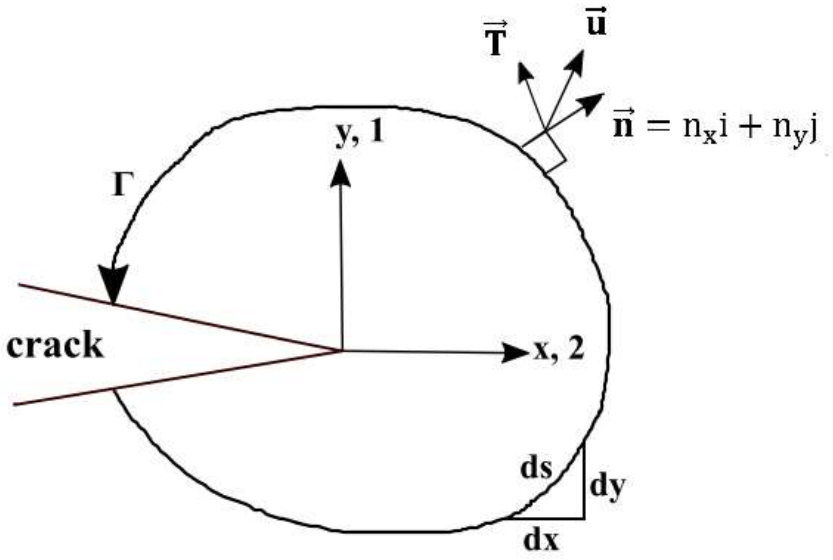

Figure 9-3: *J*-integral nomenclatures

For this expression of the *J*-integral, the in-plane stresses σ_{xx}, σ_{yy} and σ_{xy}, the in-plane strains ε_{xx} or $\frac{\partial u}{\partial x}$, ε_{yy} and γ_{xy} are already known from the DIC-hybrid stress analysis (equations (9-12)

through (9-15)). The rotation component $\frac{\partial v}{\partial x}$ can also be derived in a similar manner from the analytical concepts of the DIC-hybrid analysis. Differentiating the displacement components of equations (2-31) and (2-32) with respect to direction *x*, the following expressions for the normal strain ε_{xx} and rotation component $\frac{\partial v}{\partial x}$ are obtained [77]. The Cauchy-Reimann condition of equation (8-40) is followed while differentiating the analytic functions $\Phi(z_1)$ and $\Psi(z_2)$ with respect to the real coordinate axis *x*, Figure 9-1.

$$\varepsilon_{xx} = \frac{\partial u}{\partial x} = 2Re\{p_1\Phi'(z_1) + p_2\Psi'(z_2)\} \tag{9-28}$$

$$\frac{\partial v}{\partial x} = 2Re\{q_1\Phi'(z_1) + q_2\Psi'(z_2)\} \tag{9-29}$$

Combining equations (9-7) through (9-9) in equation (9-6), the expressions for $\Phi'(z_1)$ and $\Psi'(z_2)$ are obtained and used in the above equations (9-28) and (9-29) to establish the expressions for normal strain and rotation component as [77]

$$\frac{\partial u}{\partial x} = \varepsilon_{xx} = \sum_{j=1}^{N} Re\left\{i\left(jp_1\zeta_1^{j-2} + jp_2C\zeta_2^{j-2}\right)c_j - i\left(jp_2B\zeta_2^{j-2}\right)\bar{c}_j\right\} \tag{9-30}$$

$$\frac{\partial v}{\partial x} = \sum_{j=1}^{N} Re\left\{i\left(jq_1\zeta_1^{j-2} + jq_2C\zeta_2^{j-2}\right)c_j - i\left(jq_2B\zeta_2^{j-2}\right)\bar{c}_j\right\} \tag{9-31}$$

All required quantities to evaluate the *J*-integral using equation (9-27) are now known along any closed path Γ enclosing the crack. The *J*-integrals are path independent and equation

(9-27) should yield the same value irrespective along which path the integration is carried out as long as the path surrounds the crack in a counter clock-wise direction from the lower flank of the crack to the upper flank.

For a plane-stressed, orthotropic, tensile-loaded plate with a crack along negative *x*-axis and strong/stiff direction 1 perpendicular to the crack-face, for opening-mode fracture Griffith's strain energy release rate function, G_{I}, and SIF, K_{I}, are related as below [77,130]

$$G_{\mathrm{I}} = \frac{K_{\mathrm{I}}^2}{\sqrt{(2E_{11}E_{22})}}\left[\left(\frac{E_{22}}{E_{11}}\right)^{\frac{1}{2}} + \frac{E_{22}}{2G_{12}} - \frac{\nu_{12}E_{22}}{E_{11}}\right]^{\frac{1}{2}} \tag{9-32}$$

For linear elasticity and mode-I (i.e., $G_{\mathrm{II}} = 0$) crack, the *J*-integral is expressed as [77,150]

$$J = G_{\mathrm{I}} \tag{9-33}$$

Substituting equation (9-33) into equation (9-32) and re-arranging, K_{I} is expressed in terms of the *J*-integral and orthotropic plate's material properties as

$$K_{\mathrm{I}}^2 = \frac{J\sqrt{E_{11}E_{22}}}{\sqrt{(\alpha_1^* + \beta_1^*)/2}} \tag{9-34}$$

where $\alpha_1^* = \sqrt{E_{22}/E_{11}}$ and $\beta_1^* = \frac{E_{22}}{2G_{12}} - \frac{\nu_{12}E_{22}}{E_{11}}$

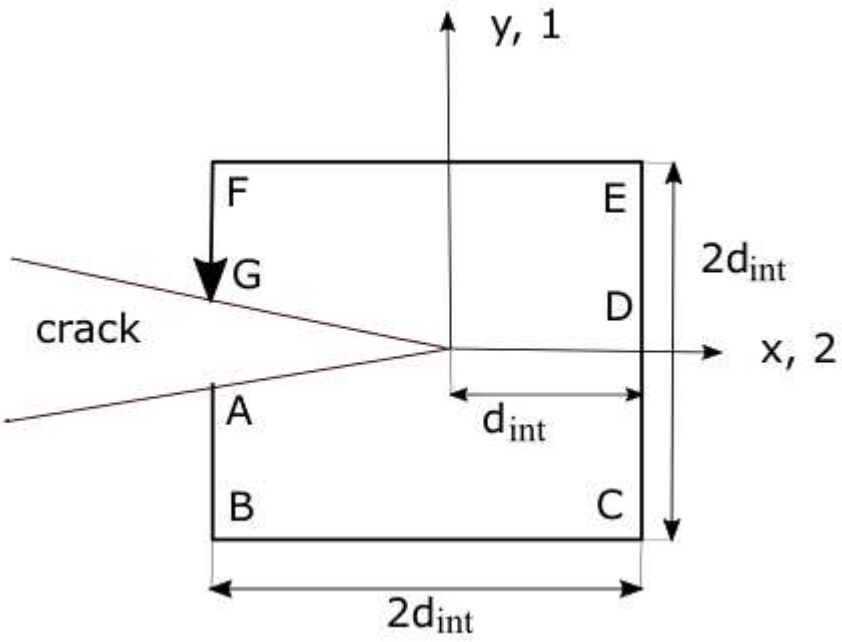

Figure 9-4: *J*-integral path ABCDEFG for the plate of Figure 9-1

Although the *J*-integral is path independent, prudent selection of the path Γ can reduce computational complexities to a great extent. Keeping this in mind, the *J*-integral here is evaluated along a square path ABCDEFG in a counter clock-wise direction from the lower to upper flank of the crack according to Figure 9-4 for various distances, d_{int}, from the crack-tip. For this purpose, for each line segment of the integration path that contributes to the *J*-integral is derived separately and then summed up to find the total *J*. For each line segment, the expression for *J*-integral can be simplified according to Table 9-1.

Table 9-1: Simplified expression of *J*-integral for sections of the ABCDEFG integration path

Line AB	$n_x = -1$, $n_y = 0$ and $\int_A^B ds = -\int_A^B dy$ $J_{AB} = \int_A^B \left[\frac{1}{2}(\sigma_{xx}\varepsilon_{xx} + \sigma_{yy}\varepsilon_{yy} + \sigma_{xy}\gamma_{xy})dy - \left(\sigma_{xx}\frac{\partial u}{\partial x} + \sigma_{xy}\frac{\partial v}{\partial x}\right)dy\right]$
Line BC	$n_x = 0$, $n_y = -1$, $dy = 0$ and $\int_B^C ds = \int_B^C dx$ $J_{BC} = \int_B^C \left[\left(\sigma_{xy}\frac{\partial u}{\partial x} + \sigma_{yy}\frac{\partial v}{\partial x}\right)dx\right]$
Line CDE	$n_x = 1$, $n_y = 0$, $dx = 0$ and $\int_C^E ds = \int_C^E dy$ $J_{CE} = \int_C^E \left[\frac{1}{2}(\sigma_{xx}\varepsilon_{xx} + \sigma_{yy}\varepsilon_{yy} + \sigma_{xy}\gamma_{xy})dy - \left(\sigma_{xx}\frac{\partial u}{\partial x} + \sigma_{xy}\frac{\partial v}{\partial x}\right)dy\right]$
Line EF	$n_x = 0$, $n_y = 1$, $dy = 0$ and $\int_E^F ds = -\int_E^F dx$ $J_{EF} = \int_E^F \left[\left(\sigma_{xy}\frac{\partial u}{\partial x} + \sigma_{yy}\frac{\partial v}{\partial x}\right)dx\right]$
Line FG	$n_x = -1$, $n_y = 0$ and $\int_F^G ds = -\int_F^G dy$ $J_{FG} = \int_F^G \left[\frac{1}{2}(\sigma_{xx}\varepsilon_{xx} + \sigma_{yy}\varepsilon_{yy} + \sigma_{xy}\gamma_{xy})dy - \left(\sigma_{xx}\frac{\partial u}{\partial x} + \sigma_{xy}\frac{\partial v}{\partial x}\right)dy\right]$

As the integrands of *J* are comparatively complex, a numerical integration based on the Gaussian Quadrature rule and employing 15 Gaussian points is used to compute the *J*-integral. The integrations are carried along the preselected path Γ, i.e., the square AB-BC-CD-DE-EF-FG, i.e., individually along the six lines. Symmetry about *x*-axis requires only half of the integration path,

i.e., AB-BC-CD or DE-EF-FG to be evaluated [77]. Knowing the Airy coefficients from the DIC-hybrid method, the in-plane stresses, strains and displacement slopes throughout the plate, including on the traction-free region and along the integration path are evaluated, from which the *J*-integral and thus the SIF, K_I, is determined.

9.4.2.3. Method-3 (Mogadpalli and Parameswaran's Concept)

Mogadpalli and Parameswaran [17] derived the near crack-tip displacement fields for single-edge cracked orthotropic members and used these to evaluate the SIF. For a single-edge crack in an orthotropic plate aligned along one of the principal material axes and the coordinate origin being located at the crack-tip, for opening-mode loading, the displacement component in the loading direction is expressed as [17]

$$v = \frac{\alpha-\beta}{2\alpha}\{a_{22} - a_{12}(\alpha+\beta)^2\}\frac{Im\bar{Z}_1}{(\beta+\alpha)} + \frac{(\alpha+\beta)}{2\alpha}\{a_{22} - a_{12}(\beta-\alpha)^2\}\frac{Im\bar{Z}_2}{(\beta-\alpha)} + \frac{\beta}{2\alpha}\{a_{12}(\alpha+\beta)^2 - a_{22}\}\frac{Im\bar{Y}_1}{(\beta+\alpha)} + \frac{\beta}{2\alpha}\{a_{22} - a_{12}(\beta-\alpha)^2\}\frac{Im\bar{Y}_2}{(\beta-\alpha)} \tag{9-35}$$

where

$$\bar{Z}_k(z_k) = \sum_{j=0}^{M} \frac{2}{2j+1} M_j z_k^{j+\frac{1}{2}}, \quad k = 1, 2 \tag{9-36}$$

$$\bar{Y}_k(z_k) = \sum_{j=0}^{N} \frac{1}{j+1} N_j z_k^{j+1}, \quad k = 1, 2 \tag{9-37}$$

$$z_1 = x + i(\beta + \alpha)y, \quad z_2 = x + i(\beta - \alpha)y \tag{9-38}$$

$$2\beta^2 = \frac{a_{66}+2a_{12}}{2a_{11}} + \sqrt{\frac{a_{22}}{a_{11}}}, \quad 2\alpha^2 = \frac{a_{66}+2a_{12}}{2a_{11}} - \sqrt{\frac{a_{22}}{a_{11}}} \tag{9-39}$$

For the DEC-plate of Figure 9-1, the strong/stiff orthotropic direction 1 being along y-axis, the elastic compliances, a_{ij}, are expressed accordingly in equation (9-16). For the physically tested plate the contribution from the rigid body motion is neglected in the expression of v in equation (9-35).

The coefficients M_j and N_j present in equations (9-36) and (9-37) are real coefficients and Shukla et al. showed that, the coefficient M_0 is directly related to the opening-mode SIF, K_I, as [16,17]

$$K_\mathrm{I} = M_0\sqrt{2\pi} \tag{9-40}$$

Using either measured or predicted in-plane displacements in the loading direction, v, in equation (9-35), the coefficients M_j and N_j are evaluated by least squares. From the evaluated coefficient, M_0 is used in equation (9-40) to find K_I. Details regarding evaluating M_j and N_j from v-displacement information are provided in Chapter 8: equations (8-72) through (8-76).

The number of terms to use in the summation series is selected by finding the root mean square (RMS) between the input displacements and the reconstructed displacements (from equation (9-35)) for various number of coefficients, $M + N$, and using the number of coefficients that gives rise to lower values of RMS[1]. The analysis can similarly be done using the measured- or predicted-displacement in the direction transverse to the loading direction, u, whose expression is provided in Chapter 8: equation (8-65) combined with equations (8-67), (8-68) and (8-70).

9.4.2.4. Method-4 (Sih, Paris and Irwin's Concept)

Sih, Paris and Irwin's near crack-tip singular stress field approximation for orthotropic materials is utilized here. For an opening-mode or mode-I crack, the in-plane stress component perpendicular to the crack-face in regions close to the crack-tip can be expressed as equation (9-41) [22,122]. The crack coordinate system is shown in Figure 9-5.

$$\sigma_{yy} = \frac{K_{\mathrm{I}}}{(2\pi r)^{\frac{1}{2}}} Re\left(\frac{1}{\mu_1 - \mu_2}\left[\frac{\mu_1}{(\cos\theta + \mu_2 \sin\theta)^{1/2}} - \frac{\mu_2}{(\cos\theta + \mu_1 \sin\theta)^{1/2}}\right]\right) \quad (9\text{-}41)$$

[1] Mogadpalli and Parameswaran [17] used Bao et al. [93] provided closed-form equations to find a SIF value which they considered as the exact SIF. They increased $M + N$ in the summation series until the computed SIF values matched closely to the expected SIF value.

where distance r is measured from the crack-tip (i.e., $z_j = x + \mu_j y = 0$ as the x-y coordinate origin is at the crack-tip) and angle θ is in a counter clock-wise direction from the crack-face or x-axis.

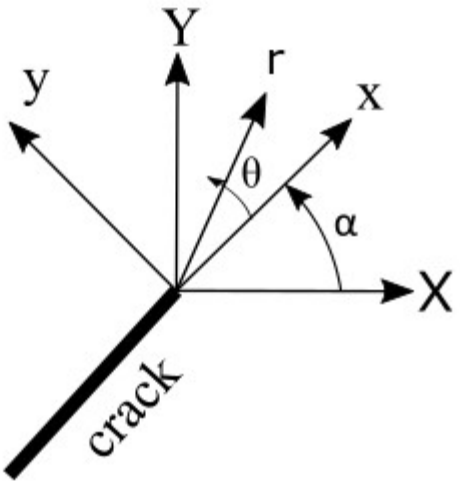

Figure 9-5: Crack coordinate system (x, y) with respect to plate's global Cartesian coordinates (X, Y)

For a crack that lies along the x-axis of material orthotropy, and crack-face aligned with global X-axis, i.e., $\alpha = 0$, Figure 9-1, then along $\theta = 0$ for $r << a$, from the above equation (9-41), for mode-I loading the SIF can be expressed as [22]

$$K_{\mathrm{I}} = \sigma_{yy}\sqrt{2\pi r} \tag{9-42}$$

where σ_{yy} is the in-plane stress component in the loading direction of the plate, Figure 9-1, and is obtained from equation (9-13) of the DIC-hybrid method.

9.5. Experimental Details

9.5.1. Plate Details

The DEC-orthotropic plate of length, L = 29.21 cm (11.5"), width, W = 63.5 mm (2.5"), thickness, t = 5.28 mm (0.208") and with each crack length, a = 19.05 mm (0.75"), was analyzed using DIC. The rectangular plate was prepared from a 5.28 mm thick $[0_{13}/90_5/0_{13}]$ graphite-epoxy laminate sheet (from Kinetic Composite, Inc., Oceanside, CA) using water-jet cutting, Table 9-2. The 0.15 mm wide by a = 19.05 mm long edge cracks were prepared by electrical discharge machining (EDM) (by Wire Works, Madison, WI) and sharpened with a razor blade. From prior experience, in order to avoid any machining-induced defects such as fiber breakage or delamination, the graphite-epoxy plate was clamped between two aluminum plates when the cracks were prepared by EDM. The adverse effects of directly introducing a discontinuity in an orthotropic plate under high pressure are discussed in the Appendix B.

Table 9-2: DEC-plate and experimental details

Material	$[0_{13}/90_5/0_{13}]$ graphite-epoxy orthotropic laminate
Supplier	Kinetic Composite, Inc., Oceanside, CA
Thickness, t	5.28 mm (0.208")
Length, L	29.21 cm (11.5")
Width, W	6.35 cm (2.5")
Individual crack length, a	19.05 mm (0.75")
Symmetry	Both horizontally and vertically
Loading for DIC analysis	From 0 to 8.9 kN (2,000 lbs) in 889.6 N (200 lbs) steps
Loading for DIC-hybrid model	7.1 kN (1,600 lbs)

The measured elastic properties of the DEC-plate are $E_{11} = 104.1$ GPa, $E_{22} = 28.1$ GPa, $\nu_{12} = 0.155$ and $G_{12} = 3.0$ GPa, with the 1-direction being in the vertical y-orientation of Figure 9-1, Table 4-1 and Appendix A.

9.5.2. Surface Preparation

The random and dense speckle pattern of Figure 9-6 was applied to the surface of the plate to act as unique markers for pixel correlation between the unloaded and loaded plate. The plate was lightly buffed initially with 400-grit emery cloth and the cracks carefully sharpened with a razor blade. The polished surface was cleaned with water-based mild cleaners (Vishay Precision Group - Micro-Measurements M-Prep Conditioner A followed by M-Prep Neutralizer 5A) and

allowed to dry. A thin layer of black paint was applied to the cleaned surface, after which the random pattern of white dots was applied. A suitable speckle pattern was achieved by applying a light pressure to the trigger of the paint container. Rust Oleum Ultra-Cover paints were used.

Figure 9-6: DEC-plate with applied speckle pattern

9.5.3. Plate Loading

The plate was loaded using a 89 kN (20,000 lbs), closed-loop, hydraulic-grip MTS machine, Figure 9-7. With care to ensure symmetrical loading about the *x*-*y* axes, the plate was mounted in the hydraulic grips and loaded from 0 to 8.9 kN (2,000 lbs) at load increments of 889.6 N (200 lbs). An oscilloscope was used to monitor the applied load with better accuracy than just relying on the control panel of the load frame. A digital image at each load increment, along with an image of the undeformed plate, was captured by the Correlated Solution, Inc.'s commercial DIC package. The properly aligned loaded plate experienced no out-of-plane motion other than the Poisson's effect. A 2D-DIC was conducted, the data from which were used to do the stress analysis.

(a) (b)

Figure 9-7: a) Experimental set-up for DIC of the finite, orthotropic, graphite-epoxy plate with DEC and b) Loaded plate with speckle pattern

9.5.4. DIC Details

A digital image of the plate was taken at each load using Correlated Solution, Inc.'s (Correlated Solutions, Inc., Irmo, SC 29063) DIC package. Only one camera was employed as the problem is plane-stress. The 2D-DIC system was manually calibrated by correlating pixel size for a known distance through Vic-2D software. A set of images at different loads was taken by the DIC camera equipped with Vic-Snap software along with a reference image, i.e., image at essentially zero load representing undeformed condition of the plate. Room lighting was used. The displacement correlation was done using Vic-2D software. A subset size of 45 and step size of 5 were used. DIC details are provided in Table 4-3. Each pixel of the DIC image was 0.17 mm (0.0067") = 0.009a in size.

9.6. Finite Element Model

Having geometric and loading symmetry about both the *x*- and *y*-axes, only a quarter of the plate was modeled using FEA tool ANSYS APDL with element type Plane 183. The plate length between the grips was considered in the FEA. Appropriate symmetrical boundary conditions were imposed and the origin of the coordinate system was located at the crack-tip. Assigned material properties are those discussed in Section 9.5.1, (Table 4-1). 'KSCON' command of the FEA tool was used to generate focused mesh at the crack-tip and the 'skewed element' option was used to make the crack-tip elements singular. The final quarter FEM of the plate had 14,989 eight-node quadratic isoparametric elements. This includes 48 quarter-point elements at the crack-tip and a total of 45,336 nodes. The quarter-point element size near crack-tip is 0.013 mm (0.0005"). This corresponds to 0.0007a and 0.0024t. An external vertical load of 7.1 kN (1,600 lbs) was applied in the strong/stiff direction of the plate. This corresponds to a nominal stress, σ_0, of 21.23 MPa (3.1 ksi) according to equation (9-43) based on the far-field cross-section of the plate.

$$\sigma_0 = \frac{F^*}{W \times t} = \frac{7{,}117.15 \text{ N}}{63.5 \text{ mm} \times 5.28 \text{ mm}} = 21.23 \text{ MPa } (3{,}076.92 \text{ psi}) \qquad (9\text{-}43)$$

The FEA quarter-model, with appropriate symmetrical boundary conditions and loading, is shown in Figure 9-8(a) and the crack opening behavior under the loading in Figure 9-8(b). Figure 9-9 and Figure 9-10 represent FEM-predicted in-plane displacements, v, and the stresses, σ_{yy}, in the loading direction y. FEM-predicted in-plane displacements and stresses for each node, along with x-y coordinates, were exported to Excel for further post-processing in MATLAB.

ANSYS APDL offers built-in commands such as ‘KCALC’ to calculate mixed-mode SIFs or ‘CINT’ to evaluate the *J*-integral for fracture problems. However, these commands are restricted to isotropic materials. The analytical concepts under Section 9.4.2. were therefore used to evaluate the *J*-integral (Section 9.4.2.2) and K_I’s for the present orthotropic plate essentially using FEM-predicted *v*-displacement data.

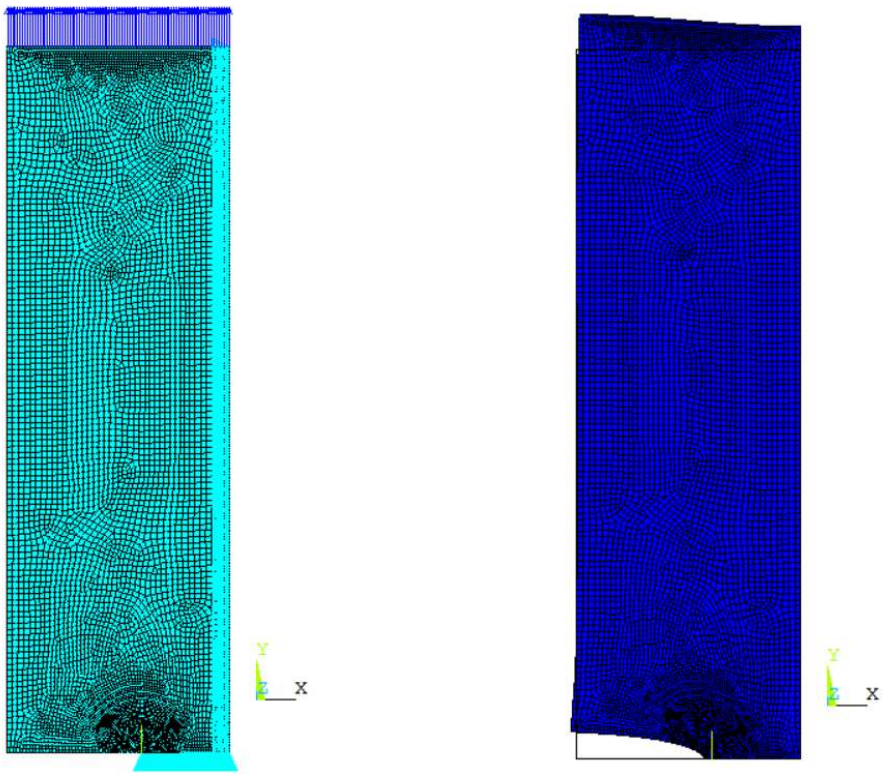

(a) (b)

Figure 9-8: (a) FEM quarter model of graphite-epoxy DEC-plate and (b) Crack opening under mode-I loading

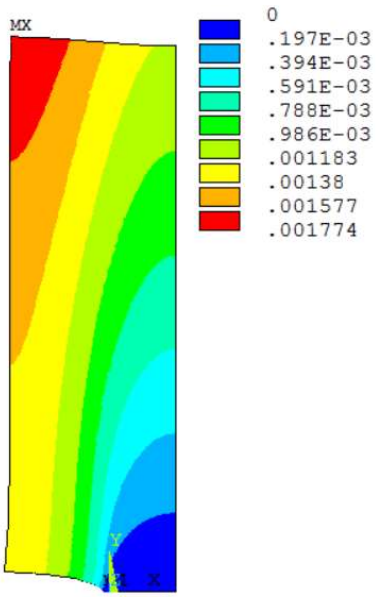

Figure 9-9: In-plane displacements, *v*, in loading direction from FEM (units in inches)

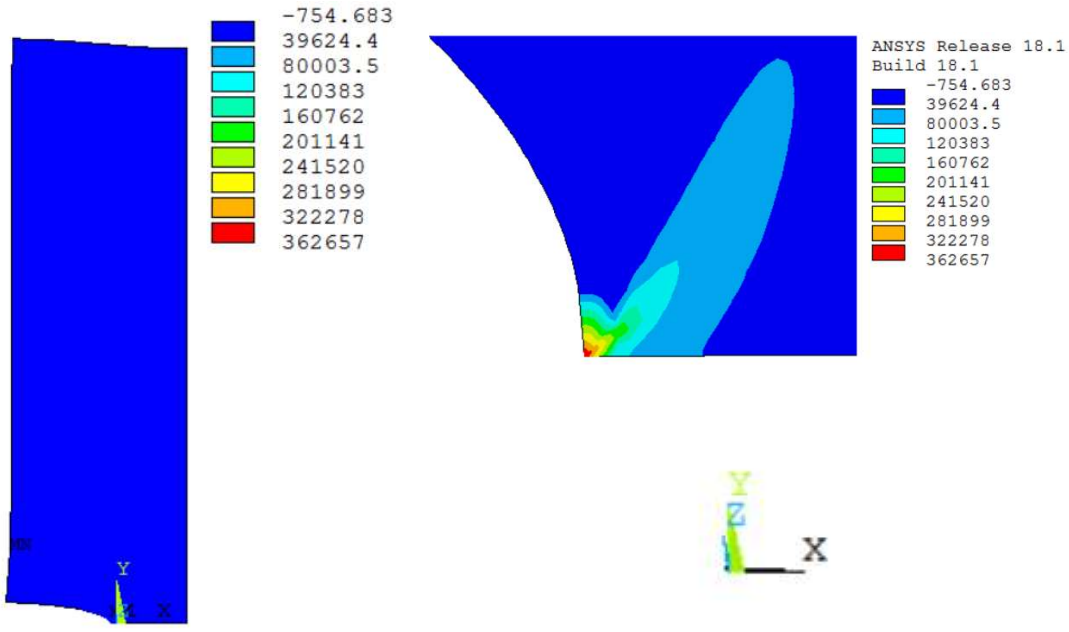

(a) (b)

Figure 9-10: FEM-predicted in-plane stress component (a) σ_{yy}, in loading direction, (b) σ_{yy} stress distribution near crack-tip, (units in psi)

9.7. System Validation Data Analyses and Results

To check the reliability of the experimentally determined SIF, a few additional analyses were conducted on the DEC graphite-epoxy plate with FEM-predicted information based on the methods mentioned previously in Section 9.4.2. These studies will be called "system validation analyses". To avoid compromising results due to discrepancies from experimental scatters in measured quantities, these studies were based mostly on FEA-predicted *v*-displacement data. SIF results from DIC-hybrid model utilizing DIC-measured *v*-displacement data are then compared with those obtained from the system validation analyses.

9.7.1. From Method-1 (Khalil/Ju's Concept)

The first system validation analysis was done according to method-1 (Khalil et al. [118] , Ju [139] and Ju and Rowlands [137]), using FEA-predicted displacement data, *v*, in the loading direction in equation (9-17) and combining equations (9-19), (9-20), (9-23) and (9-24) with equation (9-17). The simultaneous system of linear equations was formed keeping the number of equations higher than the number of unknowns. The only unknowns in this overdetermined system were the stress coefficients, γ_j, which were evaluated from the *v*-displacement data and using least squares. The number of terms to retain in the summation series was determined by checking the root mean square (RMS) between the FEA *v*-displacements, *d*, and the reconstructed *v*-displacements, *d'*, using equation (9-17) for varying number of stress coefficients, γ_{2N}, where for $j = 1, 2,\ldots N$; $\gamma_{2N} = 2j$. Once the stress coefficients, γ_j, were evaluated, the SIF for opening-mode loading, K_I, was determined from equation (9-25). Acknowledging Shukla's [16] suggestion to not use measured data less than 50% of the plate thickness from the crack-tip, the selected FEM data

originated at distances greater than $r = 0.5t \approx 0.15a$ from the crack-tip [16,17]. Analyses were done for FEA-predicted v-displacement data selected over the left quadrant of the plate at distances $r = 0.2a$, $0.3a$, $0.4a$ and $0.5a$ away from the crack-tip. For each data range, the analyses were done involving various number of stress coefficients, γ_{2N}, in equation (9-17). This was done in order to observe the effect of the selected data ranges and the number of stress coefficients, γ_{2N}, on the reconstructed displacement data and thus on the calculated SIF, K_I, Table 9-3.

Table 9-3: Normalized SIF from method-1 (Khalil/Ju's concepts) for various ranges of FEM source v-data locations and number of utilized stress coefficients

Data selection radius, r	Normalized SIF, $\frac{K_I}{\sigma_0\sqrt{a}}$ for number of stress coefficients, γ_{2N} =										
	14	16	18	20	24	28	30	34	36	40	50
$= 0.2a = 0.72t$	2.27	2.27	2.29	2.29	2.30	2.30	2.29	2.3	2.28	2.25	1.06
$= 0.3a$	2.28	2.28	2.31	2.31	2.32	2.34	2.33	2.34	2.27	2.25	0.99
$= 0.4a$	2.29	2.29	2.33	2.32	2.33	2.37	2.36	2.38	2.31	2.25	0.94
$= 0.5a$	2.30	2.30	2.34	2.34	2.35	2.39	2.38	2.43	2.30	2.25	0.89

For a finite series, using too few coefficients produces error in the computed results due to insufficient terms to express the quantities properly. Just like evaluating Airy coefficients from measured data, using too many coefficients leads to numerical problems. For this method, selecting data too far from the crack-tip also affects the results. Selecting data at a distance $r \geq 0.5a$ from

the crack-tip did not show any stable trend in the obtained SIF results and were discarded. As for selecting data beyond $r \geq 0.5a$, there are very little input data close to the crack-tip. Use of γ_{2N} = 14 to 44 is considered optimum as it gives minimum difference between the input displacements and computed displacements, Figure 9-11. Beyond γ_{2N} = 36, there is a sudden decrease in the normalized SIF values, Table 9-3 and Figure 9-12. It is hard to make a concluding statement about the SIF from this analysis, so a new analysis was conducted and will be further discussed.

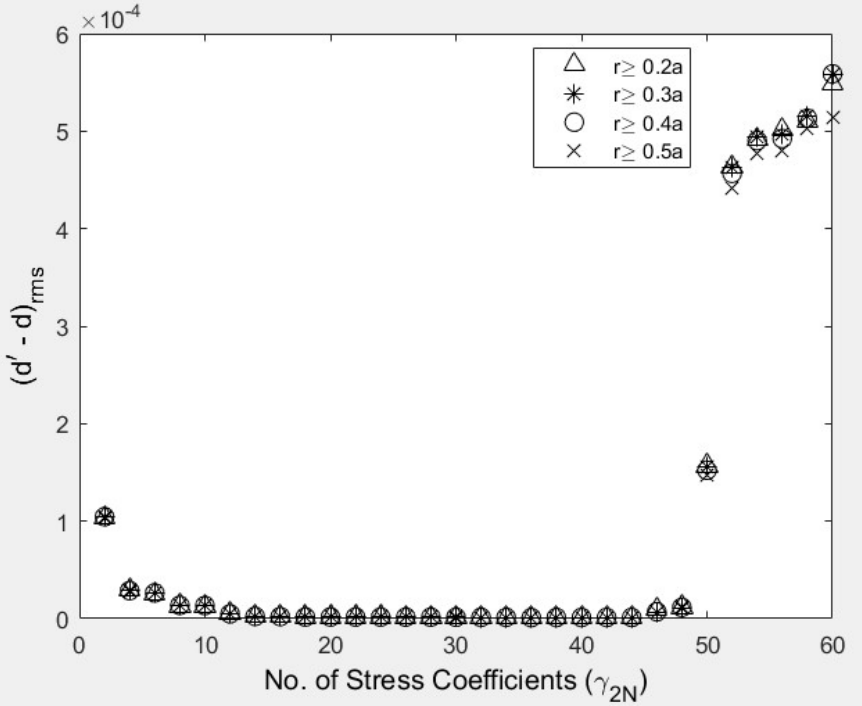

Figure 9-11: RMS for various number of γ_{2N} for four sets of FEM *v*-displacement data as input in method-1 (Khalil/Ju's concepts)

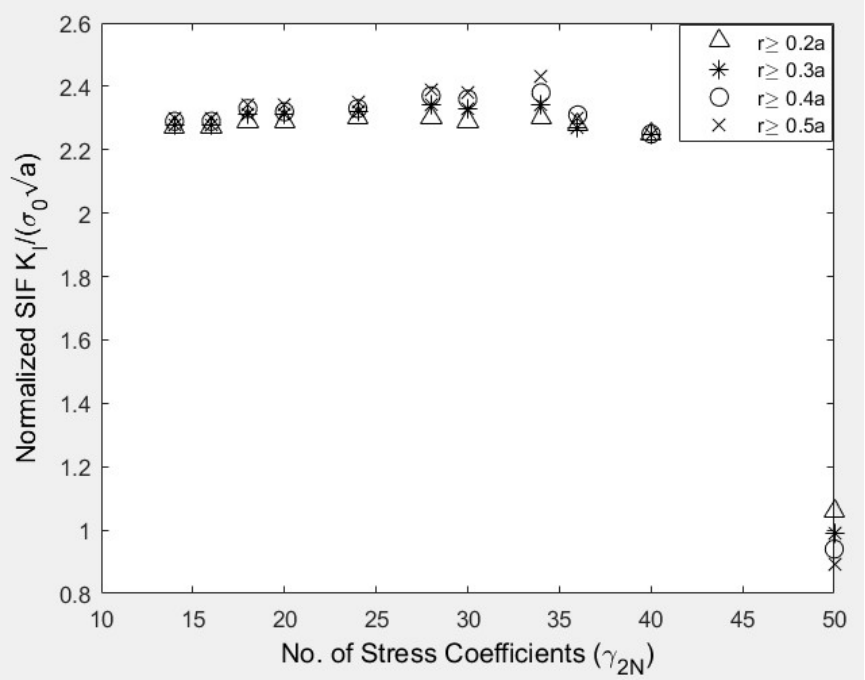

Figure 9-12: Normalized SIF from method-1(Khalil/Ju's method) for various ranges of data source location and number of utilized stress coefficients, γ_{2N}, for FEM v-displacements as input

Using method-1 (based on Khalil/Ju's concepts) and FEM-provided information, another set of analyses was conducted. In this case, the measured input included all the in-plane displacement and stress components. Combining equations (9-19) and (9-20) with equation (9-17), with once replacing q_j with p_j for j = 1, 2; the expressions for both the in-plane displacements, v and u, are obtained, respectively. Similarly combining equations (9-21) and (9-22) with equation (9-18), and equating p = 0, 1 and 2 respectively, expressions for σ_{yy}, σ_{xy} and σ_{xx} are established, respectively. Upon solving the system of linear equations for the stress coefficients, γ_j, K_I, is obtained from equation (9-25). In both cases expression of M_{1j} and M_{2j} of equations (9-23) and (9-24) were utilized. The RMS plot of Figure 9-13 now suggests using γ_{2N} = 14 to 38. Computed normalized K_I from Table 9-4 shows highly consistent results for γ_{2N} = 14 to 36 in the summation series, where normalized K_I is found to vary essentially between 2.25 and 2.27. Figure 9-14

compares the reconstructed in-plane displacement component, v, and the stress components from method-1 (Khalil/Ju's method) with the FEM-predictions. The good agreement between the respective contours confirms the validity of the computed SIF. All computed/predicted stresses are normalized by σ_0 = 21.23 MPa from equation (9-43).

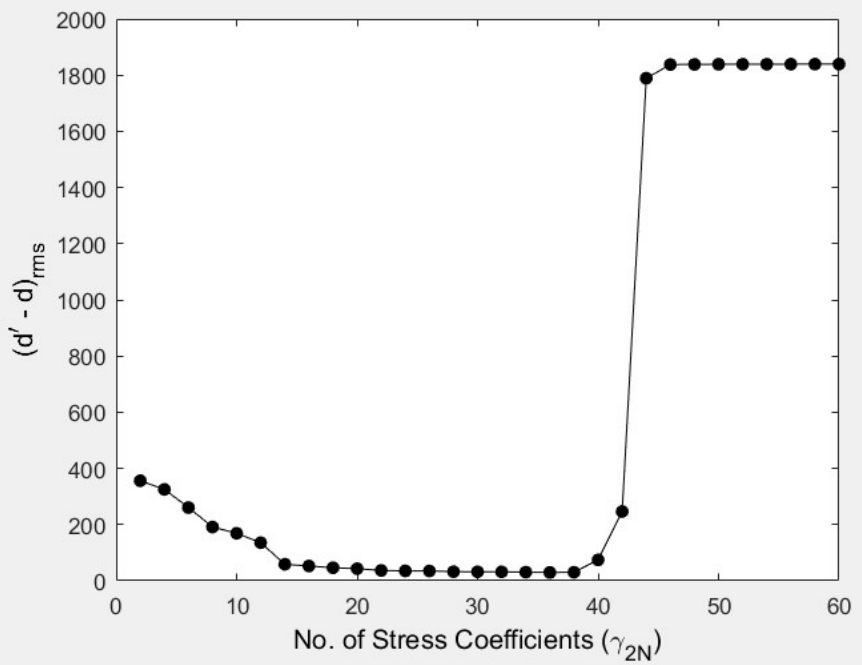

Figure 9-13: RMS for various number of γ_{2N} for FEM v, u, σ_{yy}, σ_{xx} and σ_{xy} as input in method-1 (Khalil/Ju's concepts)

Table 9-4: Normalized SIF vs number of stress coefficients, for v, u, σ_{yy}, σ_{xx} and σ_{xy} as input in method-1(Khalil/Ju's concept)

Data selection radius, r	Normalized SIF, $\frac{K_I}{\sigma_0\sqrt{a}}$, for number of stress coefficients, γ_{2N} =										
	14	16	18	20	24	28	30	34	36	40	44
$=0.2a = 0.72t$	2.21	2.23	2.25	2.26	2.25	2.25	2.25	2.26	2.26	2.25	0.01
$= 0.3a$	2.18	2.22	2.24	2.27	2.25	2.26	2.25	2.26	2.26	2.17	0.01
$= 0.4a$	2.16	2.21	2.24	2.27	2.25	2.26	2.25	2.27	2.27	2.02	0.07
$= 0.5a$	2.14	2.20	2.24	2.27	2.25	2.27	2.24	2.29	2.25	1.84	0.08

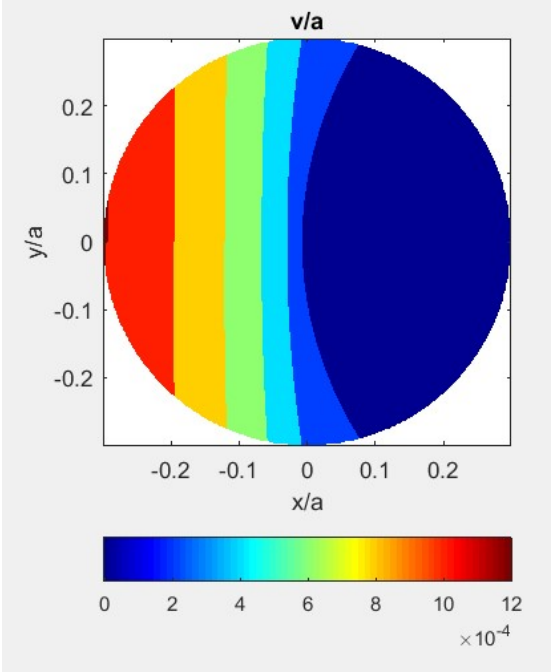

(a)

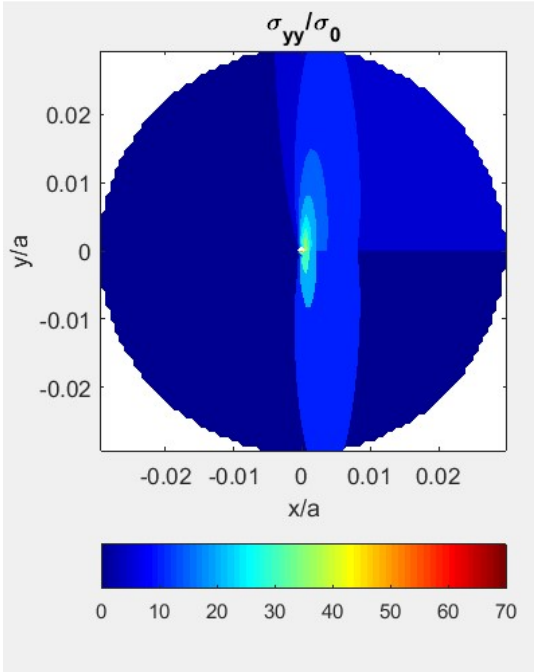

(b)

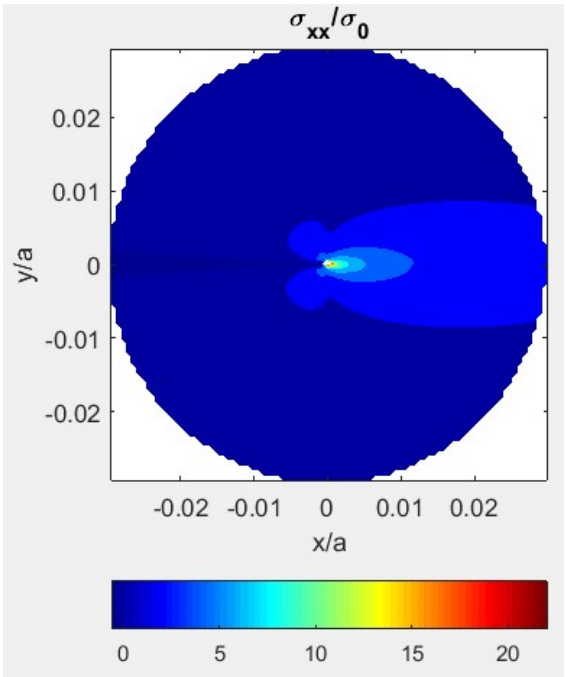

(c)

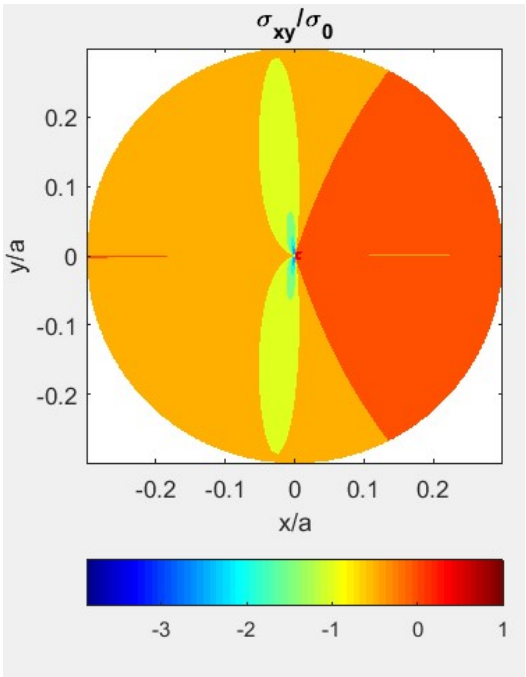

(d)

Figure 9-14: Contours of (a) v/a, (b) σ_{yy}/σ_0, (c) σ_{xx}/σ_0 and (d) σ_{xy}/σ_0 from using FEA-predicted in-plane displacements u and v and in-plane stresses σ_{xx}, σ_{yy} and σ_{xy} as input in Khalil/Ju's method (top) and FEM (bottom)

9.7.2. From Hybrid Stress Analysis and *J*-Integral

FEA-predicted *v*-displacement data were used in the hybrid stress analysis method to perform a full-field stress analysis of the DEC graphite-epoxy plate. Full-field states of stress and displacement information were computed from the hybrid-method and later post-processed using the *J*-integral concept to evaluate the SIF. For the FEA-hybrid analysis of the DEC-plate FEA-predicted *v*-displacement data were used in equation (9-11) to obtain the Airy coefficients, c_j. From equations (9-10) through (9-15) and (9-31), the components of in-plane displacements, stresses, strains and rotation components required to evaluate *J*-integral from equation (9-27) were then obtained. Knowing the *J*-integral and using equation (9-34), K_{I}, was obtained for various integration paths, Table 9-5. From the RMS plot of Figure 9-15, $k = 7$ was used in the analysis. Figure 9-16 compares the reconstructed in-plane displacement and the stress components from the hybrid stress analysis method for FEA *v*-displacements as input with the direct FEM-predictions. The agreement is again very good. Table 9-5 shows the independence of the integration path on the computed SIF.

Table 9-5: SIF by FEA-hybrid stress analysis and *J*-integral

d_{int}	$0.1a$	$0.2a = 0.72t$	$0.3a$	$0.4a$	$0.5a$	$0.6a$
$\frac{K_{\mathrm{I}}}{\sigma_0\sqrt{a}}$	2.274	2.275	2.275	2.276	2.277	2.281

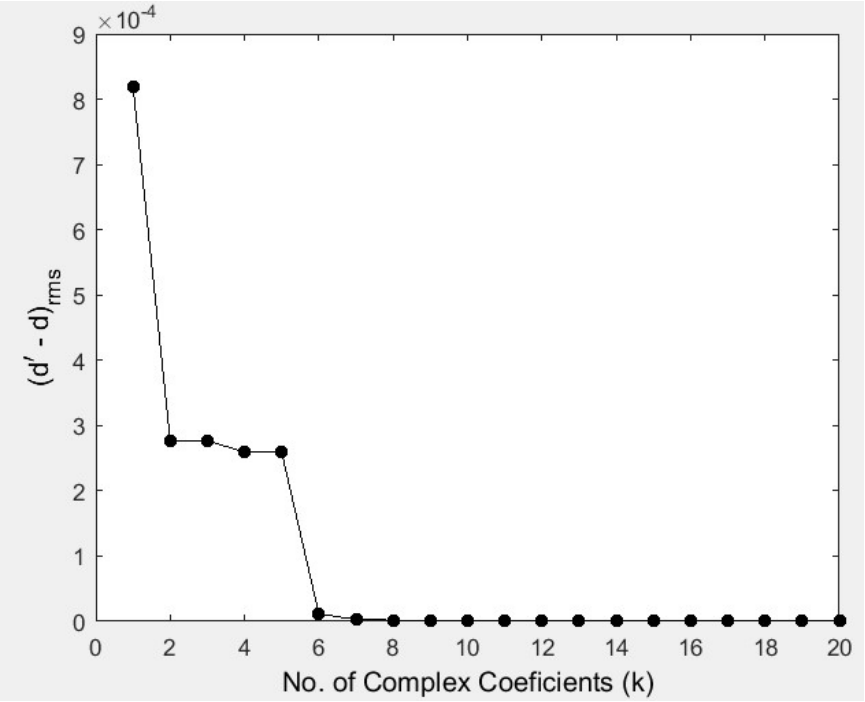

Figure 9-15: RMS for various number of complex Airy coefficients, *k*, for FEM-predicted *v*-displacements as input in the hybrid stress analysis method using Taylor series

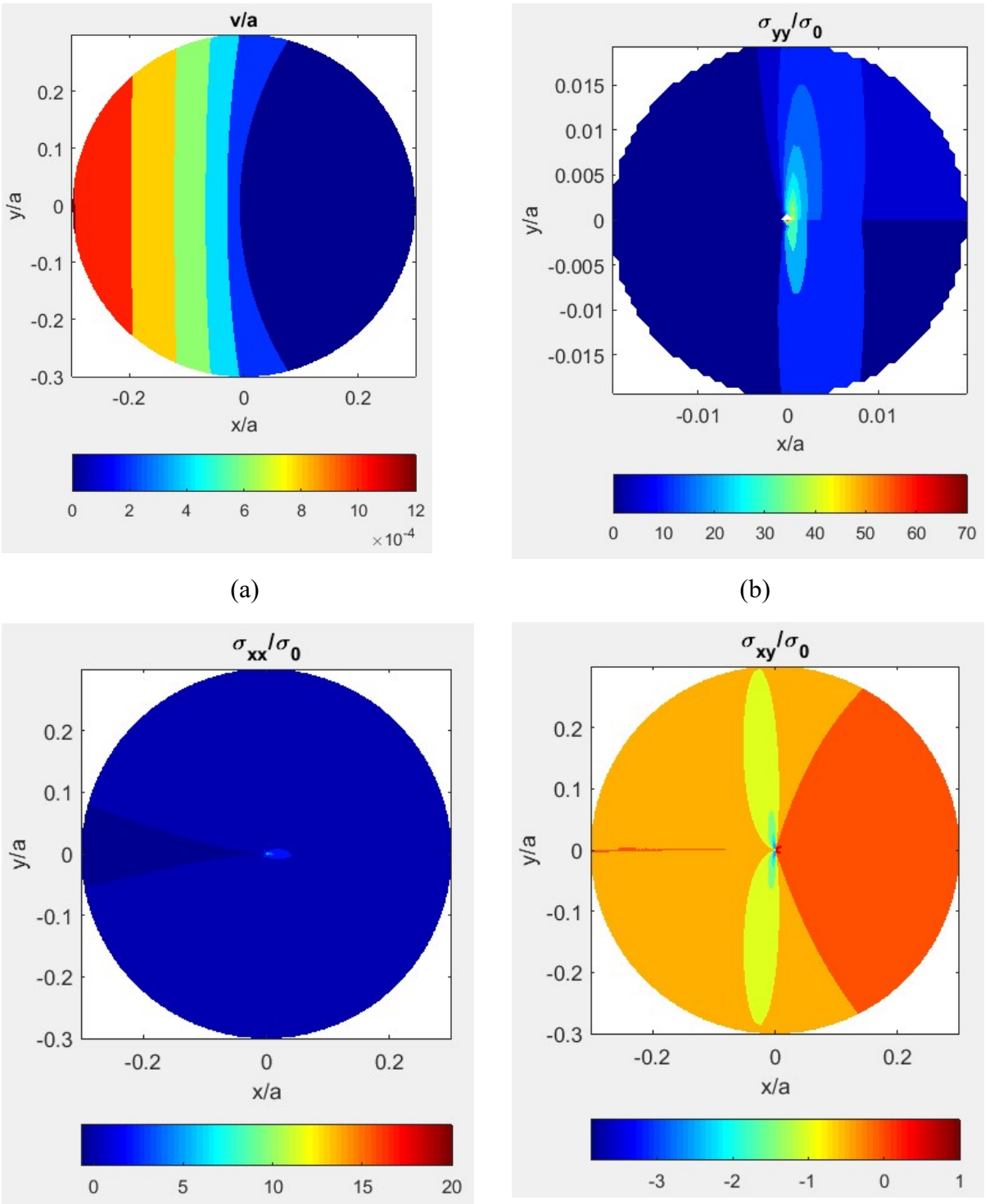

Figure 9-16: Contours of (a) v/a, (b) σ_{yy}/σ_0, (c) σ_{xx}/σ_0 and (d) σ_{xy}/σ_0 by using FEA-predicted v-displacements in the hybrid stress analysis method as input (top) and from FEM (bottom)

9.7.3. From Method-3 (Mogadpalli and Parameswaran's Concept)

The third analysis was done according to method-3 (Mogadpalli and Parameswaran [17]). FEA-simulated displacement information in the loading direction, v, was used in equation (9-35) and from combining equations (9-36) through (9-39) in equation (9-35), the unknown coefficients (M_j and N_j) were evaluated using least squares. Knowing the coefficients M_j and N_j, the SIF was determined from equation (9-40). The input data were selected at a distance of at least 50% of the plate thickness from the crack-tip as suggested by Shukla et al. [16] and as followed by Mogadpalli and Parameswaran [17] to essentially eliminate three-dimensional effects. A study similar to that by Mogadpalli and Parameswaran [17] is carried out here to check whether data selection and the number of coefficients retained to reconstruct the displacements by least squares have any significant effect on the resulting SIF. Resulting normalized SIF are presented in Table 9-6 and Figure 9-17.

Table 9-6: Normalized SIF for various ranges of data locations and number of utilized stress coefficients for FEM v-displacements as input in method-3 (Mogadpalli and Parameswaran's concept)

Data selection radius, r	Normalized SIF, $\frac{K_I}{\sigma_0\sqrt{a}}$, for $M + N =$									
	2	4	6	8	10	12	14	16	18	20
$= 0.2a = 0.72t$	1.80	2.36	2.29	2.29	2.29	2.28	2.26	2.26	2.25	2.24
$= 0.3a$	1.77	2.36	2.29	2.29	2.29	2.28	2.26	2.26	2.25	2.24
$= 0.4a$	1.76	2.36	2.30	2.30	2.30	2.29	2.26	2.27	2.25	2.24
$= 0.5a$	1.73	2.36	2.3	2.3	2.3	2.29	2.26	2.27	2.25	2.24

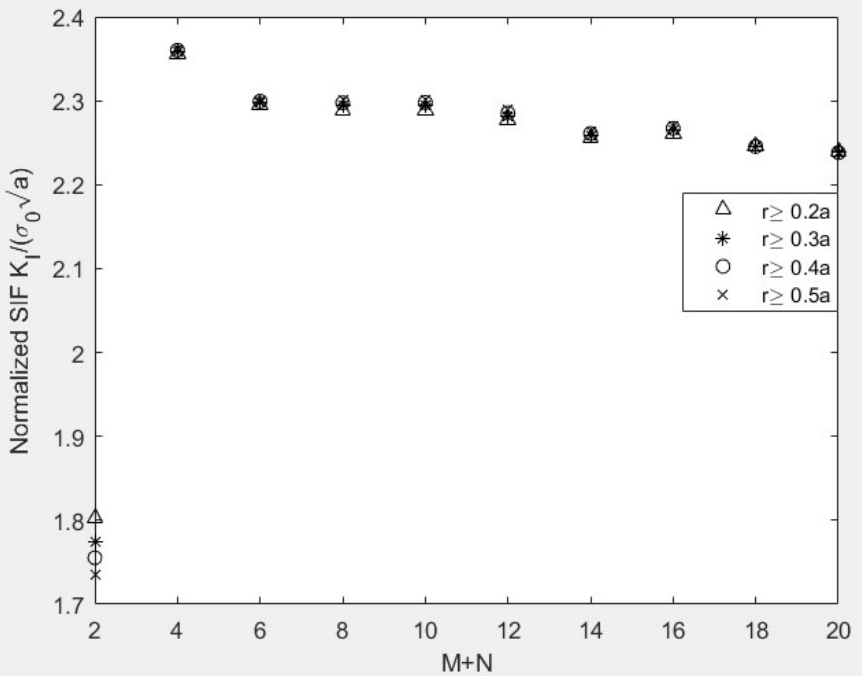

Figure 9-17: Normalized SIF for various ranges of FEM *v*-displacement input data source locations and number of utilized stress coefficients, $M + N$, in method-3 (Mogadpalli and Parameswaran's concept)

For all the four data ranges, the normalized SIF for $6 \leq M + N \leq 12$ are close to each other, Table 9-6 and Figure 9-17. For $M + N > 12$, there is a sudden slight decrease in the normalized SIF values. However, the normalized SIF for $14 \leq M + N \leq 20$ again agree well. The RMS plot of Figure 9-18 show that for $8 \leq M + N \leq 24$ in the summation series have essentially the same effect. Mogadpalli and Parameswaran [17] recommended the use of $M + N \geq 12$. Therefore, the final SIF was selected by taking the average of all these 20 SIF values between $12 \leq M + N \leq 20$ in Table 9-6. The resulting mean normalized SIF, K_I is 2.26.

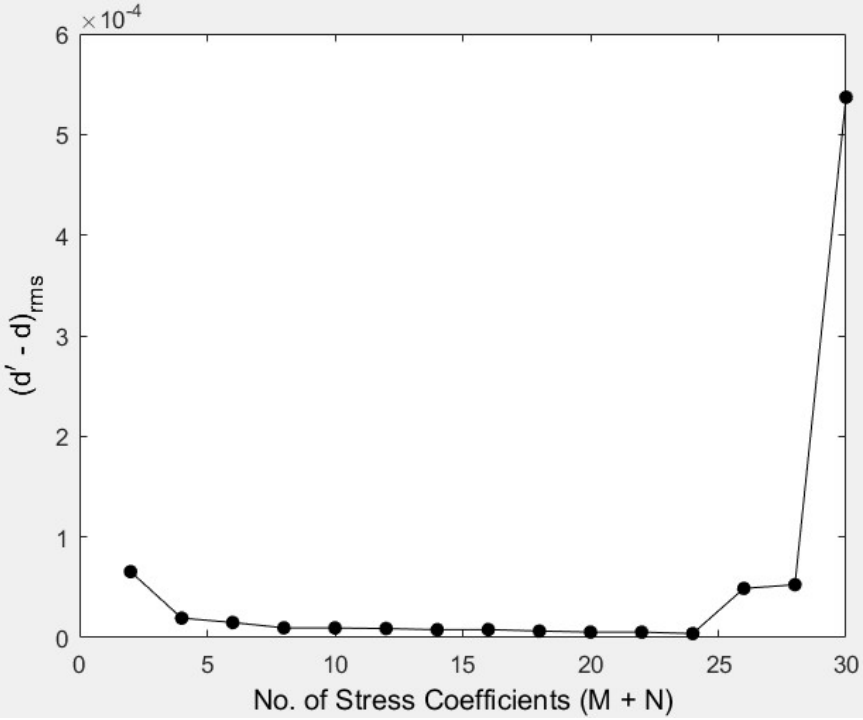

Figure 9-18: RMS for various number of stress coefficients, $M + N$, for FEM-predicted v-displacements as input in method-3 (Mogadpalli and Parameswaran's concept)

9.8. DIC Data Processing

DIC-measured data were exported into MATLAB for further processing. DIC images have a pixel size/spacing of 0.18 mm (0.0072"). While physically loading the plate, Figure 9-7, the top grip of the MTS load frame remained stationary and the bottom grip moved down to apply the tensile load. Figure 9-19 shows the non-symmetrical displacement pattern about the horizontal x-axis due to such loading. As the plate geometry and loading are symmetrical about both the x-y axes, and the analytical expressions assume that the origin of the final coordinate system is located at the crack-tip and that the plate extends equally in both vertical directions, the DIC-measured v -displacement data (Figure 9-19) in the loading direction (strong/stiff direction, y-direction) were processed (so that, $v = 0$ through the horizontal center-line) and averaged over the four quadrants

to cancel any measurement asymmetry and to reduce scatter. For the averaged *v*-displacement data in the loading direction, the plate's origin was then shifted for the coordinate system to pass through the crack-tip. The resulting averaged vertical displacements, *v*, are plotted over the top left quadrant of the plate in Figure 9-20a. Results in other quadrants are obtained through symmetry.

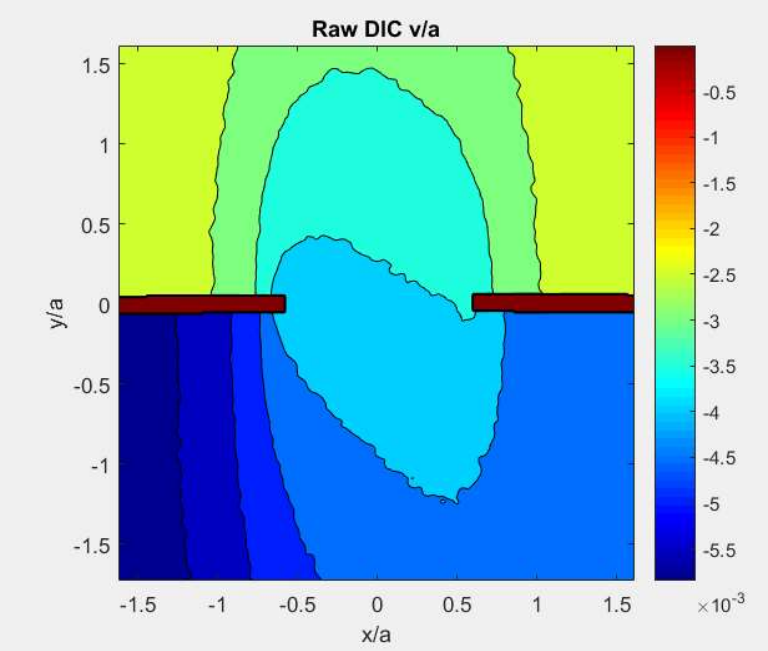

Figure 9-19: Normalized DIC raw *v*-displacement data in the strong/stiff *y*-direction

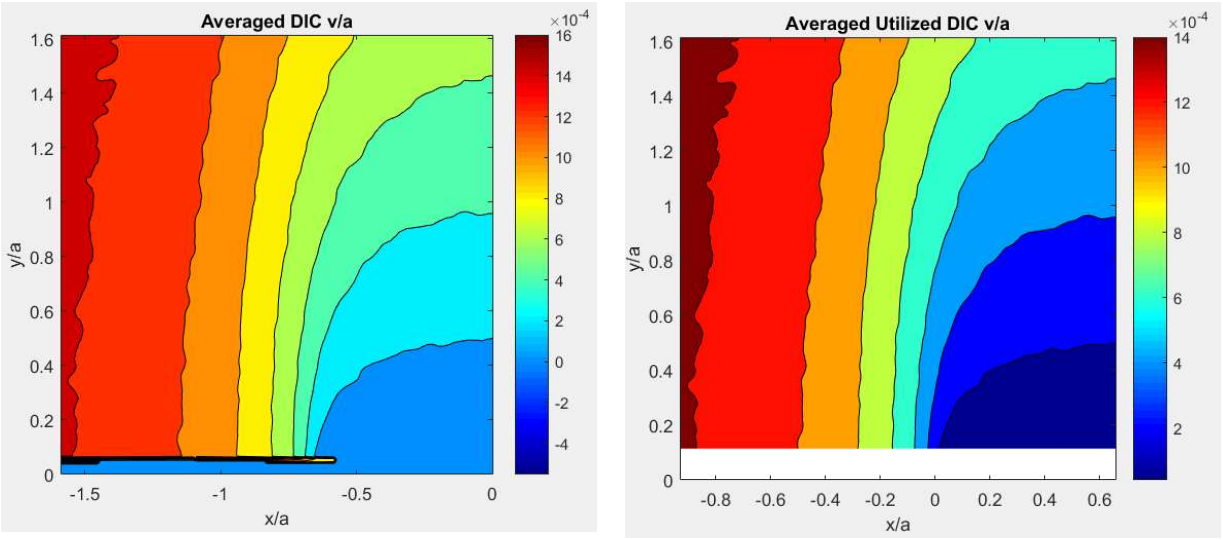

(a) (b)

Figure 9-20: (a) Recorded v-displacements averaged throughout the four quadrants and (b) Information of (a) post-processed to relocate coordinate origin at crack-tip and discarding unreliable crack-face data

The current DIC-hybrid complex variables stress analysis utilizes the Taylor power-series to express the complex variables Airy stress functions. From the averaged DIC v-displacement data (Figure 9-20(a) and Figure 9-21(a)), the measured information was considered at a distance $\geq y/a = 0.1$ (12 pixels) away vertically from the crack surface (Figure 9-20b). A total of $n_{DIC} =$ 25,718 equally-spaced DIC-recorded vertical displacements, v, were employed throughout the region defined by $-0.9 \leq x/a \leq 0.6$ and $0.1 \leq y/a \leq 1.5$. Locations of the $n_{DIC} = 25{,}718$ DIC v-displacement input values are shown in Figure 9-21(b). In addition to the DIC v-displacement information, symmetry condition $v = 0$ (equation (9-11)) was imposed at $h_1 = 6$ locations along the horizontal x-axis beyond the crack at $y = 0$, and stress $\sigma_{xy} = 0$ (equation (9-14)) was imposed at $h_2 = 3$ locations discretely along the vertical axis of symmetry (y-axis at $x/a = 0.67$, i.e., at the center of the plate). Finite boundary condition, stress $\sigma_{xy} = 0$ (equation (9-14)) was imposed at $h_3 = 3$

locations along vertical y-axis at $x/a = -1$ (left edge of plate). All the above-mentioned symmetry and boundary conditions were imposed at equally-spaced locations. Similar DIC-hybrid stress analysis results were obtained without imposing any symmetry or boundary conditions. In that case only DIC-measured v-displacement data were used as the system input, Appendix Q.

For the DIC-hybrid stress analysis and for the $n_t = n_{DIC} + h_1 + h_2 + h_3 = 25{,}730$ data values, the root mean square (RMS) between the DIC-measured v-displacements and imposed conditions, d, and the reconstructed v-displacements plus imposed conditions, d', were prepared for varying number of complex Airy stress coefficients, k, Figure 9-22. The RMS plot decreases little beyond $k = 7$ which suggests employing seven complex coefficients is reasonable. For a selected set of data, choosing an appropriate number of Airy coefficients in the stress functions can be very crucial. One typically wants to use as few coefficients as reasonable, but employing too few coefficients can give erroneous results. On the other hand, utilizing too many coefficients can cause computational problems and the solution to become singular.

The 14 real coefficients were evaluated from the $n_{DIC} = 25{,}718$ DIC v-displacement data, $h_1 = 6$ symmetry condition $v = 0$ in equation (9-11), $h_2 = 3$ symmetry condition $\sigma_{xy} = 0$ at $x = (W/2 - a)$ and $h_3 = 3$ finite boundary condition $\sigma_{xy} = 0$ at $x = -a$ in equation (9-14) and using least squares. Knowing the Airy coefficients and using equations (9-10) through (9-15), the in-plane displacement, stress and strain components were determined.

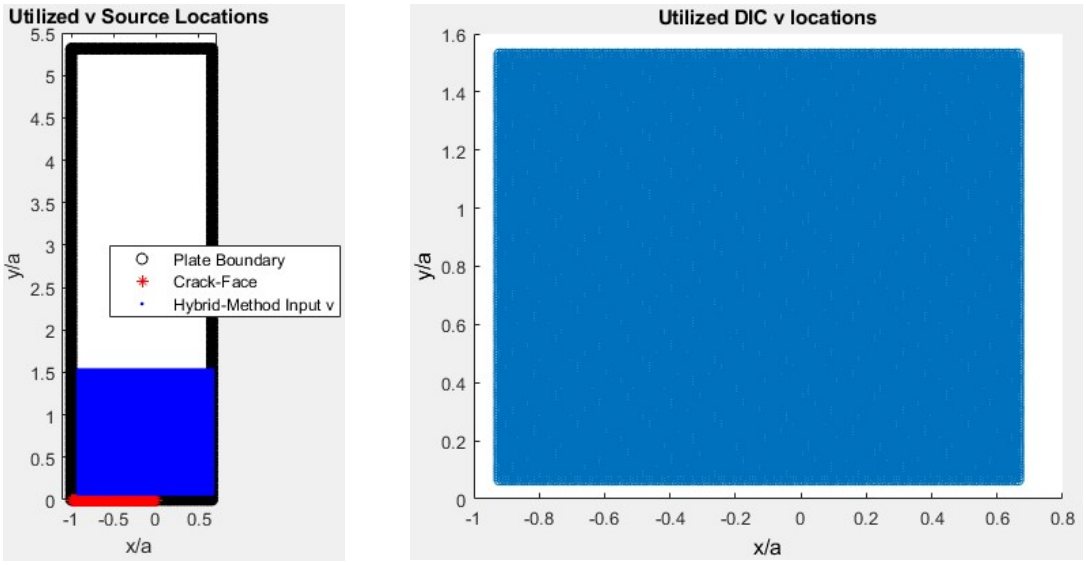

(a) (b)

Figure 9-21: (a) Quarter DEC-plate with DIC-measured *v*-displacements and (b) Source locations of utilized n_{DIC} = 25,718 DIC-measured *v* information

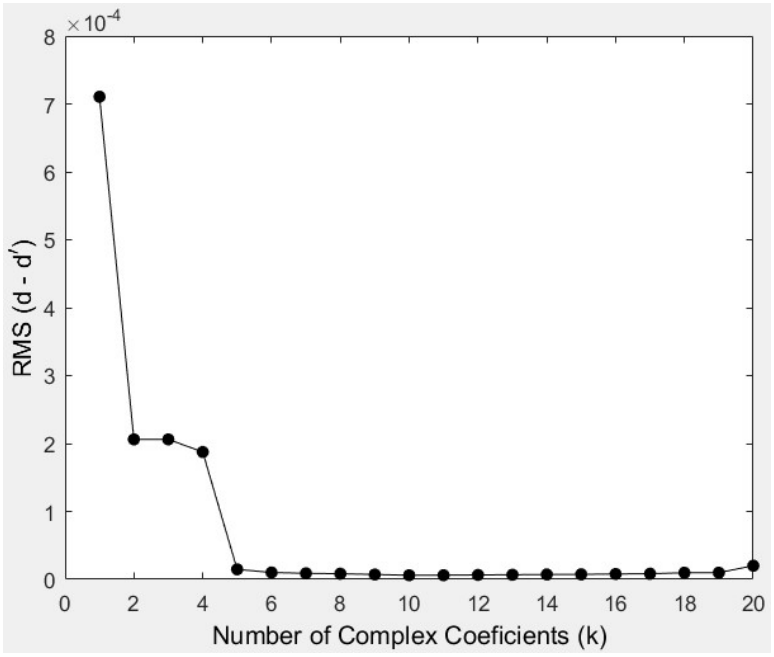

Figure 9-22: RMS values of (*d* - *d'*) versus the number of complex coefficients, *k*, for DIC-recorded n_{DIC} = 25,718 *v*-displacements and *h* = 12 imposed conditions in DIC-hybrid method using Taylor series

9.9. Results

9.9.1. DIC-Hybrid Stress Analysis

In-plane displacement and stress contours from the DIC-hybrid system are compared with FEM-predictions in Figure 9-23 through Figure 9-26. Contour plots show good agreement for the displacement and stress components derived from the two completely different methods, i.e., DIC-hybrid stress analysis method and FEA. Displayed results are for a load of $F^* = 7.1$ kN (1,600 lbs). Locations and displacement data are normalized with respect to the crack length, a, and stresses with respect to the far-field stress, $\sigma_0 = 21.23$ MPa, obtained from equation (9-43).

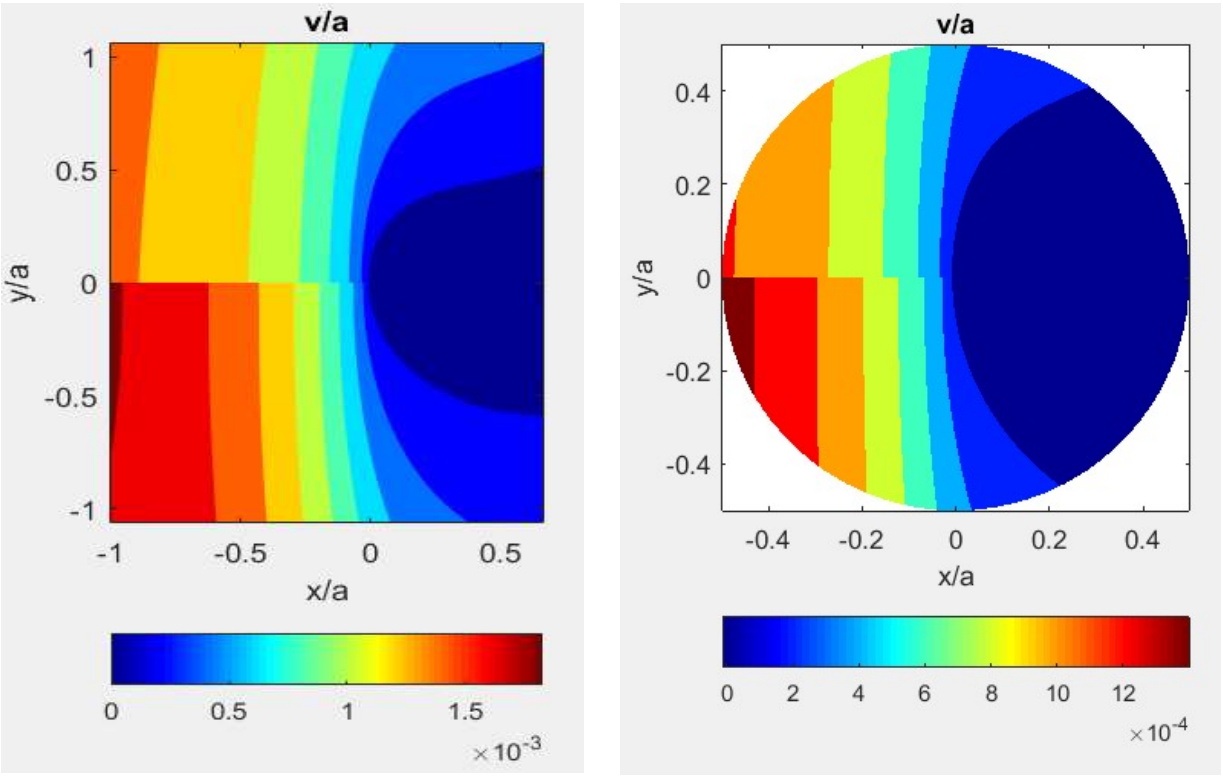

(a) (b)

Figure 9-23: Displacement v/a contours in strong/stiff y-direction from DIC-hybrid method (top) and FEM (bottom) for (a) Region of Figure 9-20(a) and (b) Region close to the crack-tip

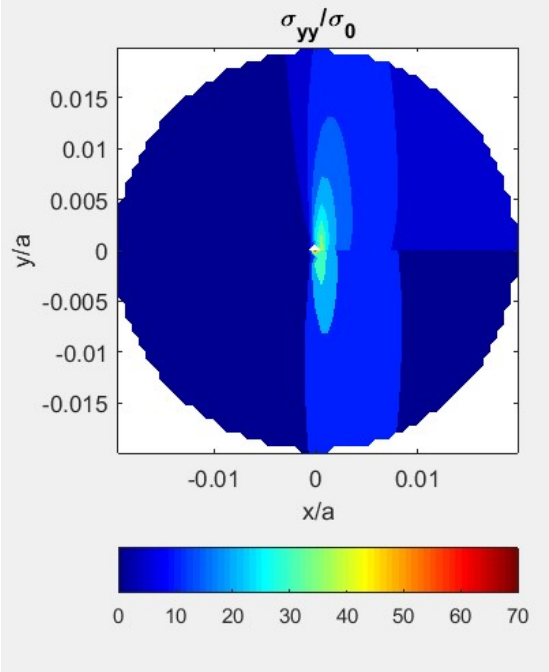

Figure 9-24: Stress σ_{yy}/σ_0 contours in region close to the crack-tip from DIC-hybrid method (top) and FEM (bottom)

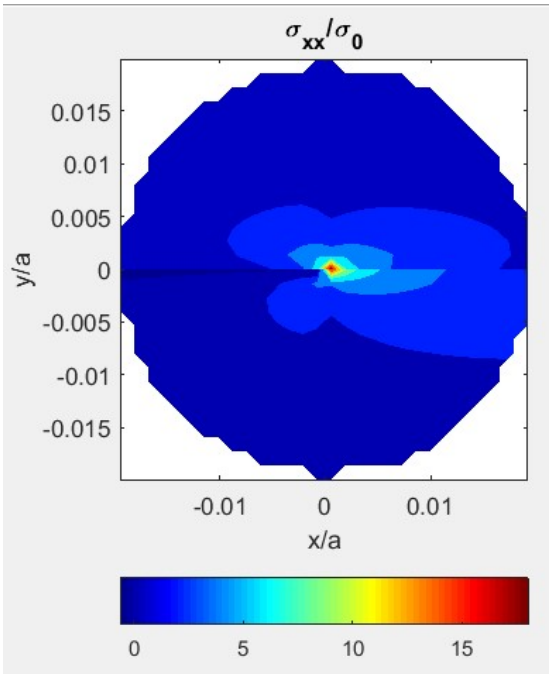

Figure 9-25: Stress σ_{xx}/σ_0 contours in region close to the crack-tip from DIC-hybrid method (top) and FEM (bottom)

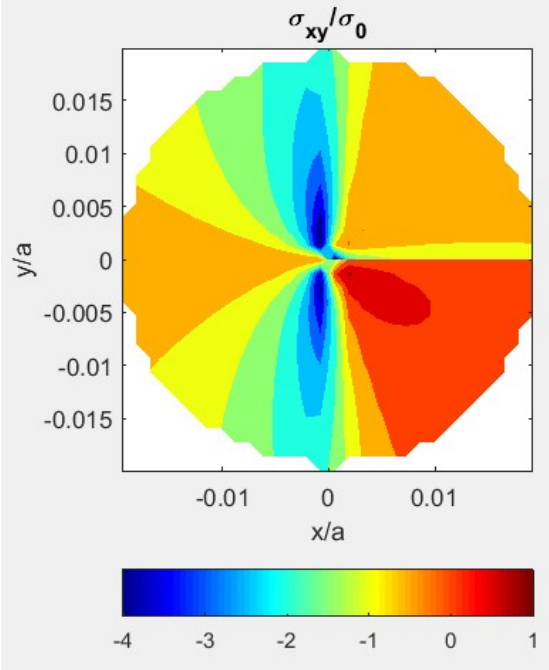

Figure 9-26: Shear stress σ_{xy}/σ_0 contours in region close to the crack-tip from DIC-hybrid method (top) and FEM (bottom)

9.9.2. SIF Determination

Knowing the full-field state of stress (in-plane displacements/stresses/strains) of the graphite-epoxy, finite-width, orthotropic plate with DEC under mode-I loading from the DIC-hybrid stress analysis method, the information was post-processed utilizing several of the previously mentioned concepts (of Section 9.4.2 'Determining SIF'**)** to evaluate K_I. Obtained results from these various methods using DIC-measured information are compared with those obtained from the system validation analyses using FEM predictions. As a result of using data from different sources (i.e., DIC vs. FEA) and different methodologies to process the data, slight differences between the obtained K_I were observed but all are within an acceptable range. The largest difference observed is from which source the utilized data is obtained, i.e., whether using

DIC-measured data or FEA-predicted data. The dependence of the results on the data selection ranges and length of the used finite series were also analyzed.

SIF was evaluated by processing DIC-measured in-plane displacements in the loading direction, v, according to the procedure illustrated in method-1 (based on Khalil/Ju's concepts). For this the DIC-recorded v-displacements were used in equation (9-17) to evaluate the unknown stress coefficients, whereas the expressions for E_j were obtained from equations (9-19), (9-20) combined with equations (9-23) and (9-24). Knowing the stress coefficients, K_{I} was obtained using equation (9-25). Details on evaluating the stress coefficients and hence K_{I} from measured v-displacement data based on Khalil/Ju's concept is provided in Chapter 8: equations (8-33) and (8-36). To observe the effect of the selected data range and the number of terms retained in the summation series, K_{I} was evaluated for various ranges of input data source locations and for varying number of stress coefficients, Table 9-7. The normalized K_{I} data of Table 9-7 and the RMS plot of Figure 9-27 show that the evaluated magnitudes of K_{I} are essentially independent of the source locations of the input data and number of retained terms in the summation series for $\gamma_{2N} > 10$. The independence of the source locations of the measured input displacement data is of particular significance in practice.

Table 9-7: Normalized SIF from method-1(Khalil/Ju's concepts) for various ranges of DIC-measured *v*-displacement input locations and number of utilized stress coefficients, γ_{2N}

Data selection radius, *r*	Normalized SIF, $\frac{K_I}{\sigma_0\sqrt{a}}$, for number of stress coefficient, γ_{2N} =							
	6	10	12	14	20	28	32	40
= 0.2*a* = 0.72*t*	1.92	2.11	2.08	2.08	2.08	2.08	2.08	2.08
= 0.3*a*	1.85	2.12	2.08	2.09	2.08	2.08	2.08	2.08
= 0.4*a*	1.79	2.13	2.08	2.08	2.08	2.08	2.08	2.08
= 0.5*a*	1.74	2.14	2.08	2.07	2.08	2.08	2.08	2.08
0.2*a* ≤ *r*≤ 0.5*a*	2.02	2.10	2.08	2.09	2.08	2.08	2.08	2.08

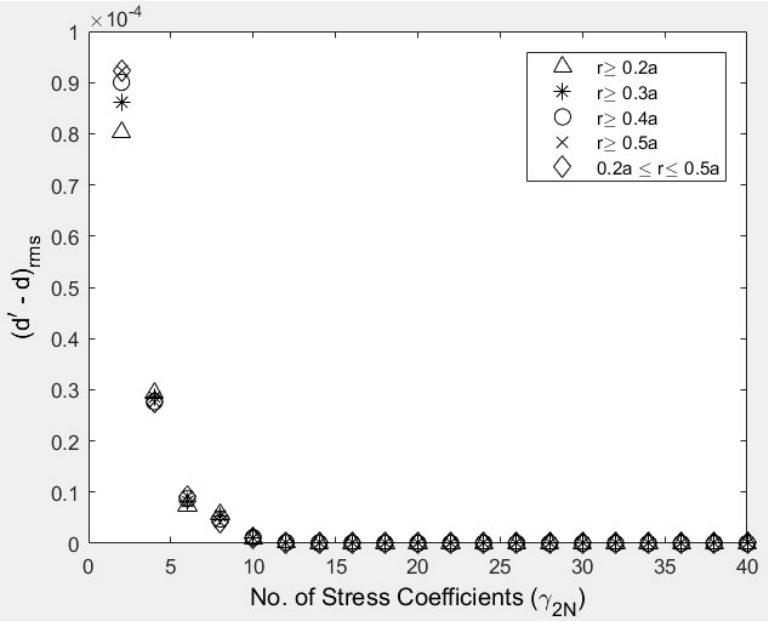

Figure 9-27: RMS for various number of stress coefficients, γ_{2N}, for four set of data locations using DIC-measured *v*-displacements as input in method-1 (Khalil/Ju's concept)

For the second experimental analysis, the DIC-hybrid method evaluated complete state of stress for the orthotropic DEC-plate (Figure 9-23 through Figure 9-26) was processed with the *J*-integral method to determine K_I. For various lengths of the integration path, d_{int}, of Figure 9-4, the *J*-integral for each separate integration path was determined using the equations of Table 9-1. Summing up the individual contribution of each segment of the square path, the total *J* value was determined and used in equation (9-34) to determine the SIF. Normalized K_I obtained by combining DIC-hybrid method and *J*-integral are shown in Table 9-8 for different integration paths.

The DIC-based experimentally determined values of K_I by the two methods, i.e., Khalil/Ju's concepts and *J*-integral agree very well with each other, Table 9-7 and Table 9-8. The FEM-based results are approximately 8% higher. That the evaluated values of K_I by the *J*-integral method (Table 9-8) are independent of the location of the integration paths (i.e., source locations of input data) is significant for practical applications.

Table 9-8: Normalized SIF for a finite orthotropic DEC-plate from DIC-hybrid and method-2 (*J*-integral) for various integration paths

Normalized SIF, $\frac{K_I}{\sigma_0\sqrt{a}}$, from hybrid-method and *J*-integral for		
Arm length of square integration path, d_{int}	FEA (ν)	DIC (ν)
$0.1a$ = 1.9 mm	2.274	2.079
$0.2a = 0.72t$	2.275	2.073
$0.3a$	2.275	2.056
$0.4a$	2.276	2.036
$0.5a$	2.277	2.022
$0.6a$ = 11.4 mm	2.281	2.021

The integration path for the *J*-integral is selected only up to $d_{int} = 0.6a$. A distance $d_{int} = 0.667a$ would reach the center of the DEC-plate. Note that d_{int} is measured from the crack-tip. There is also an edge crack on the right side of the center-line and results should not be influenced by the right-edge crack. Therefore, the plate was not analyzed beyond $r = 0.6a$.

The SIF, K_I, was also determined according to the concepts of method-4 (Sih, Paris and Irwin's concept). Using DIC-hybrid computed in-plane stresses, σ_{yy}, in direction perpendicular to the crack-face, in this case also in the loading direction, y, in equation (9-42) provides the SIF, K_I. The obtained normalized K_I at various distance along x-axis for $y = 0$ of Figure 9-1 from the crack-tip are presented in Table 9-9. Over the range $0.16a = 3$ mm $\leq r \leq 0.5a = 9.5$ mm from the crack-tip, K_I changes by less than 3%. This essential independence of location from crack-tip is significant for practical applications.

Table 9-9: Normalized K_I from method-4 (Sih, Paris and Irwin's concept) using DIC-hybrid computed normal stresses perpendicular to crack-face, σ_{yy}, at various locations, r, from the crack-tip along $y = 0$

Distance from crack-tip, $r =$	$0.16a$	$0.2a = 0.72t$	$0.3a$	$0.35a$	$0.4a$	$0.45a$	$0.5a$
Normalized SIF, $\frac{K_I}{\sigma_0\sqrt{a}}$	2.09	2.09	2.10	2.11	2.12	2.13	2.14

The determined opening-mode SIF, K_I, of the DEC graphite-epoxy plate by the various methods demonstrated here from either FEM-predicted or DIC-measured input data are shown in Table 9-10. The first three values are experimentally determined normalized K_I from method-1, -2 and -4 and the last three are normalized K_I obtained for FEM data from method-1, -2 and -3. Results, which show dependence of the evaluated SIF on the different data sources (i.e., experimental or predicted), demonstrate excellent agreement between the obtained SIF from the different methods when the data source is the same.

For Khalil/Ju's concept, the FEM-prediction/DIC-measured information is directly utilized to find the SIF. For the other two determinations, the predicted or experimental v-data is used in the hybrid-method to find structural information near the crack-tip from which the SIF are obtained.

The values of K_I by the three experimental schemes agree within 2% of each other, as do those among the three FEM-based analyses. Compatible with the good agreement between the FEM-predicted and DIC-based displacements and stresses of Figure 9-23 through Figure 9-26, the average DIC- and FEM-based values of K_I agrees within 8% of each other. Acknowledging the comment by Shukla et al. [16] to keep $r \geq 0.5t$ to avoid any local plasticity, present results for $r \geq 0.5t = 0.15a$ should be emphasized.

Table 9-10: Comparison between results of averaged normalized K_I

Averaged normalized SIF, $\frac{K_I}{\sigma_0\sqrt{a}}$, from					
DIC-measured displacement, v			FEM-predicted displacement, v		
Method-1 (Khalil/Ju)	Method-2 (J-integral)	Method-4 (Sih, Paris and Irwin)	Method-1 (Khalil/Ju)	Method-2 (J-integral)	Method-3 (Mogadpalli and Parameswaran)
2.08	2.10	2.11	2.26 (v, u, σ_{xx}, σ_{yy}, σ_{xy})	2.27	2.26

The DEC plate of Figure 9-1 was also analyzed using the concepts provided by Bao et al. [93] which are included in Appendix R. Details regarding the Bao's concepts are provided in Chapter 8, Section 8.4.5.5. Analytical concepts from fracture analyses with composites done by Bažant et al. [180] are also provided in Appendix R. The analytical concepts of Bažant's study are similar to those of Bao's [93].

9.10. Summary, Discussion and Conclusions

Combining experimentally measured information with strong mechanics-based analytical expressions of complex variables Airy stress functions, conformal mapping, analytic continuation, power-series expansions and least squares is an effective means of stress analyzing loaded, finite-width, orthotropic members with various cutouts [9,22,70,72,84,88]. This approach can be extended to analyze both isotropic and anisotropic loaded, finite, plates involving cracks.

DIC-determined stress and/or displacement fields near the crack-tip are used with concepts such as *J*-integrals or analytical expressions of near crack-tip singular stress/displacement fields to find the SIF. Obtained results from these several different techniques exhibits good agreement. Experimental reliability is demonstrated by FEM.

Not requiring experimental data very near the crack-tip or along the crack surfaces or near any other edges, nor requiring any knowledge of the external loading are advantages of this approach over other crack-analysis techniques. The (fairly) near crack-tip displacement/stress information is achieved employing measured displacement data with rigorous mechanics-based formulations of Airy stress functions instead of arbitrary schemes typically used in commercially available software. Reasonable near crack-tip states of stress and displacement are achieved without having any experimental information in those regions. This is important as experimental data very near the crack is often very unreliable.

Expressions of crack-tip nearby singular stress/displacement fields or path independent *J*-integrals are used to find the SIF directly from each of FEM-predictions, DIC-measured *v*-displacement data or from the DIC-hybrid method computed stresses and displacements. Experimental fracture analysis methods tend to need reliable input data very close to the crack-tip. In real world applications, one might face the challenge of not having reliable stress/strain information sufficiently near the crack-tip. Much of this challenge is overcome by the present experimental-analytical hybrid concept as it does not require measured data very near the crack. Using the near crack-tip singular stress field expression (method-4 Sih, Paris and Irwin's concept) is computationally a very simple way to find SIF from known stresses. On the other hand, the method of combining the concepts of *J*-integral with DIC-hybrid stress analysis (method-2) involves cumbersome, relatively complicated calculation procedures but enables one to accurately

evaluate SIF at locations either close or away from the crack-tip. The approach (method-1 Khalil's concept) where experimental displacement data are used in expressions of the near-by crack-tip displacement/stress fields based on Airy stress functions and conformal mapping is a computationally effective way to find SIF based on measured data originating close or far from the crack-tip.

The presented hybrid-method provides reliable techniques to determine SIFs in orthotropic composites from recorded displacement information without requiring measured data in the immediate vicinity of the crack. The general approach is applicable to orthotropic or isotropic materials, operating in a field or industrial environment (i.e., not restricted to the laboratory) and the concepts can be extended to other shaped or loaded structures and other crack configurations (Chapter 8). Using different mapping functions such as the Schwarz-Christoffel mapping could enable application to highly complicated crack shapes. Virtually any form of experimental data or external loading (Appendix H) can be handled by this method, as can isotropic cases (Appendix O). That the experimental results by each of the three methods are independent of the widely varying source locations is significant.

Determining K_I in a finite DEC tensile orthotropic plate is of interest in its own right. However, this geometry and loading benefited from being able to conduct a reliable FEA with which to compare the experimental results. A desirable advantage of the herein developed technique is its ability to determine SIFs in situations which preclude obtaining a confident FEA, e.g., when not knowing the loading conditions. The latter are often unknown with real-world/practical structures. Unlike the present approach, it is extremely difficult to obtain SIFs for general but finite situations by purely theoretical or numerical methods if the external loading is unknown.

Chapter 10. Summary, Discussion and Conclusions

Motivated by practical needs, the presented hybrid technique enables one to stress analyze finite structures containing cutouts/cracks full-field, including along the boundaries of the discontinuities. This is accomplished without knowing the external loading or boundary conditions and is applicable to isotropic or orthotropic composite materials. The method overcomes the shortcomings of purely experimental/analytical/numerical methods. Major contributions of this thesis include the following:

1. Experimentally demonstrated the ability to reliably stress analyze tensile-loaded, finite, orthotropic plates which contain either a circular hole, elliptical hole or double-edge cracks.

2. Numerically substantiated the hybrid-method's capability to stress analyze isotropic or orthotropic plates of virtually any elastic material, having essentially any hole-size to plate-width ratio (infinite or finite plates based on $2a/W$) and with any hole-opening ratio or sharpness (a/b). This demonstrates that when processing measured displacement data with conformal mapping and analytic continuation concepts, Lekhnitskii's theory of anisotropic elasticity can reliably analyze finite geometries.

3. The presented technique is capable of analyzing structures with significant amount of missing or unreliable input data at structurally critical locations by processing (highly) distant reliable measured information. This demonstration also illustrates the method's ability to analyze a plate with non-rectangular outer boundary.

4. Numerically illustrated the hybrid-method's ability to provide reliable fracture information for essentially any type of cracked plate (plates with any type of cracks and material properties) under mode-I loading.

5. Although both TSA and DIC measured data are employed, this thesis emphasized the use of a single component of measured displacement. Among other features, this acknowledges the comparatively simple experimental set-up and requirements of DIC.

6. Detailed analytical procedures are included for rectangular or polygonal cutouts, inclined elliptical openings or inclined cracks.

7. A systematic procedure is provided to select an appropriate number of coefficients to use.

8. This rigorous mechanics-based hybrid-method does not require knowing the external loading or boundary conditions or measured input information near the cutouts, it automatically/simultaneously separates and smooths the displacement and stress components, and does not involve differentiating the measured quantities using arbitrary techniques. Equilibrium and compatibility are satisfied. Boundary conditions can be involved/satisfied.

9. The successful ability to synergize several different fracture models with the hybrid-method and evaluate SIFs was demonstrated. The *J*-integral proved to be particularly effective in evaluating important fracture information in cracked orthotropic finite plates.

10. The use of Taylor series to fracture analyze cracked orthotropic materials offers an effective way to analyze plates having variety of crack configurations employing only a single mapping function.

Chapter 11. Future Considerations

1. Stress analyze orthotropic structures containing parabolic, triangular, rectangular, oval, polygonal, inclined elliptical openings/notches or inclined cracks. Of particular interest would be to assess if the present approach is able to handle these correctly as highly finite geometries.

2. Determine stresses in pinned/bolted joints in orthotropic composites from DIC-recorded displacement data. Consider using a stress function and imposing available/appropriate boundary conditions.

3. Stress analyze inclined-loaded perforated orthotropic plates, i.e., the applied loading not in a direction of material symmetry.

4. Stress analyze natural fiber composite/green composite (NFC) [181–183] structures and natural composites such as wood and orthopedic structures [184].

5. Stress analyze structures containing multiple geometric discontinuities and/or those with different/varying material properties, e.g., functionally-graded materials.

6. Analyze composite plates with cracks emanating from edge of a hole or notch. Might consider mapping the crack using the Taylor series.

7. Extend the approach to analyze interface cracks between dissimilar anisotropic materials [177,185] or elastoplastic heterogeneous materials [186].

8. Consider the research to structures fabricated from non-linear/non-elastic materials, e.g., plasticity, non-linear elasticity [187], viscoelasticity or polymers.

9. Extend concepts to plates/beams under bending, complex loaded plates and/or non-symmetrical cases.

10. Assess the feasibility of applying present DIC concepts to situations involving vibrations and/or fatigue.

11. Combine the present hybrid approach into commercial displacement-based (e.g., DIC) algorithm software. Such would provide accurate displacements and strains at and near the boundaries of cutouts without having to filter or differentiate the displacement information. This should eliminate the drawbacks of conventional displacement-based experimental techniques, i.e., not providing reliable measured information or masking high strain gradients near geometric discontinuities as a result of filtering the measured data.

12. Extend the concepts of Chapters 6 and 7 to orthotropic materials.

13. Extend the concept to analyze orthotropic structures with complicated arbitrary cutouts by using the Schwarz-Christoffel mapping function for polygons [188].

14. Extend the present hybrid-DIC concepts to perforated structures whose internal and external geometries are both highly complicated (e.g., Reference [189]).

15. Extend the approach to thermal stress analysis of orthotropic structures with discontinuities, i.e., structures under thermal loading [190].

16. Consider the approach for analyzing plates undergoing large deformation due to bending, where along with the Airy stress function the effect of the transverse displacements need to be considered in terms of a non-linear partial differential equation representing the structural behavior [191].

17. Consider extending the approach to non-flat/curved surfaces.

Appendices

Appendix A. Elastic Properties of $[0_{13}/90_5/0_{13}]$ Graphite-Epoxy Laminate

Material properties E_{11}, E_{22}, ν_{12} and G_{12} of the orthotropic $[0_{13}/90_5/0_{13}]$ graphite-epoxy laminate (from Kinetic Composites, Inc., Oceanside, CA) were measured. Two sets of uniaxial tests were conducted on two sets of three different types of composite tensile coupons. Coupons were tested in the 0°, 90° and ± 45° directions with respect to the strong/stiff laminate orientation. All the coupons were prepared from the same graphite-epoxy laminate sheet with a thickness, t = 5.28 mm (0.208"). The test specimens were tested according to ASTM standard D3039M-00 guidelines. Strain-gages were mounted on the specimens both in the loading direction and perpendicular to the loading direction, Figure A-1(a). Standard procedures (provided by Vishay Precision Micro-Measurements Group [82]) were followed for specimen surface preparation and gage installation. The coupons were tensile loaded along the strong/stiff direction and perpendicular to the strong/stiff direction to obtain E_{11}, ν_{12} and E_{22}, respectively. A tensile test was conducted with applied load ± 45° with respect to the principal laminate direction of material symmetry to measure E_{45}. Using the transformation relation of equation (A-1) and the measured values of E_{11}, E_{22}, E_{45} and ν_{12} the shear modulus G_{12} was obtained.

The 0° and 90° tensile coupons had a width, W = 12.7 mm (0.5") and length, L = 25.4 cm (10") and the ± 45° tensile coupons had a width, W = 9.53 mm (0.375") and length, L = 27.94 cm (11"). Tests were conducted using two different loading-frames. The first set of tensile tests was conducted using a 4.5 kN (10,000 lbs) capacity Sintech machine with screw driven wedge grips

and a MTS extensometer, Figure A-1(b). The load and strain readings were recorded using the data acquisition system equipped with the Sintech load-frame. The second set of tests was done using a 89 kN (20,000 lbs) capacity hydraulic-grip MTS machine. In this case the applied loads were monitored with an oscilloscope and the strain-gage outputs were recorded using a strain conditioner, Figure A-2. For all the tests, load and strain data were recorded upon loading and unloading the coupons.

The 0° coupons were loaded from essentially 0 to 17.79 kN (4,000 lbs) at an increment of 2.22 kN (500 lbs), the 90° coupons from 0 to 4.45 kN (1,000 lbs) in increments of 445 N (100 lbs) and the ± 45° coupon from 0 to 2.67 kN (600 lbs) in increments of 222 N (50 lbs). The maximum load for each type of specimen was selected based on approximate strength calculations for the graphite-epoxy composite according to lamination theory.

The laminate's stiffness, i.e., elastic modulus in any orientation x with respect to the axes of material symmetry 1 and 2, gives the following relationship

$$\frac{1}{E_{xx}} = \frac{m^2}{E_{11}}(m^2 - n^2 v_{12}) + \frac{n^2}{E_{22}}(n^2 - m^2 v_{21}) + \frac{m^2 n^2}{G_{12}} \qquad \text{(A-1)}$$

where m = sin (θ) and n = cos (θ), and θ is measured from direction 1 in a counter clock-wise direction. For θ = ± 45° the above equation (A-1) provides the elastic modulus in the ± 45° direction with respect to the strong/stiff fiber direction, i.e., $E_{xx} = E_{45°}$ for $\theta = 45°$ (equation (A-2)). G_{12} was consequently evaluated from measured values of E_{11}, E_{22}, E_{45} and v_{12} in equation (A-2).

$$\frac{1}{E_{45}} = \frac{(0.5)^2}{E_{11}}((0.5)^2 - (0.5)^2 v_{12}) + \frac{(0.5)^2}{E_{22}}((0.5)^2 - (0.5)^2 v_{21}) + \frac{(0.5)^2(0.5)^2}{G_{12}} \quad \text{(A-2)}$$

Obtained test results from the first set of loading (Sintech machine and extensometer) are provided in Figure A-3 through Figure A-9, and for the second set of loading (MTS and strain-gages) in Figure A-10 through Figure A-13, respectively.

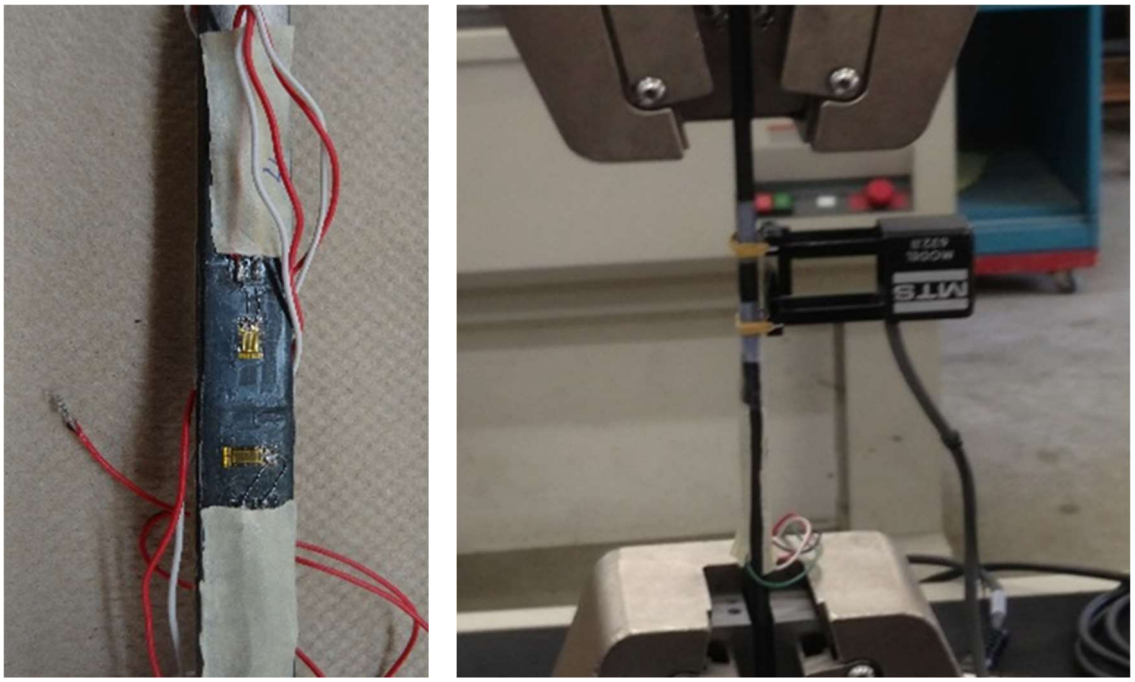

(a) (b)

Figure A-1: (a) Composite coupon mounted with strain-gages and (b) Loaded composite coupon with extensometer

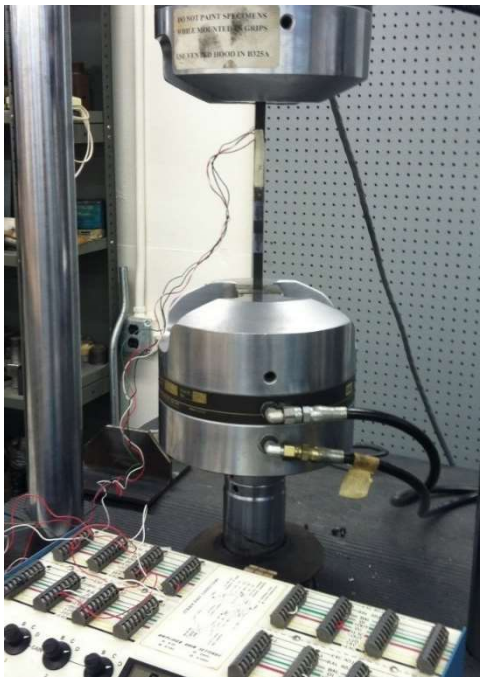

Figure A-2: Experimental set-up for tensile testing of strain-gaged graphite-epoxy coupon using a strain-conditioner

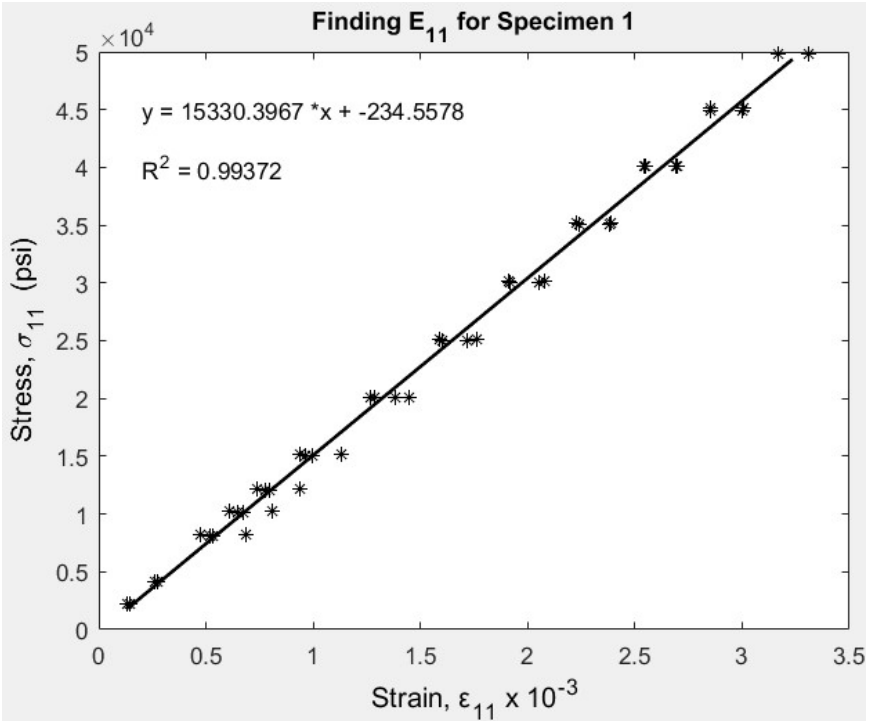

Figure A-3: Measured material property E_{11} for specimen 1 from test 1

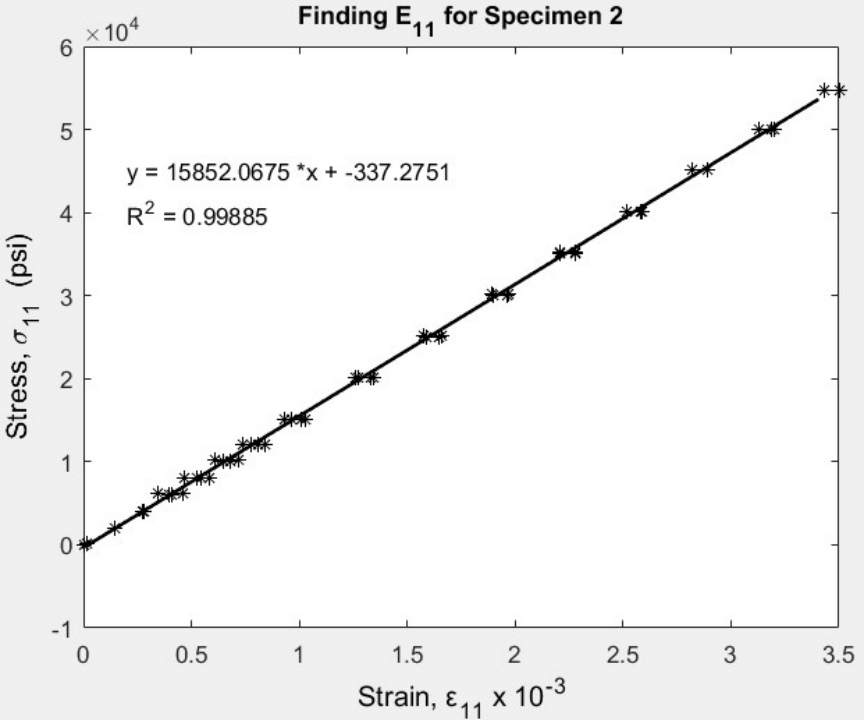

Figure A-4: Measured material property E_{11} for specimen 2 from test 1

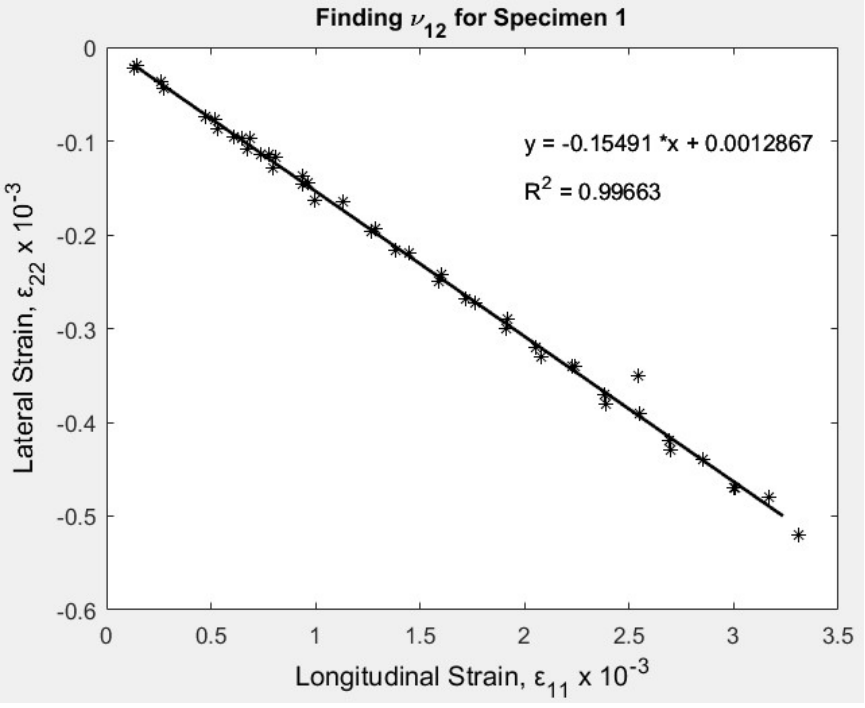

Figure A-5: Measured material property ν_{12} from test 1

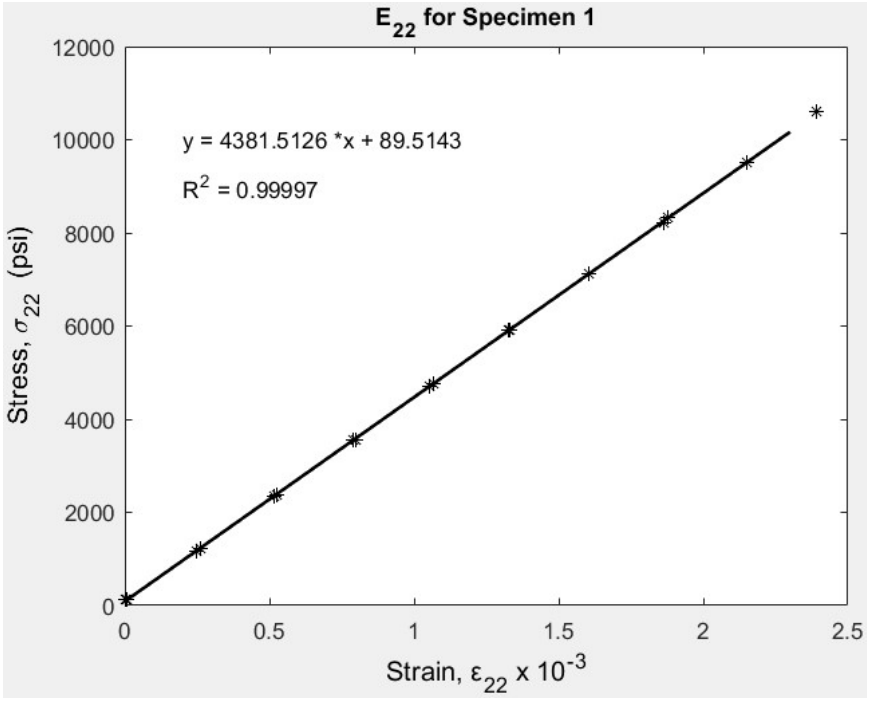

Figure A-6: Measured material property E_{22} for specimen 1 from test 1

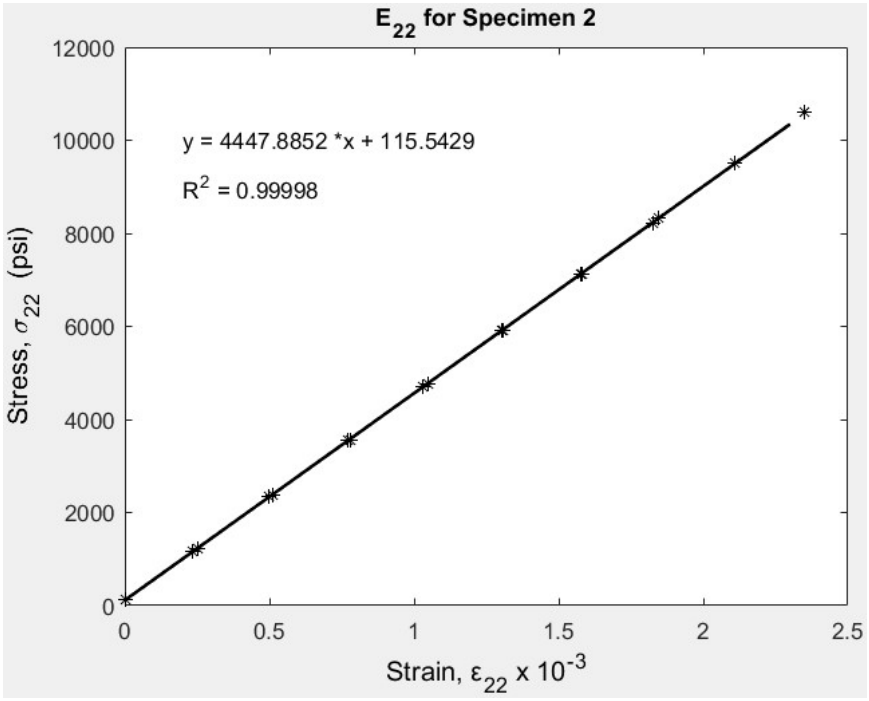

Figure A-7: Measured material property E_{22} for specimen 2 from test 1

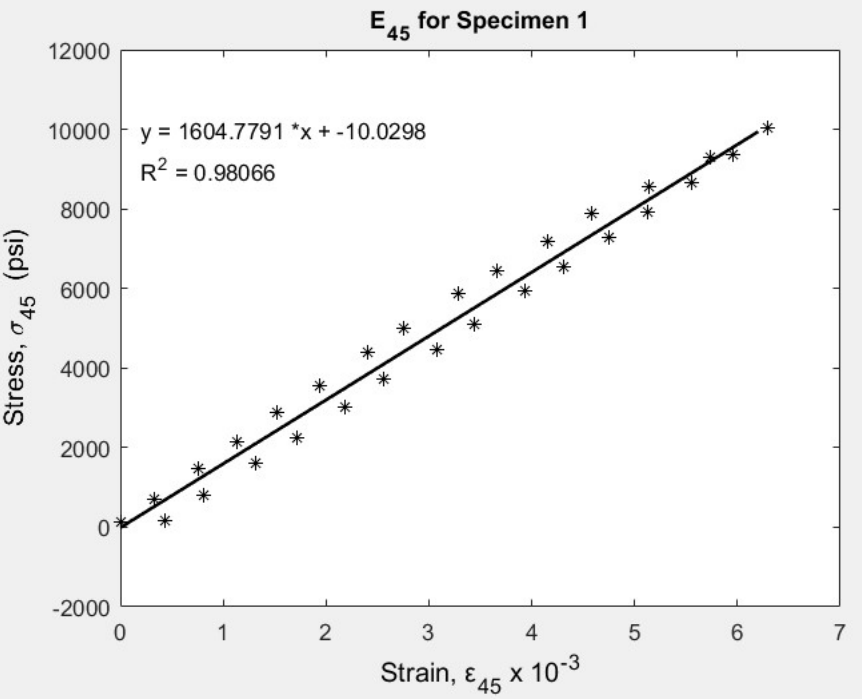

Figure A-8: Measured material property E_{45} for specimen 1 from test 1

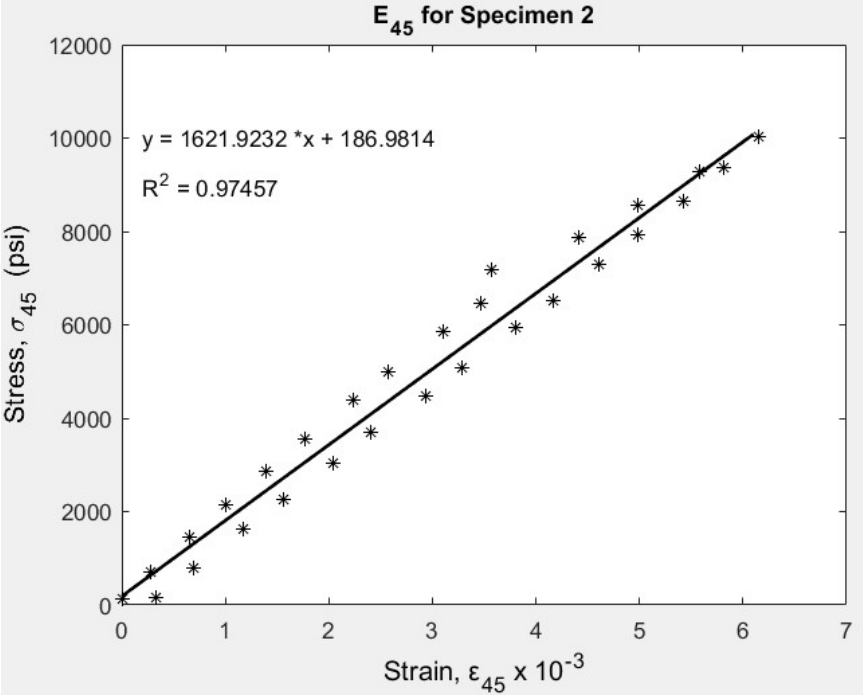

Figure A-9: Measured material property E_{45} for specimen 2 from test 1

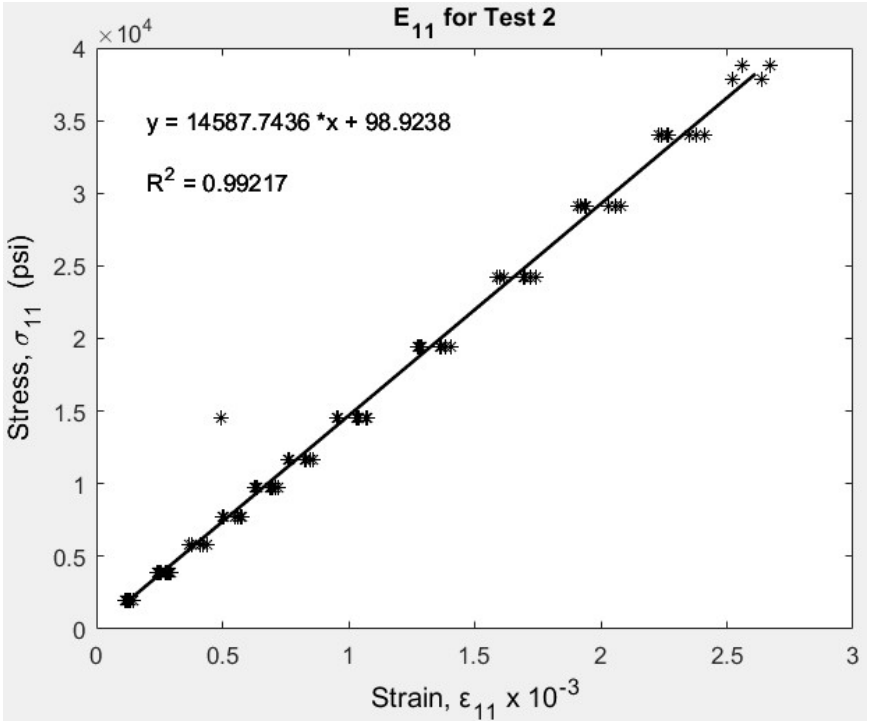

Figure A-10: Measured material property E_{11} from test 2

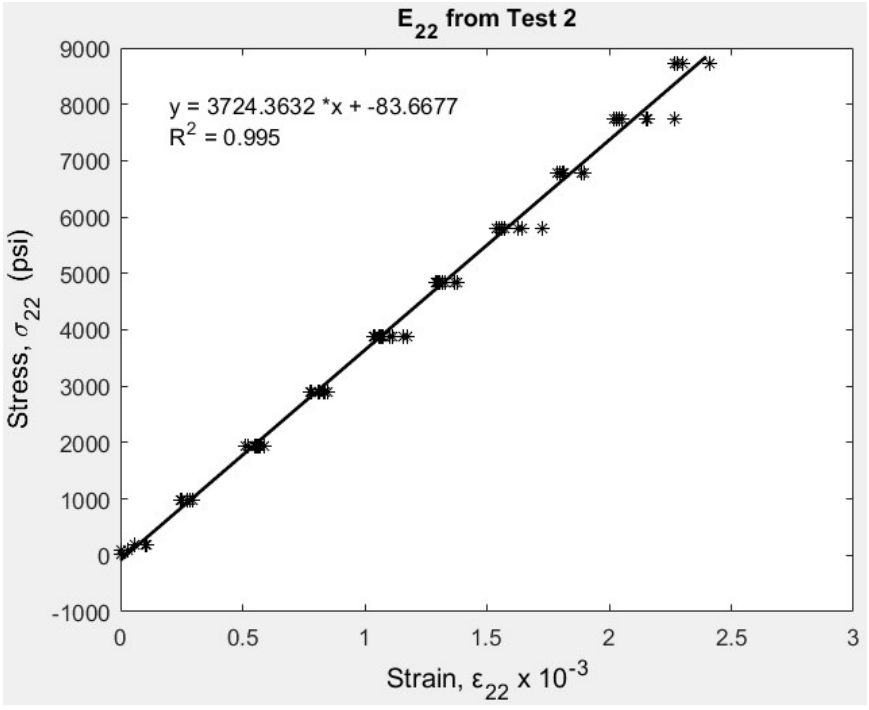

Figure A-11: Measured material property E_{22} from test 2

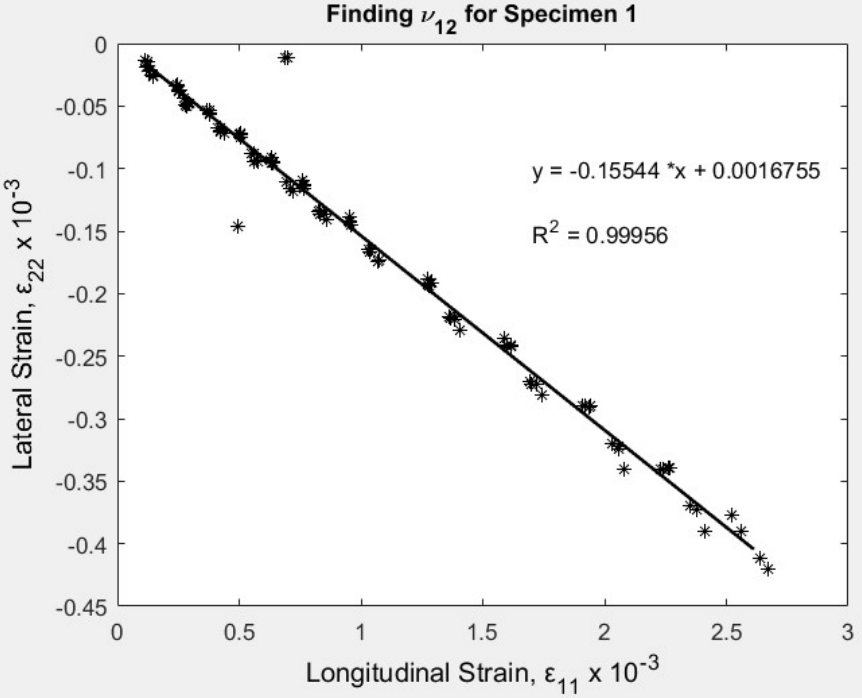

Figure A-12: Measured material property ν_{12} from test 2

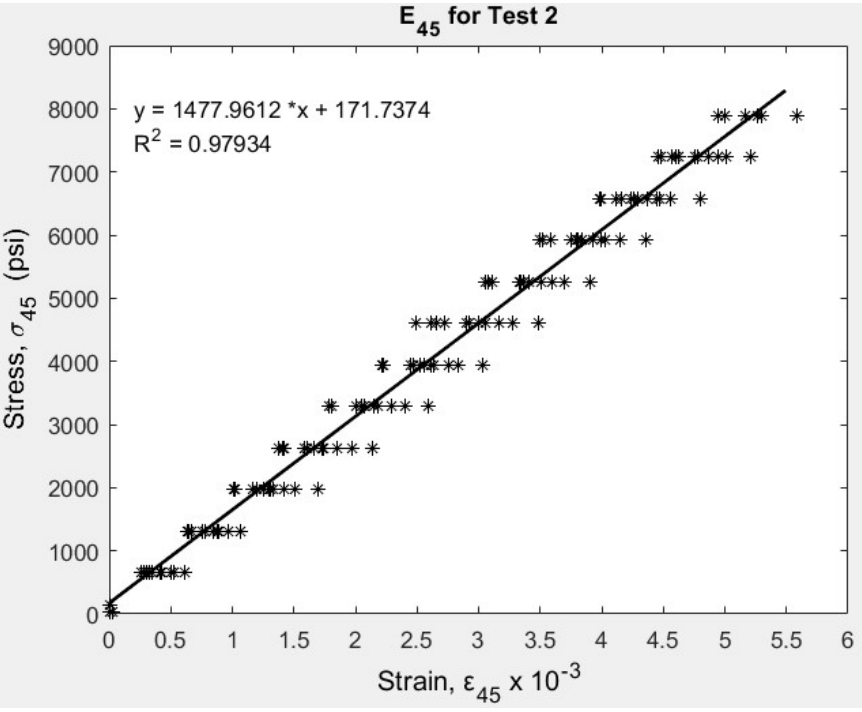

Figure A-13: Measured material property E_{45} from test 2

Averaging the values of each of the respective material properties obtained from specimen 1 and 2 in the first set of tests (Figure A-3 through Figure A-9) gives E_{11} = 107.6 GPa (15.6 × 10^6 psi), E_{22} = 30.5 GPa (4.4 × 10^6 psi), E_{45} = 11.1 GPa (1.6 × 10^6 psi) and ν_{12} = 0.16. Knowing these material quantities, averaged G_{12} = 3.12 GPa (0.453 × 10^6 psi) is obtained from equations (A-1) and (A-2). For the second set of tests, each test was done multiple times on a single coupon. Using the data from these tests (Figure A-10 through Figure A-13) the following averaged values are E_{11} = 100.7 GPa (14.6 × 10^6 psi), E_{22} = 25.7 GPa (3.7 × 10^6 psi), E_{45} = 10.2 GPa (1.5 × 10^6 psi) and ν_{12} = 0.16. From equation (A-2), G_{12} = 2.9 GPa (0.418 × 10^6 psi). The average of these two set of test results are used as material properties for the [$0_{13}/90_5/0_{13}$] graphite-epoxy laminate (provided by Kinetic Composites, Inc.) for all analyses conducted in this thesis. The final averaged material properties are E_{11} = 104.1 GPa, E_{22} = 28.1 GPa, G_{12} = 3.0 GPa and ν_{12} = 0.16.

Appendix B. Machining Perforated Composite Plates using Water-Jet Cutting

Composites, due to their non-homogeneity and strength, requires special cutting tools when machining composite parts. Use of conventional machining tools for composite cutting often leads to early tool wear. The machined parts can also experience fiber breakage or pull-out, cracking, fraying and/or delamination, and thus a possible compromise in the material's strength. Water-jet cutting is a reliable, cost effective and fast machining technique for composites. Abrasive water-jet cutting can cut most materials with high precision. Water-jet cutting relies on supersonic erosion to cut materials rather than on friction and shearing like conventional cutting techniques. This generates satin-finished edges in the final product (eliminates the need for secondary finishing), reduces machining induced defects and has no thermal damages. It is also an environment friendly procedure as it produces no toxic fumes or cut dust/particles or unnecessary wastage of the raw materials [192,193].

Water-jet cutting (located at UW-Madison College of Engineering Student Shop) was used to machine circularly-perforated graphite-epoxy plates from a 5.28 mm (0.208") thick laminate. A water pressure of 413.69 MPa (60,000 psi), along with abrasive substances (garnet), were used for the water-jet. To avoid any machining induced defects while creating the holes, the composite was clamped between aluminum plates and a small starter hole was initially drilled. Using the abrasive impregnated water-jet around the starter hole, the final hole diameter was achieved, Figure 4-3(a).

Some challenges exist when water-jet cutting high-strength composite laminates and measures taken to avoid these will be discussed. To cut composite coupons, if the water-jet directly

impacts the composite laminate, sudden exposure to a high-pressurized jet can cause delamination or flaking of the composite. Therefore, the cutting path is selected such that initially the water-jet starts at a location exterior to the laminate and then slowly moves on to the composite laminate. After a component is made by the water-jet according to desired dimensions, then one should move the water-jet to an exterior location before it is turned off. A few different procedures were tested to create round holes, not all of which were successful. In the first attempt the water-jet itself was used to pierce a small hole and gradually go around in a circular path to create the desired round cutout. This procedure led to severe delamination (Figure B-1). In the second attempt a piece of stainless-steel was held on top of the graphite-epoxy laminate and again the water-jet was used to initially pierce through the steel and the laminate and eventually create the circular hole. This was less aggressive on the laminate, but the composite plate still suffered noticeable delamination (Figure B-2). The third attempt involved drilling a small pre-hole in the laminate and then the water-jet was used to remove more material long the circumference of the start-up hole and create the circular hole of desired radius. This avoided any composite delamination but drilling the start-up hole initiated flaking of the material around the edge of the hole (Figure B-3). The final attempt involved clamping the composite between two aluminum plates (like a sandwich structure with the composite plate as the core). A very small central pre-hole was initially drilled through the sandwich plate. By water-jet cutting around the start-up hole, a circular hole was eventually machined to the final diameter. This procedure avoided any machining induced defects in the machined circularly-perforated graphite-epoxy plate (Figure 4-3(a)) and was used for the DIC experiment.

Figure B-1: Severe delamination in the composite laminate due to creating a circular hole directly using water-jet cutting

Figure B-2: Delamination in the composite laminate when using a stainless-steel plate on top of the composite coupon when creating a circular hole using water-jet cutting

Figure B-3: Flaking in the composite laminate when directly drilling into the coupon to create a start-up hole

Appendix C. Out-of-Plane Displacement Monitoring in Circularly-Perforated Orthotropic Plate

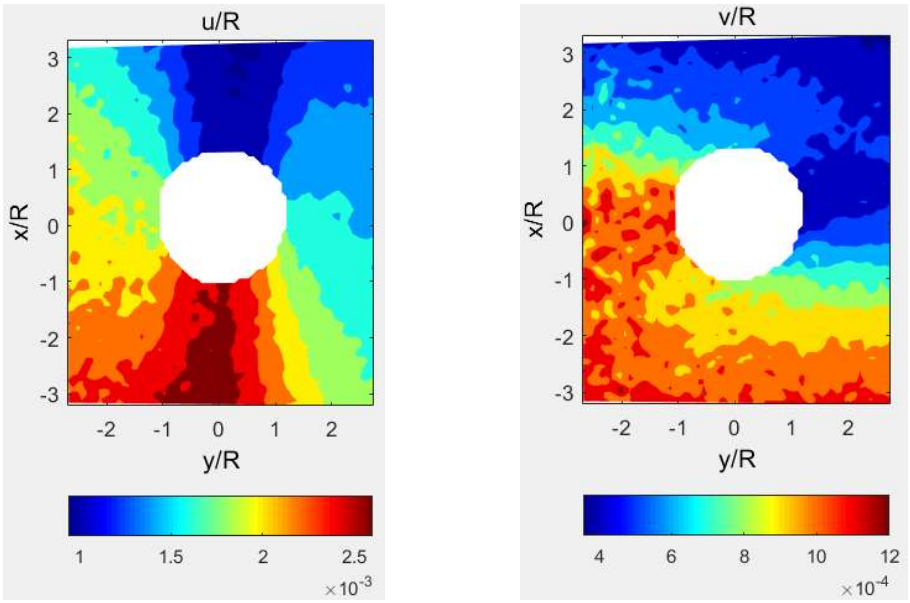

(a) (b)

(c)

Figure C-1: Contours of 3D-DIC provided raw displacements (a) u/R, (b) v/R and (c) w/R, showing no sign of out-of-plane bending for the loaded circularly-perforated plate of Figure 4-2

From the 3D-DIC measured raw data of the above Figure C-1 for the circularly-perforated orthotropic plate of Figure 4-2, it can be seen that the out-of-plane displacements, w, is significantly smaller than the in-plane displacements along the loading direction, u, and transverse to the loading direction, v. The maximum value of u is 88.88 times larger than the maximum value of w. Similarly, the maximum value of v is 36.08 times larger than the maximum value of w. This indicates there was no out-of-plane bending other than Poisson's effect while loading the circularly-perforated orthotropic plate (Figure 4-4).

Appendix D. Mapping Function for Elliptical Hole

While using a conformal mapping function to map an elliptical cutout from the physical z-plane into a unit circle in the mapped ζ-plane, along the contour of the ellipse in the x-y plane, the contour of the unit circle in the ζ-plane is as [5]

$$\zeta = \zeta_1 = \zeta_2 = e^{\theta i} \tag{D-1}$$

For the plate of Figure 5-1, i.e., an ellipse with major-axis, $2a$, and minor-axis, $2b$, along y and x axis, respectively, the equation for the ellipse is

$$\frac{x^2}{b^2} + \frac{y^2}{a^2} = 1 \tag{D-2}$$

For the coordinate system shown in Figure 5-1, the polar to Cartesian coordinate transformation takes place according to

$$x = r\cos\theta \quad \text{and} \quad y = r\sin\theta \tag{D-3}$$

where r is the radial coordinate measured from the center of the ellipse and angle θ is measured clock-wise from the vertical x-axis. Substituting x and y of equations (D-3) into equation (D-2) gives

$$r = \frac{ab}{\sqrt{a^2 \cos^2\theta + b^2 \sin^2\theta}} \tag{D-4}$$

In Figure 5-1, at $\theta = 0°$ and $(x, y) = (b, 0)$, equation (D-4) gives, $r = b$. Substituting this expression for r in equation (D-3) produces $x = b \cos\theta$. Similarly, at $\theta = 90°$ and $(x, y) = (0, a)$, from equation (D-4) the expression of r comes out to be $r = a$. Substituting this into equation (D-3) gives $y = a \sin\theta$. Moreover, expressing the sine and cosine functions as weighted sums of the exponential function and combining equation (D-1) with it one gets the following

$$\begin{aligned} \cos\theta &= Re\{e^{i\theta}\} = \frac{e^{i\theta} + e^{-i\theta}}{2} = \frac{\zeta + \zeta^{-1}}{2} \\ \sin\theta &= Im\{e^{i\theta}\} = \frac{e^{i\theta} - e^{-i\theta}}{2i} = -i\frac{\zeta - \zeta^{-1}}{2} \end{aligned} \tag{D-5}$$

Expressing cos θ and sin θ according to equations (D-5), and substituting $x = b \cos\theta$ and $y = a \sin\theta$ into the expression of the complex variables $z_j = \omega_j(\zeta_j) = x + \mu_j y$ of equation (2-38), the mapping function for an elliptical hole in an orthotropic plate is thereby expressed as equation (D-6).

$$z_j = \omega_j(\zeta_j) = x + \mu_j y = b\frac{\zeta_j + \zeta_j^{-1}}{2} - ia\mu_j\frac{\zeta_j - \zeta_j^{-1}}{2}, \quad j = 1, 2 \tag{D-6}$$

After re-arranging equation (D-6), the mapping function takes the following form

$$z_j = \omega_j(\zeta_j) = \frac{b + ia\mu_j}{2}\frac{1}{\zeta_j} + \frac{b - ia\mu_j}{2}\zeta_j, \quad j = 1, 2 \tag{D-7}$$

which is that of equation (5-6). Equation (5-6) or (D-7) differ slightly from the mapping expressions for an elliptical hole appearing in sources such as References [5] and [8]. This is because of the *x*-*y* coordinate orientation relative to the major and minor elliptical axes and from where θ is measured.

Appendix E. Out-of-Plane Displacement Monitoring for Elliptically-Perforated Orthotropic Plate

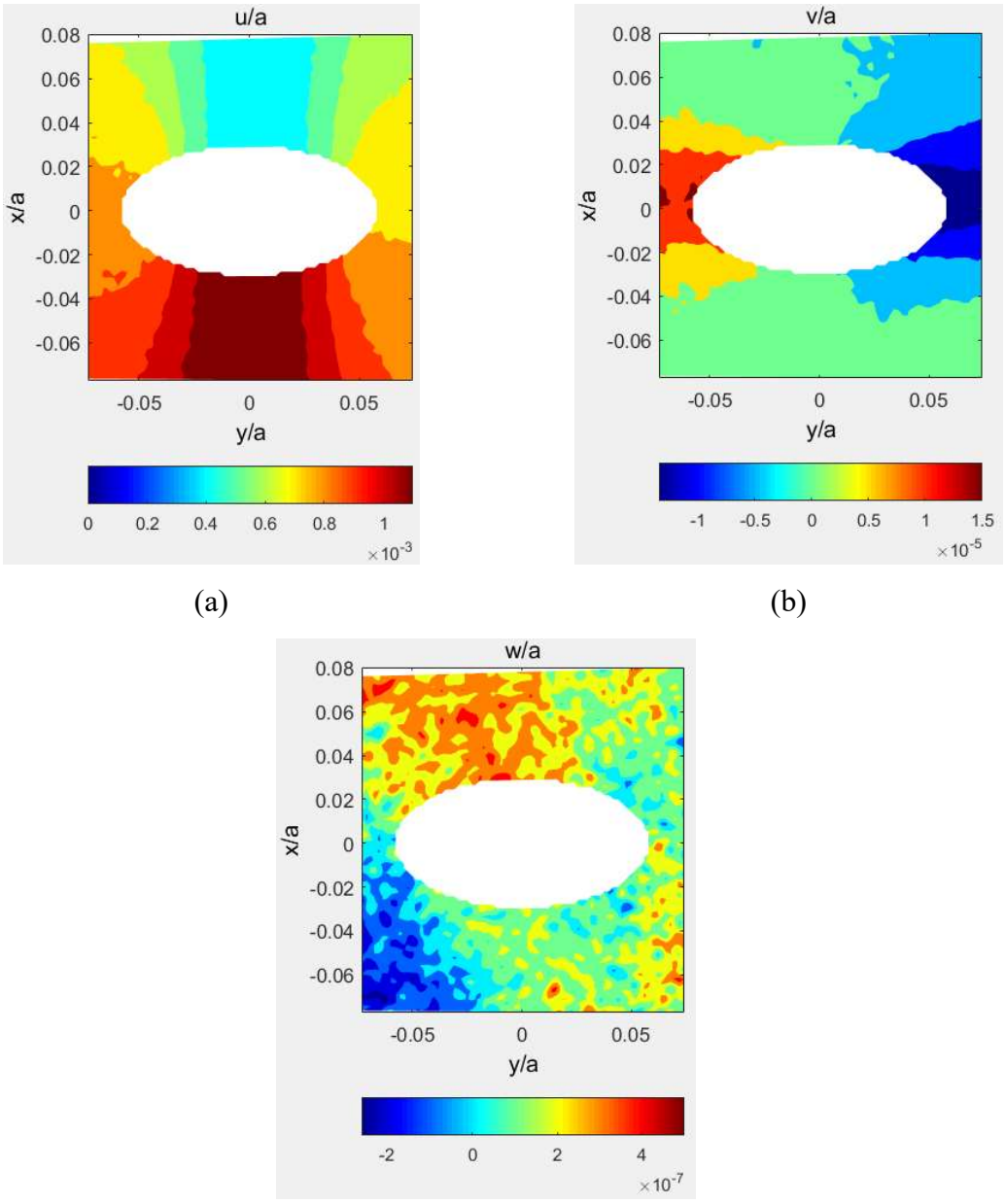

(a) (b)

(c)

Figure E-1: Contours of 3D-DIC provided raw displacements (a) *u*/*a*, (b) *v*/*a* and (c) *w*/*a*, showing no sign of out-of-plane bending for elliptically-perforated plate of Figure 5-1

Figure E-1(c) show that the 3D-DIC recorded raw out-of-plane displacements, w, are significantly less (negligible) compared to in-plane displacements of Figures E-1(a) and (b). The maximum in-plane displacement in the loading direction, u, is 2.24×10^3 times larger than w and that transverse to the loading direction, v, is 31.40 times larger than w, Figure E-1. Therefore, showing there was no out-of-plane motion other than Poisson's effect when loading (Figure 5-4) the elliptically-perforated plate of Figure 5-1. The comparison among the three components of the displacement was done from unprocessed raw DIC data to keep everything consistent. The measured data at locations $r = 0.45a$ beyond the hole's boundary were considered to exclude the unreliable edge data.

Appendix F. Effect of Number of Airy Coefficients, *k*, on the Elliptically-Perforated, Finite, Orthotropic Plate

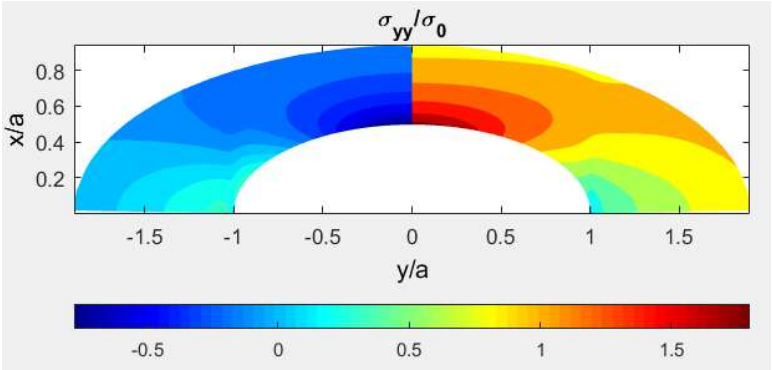

(a)

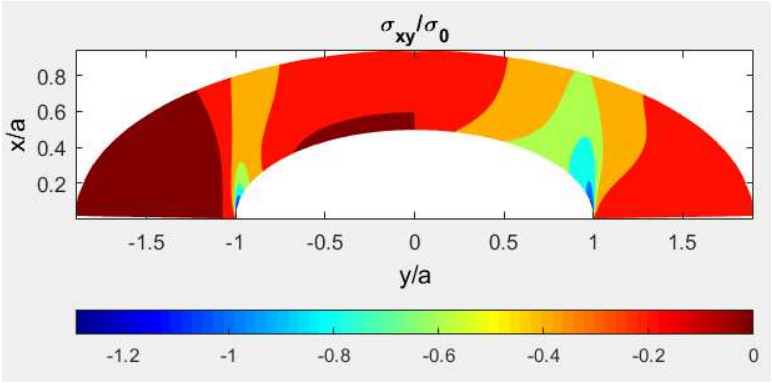

(b)

Figure F-1: Contours of stresses (a) σ_{yy}/σ_0 and (b) σ_{xy}/σ_0 from FEM (left side) and hybrid-method based on DIC-measured displacement information, u, in vertical loading direction for $k = 4$ (right side)

Figure F-1 further supports the selection of $k = 2$ in DIC-hybrid method to stress analyze the elliptically-perforated, finite, orthotropic graphite-epoxy plate of Figure 5-1. Although their magnitudes are relatively small, as the number of Airy coefficients is increased to $k = 4$, the in-plane normal stresses transverse to the loading direction, Figure F-1(a), and the shear stresses,

Figure F-1(b), start to deviate from their expected behavior. The in-plane normal stresses in the loading direction remains essentially unchanged.

Appendix G. Determination of Experimental Stress Concentration Factor from Durelli et al. [94]

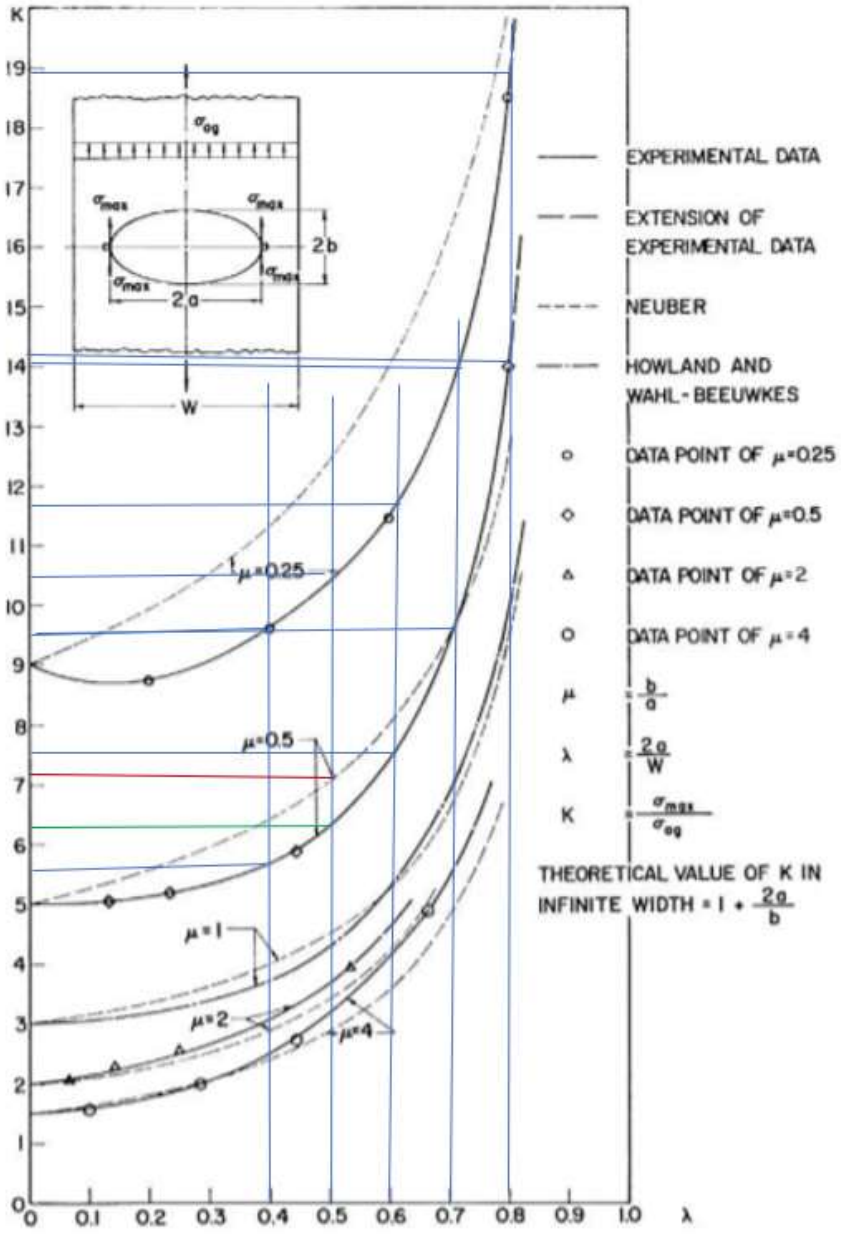

Figure G-1: Experimental stress concentration factor versus hole-opening to plate-width ratio for finite, elliptically-perforated, isotropic plate from Durelli et al. [94]

Durelli et al. [94] in Figure G-1 used the symbols K for the experimentally-determined stress concentration factor, λ for the elliptical hole-opening to plate-width ratio, $2a/W$, and μ for the ratio of the minor to major ellipse radii, b/a. Stress concentration factor results obtained from Neuber's rule are also included in Figure G-1. It should be noted that for the elliptically-perforated plates of Chapter 5, including the plate of Figure 5-1, all presented results consider the hole-opening sharpness as the ratio of the major to the minor ellipse radii, a/b, which is the inverse of the μ used in Figure G-1.

Appendix H. Complex Variables Hybrid-Method Validity for Bi-Axial Tensile and In-Plane Shear Loading

The displacement-based complex variables method was utilized in this section to individually analyze a bi-axial tensile and an in-plane shear loaded, finite, orthotropic plate with a central circular hole. The plate dimensions and material properties are provided in Table H-1 and Table H-2, respectively. Quarter-FEA models of the two plates were created in ANSYS APDL using isoparametric elements Plane 183. The FEM details are provided in Chapter 4, Section 4.8. The plates individually experienced bi-axial tensile stresses and in-plane shear stresses of 11.05 MPa (1.6 ksi) along all far-field boundaries, Figure H-1.

Table H-1: Details of bi-axial tensile or in-plane shear loaded circularly-perforated orthotropic plate

Plate Parameters	Orthotropic Circularly-Perforated Plate
Circular hole diameter, D	25.4 mm (1")
Hole-opening to plate-width ratio	$D/W = 0.33$
Width, W	76.2 mm (3")
Length, L	279.4 mm (11")
Thickness, t	5.28 mm (0.208")
Far-field stress, σ_0	11.05 MPa
Degree of anisotropy, E_{11}/E_{22}	1.03
Symmetry	Horizontally and vertically

Table H-2: Material properties of bi-axial tensile or in-plane shear loaded circularly-perforated orthotropic plate

Properties	Symbol	Value	Units
Elastic modulus in strong/stiff direction	E_{11} or E_{xx}	210.29	GPa
Major Poisson's ratio	ν_{12} or ν_{xy}	0.25	Dimensionless
Elastic modulus perpendicular to direction -1	E_{22} or E_{yy}	203.39	GPa
Shear modulus	G_{12} or G_{xy}	82.74	GPa

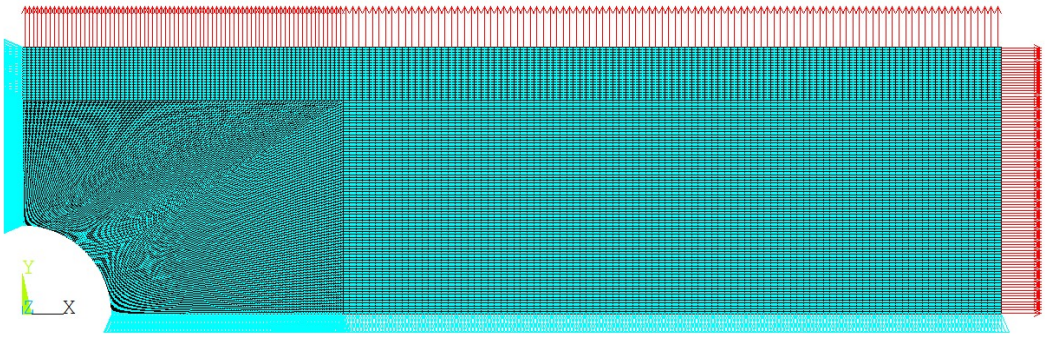

(a)

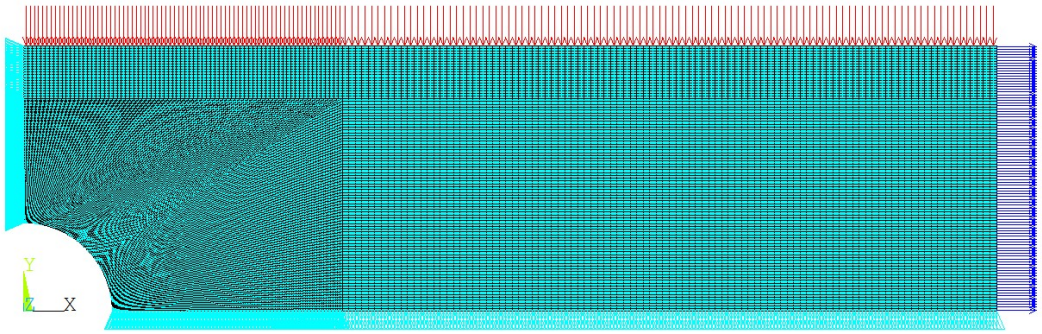

(b)

Figure H-1: Quarter-plate FEMs of circularly-perforated orthotropic plate under (a) Bi-axial tensile and (b) In-plane shear stresses

The plates were analyzed using FEA-determined displacements in the x-direction, u. The direction x is along the plate's strong/stiff material direction 1. FEA-predicted u-displacements

were processed by the complex variables hybrid stress analysis method according to the procedure outlined in Chapter 4, Section 4.4. The FEA-determined u-displacements (individually for either the bi-axial tensile or shear loaded plate) were processed with equation (4-1) combined with equation (4-7) to evaluate the Airy coefficients, c_j. Once the Airy coefficients are known, using them in equations (4-1) through (4-5) the in-plane displacements and stresses in the plate under bi-axial tensile or in-plane shear loading were evaluated individually. Both the analyses were done for n_{FEA} = 31,087 FEA-predicted displacements in the x-direction, u. Based on the respective RMS plots, number of Airy coefficients, $k = 8$ and $k = 10$, were employed in the Laurent series expansion of the stress functions for the plates under bi-axial tensile and in-plane shear loading, respectively. The method requires no knowledge of the external loading or boundary conditions.

Hybrid-method provided results are compared with the direct FEA-predictions in Figure H-2 through Figure H-5. All distances and displacements are normalized by the radius of the circular hole, R = 12.7 mm (0.5"), and stresses with respect to the applied external stress, σ_0 = 11.05 MPa (1.6 ksi). The stress concentration factor (SCF) of the plates were determined using either direct FEA-predicted or complex variables hybrid-method evaluated in-plane stresses, σ_{xx}, in the loading direction at $x = 0$ for $y = R$, in equation (5-14), Table H-3. SCFs from direct FEA prediction and obtained by using FEA-predicted u-displacements in the complex hybrid-method show good agreement. In addition, from a study by Kotousov and Wang [194] done with a similar isotropic plate under in-plane shear as of the current orthotropic plate with E_{11}/E_{22} = 1.03 experiencing shear loading, Figure H-1(b), the SCF was evaluated and compared with the ones from FEA and complex variables hybrid-method, Table H-3. Kotousov and Wang [194] studied infinite plates whereas the present plate under shear loading has a finite-width compared to the hole diameter, i.e., $D/W = 0.33$. Thus, the evaluated K_T for the current in-plane shear loaded plate

as expected is slightly higher than that from Kotousov and Wang's study. From Figure 2 of Kotousov and Wang's paper [194], for a circularly-perforated infinite isotropic plate the K_T are determined as a function of the plate's half thickness to hole radius ratio, i.e., $t/2R = 0.208$ for the current plate and for Poisson's ratio, $\nu = 0.25 \approx 0.3$.

The agreement between the displacement-based hybrid and FEA results demonstrate the complex variables hybrid-method's ability to reliably analyze a bi-axially tensile loaded plate or a plate experiencing in-plane shear loading. This validate the hybrid-method's ability to analyze orthotropic plates under a variety of loading. When analyzing orthotropic plates under various in-plane loading, the concept of the complex variables hybrid-method is computationally more convenient than other approaches available in literature. Such example is a study done by Lim et al. [195] to analyze bi-axially loaded anisotropic plates.

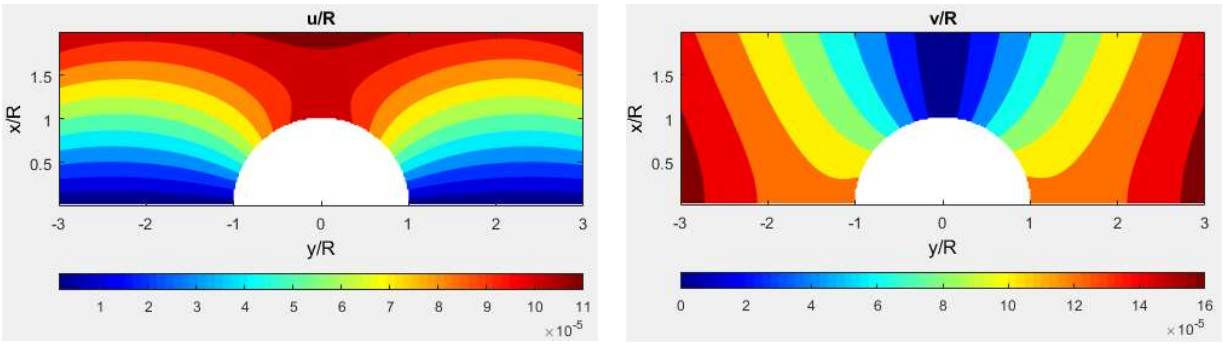

(a) (b)

Figure H-2: Contours of (a) u/a and (b) v/a from FEA (left side) and hybrid-method (right side) based on FEA-predicted displacement information, u, for circularly-perforated, $D/W = 0.33$, orthotropic plate with $E_{11}/E_{22} = 1.03$ under bi-axial tensile load

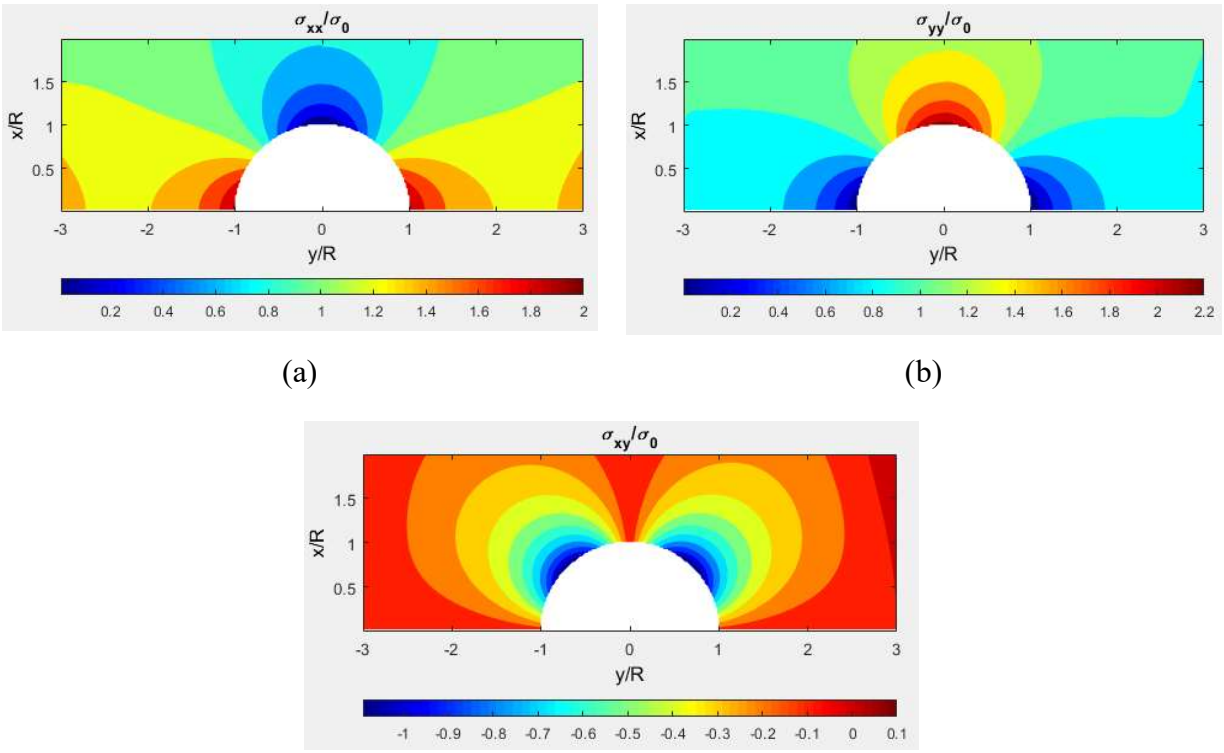

(a) (b)

(c)

Figure H-3: Contours of (a) σ_{xx}/σ_0, (b) σ_{yy}/σ_0 and (c) σ_{xy}/σ_0 from FEA (left side) and hybrid-method (right side) based on FEA-predicted displacement information, u, for circularly-perforated, $D/W = 0.33$, orthotropic plate with $E_{11}/E_{22} = 1.03$ under bi-axial tensile load

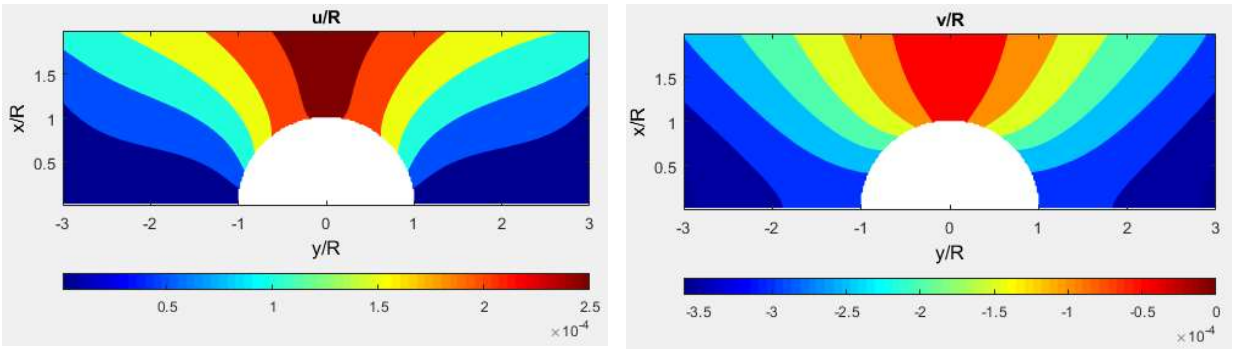

(a) (b)

Figure H-4: Contours of (a) u/a and (b) v/a from FEA (left side) and hybrid-method (right side) based on FEA-predicted displacement information, u, for circularly-perforated, $D/W = 0.33$, orthotropic plate with $E_{11}/E_{22} = 1.03$ under in-plane shear loading

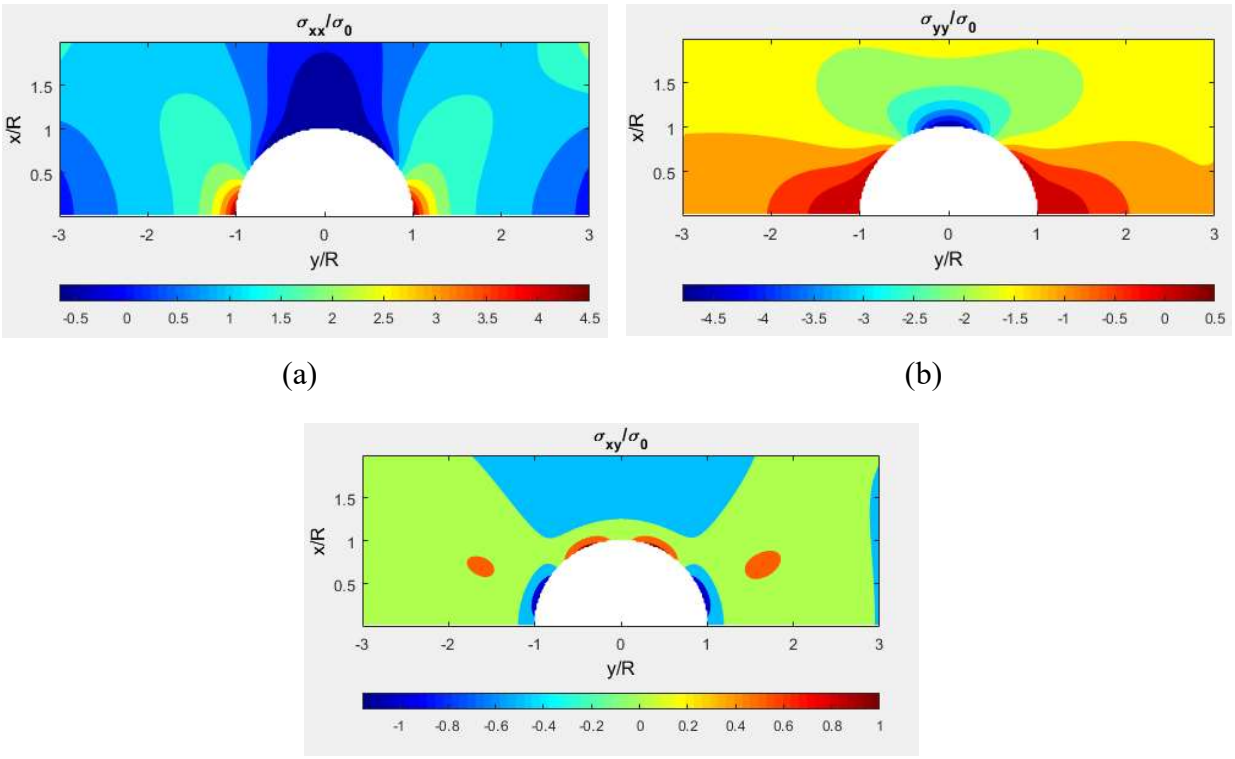

Figure H-5: Contours of (a) σ_{xx}/σ_0, (b) σ_{yy}/σ_0 and (c) σ_{xy}/σ_0 from FEA (left side) and hybrid-method (right side) based on FEA-predicted displacement information, u, for circularly-perforated, $D/W = 0.33$, orthotropic plate with $E_{11}/E_{22} = 1.03$ under in-plane shear loading

Table H-3: SFC for circularly-perforated orthotropic plates with $D/W = 0.33$ and $E_{11}/E_{22} = 1.03$ under variety of loadings

Load type	SCF, K_T, from		
	Hybrid-method	FEA	Literature
Bi-axial tension	2.04	2.04	-
In-plane shear	4.96	4.95	4.02 (for similar infinite plate from Kotousov and Wang [194])

Appendix I. Environmental Effects on Thermoelastic Coefficient, *K*

To stress analyze mechanical members employing thermoelastic stress analysis (TSA) requires the TSA-recorded load-induced temperature signal, S^*, be converted to the first invariant of stresses or the isopachic stress, S. This is done by experimentally knowing the thermoelastic coefficient, K. Therefore, accuracy of the TSA-stresses depends on accurately determining K.

To avoid reflection from the TSA specimen surface and to provide uniform and enhanced thermal emissivity, one typically applies a layer of black paint to the TSA specimen surface priori to testing. The TSA coefficient, K, can be determined from a uniform tensile coupon also coated with a thin layer of the same black paint. It is good practice to paint and load the calibration coupon on the same day under the same temperature and humidity conditions and cyclic rate as those of the TSA test specimen. Following these steps avoids any environmental or time-dependent effects.

The studies conducted in this research involve graphite-epoxy laminates and aluminum. Neither of these materials experiences time-dependent deformation at room temperature. However, as the TSA specimens are provided with a thin layer of paint, the effects of temperature and humidity on the paint need to be investigated. Any influence of time-dependent deformation or environmental factors can contaminate the TSA-recorded information and/or the measured thermoelastic coefficient, K, and therefore compromise the resulting stress analysis.

The effects of temperature and humidity on the applied paint layer was experimentally investigated. Two aluminum tensile plates of width, W = 5.08 cm (2") and thickness, t = 6.34 mm (0.25"), were surface prepared and coated with a thin layer of Krylon Ultra-Flat black paint and

allowed to dry for an hour. This is slightly more than the paint manufacturer's suggested cure time of 30 minutes. A TSA test was conducted on each of the two painted plates just shortly after the one-hour cure time. The plates were cyclically loaded in a 89 kN capacity, closed-loop, hydraulic-grip MTS loading-frame. The thermoelastic coefficients, *K*, were determined with the Delta Therm Stress Photonics TSA system software and Delta Therm DT1410 infrared camera. The specimens were cyclically loaded at 8,896.4 N ± 5,337.7 N (2,000 lbs ± 1,200 lbs). Tests were conducted at loading frequencies of 10 Hz and 20 Hz. The initial thermoelastic coefficients are determined essentially just an hour after applying the paint layer and are considered as the reference *K* value for the respective testing.

One of the aluminum plate was exposed to relatively elevated temperature (maximum of 110 °F) and high humidity (50% RH) for a time duration. The other aluminum plate was kept at room environment. Determined values of *K* were determined intermittently and plotted against the exposure time. Values of *K* were calculated from the TSA-measured data according to equation (I-1)

$$K = S^*/\Delta\sigma \tag{I-1}$$

where S^* is the TSA-recorded thermal information. For a uniform tensile calibration plate/coupon under proportional loading, $\Delta\sigma$ is related to the stress range it experiences under the applied cyclic load. The highest and lowest peaks of the cyclic loading were recorded using an oscilloscope. Using these maximum-minimum loads and the uniform cross-sectional area of the specimen, the stress range, $\Delta\sigma$, of the applied cyclic load is calculated. *K* has a unit of *U*/MPa or *U*/psi, where '*U*' denotes the uncalibrated TSA-recorded signal output.

For the aluminum plate kept at room enviorment, Figure I-1, there were slight variations in the measured values of *K*. For the 10 Hz frequency over a time interval of 53 days, the measured thermoelastic coefficient, *K*, varied within 1% to 6% (% of error) from the reference *K* value and from 1% to 5% for 20 Hz frequency. For the plate exposed to elevated conditions over 24 days, Figure I-2, it was seen that after the first exposure to extreme conditions there was a noticeable change in the obtained thermoelastic coefficient, *K*; 24% for 10 Hz frequency and 17% for 20 Hz frequency compared to the reference *K* values, respectively. Subsequent relative changes were smaller. The *K* values of Figure I-1 and Figure I-2 are normalized with respect to the stress amplitude ($\Delta\sigma/2$) of the cyclically applied load.

Results show that at room/ambient conditions, the paint exhibits only slight or negligible changes in the *K* values over time. The paint's melting temperature is not provided by the manufacture. When exposed to elevated conditions of temperature and % RH, the thermoelastic coefficient, *K*, noticeably changes after the first exposure. The viscoelastic effect of the coating probably plays a role here. Any change in the *K* values can significantly affect the TSA-determined stresses. The present results suggest it is good practice to paint and test the TSA test specimen and calibration plate/coupon on the same day, at the same frequency and under same environmantal conditions.

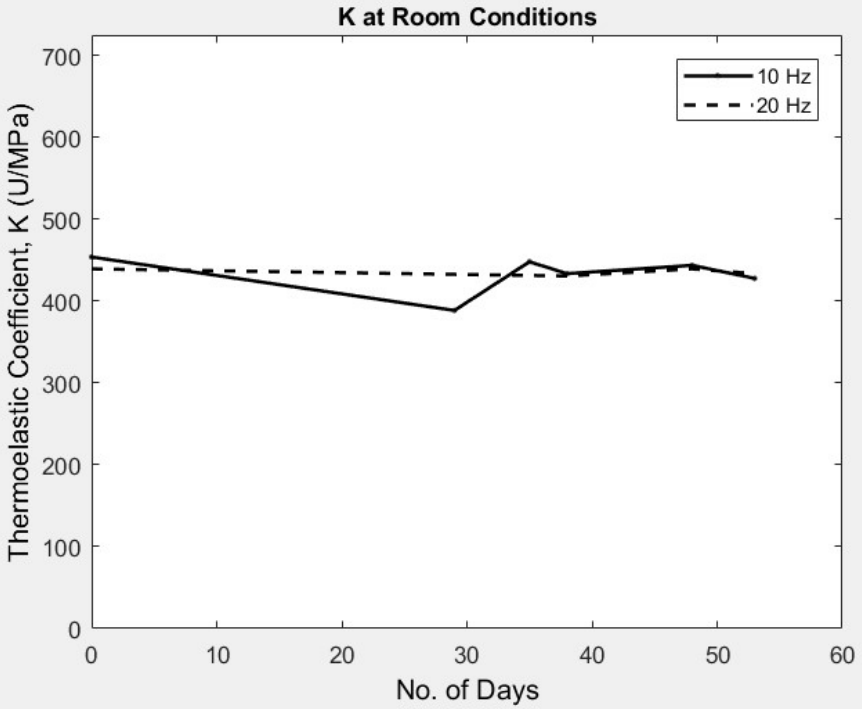

Figure I-1: Cyclic effect on thermoelastic coefficient, *K* (ambient conditions)

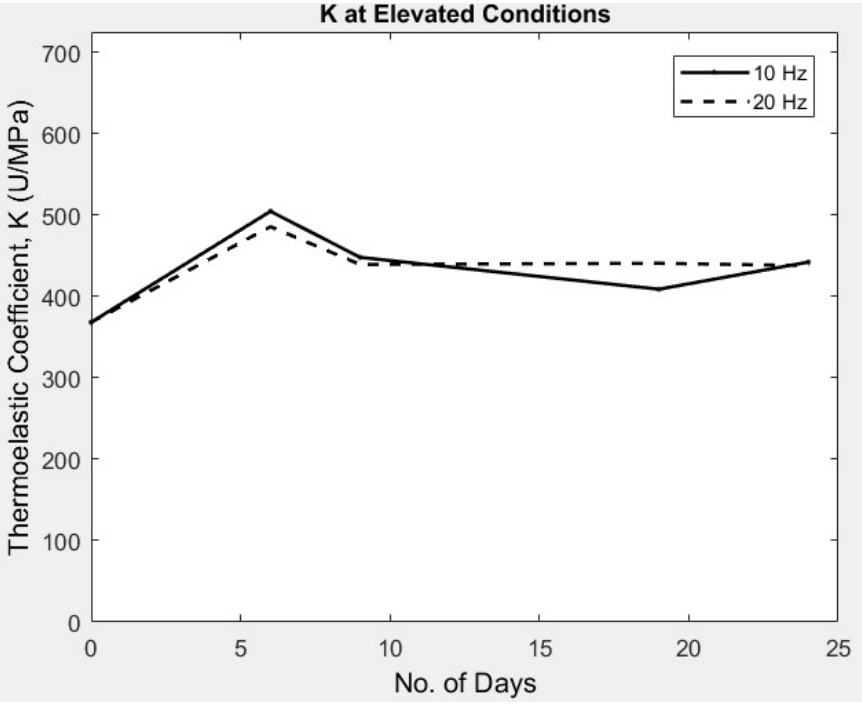

Figure I-2: Effect of elevated temperature and high humidity on thermoelastic coefficient, *K*

Appendix J. Effect of Varying Number of Airy Coefficients, *k*, for the Circularly-Perforated, Finite, Isotropic Plate

The computed load F_c^* of Table J-1 further validates the use of $k = 21$ in the TSA stress analysis of the plate of Figure 6-1. $k = 21$ best satisfies the load equilibrium. Note that the TSA-computed load, F_c^*, was calculated using the expression of the load equilibrium of equation (6-23) at $y = R$.

Table J-1: Comparison between applied load (1,779.29 N) and TSA-computed load versus number of Airy coefficients, k, for $n_t = 12{,}592 + 244$

No. of Airy coefficients, k	Computed load, F_c^*, from TSA-hybrid method (N)	% of error with physically applied load
9	1,719.82	3.34
11	1,693.39	4.83
13	1,717.41	3.48
15	1,707.14	4.05
17	1,759.05	1.34
19	1,766.43	0.72
21	1,785.43	0.34
25	1,590.86	10.59

Appendix K. How Far Should One Stay Away from an Edge

For the off-axis perforated aluminum plate of Chapter 6 (Figure 6-1), some additional analyses were conducted to demonstrate the effect of the TSA-recorded data selection ranges on the TSA results. The initial analysis used n_{TSA} = 12,592, excluded three pixels of TSA-recorded data along the two vertical sides of the plate and omitted data within $0.1R$ (≈ 1 mm) distance from the hole's boundary. In addition, an assumption was made of having no sufficiently reliable TSA-recorded information throughout the region to the right of the hole up as far as y/R = 0.75 (19 pixels from point 'A') from the plate's horizontal center-line, Figure 6-8. A total of $2h$ = 244 boundary conditions, $\sigma_{xy} = \sigma_{xx} = 0$, were imposed along the two vertical edges of the plate at 61 equally-spaced locations and k = 21 Airy coefficients were employed. The additional analyses investigate how the TSA data selection along the plate's vertical edges and the varying amount of missing/unreliable data at structurally critical locations affects the overall performance of the TSA method.

For the first of these two analyses, while keeping everything else the same as the initial analysis, the number of excluded pixels of input data along the vertical edges of the plate was changed from three pixels to two pixels (n_{TSA} = 12,882) then to one pixel (n_{TSA} = 12,998), respectively. The TSA evaluated stresses at location 'A' (Figure 6-1) for these situations are compared with those obtained from FEA and strain-gage, Table K-1. Load equilibrium was also checked, Table K-1.

From comparison of the TSA results with strain-gage data, Table K-1, it is observed that as more TSA data are excluded from the two vertical edges of the plate, the TSA results improve,

i.e., TSA-computed stress at location ‘A’ agrees better with the strain-gage result. The load equilibrium is also better satisfied when excluding recorded data within three pixels from each of the vertical edges. These results suggest improved results by excluding possibly unreliable data from the TSA analysis.

Table K-1: TSA-hybrid method computed stress at location ‘A’ for various data ranges and k = 21

No. of pixels omitted from each vertical side	TSA-hybrid method utilized data, $n_t = n_{TSA} + 2h$	% of error between TSA-hybrid method		
		Computed stresses at location ‘A’ with		Computed and physically applied load
		FEA	Strain-gage	
1	12, 998 + 2×122	2.12	3.73	2.84
2	12, 882 + 2×122	2.94	2.97	3.20
3	12, 592 + 2×122	4.51	1.49	0.34

For the third analysis, TSA-recorded data were excluded within three pixels from each vertical side of the plate, and the region to the right of the hole where no reliable TSA-measured S^* data existed (Figure 6-8) was slightly enlarged. The TSA-measured S^* data were now considered unreliable/absent up to $y/R = 1$ from the horizontal center-line instead of $y/R = 0.75$, Figure K-1 and Figure 6-8, respectively. The closest available TSA-recorded data from location ‘A’ is now 25 pixels away vertically, instead of the initial 19 pixels, from location ‘A’. The utilized TSA-measured load-induced thermal information, S^*, for this analysis reduced to n_{TSA} = 12,479, Figure K-1. Results obtained from this analysis are tabulated in Table K-2 and Figure K-2.

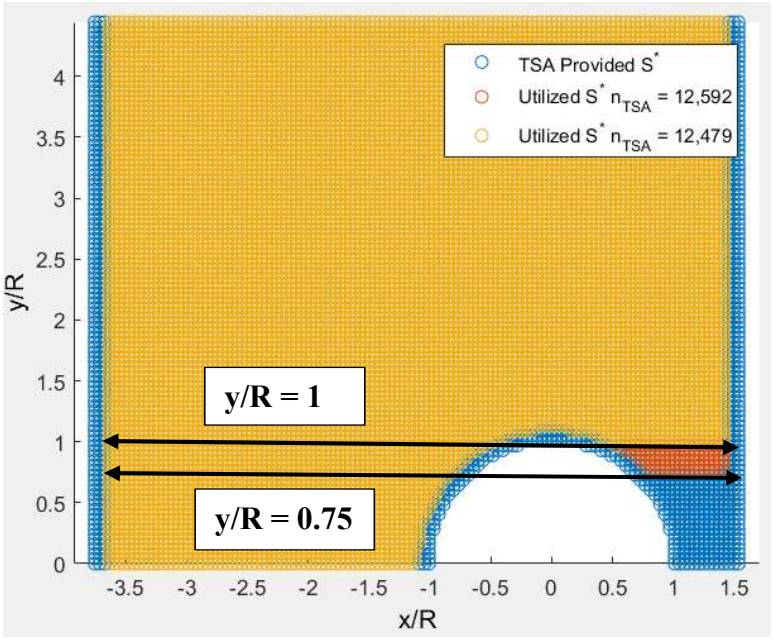

Figure K-1: Utilized data source locations of S^*

Table K-2: TSA computed stress at location 'A' for $n_t = n_{TSA} + 2h$ = 12,723 and unreliable data up to y/R = 1

TSA		Absolute % of error compared with	
No. of Coefficients, k	σ_{yy}/σ_0	FEA, σ_{yy}/σ_0 = 5.67	Strain-gage, σ_{yy}/σ_0 = 5.34
17	5.26	7.23	1.50
19	5.34	5.82	0.10
21	5.30	6.53	0.75
23	5.31	6.35	0.56

Based on the strain-gage information compared with the three situations of Table K-1, results of Table K-2 suggest that omitting additional questionable TSA-measured data between

right edge of the hole and the right vertical edge of the plate enables the TSA result at point ‘A’ to agree more closely with the strain-gage result. However, the FEA results suggest otherwise. Note that the case of Table K-2 now involves less input data and the closet input values are further away from point ‘A’ then are those of Table K-1.

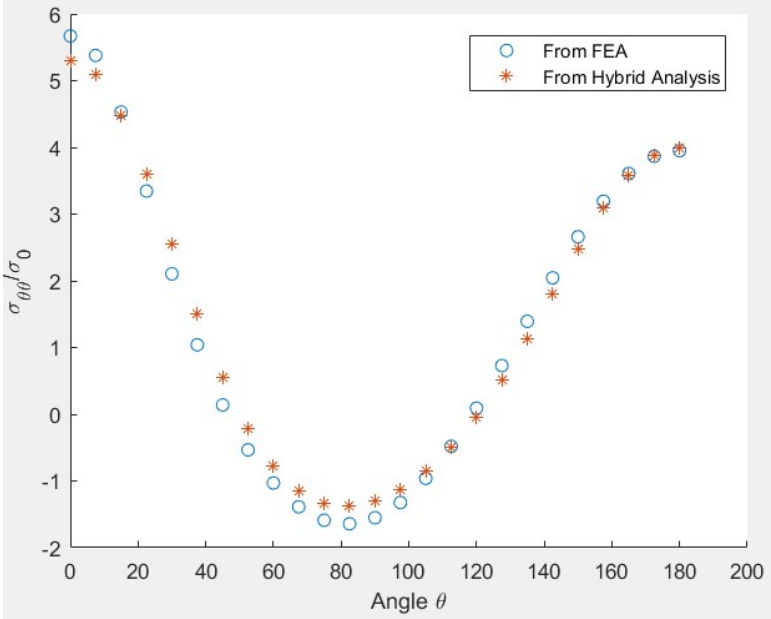

Figure K-2: Plot of $\sigma_{\theta\theta}/\sigma_0$ along the hole’s boundary from FEM and TSA-hybrid method for n_t = 12,723, missing data up to y/R = 1 and k = 21

For the two cases where the experimental information is unreliable vertically up to y/R = 1 (Figure K-2) and y/R = 0.75 (Figure 6-20) to the right of the hole, comparing the tangential stresses it can be seen that the largest changes in the TSA results along the hole’s boundary are at θ = 0°, i.e., location ‘A’. Elsewhere along the hole’s boundary both the analyses give similar results. Experience suggests that it is good practice to not use TSA data within two-to-three pixels of edges.

Since TSA pixels are usually about 0.3 mm in size, this implies typically staying away at least one millimeter from an edge.

The objective of these additional analyses was not to find the worst-case scenario under which the present TSA-hybrid method is capable of providing reliable information at structurally important locations. This is investigated in Chapter 7 using DIC-measured displacement information. Instead these analyses were intended to see how the close-to-edge experimental data filtration can affect the TSA results.

Appendix L. Complex Variables Hybrid Stress Analysis of Isotropic Ring with FEA-Predicted *v*-Displacements

The isotropic ring of Figure 7-1 and Table 7-1 was stress analyzed using the complex variables hybrid-method, i.e., displacement information was processed with a combination of complex variables Airy stress functions, conformal mapping, analytic continuation and least squares. No symmetry or external boundary conditions were imposed. The analytical procedures outlined in Chapter 4, Section 4.4 were followed, i.e., equations (4-1) through (4-8). The mapping function of equation (4-7) for $R = R_i$, was used to map the inner circular hole of the ring and its adjacent exterior region from the physical z-plane to a unit circle and its exterior region in the mapped ζ-plane. The Laurent series expansion of the stress functions were employed and the complete states of stress and displacement of the ring were determined employing equations (4-1) through (4-5). For isotropy the elastic compliances of equation (2-18) are simplified according to elastic modulus, $E_{22} = E$ and $E_{11} \approx E$, Poisson's ratio, $v_{12} = v$ and shear modulus, $G_{12} = G = E_{11}/2(1 + v)$. For the aluminum ring of Figure 7-1 the direction 1 is considered in the ring's Cartesian y-direction. For isotropy from equation (2-17) one gets the complex material properties as $\mu_1 = \mu_2 \approx i$.

FEA-predicted displacements in the loading direction, v, (Figure 7-10) from the quarter FEM of the isotropic ring of Figure 7-9 were employed to conduct the full-field stress analysis. Details regarding the FEM are provided in Chapter 7, Section 7.8. FEA-predicted v-displacement data were selected within the range of $1.08R_i \leq r \leq 0.95R_i$, Figure M-1, where radial direction r is measured from the center of the ring and R_i is the ring's inner radius, Figure 7-1. Within this

selected region data were omitted over a small region close to the center of the ring where the concentrated load was applied, Figure M-1. This was done acknowledging that the FEA information of Figure 7-10 includes the effect of the top concentrated load. However, the stress functions and its associated stress and displacement expressions, do not. A total number of n_{FEA} = 2,225 FEA-predicted v-displacements along the loading direction y were selected.

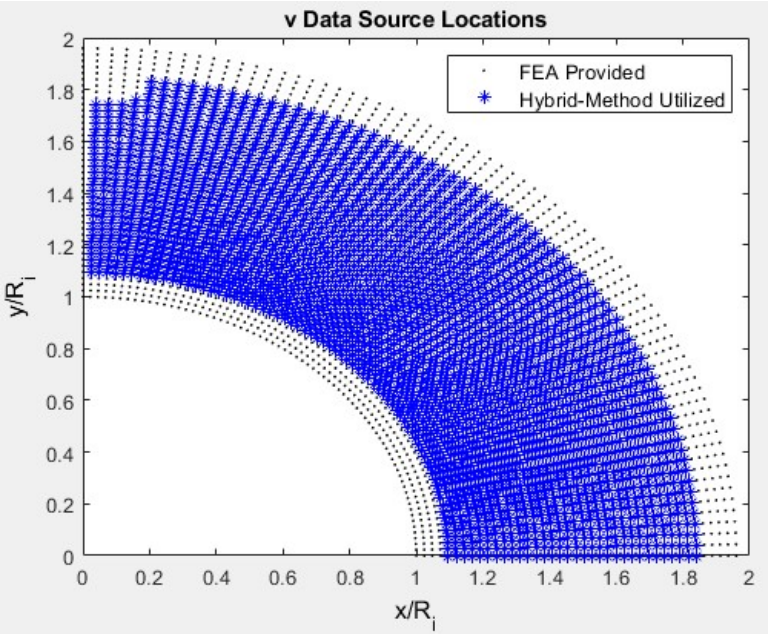

Figure L-1: One quarter of the ring of Figure 7-1 showing regions of FEA-provided (black dots) and hybrid-method utilized (blue star) v-displacements source data locations

The n_{FEA} = 2,225 FEA-predicted v-displacements, Figure L-1, were employed in equation (4-2) along with the expression of ζ_j for j = 1, 2, and $R = R_i$ from equation (4-7) to find the Airy stress coefficients, $c_j = a_j + ib_j$, according to the following equation (L-1) by least squares. Equation (L-1) can be re-written in terms of matrices as equation (L-2).

$$\{d\}$$

$$= 2 \sum_{\substack{j=-m \\ j \neq 0}}^{j=m} Re\left(\begin{bmatrix} q_1 \zeta_1^j + q_2 \left(C \zeta_2^j + B \zeta_2^{-j} \right) & i\left[q_1 \zeta_1^j + q_2 \left(C \zeta_2^j - B \zeta_2^{-j} \right) \right] \end{bmatrix} \begin{Bmatrix} a_j \\ b_j \end{Bmatrix} \right) \qquad \text{(L-1)}$$

$$= \{\text{FEA } v - \text{Displacement Data}\}$$

$$[A]_{n_{FEA} \times 2(m+1)} \{c\}_{2(m+1) \times 1} = \{d\}_{n_{FEA} \times 1} \qquad \text{(L-2)}$$

where for m = 1, 3… there are 2(m + 1) real Airy coefficients and $k = m + 1$ complex coefficients. Matrix [A] depends on the material properties, the mapping function and the source locations of the recorded input displacement values, vector $\{c\}$ involves the Airy coefficients and $\{d\}$ consists of the FEA-predicted v-displacement data. The only unknowns in the above equation (L-2) are the Airy coefficients in vector $\{c\}$. They are evaluated by the least-squares method. MATLAB's backlash operator is used for this purpose, equation (L-3). In these overdetermined system of linear equations (L-1) and (L-2), the number of equations, n_{FEA}, are kept higher than the number of unknown, 2(m + 1), real Airy coefficients, a_j and b_j.

$$\{c\} = [A] \backslash \{d\} \qquad \text{(L-3)}$$

For the selected n_{FEA} = 2,225 FEA-predicted v-displacements, from the RMS plot of Figure L-2 and the plot of condition number of Figures L-3, the number of Airy coefficients to employ in the finite summation series was chosen as k = 14. Details regarding selecting the appropriate number of Airy coefficients to use in the hybrid-method are provided in Chapter 4, Section 4.9.1.

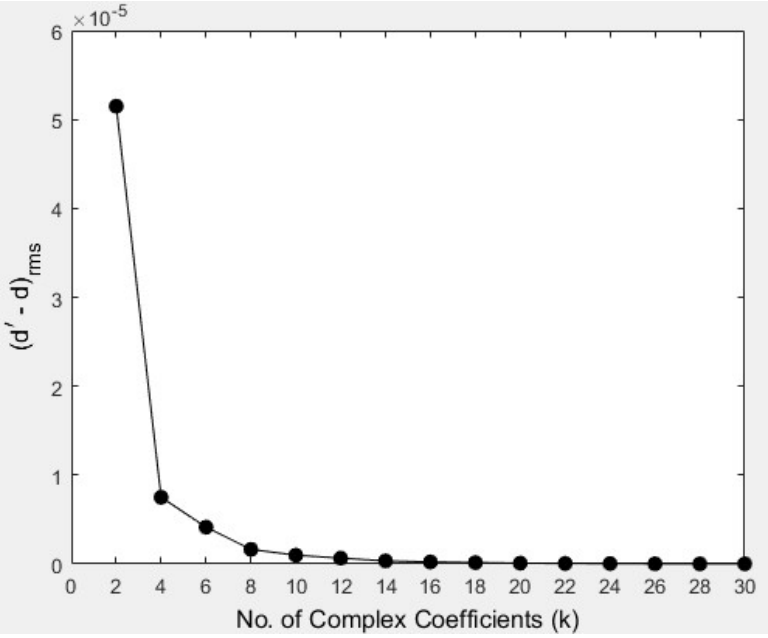

Figure L-2: RMS of the measured and reconstructed displacement data versus the number of Airy stress coefficients, k, for n_{FEA} = 2,225 of Figure L-1

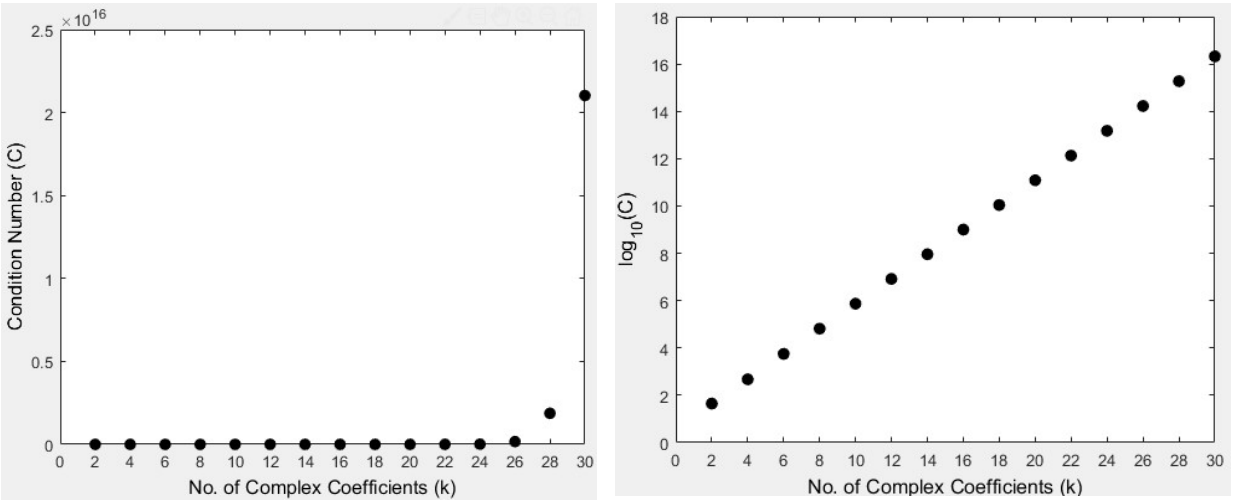

(a) (b)

Figure L-3: (a) Condition number, C, and (b) $\log_{10}(C)$ for varying number of Airy stress coefficients, k, for n_{FEA} = 2,225 of Figure L-1

Results

Employing the FEA-predicted *v*-displacement data the Airy coefficients are evaluated according to equations (L-1) through (L-3). The analysis involves no imposed boundary conditions. The traction-free boundary conditions were analytically satisfied by the conformal mapping function and the outer circular boundary conditions inherently by the measured (in this case FEA simulated) information. Knowing the Airy coefficients, the in-plane Cartesian displacements and stresses of the ring are determined from equations (4-1) through (4-5), whereas stresses in polar coordinates from equation (2-73). Angle θ is measured from the horizontal x-axis in a counter clock-wise direction, Figure 7-1.

Figure L-4 through Figure L-9 compare the results obtained from the hybrid-method based on FEA-predicted *v*-displacement data with those directly predicted by FEA. All distances and displacements are normalized by the inner radius of the ring, R_i = 25.4 mm, and stresses with respect to the nominal stress, σ_{net} = 7.18 MPa of equation (7-15). The hybrid and FEA results are also compared with strain-gage readings in between locations of θ = 0° to 90° at 10° intervals, Figure L-10. Details regarding the strain-gage analysis are provided in Chapter 7, Section 7.9.

The hybrid-method evaluated displacement and stress contours of Figure L-4 through Figure L-9 show very good agreement with the direct FEA-predictions. The tangential stresses along the inner boundary of the ring match exactly with those directly predicted by FEA and the strain-gage readings, Figure L-10.

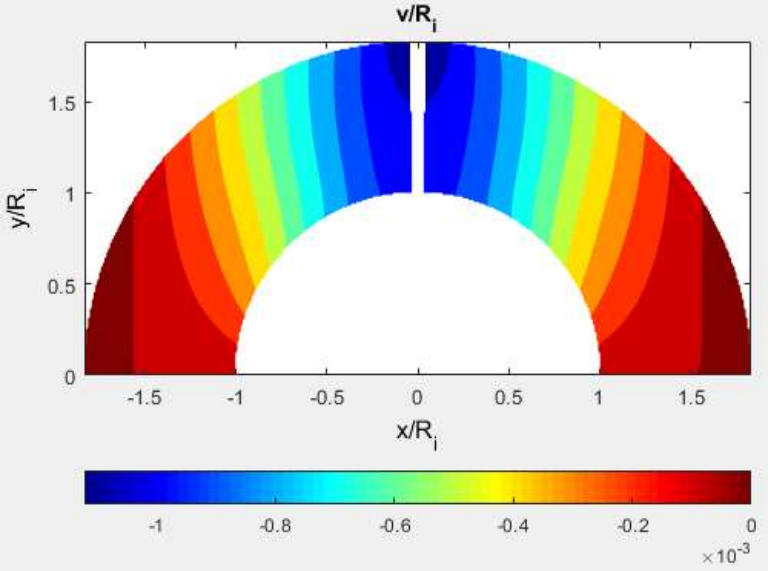

Figure L-4: Contours of displacements v/R_i (displacements along the loading direction) from complex variables hybrid-method (right) and FEM (left) for n_{FEA} = 2,225 and Laurent series of the aluminum ring loaded along direction y

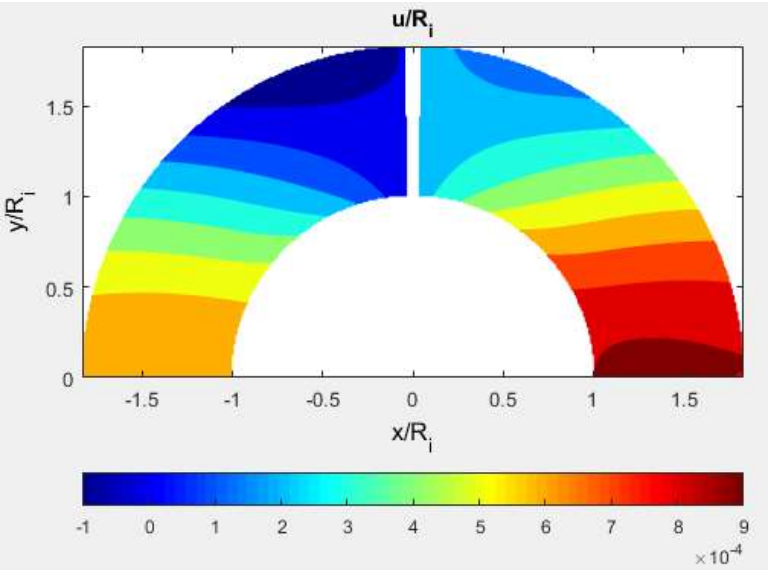

Figure L-5: Contours of displacements u/R_i (displacements transverse to the loading direction) from complex variables hybrid-method (right) and FEM (left) for n_{FEA} = 2,225 and Laurent series of the aluminum ring loaded along direction y

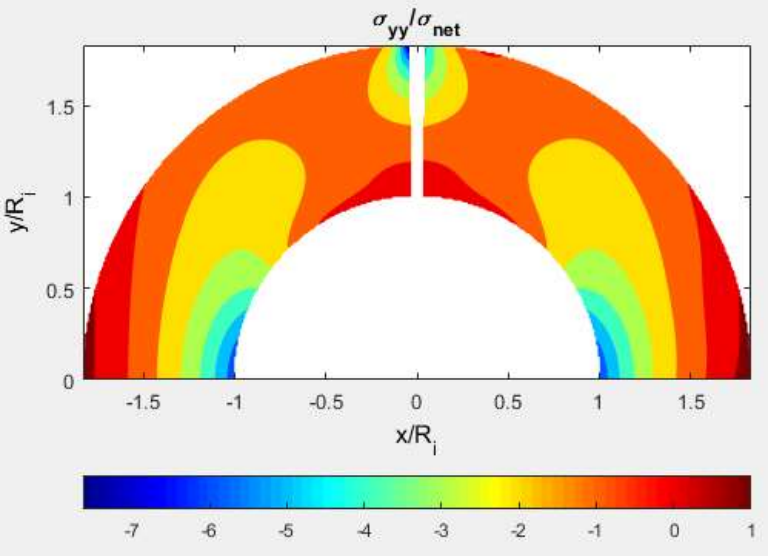

Figure L-6: Contours of stresses σ_{yy}/σ_{net} from complex variables hybrid-method (right) and FEM (left) for n_{FEA} = 2,225 and Laurent series of the aluminum ring loaded along direction y

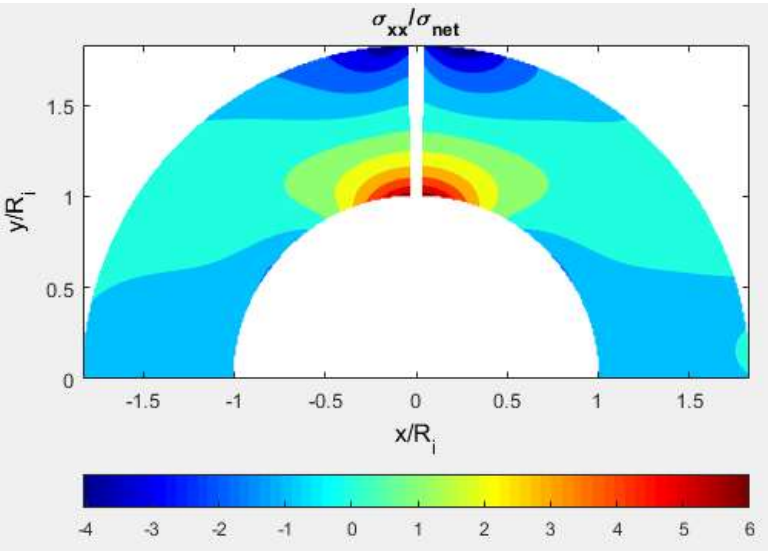

Figure L-7: Contours of stresses σ_{xx}/σ_{net} from complex variables hybrid-method (right) and FEM (left) for n_{FEA} = 2,225 and Laurent series of the aluminum ring loaded along direction y

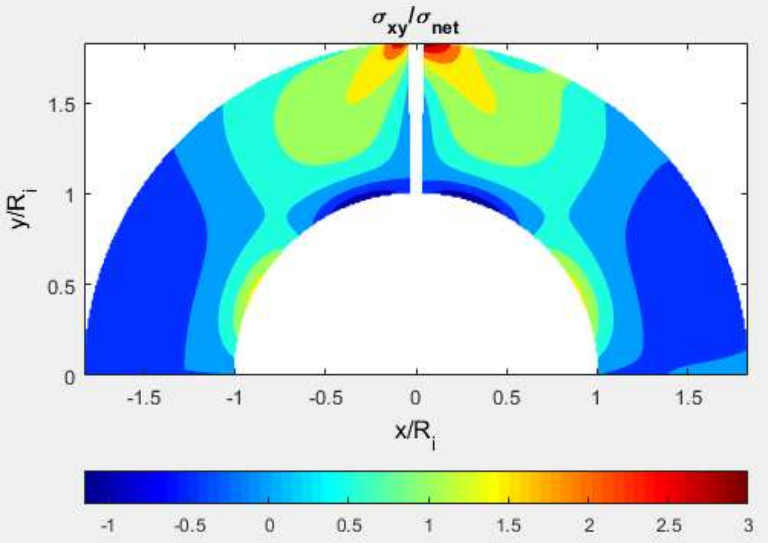

Figure L-8: Contours of stresses σ_{xy}/σ_{net} from complex variables hybrid-method (right) and FEM (left) for n_{FEA} = 2,225 and Laurent series of the aluminum ring loaded along direction y

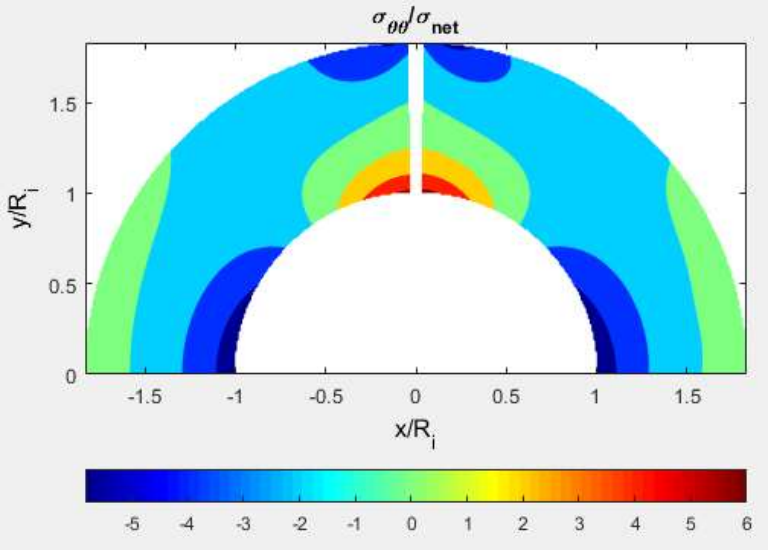

Figure L-9: Contours of stresses $\sigma_{\theta\theta}/\sigma_{net}$ from complex variables hybrid-method (right) and FEM (left) for n_{FEA} = 2,225 and Laurent series of the aluminum ring loaded along direction y

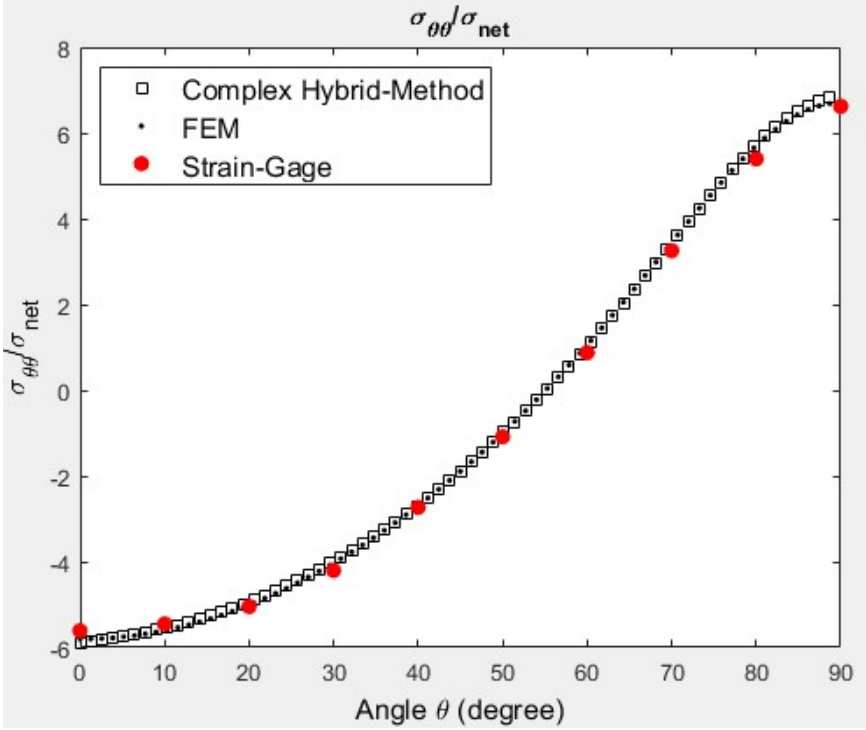

Figure L-10: Plot of tangential stresses, $\sigma_{\theta\theta}/\sigma_{net}$, along inner boundary of the aluminum ring from strain-gage, direct FEA and complex variables hybrid-method (FEA-predicted v-displacements as input) for n_{FEA} = 2,225 and Laurent series

Summary, Discussion and Conclusions

The hybrid-method results demonstrate good agreement with those from direct FEA-predictions and strain-gage readings. This supports the present hybrid-method's ability to reliably stress analyze members with non-rectangular outer boundaries and non-uniform loading by processing a single measured displacement component with mechanics-based algorithms established on the concepts of complex variables Airy stress functions, conformal mapping, analytic continuation and Laurent series combined with numerical method such as least squares. In addition, the hybrid-method's ability to reliably analyze isotropic materials is demonstrated.

Appendix M. Complex Variables Hybrid Stress Analyses of Aluminum Ring with DIC-Measured *v*-Displacements

In this section the aluminum ring of Figure 7-1 and Table 7-1 was experimentally stress analyzed using the complex variables hybrid-stress analysis concepts according to the details provided in Appendix L. DIC-measured displacement data in the loading direction, v, were utilized in the analytical expressions based on the concepts of complex variables Airy stress functions, conformal mapping, analytic continuation and power-series expansion combined with numerical tools such as least squares. Details regarding the DIC surface preparation, loading, data acquisition and processing are provided in Chapter 7, Sections 7.6 and 7.7. From the processed and averaged DIC-measured v-displacements of Figure 7-6, $n_{DIC} = 22{,}039$ input v-data were selected by omitting measured data close to inner and outer boundaries and near the location where the concentrated external load was applied. These selected DIC-measured information was processed according to the procedures outlined in Appendix L, i.e., according to Chapter 4, Section 4.4, equations (4-1) through (4-8) for $R = R_i$, $E_{22} = E$, $E_{11} \approx E$, $\nu_{12} = \nu$, $G_{12} = G = E_{11}/2(1 + \nu)$ and $\mu_1 = \mu_2 \approx i$.

The Airy stress coefficients, c_j, were evaluated using the $n_{DIC} = 22{,}039$ DIC-measured v-displacements in equations (4-2). The number of Airy coefficients retained in the summation series, $k = 4$ or $m = 8$, were selected based on the RMS plot of Figure M-2 and plot of condition numbers of Figure M-3. Here k is the number of complex Airy coefficients, c_j, and m is the number of real Airy coefficients, a_j and b_j.

Using the hybrid-method evaluated Airy stress coefficients in equations (4-1) through (4-5) the complete states of displacement and stress are obtained for the aluminum ring, Figure M-4

through Figure M-7. Knowing the in-plane stresses in the Cartesian coordinates from equations (4-3) through (4-5), using those in equation (2-73) the in-plane stresses in the Polar coordinates are obtained. The tangential stress contours are provided in Figure M-8. The hybrid displacement and stress contours obtained from DIC-measured *v*-displacements are compared with those directly predicted by FEA in Figure M-4 through Figure M-9. All distances and displacements are normalized by the inner radius of the ring, R_i = 25.4 mm, and stresses with respect to the nominal stress, σ_{net} = 7.18 MPa of equation (7-15).

A strain-gage analysis was conducted on the aluminum ring of Figure 7-1 as outlined in Chapter 7, Section 7.9. The tangential stresses along the inner boundary of the ring obtained from the DIC-hybrid method, direct FEA and strain-gage reading are plotted in Figure M-9. For the current aluminum ring the 0° and 90° locations are structurally the most significant. At these two locations the agreement between all the three approaches are significant, Figure M-9. However, noticeable discrepancies occur between DIC results with FEA and strain-gage readings away from θ = 0° or 90° locations, Figure M-9. Imposing certain boundary conditions and working with measured data very close to the inner boundary are possible ways of overcoming these discrepancies.

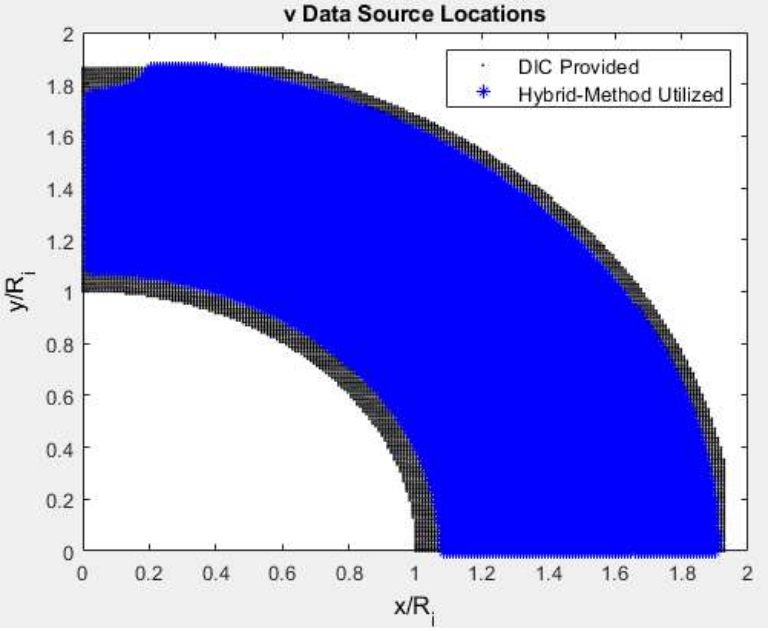

Figure M-1: One quarter of the ring of Figure 7-1 showing regions of DIC-provided (black dots) and hybrid-method utilized (blue star) *v*-displacements source data locations

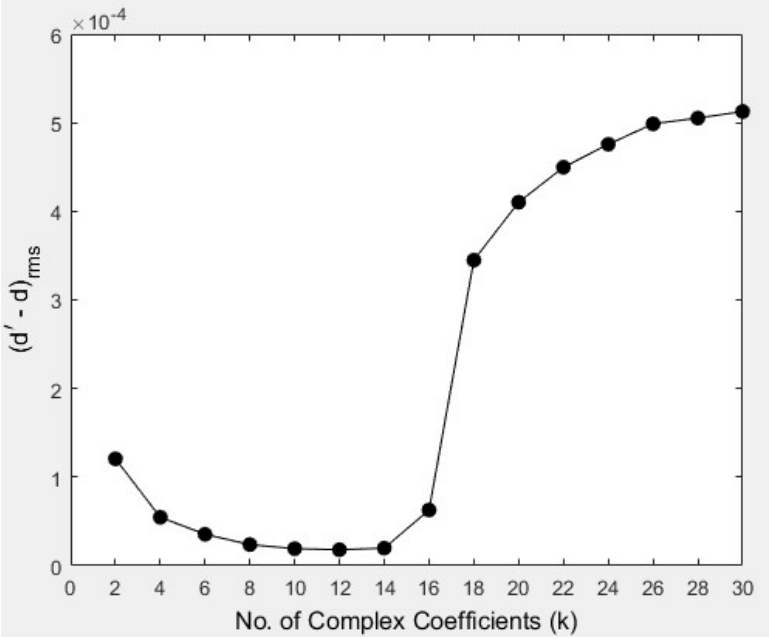

Figure M-2: RMS of the DIC-measured and hybrid-method reconstructed displacement data versus the number of Airy stress coefficients, *k,* for n_{DIC} = 22,039 of Figure M-1

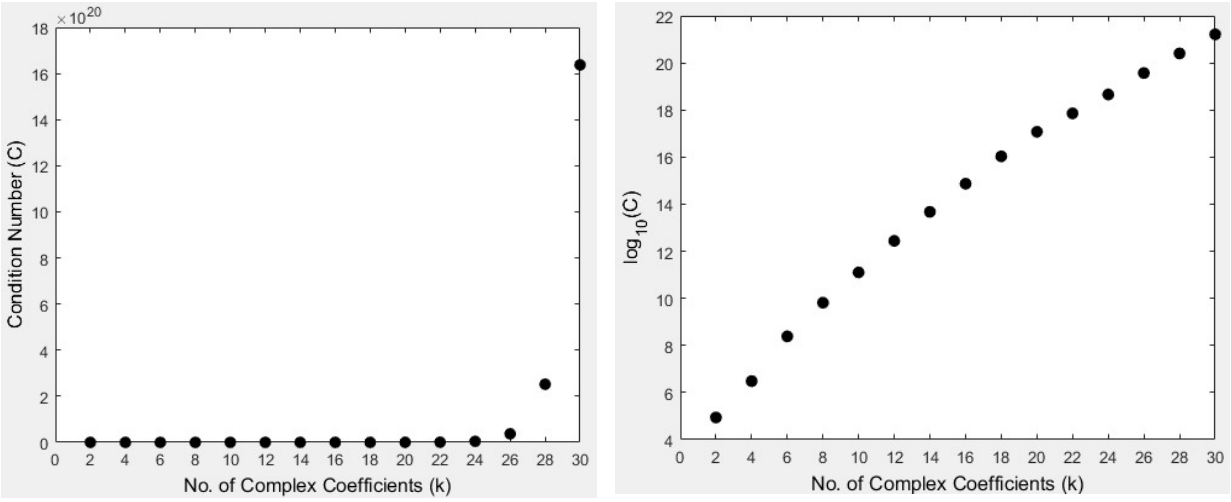

(a) (b)

Figure M-3: (a) Condition number, C, and (b) $\log_{10}(C)$ for varying number of Airy stress coefficients, k, for n_{DIC} = 22,039 of Figure M-1

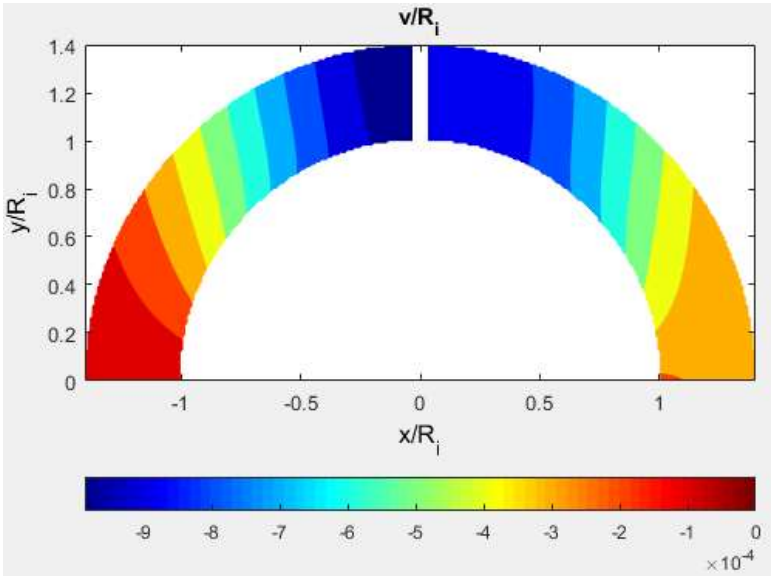

Figure M-4: Contours of displacements v/R_i from complex variables DIC-hybrid method (right) and FEM (left) of the aluminum ring loaded along direction y for DIC-measured n_{DIC} = 22,039 v-displacements and Laurent series

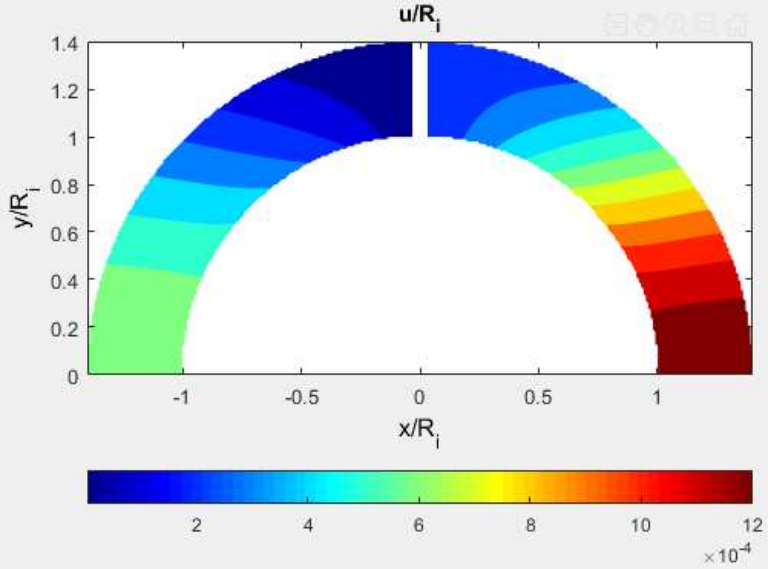

Figure M-5: Contours of displacements u/R_i (displacements transverse to the loading direction) from complex variables DIC-hybrid method (right) and FEM (left) of the aluminum ring loaded along direction y for DIC-measured n_{DIC} = 22,039 v-displacements and Laurent series

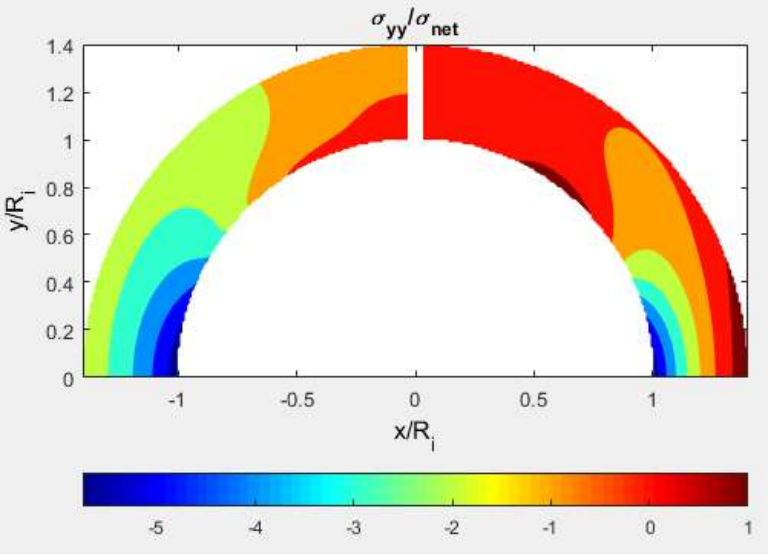

Figure M-6: Contours of stresses σ_{yy}/σ_{net} from complex variables DIC-hybrid method (right) and FEM (left) of the aluminum ring loaded along direction y for DIC-measured n_{DIC} = 22,039 v-displacements and Laurent series

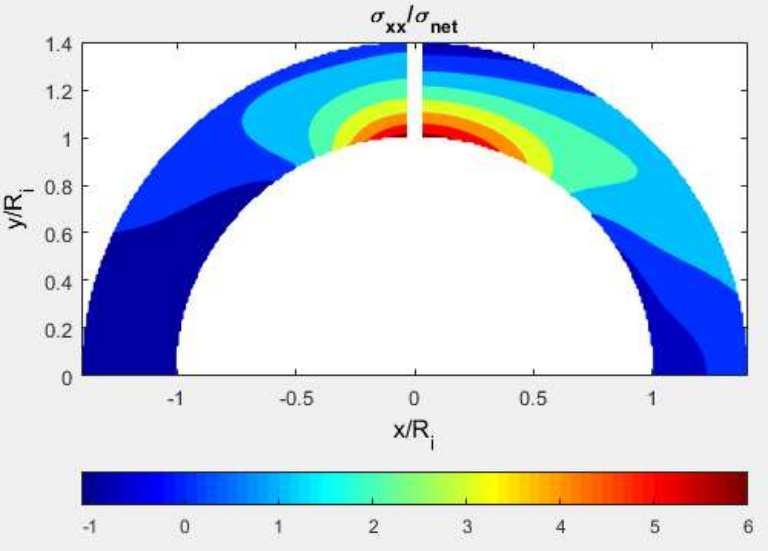

Figure M-7: Contours of stresses σ_{xx}/σ_{net} from complex variables DIC-hybrid method (right) and FEM (left) of the aluminum ring loaded along direction y for DIC-measured n_{DIC} = 22,039 v-displacements and Laurent series

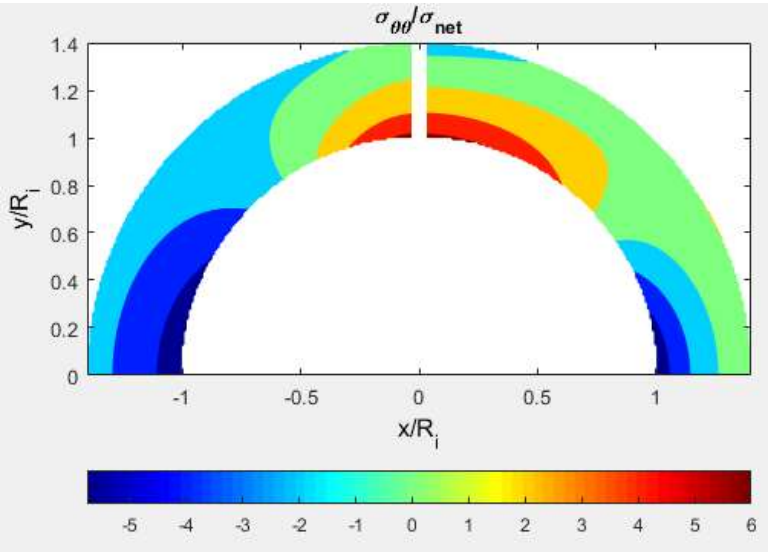

Figure M-8: Contours of stresses $\sigma_{\theta\theta}/\sigma_{net}$ from complex variables DIC-hybrid method (right) and FEM (left) of the aluminum ring loaded along direction y for DIC-measured n_{DIC} = 22,039 v-displacements and Laurent series

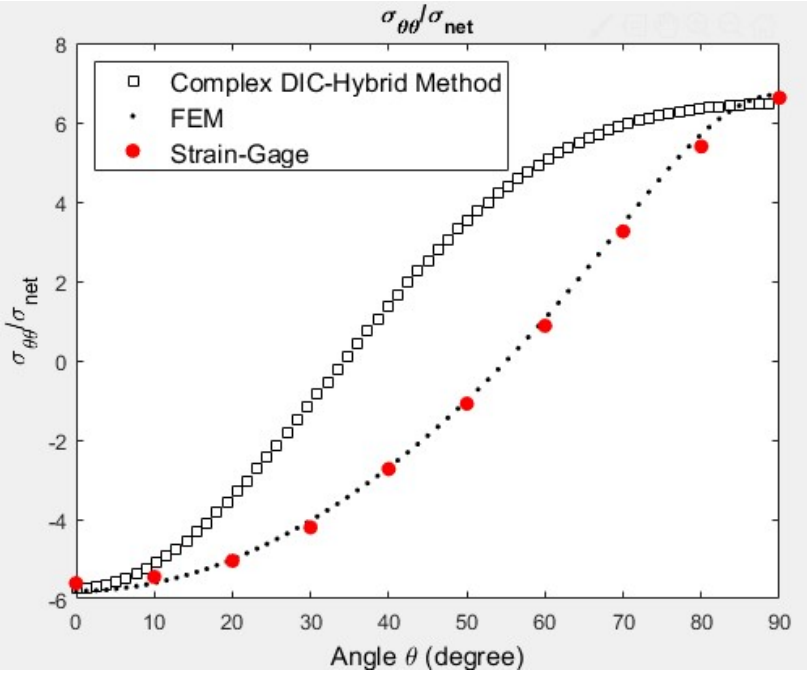

Figure M-9: Plot of tangential stresses, $\sigma_{\theta\theta}/\sigma_{net}$, along inner boundary of the ring from strain-gage, direct FEA and complex variables DIC-hybrid method (DIC *v*-displacements as input) for n_{DIC} = 22,039 and Laurent series

Appendix N. Edge-Crack Mapping Function and Laurent Series

The mapping function of equation (8-7), which maps a unit circle and its exterior region from the ζ-plane to an edge crack and its exterior region in the z-plane, Figure 8-2, is a special case of Andersson's mapping. For an orthotropic material in the physical plane $z = x + \mu_j y$, for $j = 1, 2$, Andersson's mapping function is [22,172]

$$\omega_j(\zeta_j) = z_j = \frac{(1-i\mu_j)}{2} a\zeta_j^{-1}(\zeta_j - 1)^k(\zeta_j + 1)^{2-k} + \frac{1+i\mu_j}{2} a\overline{\zeta_J^{-1}(\zeta_J - 1)^k(\zeta_J + 1)^{2-k}} + z_c \qquad j = 1, 2 \tag{N-1}$$

where the edge crack is inclined by an angle $k\pi/2$ to the x-axis. Using $k = 1$ in equation (N-1) gives the mapping function of equation (8-7) in which the edge crack is transverse to the x-axis. The mode-I loading is in the x-direction of the plate perpendicular to the crack-face.

Appendix O. Complex Variables Hybrid-Method and *J*-Integral to Fracture Analyze Isotropic Plates Containing Cracks

General Overview

The ability of the displacement-based complex variables hybrid-method combined with the *J*-integral concepts to fracture analyze members fabricated with isotropic materials containing cracks is demonstrated here. A double-edge crack (DEC) plate (plate-5) with dimensions according to Figure 9-1 and material properties of Table O-1 was modeled and analyzed in ANSYS APDL. The orthotropic material properties of plate-5 (Table O-1) have directional properties with very low degree of anisotropy, E_{11}/E_{22} = 1.034, i.e., properties of plate-5 are similar to an isotropic material. In addition, FEA of a steel DEC-plate (plate-6) with dimensions and elastic properties of Figure 9-1 and Table O-2, respectively, was conducted.

Hybrid-Method

FEM quarter models of plate-5 and -6 were created and analyzed using ANSYS APDL with the coordinates and dimensions as shown in Figure 9-1 and properties of Table O-1 and Table O-2, respectively. Details regarding the FEA models are provided in Chapter 9, Section 9.6. FEA predicted *v*-displacements were processed by the hybrid-method combined with the *J*-integral approach according to Chapter 9, Sections 9.4.1 (displacement-based hybrid-method) and 9.4.2.2

(*J*-integral concepts). The FEA-predicted *v*-displacements are processed with equation (9-11) combined with the mapping function of equation (9-3) to evaluate the Airy coefficients, c_j. The mapping function maps an edge crack and its surrounding region from the *z*-plane to a half-plane with the crack-face along the real axis in the mapped ζ-plane and vise-versa. Knowing the Airy coefficients and plate's material properties and using equations (9-11) through (9-15) and equations (9-30) and (9-31) the plate's states of stress, displacement and rotation components are evaluated. From these hybrid-method evaluated results in equation (9-27) the *J*-integral of the DEC-plates are obtained along a path surrounding the crack from the lower flank to the upper flank in a counter clock-wise direction at a distance d_{int} from the crack-tip, Figure 9-4. Details regarding evaluating the *J*-integral for each of the line segments of the path shown in Figure 9-4 are provided in Table 9-1. Once the *J*-integral is evaluated one can obtain SIF, K_I from equation (9-34). Only the *v*-displacements were employed in the hybrid analyses without requiring to use any other boundary conditions.

Hybrid Analyses Details

While processing the FEA-predicted *v*-displacements using the displacement-based complex hybrid-method for both plate-5 and -6, n_{FEA} = 2,404 displacements were selected close but slightly away from the crack-face and -tip over the region $0.1a \le y \le 0.2(L/2)$, $-a \le x \le (W/2 - a)$ and $r \ge 0.1a$, Figure O-1. This is due to the fact that measured data close to the crack-face are unreliable and also to avoid any three-dimensional effect prevailing close to the crack-tip. For these n_{FEA} = 2,404 selected FEA-predicted *v*-displacements to obtain reliable results the RMS plot of Figure O-2 suggests using $k \ge 14$ Airy coefficients in the finite series employed in the analytical

expressions of displacements, stresses and rotation components. For the current analyses $k = 30$ were selected. Some details regarding the hybrid analyses for plate-5 and 6 are provided in Table O-3. Using the evaluated c_j in equations (9-10) through (9-15) the in-plane displacements, stresses and strains were obtained, Figure O-4 through Figure O-7 for plate-5 and Figure O-9 through Figure O-12 for plate-6.

Fracture Analyses Details

ANSYS APDL provides built-in commands to find important fracture-related parameters for isotropic materials, Figure O-8 and Figure O-13. For the steel plate-6 ANSYS APDL command 'CINT' was used to evaluate the *J*-integral around contours surrounding the edge crack of the quarter FEM model of the DEC-plate, Figure O-13. As plate-5 has properties close to an isotropic material, the *J*-integral of the plate was also evaluated using ANSYS command 'CINT', Figure O-8.

The *J*-integrals of plate-5 and -6 also evaluated by post-processing the hybrid-method provided information according to the *J*-integral concepts of Chapter 9, Section 9.4.2.2, are provided in Table O-4 and Table O-5, respectively. The integrations were computed using the Gaussian-Quadrature rule employing 15 Gaussian points.

Table O-1: Material properties of almost isotropic plate-5 with double-edge cracks

Plate's Elastic Properties	Double-Edge Cracks (Almost Isotropic)
Elastic modulus in loading direction, E_{22} or E_{yy}	203.39 GPa (29.5×10^6 psi)
Elastic modulus transverse to loading direction, E_{11} or E_{xx}	210.29 GPa (30.5×10^6 psi)
Major Poisson's ratio, v_{12} or v_{xy}	0.25
Shear modulus, G_{12} or G_{xy}	82.74 GPa (12×10^6 psi)

Table O-2: Material properties of isotropic plate-6 with double-edge cracks

Plate's Elastic Properties	Double-Edge Cracks (Isotropic)
Elastic modulus, E	206.84 GPa (30×10^6 psi)
Poisson's ratio, v	0.25
Shear modulus, G	84.12 GPa (12.2×10^6 psi)

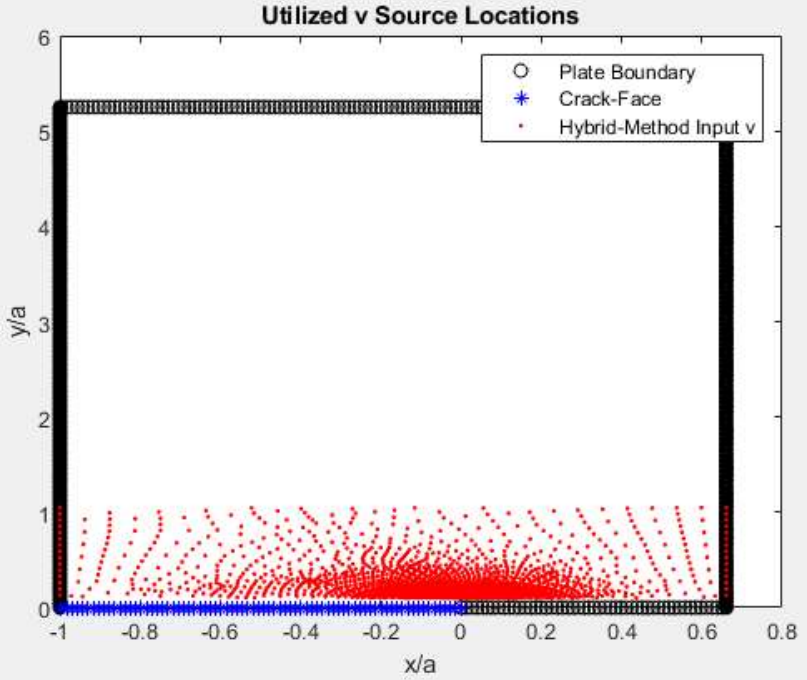

Figure O-1: Hybrid-method utilized FEM-predicted *v*-displacements source locations for plate-5 and plate-6 for $0.1a \leq y \leq 0.2(L/2)$, $-a \leq x \leq (W/2 - a)$ and $r \geq 0.1a$

4.2

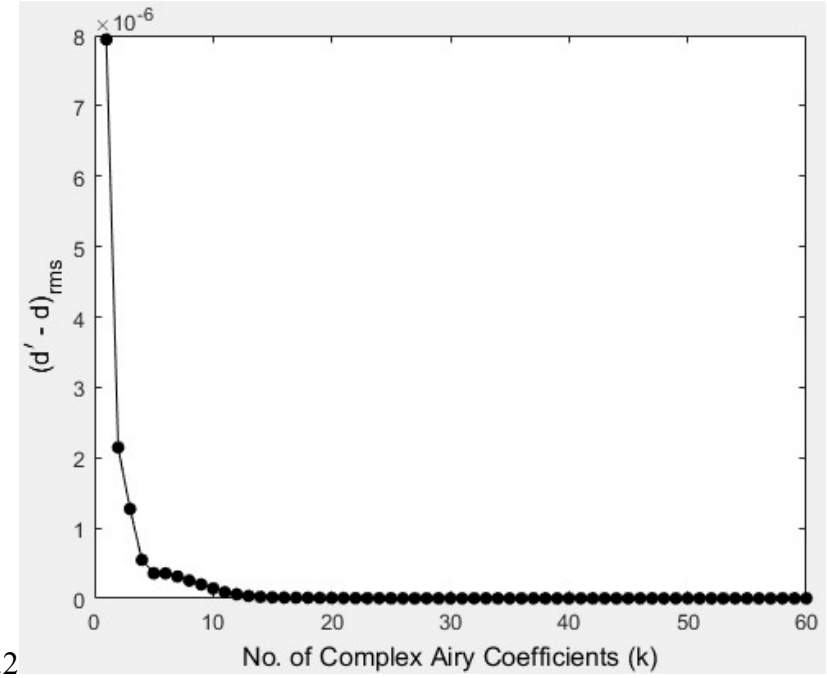

Figure O-2: RMS of the FEA-predicted and hybrid-method reconstructed *v*-displacement data versus the number of Airy stress coefficients, *k,* for n_{FEA} = 2,404 of the almost isotropic DEC-plate-5 and Taylor series

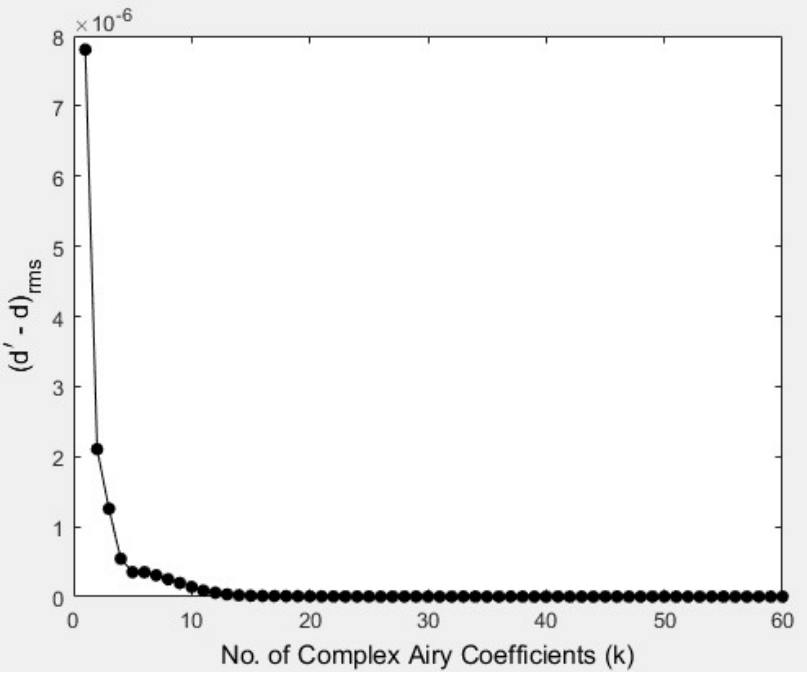

Figure O-3: RMS of the FEA-predicted and hybrid-method reconstructed *v*-displacement data versus the number of Airy stress coefficients, *k,* for n_{FEA} = 2,404 of steel DEC plate-6 and Taylor series

Table O-3: Hybrid analyses details for plate-5 and -6

Plate Type	Complex material properties	Hybrid-method's input quantity	Employed FEA-predicted displacements	Imposed boundary condition	No. of complex Airy coefficients employed
DEC almost isotropic (E_{11}/E_{22} = 1.034)	$\mu_1 = -0.0472 + 1.0073i$ $\mu_2 = 0.0472 + 1.0073i$	*v*	n_{FEA} = 2,404	$h = 0$	$k = 30$ (Taylor series)
DEC isotropic (E_{11}/E_{22} = 1.00)	$\mu_1 = \mu_2 = 1.00i$	*v*	n_{FEA} = 2,404	$h = 0$	$k = 30$ (Taylor Series)

Results

For plate-5 (almost isotropic DEC-plate) Figure O-4 through Figure O-7 and for plate-6 (steel DEC-plate) Figure O-9 through Figure O-12 compare the results obtained from the hybrid-method employing FEA-predicted v-displacement data with those directly predicted by FEA. All distances and displacements are normalized by the length of the individual edge crack, a = 19.05 mm, and stresses with respect to the far-field stress, σ_0 = 21.23 MPa according to equation (9-43).

The J-integrals evaluated using the ANSYS in-build 'CINT' command, Figure O-8 and Figure O-13, agree well with those evaluaed by the hybrid-method combined with the J-integral concepts, Table O-4 and Table O-5, for various integration paths, d_{int}.

The excellent agreement between the hybrid-method reconstructed and direct FEA-predicted displacement and stress contours of Figure O-4 through Figure O-7 and Figure O-9 through Figure O-12 for plate-5 and -6, respectively, demonstrate the hybrid-method's capability in reliably stress analyzing members fabricated of isotropic or orthotropic materials with lower degree of anisotropy containg cracks. The hybrid-methods capability in effectively treating orthotropic members with different material properties and crack types was demonstrated in Chapter 9.

The J-integral value obtained from ANSYS relates closely with those obtained from the hybrid-method, within $0.017\% - 0.717\%$ for plate-5 and $0.096\% - 0.296\%$ for plate-6 , Table O-4 and Table O-5, respectively. This validates that the hybrid-method combined with the J-integral concept is an effective approach to reliably analyze istropic members involving cracks.

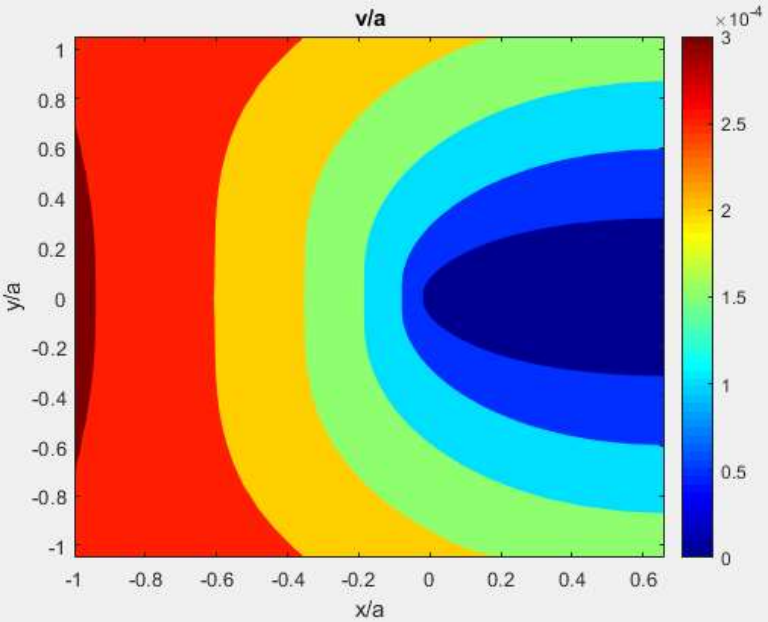

Figure O-4: Contours of displacements v/a for almost isotropic DEC plate-5 from hybrid-method (top half) using n_{FEA} = 2,404 FEM-predicted v-displacements, Taylor series and k = 30 and from FEA (bottom half)

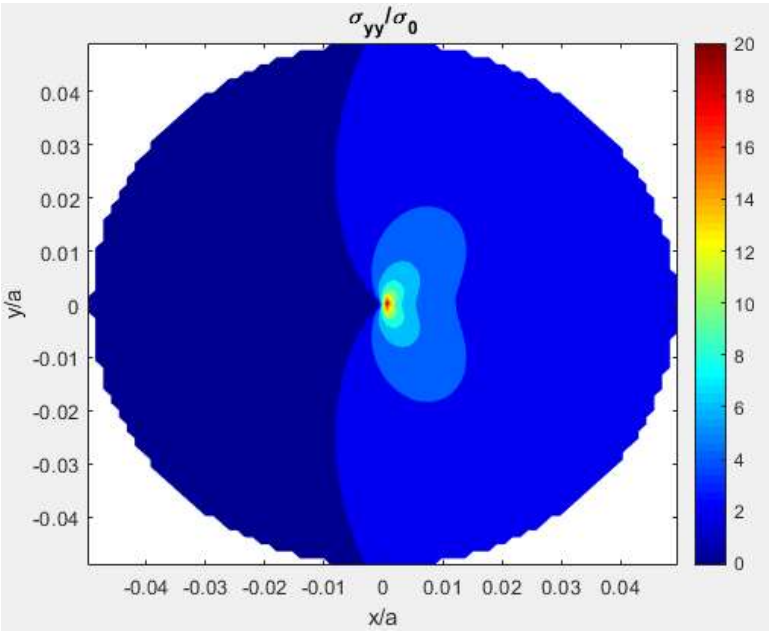

Figure O-5: Contours of stresses σ_{yy}/σ_0 for almost isotropic DEC plate-5 from hybrid-method (top half) using n_{FEA} = 2,404 FEM-predicted v-displacements, Taylor series and k = 30 and from FEA (bottom half)

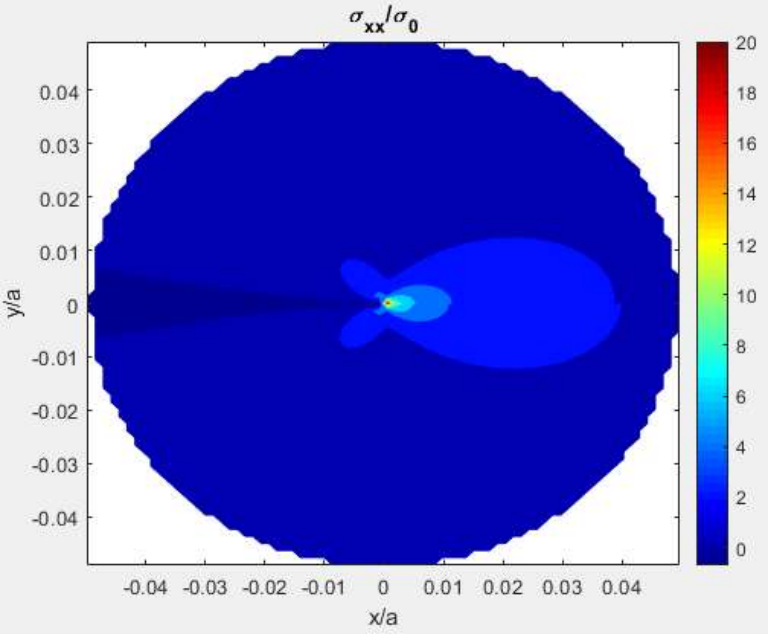

Figure O-6: Contours of stresses σ_{xx}/σ_0 for almost isotropic DEC plate-5 from hybrid-method (top half) using n_{FEA} = 2,404 FEM-predicted v-displacements, Taylor series and k = 30 and from FEA (bottom half)

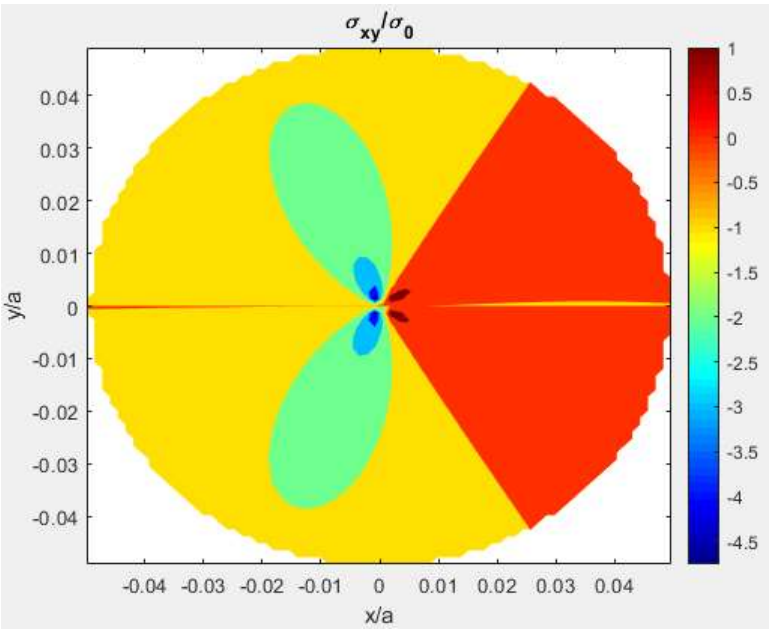

Figure O-7: Contours of stresses σ_{xy}/σ_0 for almost isotropic DEC plate-5 from hybrid-method (top half) using n_{FEA} = 2,404 FEM-predicted v-displacements, Taylor series and k = 30 and from FEA (bottom half)

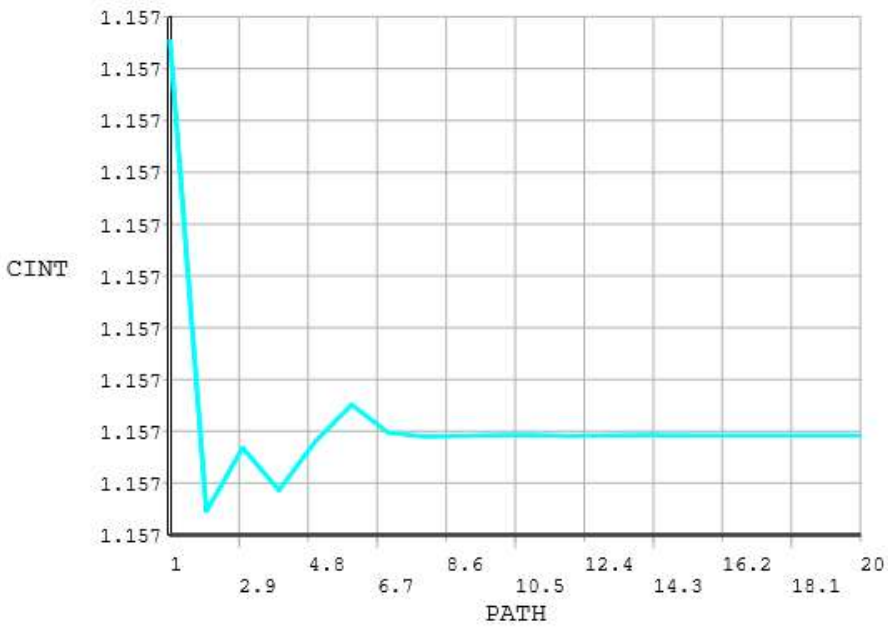

Figure O-8: *J*-integral along various paths enclosing the crack for the almost isotropic DEC plate-5 using ANSYS APDL 'CINT' command (units of *J*, i.e., 'CINT' along *y*-axis are in inch-lbs/inch^2)

Table O-4: Hybrid-method computed *J*-integral values for various paths surrounding the crack and *J*-integral value from FEA for almost isotropic DEC plate-5

d_{int}	*J* value (hybrid-method)	*J* (FEA)
0.2*a*	202.56 Joules/m^2 (1.15647 inch-lbs/inch^2)	
0.4*a*	202.56 Joules/m^2 (1.15649 inch-lbs/inch^2)	202.60 Joules/m^2 (1.1567 inch-lbs/inch^2)
0.6*a*	201.14 Joules/m^2 (1.14836 inch-lbs/inch^2)	

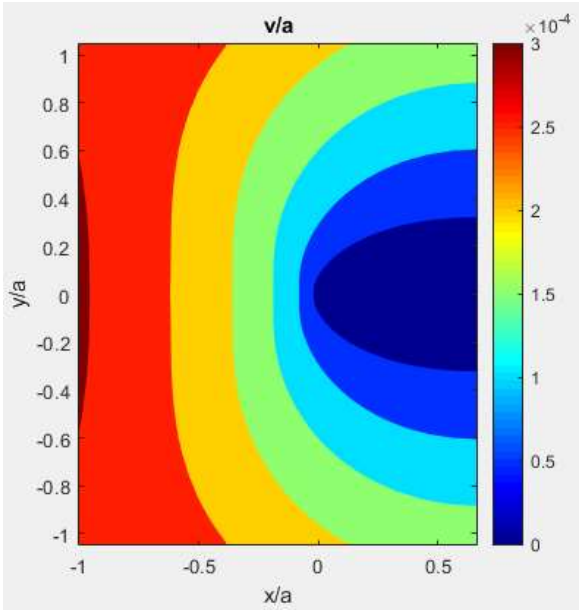

Figure O-9: Contour of displacements v/a for isotropic (steel) DEC plate-6 from hybrid-method (top half) using n_{FEA} = 2,404 FEM-predicted v-displacements, Taylor series and k = 30 and from FEA (bottom half)

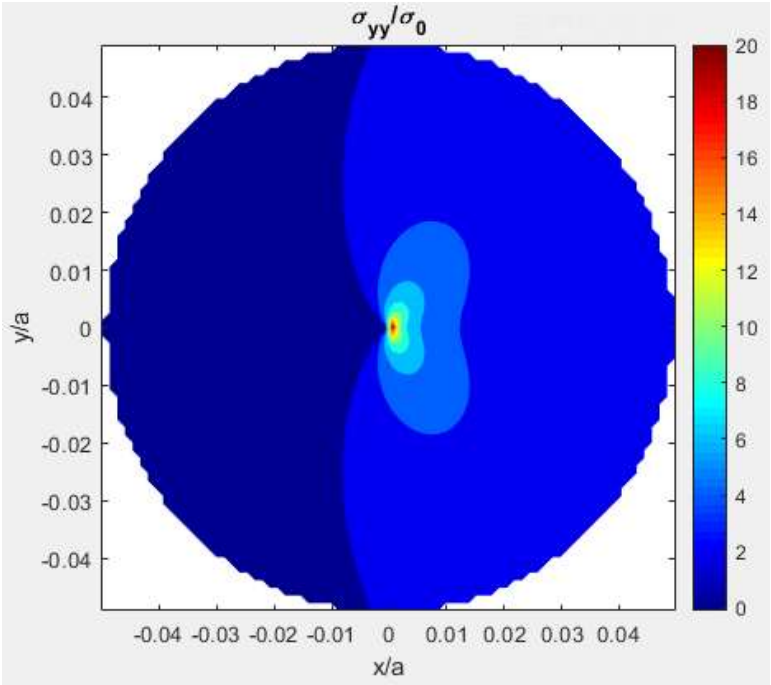

Figure O-10: Contour of stresses σ_{yy}/σ_0 for isotropic (steel) DEC plate-6 from hybrid-method (top half) using n_{FEA} = 2,404 FEM-predicted v-displacements, Taylor series and k = 30 and from FEA (bottom half)

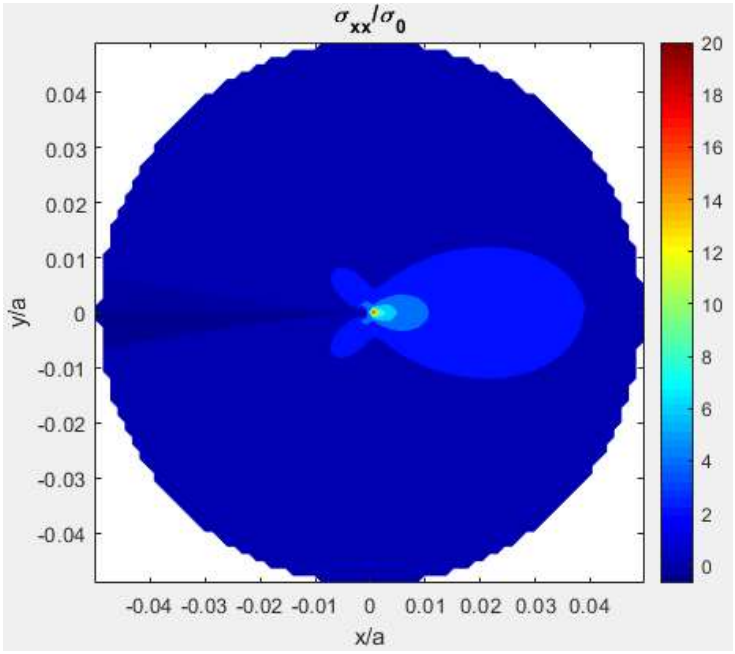

Figure O-11: Contour of stresses σ_{xx}/σ_0 for isotropic (steel) DEC plate-6 from hybrid-method (top half) using n_{FEA} = 2,404 FEM-predicted v-displacements, Taylor series and k = 30 and from FEA (bottom half)

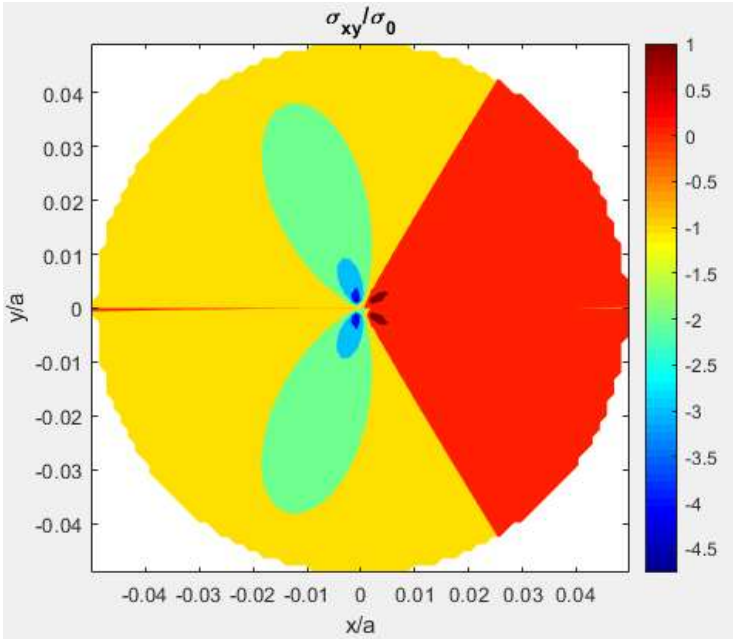

Figure O-12: Contour of stresses σ_{xy}/σ_0 for isotropic (steel) DEC plate-6 from hybrid-method (top half) using n_{FEA} = 2,404 FEM-predicted v-displacements, Taylor series and k = 30 and from FEA (bottom half)

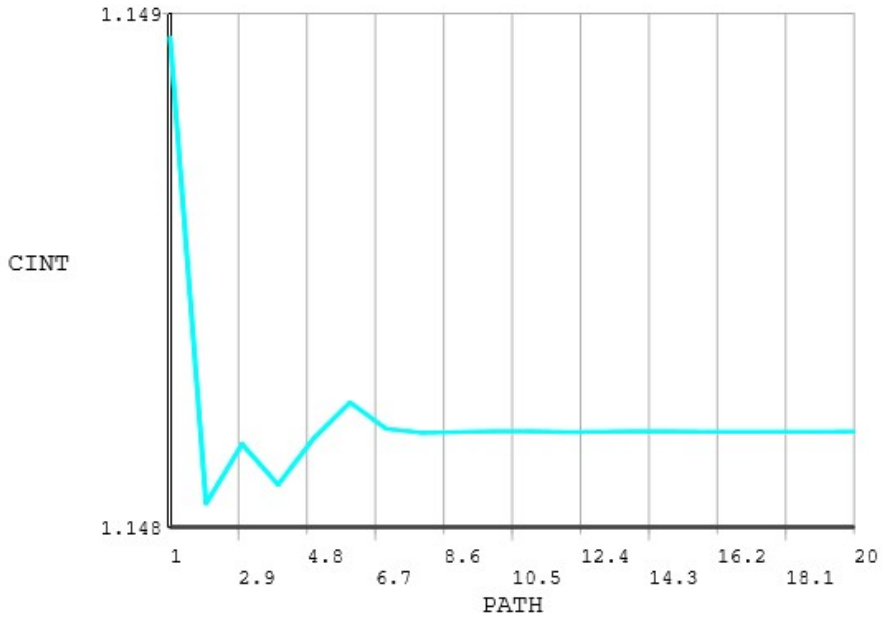

Figure O-13: *J*-integral along various paths enclosing the crack for the steel DEC plate-6 using ANSYS APDL 'CINT' command (units of *J*, i.e., 'CINT' along *y*-axis are in inch-lbs/inch^2)

Table O-5: Hybrid-method computed *J*-integral values for various path surrounding the crack and *J*-integral value from FEA for steel DEC plate-6

d_{int}	*J* value (hybrid-method)	*J* (FEA)
0.2*a*	200.99 Joules/m^2 (1.1475 inch-lbs/inch^2)	201.09 Joules/m^2 (1.1481 inch-lbs/inch^2)
0.4*a*	201.28 Joules/m^2 (1.1492 inch-lbs/inch^2)	
0.6*a*	200.49 Joules/m^2 (1.1447 inch-lbs/inch^2)	

Discussion and Conclusions

The displacement-based complex hybrid-method combined with the *J*-integral concepts is an effective and reliable means of fracture analyzing both orthotropic and isotropic members involving cracks. The method can reliably analyze virtually any type of plates. The use of the Taylor series further allows any type of crack configuration to be analyzed using a single mapping function. The stress and fracture analyses were done employing only a single component of measured information (in this case FEA-predicted *v*-displacements in the loading direction). No other boundary condition needs to be imposed nor the method require knowing the external loading.

It was observed from these analyses that for the complex hybrid-method instead of selecting input displacement data over the entire plate, selecting data closer to the crack-face improved the hybrid results. This will be further discussed in Appendix P. A limitation of the hybrid-method especially when treating edge cracks is the difficulty in evaluating the transverse displacement component, *u*, from using displacements in the loading direction, *v*, as input and vice-versa. The hybrid-method evaluated *u* by using FEA *v* as the hybrid-method's input does not exactly match with the ones directly predicted by FEA. However, as *u*-displacements are significantly smaller compared to *v*-displacements.

Appendix P. Effect of Source Data Locations on Complex Hybrid-Method Evaluated *J*-Integral Values

This study observes the effect of the hybrid-method selected input ranges and locations on the *J*-integral results evaluated by processing the hybrid-method computed information. The analyses were done for the orthotropic DEC plate-5 (with elastic properties close to isotropy) using FEA-predicted *v*-displacements, according to the procedures outlined in Appendix O. For various ranges of data source locations using the FEA-predicted *v*-displacements in the complex hybrid-method the plate was analyzed. The hybrid-method computed results were processed with the concept of *J*-integrals to evaluate fracture parameter *J*-value, which is related to the SIF of the crack plate. The *J*-integral of the almost isotropic DEC plate-5 was also determined using the ANSYS APDL command 'CINT' in Appendix O and found to be 202.60 Joules/m^2 (1.1567 inch-lbs/inch^2). It is observed from the analyses done under this section that as the hybrid-method input data are selected closer to the crack-face improves the method's result accuracy and subsequently provides better estimation of the *J*-integral value. The hybrid-method obtained *J*-integral values for the varying data source locations are compared to that provided by the FEA 'CINT' command.

The analyses first considers *v*-displacement data over the entire plate, Figure P-1, and gradually reduces the amount of data selected considering input data closer to the crack-face, Figure P-2 and Figure P-3. Then the analyses were conducted selecting reasonably amount of input data considerably close to the crack-face, Figure O-1. Finally, the analysis was done by considering limited amount of data close to the crack-face. Results from these analyses are provided in Table P-1.

Obtained results demonstrate that as one selects the hybrid-method input data close to the crack-face, cases 4 through 7 of Table P-1, better results for the *J*-integral are obtained with respect to that evaluated from FEA, compared to selecting data over a larger region, cases 1 through 3 of Table P-1. However, if the selected data source locations are adjacent to the crack-face but over a comparatively small region, then the small number of selected input quantity are not sufficient to reliably analyze the plate, thus effecting the hybrid-method's accuracy. For case 8 of Table P-1 due to inadequate number of input quantities, the hybrid-method evaluated states of stress and displacement contours start to deviate from the ones directly determined from the FEA.

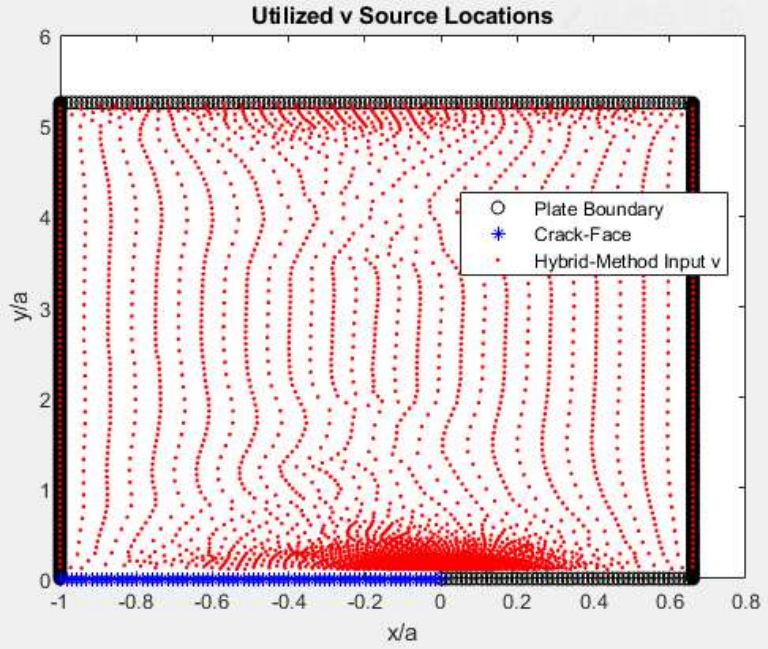

Figure P-1: Hybrid-method utilized FEM-predicted *v*-displacement data source locations for plate-5 for $0.1a \leq y \leq (L/2)$, $-a \leq x \leq (W/2 - a)$ and $r \geq 0.1a$

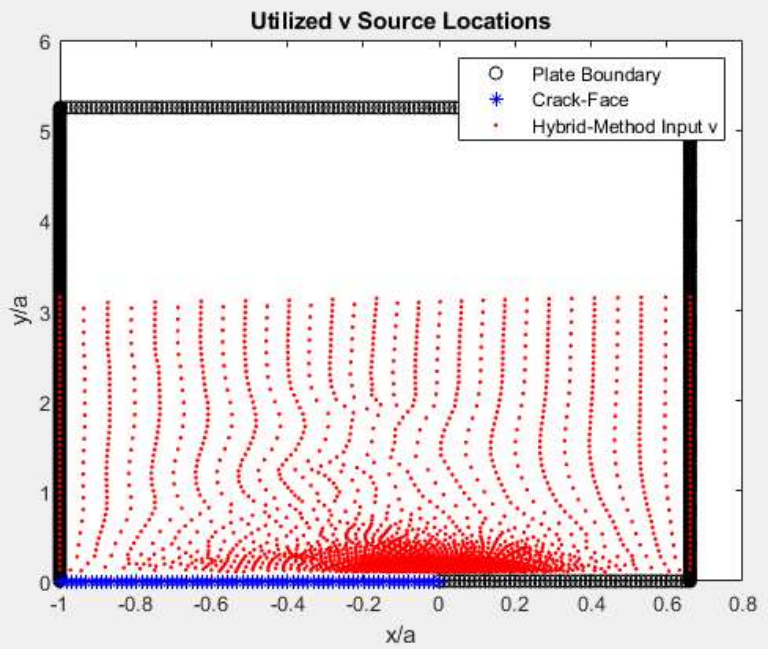

Figure P-2: Hybrid-method utilized FEM-predicted *v*-displacement data source locations for plate-5 for $0.1a \leq y \leq 0.6(L/2)$, $-a \leq x \leq (W/2 - a)$ and $r \geq 0.1a$

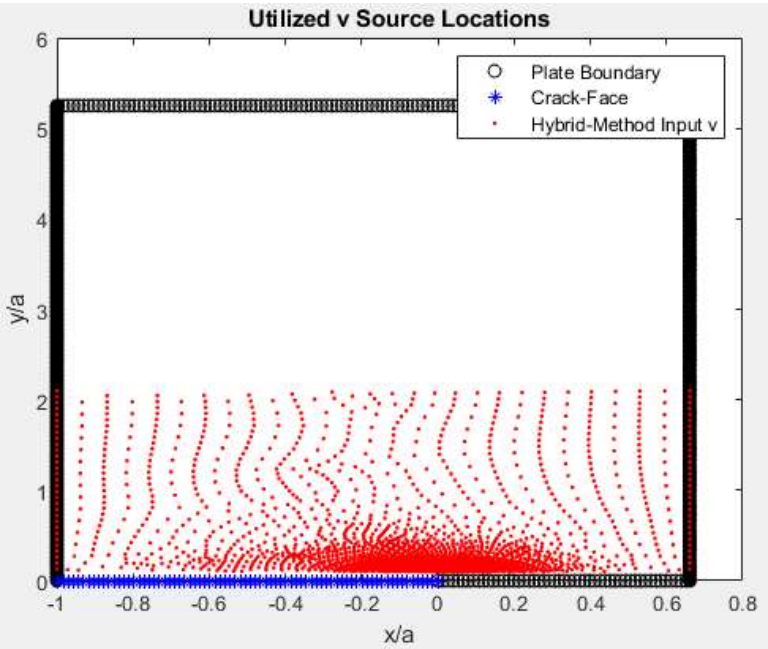

Figure P-3: Hybrid-method utilized FEM-predicted *v*-displacement data source locations for plate-5 for $0.1a \leq y \leq 0.4(L/2)$, $-a \leq x \leq (W/2 - a)$ and $r \geq 0.1a$

Table P-1: Effect of hybrid-method input v-displacement data source locations on the evaluated J-integral value

Case	Selected region for input v-displacements	Radius from crack-tip beyond which input data are selected	Employed FEM-predicted v-displacement input, n_{FEA}	Computed J-integral value
1 (Figure P-1)	$0.1a \le y \le (L/2)$, $-a \le x \le (W/2 - a)$	$r \ge 0.1a$	4,066	189.62 Joules/m^2 (1.0826 inch-lbs/inch^2)
2	$0.1a \le y \le 0.8(L/2)$, $-a \le x \le (W/2 - a)$	$r \ge 0.1a$	3,432	189.04 Joules/m^2 (1.0793 inch-lbs/inch^2)
3 (Figure P-2)	$0.1a \le y \le 0.6(L/2)$, $-a \le x \le (W/2 - a)$	$r \ge 0.1a$	3,099	194.17 Joules/m^2 (1.1086 inch-lbs/inch^2)
4 (Figure P-3)	$0.1a \le y \le 0.4(L/2)$, $-a \le x \le (W/2 - a)$	$r \ge 0.1a$	2,746	201.62 Joules/m^2 (1.1511 inch-lbs/inch^2)
5 (Figure O-1)	$0.1a \le y \le 0.2(L/2)$, $-a \le x \le (W/2 - a)$	$r \ge 0.1a$	2,404	202.56 Joules/m^2 (1.1565 inch-lbs/inch^2)
6	$0.1a \le y \le 0.1(L/2)$, $-a \le x \le (W/2 - a)$	$r \ge 0.1a$	2,157	202.75 Joules/m^2 (1.1576 inch-lbs/inch^2)
7	$0.1a \le y \le 0.08(L/2)$, $-a \le x \le (w/2 - a)$	$r \ge 0.1a$	2,044	202.91 Joules/m^2 (1.1585 inch-lbs/inch^2)
8	$0.1a \le y \le 0.05(L/2)$, $-a \le x \le (w/2 - a)$	$r \ge 0.1a$	1,677	203.10 Joules/m^2 (1.1596 inch-lbs/inch^2) (contours start to deviate)

Appendix Q. DIC-Hybrid Results for DEC-Plate using only Measured *v*-Displacements

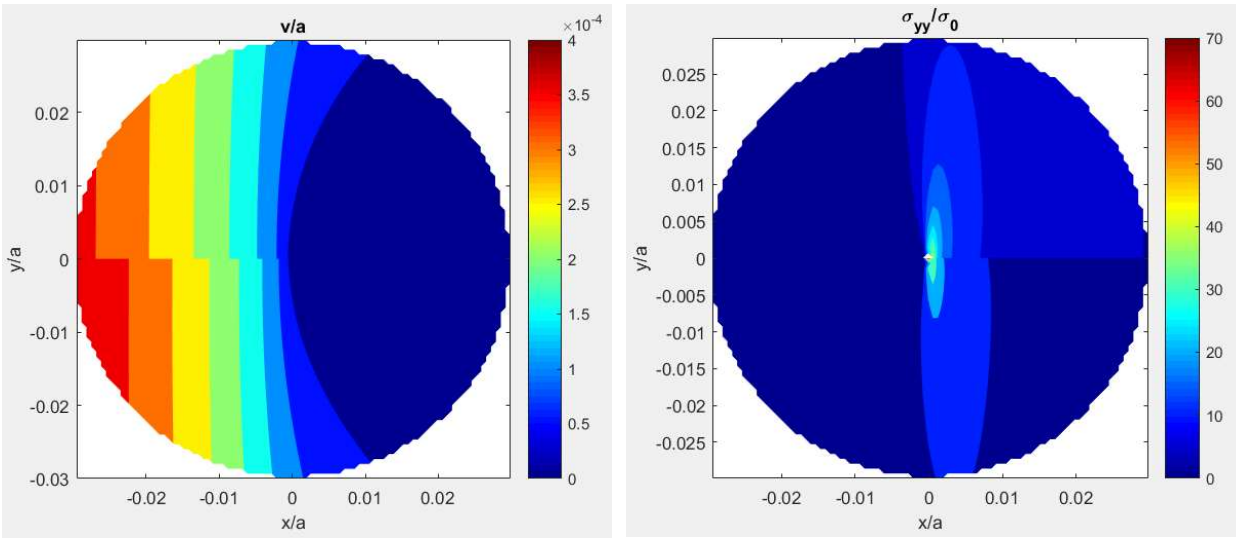

Figure Q-1: Contours of (a) v/a, (b) σ_{yy}/σ_0, (c) σ_{xx}/σ_0 and (d) σ_{xy}/σ_0 from DIC-hybrid method (top) and FEM (bottom) with only DIC v-displacements as input for Figure 9-1

In Figure Q-1, in-plane stress and displacement contours of Figure 9-1 are evaluated from the DIC-hybrid stress analysis method by only using DIC-measured v-displacements as input and without imposing any symmetry or finite boundary conditions. Here $k = 6$ and $n_{DIC} = 27{,}221$ were used.

Appendix R. Evaluating SIF for the [$0_{13}/90_5/0_{13}$] Graphite-Epoxy DEC-Plate using Bao's Closed-Form Solutions

Bao et al. [93] provided closed-form solutions to find SIFs for orthotropic plates containing various shaped cracks. According to Bao's study for an orthotropic DEC-plate under a uniform stress of σ_0, the mode-I SIF, K_I, is of the following form

$$K_I = \sigma_0\sqrt{\pi a}Y(\rho)H\left(\frac{a}{W}\right) \tag{R-1}$$

where λ and ρ are the dimensionless parameters and equation (R-2) provides the general expression of these quantities in terms of the material's elastic compliances [177]. For the orthotropic [$0_{13}/90_5/0_{13}$] graphite-epoxy DEC-plate of Figure 9-1 with elastic properties of those provided in Table 4-1, λ and ρ are obtained from the below expressions

$$\lambda = \frac{a_{1'1'}}{a_{2'2'}},\ \ \rho = \frac{1}{2}(2a_{1'2'} + a_{6'6'})(a_{1'1'}a_{2'2'})^{-\frac{1}{2}} \tag{R-2}$$

According to the coordinate system of Figure 9-1 the elastic compliances for the present DEC-plate are

$$a_{1'1'} = \frac{1}{E_{22}}, a_{1'2'} = \frac{-\nu_{12}}{E_{11}} = \frac{-\nu_{21}}{E_{22}}, a_{2'2'} = \frac{1}{E_{11}} \text{ and } a_{6'6'} = \frac{1}{G_{12}} \tag{R-3}$$

where coordinates 1'-2' define directions parallel and perpendicular to the crack-face and coordinates 1-2 represent directions along and transverse to the strong/stiff fiber direction, respectively.

Thus, combining equation (R-3) into equation (R-2), the material constants λ and ρ are

$$\lambda = \frac{E_{11}}{E_{22}} = 3.7 \text{ and } \rho = \frac{(E_{11}E_{22})^{\frac{1}{2}}}{2G_{12}} - (\nu_{12}\nu_{21})^{\frac{1}{2}} = 8.7 \tag{R-4}$$

For a tensile-loaded orthotropic plate the material orthotropy correction factor, $Y(\rho)$, and for a DEC-plate the geometry dependence rescaling factor, $H(a/W)$, are provided in equations (R-5) and (R-6), respectively, [93]

$$Y(\rho) = 1 + 0.1(\rho - 1) - 0.016(\rho - 1)^2 + 0.002(\rho - 1)^3 \tag{R-5}$$

and

$$H\left(\frac{a}{W}\right) = \left[1 + 0.122\cos^4\frac{\pi a}{W}\right]\sqrt{\frac{W}{\pi a}\tan\frac{\pi a}{W}} \tag{R-6}$$

Moreover, the K_I becomes independent of plate's length-to-width ratio, L/W, and the degree of material anisotropy, λ, if the composite parameter $\lambda^{1/4}(L/W) \geq 2$. For the present plate of Figure 9-1 the value of $\lambda^{1/4}(L/W)$ is 6.38. Thus, the theory by Bao et al. would suggest the effects of λ and L/W on K_I are negligible.

For the current $[0_{13}/90_5/0_{13}]$ graphite-epoxy DEC-plate using ρ of equation (R-4) into equation (R-5), $Y(\rho)$ is obtained. From the double-edge cracks length to plate-width ratio, $2a/W$, of 0.6 and equation (R-6), $H(a/W)$ is obtained. Substituting the values of $Y(\rho)$ and $H(a/W)$ into equation (R-1) gives K_I. The normalized SIF, $K_I/\sigma_0\sqrt{a}$, is 3.7, which is much higher than those evaluated by the previously-mentioned methods, Table 9-10. One possible reason is that, the value of ρ for the current graphite-epoxy DEC-plate is 8.7. However, the expression of K_I provided by Bao et al. [93] in equation (R-1) is typically valid for materials with $0 \leq \rho \leq 4$ and $0.05 \leq \lambda \leq 20$. The value of ρ for the current plate exceeds the highest limit of $0 \leq \rho \leq 4$ by a factor of 2.2 and equation (R-1) over-estimates K_I. Again Bao et al. [93] study was conducted considering the crack to be aligned with material orthotropy direction 1, i.e., most compliant direction.

However, if the expression of equation (R-1) did not include the mathematical constant $\sqrt{\pi}$, i.e., the expression of K_I was as of that provided in equation (R-7), then the K_I normalized by $\sigma_0\sqrt{a}$ comes out to be 2.09, which agrees with the normalized K_I obtained from the other methods illustrated in Chapter 9, Table 9-10.

$$K_I = \sigma_0\sqrt{a}Y(\rho)H\left(\frac{a}{W}\right) \tag{R-7}$$

A similar study done by Bažant et al. [180] provides slightly different expressions for the SIF of an orthotropic structure containing cracks. For composite laminates involving fracture Bažant study considers the structural size effect, i.e., effect of the structure's characteristic dimension, on its nominal strength and fracture characteristics. Bažant combined the concept of the size effect of a structure with Bao's concept. The K_I for an orthotropic structure according to Bažant's study is

$$K_{\mathrm{I}} = \sigma_N \sqrt{\pi D_c \alpha_c} Y(\rho) H(\alpha_c) \tag{R-8}$$

where D_c is the characteristic structure size, α_c is the ratio of crack length, a, to characteristic size, D_c, and σ_N is the nominal stress. Expression of these parameters are provided as below

$$D_c = \begin{cases} W, & \text{for SEC} \\ W/2, & \text{for DEC} \end{cases}, \quad \alpha_c = a/D_c \quad \text{and} \quad \sigma_N = P/D_c t \tag{R-9}$$

The material parameter $Y(\rho)$ in equation (R-8) is a function of the orthotropic material coefficient, ρ, from Bao's study provided in equation (R-4). However, the expression of $Y(\rho)$ provided in Bažant's study is as

$$Y(\rho) = [1 + 0.1(\rho - 1) - 0.015(\rho - 1)^2 + 0.002(\rho - 1)^3] \left(\frac{1 + \rho}{2}\right)^{-1/4} \tag{R-10}$$

The geometry correction factor $H(\alpha_c)$ in this case is a function of α_c. Expressions for $H(\alpha_c)$ are provided below and for DEC configuration is the same as equation (R-6).

$$H(\alpha_c) = \begin{cases} \left[1 + 0.122 \cos^4 \frac{\pi \alpha_c}{2}\right] \sqrt{\frac{2}{\pi \alpha_c} \tan \frac{\pi \alpha_c}{2}} & \text{for DEC} \\ 1.122 - 0.231\alpha_c + 10.55\alpha_c^2 - 21.71\alpha_c^3 + 30.38\alpha_c^4 & \text{for SEC} \end{cases} \tag{R-11}$$

For the DEC plate of Figure 9-1 with dimensions and properties in Table 9-2 and Table 4-1, respectively, combining equations (R-9) through (R-11) in equation (R-8) the mode-I K_{I} is obtained. The normalized SIF, $K_{\mathrm{I}}/\sigma_N\sqrt{a}$, is obtained as 2.63, which is 13.56% larger than the

normalized K_I obtained from the hybrid-method using FEA-predicted *v*-displacements and 19.67% larger when using DIC-measured *v*-displacement data, Table 9-10.

References

[1] Barbero EJ. Finite Element Analysis of Composite Materials using ANSYS. 2nd ed. Boca Raton, Florida, USA: CRC Press; 2013.

[2] Lian W, Yao W. Fatigue Life Prediction of Composite Laminates by FEA Simulation Method. Int J Fatigue 2010;32:123–33.

[3] Ambur D, McGowan D. Response of Composite Plates with Inclined Elliptical Notches and Subjected to Axial Compression. AIAA 40th Struct. Struct. Dyn. Mater. Conf., vol. 99–1276, St. Louis, MO, USA: AIAA; 1999.

[4] Meleshko V. Selected Topics in the History of the Two-Dimensional Biharmonic Problem. Appl Mech Rev 2003;56:33–85.

[5] Lekhnitskii SG. Anisotropic Plates. New York: Gordon and Breach; 1968.

[6] Savin GN. Stress Distribution Around Holes. Springfield, WA, USA: National Aeronautics and Space Administration; 1970.

[7] Bowie OL, Freese CE. Central Crack in Plane Orthotropic Rectangular Sheet. Int J Fract Mech 1972;8:49–57.

[8] Gerhardt TD. A Hybrid/Finite Element Approach for Stress Analysis of Notched Anisotropic Materials. J Appl Mech 1984;51:804–10.

[9] Lin ST. Quantitative Thermoelastic Stress Analysis of Orthotropic Composite Structures. PhD Thesis. University of Wisconsin - Madison, 1994.

[10] Schinzinger R. Conformal Mapping: Methods and Applications. New York, USA: Elsevier; 1991.

[11] Nehari Z. Conformal Mapping. New York, USA: McGraw-Hill; 1952.

[12] Krantz SG. Conformal Mappings. Am Sci 1999;87:436–45.

[13] Ashrafi M, Tuttle ME. High Strain Gradient Measurements in Notched Laminated Composite Panels by Digital Image Correlation. In: Tandon G, editor. Compos. Hybrid Multifunct. Mater. Vol. 4 Proc. 2014 Annu. Conf. Exp. Appl. Mech., Cham: Springer International Publishing; 2015, p. 75–81.

[14] Sutton MA, Orteu J-J, Schreier HW. Image Correlation for Shape, Motion and Deformation Measurements Basic Concepts, Theory and Applications. Springer; 2009.

[15] Muskhelishvili NI. Some Basic Problems of the Mathematical Theory of Elasticity: Fundamental Equations, Plane Theory of Elasticity, Torsion, and Bending. Groningen: Noordhoff International; 1975.

[16] Shukla A, Agarwal BD, Bhushan B. Determination of Stress Intensity Factor in Orthotropic Composite Materials using Strain Gages. Eng Fract Mech 1989;32:469–77.

[17] Mogadpalli GP, Parameswaran V. Determination of Stress Intensity Factor for Cracks in Orthotropic Composite Materials using Digital Image Correlation. Strain 2008;44:446–52.

[18] Lin ST, Rowlands RE. Thermoelastic Stress Analysis of Orthotropic Composites. Exp Mech 1995;35:257–65.

[19] Alshaya AA. Experimental, Analytical and Numerical Analyses of Orthotropic Materials and Biomechanics Application. PhD Thesis. University of Wisconsin -Madison, 2017.

[20] Dai M, Schiavone P, Gao CF. Surface Tension-Induced Stress Concentration Around an Elliptical Hole in an Anisotropic Half-Plane. Mech Res Commun 2016;73:58–62.

[21] Tong P. A Hybrid Crack Element for Rectilinear Anisotropic Material. Int J Numer Methods Eng 1977;11:377–403.

[22] Rhee J, Rowlands RE. Thermoelastic-Numerical Hybrid Analysis of Holes and Cracks in Composites. Exp Mech 1999;39:349–55.

[23] Dave JM, Sharma DS. Stress Field Around Rectangular Hole in Functionally Graded Plate. Int J Mech Sci 2018;136:360–70.

[24] Chauhan MM, Sharma DS. Stresses in Finite Anisotropic Plate Weakened by Rectangular Hole. Int J Mech Sci 2015;101–102:272–9.

[25] Dai M, Gao CF. Perturbation Solution of Two Arbitrarily-Shaped Holes in a Piezoelectric Solid. Int J Mech Sci 2014;88:37–45.

[26] Sharma DS. Stresses Around Polygonal Hole in an Infinite Laminated Composite Plate. Eur J Mech - ASolids 2015;54:44–52.

[27] Allam MNM, Zenkour AM, El-Mekawy HF. Stress Concentrations in a Viscoelastic Composite Plate Weakened by a Triangular Hole. Compos Struct 2007;79:1–11.

[28] Soutas-Little RW. Elasticity. Mineola, New York, USA: Dover Publication Inc.; 1998.

[29] Foust BE. Individuals Stress Determination in Inverse Problems by Combining Experimental Methods and Airy Stress Functions. MS Thesis. University of Wisconsin - Madison, 2003.

[30] Pan B, Qian K, Xie H, Asundi A. Two-Dimensional Digital Image Correlation for In-Plane Displacement and Strain Measurement: A Review. Meas Sci Technol 2009;20:17.

[31] Dally JW, Riley WF. Experimental Stress Analysis. 3rd ed. New York: McGraw-Hill; 1991.

[32] Yang L, Wang Y, Lu R. Advanced Optical Methods for Whole Field Displacement and Strain Measurement. 2010 Int. Symp. Optomechatronic Technol., Toronto, Canada: 2010, p. 1–6.

[33] Xu ZH, Li XD, Sutton MA, Li N. Drift and Spatial Distortion Elimination in Atomic Force Microscopy Images by the Digital Image Correlation Technique. J Strain Anal Eng Des 2008;43:729–43.

[34] Jin H, Lu WY, Korellis J. Micro-Scale Deformation Measurement using the Digital Image Correlation Technique and Scanning Electron Microscope Imaging. J Strain Anal Eng Des 2008;43:719–28.

[35] Backman D, Liao M, Crichlow L, Yanishevsky M, Patterson EA. The Use of Digital Image Correlation in a Parametric Study on the Effect of Edge Distance and Thickness on Residual Strains After Hole Cold Expansion. J Strain Anal Eng Des 2008;43:781–9.

[36] Reu PL, Miller TJ. The Application of High-Speed Digital Image Correlation. J Strain Anal Eng Des 2008;43:673–88.

[37] Jerabek M, Major Z, Lang RW. Strain Determination of Polymeric Materials using Digital Image Correlation. Polym Test 2010;29:407–16.

[38] McCormick N, Lord J. Digital Image Correlation. Mater Today 2010;13:52–4.

[39] Du Y, Díaz FA, Burguete RL, Patterson EA. Evaluation using Digital Image Correlation of Stress Intensity Factors in an Aerospace Panel. Exp Mech 2011;51:45–57.

[40] Zhou X, Chen HB, Chen J, Chen SB, Feng Z. High Temperature Full-Field Strain Measurement Based on Digital Image Correlation During Arc Welding. 2016 IEEE Workshop Adv. Robot. Its Soc. Impacts ARSO, Shangai: 2016, p. 203–7.

[41] Agarwal G, Gao H, Amirthalingam M, Hermans MJM. In Situ Strain Investigation During Laser Welding using Digital Image Correlation and Finite-Element-Based Numerical Simulation. Sci Technol Weld Join 2018;23:134–9.

[42] Peters WH, Ranson WF. Digital Imaging Techniques in Experimental Stress Analysis. Opt Eng 1982;21:213427.

[43] Sutton MA, Wolters WJ, Peters WH, Ranson WF, McNeill SR. Determination of Displacements using an Improved Digital Correlation Method. Image Vis Comput 1983;1:133–9.

[44] Bruck HA, McNeill SR, Sutton MA, Peters WH. Digital Image Correlation using Newton-Raphson Method of Partial Differential Correction. Exp Mech 1989;29:261–7.

[45] Chen J, Zhang X, Zhan N, Hu X. Deformation Measurement Across Crack using Two-Step Extended Digital Image Correlation Method. Opt Lasers Eng 2010;48:1126–31.

[46] Davis CQ, Freeman DM. Statistics of Subpixel Registration Algorithms Based on Spatiotemporal Gradients or Block Matching. Opt Eng 1998;37:37–9.

[47] Jin GC, Yao XF, Bao NK. Applications of Speckle Metrology to Vibration and Deformation Measurements of Electronic Devices. ITHERM 2000 Seventh Intersoc. Conf. Therm. Thermomechanical Phenom. Electron. Syst., vol. 2, Las Vegas, NV, USA: 2000, p. 253–5.

[48] Pan B, Asundi A, Xie H, Gao J. Digital Image Correlation using Iterative Least Squares and Pointwise Least Squares for Displacement Field and Strain Field Measurements. Opt Lasers Eng 2009;47:865–74.

[49] Pan B. Reliability-Guided Digital Image Correlation for Image Deformation Measurement. Appl Opt 2009;48:1535–42.

[50] Pan B, Li K. A Fast Digital Image Correlation Method for Deformation Measurement. Opt Lasers Eng 2011;49:841–7.

[51] Pan B, Li K, Tong W. Fast, Robust and Accurate Digital Image Correlation Calculation without Redundant Computations. Exp Mech 2013;53:1277.

[52] Zhang J, Sweedy A, Gitzhofer F, Baroud G. A Novel Method for Repeatedly Generating Speckle Patterns used in Digital Image Correlation. Opt Lasers Eng 2018;100:259–66.

[53] Niu Y, Shao S, Park SB, Kao CL. A Novel Speckle-Free Digital Image Correlation Method for In Situ Warpage Characterization. IEEE Trans Compon Packag Manuf Technol 2017;7:276–84.

[54] Pan B, Xie H, Wang Z, Qian K, Wang Z. Study on Subset Size Selection in Digital Image Correlation for Speckle Patterns. Opt Express 2008;16:7037–48.

[55] Correlated Solutions n.d. http://www.correlatedsolutions.com/ (accessed April 21, 2016).

[56] Yaofeng S, Pang JHL. Study of Optimal Subset Size in Digital Image Correlation of Speckle Pattern Images. Opt Lasers Eng 2007;45:967–74.

[57] Wang ZY, Li HQ, Tong JW, Ruan JT. Statistical Analysis of the Effect of Intensity Pattern Noise on the Displacement Measurement Precision of Digital Image Correlation using Self-Correlated Images. Exp Mech 2007;47:701–7.

[58] Mudassar AA, Butt S. Improved Digital Image Correlation Method. Opt Lasers Eng 2016;87:156–67.

[59] Greene RJ, Patterson EA, Rowlands RE. Thermoelastic Stress Analysis. In: Sharpe WN, editor. Springer Handb. Exp. Solid Mech., Boston, MA: Springer; 2008, p. 743–68.

[60] Thomson (Lord Kelvin) W. On Dynamical Theory of Heat Transfer. R. Soc. Edinburg, vol. 20, Edinburgh, Scotland: 1953, p. 261–83.

[61] Compton KT, Webster DB. Temperature Changes Accompanying the Adiabatic Compression of Steel. vol. 5. Ithica, New York: Physical Review; 1915.

[62] Biot MA. Thermoelasticity and Irreversible Thermodynamics. Buffalo, NY, USA: Cornell Aeronautical Laboratory, Inc.; 1955.

[63] Belgen MH. Structural Stress Measurements with an Infrared Radiometer. Instrum Syst Autom Soc 1967;6:49–53.

[64] Mountain DS, Webber JMB. Stress Pattern Analysis by Thermal Emission (SPATE). 4th Eur. Electro-Opt. Conf, vol. 0164, Utrecht, Netherlands: 1979, p. 189–96.

[65] Darken LS, Gurry RW. Physical Chemistry of Metals. New York: McGraw-Hill; 1953.

[66] Salerno A, Costa A, Fantoni G. Calibration of the Thermoelastic Constants for Quantitative Thermoelastic Stress Analysis on Composites. Rev Sci Instrum 2009;80.

[67] Pilkey WD, Pilkey DF. Peterson's Stress Concentration Factors. 3rd ed. New York: Wiley; 2008.

[68] Rowlands RE, Daniel IM, Whiteside JB. Stress and Failure Analysis of a Glass-Epoxy Composite Plate with a Circular Hole. Exp Mech 1973;13:31–7.

[69] Whiteside JB, Daniel IM, Rowlands RE. The Behavior of Advanced Filamentary Composite Plates with Cutouts. Grumman Aerospace Corp Bethpage NY, USA: Defense Technical Information Center; 1973.

[70] Rhee J, He S, Rowlands RE. Hybrid Moiré-Numerical Stress Analysis Around Cutouts in Loaded Composites. Exp Mech 1996;36:379–87.

[71] Baek TH, Rowlands RE. Hybrid Stress Analysis of Perforated Composites using Strain Gages. Exp Mech 2001;41:195–203.

[72] Baek TH, Rowlands RE. Experimental Determination of Stress Concentrations in Orthotropic Composites. J Strain Anal Eng Des 1999;34:69–81.

[73] Baek TH, Chung TJ, Panganiban H. Full-Field Stress Determination Around Circular Discontinuity in a Tensile-Loaded Plate using x-Displacements only. J Solid Mech Mater Eng 2008;2:756–62.

[74] Khaja AA. Experimentally Determined Full-Field Stress, Strain and Displacement Analyses of Perforated Finite Members. PhD Thesis. University of Wisconsin - Madison, 2012.

[75] Rhee J, Rowlands RE. Stresses Around Extremely Large or Interacting Multiple Holes in Orthotropic Composites. Comput Struct 1996;61:935–50.

[76] Chen HC. Stress Analysis of Laminates with Holes by Special Finite Element. Compos Struct 1995;31:99–106.

[77] Lin ST, Feng Z, Rowlands RE. Thermoelastic Determination of Stress Intensity Factors in Orthotropic Composites using the *J*-Integral. Eng Fract Mech 1997;56:579–92.

[78] Emery TR, Dulieu-Barton JM. Thermoelastic Stress Analysis of Damage Mechanisms in Composite Materials. Compos Part Appl Sci Manuf 2010;41:1729–42.

[79] Lagattu F, Brillaud J, Lafarie-Frenot MC. High Strain Gradient Measurements by using Digital Image Correlation Technique. Mater Charact 2004;53:17–28.

[80] Caminero MA, Lopez-Pedrosa M, Pinna C, Soutis C. Damage Monitoring and Analysis of Composite Laminates with an Open Hole and Adhesively Bonded Repairs using Digital Image Correlation. Compos Part B Eng 2013;53:76–91.

[81] Laurin F, Charrier JS, Lévêque D, Maire JF, Mavel A, Nuñez P. Determination of the Properties of Composite Materials Thanks to Digital Image Correlation Measurements. IUTAM Symp Full-Field Meas Identif Solid Mech 2012;4:106–15.

[82] Vishay Precision Group - Micro-Measurements - Home Page n.d. http://www.vishaypg.com/micro-measurements/ (accessed October 5, 2018).

[83] Samad WA. Hybrid Full-Field Stress Analysis of Structures Containing Irregularly-Shaped Cutouts. PhD Thesis. University of Wisconsin - Madison, 2013.

[84] Fatima NS. Stress Analysis of a Circularly-Perforated Finite Orthotropic Composite Plate. J Mech Eng Autom 2017;7:209–20.

[85] Samad WA, Rowlands RE. Nondestructive Full-Field Stress Analysis of a Finite Structure Containing an Elliptical Hole using Digital Image Correlation. Int. Symp. Exp. Mech. ISEM, vol. 12, Taipei, Taiwan: 2012, p. 8–11.

[86] Lin CC, Ko CC. Stress and Strength Analysis of Finite Composite Laminates with Elliptical Holes. J Compos Mater 1988;22:373–85.

[87] Xu X, Sun L, Fan X. Stress Concentration of Finite Composite Laminates with Elliptical Hole. Comput Struct 1995;57:29–34.

[88] Alshaya A, Shuai X, Rowlands RE. Stress Analysis of a Finite Orthotropic Plate Containing an Elliptical Hole from Recorded Temperature Data. In: Quinn S, Balandraud X, editors. Residual Stress Thermomechanics Infrared Imaging Hybrid Tech. Inverse Probl. Vol. 9 Proc. 2016 Annu. Conf. Exp. Appl. Mech., Cham: Springer International Publishing; 2017, p. 47–56.

[89] Zakharov DD, Becker W. Boundary Value Problems for Unsymmetric Laminates, Occupying a Region with Elliptic Contour. Compos Struct 2000;49:275–84.

[90] Madenci E, Barut A, Nemeth MP. A Complex Potential-Variational Method for Stress Analysis of Unsymmetric Laminates with an Elliptical Cutout. J Appl Mech 2001;68:731–9.

[91] Tan SC. Finite-Width Correction Factors for Anisotropic Plate Containing a Central Opening. J Compos Mater 1988;22:1080–97.

[92] Tan SC. Laminated Composites Containing an Elliptical Opening. I. Approximate Stress Analyses and Fracture Models. J Compos Mater 1987;21:925–48.

[93] Bao G, Ho S, Suo Z, Fan B. The Role of Material Orthotropy in Fracture Specimens for Composites. Int J Solids Struct 1992;29:1105–16.

[94] Durelli AJ, Parks VJ, Feng HC. Stresses Around an Elliptical Hole in a Finite Plate Subjected to Axial Loading. J Appl Mech 1966;33:192–5.

[95] Daniel IM, Ishai O. Engineering Mechanics of Composite Materials. vol. 3. 2nd ed. Oxford University Press; 2005.

[96] Lin SJ, Quinn S, Matthys DR, New AM, Kincaid IM, Boyce BR, et al. Thermoelastic Determination of Individual Stresses in Vicinity of a Near-Edge Hole Beneath a Concentrated Load. Exp Mech 2011;51:797–814.

[97] Wang WC, Chen YM, Lin MS, Wu CP. Investigation of the Stress Field of a Near-Surface Circular Hole. Exp Mech 2005;45:244–9.

[98] Lin SJ, Matthys DR, Rowlands RE. Separating Stresses Thermoelastically in a Central Circularly Perforated Plate using an Airy Stress Function. Strain 2009;45:516–26.

[99] Ryall TG, Heller M, Jones R. Determination of Stress Components from Thermoelastic Data without Boundary Conditions. J Appl Mech 1992;59:841–7.

[100] Lin SJ, Matthys DR, Quinn S, Davidson JP, Boyce BR, Khaja AA, et al. Stresses at and in the Neighborhood of a Near-Edge Hole in a Plate Subjected to an Offset Load from Measured Temperatures. Eur J Mech - ASolids 2013;39:209–17.

[101] Philip SK. Stress Analysis of a Finite Structure Containing an Asymmetrical, Arbitrarily-Shaped Cutout Based on Recorded Temperature Data. MS Thesis. University of Wisconsin - Madison, 2015.

[102] Paneerselvam S, Samad WA, Venkatesh R, Song KW, El-Hajjar RF, Rowlands RE. Displacement-Based Experimental Stress Analysis of a Circularly-Perforated Asymmetrical Isotropic Structure. Exp Mech 2017;57:129–42.

[103] McKelvie J. Consideration of The Surface Temperature Response to Cyclic Thermoelastic Heat Generation. Proc SPIE, vol. 731, 1987, p. 44–55.

[104] Mackenzie AK. Effects of Surface Coatings on Infra-Red Measurements of Thermoelastic Responses. Stress Vib. Recent Dev. Ind. Meas. Anal., vol. 1084, London, UK: 1989, p. 59–71.

[105] Quinn S, Dulieu-Barton J. Identification of the Sources of Non-Adiabatic Behaviour for Practical Thermoelastic Stress Analysis. J Strain Anal Eng Des 2002;37:59–71.

[106] Joglekar NS. Separating Stresses using Airy's Stress Function and TSA, Effects of Varying the Amount and Source Locations of the Input Measured TSA Data and the Number of Airy Coefficients to Use. MS Thesis. University of Wisconsin - Madison, 2009.

[107] Offermann S, Beaudoin JL, Bissieux C, Frick H. Thermoelastic Stress Analysis Under Nonadiabatic Conditions. Exp Mech 1997;37:409–13.

[108] Salerno A, Desiderati S. Procedure Proposal for the Correction of Nonadiabatic Thermoelastic Stress Analysis Results. Rev Sci Instrum 2004;75:507–14.

[109] Gallotti A, Salerno A. Automatic Procedure for the Correction of Thermoelastic Stress Analysis Data Acquired in Nonadiabatic Conditions. Rev Sci Instrum 2005;76:124903.

[110] Gallotti A, Salerno A, Desiderati S, Fantoni G. Thermoelastic Investigation of an Aluminium Helicopter Component Under Non-Adiabatic Conditions. Fatigue Fract Eng Mater Struct 2008;31:405–13.

[111] Timoshenko S, Goodier JN. Theory of Elasticity. Auckland, London: McGraw-Hill; 1951.

[112] Serati M, Alehossein H, Williams DJ. Elastic Stress Analysis of Partially Loaded Hollow Discs. Int J Eng Sci 2012;53:19–37.

[113] Boone TJ, Wawrzynek PA, Ingraffea AR. Finite Element Modelling of Fracture Propagation in Orthotropic Materials. Eng Fract Mech 1987;26:185–201.

[114] Bueckner HF. Novel Principle for the Computation of Stress Intensity Factors. Z Fuer Angew Math Mech 1970;50:529–46.

[115] Rice JR. Some Remarks on Elastic Crack-Tip Stress Fields. Int J Solids Struct 1972;8:751–8.

[116] Tamayo DR, Montoya A, Millwater H. A Virtual Crack Extension Method for Thermoelastic Fracture using a Complex-Variable Finite Element Method. Eng Fract Mech 2018;192:328–42.

[117] Chakraborty D, Murthy KSRK. Experimental Determination of Mode I Stress Intensity Factor in Orthotropic Materials using a Single Strain Gage. Eng Fract Mech 2017;173:130–45.

[118] Khalil SA, Sun CT, Hwang WC. Application of a Hybrid Finite Element Method to Determine Stress Intensity Factors in Unidirectional Composites. Int J Fract 1986;31:37–51.

[119] Barsoum RS. On the Use of Isoparametric Finite Elements in Linear Fracture Mechanics. Int J Numer Methods Eng 1976;10:25–37.

[120] Henshell RD, Shaw KG. Crack Tip Finite Elements are Unnecessary. Int J Numer Methods Eng 1975;9:495–507.

[121] Nejati M, Paluszny A, Zimmerman RW. A Disk-Shaped Domain Integral Method for the Computation of Stress Intensity Factors using Tetrahedral Meshes. Int J Solids Struct 2015;69–70:230–51.

[122] Sih GC, Paris PC, Irwin GR. On Cracks in Rectilinearly Anisotropic Bodies. Int J Fract Mech 1965;1:189–203.

[123] Bowie OL, Neal DM. A Modified Mapping-Collocation Technique for Accurate Calculation of Stress Intensity Factors. Int J Fract Mech 1970;6:199–206.

[124] Bowie OL, Freese CE, Neal DM. Solution of Plane Problems of Elasticity Utilizing Partitioning Concepts. J Appl Mech 1973;40:767–72.

[125] Bowie OL. Rectangular Tensile Sheet with Symmetric Edge Cracks. J Appl Mech 1964;31:208–12.

[126] Meyerson MD. Conformal Mapping and Fracture Mechanics. Eng Fract Mech 1992;41:951–3.

[127] Li JL, Cheng HX. An Application of Conformal Mapping to Fracture Analysis of Composite Plate with Curved Crack. Appl Mech Mater 2012;121–126:1759–63.

[128] Tong P, Pian THH, Lasry SJ. A Hybrid-Element Approach to Crack Problems in Plane Elasticity. Int J Numer Methods Eng 1973;7:297–308.

[129] Joshi S, Manepatil S. Stress Intensity Factors for an Inclined and/or Eccentric Crack in a Finite Orthotropic Lamina. Lat Am J Solids Struct 2014;11:1886–905.

[130] Mandell JF, Mcgarry FJ, Wang SS, Im J. Stress Intensity Factors for Anisotropic Fracture Test Specimens of Several Geometries. J Compos Mater 1974;8:106–16.

[131] Saxce GD, Kang CH. Application of the Hybrid Mongrel Displacement Finite Method to the Computation of Stress Intensity Factors in Anisotropic Material. Eng Fract Mech 1992;41:71–83.

[132] Abdullah AM. Comparison the Values of Stresses for the Mode I Stress Intensity Factor for a Double Edge Cracked Tension (Isotropic & Orthotropic) Plates. AL Rafdain Eng J 2013;21:14–28.

[133] Arakere NK, Knudsen EC, Wells D, McGill P, Swanson GR. Determination of Mixed-Mode Stress Intensity Factors, Fracture Toughness, and Crack Turning Angle for Anisotropic Foam Material. Int J Solids Struct 2008;45:4936–51.

[134] Feng Z, Sanford RJ, Rowlands RE. Determining Stress Intensity Factors from Smoothing Finite-Element Representation of Photomechanical Data. Eng Fract Mech 1991;40:593–601.

[135] Feng Z, Rowlands RE, Sanford RJ. Stress Intensity Determination by an Experimental-Numerical Hybrid Technique. J Strain Anal Eng Des 1991;26:243–51.

[136] He KY, Rowlands RE. Determining Stress Intensity Factors in Orthotropic Composites from Far-Field Measured Temperatures. Exp Mech 2004;44:555–61.

[137] Ju SH, Rowlands RE. Thermoelastic Determination of K_I and K_{II} in an Orthotropic Graphite-Epoxy Composite. J Compos Mater 2003;37:2011–25.

[138] Ju SH, Rowlands RE. Mixed-Mode Thermoelastic Fracture Analysis of Orthotropic Composites. Int J Fract 2013;120:601–21.

[139] Ju SH. Simulating Stress Intensity Factors for Anisotropic Materials by the Least-Squares Method. Int J Fract 1996;81:283–97.

[140] Ju SH, Rowlands RE. Thermoelastic Determination of Crack-Tip Coordinates in Composites. Int J Solids Struct 2007;44:4845–59.

[141] Baek TH, Chen L, Hong DP. Hybrid Determination of Mixed-Mode Stress Intensity Factors on Discontinuous Finite-Width Plate by Finite Element and Photoelasticity. J Mech Sci Technol 2011;25:2535–43.

[142] Farahani BV, Tavares PJ, Moreira PMGP. SIF Determination with Thermoelastic Stress Analysis. Procedia Struct Integr 2016;2:2148–55.

[143] Liu C, Rosakis AJ, Ellis RW, Stout MG. A Study of the Fracture Behavior of Unidirectional Fiber- Reinforced Composite using Coherent Gradient Sensing (CGS) Interferometry. Int J Fract 1998;90:355–82.

[144] Periasamy C, Tippur HV. Measurement of Crack-Tip and Punch-Tip Transient Deformations and Stress Intensity Factors using Digital Gradient Sensing Technique. Eng Fract Mech 2013;98:185–99.

[145] Dai JJ, Liang XD, Yao XF, Yeh HY. Study of Cracked Unidirectional Glass Fiber-reinforced Composites by Digital Speckle Correlation Method. J Reinf Plast Compos 2005;24:1737–46.

[146] Kim JW. A Contour Integral Computation of Stress Intensity Factors in the Cracked Orthotropic Elastic Plates. Eng Fract Mech 1985;21:353–64.

[147] Perry KE, Mckelvie J. Measurement of Energy Release Rates for Delaminations in Composite Materials. Exp Mech 1996;36:55–63.

[148] Kawahara WA, Brandon SL. *J*-Integral Evaluation by Resistance Strain Gauges. Eng Fract Mech 1983;18:427–34.

[149] Frediani A. Experimental Measurement of the *J*-Integral. Eng Fract Mech 1984;19:1105–37.

[150] Rice JR. A Path Independent Integral and the Approximate Analysis of Strain Concentration by Notches and Cracks. J Appl Mech 1968;35:379–86.

[151] Vavrik D, Jandejsek I. Experimental Evaluation of Contour *J* Integral and Energy Dissipated in the Fracture Process Zone. Eng Fract Mech 2014;129:14–25.

[152] Valaire BT, Yong YW, Suhling J, Jang BZ, Zhang SQ. Application of the *J*-Integral to Mixed Mode Fracture Analysis of Orthotropic Composites. Eng Fract Mech 1990;36:507–14.

[153] Hein J, Kuna M. 3D *J*-Integral for Functionally Graded and Temperature Dependent Thermoelastic Materials. PROSTR Procedia Struct Integr 21st Eur Conf Fract ECF21 20-24 June 2016 Catania Italy 2016;2:2246–54.

[154] Rabbolini S, Pataky GJ, Sehitoglu H, Beretta S. Anisotropic Stress Intensity Factor Ranges Measurements with DIC. MSPRO Procedia Mater Sci 20th Eur Conf Fract 2014;3:2104–10.

[155] Dag S, Yildirim B, Topal S. Computational Methods for Inclined Cracks in Orthotropic Functionally Graded Materials under Thermal Stresses. J Therm Stress 2013;36:1001–26.

[156] Dag S. Thermal Fracture Analysis of Orthotropic Functionally Graded Materials using an Equivalent Domain Integral Approach. Eng Fract Mech 2006;73:2802–28.

[157] Lee D, Tippur H, Bogert P. Quasi-Static and Dynamic Fracture of Graphite/Epoxy Composites: An Optical Study of Loading-Rate Effects. Compos Part B Eng 2010;41:462–74.

[158] Stroh AN. Dislocations and Cracks in Anisotropic Elasticity. Philos Mag Jounal Theor Exp Appl Phys 1958;3:625–46.

[159] Tracy J, Waas A, Daly S. Experimental Assessment of Toughness in Ceramic Matrix Composites using the *J*-Integral with Digital Image Correlation Part I: Methodology and Validation. J Mater Sci 2015;50:4646–58.

[160] Cahill LM, Natarajan S, Bordas SPA, O'Higgins R, McHugh P, Mccarthy CT. Experimental-Numerical Determination of the Fracture Toughness of a Unidirectional Composite Material using DIC and a *J*-Integral Approach. IWCMM Int. Workshop Comput. Mech. Mater., Ireland: 2011.

[161] Catalanotti G, Camanho PP, Xavier J, Dávila CG, Marques AT. Measurement of Resistance Curves in the Longitudinal Failure of Composites using Digital Image Correlation. Compos Sci Technol 2010;70:1986–93.

[162] Gonzáles GLG, Gonzáles JAO, Castro JTP, Freire JLF. A *J*-Integral Approach using Digital Image Correlation for Evaluating Stress Intensity Factors in Fatigue Cracks with Closure Effects. Theor Appl Fract Mech 2017;90:14–21.

[163] Hedan S, Valle V, Cottron M. Calculation of *J*-integrals using experimental and numerical data: Influences of ratio (a/W) and the 3D structure. Eng Fract Mech 2011;78:1976–85.

[164] Pataky GJ, Sangid MD, Sehitoglu H, Hamilton RF, Maier HJ, Sofronis P. Full Field Measurements of Anisotropic Stress Intensity Factor Ranges in Fatigue. Eng Fract Mech 2012;94:13–28.

[165] Samarasinghe S, Kulasiri D. Stress Intensity Factor of Wood from Crack-Tip Displacement Fields Obtained from Digital Image Processing. Silva Fenn 2004;38:267–78.

[166] Meite M, Dubois F, Pop O, Absi J. Mixed Mode Fracture Properties Characterization for Wood by Digital Images Correlation and Finite Element Method Coupling. Eng Fract Mech 2013;105:86–100.

[167] Nunes LCS, Reis JML. Estimation of Crack-Tip-Opening Displacement and Crack Extension of Glass Fiber Reinforced Polymer Mortars using Digital Image Correlation Method. Mater Des 2012;33:248–53.

[168] Koohbor B, Mallon S, Kidane A, Sutton MA. A DIC-Based Study of In-Plane Mechanical Response and Fracture of Orthotropic Carbon Fiber Reinforced Composite. Compos Part B Eng 2014;66:388–99.

[169] Mallon S, Koohbor B, Kidane A, Sutton MA. Fracture Behavior of Prestressed Composites Subjected to Shock Loading: A DIC-Based Study. Exp Mech 2015;55:211–25.

[170] Han Q, Wang L, Xu J. Experimental Research on Fracture Behaviors of Damaged CFRP Tendons: Fracture Mode and Failure Analysis. Constr Build Mater 2016;112:1013–24.

[171] Rhee J. Geometric Discontinuities in Orthotropic Composites. PhD Thesis. University of Wisconsin - Madison, 1995.

[172] Andersson H. Stress-Intensity Factors at the Tips of a Star-Shaped Contour in an Infinite Tensile Sheet. J Mech Phys Solids 1969;17:405–6.

[173] Liebowitz H, Sih GC. Mathematical Theories of Brittle Fracture. In: Liebowitz H, editor. Fracture, New York: Academic Press; 1968, p. 67–190.

[174] Irwin GR. Analytical Aspects of Crack Stress Field Problems. University of Illinois, Department of Theoretical and Applied Mechanics; 1962.

[175] Westergaard HMW. Bearing Pressures and Cracks. J Appl Mech 1939;6:49–53.

[176] Sanford RJ. A Critical Re-Examination of the Westergaard Method for Solving Opening-Mode Crack Problems. Mech Res Commun 1979;6:289–94.

[177] Suo Z, Hill R. Singularities, Interfaces and Cracks in Dissimilar Anisotropic Media. Proc R Soc Lond Ser Math Phys Sci 1990;427:331–58.

[178] Tada H, Paris PC, Irwin GR. The Stress Analysis of Cracks Handbook. 3rd Edition. St. Louis, MS, USA: Paris Productions and Del Research Corp.; 1985.

[179] Huang H, Kardomateas GA. Single-Edge and Double-Edge Cracks in a Fully Anisotropic Strip. J Eng Mater Technol 1999;121:422–9.

[180] Bažant ZP, Daniel IM, Li Z. Size Effect and Fracture Characteristics of Composite Laminates. J Eng Mater Technol 1996;118:317–24.

[181] Koronis G, Silva A, Fontul M. Green Composites: A Review of Adequate Materials for Automotive Applications. Compos Part B Eng 2013;44:120–7.

[182] Pickering KL, Efendy MGA, Le TM. A Review of Recent Developments in Natural Fibre Composites and Their Mechanical Performance. Compos Part Appl Sci Manuf Spec Issue Biocomposites 2016;83:98–112.

[183] Akampumuza O, Wambua PM, Ahmed A, Li W, Qin XH. Review of the Applications of Biocomposites in the Automotive Industry. Polym Compos 2017;38:2553–69.

[184] Ramakrishna S, Mayer J, Wintermantel E, Leong KW. Biomedical Applications of Polymer-Composite Materials: A Review. Compos Sci Technol 2001;61:1189–224.

[185] Cho SB, Lee KR, Choy YS, Yuuki R. Determination of Stress Intensity Factors and Boundary Element Analysis for Interface Cracks in Dissimilar Anisotropic Materials. Eng Fract Mech 1992;43:603–14.

[186] Latourte F, Chrysochoos A, Pagano S, Wattrisse B. Elastoplastic Behavior Identification for Heterogeneous Loadings and Materials. Exp Mech 2008;48:435–49.

[187] Hori M, Kameda T. Inversion of Stress from Strain without Full Knowledge of Constitutive Relations. J Mech Phys Solids 2001;49:1621–38.

[188] Patel NP, Sharma DS. On the Stress Concentration Around a Polygonal Cut-Out of Complex Geometry in an Infinite Orthotropic Plate. Compos Struct 2017;179:415–36.

[189] Kalayciogli B, Alshaya A, Rowlands RE. Experimental Stress Analysis of Unsymmetrical, Irregularly-Shaped Structure Containing an Arbitrarily-Shaped Hole. In: Baldi A, Considine J, Quinn S, Balandraud X, editors. Conf. Proc. Soc. Exp. Mech. Ser., vol. 8, Greese: Springer, Cham; 2018, p. 9–12.

[190] Jafari M. Thermal Stress Analysis of Orthotropic Plate Containing a Rectangular Hole using Complex Variable Method. Eur J Mech - ASolids 2019;73:212–23.

[191] Kim CH. Airy Stress Function for Describing the Non-Linear Effect of Simply Supported Plates with Movable Edges. Int J Non-Linear Mech 2010;45:395–408.

[192] Cutting Composites with Abrasive Waterjet Systems - Flow Waterjet n.d. https://www.flowwaterjet.com/Applications/Composites (accessed October 5, 2018).

[193] Composite Cutting with Abrasive Waterjet Composite Machines. n.d. https://www.kmtwaterjet.com/kmt-cutting-composites.aspx (accessed October 5, 2018).

[194] Kotousov A, Wang CH. Three-Dimensional Stress Constraint in an Elastic Plate with a Notch. Int J Solids Struct 2002;39:4311–26.

[195] Lim WK, Choi SY, Sankar BV. Biaxial Load Effects on Crack Extension in Anisotropic Solids. Eng Fract Mech 2001;68:403–16.